AMES

Supercomputing in Aerospace

*Proceedings of a symposium held at
NASA Ames Research Center
Moffett Field, California
March 10-12, 1987*

NASA

Supercomputing in Aerospace

NASA

National Aeronautics and
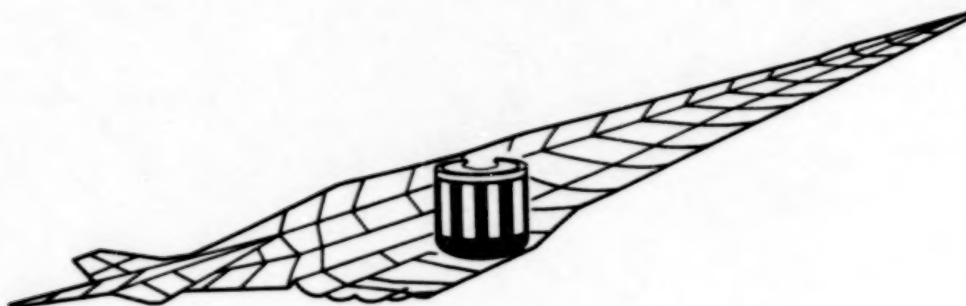Space Administration

**Scientific and Technical
Information Branch**

1987

CONFERENCE COMMITTEE

General Chairperson ....Paul Kutler

Accommodations and Food
   and Beverage......................Sonja S. Glenn

Budget.............................Karl S. Talarico

Communications...................Marshal L. Merriam

Graphics Display..................Velvin R. Watson

NAS Tutorial Committee.............Leslie J. Chow
                                     Lynda L. Haines

Publications...........................Helen C. Yee

Publicity...........................Anthony R. Gross

Security and Transportation.........John R. Viegas

Tours.............................Sanford S. Davis

Conference Secretary.................Betty Beyerly

PREFACE

This volume is a collection of papers presented at the NASA Conference on Supercomputing in Aerospace, March 10-12 1987, at the NASA Ames Research Center, Moffett Field, California. The conference was held to commemorate the opening of the Numerical Aerodynamic Simulation (NAS) Facility, which became officially operational in the first part of 1987. The theme for the 3-day technical meeting was "Computational Aerophysics and the NAS System--Essential Elements of the U.S. Aerospace Program." The conference consisted of invited speakers from industry, government, and academia, and was sponsored by the Fluid Dynamics Division at NASA Ames.

The conference consisted of four sessions: 1) NAS History and NASA Computational Programs, 2) Future Computing Prospects, 3) Design Applications, and 4) Fluid Dynamics. In the first session papers were presented that discussed the history of the NAS project, its advocacy, current status, and future plans. In the second session, two computer manufacturers presented their outlook for the future of supercomputer development within their organizations. Session 3 consisted of invited talks from users of computational fluid dynamics (CFD) technology with real-world applications. Session 4 was composed of talks that centered around the development and use of CFD for understanding fluid physics. In addition, several talks on other computationally demanding disciplines were presented.

The conference concluded with a NAS Tutorial. In it information on the NAS system was presented, including proposing projects for NAS use, administrative and operational procedures for accepted projects, code experiments on NAS Cray 2, long-haul communications, and user support services.

TABLE OF CONTENTS

Session 3--Design Applications II

Session 4--Fluid Dynamics I

Session 5--Fluid Dynamics II

N87
25999
UNCLAS

HISTORY OF THE NUMERICAL AERODYNAMIC SIMULATION PROGRAM

Victor L. Peterson and William F. Ballhaus, Jr.
NASA Ames Research Center

ABSTRACT

NASA's Numerical Aerodynamic Simulation (NAS) program has reached a milestone with the completion of the initial operating configuration of the NAS Processing System Network. This achievement is the first major milestone in the continuing effort to provide a state-of-the-art supercomputer facility for the national aerospace community and to serve as a pathfinder for the development and use of future supercomputer systems. The underlying factors that motivated the initiation of the program are first identified and then discussed. These include the emergence and evolution of computational aerodynamics as a powerful new capability in aerodynamics research and development, the computer power required for advances in the discipline, the complementary nature of computation and wind tunnel testing, and the need for the government to play a pathfinding role in the development and use of large-scale scientific computing systems. Finally, the history of the NAS program is traced from its inception in 1975 to the present time.

INTRODUCTION

The Numerical Aerodynamic Simulation (NAS) program is an outgrowth of the discipline of computational fluid dynamics. However, the NAS system is now recognized to be an important facility for advancing all of the computationally intensive aerospace disciplines and for serving in a pathfinder role for the development and use of future supercomputer systems. In fact, the NAS Program began to influence both discipline-oriented users and developers of supercomputers even before the system was first assembled. The NAS has drawn national attention to the importance of scientific computers to the country's technology base and has served as a focal point for the large-scale scientific computing community.

The NAS program will provide a leading edge computational capability to the national aerospace community. It will stimulate improvements to the entire computational process ranging from problem formulation to publication of results. The program has been structured to focus on the development of a complete computer system that can be upgraded periodically with minimum impact on the user and on the ever increasing inventory of applications software. The NAS system, in its initial operating configuration, is already serving over 200 users nationwide at over 20 remote

locations. These numbers will continue to increase as the system matures to its extended operating configuration including two powerful supercomputers, all of the necessary supporting equipment, and well established communications links.

The objectives of this paper are twofold: 1) to identify the factors that led to the initiation of the NAS Program, and 2) to review the evolution of the NAS Program from its inception in 1975 to the present time. Included in the discussion are brief reviews of the evolution of computational aerodynamics, computer requirements for future advances, the complementary roles of computation and experiment, and the historical role of the government in the development and use of large-scale scientific computing systems.

FACTORS MOTIVATING THE NAS PROGRAM

The underlying motivations for the NAS program are a composite of four principal factors: 1) the emergence and evolution of computational aerodynamics as a powerful new capability in aerodynamics research and development; 2) the demands that this relatively new discipline places on computer systems; 3) the use of computation as a complement to wind-tunnel testing; and 4) the long standing, recognized need for the government to play a pathfinding role in the development and use of large-scale scientific computing systems. Each of these factors will be briefly discussed prior to describing the evolution of the program.

Emergence and Evolution of Computational Aerodynamics

Electronic computers were used to assist with aerodynamic analyses ever since they became available to the aeronautical researchers in the 1950s. Prior to 1970, aerodynamic analyses were limited primarily to the solution of the linearized inviscid flow equations and to the equations governing the behavior of the viscous boundary layer adjacent to an aerodynamic surface. Computers of the IBM-360 and CDC-6600 class permitted these equations to be solved for the flows about idealized complete aircraft configurations, but only for situations where the flows were everywhere either subsonic or moderately supersonic and everywhere attached to the surfaces over which they passed. Some attempts were made to include the nonlinear terms in the inviscid flow equations and solve for transonic flows about airfoils, but

these were limited to the very restrictive situations of either nonlifting airfoils or airfoils with detached bow shock waves.

The year 1970 marked the beginning of a series of advances in computational aerodynamics that would not have been possible without computers. The first major advance in solving for the nonlinear transonic flows about practical lifting airfoils with embedded shock waves was reported in the literature by Magnus and Yoshihary (1970). Subsequent milestones in the development of the technology for treating the nonlinear inviscid equations, and enabled only by the computer, are shown in figure 1. By about 1973, solutions for wing-body combinations treated with the steady-flow, small-disturbance equations were being published. Results of the first treatment of unsteady flows about airfoils appeared in the literature by Ballhaus, Jr., et al. (1975), and the first flutter analysis for a swept wing was published about 6 yr ago by Borland and Rizzetta (1981). Research on the aeroelastic behavior of wings is still limited by the performance of currently available computers to the treatment of the equations governing inviscid flows. These equations, with corrections for boundary-layer effects, are still used extensively for a wide range of aerodynamic problems. However, the really important problems facing the designers today require the use of the Reynolds-averaged, Navier-Stokes equations, both with and without the inclusion of the additional equations governing real-gas chemistry.

Milestones in the use of the Reynolds-averaged, Navier-Stokes equations for treating compressible viscous flows are shown in figure 2. These equations account for most of the physics of interest in fluid-dynamic flows. The process of time-averaging the Navier-Stokes equations over a time interval that is long relative to turbulent eddy fluctuations, yet small relative to macroscopic flow changes, introduces new terms representing the time-averaged transport of momentum and energy, which must be modeled using empirical information. Very powerful computers are required for simulations with this level of approximation, but the potential advantages over the inviscid equations are enormous. Realistic simulations of separated flows and of unsteady viscous flows, such as buffeting, will become commonplace as the ability to model the turbulence terms matures. Combined with computer-optimization methods, these simulations should make it possible to develop designs optimized for various missions while adhering to practical constraints such as available engine power and sufficient fuel volume to meet range requirements. Landmark advances include the investigation of a shock-wave interaction with a laminar boundary layer reported by MacCormack (1971), the treatment of high-Reynolds-number transonic airfoil flows by Deiwert (1974), the first turbulent flow over a lifting wing by Mansour (1984), and the first turbulent flow over a realistic fighter

configuration at angle of attack by Flores et al. (1987). Relatively large amounts of computer time are still required for the application of these equations to practical problems, but advances in technology continue to improve computational efficiency.

Figure 3 displays a perspective on the effect that increasing computer power has had on computational aerodynamics in a practical engineering sense. Presently available machines are adequate for calculating the flows about relatively complex configurations with the inviscid-flow equations. However, the type of information derived from the computations is limited (e.g., no total drag and no effects of flow separation). The viscous-flow equations, being more complex and requiring finer computational meshes, demand substantially greater computational power to solve. Thus, the types of problems that can be solved with a given computer are necessarily less complex. In effect, a designer has to make the choice between treating simple configurations with complex physics or treating complex configurations with simple physics. Yet, in both inviscid- and viscous-flow situations, each new generation of computers has resulted in advances in the value of computational aerodynamics as a design tool. The discipline will begin to mature when both complex configurations and complex physics can be treated simultaneously with a reasonable amount of computer time.

Computer Requirements

Computer requirements for computational aerodynamics can be related to the four major levels of approximation to the Navier-Stokes equations that were identified in the work by Chapman (1979). Each level of approximation resolves the underlying physics to a different degree, provides a different level of understanding, and requires a different level of computer capability. Table 1 and the works of Chapman (1979) and Peterson (1984) discuss in some depth these approximations, their capabilities to solve problems associated with aircraft aerodynamics, and the computer requirements to solve them in a reasonable amount of time (about 15 min) for flows about relatively complete aircraft configurations. Computer requirements are expressed in terms of the power of a Class VI machine, which is defined here to have a processing speed of 30 million floating-point operations per second (MFLOPS) and a memory of about 8 million words. Machines of this class are widely available at the present time. Computer requirements increase with each higher level of approximation, both because more flow variables are involved and because either more panels or more grid points are required to resolve the flows to a level of detail that is commensurate with the physics embodied in the approximation. Experience indicates that the Reynolds-averaged form of the Navier-Stokes equations probably will be adequate for most design-oriented problems. The effects of all scales of turbulence are modeled in this level

2

of approximation; the development of appropriate turbulence models is the subject of current research by both computational and experimental fluid dynamicists. In fact, the experimentalists are being guided, to a large extent, by computational research programs which are based either on the large-eddy simulation approximation or on the use of the full Navier-Stokes equations for simple flow geometries.

Speed and memory requirements for computing the aerodyamic behavior of shapes of varying complexities are compared with several existing and planned computers in figure 4 . Computers large enough to provide solutions in 15 min or less to the Reynolds-averaged, Navier-Stokes equations for the flow about a complete aircraft are expected to be available before the end of this decade. This advance should mark the time when computers will not be just a supplement to the aircraft design process, but will be an absolute necessity to be competitive in meeting economic and performance requirements. Computers having even more power will be required in the future, however, to treat routine problems involving real-gas chemistry, the coupling of the disciplines of aerodynamics, structures, propulsion and controls, and the optimization of a complete aircraft design.

Complementary Nature of Computation and Experiment

In the early 1970s, computations were recognized by a few visionaries to have the potential for becoming an effective complement to fluid- and aero-dynamic experiments for a number of reasons. First, the physics of fluid flows could be represented by mathematical equations, and computers, beginning with the IBM 360 and the CDC 6600 machines, were becoming sufficiently powerful to solve meaningful approximating sets of these equations in a practical amount of time and at reasonable cost.

Second, wind tunnel costs and computational costs were recognized to be changing in importantly different ways. Increased complexity and broadened performance envelopes of aircraft caused the number of wind tunnel hours expended in the development of new aircraft to increase exponentially with time. In fact, this increase amounts to as much as a factor of about 1,000 over an 80 yr period (50 hr for the Wright Flyer compared to 50,000 hr for the Space Shuttle). Concurrently, the cost per hour of testing also increased by a factor of about 1,000 over the same period. Thus, wind tunnel testing costs escalated by nearly a million fold in 80 yr, while the cost of numerically simulating a given flow is shown by the data in figure 5 to have decreased by a factor of 100,000 in just 15 yr during the period from 1969 to 1984. This decrease was due to improvements in both computers and algorithms.

Third, on the one hand, all wind tunnels are known to have all or some of the fundamental limitations such as model size (Reynolds number), temperature, wall interference, model support interference, unrealistic aeroelastic model distortions under load, stream nonuniformity, unrealistic turbulence levels, and test gas (of concern for the design of vehicles for flight in the atmospheres of other planets). On the other hand, if it is accepted that the physics of fluid flows can be described precisely by mathematical equations, then the only fundamental limitations of the computational approach are the limits of computer speed and memory, and speed and memory appear to be expandable with time by many more orders of magnitude.

Finally, wind tunnels and computers each bring different strengths to the research and development process. The wind tunnel is superior in providing detailed performance data once a final configuration is selected, especially for cases involving complex geometry and complex aerodynamic phenomena. Computers are especially useful for other applications including: 1) making detailed fluid physics studies, such as simulations designed to shed light on the basic structure of turbulent flows; 2) developing new design concepts, such as swept forward wings or jet flaps for lift augmentation; 3) sorting through many candidate configurations and eliminating all but the most promising before wind tunnel testing; 4) assisting the aerodynamicist in instrumenting test models to improve resolution of the physical phenomena of interest; and 5) correcting wind tunnel data for scaling and interference errors. The combined use of computers and wind tunnels captures the strengths of each tool.

Pathfinding Role of the Government

A concern in the mid-1970s was that computer power was only marginally adequate for calculating the aerodynamics of simple aircraft shapes at cruise conditions. More power was needed to provide both for increased resolution of geometry and for including more complete flow physics in the analyses to predict performance during maneuvers and near performance boundaries. In fact, treatment of these more complex problems in an effective manner required advances not only in computing engines, but also in operating systems, languages, compilers, central storage capabilities, networking, remote communications, graphics, and user workstations. There seemed to be no assurance that the advances required to meet government needs would be provided without government stimulus. In fact, this view was reinforced by the information summarized in table 2 which shows the historical role of the government in stimulating the development of advanced computers. Every major new digital computer from the IBM 701 to the current Cray and Control Data Corporation (CDC) machines has evolved from technology developments accelerated by a government-sponsored pioneering

computer development undertaken to satisfy a driving need. The need for a superior design capability for aerospace vehicles was, and still is, a strong driver for the NAS Program.

NASA first became involved with the pathfinding role in large-scale scientific computers in a formal way when, in 1972, it joined with the Advanced Research and Development Projects Agency (now DARPA) to test the feasibility of the ILLIAC-IV computer. The ILLIAC Project was originally undertaken for the purposes of exploring the feasibility of parallel processing and advanced-computer-logic circuit technology, and researching new ideas for high-speed computer memory. When ARPA started the ILLIAC Project, their driving need was for an anti-ICBM control system. NASA's motivation for later joining in the development was, of course, the need for more computer power for the development of computational aerodynamics.

The CDC was experimenting with the STAR-100 computer at the same time the ILLIAC-IV was being tested. Only four of these machines, featuring new ideas in pipeline architecture, were produced. Three of these were obtained by Government laboratories and one was retained by CDC. Cray Research, Inc. had yet to produce a machine and IBM elected not to compete in the large-scale scientific computer market. Two other companies, Burroughs and Texas Instruments, were on the verge of discontinuing their supercomputer efforts. Technology surveys showed that computers having many times the power of the ILLIAC-IV and the STAR-100 could be developed, but the development would not happen without Government sponsorship since the market for supercomputers was still very small and limited primarily to government laboratories. In the mid-1970s, ARPA's interests had been largely satisfied with the ILLIAC-IV, and no government organization other than NASA appeared to be interested in first defining long-range requirements for supercomputers and then strongly urging their development.

The experience gained with the ILLIAC-IV project and the clear benefits derived from it provided further motivation for proceeding with a major thrust to develop an advanced computational system and the confidence that success could be achieved. Benefits from the ILLIAC-IV Project accrued in four major areas. First, in computer technology, the ILLIAC-IV was the first large machine to have multiple processors working in parallel, the first to employ emitter-coupled logic (ECL), and the first to have multilayered (12 layers) printed circuit boards designed with automated methods. Second, in algorithm technology, the existence of the machine forced the development of numerical methods for parallel processing. This new method also led to the revelation that some principles of parallel algorithms could be utilized to obtain faster execution of problems on conventional computers of that time period that could perform some functions simultaneously, such as the CDC 7600, than could

be obtained using algorithms based on sequential computing concepts. Third, a deeper understanding evolved from the problems associated with large one-of-a-kind scientific computers. These problems included operating-system software costs, problems associated with applications software transportability to machines having different architectures, and a need to provide extensions to the common FORTRAN language to obtain maximum performance gains. In fact, the NASA Ames Research Center's investigators developed a language called "CFD" which enabled fluid dynamics codes to be run efficiently on the parallel-processing architecture. For problems that could be structured in parallel, the ILLIAC-IV was substantially more powerful than the other scientific computers of its era.

This advanced computer power enabled a number of pioneering advances in CFD, including the first simulation of viscosity-induced unsteady flow (buffett) about an airfoil, the first simulation of control-surface buzz, and detailed simulations of turbulent flows. The ILLIAC-IV experience provided the foundation and motivation for continuing to advance both CFD and supercomputer systems technology, which led to the conception of the NAS program.

EVOLUTION OF THE NAS PROGRAM

The potential value of the computational approach to aerodynamics research and development was clearly established by the mid-1970s. Also clear was the importance of pursuing every conceivable opportunity for improving aerospace vehicle design tools to maintain a leadership position in the intensifying international competition in both the commercial and military aircraft arenas. Thus, in 1975, a small group of people associated with the computational fluid dynamics effort at the Ames Research Center conceived the NAS program as a vital underpinning of the country's future in aeronautics.

The group recognized the importance to computational aerodynamics of a sustained effort to increase computer power as rapidly as technology would allow. They also recognized the need for the government to assume some responsibility for a pathfinding role to accelerate the attainment of new milestones in computer performance.

The initial proposal called for the development of a special-purpose processor called the Navier-Stokes Processing Facility. The central processor was to have a minimum effective speed of one-billion floating-point operations per second when operating on the three-dimensional, Reynolds-averaged, Navier-Stokes equations and to have performance comparable to the best general-purpose computers when used for processing the equations of other scientific disciplines. Its main memory had to accommodate a problem data base of

31-million 64-bit words. To keep development risks low, the goal of the project was to assemble existing computer component technologies into a specialized architecture rather than to develop new electronic components. Finally, the machine had to be user-oriented, easy to program, and capable of detecting systematic errors when they occurred. The proposal was endorsed in principle by NASA management in November, 1975; then in-house studies began to gather momentum and the name of the project was changed to the Computational Aerodynamic Design Facility (CADF).

Computational Aerodynamic Design Facility Project

The first formal exposure of NASA's objectives occurred in October, 1976 when proposals were requested from industry to "perform analysis and definition of candidate configurations for a computational facility in order to arrive at the best match between aerodynamic solution methods and processor system design." These analyses were to be directed toward the selection, preliminary design, and evaluation of candidate system configurations that would be best suited to the solution of given aerodynamic flow models. Design requirements that were established for this study included: 1) the capability to complete selected numerical solutions of the Navier-Stokes equations for grid sizes ranging from 5×10^5 to 1×10^6 points and wall-clock times (exclusive of input-data preparation and output-data analysis) ranging from 5 to 15 min; 2) a working memory of 40×10^6 words; 3) an archival storage of at least 10×10^9 words; and 4) 120 hr/wk of availability to the users.

Two parallel contracts were awarded in February 1977 to develop preliminary designs for the most promising configurations and to develop performance estimates, risk analyses, and preliminary implementation cost and schedule estimates for each of the designs. During these initial studies, which lasted about 12 mo, it became apparent that the overall approach to developing the facility was sound and that performance goals could be reached with new architectural concepts and proven electronic components.

A 3-day workshop on Future Computer Requirements for Computational Aerodynamics was held at the Ames Research Center in October 1977 for the purposes of further clarifying the need for a large-scale computer system for computational aerodynamic work, for confirming that the design goals were consistent with the needs of the projected users of the facility and for validating the feasibility of meeting the requirements with emerging technology. Representatives from all of the appropriate technical communities were invited, including aircraft companies, computer companies, software houses, private research institutions, universities, the Departments of Defense and Energy, and other NASA Centers. An unanticipated large attendance of over 250 people confirmed the existence of broad national interest and need for more powerful computers in science and engineering. The feasibility of meeting processing speed and memory requirements was further solidified, although it was clear that the goals could only be met with a multiple-processor architecture. Projected near-term advances in electronic component performance would not permit the goals to be met with a single-processor machine. The workshop also confirmed that computer industry economics at that point in time would not support the development of large specialized processors without the infusion of government capital. The market at that time was uncertain, and it was not clear that enough machines could be sold to amortize the development costs. Finally, the aircraft industry reaffirmed the need for the proposed facility for use in solving special design problems and for serving as a pathfinder for the development and use of large-scale scientific computer systems. The workshop proceedings were edited by Inouye (1978).

An assessment of the utility of the Computational Aerodynamic Design Facility for disciplines of interest to NASA, other than fluid- and aerodynamics, was also conducted in 1977. This assessment was initiated to provide assurance that the facility would not be so highly optimized for solving the fluid dynamic equations that it would not be useful for other work. It would also provide guidance as to how the design could be altered, if required, to make it useful for general science and engineering calculations without seriously impacting its capabilities for the originally intended problems. Experts involved with research on weather and climate, structures, chemistry, astrophysics, and propulsion reviewed the proposed architectures and analyzed how the various solution algorithms peculiar to those disciplines could be mapped onto the designs. Results of the assessment confirmed the expected conclusion that the CADF would provide a powerful new capability for a broad range of problems of importance to NASA.

Numerical Aerodynamic Simulation Facility Project

After it was recognized that the facility would be used primarily for computational research rather than for routine aircraft design, the name was changed during the course of the first study contracts to the Numerical Aerodynamic Simulation Facility (NASF). Even though it became apparent after the workshop that a computational resource of this magnitude would be a valuable tool for the solution of complex problems in other technical areas of interest, aerodynamics would still be the discipline used to drive the requirements. However, before the conclusion of the first round of contracted efforts, the need for further studies with greater emphasis on a computer suitable for a broader range of disciplines was recognized.

Accordingly, 12-mo follow-on feasibility study contracts were awarded in March 1978. The results of these efforts were expected to provide data of sufficient accuracy to permit formulation of a definitive plan for the development of the facility. Several events occurred during the period of these studies which resulted in some revisions to the basic performance specifications and a deeper involvement of the user community in the project activities.

The discipline of computational aerodynamics had matured significantly in the 3 yr since the project was first conceived. New numerical methods were developed and existing methods were refined. This led to the realization that if the size of the on-line or working memory was increased to 240×10^6 words, the facility could be used not only to estimate the performance of relatively complete aircraft configurations, but also to serve as an effective tool to study the physics of turbulent flows, a subject that had eluded researchers for more than 80 years. A corresponding increase in the off-line file storage from 10×10^9 to approximately 100×10^9 words was required to accommodate the larger data sets.

A User Steering Group was formed in July 1978 to provide a channel for the dissemination of information regarding project status, a forum for user-oriented issues needing discussion, and a sounding board by which the project office could obtain feedback from future user organizations. Examples of user-oriented issues of interest were: 1) selection of user languages; 2) management policy; 3) equipment required for remote access; and 4) data protection. The User Steering Group was composed of representatives of the aerospace industry, universities, and other government agencies. The group is still active, although its name was eventually changed to the User Interface Group to reflect its current role more accurately. Organizations currently represented on the User Interface Group are shown in table 3.

The feasibility studies were completed in the spring of 1979. Each study produced a refined baseline configuration, a functional design, and rough estimates of cost and schedule. Both studies concluded that about 5 yr would be required to complete the detailed design and to develop, integrate, and test the facility. While preparations were being made to continue the contracted development process, the name of the project was changed once again to the Numerical Aerodynamic Simulator (NAS) Project.

Numerical Aerodynamic Simulator Project

A detailed plan for the design-definition phase of the activity was prepared during the winter of 1979 by the NAS Project Office, which was established at Ames Research Center earlier in the year. This plan included refining the specifications for: 1) the computing engine; 2) the

support processing system; and 3) the collection of other peripherals, including intelligent terminals, graphical display devices, and data communication interfaces to both local and remote users. Two 40-week, parallel, design-definition contracts were awarded in September 1980. Upon their completion in July 1981, the contractors were awarded follow-on contracts related to further design definition. These were concluded in April 1982 when the proposals for the detailed design, development, and construction were submitted by the contractors for evaluation.

After an evaluation of the proposals, the decision was made in June 1982 to discontinue the procurement. This decision was based on evaluation findings which were that the risks involved in achieving the proposed technical objectives within the critical resource and schedule limitations were unacceptable. Following this decision, efforts began to chart a new course of action. A reassessment was made of the needs of the user community and the evolving state of the art in computer technology. Three principal conclusions resulted from this reassessment.

First, the application and essential importance of computational aerodynamics to aeronautical research and development had grown significantly since the mid-1970s. Thus, it was deemed important to establish and to maintain a leading-edge computational capability as an essential step toward maintaining the nation's leadership in aeronautics. To achieve this goal the NAS project was to be restructured as an on-going NAS program in which significant advances in high-speed computer technology would be continuously incorporated as they became available.

Second, the supercomputer environment had changed since the inception of the NAS activity in the mid-1970s. Increased interest in supercomputing, advances in computer technology stimulated in part by the NAS Program, and the increasing threat of foreign competition changed the environment to the extent that it no longer appeared necessary for the government to directly subsidize the development of the next generation of scientific computers. These factors provided an environment permitting a more systematic, evolutionary approach toward developing and maintaining an advanced NAS computational capability.

Third, the importance of coupling advancements in the state of the art of supercomputers with advanced system networks and software architectures was recognized. This capability is necessary to accommodate successive generations of supercomputers from different vendors and to provide the capabilities needed to enhance productivity of the user. This step led to a strategy that minimizes the dependence of the entire system on single vendors and to the establishment of a strong in-house technical capability to direct the initial and ongoing development efforts.

This reassessment highlighted the importance of the pathfinding role of the NAS program. It would be particularly challenging to develop a system with components ranging from supercomputers to user workstations that could be maintained at the leading edge of the state of the art, while simultaneously providing uninterrupted service to a large community of users working on important national problems.

Numerical Aerodynamic Simulation Program

A plan for the redefined program was approved in February 1983. It included: 1) the design, implementation, testing, and integration of an initial operating configuration of the NAS Processing System Network; 2) the systematic and evolutionary incorporation of advanced computer-system technologies to maintain a leading-edge performance cappability; and 3) the management and operation of the complex.

The new plan was presented to the various NASA Advisory Groups, the Office of Management and Budget, the Office of Science Technology and Policy and appropriate Congressional Subcommittees. It received strong support, and the Program was approved by Congress as a new start for NASA in the President's budget for fiscal year 1984. The Administrator of NASA at that time termed the NAS Program "the Centerpiece of NASA's Aeronautical Program."

Following Program approval, the development of the initial operating capability began in earnest. The in-house project team was expanded, and it was supplemented by a force of on-site contractor personnel. Procurements of both hardware and software were initiated and the evolving test-bed network was ready to receive the first High-Speed Processor, the Cray-2, in the Fall of 1985. After about 9 mo of test and integration, and with the help of a select group of users, the system was unveiled for national use in its Interim Initial Operating Configuration in July 1986. Within a few months the system was being used effectively by over 200 national users located both at Ames Research Center and at 20 remote sites.

The term "Interim Initial Operating Configuration" was selected to emphasize the fact that the system would not reach its first stage of maturity until it could be located in the new building that was being constructed as its ultimate home. Construction of this new building started in the Spring of 1985, and it was ready for occupancy at the end of 1986. The system was shut down for several weeks, dismantled, reassembled in the new building, and brought back into operation prior to meeting the goals of the Initial Operating Configuration. This conference celebrates the achievement of the goals of the Initial Operating Configuration, and commemorates the dedication of this new national capability.

Plans are now well along for expanding the system and installing the second high-speed processor prior to reaching the goals of the first Extended Operating Configuration in 1988.

SUMMARY AND CONCLUDING REMARKS

A major milestone in aerodynamics research and development was reached in 1970 when, for the first time, computers began to solve problems not previously amenable to solution. Within several years, it became apparent that insufficient computer power would impose serious limitations on the growth of computational aerodynamics as a useful discipline. It was possible to calculate the flows about three-dimensional shapes such as wings and simple wing bodies, but only with highly approximate forms of the governing equations that neglected full treatment of important nonlinear and viscous phenomena. Consideration of more comprehensive physics forced the analyses to be restricted to simple two-dimensional shapes, such as airfoils or axisymmetric aircraft components. Even in this primative state, computational aerodynamics was recognized to have the potential to become a major complement to wind-tunnel testing. Working together, computers and wind tunnels would provide a formidable capability for designing aerospace vehicles.

Recognizing the potential importance of computational methods to the aerodynamics design process, a group of people at the Ames Research Center initiated an effort in 1975 to drive the development of a computer system powerful enough to take the next major step in the development and use of computational aerodynamics. This small initial effort grew with time and, in the fall of 1983, it became a major new program for NASA with two principal objectives: 1) to provide a supercomputer facility for the national aerospace community that would be maintained as close to the state of the art as possible, and 2) to serve as a pathfinder for the development and use of future supercomputer systems. The NAS Program will reach its first major milestone in March of 1987 when its initial capability was declared operational. Already, it was serving over 200 users nationwide, and plans were well underway for its extended operating capability having two powerful supercomputers, all of the necessary supporting equipment and well-established communications links.

Computational aerodynamics was in a relatively immature stage when the NAS Program was conceived in 1975. Even so, initial forecasts of the importance of the discipline to the country's aeronautics program and of the amount of computer power required to reach various plateaus have been remarkably accurate. Nothing has transpired in the intervening 12 yr that would temper the desire to push the developement of large-scale computer systems for the country's aerospace program as fast as the technology will allow. In fact,

supercomputers are now recognized as being absolutely essential for many fields of science and engineering, and all are benefiting from the efforts of the NAS Program to develop and maintain a leading-edge computational system.

REFERENCES

1. Magnus, R.; and Yoshihara, H.: Inviscid Transonic Flow Over Airfoils. AIAA J., Vol. 8, No. 12, Dec. 1970, pp. 2157-2162.

2. Ballhaus, W. F., Jr.; Magnus, R.; and Yoshihara, H.: Some Examples of Unsteady Transonic Flows Over Airfoils. Unsteady Aerodynamics, Vol. II, University of Arizona Press, 1975, pp. 769-791.

3. Borland, C. J.; and Rizzetta, D. P.: Nonlinear Transonic Flutter Analysis. AIAA Paper 81-0608-CP, May 1981.

4. MacCormack, R. W.: Numerical Solutions of the Interaction of a Shock Wave With a Laminar Boundary Layer. Lecture Notes in Physics, Vol. 8, Springer-Verlag, 1971, pp. 151-163.

5. Deiwert, G. S.: Numerical Simulation of High Reynolds Number Transonic Flow. AIAA Paper 74-603, June 1974.

6. Mansour, N. N.: Numerical Simulation of the Tip Vortex Off a Low-Aspect-Ratio Wing at Transonic Speed. NASA TM 85932, April 1984.

7. Flores, J.; Reznick, S. G.; Holst, T. L.; and Gundy, K.: Transonic Navier-Stokes Solutions for a Fighter-Like Configuration. AIAA Paper No. 87-0032, Jan. 1987.

8. Chapman, Dean R.: Computational Aerodynamics Development and Outlook. AIAA J. Vol. 17, No. 12, Dec. 1979, pp. 1293-1313.

9. Peterson, Victor L.: Impact of Computers on Aerodynamics Research and Development. IEEE Proc., Vol. 72, pp 68-79, Jan. 1984.

10. Inouye, M. (ed.): Future Computer Requirements for Computational Aerodynamics. NASA CP 2032, 1978.

Table 1.- Governing equations, results, and computer requirements for computational aerodynamics.

APPROXIMATION	CAPABILITY	GRID POINTS REQUIRED	COMPUTER REQUIREMENT
LINEARIZED INVISCID	SUBSONIC/SUPERSONIC PRESSURE LOADS VORTEX DRAG	3×10^3 PANELS	1/10 CLASS VI
NONLINEAR INVISCID	ABOVE PLUS: TRANSONIC PRESSURE LOADS WAVE DRAG	10^5	CLASS VI
REYNOLDS AVERAGED NAVIER-STOKES	ABOVE PLUS: SEPARATION/REATTACHMENT STALL/BUFFET/FLUTTER TOTAL DRAG	10^7	30 × CLASS VI
LARGE EDDY SIMULATION	ABOVE PLUS: TURBULENCE STRUCTURE AERODYNAMIC NOISE	10^9	3000 × CLASS VI
FULL NAVIER-STOKES	ABOVE PLUS: LAMINAR/TURBULENT TRANSITION TURBULENCE DISSIPATION	10^{12} TO 10^{15}	3 MILLION TO 3 BILLION CLASS VI

Table 2.- Historical role of the Government as a prime driver in advancing computer capability.

TIME	DRIVING NEED	SPONSOR	COMPUTER DEVELOPED	KEY TECHNOLOGY	COMMERCIAL FOLLOW ONS
MID 1940'S (WW II)	MULTITUDE OF BALLISTIC TABLES	BRL	ENIAC	VACUUM TUBE ELECTRONIC COMPUTING	IBM 701, UNIVAC I
EARLY-MID 1950'S	DEW AIR DEFENSE FOR TRACKING BOMBER FLEET	USAF	AN FSQ-7	MAGNETIC CORE MEMORY	IBM 709
EARLY 1960'S	SUPERIOR DESIGN CAPABILITY FOR SMALL NUCLEAR DEVICES	AEC	CDC 6600	INTEGRATED CIRCUITS	CDC 7600, IBM 370
LATE 1960'S	ANTI-ICBM CONTROL SYSTEM (NEED ELIMINATED POLITICALLY PRIOR TO COMPLETION IN 1972)	DARPA	ILLIAC IV	SEMICONDUCTOR MEMORY AND PARALLEL PROCESSING	CDC STAR, CRAY 1
CIRCA 1980	SUPERIOR DESIGN CAPABILITY FOR AIRCRAFT	NASA	NAS PROCESSING SYSTEM NETWORK	NETWORKING OF SUPERCOMPUTERS, COMMON USER INTERFACE	

Table 3.- NAS User Interface Group.

FUNCTION
- INFORMATION CHANNEL BETWEEN USER COMMUNITY AND PROJECT
- IDENTIFY AND DISCUSS USER-ORIENTED ISSUES, e.g., REMOTE ACCESS

PARTICIPATING ORGANIZATIONS
- AIRFRAME COMPANIES
  BOEING AEROSPACE, GENERAL DYNAMICS, GRUMMAN AEROSPACE, LOCKHEED-CALIF., LOCKHEED-GA, McDONNELL DOUGLAS, NORTHROP, ROCKWELL, VOUGHT
- ENGINE COMPANIES
  DETROIT DIESEL ALLISON, GENERAL ELECTRIC, PRATT AND WHITNEY
- DEFENSE DEPARTMENT
  AFWAL, AEDC, BRL, DTNSRDC, NUSC
- GENERAL AVIATION
  GENERAL AVIATION MANUFACTURERS ASSOC. (GATES-LEARJET)
- ROTORCRAFT
  AMERICAN HELICOPTER SOCIETY (UNITED TECHNOLOGY CORP. R&D CENTER)
- UNIVERSITIES
  STANFORD, UNIVERSITY OF COLORADO, SCRIPPS INSTITUTION OF OCEANOGRAPHY, PRINCETON, MASSACHUSSETTS INSTITUTE OF TECHNOLOGY
- NATIONAL SCIENCE FOUNDATION (NSF)
- NATIONAL CENTER FOR ATMOSPHERIC RESEARCH (NCAR)
- NASA
  AMES, GODDARD, LANGLEY, LEWIS
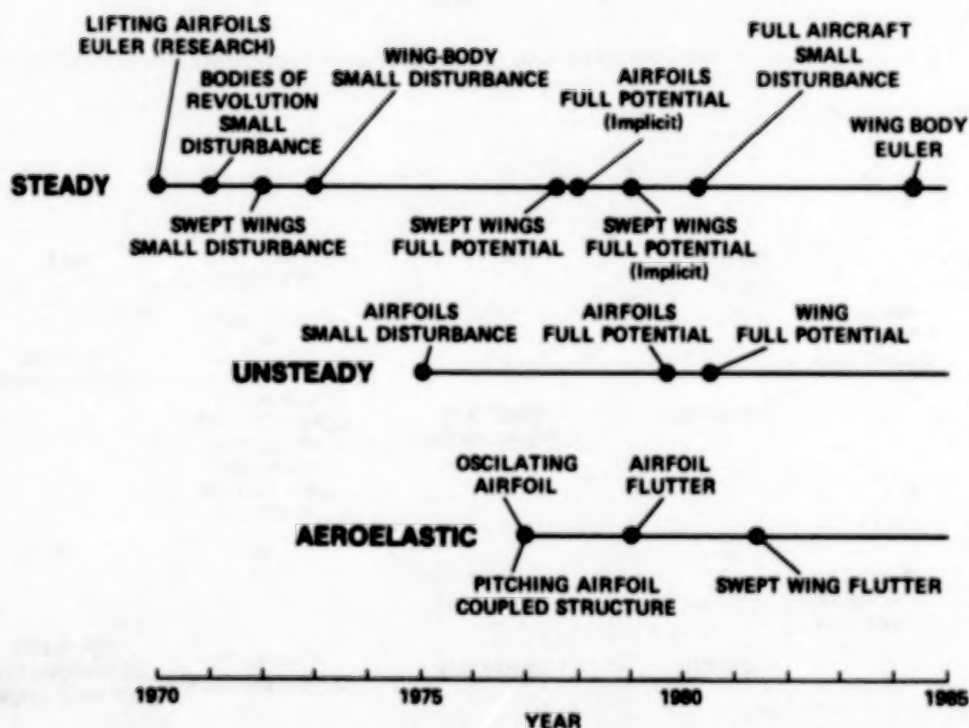
Figure 1.- Milestones in the development of computational aerodynamics; inviscid transonic flows.
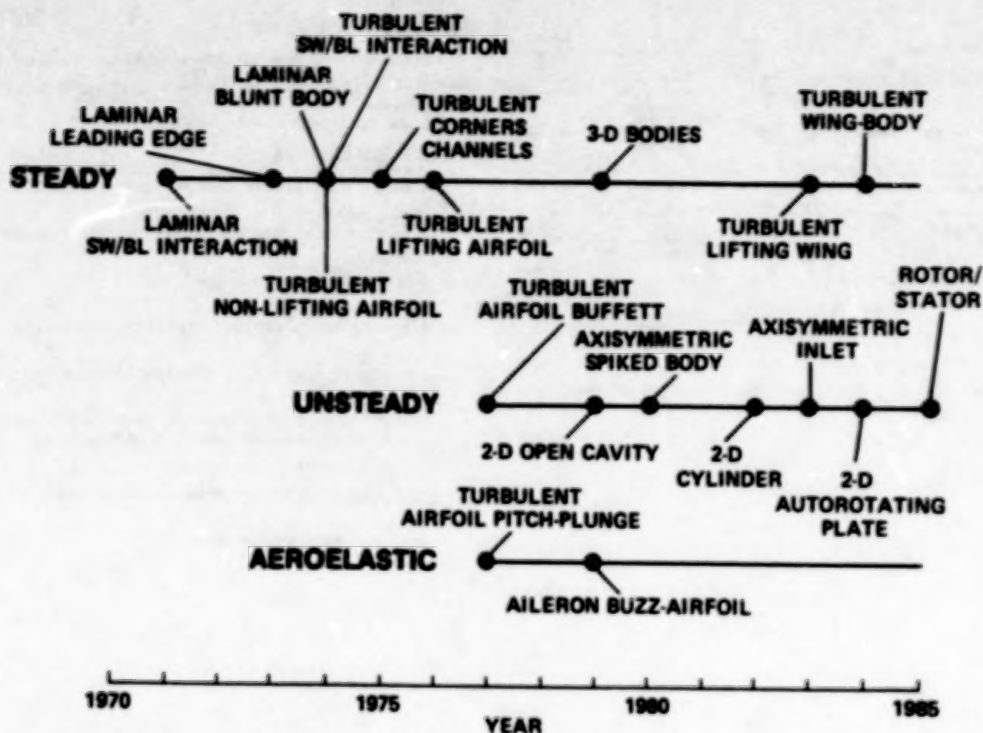
Figure 2.- Milestones in the development of computational aerodynamics; compressible viscous flows.
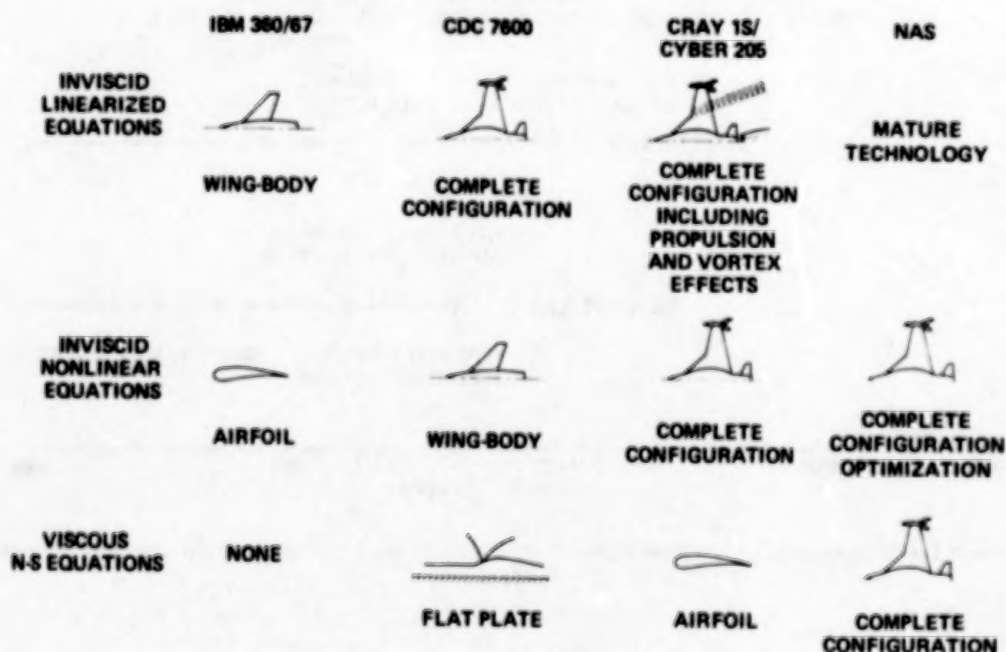
Figure 3.- Pictorial representation of the effect that increasing computer power has had on computational aerodynamics.

10

Figure 4.- Computer speed and memory requirements for aerodynamic calculations compared with the capabilities of various machines; 15-min runs with 1985 algorithms.

IMPROVEMENT IN COMPUTERS

IMPROVEMENT IN METHODS
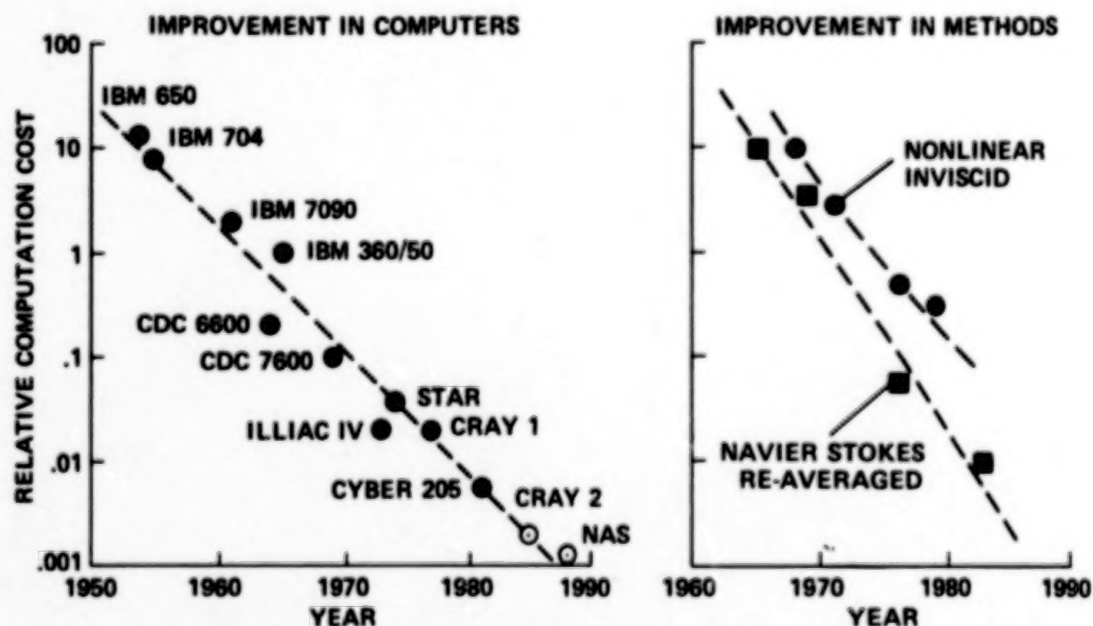
IMPROVEMENTS COMPOUND TO RESULT IN 10^5 REDUCTION IN COST OF PERFORMING A COMPUTATION OVER A 15-YEAR PERIOD

Figure 5.- Comparison of numerical simulation cost trend resulting from improvements in computers with that resulting from improvements in algorithms.

11

N87
26000
UNCLAS

INTRODUCTION

F. R. Bailey
NASA Ames Research Center
Moffett Field, California

The Numerical Aerodynamic Simulation (NAS) Program had its inception in 1975 at the Ames Research Center (ARC) when a small group of researchers associated with the computational fluid dynamics program set out to obtain significantly greater computer power and the memory capacity needed to solve three-dimensional fluid flow models (Peterson et al., 1984). The state of the art in computational aerodynamics was at the point where problems involving complex geometries could be treated only with very simple physical models and only those involving simple two-dimensional geometry could be treated with more complex physical models. It was clear that to treat problems with both complex three-dimensional geometries and complex physics required more computer power and memory capacity than was available. This is illustrated in figure 1, where the estimated computer speed and memory requirements

derived from assuming a solution in 15 min of central-processor time are compared with the capabilities of several supercomputer generations (Peterson et al., 1985). As indicated, current supercomputers can adequately address inviscid flows, but the computers needed to adequately address more complex Reynolds-averaged approximations to turbulent flows about full aircraft configurations will not be available until the end of this decade. Large-eddy simulations for complete aircraft must wait for future, more powerful computers.

Sparked by this need for increased computer power, the ARC team spent several years performing requirements refinement, technical studies, and advocacy that resulted in the establishment of the NAS Program in 1983. The ongoing objectives of the program are: (1) to provide a national computational capability, available to NASA, Department of Defense, and other Government agencies, industry, and universities, as a necessary element in
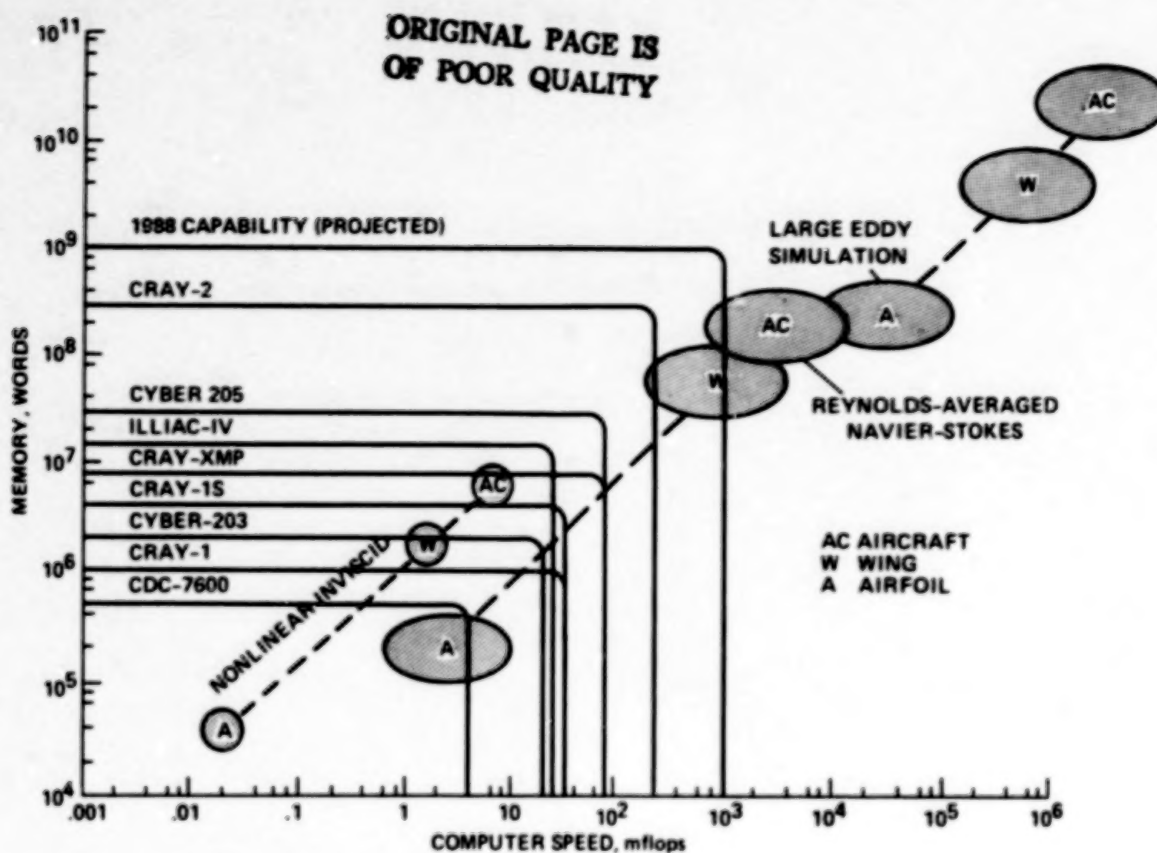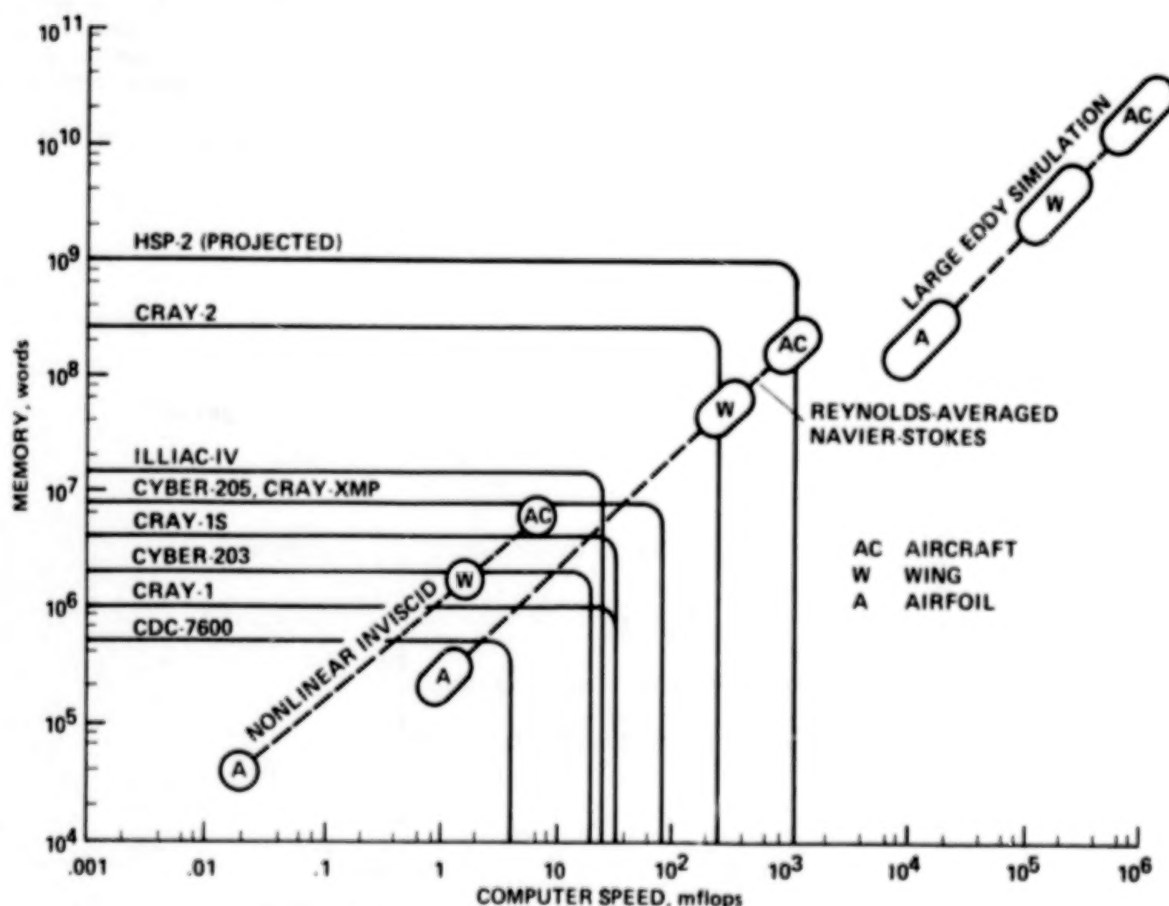

Fig. 1 Computer speed and memory requirements for aerodynamic calculations compared with the capability of various supercomputers.

ensuring continuing leadership in computational fluid dynamics and related disciplines; (2) to act as a pathfinder in advanced, large-scale computer system capability through systematic incorporation of state-of-the-art improvements in computer hardware and software technologies; and (3) to provide a strong research tool for NASA's Office of Aeronautics and Space Technology.

An early task in implementing the NAS Program was to ensure its role as a pathfinder in providing advanced supercomputing capabilities to the computational fluid dynamics community. To accomplish this a long-term strategy of installing, at the earliest opportunity, a system representing each new generation of increasingly more powerful high-speed processors was initiated. Each generation may be a prototype or early production model. The strategy, illustrated in figure 2, has already started with the installation of Ser. No. 2 of the Cray-2 as the first generation, high-speed processor. Introduction of the Cray-2 required an 8-mo period of test and integration before production operations began. The second high-speed processor will be added in 1987 followed by several months of test and integration leading to an operational capability in 1988. The third generation will replace the first in the 1989/90 time frame. In subsequent years, new advanced high-speed processors will replace the older installed systems, thereby maintaining a steady state in which there are two high-speed processors, one of which is the most advanced available.

Coupled with the high-speed processor installation strategy, is the ongoing design and development of the NAS Processing System Network (NPSN). The NPSN is a network of high-speed processors and support computers configured to provide a state-of-the-art, scientific, supercomputing environment to the computational fluid

dynamics and computational physics community. The NPSN will be implemented in phases, with the completion of each phase resulting in an NPSN configuration keyed to the introduction of a new-generation, high-speed processor. The NAS Program defined the first two configurations in 1983. These are the Initial Operating Configuration (IOC) and Extended Operating Configuration (EOC) defined below.

Initial Operating Configuration:

- High-speed processor-1 (HSP-1)
    - 250 million floating-point operations/sec (MFLOPS) computing rate for optimized, large-scale, computational aerodynamic applications
    - 256 million 64-bit words of central memory
- Integrated and expandable NPSN configuration
    - Common-user interface for all subsystems
    - Medium-band (56 kilobits/sec) communications for remote sites
    - Wide-band (1.544 megabits/sec) communications to NASA centers

Extended Operating Configuration:

- Additional High-Speed Processor-2 (HSP-2)
    - 1000 MFLOPS computing rate for optimized, large-scale, computational aerodynamic applications
- Upgraded subsystems to accommodate HSP-2 and graphics subsystems
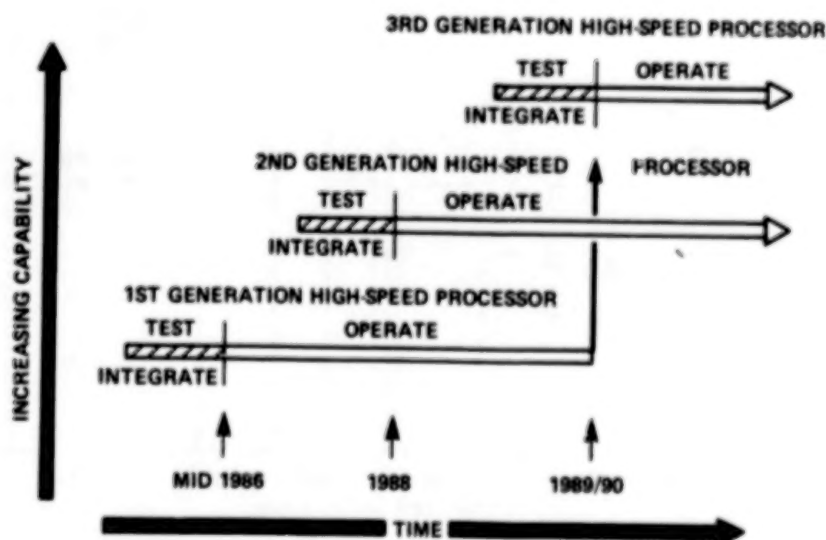- 6.2 Megabits/sec communications to NASA centers

Fig. 2 NAS Program strategy for introducing state-of-the-art high-speed processors.

The NAS Facility, completed in January 1987, provides the physical location for the NAS Program. It houses the NPSN, system support and development staff, and computational fluid dynamics research staff. This new 90,000-ft^2 building was designed with approximately 15,000 ft^2 of raised computer floor which is sufficient to accommodate future expanded NPSN configurations. Approximately 15,000 ft^2 of additional raised floor is available for technical support space, laboratories, and user colocated workstation equipment. Office space was designed to allow the computer systems staff and computational fluid dynamics researchers to share the building. These accommodations provide a strong bonding between the computer service providers and their researcher clients.

The NAS Systems Division, formerly the NAS Projects Office, at ARC has completed the initial tasks and is responsible for accomplishing the NAS Program long-term objectives on a continuing basis. The Division includes a skilled staff of computer scientists and engineers who are responsible for planning, designing, and implementing the advanced technology necessary to keep NAS attuned to its pathfinding role. The Division also provides day-to-day computer operations; ongoing computer system support functions such as hardware and software maintenance; and logistics; as well as computer services personnel to provide the training, consulting and trouble-shooting necessary to offer premier supercomputing service to a national user base.

NAS IOC DESCRIPTION

The IOC of the NPSN consists of the following functional subsystems: high-speed processor, support processing, workstation, mass-storage, and long-haul communications. The configuration, shown in figure 3, is a local-area-network-oriented architecture consisting of hardware from a number of vendors. To reduce hardware and vendor-specific dependencies, the NPSN software presents a common user interface across the system that provides users with the same environment on all user-accessible machines, i.e., provides common utilities and commands on user-visible subsystems. This uniform environment enables users to move easily between processors, allows for easy file access and command initiation across machine boundaries, and enhances user-code portability within the NPSN.

The operating system on all user-visible computers is based on AT&T's UNIX™ System V.2 operating system with network software modeled after the Berkeley 4.2/4.3 bsd UNIX operating system. Jobs on all user-visible systems can be run in batch or interactive modes. Communications protocols come from the DoD Internet family of protocols, commonly referred to as TCP/IP.
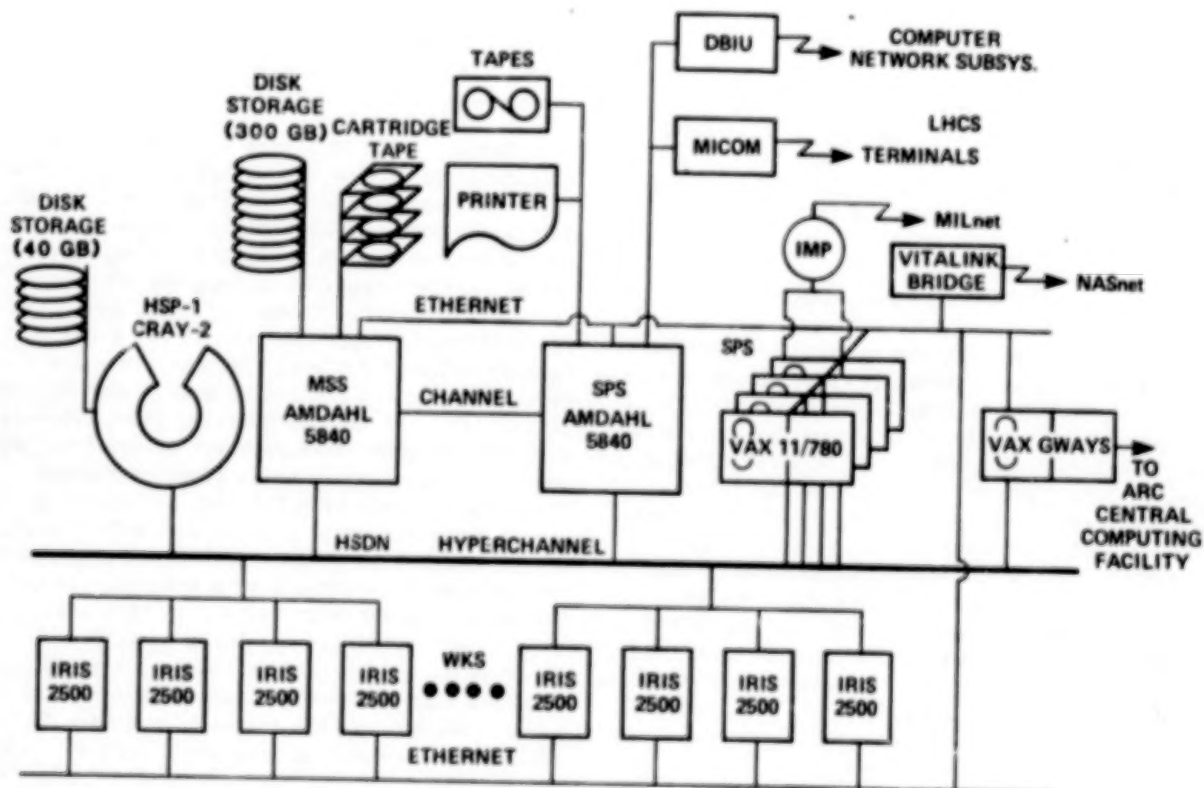

Fig. 3 IOC of the NPSN.

High-Speed Processor

The first HSP, a Cray-2, is a four-processor system with 268,435,456 words of dynamic memory--or as more commonly referenced, with 256 megawords (where each 1k equals 1024 64 bits/word) of dynamic memory. The four processors can operate independently on separate jobs or in a multiprocessing mode on a single job. The NAS Cray-2 has achieved a peak computing speed of 1720 MFLOPS for assembly-language matrix multiplies and a sustained aggregate-speed in excess of 250 MFLOPS for a job mix of computational physics FORTRAN codes.

Common memory is accessed automatically by the hardware, and can be accessed randomly from any of the four processors as well as from any of the common data channels. Any job can utilize all or part of the common memory. This memory is divided into four quadrants, each of which has 128 interleaved banks. In addition to the common memory, each of the processors has a very-high-speed local memory for temporary storage of vector and scalar data. Externally, there are 34 DD49 disks attached to the Cray-2, giving a combined storage capacity of approximately 40 gigabytes. Cray-2 software includes an operating system (UNICOS) based on AT&T UNIX System V.2; an automatic vectorizing FORTRAN compiler; a C-language compiler; a large set of batch and interactive utilities; a large set of libraries, including a multitasking library; TCP/IP networking; and Berkeley "r" commands.

Support Processing Subsystem

The support processing subsystem (SPS) consists of an Amdahl 5860 mainframe computer and four VAX 11/780 minicomputers. This subsystem supports general-purpose interactive processing for local and remote users. In addition, it provides the interface to local and remote terminals and to tapes and high-speed printers.

Workstation Subsystem

The Workstation Subsystem (WKS) consists of microprocessor-based workstations which produce graphical displays of Cray-2-generated datasets and manipulate text and data as well as perform small-scale computations. The IRIS™ (Integrated Raster Imaging System), selected as the initial NAS workstation, is manufactured by Silicon Graphics Inc. and interfaces to both Ethernet™ and Network Systems Corporation's HYPERchannel™ network. A key element of the IRIS is a set of special-purpose graphics microprocessors, called a "geometry engine," which transforms and displays three-dimensional data at rates exceeding 50,000 floating point coordinates/sec. Other workstations with TCP/IP interface capabilities are also compatible with the NPSN System.

Mass Storage Subsystem

The Mass Storage Subsystem (MSS) consists of an Amdahl 5860 mainframe computer, Amdahl 6380 disks, and IBM 3480 cartridge tape drives; this subsystem serves the global online and archival storage needs of the NPSN. The MSS checks and coordinates requests for files to be stored or retrieved within the NPSN and maintains a directory of all contained files. The MSS also acts as a file server for the other NPSN subsystems, controls its own internal devices, and performs file duplication, media migration, storage allocation, accounting and file management. The aggregate Amdahl 6380 disk-storage capacity is approximately 300 gigabytes at present.

High-Speed Data Network

The High-Speed Data Network (HSDN) is the local communications network which allows the exchange of data and control messages within the NPSN. Major design emphasis was placed on its ability to support large file transfers between the subsystems. The local network includes HYPERchannel, Ethernet, and the driver-level network software to support the intra-NAS data communications.

Long-Haul Communication Subsystem

NPSN access by the nationwide remote user community is provided by the Long-Haul Communication Subsystem (LHCS). LHCS consists of a NAS-unique remote-connection network, NASnet, and hardware/software interfaces to existing Government-sponsored networks.

NASnet, shown in figure 4, is a starlike configuration of data communication links connecting remote user sites to the NPSN. The physical data links between NASA Centers are provided by NASA's Program Support Communication Network. These links are extended to non-NASA sites via AT&T tail circuits. Except for dedicated 224 Kbit/sec terrestrial links to Lewis and Langley Research Centers, all data links are switched terrestrial circuits with a capacity of 56 Kbit/sec. At each termination point there is a Vitalink TransLAN™ communication bridge that connects the data circuit to an Ethernet network. The bridges permit NPSN Ethernet packets with remote addresses to be sent to destination hosts on the remote-site Ethernets. Conversely, Ethernet packets on a remote site's Ethernet can be routed to NPSN Ethernet hosts. In this way, remote users see their own local host, i.e., workstation, as just another node on the NPSN Ethernet. Since NASnet is implemented by switch circuit technology, the remote user literally dials up the connection only when required. From the software viewpoint, the selection of the DoD Internet Protocol (TCP/IP) suite for the NPSN

NASnet User Sites

Fig. 4 NASnet configuration.

allows the most straightforward implementation of NASnet since it not only supports a rich set of applications (mail, file transfer, remote login, etc.), but implementation also exists for a large number of various computers ranging from IBM PCs to Cray supercomputers. In summary, NASnet, whose first prototype implementation was in July 1985, provides the remote user with all the functional capabilities of a local user of the NPSN and, in particular, gives the ability to use all the interactive capabilities of powerful graphics workstations. For example, experience has shown NASnet to be very effective in supporting NAS workstation clusters at Lewis and Langley Research Centers. Users at these Centers not only access the NPSN in the same manner as ARC users, but also utilize their Ethernet connected workstations to access computer resources at their own Centers.

In addition to NASnet, PSCN circuits support two other long-haul communication capabilities. The first is the Computer Network Subsystem (CNS) that provides batch-oriented bulk file transfer service among NASA Office of Aeronautics and Space

Technology (OAST) Research Centers (Ames-Moffett, Ames-Dryden, Lewis and Langley) using T1 (1.544 mbit/sec) satellite links.

The second PSCN-provided capability is the NASA Packet Switch System (NPSS). NPSS provides 9600 bit/sec terminal access to the NPSN from NASA Centers. Since NPSS is also connected to GTE's Telenet™ packet switched network, remote users outside NASA Centers can gain access to the NPSN at rates of 1200-2400 bits/sec.

Access by DoD research installations and many universities is provided by MILnet and ARPAnet. Additional university access will be provided in the future by a newly formed network sponsored by the National Service Foundation (NSF) (Jennings et al., 1986). This network (popularly called NSFnet) is designed to provide remote access to NSF-sponsored supercomputer centers by connecting several regional networks to a national backbone circuit. One of these regional networks is the NSF-funded Bay Area Regional Research Network (BARRnet) which includes ARC, University of

California campuses (Berkeley, Davis, San Francisco, and Santa Cruz), and Stanford University. When operational in 1987, BARRnet will provide T1 communications links between participating member sites and will connect to ARPAnet at Stanford and to the NSF funded San Diego Supercomputer Center (SDSC) through a remote user access computer (RUAC) at UC Berkeley.

NAS COMPUTATIONAL SERVICES

The NAS Program provides all users with consulting, training, and documentation services. A telephone hotline is manned around the clock, excluding Government holidays. Consulting advice is also available by computer mail and in person (for local and visiting scientists). Consulting expertise includes NPSN operating systems, compilers, communications, code conversion, code optimization, file handling, tape usage, workstation graphics, and other areas of user interest.

Training services include 3-day user training classes which are held monthly at ARC. These classes cover introductory UNIX, code conversion aids, code optimization, file archival methods, tape usage, and user responsibilities. User training classes can be presented at remote sites by special arrangement. NPSN usage information is also available online in the form of manual pages as well as tutorials and sample sessions.

In the area of documentation, the NAS User Guide is sent to each account holder. The User Guide presents basic, high-level information. Other user documents are referenced for more in-depth information. The User Guide contains a complete list of Cray-2 manuals, editor manuals, reference cards, etc., which are available by request for all users.

In addition, NAS System Bulletins are sent to each user when major systems changes occur, and a monthly NAS newsletter is sent to users and other interested people. The newsletters contain NAS usage information along with items about the user projects and general NAS news and developments.

NAS USAGE

The NAS Program is intended to support pioneering work in basic and applied research. Approximately 90% of the scientific research pertains to the areas of fluid dynamics, aerodynamics, structures, material science, aerothermal dynamics, and other aeronautical applications. The remaining 10% includes work in other disciplines such as chemistry, atmospheric modeling, astrophysics, and other areas of interest to NASA. About 55% of the available computer resources supports NASA programs and is used by both in-house staff and organizations involved in NASA

grants, contracts, and joint programs. The approximate allocation of the remaining amount is 20% to DoD, 15% to industry, 5% to other Government agencies, and 5% to universities. Only the costs of industry proprietary work are reimbursed to the Government in accordance with a formula that includes operating and capital improvement costs.

The NAS Program has implemented project selection and resource allocation procedures which invite applications for NAS usage from the scientific user community and provide for peer review of projects and equitable resource allocation. The NASA Office of Aeronautics and Space Technology receives approximately 45% of the resources, to be shared among Ames, Langley, and Lewis Research Centers. Each Center suballocates its share to individual in-house and supported research projects. The university allocation is administered by the National Science Foundation. Overall resource availability is determined by the NAS Systems Division.

To be selected for NAS usage, potential users must propose technically sound and relevant projects which require the unique capabilities offered by the NPSN. The NAS selection criteria are: technical quality, national need, timeliness, and suitability to NAS resources. Selection criteria and allocation guidelines are periodically reviewed to ensure maximum benefits. The guidelines for usage described here apply only to NAS computers in an operational status. When new computers are being integrated into the NPSN, they are devoted primarily to testing and software development.

During the interim operational period, from July 1986 through February 1987, Cray-2 computer time was allocated to 123 projects. The selection process is now under way for the first full operational period, which is for 1 year, March 1987 through February 1988. For the interim period, Cray-2 time was distributed over a wide range of disciplines as shown in figure 5. Note that a high percentage of the Cray-2 was allocated to projects related to the National AeroSpace Plane (NASP). This reflects the importance of supercomputing to this new initiative. NASP technology applications are expected to increase in future years.

EARLY NAS OPERATIONAL EXPERIENCE

The NAS Program initiated pilot operations for a select group of users in December 1985, shortly after the Cray-2 had completed acceptance testing. In July 1986, interim operations of a completely integrated NPSN began. User access during these periods increased rapidly and appreciable operational experience was gained by NAS users.
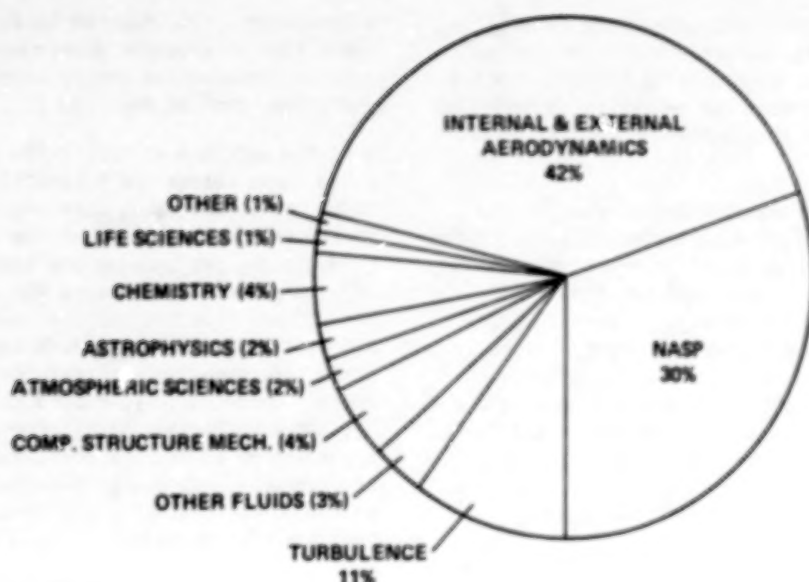
Fig. 5 Cray-2 computer time allocation distribution based on 123 interim operational period allocations.

Even within the context of pilot operations, which included a high level of system development activities, initial NAS users provided overwhelmingly positive feedback on their increased productivity while using the NFSN. In particular, most users indicated a significant reduction in code development debugging time, start-up time for changes in configuration geometry or grid resolution, and job turnaround times, as well as improvements in the graphical analysis of computed results.

The reduction in code development and debugging time can be attributed mainly to the availability of interactive supercomputing and the rich variety of tools in the UNIX environment. Prior to the development of the UNICOS operating system, vendor-supplied operating systems for supercomputers had remained, almost exclusively, as batch mode processing. While batch processing may be desirable for long production runs, debugging and code development are not best handled in this mode. UNIX provides both the interactive capability necessary for efficient code development and debugging, and the batch capability for production runs via the Network Queuing System (NQS) software. For the system developer, many of the same advantages are realized. In addition, it has been reported that the introduction of new systems, as well as software enhancements and "bugfixes," are more easily and quickly completed with the uniform UNIX environment and consistent protocol suite across the NAS machines.

The NAS Cray-2 is the first full-memory, four-processor Cray-2. The 256-megaword central memory capacity represents a two-orders-of-magnitude increase over previously available capacity. Prior to the Cray-2, increased resolu-

tion or geometric complexity required the use of a Solid State Disk (SSD). The input/output (I/O) delays associated with paging data between the central memory and disk were significant and, not infrequently, reached 10 or 20 times the actual CPU time for the job. Therefore, specialized, machine-specific code modifications were required for efficient utilization of SSD memory.

For example, a typical three-dimensional Reynolds-averaged Navier-Stokes simulation is constrained to resolve less than 69 cubed (approximately 0.3 megaword) spatial points if the job is to remain in the central memory of an 8-megaword machine. Full use of 256 megawords would allow for 217 cubed, or 10.24 million points, to be resolved for an in-core run of this example code. Thus the increased memory of the Cray-2 allows for both increased job complexity without significant code modification and virtual elimination of I/O wait time. The net effect is decreased startup time for increasingly complex problems and improved job turnaround.

As the speed and memory of supercomputers continue to increase, larger and more physically complex problems can be solved more routinely. To analyze these larger and more complex datasets, graphical displays are not only desirable but necessary. Specialized graphical processors such as the "geometry engine" of the IRIS workstation help to provide pseudo-real-time visualization of computed results, i.e., real-time manipulation of graphical images which are created from previously computed datasets.

It is probably realistic to assume that the demand for supercomputers and graphical displays expands to fill any available resource. However,

19

because of the distributed processing capability of the NPSN and its uniform software environment and protocol suite, coprocessing between workstation and supercomputers can be easily implemented for more effective utilization of available resources.

Graphical coprocessing tasks, such as the ARC-developed Realtime Interactive Particle Traces (RIP) software package which interactively calculates particle paths in a computed flow field, involve initiating two coupled processes simultaneously: a computational and memory intensive process residing on the Cray-2 and a graphical display and manipulation process residing on the workstation. Information is passed back and forth between the two machines via HYPERchannel and Ethernet links for remote workstations. In this way, a processing task can be intelligently divided to make use of the strong points of the various machines in the NAS system. For the user, this translates into a substantial savings in time for the display of a particle trace on a workstation, since the Cray-2/IRIS combination offers a 10:1 performance improvement over an IRIS alone. Because of the uniform UNIX environment across the Cray-2 and workstations, the creation and installation of RIP required one afternoon to coordinate among three people with existing but decoupled codes.

Quality film output of workstation-generated displays is provided by Model 655 Dunn cameras and prototype Seiko printers. Users can make high quality photographs, transparencies, or negatives with the Dunn cameras. The Dunn system works directly off the RGB output of the workstations. For 16-mm movies, the computer-controlled Model 632 Dunn camera functions with the aid of a workstation patch panel.

Video animation capabilities are provided by an ABEKAS digital disk recorder. This system takes an RS170 output from the IRIS, converts it to NTSC signals, and records it on disk. This represents a significant improvement in recording speed, editing, and special effects capabilities over older tape-recording devices. To assist the user in making animation sequences, a program called the Graphics Animation System (GAS) has been developed. GAS lets the user create scripts on the IRIS which can be played back at a later time on the animation system. GAS is a fairly "user friendly" program in that it records a user's actions as graphic images are manipulated on the IRIS screen, automatically generating a playback script. If needed, the user can edit this script to either correct the errors or to add steps to smooth out the animation.

FUTURE CHALLENGES AND PLANS

The NAS Program is engaged in planning the implementation of the EOC and its follow-on con-

figurations. EOC, planned to be operational in 1988, adds an advanced supercomputer, the HSP-2, with performance and memory capacity targeted at four times that of the Cray-2.

The addition of this large increment in computer power raises the potential for inbalance among processing rate, data transport bandwidth, and storage capacity across the entire NPSN. At present, the performance and storage capacity of supercomputers is outpacing the ability to move data to and from the computer and to store it. New storage technologies such as optical, magneto-optic, and magnetic vertical recording look promising. Unfortunately, supercomputing needs alone are not a sufficient market force to drive these technologies to the desired level of performance and capacity. As a consequence, new strategies with older technologies are being investigated to meet near-future needs.

Increased high-speed processor data production, higher graphics data consumption, and higher storage capacity will require increased data communication bandwidth in the NPSN. An analysis of the bandwidth requirement for a 20-fold increase in processing power, based on models of the NPSN projected workload and system architecture, shows an effective bandwidth of 100 megabits/sec is necessary (Levin et al., 1987). To meet this requirement, the NAS Program has efforts under way to establish a network test bed for hands-on investigation of new networking technologies.

Long-haul data communications is also an important area for future improvement. The experience gained with NASnet has demonstrated the value of high-bandwidth and low-delay terrestrial circuits. The NAS Program plans to aggressively pursue opportunities to economically increase bandwidth capability when high capacity transcontinental fiber-optic data trunks become available in the next few years. In addition, an advanced remote-communications gateway prototype is planned. The objective of this effort is to meter circuit capacity as throughput demand rises and falls. This will be accomplished by a type-of-service routing gateway that establishes the optimum bandwidth and delay characters to match a particular application service (interactive character stream, on-demand data transfer, bulk file transfer, etc.). The bandwidth will be optimized by adding or deleting subchannel allocations of the backbone circuit and the delay optimized by switching to either low-delay terrestrial or high-delay satellite circuits.

The first-order software challenge for the future is to provide the algorithms, languages, and programming tools to effectively use the potential of parallel architecture computers. Future high-speed processors, without a doubt, will consist of several if not many processors. Parallel supercomputers are here now in the form of the four-processor Cray XMP and Cray-2, but their parallel multitasking capability is greatly

under utilized. When the multitasking of many processors becomes necessary to achieve greater performance, much improved software will be critically needed. The NAS Program is placing greater emphasis on improved techniques for multitasking and will aggressively pursue research in massively parallel architectures.

Future technology will also support more parallelism across computer boundaries as in the case of coprocessing between supercomputers and workstations. Special-purpose processors, designed to perform very well on a piece of the total problem, connected to very fast networks are a fertile area for research and development. The NAS Program is actively engaged in research and advance development in these areas, with the goal of introducing them into the NPSN by the end of the decade.

SUMMARY

The NAS program has met its first major milestone—the NPSN IOC. The program has met its goal of providing a national supercomputer facility capable of greatly enhancing the Nation's research and development efforts. Furthermore, the program is fulfilling its pathfinder role by defining and implementing a new paradigm for supercomputing system environments. The IOC is only the begin-

ning and the NAS Program will aggressively continue to develop and implement emerging supercomputer, communications, storage, and software technologies to strengthen computations as a critical element in supporting the Nation's leadership role in aeronautics.

REFERENCES

Jennings, D. M.; Landweber, L. H.; Fuchs, I. H.; Farber, D. J.; and Adrion, W. R.: Computer Networking for Scientists, Science, Vol. 231, Feb. 1986.

Levin, E.; Eaton, C. K.; and Young, B.: Scaling of Data Communications for Advanced Supercomputer Network. To be pres. to the IFIP/IEEE/ITC Intern. Conf. Data Commun. Systems and Their Performance, Rio de Janeiro, June 22-25, 1987.

Peterson, V. L.; and Arnold, J. O.: Impact of Supercomputers on Experimentation: A View from a National Laboratory, Proc. Amer. Soc. Eng. Symp., Atlanta, June 17-19, 1985.

Peterson, V. L.; Ballhaus, W. F., Jr.; and Bailey, F. R.: Numerical Aerodynamic Simulation (NAS), in Large Scale Scientific Computation (Seymour V. Parter, ed.), Academic Press, New York, 1984.

COMPUTATIONAL MECHANICS AND PHYSICS AT NASA LANGLEY RESEARCH CENTER

Jerry C. South, Jr.
Chief Scientist
NASA Langley Research Center
Hampton, Virginia 23665

Abstract

An overview is given of Computational Mechanics and Physics at NASA Langley Research Center. Computational analysis is a major component and tool in many of Langley's diverse research disciplines, as well as in our interdisciplinary research. Examples are given for algorithm development and advanced applications in aerodynamics, transition to turbulence and turbulence simulation, hypersonics, structures, and interdisciplinary optimization.

Introduction

Research disciplines at Langley include aerodynamics, acoustics, structures, materials, electronics, controls, and atmospheric sciences. Computational analysis has become a dominant tool in most of these disciplines, providing enhanced insight into the physical processes that underlie our engineering and scientific problems. The use of computational analysis is so pervasive, and the expectations so great, that the demand by our researchers for more computer power seems insatiable. We have at our disposal a VPS-32 supercomputer (a 2-pipeline CYBER 205 with a 32 million, 64-bit word memory) in our central complex; access to a 4-pipeline 205 (with 8 million words of memory) in the Ames central facility; and of course, the NAS Cray-2. We have a parallel processor, a FLEX-32, which has 20 independent processors, each with 1 megabytes local memory and 2 megabytes shared memory. Additionally, there are a number of "super" minicomputers and over 100 other minicomputers sited in local research areas and associated printing and graphics terminals for pre- and post-processing computational results, and a local network for file transfers among the various resources.

In spite of what seems to be a considerable amount of computing power, we have saturated not only our VPS-32, but also "our half" of the Ames 205. As more codes are converted to CRAY FORTRAN or developed from scratch, we will saturate our share of the NAS as well (the usage rate as of this writing was about 300 hr/mo). This story is probably repeated at most research laboratories, and certainly many industries today, for several reasons. For example, nearly everyone seems to expect to make 7-hour runs on a supercomputer. The computations are usually three-dimensional simulations of physical problems and contain a wealth of detailed information not obtainable (or infeasible) by other means. Further, many more engineers and scientists are aware of, and use supercomputers in their research than was the case just 10 years ago. In the late 1960's, there were four supercomputers at Langley alone; namely CDC 6600's, which were ten times faster than their forerunners! However, it was almost unthinkable to make a 7-hour run, for the results of such a run would be so limited in use and would contain only a tiny fraction of the information compared to today's analyses.

We join with universities and industry to develop advances in computational methods for use in aerospace research. To assist in this thrust, the Institute for Computer Applications in Science and Engineering (ICASE) was created over 10 years ago at Langley to provide a direct interaction between university mathematicians and computer scientists and NASA research engineers to find an optimum blend among the theoreticians and the practitioners. The Institute has been an unqualified success. Mathematicians have been stimulated by association with difficult engineering problems, and research engineers have found the expertise of world-class numerical analysts, applied mathematicians, and computer scientists to be invaluable. A prime focus for ICASE researchers is development and analysis of computational algorithms for vector and parallel computers, such as the FLEX-32 mentioned previously.

In this paper an overview will be given of the algorithm developments and diverse applications of computational analysis at Langley which may be of interest to this conference. The main body of the paper is presented in the form of individual, self-contained briefs which were prepared by the researchers involved. It is intended that the briefs be as free of unexplained jargon and symbols as possible, in order to convey the scope of computational mechanics and physics at Langley, rather than exquisite details.

The majority of the briefs are in the area of computational fluid dynamics (CFD), as would be expected. Shown are examples of new Navier-Stokes and Euler equation algorithms for three-dimensional flows, and advanced viscous-inviscid computations using Euler and potential equations coupled with boundary-layer methods for three-dimensional aerodynamic problems. Some of the important CFD applications and developments in spectral methods coupled with Multigrid convergence acceleration are given. Vortex flows are a subject of intensive theoretical, computational, and experimental study at Langley, and some CFD applications are given here.

Researchers have developed CFD techniques for direct simulation of transition to turbulence, fully turbulent flows, and "large-eddy" simulations where the sub-grid scales of turbulent eddys are modeled. Both incompressible and compressible flows have been treated, and spectral methods are the predominant spatial differencing choice, due to the high accuracy of such schemes. This area of computational research consumes enormous computational resources, even for very simple geometry, and it has been one of our prime early focuses for NAS applications. Because transition and turbulence remain as a major stumbling block to the accurate prediction of complex flows, it continues to be a major research area at Langley, and NASA in

general. In another paper, M. Y. Hussaini presents a more comprehensive discussion of this area. Two examples of this research are shown in the main section.

The area of hypersonic flow is one which contains certain important problems that can be studied only by computational analysis, because of lack of experimental facilities capable of simulating the full range of hypersonic flight conditions. Hypersonics has been reborn as a top-priority engineering research field in the Nation, and NASA in particular, with the National Aero-Space Plane as a focus, along with advanced missions in support of our space program. Direct-simulation Monte-Carlo (DSMC) methods are used to explore and predict rarified flows, and to calibrate continuum Navier-Stokes codes which require slip boundary conditions at the solid walls of a vehicle. Finite-element and finite-difference methods are being developed for treating high-enthalpy, nonequilibrium flows and their inter-action with structural elements. A significant focus area at Langley is the scramjet engine and its integration with the external aerodynamics of an Aero-Space plane, as regards spillage, combus-tion, and overall vehicle performance. The NASA hypersonic computational research will be covered in some detail in this conference in the paper by D. L. Dwoyer. Here we present one example in computational hypersonics, comparing Navier-Stokes, viscous-shock-layer, and DSMC algorithms for a rarified, nonequilibrium flow.

Computational structural mechanics at Langley is likely to become the fastest-growing community of supercomputer users. Structures researchers and designers in NASA and industry have developed and applied both linear and nonlinear finite-element methods with a high degree of sophistication for analysis of major problems in solid mechanics. The general software in use today evolved on computers with memory which was small relative to that avail-able on current supercomputers; the solution tech-niques usually involve the generation of large linear systems of equations which are solved by some direct methods, such as elimination or inver-sion. The largest codes can require huge amounts of auxiliary storage, but are often relatively modest in terms of actual compute time (at least compared to CFD codes). Data generation and efficient input-output are a major concern. The NAS should be a particularly adept machine for such applications, for most problems which are presently analyzed will fit in the 256MW memory of the Cray-2. Static and dynamic analysis of large, complex structures, and fracture analysis of composite structures are two areas of research at Langley which require significant supercomputing resources, and the demand is growing rapidly. They are extremely well-suited for the NAS. Two examples of this work are shown in the following section, one of which relied on intensive use of the Cray XMP and Cray-2 at Ames via the NAS network to solve the analysis problem of the space shuttle solid-rocket booster joints. For this problem of national importance, the NAS network and its supporting personnel performed in admirable fashion.

The final example in the next section is one illustrative of our interdisciplinary research. A Langley research goal is to develop methods for integrating advances in our disciplines to achieve safer and more efficient aerospace vehicle and system designs. The example shown is a direct approach to maximizing electromagnetic performance of a large space antenna while minimizing the system mass.

Examples of Computational Analysis

Implicit Upwind-Biased Algorithm for Navier-Stokes Equations

An efficient computational algorithm for the compressible Navier-Stokes equations has been developed. The spatial differencing reflects the predominant nature of the equations in the limit of Reynolds number $R_e \rightarrow \infty$ (hyperbolic) and $R_e \rightarrow 0$ (parabolic) through upwind differencing of the convective and pressure terms and central differ-encing of the viscous shear stress and heat flux terms. The method is naturally dissipative so that no additional smoothing terms are required and is particularly well-suited for transonic and super-sonic flows where strong shock waves are prevalent.

The algorithm is advanced implicitly in time by applying the backward-time Euler integration scheme to the governing equations, linearizing the equations in time, and using the delta form so that the steady-state solution is independent of the time step. Efficient solutions to the systems of equations are obtained at subsonic and transonic speeds through spatially split approximate factori-zation and at supersonic speeds through a hybrid relaxation/approximate-factorization technique. Extremely efficient solutions to the steady-state equations are obtained with multigrid acceleration.

Results from an example computation for the subsonic flow over an aspect ratio AR equal to one delta wing are shown in Figure 1. In this figure, Reynolds number based on length is represented by Re_L, free-stream Mach number by M_∞, lift coeffi-cient by C_L, and trailing-edge flap angle by δ. The total pressure contours (shown in Fig. 2 at an angle of attack α of 20.5°) indicate the primary vortex, which is shed from the leading edge, and the secondary vortices (underneath the primary) which are induced by boundary-layer crossflow separation. The computation of lift versus angle of attack shows good agreement with experimental data and includes the prediction of maximum lift associated with the onset of vortex breakdown.
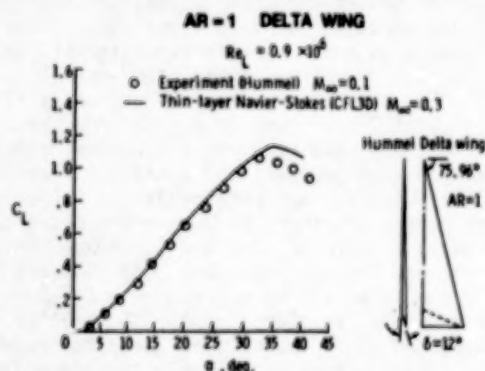

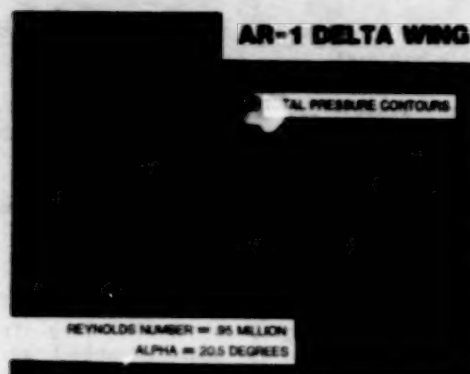Fig. 1 Lift versus angle of attack of highly swept delta wing.

Fig. 2 Total pressure contours for highly
swept delta wing.

Fig. 3 Comparison of computational and experi-
mental pressures for the Pathfinder I at
$M_\infty = 0.82$, $\alpha = 1.93°$, $R_e = 17 \times 10^6$.

Three-Dimensional Transonic Viscous-Inviscid Interaction Program

Over the past 5 years, the computer code
TAWFIVE (Transonic Analysis of a Wing and Fuselage
with Interacted Viscous Effects) has been under
development at NASA Langley. The program was
developed to accurately predict the transonic flow
about wing-body configurations. In TAWFIVE, the
conservative full-potential equation is used to
model the outer inviscid portion of the flow field
on a boundary-fitted grid. A three-dimensional
integral boundary-layer method is used to model the
inner viscous region of the flow field. Wake
curvature and displacement thickness effects are
also included.

The TAWFIVE code has recently been modified in
an effort to significantly decrease its computation
time and to add several new capabilities.
Originally, TAWFIVE used a relaxation scheme to
solve the outer inviscid portion of the flow. To
accelerate convergence, the multigrid method has
been incorporated. This method reduces total run
times by at least 50%. Some improvements in the
grid have also been made, and user input to the
program has been reduced. Also, the capability to
allow the wing lift level to be specified and the
angle of attack to be a result of the calculation
have been added.

As a sample of the capability of TAWFIVE,
results from a TAWFIVE calculation for the
Pathfinder I configuration are compared with
experimental data from the National Transonic
Facility. The flow conditions are $M_\infty = 0.82$,
$\alpha = 1.93°$, and a Reynolds number R_e of 17×10^6
based on mean chord. Figure 3 shows good agreement
for pressure coefficient C_p versus chord fraction
x/c at three span fraction η locations.

Euler Code With Interacted Viscous Effects

An Euler code coupled with a boundary-layer
solver has been developed by Keith Koenig,
Mississippi State University, under contract to
NASA. The code solves for the viscous flow field
around a wing/fuselage combination. The finite-
volume Euler solver uses flux-vector splitting of
the governing equations and solves the discretized
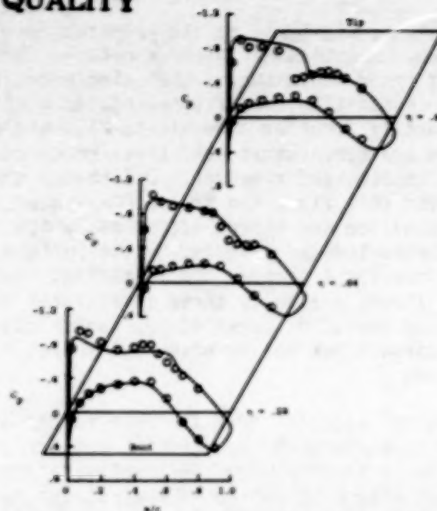split equations with an implicit, upwind, second-

order predictor-corrector scheme. The viscous
solver is an inverse integral technique that has
analytical expressions for the velocity profiles
which are valid for attached and separated
turbulent boundary layers. The code is structured
such that results can be obtained to engineering
accuracy on the Control Data Corporation's VPS-32
computer in a DEBUG category run.

Results are presented for an advanced trans-
port configuration at $\alpha = 2.41°$, $M = 0.819$, and
$R_e = 5.9 \times 10^6$ and compared with experimental
pressure coefficients at a midspan location on the
wing. The computations were performed on a medium
density C-H-shaped mesh (97×17×17). Comparisons of
computed and experimental results on other configu-
rations (including Pathfinder 1) have also been
made and are good. Plans are underway to apply the
code to lower-aspect-ratio fighter-type configura-
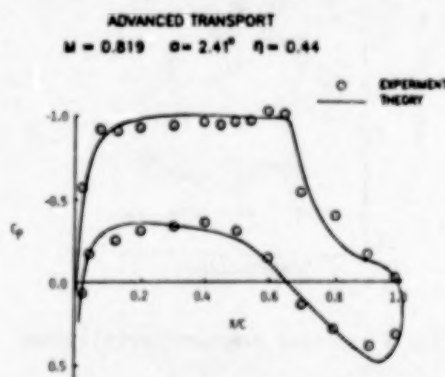tions to further validate its capability.

Fig. 4 Euler calculation with interacted
viscous effects.

Aerodynamic Loads for Slender-Wing/Body Configurations

Low-aspect-ratio wings are desirable for
vehicles that require supersonic or hypersonic
capability, such as advanced fighter

configurations, missiles, or the proposed Aero-Space Plane. Due to their slender nature, these configurations exhibit substantial wing/body inter-ference. In addition, separation-induced vortex flows naturally occur at moderate-to-high angles of attack and are dominant at conditions required for takeoff, landing, and maneuver. One theory that accounts for this flow, the free-vortex-sheet, has recently provided successful estimates, which include vortex-induced effects, of the surface load distributions for a slender configuration. Results from this theory are fully three dimensional and represent an inviscid "upper bound," which data tend to approach but not surpass as Reynolds number is increased.

A typical solution from the free-vortex-sheet theory is compared with experimental results in Figure 5 for a slender-wing/body configuration at an angle of attack of 20° and a free-stream Mach number of 0.5. The results are presented at a longitudinal station in which the body radius is approximately one-half of the configuration semi-span. Both theory and experiment show a double suction peak on the upper surface. The maximum pressure coefficient between these two peaks occurs at the wing/body juncture. The outboard suction peak occurs on the wing and is typical of leading-edge vortex flow; the inboard peak occurs on the fuselage and, for the theory, is solely due to induced effects of the wing primary vortex on the body.
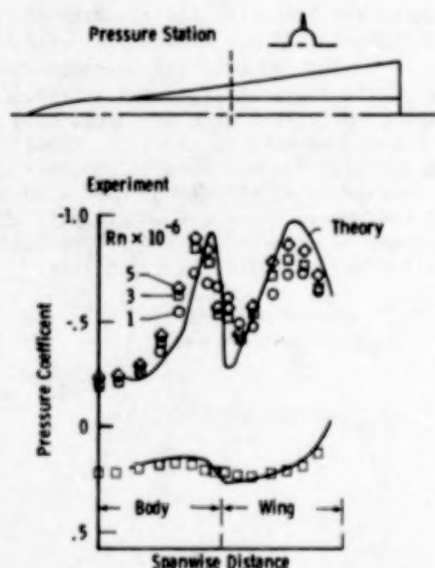

Fig. 5 Surface pressure correlation.

The correlation between theory and experiment is good on both the upper and lower surfaces. Similar correlations were achieved at other longitudinal stations. The experimental Reynolds number effects shown are significant, and, in this sense, the inviscid free-vortex-sheet theory may provide useful estimates of the full-scale flow that occurs at significantly higher Reynolds numbers than those shown.

New Algorithm Development for Efficient Transonic Unsteady Aerodynamic Analyses

An approximate factorization (AF) algorithm was developed at NASA Langley for solution of the unsteady small-disturbance potential equation for transonic flow. The new algorithm is very efficient for transonic unsteady aerodynamic and aeroelastic analyses when compared with the alternating-direction implicit (ADI) algorithm of the Air Force/Boeing XTRAN3S computer code. Figure 6 shows results of applications of the AF algorithm to an F-5 fighter wing. The free-stream Mach number was 0.9 and the angle of attack was 0°. A comparison of convergence histories of the AF and ADI algorithms is shown in the upper part of Figure 6.
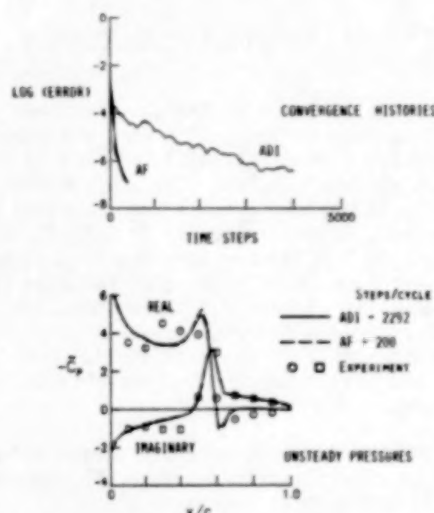

Fig. 6 Convergence histories and unsteady pressures.

The AF algorithm provides a converged steady-state solution in one-tenth the number of time steps that the ADI algorithm requires. The AF algorithm gives similar improvements in computa-tional expense for subsequent unsteady calculations required for aeroelastic analyses. A comparison of unsteady pressure coefficients per unit pitch angle $\bar{c}_p$, versus fractional chord at the wing midsemispan x/c, is shown in the lower part of Figure 6. The calculations were performed for the rigid wing pitching harmonically with a reduced frequency of $k = 0.14$. The AF results were obtained in a fraction of the number of time steps per cycle that the ADI results require, and both sets of results compare well with the experimental data. Therefore, the new AF algorithm is accurate and efficient for transonic unsteady aerodynamic analyses.

The research was conducted as part of a larger effort directed toward developing computational methods of predicting unsteady flows with emphasis on the flutter critical transonic speed range. In addition, the algorithm has been demonstrated to be effective in the supersonic regimes (not shown). Work is continuing to further assess the accuracy and efficiency of the new AF algorithm.

Automated Transonic Aeroelasticity Analysis Program Development

A procedure developed at NASA Langley for nonlinear transonic aeroelastic analysis of three-dimensional wings is based on the sequential and iterative use of a series of independent programs. For a fabricated wing shape, wing surface pressures are calculated using the FLO22 aerodynamic program. A new wing shape resulting from the pressure loadings is then used in the next iteration. Three to six iterative loops are normally required to achieve convergence.
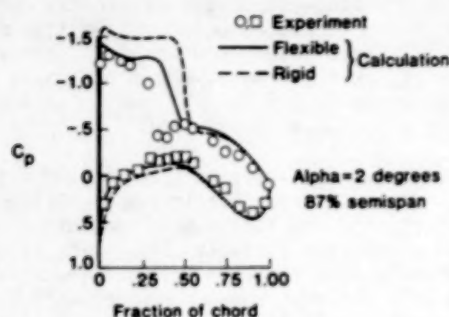

Fig. 7 Calculated and measured wing surface pressures.

Running the individual programs, transferring files, and evaluating intermediate results for a converged solution were found to be extremely time-consuming tasks. Linking programs, automating file transfers, and adding logic to exit the iterative loop when the convergence criteria were met have resulted in significant savings in user time and computer resources.

The automated procedure was used to provide results for comparison with experimentally measured data for a flexible transport-type wing tested in the Langley Transonic Dynamics Tunnel. Computed pressure coefficients for a rigid and a flexible wing show the calculated aeroelastic effects. The calculated pressure coefficients for the flexible wing agree well with the measured data, although the computed location for the recompression shock is slightly farther aft when compared with measured data. Also shown are computed and measured wing vertical deflections that are also in close agreement.
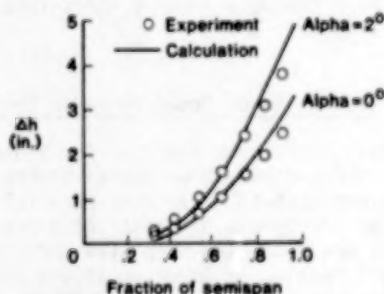

Fig. 8 Calculated and measured wing vertical deflections.

Transonic Airfoil Design Procedure

Transonic computational methods have matured to the point that they are being extensively used in the design of new configurations and the modification of existing aircraft. Their role in the design process has generally been to predict the flow field about a given configuration and to give the designer information about how changes affect the aerodynamic characteristics of the aircraft. More recently, automated design methods have been incorporated into some of the codes in an effort to expedite the design process.

A new algorithm at NASA Langley has been developed for use in the design of airfoils or wings that have a specified pressure distribution. This algorithm relates differences between the calculated and target pressure distributions to changes in airfoil surface curvature, then iteratively modifies the initial airfoil to achieve the desired pressures. This method works well for subsonic or transonic conditions because it accurately locates shocks when they are present, allows only a portion of the airfoil to be modified (if desired), and guarantees trailing-edge closure.

The Garabedian and Korn two-dimensional airfoil code has been modified to include this design procedure, and a number of test cases have been run at subsonic and transonic conditions. Results thus far indicate that the procedure is robust and accurate. An example of these results is shown in Figure 9. The target pressure coefficients were generated from an analysis run of the code for an existing supercritical-type airfoil at a Mach number of 0.734 and a lift coefficient of 0.60. The code was then run in the design mode using an NACA 0012 as the initial airfoil. At these conditions, both the initial and final pressure distributions show a considerable amount of supercritical flow on the upper surface terminating in a shock. The final pressure distribution for the modified airfoil was very close to the target pressure distribution.
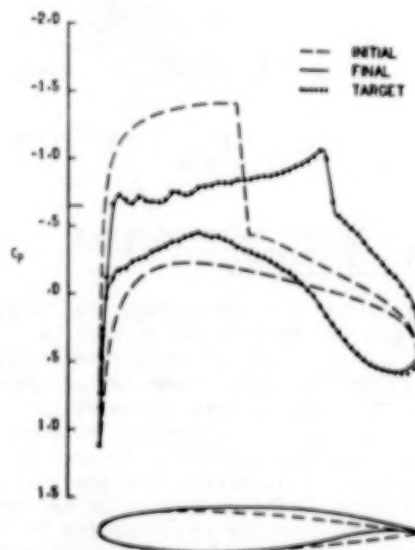

Fig. 9 Airfoil design code pressure distributions C_p.

Multiple-Domain Extension to Spectral Collocation Methods

Spectral collocation methods have proved to be efficient discretization schemes for many aerodynamic and fluid mechanic problems. The high-order accuracy shown by these methods allows either engineering-accuracy solutions on coarse meshes or, alternatively, very accurate solutions that are essential for fluid mechanic simulations. One drawback to spectral collocation has been the requirement that a complicated physical domain must be mapped onto a simple computational domain via a high-order mapping if the spectral advantages are to be preserved. Additionally, problems with discontinuous boundary conditions cannot be treated with conventional spectral methods. Such restrictions are overcome by splitting the domain into regions; adjoining regions are interfaced by enforcing a global flux balance that preserves the high-order continuity of the solution.

This multidomain method has proved to be effective on a wide range of test problems, which include resolution of a singular perturbation problem with spatial scales different by 5 orders of magnitude, and an elliptic equation in generalized nonorthogonal curvilinear coordinates. Figure 10 shows the solution isolines for Laplace's equation in a region that contains a line of fixed conditions within the domain. This discretization will be used in the simulation of transition in the shear layer behind the trailing edge of a splitter plate.
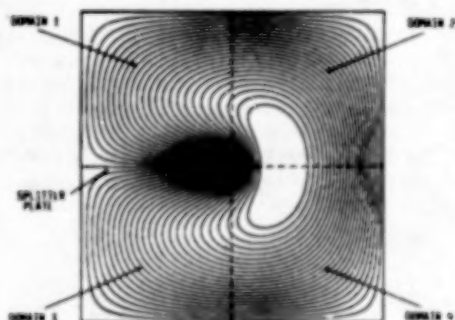

Fig. 10   Solution to Laplace's equation on splitter plate geometry.

Application of Spectral Multigrid Methods to Engineering Calculations

The high-order error decay rate that is associated with spectral methods can be used to an advantage in multidimensional engineering calculations by reducing the rapid growth in the number of points required by even modest increases in accuracy. To realize this advantage, however, efficient solution techniques must be devised to solve the equations that result from spectral discretization; these equations tend to be far more difficult to solve than the corresponding finite-difference equations. A number of techniques have been applied to spectral methods with considerable success. One such method involves preconditioning the spectral equations with a solution to the corresponding finite-difference equations and computing, at each step, the iteration parameters that yield fastest convergence. Preconditioning is a classical technique in which an algebraic system, which is to be solved iteratively, is modified by the inverse matrix of a related system which is easier to solve. This preconditioning clusters the eigenvalues of the system and results in faster convergence. Another powerful technique that has been employed is the well-know multigrid method. In this method, convergence is accelerated by taking advantage of the characteristic that is inherent in most relaxation schemes: convergence is rapid for short-wavelength error components, but it is slow for long-wavelength components. Relaxation solutions of related equations (written on a sequence of progressively coarser grids) are used to remove the entire error spectrum because a long-wavelength error on a fine grid appears as a short-wavelength error on a coarse grid.

An example of a solution that is produced by a spectral multigrid technique is shown in Figure 11, which illustrates the Mach number contours about a transonic shock-free airfoil. Simulation of shock-free transonic flow presents a severe test of the accuracy of a method. Low-accuracy flow field solutions often bear little resemblance to the true solution because nearly sonic flow is extremely sensitive to small area changes in the stream tubes. The equations produced by the spectral discretization of the potential equation could not be solved for this example by any other iterative method than the multigrid method.
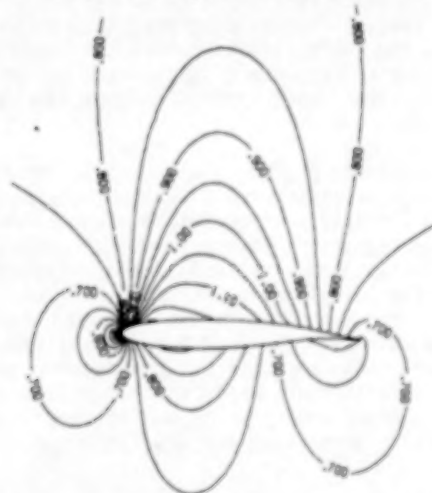

Fig. 11   Mach contours about a shock-free transonic airfoil.

Numerical Simulation of Boundary-Layer Transition

Spectral algorithms are used to conduct time-dependent, three-dimensional Navier-Stokes simulations of transition in idealized, parallel boundary layers. For incompressible water boundary layers, simulations are conducted both with and without passive wall heating in order to assess the effectiveness of this control mechanism in the strongly nonlinear regime. For compressible air boundary layers, the simulation is conducted at a free-stream Mach number of 4.5 in order to determine the influence of nonlinear, three-dimensional effects on compressible transition.

The numerical simulations indicate that wall heating can delay the transition process. One of the clearest diagnostics of the transition process is the development of a strong detached shear layer, i.e., a region (removed from the wall) in which the streamwise velocity has a high gradient in the direction normal to the wall. Figures 12(a) to 12(c) compare the flow field in an uncontrolled water boundary layer with that in one in which the wall has been heated to 2.75% above the free-stream temperature. After a nondimensional time of 3, the uncontrolled boundary layer has a strong detached shear layer, whereas the heated case still exhibits only a small perturbation to the mean flow.
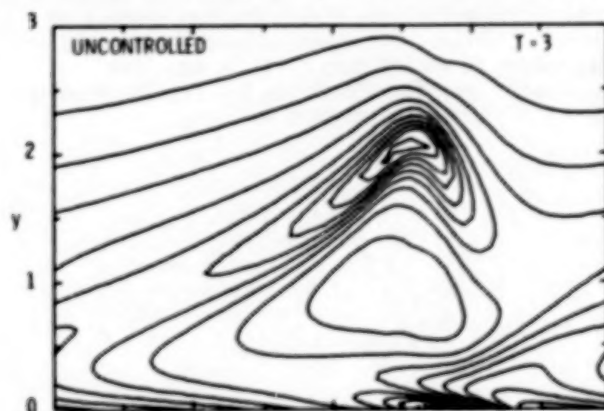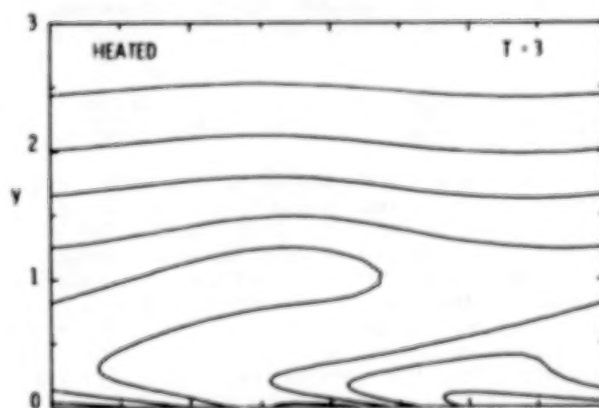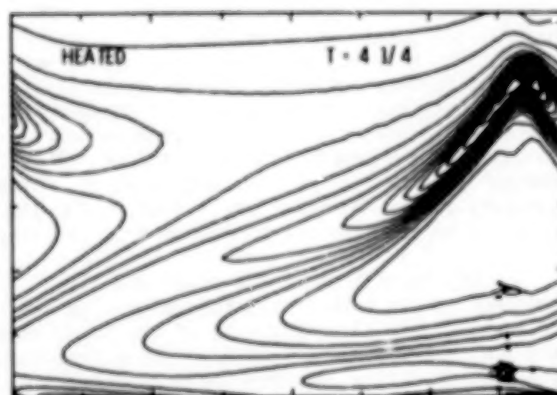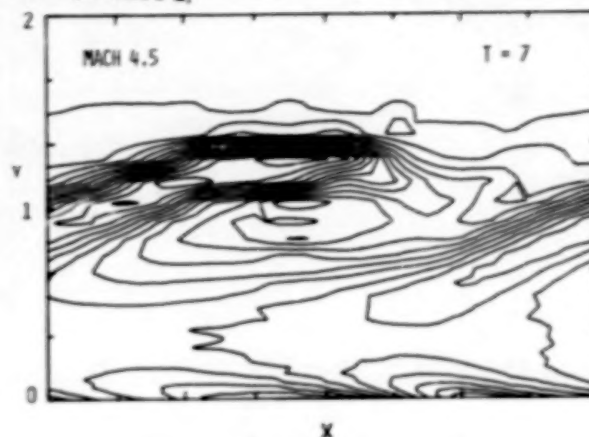

Fig. 12(a)

Fig. 12(b)

Fig. 12(c)

Fig. 12(d)

However, after a time of 4-1/4 even the heated case is undergoing transition. Wall heating delays transition but does not prevent it. The simulations of compressible flow have yielded the first theoretical evidence that nonlinear, secondary instabilities operate in the supersonic regime. Figure 12(d) presents a detached shear layer arising from a secondary instability in supersonic flow.

Subgrid-Scale Modeling of Compressible Turbulence

Highly accurate, spectral codes for both direct and large-eddy simulations of compressible, homogeneous turbulence were developed. The direct simulation (DS) code was used to generate fully resolved, low Reynolds number turbulent flow fields on 96×96×96 and 128×128×128 grids. The computed flow fields were separated, via a large-eddy simulation (LES) filtering process, into resolved and unresolved (subgrid) components with respect to both 16×16×16 and 32×32×32 grids. The subgrid-scale model was applied to the resolved fields to produce predictions for the subgrid-scale stresses. These were then compared with the exact subgrid-scale stresses as determined from the DS data. This comparison was used to find the optimal model constants and to compute the correlation between the modeled and exact subgrid-scale stresses.

A new subgrid-scale model for compressible turbulence has been developed and tested. It satisfies basic physical principles, includes compressibility effects, and can be implemented efficiently within an LES code. The DS and LES codes employ a novel, semi-implicit treatment of the pressure that permits efficient computation of very low Mach number flows. Direct simulations have been performed for Mach numbers (based on the rms value of the fluctuating velocity field) between 0.1 and 0.6. Figure 13(a) compares the energy spectrum for the Mach 0.6 case with a comparable spectrum for an incompressible case. Figure 13(b) illustrates the density fluctuations in the compressible case. Detailed data analysis has revealed that the compressible subgrid-scale model correlates well with the data, with correlations on the tensor level which are above 80%. Moreover, the constants in the model have only a weak dependence upon Mach number, changing by no more than 5% between Mach 0 and Mach 0.6.
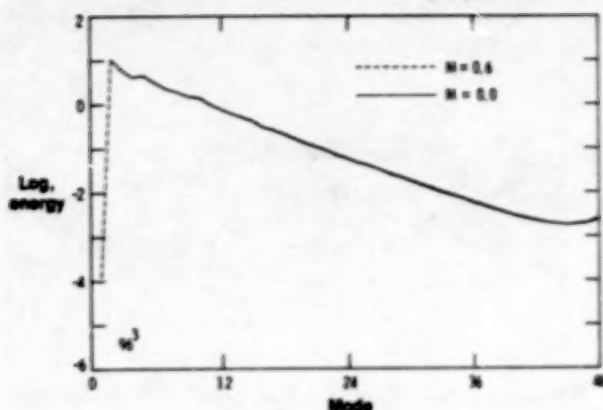
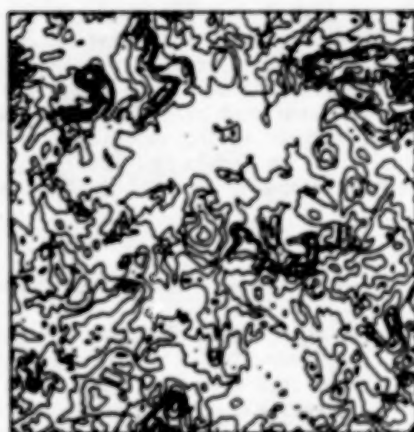Fig. 13(a) Energy spectrum for isotropic turbulence.

Fig. 13(b) Density contours.

Navier-Stokes Simulations for Hypersonic Low-Density Flows

For an accurate prediction of the aerothermal environment of a space vehicle entering the Earth's atmosphere in the high-altitude (low-density) flight regime, the multicomponent nonequilibrium gas chemistry, as well as the surface slip effects, must be included in modeling the flow field. Such rarefied and highly energetic flows are of particular interest for current and future space transportation systems. Recent numerical simulation studies have been performed in which the Navier-Stokes (N-S) equations were used to model chemical nonequilibrium flows with multicomponent surface slip boundary conditions. These solutions are applicable along the stagnation streamline of a blunt nose tip at low-density hypersonic flow conditions. The governing equations are highly nonlinear and are solved by a numerical finite-difference method known as Successive Accelerated Replacement (SAR).

The comparison of the N-S stagnation-point heat-transfer results with those obtained with the direct simulation Monte Carlo (DSMC) method (a particle approach) provides an indication of the applicability of continuum methods to low-density hypersonic flows. Also shown are the continuum

viscous shock-layer (VSL) results without either surface or shock slip boundary conditions. The VSL data begin to depart from the DSMC results for free-stream Knudsen numbers (λ_∞/R_N where λ_∞ is the undisturbed mean free path length and R_N is the nose radius, which is 1.3 m) of about 0.03. The departure is rapid for the VSL results. The departure of the N-S results without surface slip is less rapid because the N-S simulation included the shock wave structure by integrating all the way to free-stream conditions and also because it contains higher order terms than the VSL equations. Finally, the N-S solution with surface slip provides good agreement with the DSMC heat-transfer calculations for free-stream Knudsen numbers as large as unity. The three methods are in good agreement at an altitude of 92.35 km. For altitudes less than 92.35 km, the results from the N-S and VSL methods compare well[1].
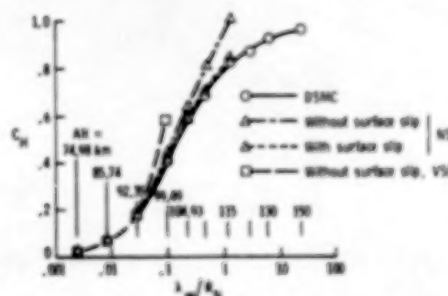

Fig. 14 Heat transfer coefficient versus Knudsen number.

Structural Behavior of the Space Shuttle SRM Tang-Clevis Joint

The space shuttle Challenger accident investigation focused on the failure of a tang-clevis joint on the right solid rocket motor (SRM). The existence of relative motion between the inner arm of the clevis and the O-ring sealing surface on the tang has been identified as a potential contributor to this failure. This motion can cause the O-rings to become unseated and therefore lose their sealing capability. Finite-element structural analyses have been performed where particular attention has been paid to modeling concerns such as mesh discretization and contact of the joint components. To model the details of the contact between tang, pin, and clevis and also to predict the general three-dimensional stress state in the joint, three-dimensional elastic, solid finite elements were selected for the analysis. The elements have elastic material properties for all analyses performed in this study. These computations were carried out via remote link with the Cray XMP-12 and XMP-48 sited at Ames Research Center. Further analyses of the nonlinear shell problem for the complete booster are being performed on the Cray-2.

A key ingredient of the joint modeling approach is the method used for connecting the separate finite element models of the tang, clevis, and pin. It was recognized from the outset that the contact regions between these components would change as a function of loading, leading to a nonlinear analysis problem. This nonlinearity

occurs, for example, when a gap that exists between unloaded components closes when loaded. The actual contact is modeled by adding a nonlinear spring between two adjacent contact nodes. The nonlinear spring stiffness curves are piecewise-linear functions of the relative displacement and are generated, for example, such that a high stiffness results for any compression of the spring and a low or zero stiffness results if the spring stretches.

Following the accident, structural tests ("referee tests") at Morton-Thiokol Incorporated were designed to gain a better understanding of the deflection behavior of the tang-clevis joint and to aid in the verification of analytical models. The test article consisted of a case segment tang joined to a case segment clevis; domed end closures seal the ends of the two-segment test article. This assembly was tested under hydrostatic pressure from zero to 1004 psi.

The finite-element model of a one-degree slice of the original SRM joint used in the comparisons is shown on Figure 15. For the baseline analysis case, no clearance around the pin is assumed. High contact forces develop around the pin under the pressure load. Even with a low coefficient of friction, these contact forces are sufficient to prevent the tang and clevis arms from sliding along the pin. The applied loading is 1000 psi internal pressure which is assumed to act on the surfaces of the tang and inner clevis arm and all surfaces of the primary O-ring groove. This loading condition implies that the primary O-ring forms a seal at the downstream corner of the O-ring groove.

Fig. 15 Finite element model of local joint (4405 nodes and 2868 elements).

A comparison of deflections from the referee test and analysis is shown in Figure 16. These deflections have been exaggerated in the deformed geometry plot. Agreement between test and analysis for the relative tang and clevis motions in the joint itself as indicated by the results on Figure 16 is generally good. Gap motion midway between the two O-ring grooves is measured in the referee tests using eight displacement transducers located around the circumference of the case. The measured values of gap motion ranged from 0.035 to 0.041 inches with an average value of 0.037 inches for a 1000 psi pressure loading. As shown in

Figure 16, the predicted value of the gap motion is approximately 17% below this average measured value. The close-up view of the deformed geometry qualitatively indicates the severity of the pin bending due to the bearing forces and the tang rotation.

Relative displacement between tang and clevis arms

Direction/Test, in./Analysis, in.
- Axial/.016/.011
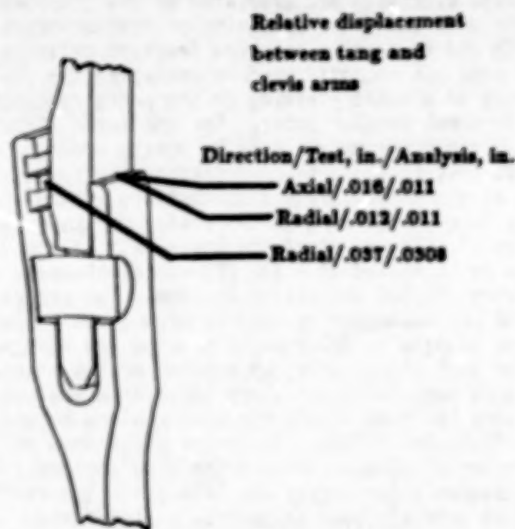- Radial/.012/.011
- Radial/.037/.0308

Fig. 16 Deformed geometry (exaggerated deflections).

The largest stress values occur in the joint itself in the vicinity of the pin. The pin contacts the tang at the lower edge of the tang hole and at the upper edges of the clevis holes. High compressive stresses are present in these locations and many of the stresses substantially exceed yield values for both the D6AC case material (180 ksi) and the MP35N pin material (250 ksi).

These analyses have demonstrated the difficulty of accurately predicting the structural behavior of the tang-clevis joint. Stresses in the vicinity of the connecting pins, obtained from elastic analyses, considerably exceed the material yield allowables indicating that inelastic analyses are probably necessary. Parametric variation of pin-hole taper, used to approximate the inelastic behavior of deformations in the tang hole, agreed with the measured gap motions.

Three-Dimensional Stress Analysis of Cracked or Uncracked Structures

Three-dimensional, elastic and elasto-plastic, finite-element codes for analysis of structures with or without cracks have been developed at NASA Langley. Advanced finite-element formulations are coupled with highly vectorized computer codes for use on the VPS-32 supercomputer.

Finite-element formulations using 8- or 20-noded isoparametric hexahedron elements are used for stress analyses of cracked or uncracked structures. For cracked elastic structures, a square-root singularity is incorporated around crack fronts. The strength of the singularity (the stress-intensity factor) is calculated for various

crack sizes and shapes in common aircraft components, such as surface cracks emanating from rivet holes. The stress-intensity factors are used to predict the fatigue life and fracture strength of damaged aircraft structures. For elastic-plastic materials, the fatigue-crack growth and fracture processes are simulated on the computer to better understand the mechanism of fatigue-crack growth and to develop improved fracture criteria. This code was recently used in analyzing the influence of plastic yielding on the performance of a solid-rocket booster joint. For uncracked structures, the programs are used to obtain accurate stress distributions in complicated structures, such as the shear-stress distributions around pin holes in a wooden wing-tunnel blade, as shown in Figure 17. The model of the lower half of the blade was composed of 3,300 (20-noded) elements and had about 50,000 degrees of freedom. The program PATRAN was subsequently used to reduce the enormous amount of data to color plots showing the stresses in the most highly stressed regions of the blade. The dark regions in the slice taken from the wooden hub show the most highly stressed regions around the pin-loaded holes. (The color plots show distribution of stresses within the dark regions.) The maximum shear stress was 1400 psi. The finite-element code was used to analyze a redesigned blade, with a smoother transition from the blade to hub region, and the results showed a 30% reduction in maximum stress.

The application of three-dimensional stress analyses to both cracked and uncracked structures will significantly enhance certainty in stress distributions and may prevent many previously unanticipated failures. These computer codes will be made more accessible to other researchers by developing more friendly codes and user guides.
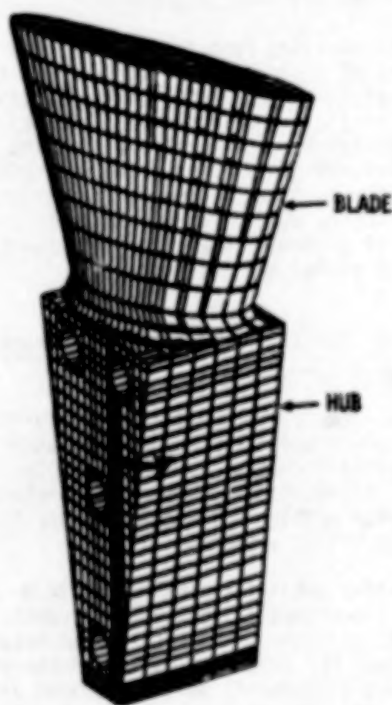

Fig. 17(b)   Shear stress distribution around pin-loaded hole.

Integrated Interdisciplinary Optimization Procedure for Large Space Antenna Design

Previous work in optimizing large space antenna structures generally concentrated on minimizing root mean square (rms) surface distortions, thereby indirectly maximizing electromagnetic (EM) antenna performance. The present work involves a direct approach to maximizing EM performance while minimizing mass. Integrating the thermal, structural, and EM analyses in the context of an optimization procedure is an effective design approach because the influence of each type of response on the other is accounted for directly and automatically. A finite-element thermal analysis and structural deformation analysis program is combined with a NASA-Langley-developed electromagnetic radiation program and a standard optimization program. The system is used to perform a thermal analysis, transfer the temperatures to the structural model, and compute the deformed shape of the antenna reflector. The deformed shape in the EM analysis is used to determine performance parameters including peak gain, side lobe levels, beam width, pointing direction, and cross-polarization.

The procedure has been tested on a 55-m tetrahedral antenna reflector shown in Figure 18. A representative orbital position was chosen as the design point and a design was sought which minimized structural mass while attaining a peak gain of at least 19,000. The results of the optimization are shown in the lower part of Figure 18. Structural mass, rms surface distortion, and peak gain are shown for the initial design and for the first three design cycles. Design goals are essentially achieved at the third cycle. The contour plots show the evolution of surface distortion as the design is improved.

Fig. 17(a)   Model of wood blade and hub.

Fig. 18 Application of optimization procedure
to space antenna design.

Solid lines are displacements toward the feed, and
dashed lines are displacements away from the
feed. Initially, there is a deep valley in the
reflector, but at the end of the third cycle, the
distortion is much smaller, and the reflector shape
is nearly a perfect paraboloid as required. The
remaining distortion occurs near the outer edges,
which are not as important to EM performance as the
center because of feed taper.

Concluding Remarks

Computational analysis at Langley Research
Center covers a wide range of aerospace research
disciplines, and is crucial to our inter-
disciplinary research goals. The demand for
supercomputing resources seems unlimited, spurred
by the quantity and quality of information now
derived from the results. This paper attempts to
convey the scope of computational research and
advanced applications at Langley by showing some
examples from several areas: Aerodynamics, fluid
dynamics, hypersonics, structures, and optimization
of space systems. Areas which were not shown, but
which are important elements of our program,
include atmospheric dynamics modeling; quantum
physics computations related to materials char-
acterization; and severe storm downburst computa-
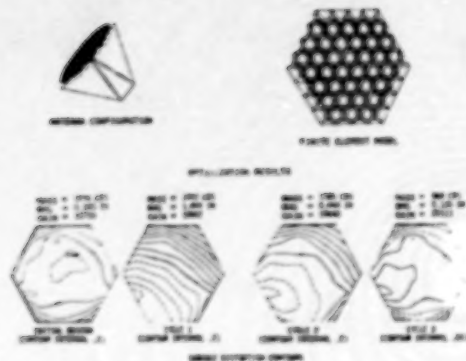tions in support of wind-shear prediction and
avoidance.

N87
26002

INTERNAL COMPUTATIONAL FLUID MECHANICS ON SUPERCOMPUTERS
FOR AEROSPACE PROPULSION SYSTEMS

Bernhard H. Anderson
Thomas J. Benson
NASA Lewis Research Center

SUMMARY

The accurate calculation of three-dimensional internal flowfields for application towards aerospace propulsion systems requires computational resources available only on supercomputers. This paper presents a survey of three-dimensional calculations of hypersonic, transonic and subsonic internal flowfields conducted at the Lewis Research Center. A steady state PNS solution of flow in a Mach 5.0 mixed compression inlet, a Navier-Stokes solution of flow in the vicinity of a terminal shock, and a PNS solution of flow in a diffusing S-bend with vortex generators will be presented and discussed. All of these calculations have been performed on either the NAS Cray 2 or the Lewis Research Center's Cray XMP.

INTRODUCTION

The accurate calculation of three-dimensional internal flowfields for application towards aerospace propulsion systems requires computational resources available only on supercomputers. Aerospace flowfields in physically realistic situations are strongly three-dimensional and viscous (as well as usually turbulent) and contain strong shock wave interactions. It is also important to predict and validate the relevant flow physics which may require large numbers of grid points. The geometry associated with aerospace and/or special performance aircraft inlets and nozzles are highly complex. These ducts typically contain large area variations, highly curved or offset centerlines, and various flow control devices including boundary layer bleed or blowing slots or vortex generators. A detailed description of these geometric features requires very fine grid systems while the flow within these geometries requires an even finer grid. Boundary layers which must be computationally resolved are generated on all internal surfaces. Strong secondary flows which are often generated in the ducts must also be resolved. If the flow is supersonic one must also accurately compute shock wave strength and location, the interaction of multiple shock waves, and the interaction of the shock waves with boundary layers within the duct. To computationally resolve all of these phenomena requires extremely fine grid systems with the accompanying large computer storage and execution time requirements.

Computer code modelling of internal flows has increased recently due to improved computer algorithms and more powerful supercomputers such as the Cray-XMP and Cray 2. Some researchers, Refs (1 to 3), have used the unsteady Reynolds-averaged Navier-Stokes (NS) equations marched in time to a steady state solution to describe the flow in the duct. At NASA Lewis, ducts have been analyzed with a zonal methodology, Ref (4); NS codes are used only in the transonic terminal shock region, while higher speed Parabolized Navier-Stokes (PNS) codes are used in the hypersonic and subsonic diffusers. Through an extensive code verification effort, Ref (4), it has been found that the higher computational speed of the PNS codes provides the analyst sufficient grid resolution to resolve critical flow phenomenon and that lack of sufficient grid resolution often leads to erroneous results. However, these codes have their limitations; they typically cannot calculate through transonic regions of mixed supersonic and subsonic flows, and they cannot properly model regions with large recirculations. Because such flow phenomenon are present near strong normal shock waves, NS codes are used in these cases.

This report will survey the results from three studies using supercomputers at the NASA Lewis Research Center on internal computational fluid mechanics which are typical of aerospace propulsion systems. Details of two of the computations can be found in the literature, Refs (5 and 6), while the third is originally presented here. The first case involves the three-dimensional calculation of hypersonic flow in a Mach 5.0 mixed compression inlet, Ref (5), which will be tested in the Lewis 10x10 foot supersonic wind tunnel. The results of the analysis are compared with preliminary experimental results. In the second case, the two-dimensional Navier-Stokes calculations of a Mach 1.3 and Mach 1.6 normal shock/boundary layer interaction in a rectangular wind tunnel is studied. The results of the analysis are compared with LDV experimental results obtained in the Lewis 1x1 supersonic wind tunnel. The third case involves the three-dimensional subsonic calculation of flow in a diffusing S-bend duct, Ref (6), with vortex generators. The results of the analysis are compared with experimental results from the University of Tennessee, Ref (7).

RESULTS

3D Hypersonic Inlet

The Mach 5.0 hypersonic mixed compression to be analyzed is shown in Figure (1). This inlet has rectangular cross-section, a pre-compression ramp and three compression ramps external to the cowl. A shock is generated on the pre-compression ramp when the aircraft is at angle of attack. This shock and the shocks from the ramps are designed to fall just outside the cowl lip at the design Mach number. The cowl lip generates a shock which is cancelled at the ramp shoulder and the cowl is contoured to further compress the flow internally. A swept sideplate runs from the leading edge of the pre-compression plate to the

leading edge of the cowl to minimize the drag generated by compressed flow spilling over the sides of the inlet.

The Mach 5.0 inlet has been analyzed three-dimensionally using a PNS analysis program. The free stream Mach number was 5.0, angle of attack was 9.0 degrees and Reynolds number per foot was 2500000. The computations were performed on an 80x60 cross-sectional grid, which corresponds to the levels of grid resolution required for accurate modelling of the glancing shock/boundary layer interaction (GSBLI), Ref (4), and were marched 630 stations from free stream to near the inlet throat. The calculation required nearly three million mesh points and slightly less than two hours cpu time on the Cray 2.

The results from the three-dimensional calculation are presented in a series of figures (2 to 9). At the top of each figure is a schematic of the inlet, with the location of the cross-sectional plane given by a vertical line and a prescribed distance from the inlet leading edge. The bottom of the figure shows the flowfield in a cross-section of the inlet; the ramp surface is at the bottom, the cowl surface at the top, and sideplates are on both sides. Because of flow symmetry, only half of the inlet was calculated. The left side of the figure shows Mach number contours, while the right side shows secondary velocity within the cross-sectional plane. The figures proceed from a location just downstream from the inlet leading edge to a location inside the cowl near the throat. On the solid surface of the ramp, cowl and sideplate, one will note the development and growth of the boundary layer by a concentration of Mach contours near these surfaces. Shock waves are noted by a concentration of Mach contours away from the solid surfaces. They can also be detected by an abrupt change in the secondary velocity vectors. In this calculation, the compression shocks and the Mach contours are parallel to the ramp and cowl surfaces.

Initially, Figure (2), the incoming flow is uniform at Mach 5.0 and 9.0 degrees angle of attack. The velocity vectors point down because the flow is at angle of attack. A shock generated by the pre-compression ramp appears as a horizontal line in the Mach contours. At the initial station, no boundary layers are noted and there are no sideplates present. As one proceeds downstream to the first ramp, Figure (3), the boundary layer has grown uniformly on the ramp surface and is thicker near the ramp than near the edge of the sideplate, as shown in the Mach contours. The non-uniformity of the sideplate boundary layer is due to the cut-back leading edge of the plate; the lower portion of the sideplate has a longer run than the upper and has therefore a thicker boundary layer. The shock from the pre-compression ramp lies just near the edge of the sideplate.

Entering the region of the compression ramps, Figure (4) shows the flowfield just downstream of the first ramp. The shock generated by this ramp is evident in the Mach contours; near the center of the flowfield this shock is flat while near the sideplate the shock forms a characteristic lamda as it interacts with the boundary layer of

the sideplate. In the secondary velocity vectors, one sees a cross-flow being induced along the sideplate and feeding forward of the inviscid shock location; flow conditions which have previously been found in the GSBLI calculations. Each of the succeeding compression ramps generates another GSBLI along the sideplate which increases the secondary flow, as shown in Figure (5). A circulation region has been generated near the sideplate corner, pulling in flow along the ramp surface.

Near the cowl lip, the flow field appears as Figure (6). The secondary velocity vectors show extremely strong flow along the sideplate, while the Mach number contours show the sideplate boundary layer to be highly distorted. The boundary layer has been thickened in the vicinity of the shock waves and thinned in the corner formed by the ramp and sideplate. The secondary velocity vectors also show flow being drawn along the ramp surface into this corner. The boundary layer along the ramp surface is quite thick and corresponds to the thickness predicted in the two-dimensional calculations. The strong secondary flows induced by the multiple GSBLI persist even though the shock waves have left the flow domain over the cowl. The flowfield from the inlet leading edge to the cowl lip has been shaped by the thick boundary layer that grows on the ramp and sideplate and the multiple GSBLI that occur on the sideplate due to the compression ramps. The flow is highly three-dimensional at the cowl lip with low energy boundary layer flow being swept up along the sideplate.

As the flow enters the cowl, Figure (7) shows that a shock wave is generated by the cowl lip. This shock, indicated by the horizontal lines in the Mach contours, moves down through the flow field as shown in Figures (8 and 9). The strong secondary flow moving up the sideplate encounters the internal cowl surface and the secondary velocity vectors indicate that this flow turns through the corner formed by the cowl and sideplate. Figures (8 and 9) show that two things happen as the secondary flow turns this corner; first, the secondary flow rolls up into a vortex, and second, the low energy flow is concentrated in the corner. The internal surface of the cowl has been shaped to further compress the flow. As the low energy flow in the corner is subjected to the adverse pressure gradient created by this turning, a large separation occurs.

The last calculated cross-section is shown in Figure (9). The shock from the cowl is about to hit the ramp surface, while the large separation region exists in the corner. The secondary flow has rolled into a vortex near the sideplate, while along the ramp flow continues into the corner. Figure (10) shows another view of the ramp flow near the inlet cowl. This figure shows oil flow results from a subscale model of the inlet which was tested at NASA Lewis. The oil flow indicates that the flow near the ramp surface is drawn in towards the sideplate. This figure shows velocity vectors on the surface of the ramp from the third ramp to the cowl. In the lower left corner of the figure the computed velocity vectors near the ramp surface are shown. The velocity vectors also indicate that flow is drawn in toward the sideplate because of the GSBLI. This is the first

qualitative verification of the results of the Mach 5.0 inlet study.

Normal Shock Wave Turbulent Boundary Layer Interaction

As part of a continuing code verification effort at NASA Lewis, the three-dimensional normal shock/boundary layer interaction is being studied both analytically and experimentally. In this study, a normal shock is formed in the constant area, square cross section, test section of a wind tunnel with free stream Mach numbers of 1.3 and 1.6. The normal shock interacts with the boundary layers that have grown on the tunnel walls; the pressure rise across the shock is felt upstream through the subsonic part of the boundary layer, the boundary layer thickens and in some cases separates from the wall. The normal shock in the vicinity of the wall is lamda shaped, with the flow passing through two oblique shocks instead of the single normal shock. In some cases, this can produce a supersonic tongue region downstream of the normal shock and near the tunnel wall. The thickening of the boundary layer can also cause reacceleration of the flow to supersonic conditions and formation of multiple normal shocks.

Because of the mixed supersonic/subsonic nature of the flowfield in the normal shock/boundary layer interaction, and because of the possible large recirculation region, a full Navier-Stokes calculation of this flowfield is required. In the present study, a time dependent linearized block implicit scheme has been time marched to a steady state solution of the normal shock/boundary layer interaction problem. In the preliminary stages of the study, the calculations have been performed two-dimensionally on 30x60 grids, on the Lewis Cray-XMP. These studies will be extended to much finer grids and three dimensions on the Cray 2. Two cases have been run; one at Mach number 1.3 and the other at Mach number 1.6. In both cases the initial conditions were uniform free stream flow with a turbulent boundary layer profile near the wall equal in thickness to the measured experimental upstream thickness. The incoming conditions were then held fixed, while the downstream pressure was set equal to the normal shock static pressure rise. This caused a normal shock to be formed near the exit of the computed flowfield. This shock moved upstream, interacting with the boundary layer on the wall until it finally stabilized near the middle of the computational flowfield. No slip boundary conditions were applied along the wall, symmetry conditions along the upper boundary, and extrapolation conditions, except for pressure, along the exit. The solution was time marched until the magnitude of the residuals was less than 10-04.

The results of the calculations are compared to experimental results in Figures (11 and 12). Figure (11) shows Mach number contours for free stream Mach number 1.3. The calculated results are shown in the upper half of the figure, while the lower half shows experimental LDV results. The shock location is noted by the vertical and contour lines, the flow is from left to right, and the wall boundary layers are indicated by

the contour lines at the top and bottom. The comparison between calculated and experimental results is quite good; the boundary layer is seen to thicken downstream of the shock, the shock strength is correctly modelled, and the calculations correctly indicate no flow separation in the vicinity of the shock. A rather weak lamda is formed both analytically and experimentally at the foot of the normal shock. When the free stream Mach number is increased to 1.6, the flowfield appears as in Figure (12). Again the calculated two-dimensional results are in the upper half of the figure while the LDV results along the tunnel centerline are given in the lower half. Upstream of the normal shock, the comparison between analysis and experiment are quite good; the analysis correctly predicts flow separation beneath the shock and correctly predicts the shape, height and upstream extent of the lamda at the foot of the shock. Downstream of the shock, however, the experiment indicates that the flow is reaccelerated to supersonic conditions and forms an additional weak normal shock, while the analysis does not predict this behavior. Additional oil flow results from the experiment show that there are large separation regions in the corners of the test section which introduce important three-dimensional effects. These three-dimensional effects are not currently modelled in the two-dimensional analysis; it is hoped that the Cray 2 calculations will better agree with the experimental results.

Subsonic S-Bend Diffuser with Vortex Generators

The flow in a diffusing S-bend duct with vortex generators has been studied both computationally, Ref (6) and experimentally, Ref (7). Figure (13) shows a schematic drawing of the 30 degree-30 degree diffuser. The flow in this duct was turbulent with a Mach number of 0.6 and a Reynolds number based on the duct diameter of 1760400. The initial conditions were measured at 1.65 duct diameters upstream of the first bend to remove the influence of the bend on the static pressure. The initial boundary layer thickness was 0.1 times the initial duct radius and the area ratio was 1.51. Without the vortex generators present, a large flow separation is detected in the diffuser both analytically and experimentally because of the high degree of offset and shortness of the diffuser. To remove this separation, three pairs of vortex generators were placed in the duct at the location noted in the figure.

The flow in the S-bend diffuser was computed using a three-dimensional PNS analysis. The standard analysis was modified to include a model of the vortex generators which accounted for both the vorticity and drag of the devices. This model was verified for benchmark configurations before being applied to the diffusing S-duct. The computations were performed on a 50x50 cross section with 100 streamwise stations and required less than six minutes cpu time on the Lewis Cray-XMP.

Figures 14(a) and 14(b) show the computed and experimental total pressure coefficient in the S-bend for the vortex generator configuration described above. The maximum and minimum values

are shown at each streamwise station. At the theta = 15 degrees point the effect of the vortex generators is evident in the contours. The computed results compare qualitatively well with the experimental results. In both set of contours the distortion caused by the generators is pushed toward the outside of the first bend opposing the pressure driven secondary flow. Although Figures 14(a) and (b) still show a very distorted flow, the difference between the maximum and the minimum values is much less here than in the duct without vortex generators. Figures (15) and (16) show the secondary flow development at the inflection plane and at the duct exit. In the experimental results at the inflection plane, the vortex due to the pressure driven secondary flow has washed out the vortices from the vortex generators except near the inside of the first bend. The contour plot indicates that in this region there may still be some interaction between the vortex generator vortex and the one induced by the pressure difference. The computed results at the inflection point show that all of the vortices have been washed out by the pressure driven secondary flow. At the exit of the bend both the experimental and computed results indicate less secondary flow into the outside of the second bend than without the vortex generators. Also near the walls they indicate more flow back toward the inside of the second bend. The experimental results show a higher level of flow toward the outside of the bend in the core flow than do the computed results.

CONCLUSIONS

A survey of supercomputer calculations of internal flows which have application towards aerospace propulsion systems at the Lewis Research Center have been presented. These calculations require large amounts of computer storage and the high computational speeds which are currently available only on supercomputers. In each of the cases presented, supercomputer analysis was able to properly model physical phenomenon seen experimentally. The need to resolve critical interactions within aerospace propulsion systems and the desire to analyze more complex flowfields are driving the need for supercomputers.

REFERENCES

1. White, M. E., Drummond, J. P., and Kumar, A., "Evolution and Status of CFD Techniques for Scramjet Applications," AIAA Paper No. 86-0160, January 1986.

2. Knight, D. D., "Improving Numerical Simulation of High Speed Inlets Using the Navier-Stokes Equations," AIAA Paper No. 80-0383, January 1980.

3. Campbell, A. F., and Forester, C. K., "Evaluation of a Method for Analyzing the Aperture Region of Two-Dimensional External Compression Inlets," AIAA Paper No. 85-3072, October, 1985.

4. Anderson, B. H., "Three-Dimensional Viscous Design Methodology for Advanced Technology Aircraft Supersonic Inlet Systems," NASA TM 83558, January 1984.

5. Benson, T. J., "Three-Dimensional Viscous Calculation of Flow in a Mach 5.0 Hypersonic Inlet," AIAA Paper No. 86-1461, June 1986.

6. Kunik, W. G., "Application of a Computational Model for Vortex Generators in Subsonic Internal Flows," AIAA Paper No. 86-1458, June 1986.

7. Vakili, A. D., Wu, J. P., Liver, P., and Bhat, M. K., "Flow Control in a Diffusing S-Duct," AIAA Paper 85-0524, March 1985.
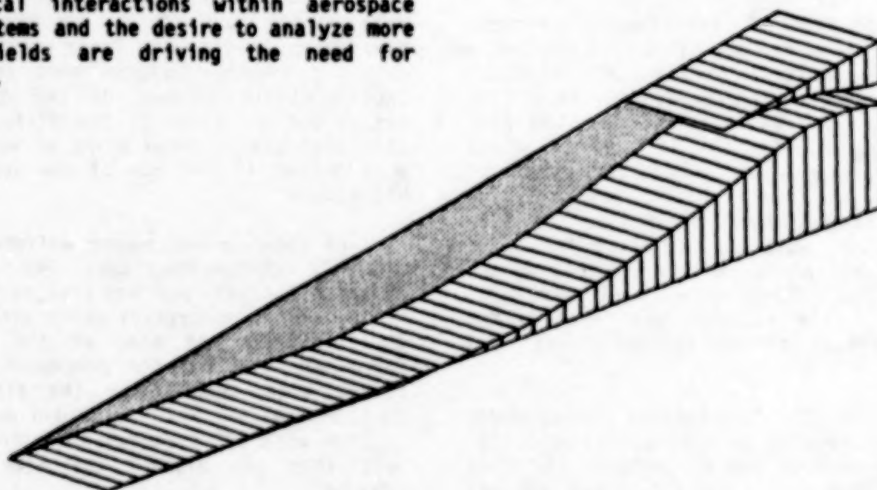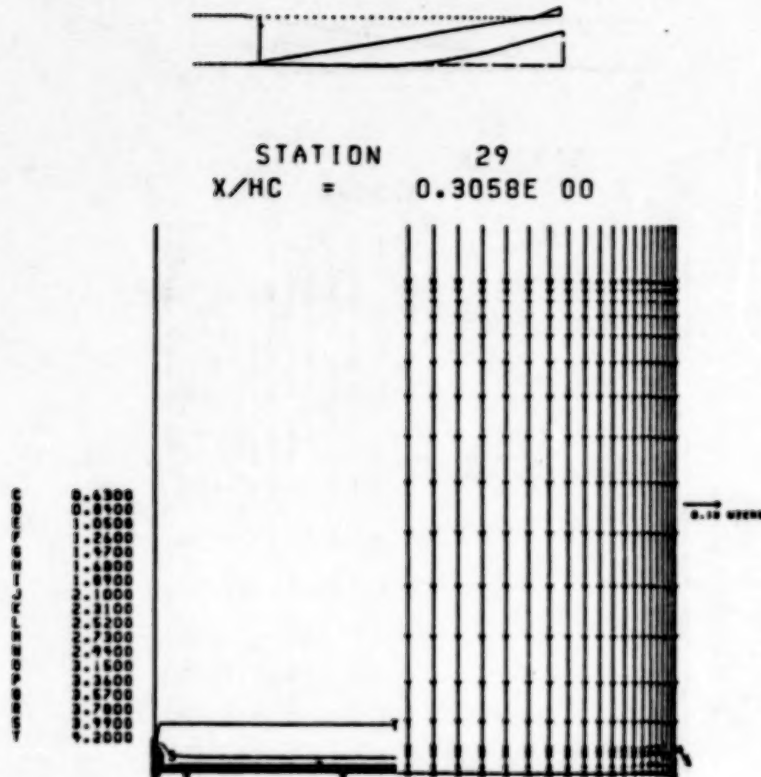
Figure 1. — Mach 5.0 hypersonic inlet geometry

Figure 2. —Mach number contours and secondary velocity vectors on pre-compression ramp
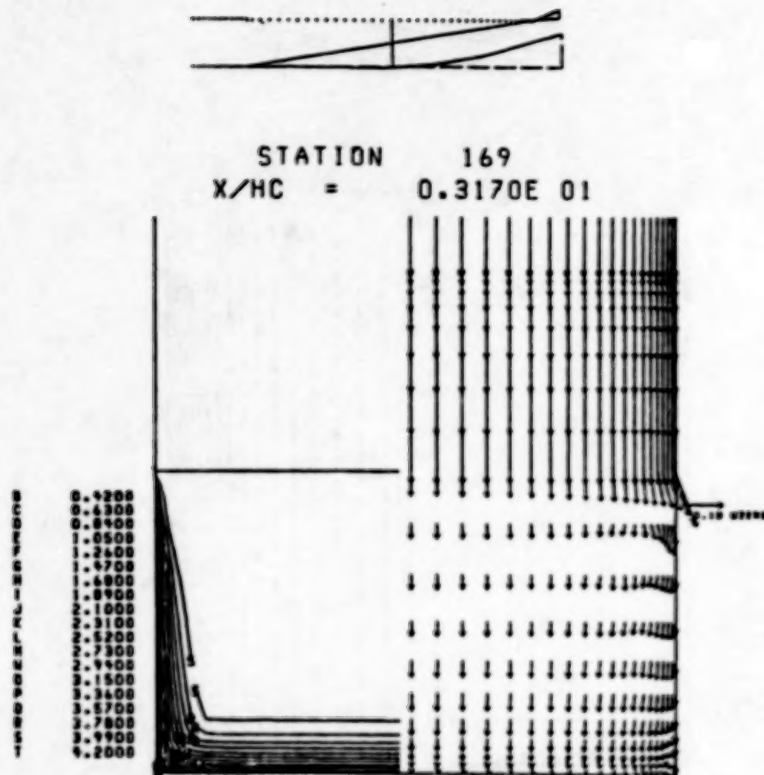
Figure 3. –Mach number contours and secondary velocity vectors before first ramp
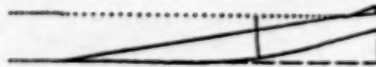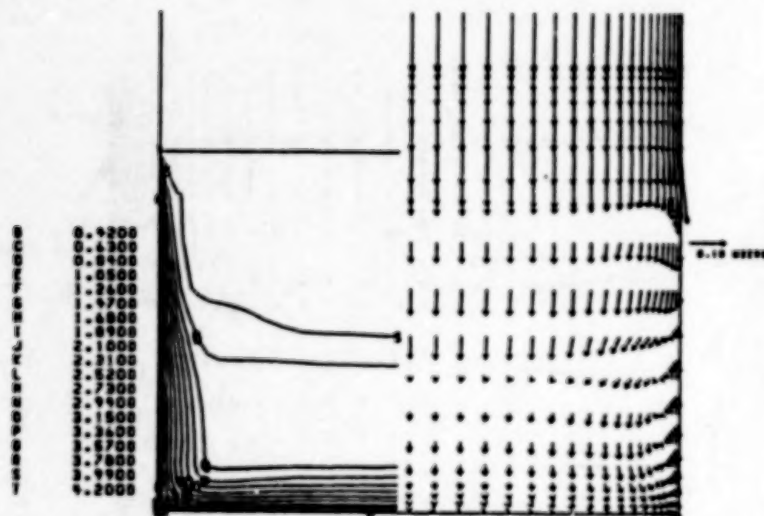
Figure 4. —Mach number contours and secondary velocity vectors aft of first ramp.

STATION 289
X/HC = 0.5345E 01
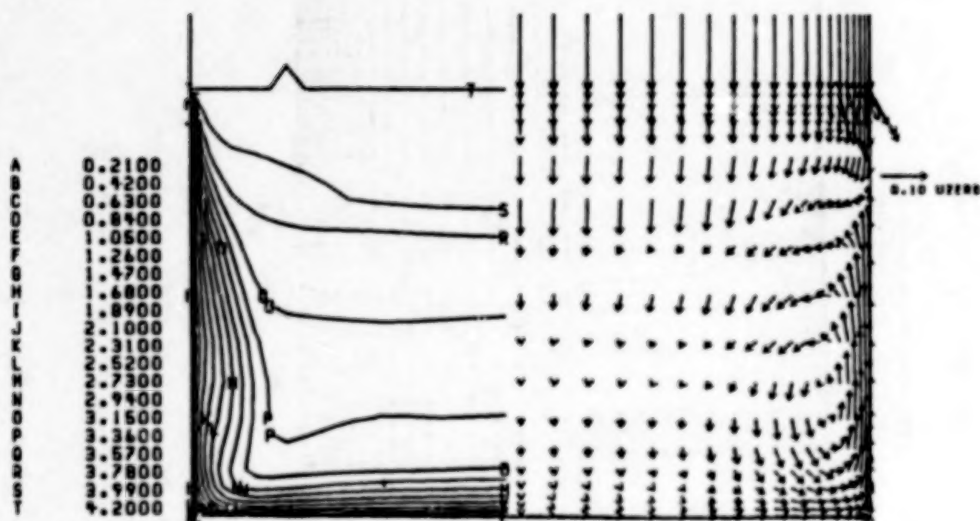
Figure 5. —Mach number contours and secondary velocity vectors
aft of third. ramp.
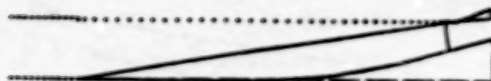
STATION 369
X/HC = 0.6158E 01
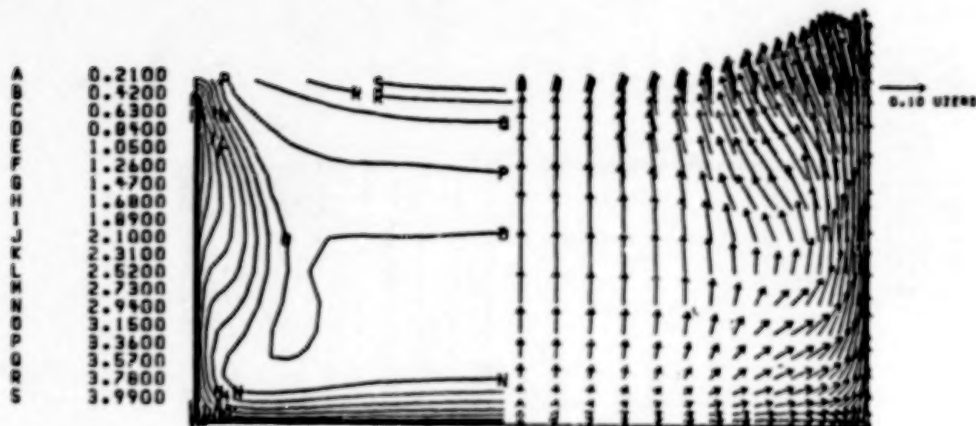
Figure 6.–Mach number contours and secondary velocity vectors
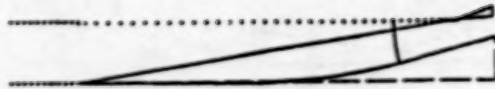before cowl lip.
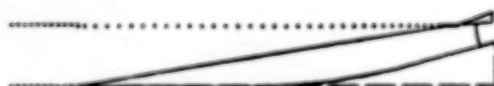
STATION 549
X/HC = 0.6655E 01
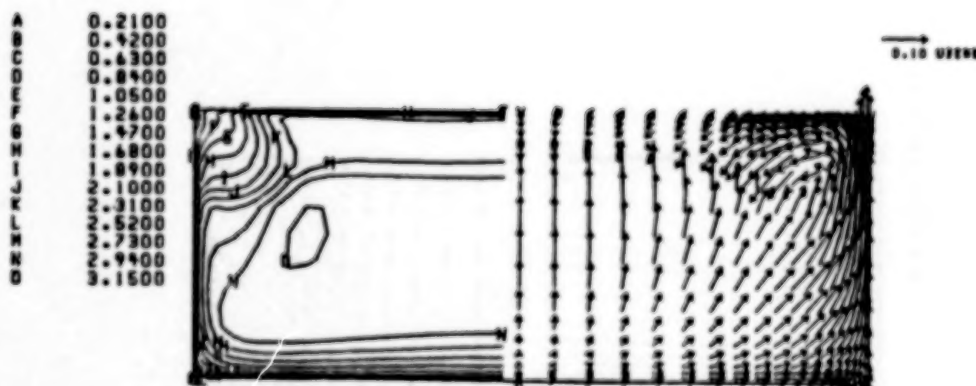
Figure 7.–Mach number contours and secondary velocity vectors
aft of cowl lip.

43

STATION 589
X/HC = 0.6802E 01
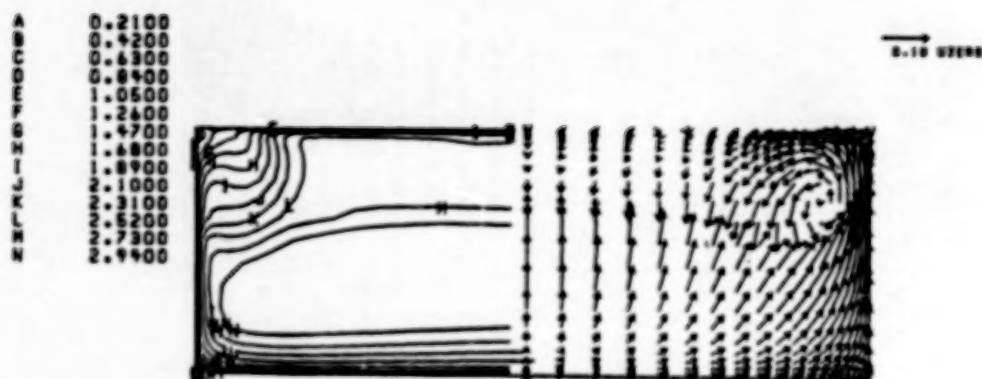
Figure 8. —Mach number contours and secondary velocity vectors
for 3D inlet calculation.

STATION 629
X/HC = 0.6887E 01
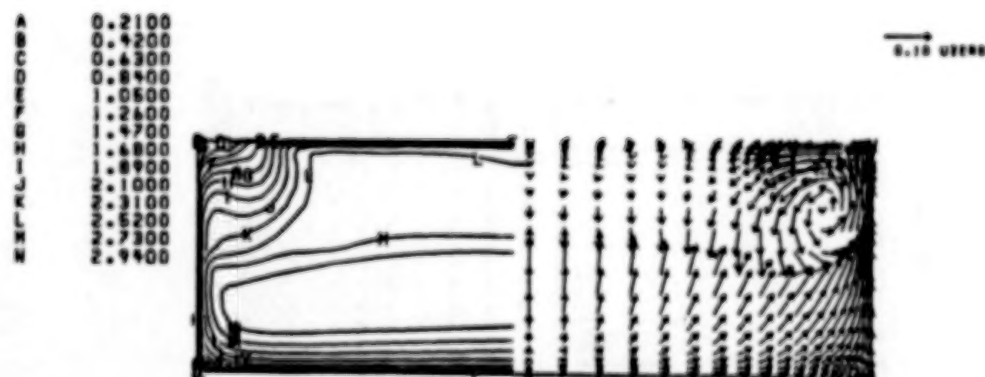
Figure 9. —Mach number contours and secondary velocity vectors
at corner separation.

44
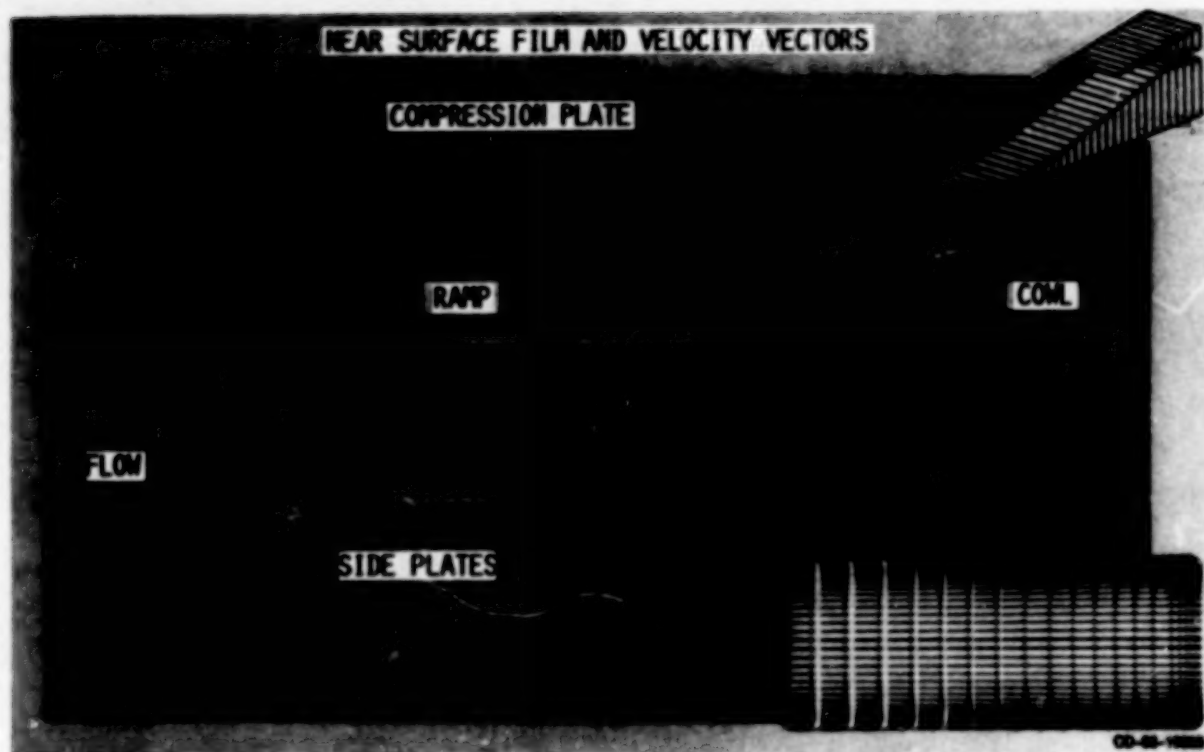
Figure 10. Surface oil flow and calculated velocity vectors for inlet ramp surface.
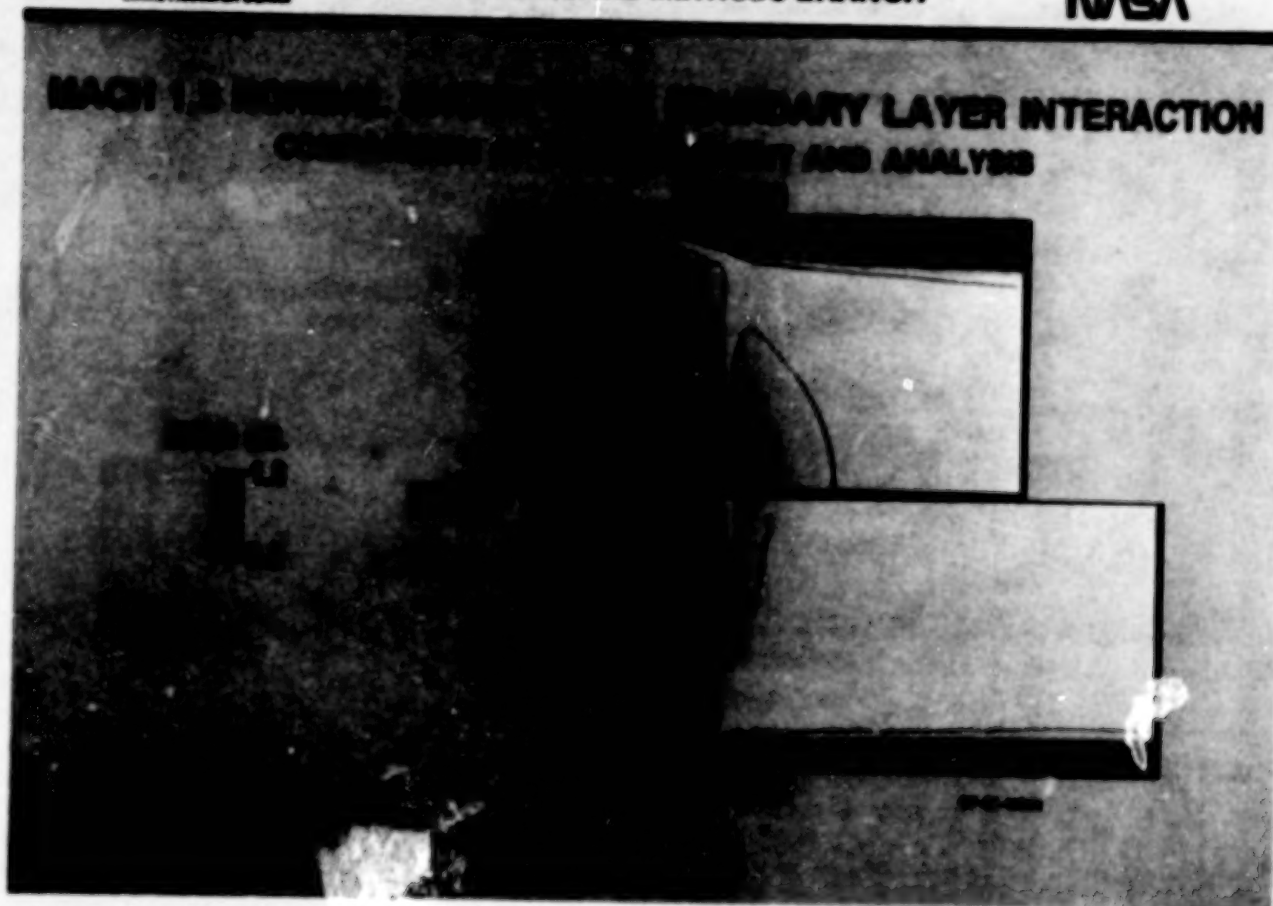
Figure 11. Comparison of experiment and analysis for Mach 1.3 normal
shock boundary layer interaction

MACH 1.6 NORMAL SHOCK WAVE BOUNDARY LAYER INTERACTION

COMPARISON OF LDV EXPERIMENT AND ANALYSIS
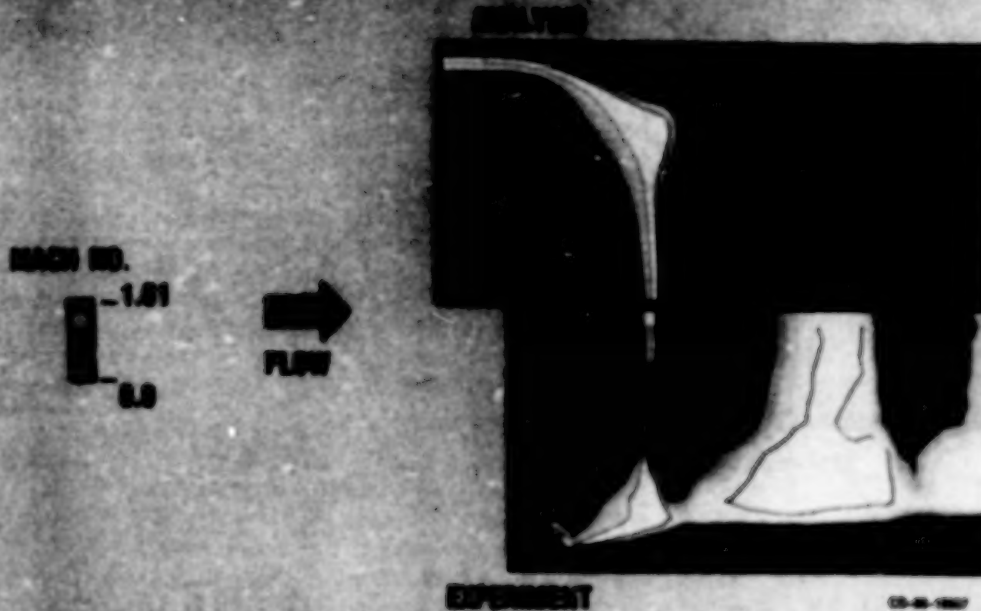
Figure 12. Comparison of experiment and analysis for Mach 1.6 normal
shock boundary layer interaction

Figure 13. - Schematic of diffusing S-duct showing the axial location of
the vortex generators.

(a) Computed total pressure coefficient contours for S-duct with v. g.'s.

(b) Experimental total pressure coefficient contours for S-duct with v. g.'s.

Figure 14.

EXPERIMENTAL RESULT

COMPUTED RESULT

Figure 15. – Comparison of secondary flow at the inflection plane for S-duct with v. g.'s.

N87
26003

YESTERDAY, TODAY, AND TOMORROW--A PERSPECTIVE OF CFD
AT NASA'S AMES RESEARCH CENTER

Paul Kutler[*] and Anthony R. Gross[†]
NASA Ames Research Center

I. ABSTRACT

This paper affords the opportunity to reflect
on the computational fluid dynamics (CFD) program
at NASA's Ames Research Center--its beginning, its
present state, and its direction for the future.
Essential elements of the research program during
each period are reviewed, including people, facil-
ities, and research problems. The burgeoning role
that CFD is playing in the aerospace business is
discussed, as is the necessity for validated CFD
tools. The current aeronautical position of this
country is assessed, as are revolutionary goals to
help maintain its aeronautical supremacy in the
world.

II. INTRODUCTION

The discipline of computational fluid
dynamics (CFD) at NASA Ames Research Center has
been a mainstay in its research program for over
15 years, and is predicted to remain so well into
the next century. It is a technical discipline
that was nurtured at Ames and has experienced
considerable growth as a result of its demon-
strated potential to aid in "building a better
plane." It has received considerable support from
local senior management and leaders from NASA
Headquarters. The Numerical Aerodynamic Simula-
tion (NAS) Facility is testimony to that fact.

In the following sections the past, present,
and future of CFD at Ames is discussed. In each
of those sections, some of the research efforts
and scientists are mentioned. In addition, the
facilities at their disposal for carrying out
their research are discussed. In the section on
Tomorrow, in addition to the planned research
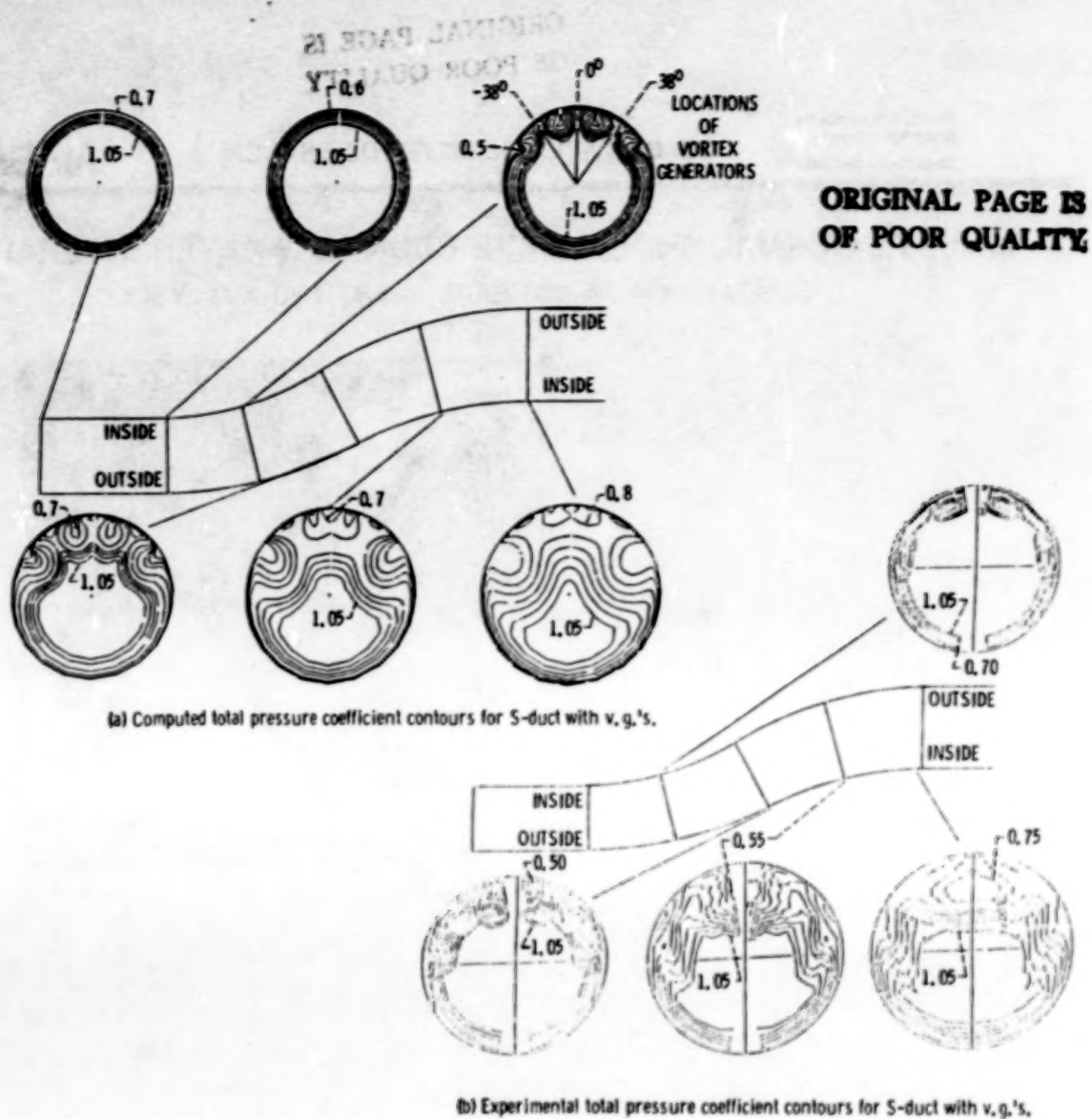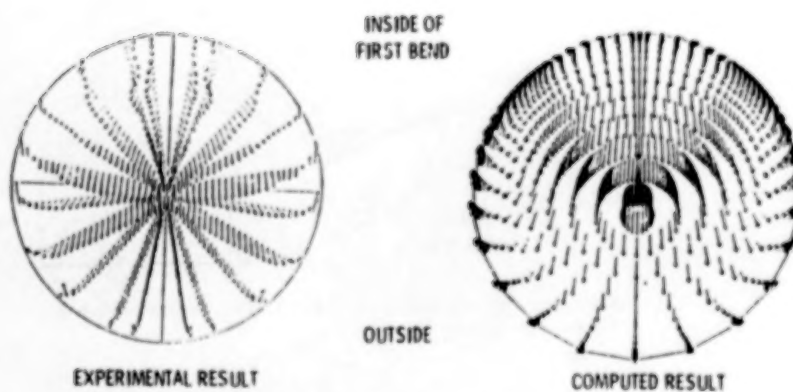program, a discussion is presented on CFD valida-
tion, computer technology, and artificial
intelligence.

In the Concluding Remarks section, NASA's
role in fluid dynamics is discussed and an assess-
ment on our country's current aerospace industry
is made. National aeronautical goals that should
challenge the aerospace engineer for many years
and keep this country in a lead position are
reiterated.

---

[*]Chief, Fluid Dynamics Division.
[†]Deputy Chief, Fluid Dynamics Division.

III. YESTERDAY'S ACCOMPLISHMENTS

Computational fluid dynamics at Ames Research
Center dates back to the days when mechanical
calculators were used by computationalists to
arduously and meticulously obtain results to very
simple (by today's standards) linear aerodynamics
problems. This period occurred before CFD was a
formal program at Ames and therefore will not be
discussed. We would, however, like to begin the
history review in the fall of 1968. At that time
two Ames scientists, Harvard Lomax and Harry
Bailey, were developing research tools for the
analysis and application of computer software to
simulate fluid flows. At the same time and with
help from many others, they were assembling a
hardware system for executing and visualizing the
CFD software they were developing.

Their computer hardware at the time included
an IBM 1800 (arriving at Ames circa 1968) linked
with an IBM 2250 cathode-ray display device. Also
available, but not in an interactive mode, was an
IBM 7094 (circa 1962) for performing calculation
in a batch mode. The beauty of the IMB 1800/2250
complex was that it was an interactive system on
which the users could display their calculations
while the calculations were being computed and
interact with the computer to modify parameters
such as the mesh size, step size, or smoothing
constants. Instabilities in the numerical solu-
tion that were observed could be instantaneously
ameliorated. The disadvantage of the system, of
course, was its speed and storage limitations (in
that regard things haven't changed much).

In the fall of 1968, two graduate students
(Joseph L. Steger and Paul Kutler), from Iowa
State University under a cooperative arrangement
with NASA Ames, joined the ranks of the Theoreti-
cal Branch led by its Acting Branch Chief,
Dr. Vernon Rossow. Mentored by Lomax and Bailey,
both students studied the discipline of CFD and
developed research projects to be used for their
dissertations. Steger studied relaxation algo-
rithms, their analysis, and their application to
transonic flows while Kutler studied explicit
algorithms and their application to supersonic
flows.

The potential of CFD as an analysis and design tool was recognized by senior management, and the discipline flourished at NASA Ames. Other students, such as F. R. Bailey and W. F. Ballhaus, Jr., studied the discipline and performed pioneering work. They were followed by many others who performed original applications or developed innovative procedures in CFD. Similar student programs exist today and continue to benefit the laboratory.

The computational facilities were constantly being upgraded as a result of management's belief in the discipline. The IBM 360-67 (circa 1969) was a milestone in Ames' CFD program because it could be directly linked with the IBM 2250 to provide the computer power and additional storage needed to perform more complex flow-field calculations.

This method of operation--namely, interactive computer graphics--was an enormous time-saver, especially in the early days of CFD, when there was such a large parameter space to explore. Research that would normally take a week to do by reducing data from computer paper output took a few hours on the interactive system. However, the disadvantage of this method of operation was that the developed software was not easily portable and required major modifications before it could be disseminated to outside users.

The information generated by the CFD scientists at Ames was sometimes displayed in the form of movies not only for scientific analysis, but also for presentation at technical meetings. Movies were shot directly from the screen of the IBM 2250 by an ingenious device conjured up by Lomax. The screen was shrouded in a black cloth with the camera mounted on a tripod at one end. The room was darkened, and the computer tripped the camera lens. It worked, and it provided some of the first CFD flow-field movies. This procedure was later refined to include a fiberglass shroud, and color was added by taping different colored plastic overlays on various parts of the monochrome screen.

An ambivalent time in the lives of the CFD scientists at Ames occurred when the CDC 7600 arrived (circa 1974). On the one hand, it provided computational relief because it was a much faster machine, but on the other hand, it meant that they could no longer run interactively, and that their computer codes had to be converted to operate in a batch mode.

The arrival of the Illiac IV (circa 1972) produced a traumatic time for some CFD scientists and a challenge for others. It introduced a completely new computer architecture, i.e., parallelism. It was unique with its 64 processors operating in parallel, each with the speed of a CDC 6600, and it was the first "Class VI" machine for Ames. Input and output on the Illiac was difficult at best, with little or no debugging capabilities. Hardware failures were many. It

required calculation checks to validate its own accuracy (two-thirds of the processors were used to check the other third). The Illiac IV (parts of which now reside in the Smithsonian Museum in Washington, D.C.) was finally replaced by the Cray 1-S (circa 1982). That was followed by the Cray X-MP/22 (circa 1984) and the Cray X-MP/48 (circa 1986).

In the formative stages of the CFD effort at Ames, the research program consisted of both theoretical and applied elements. The theoretical efforts involved the development and analysis of numerical algorithms for solving the fluid dynamic equations. The applied program involved the solution of those equations on practical aerodynamic problems.

Much of the early theoretical research involved the development of CFD methods and techniques that could handle difficult flow regions, such as transonic speeds, unsteady flows, shock-wave/boundary-layer interaction flows and shock interaction flows. MacCormack[1,2] developed a number of algorithms and techniques that were quickly accepted and widely used, including a simple, explicit, predictor-corrector scheme, and one of the first Navier-Stokes solution algorithms. Steger[3,4] developed relaxation procedures for solving the transonic potential equation. Beam and Warming[5,6] developed an implicit approximate factorization algorithm that has been the basis for many of the present day operational codes. Lomax,[7,8] in addition to his leadership of the CFD group, made many important, pioneering contributions to the development of CFD, including numerical algorithms and analysis procedures for evaluating newly developed algorithms. Holst[9-12] developed a shock-interaction procedure, a method to simulate boattail flows, and one of the first practical airfoil and wing transonic full-potential codes (TAIR and TWING).

When the Illiac IV arrived at the Center, with its 64 parallel processors, Rogallo[13] developed a programming language called "CFD" for this radically different machine that made programming it similar to programming in FORTRAN. In addition, he developed fast-Fourier-transform schemes for it and one of the early large eddy simulation (LES) codes.

There were many important problems that were solved using CFD on these early machines; problems that were instrumental in establishing CFD as a contributing analysis tool and problems that helped mature CFD into a demonstrated and useful technology. Two important problems that helped to establish CFD as a tool that could be useful in solving practical aerodynamic problems were the modification of the highly maneuverable aircraft technology remotely piloted research vehicle (HiMAT RPRV) and the redesign of the North American Sabre 60 wing. In both of these cases, the Bailey-Ballhaus Transonic Small-Disturbance-Steady-Flow Code[14] was used to achieve designs

that met performance requirements where conventional methods had previously been unsuccessful, and with considerable cost savings relative to those methods.

Another important CFD problem that demonstrated the usefulness of CFD and resulted in a considerable savings to the government (by eliminating the need to redesign the SPRINT antiballistic missile system) was the three-dimensional shock-on-shock problem solved by Kutler[15] using his patented "shock-capturing technique." In addition, Kutler[16-18] developed several codes and techniques that have been widely used, including inviscid codes for prediciting sonic booms about simplified configurations and flows about such supersonic configurations as the Space Shuttle, and viscous codes for treating supersonic blunt bodies. He also developed a code for analyzing the flow through an advanced propeller called the prop-fan. His code for determining the flow field about the Space Shuttle Orbiter was a major step forward in establishing CFD as a viable analysis tool.

IV. TODAY'S PROGRAM

Today the capability of CFD to effectively and accurately simulate the complexities of fluid flows of practical interest has grown tremendously relative to the capability of even a few years ago, and stands as a testament to the ingenuity and imagination of both the computer system developers and the CFD scientists. A few selected examples will demonstrate the great strides that have been made in recent years, and help illustrate the present state of the art in CFD at Ames.

In 1981, researchers recognized that the building blocks for a three-dimensional Navier-Stokes code existed and that an organized effort could produce a demonstration calculation about a complex configuration. They selected the F-16A fighter was selected as the target for a full, three-dimensional, transonic computation. Its geometry was complex and during maneuvers it would generate interesting fluid physics. A group was formed led by Holst that simultaneously addressed the geometry, grid development, and flow-solver problems necessary to simulate the flow about this configuration. The key problems were 1) how to divide the flow field into subelements that were small enough to be tractable to the existing computer system, 2) how to organize and manage the massive amount of information that would be generated by such a calculation, and 3) how to display the results in a manner usable to the CFD scientist. The Calma CAD/CAM system was used to develop the computer geometry, with data supplied by General Dynamics. Using the Ames ARC3D flow code as a basis, and the concepts of the two-dimensional GRAPE grid genration code, the flow field was divided into 16 separate zones to facilitate the initial computations on the Cray X-MP/22 computer.

Present computations are done on the Cray X-MP/48, a much larger and faster machine. A key advance was made during this program with the development of a boundary-condition procedure for the efficient transfer of information across each zonal boundary within the flow field. Significant efficiencies were introduced into the flow-solver coding, including accelerating the convergence of the basic algorithm by a factor of 40. Typical results are shown in figures 1 and 2. Figure 1 shows the grid system developed for the F-16A, and the flow-field results are shown in figure 2. Notice the great detail in the separated flow regions on the wing, resulting in a simulation that compares well with wind tunnel experiments.

The problem of simulating the flow about multiple moving bodies was a difficult one, and one whose solution provided the basis for many important applications. Computationally simulating such a flow usually involves one grid system moving relative to another, with the attendant requirement that information be passed across the interface boundary in a time-accurate basis. Rai[19,20] developed such a solution procedure that has resulted in the ability to simulate the flow through rotor-stator systems in two dimensions. The results have been spectacular in terms of visual and flow system detail. Figure 3 presents a simulation of the supersonic flow through a cascade of circular-arc airfoils, showing details of the shock and expansion wave interactions. This result was used on the cover of the March 25, 1985, issue of Aviation Week and Space Technology. In figure 4 the flow through a cascade of typical jet engine airfoils is shown, illustrating the detail to which the flow can be simulated. The use of present graphic workstation technology makes it practical to show the development of alternating trailing-edge vortices, and to show how these are propagated through the cascade system.

With the incentive to understand the fluid physics and to increase the thrust performance of the Space Shuttle Main Engine (SSME) without major modifications, thus resulting in a greater payload capability, a cooperative computational program with industry, was undertaken. This program resulted in the development of an incompressible Navier-Stokes code that could treat the complex internal geometry of the engine powerhead. Kwak,[21-24] beginning in 1981, developed a three-dimensional, incompressible Navier-Stokes code (INS3D) for that application that has provided an extensive low-speed simulation capability. Working with engineers from Rocketdyne (the builders of the SSME), researchers applied this code to simulate the flow within the hot-gas manifold, transfer ducts, and main injector of the SSME. It was determined that flow within the present three-duct design (fig. 5) was inefficient. A large, separated-flow region existed in the center duct,

and it was transmitting only 9% of the total flow. A proposed two-duct design showed significantly improved flow characteristics. As a result of this demonstration, it has been determined by Rocketdyne management that CFD simulation will be used to analyze all future SSME designs.

Using a parabolized Navier-Stokes code (PNS), Chaussee[25,26] has developed a flow-simulation capability for supersonic configurations, including the Space Shuttle Orbiter. This research program was also used to develop the first graphics application on the new Silicon Graphics IRIS workstations. The flow field about the Orbiter at reentry conditions is shown in figure 6, a picture that has appeared in many publications during the past year. The development and propagation of vortices are clearly shown, as is the flow along the surface. With present workstation capability it is possible for the computational aerodynamicist to carefully examine any selected aspect of the flow field, once a complete solution has been obtained.

Building on the PNS code technology, Rizk and Chaussee[27] extended the CFD simulation capability to hypersonic speeds and applied it to a configuration similar to that of the National Aerospace Plane (NASP). Figure 7 shows the pressure contours about a research configuration at Mach 25. Additional flow-field realism will be obtained by including real gas chemistry effects in the computations.

Modern aircraft wings, including those with tip stores, frequently show pronounced aeroelastic effects. Guruswamy and Goorgian[28-31] have combined a flow simulation code with a structural response code to develop an aeroelasticity simulation capability. It has been applied to the B-1 and F-5 aircraft wings. Typical results are shown in figure 8, where the pressure distributions for a wing with and without a tip missile are presented.

Turbulence, its formation and propagation, is not very well understood, and it is very difficult to predict for the fluid dynamicist. It is very important to be able to model the behavior of turbulence for use in Reynolds-averaged Navier-Stokes codes. With modern CFD software simulation tools in conjunction with the latest computer systems at Ames, the ability to computationally simulate turbulent flows is possible (i.e., for simple shapes and low Reynolds numbers). The program at Ames is the most advanced in the nation and possibly in the world. Both LES and direct simulation (DS) techniques are employed, with computations on three-dimensional grids taking about 100 hr of computer time. A typical result from an LES calculation by Kim and Moin[32,33] is shown in figure 9, which depicts a horseshoe vortex.

The CFD scientists at Ames have been fortunate in having easy access to some of the best computational facilities in the world. These facilities have included advanced supercomputers, graphics workstations, and a myriad of support systems, such as a VAX farm to serve as front- and back-end processors for the supercomputer solutions, and personal computers and modems to permit maximum flexibility in accessing the main computer systems.

The Central Computer Facility (CCF) provides a wide range of support for CFD scientists, from supercomputer systems to individual terminals, graphics support, and communications support. The present CCF consists of two supercomputers, a number of DEC VAX advanced minicomputers, and many smaller supporting systems. The supercomputers include a Cray X-MP/48, with four processors and 8 million 64-bit words of memory, and a CDC Cyber 205, which is a four-pipe machine with 8 million words of memory. The Cyber 205 was installed in June 1984, and has been extensively used by the turbulence physics researchers and the computational chemists. Data storage systems are an important part of the computational facility, and have been growing steadily in size and speed to support the new supercomputer systems and the new, more complex problems. For example, there is a 128-million-word solid-state disk (SSD) connected to the Cray X-MP that greatly enhances the practical size of problems that can be solved. In addition to the computational facilities, Ames research scientists benefit from a management policy that provides maximum access to the machines, without regard for individual program funding. It is a true Centerwide resource, available to everyone. The result of this policy is an open-access system, with a greater opportunity and incentive for innovation and the encouragement to experiment with new ideas.

In addition to the CCF capability, Ames has been chosen as the site of the NASA Numerical Aerodynamic Simulation (NAS) program. The NAS program is a national computing system that is designed to provide a large, fast computational system dedicated to solving aerospace problems. It will also serve as a pathfinder in the development of advanced-numerical-simulation technology and techniques. The governing concept is to remain at the leading edge of research computers by utilizing a continuing series of high-speed processors (HSP), each to be the prototype of the latest available technology, which will ensure availability for the scientists of the maximum computational capability. Through a network of satellite and land lines, researchers from all over the country can access this new capability. A new 90,000-ft² building has been constructed to house the NAS system and the CFD scientists who will use that capability at Ames. The first HSP, HSP-1, is the Cray 2, with a sustained operating speed of 250 Mflops, 256 million words of memory, and over a gigabyte of mass storage. It has been operational since July 1986. The second HSP is planned to be installed during 1987.

In addition to the advanced "number-crunching" capability, and the extensive communications network, computer graphics has been recognized as a critical element in the present numerical simulation process. Such tasks as developing the geometry for a complex configuration, building a multizone, three-dimensional grid system, and examining the details of a complicated flow solution, require a high-resolution, high-throughput graphics capability to most effectively exploit both the computer system and the scientists' creativity. A large number of state-of-the-art graphic workstations have been provided to the Ames scientists to both display computed results and to develop advanced graphics software. The Silicon Graphics IRIS workstation is the most common example, with upgrades being installed as they become available.

Finally, Ames utilizes a large number of ancillary systems to both support and augment the main computing systems and the work of the CFD scientists. These include both front and back-end processors to facilitate the solution procedure, as well as "smart" and "dumb" terminals to interface with the CFD scientists. A VAX farm, using both VAX 11/780-785 and VAX 8650 machines, serves as the pre- and post-data processors. Personal computers and dedicated VAX terminals serve the interface function, in addition to the IRIS graphics workstations. Finally, modems are provided to those who wish to augment their normal working time with time at home, using either their own computer, or one borrowed from their office, which permits them to connect to the Ames computer system.

V. TOMORROW'S RESEARCH PROGRAMS

NASA Ames has a vision labeled "Computation to Flight" that will govern the CFD research performed at the Center:

"Ames will be known for its capabilities in computational analysis, experimental investigations, flight simulations and flight testing, and will be acknowledged as the lead Center in the integration of these capabilities into a technology for the design of aerospace vehicles. This integrated capability will also be used to advance basic aerodynamics science, particularly the understanding of those real fluid- and aero-dynamic phenomena that determine component and total configuration performance."

In support of that vision, Ames has defined various "targets of opportunity," i.e., a set of more refined statements of the future, expressed in terms that are measurable. These targets have been divided into three categories: 1) integrated programs, 2) aerodynamic science, and 3) research

tools. Short descriptors for the targets in the three categories include: under 1) integrated programs such areas as high-angle-of-attack aerodynamics (HARV), circulation control (X-Wing), powered lift (ASTOVL), and hypersonics (NASP); under 2) aerodynamics science such areas as turbulence, viscous flows, chemically reacting flows, unsteady aerodynamics, advanced rotorcraft, space technology, and interdisciplinary physics; and under 3) research tools in such areas as algorithm enhancements, advanced computational/ experimental facilities, and advanced instrumentation.

Most of the projects under "integrated programs" satisfy the five criteria used to determine whether or not Ames embarks on a CFD research program, i.e., 1) is the problem of national importance, 2) will its solution lead to a new design tool, 3) will it aid the understanding of complex fluid physics or the discovery of new flow phenomena, 4) will it push the state of the art in computational fluid dynamics, and 5) is the problem tractable in a finite amount of time.

Three important areas that are addressed in this section and will support the planned research programs mentioned above include CFD validation, computer technology, and artificial intelligence. A perspective of each is presented below.

CFD Validation

Computational fluid dynamics is experiencing greater visibility by the aerospace community as a tool to aid in the aerospace vehicle design process. Along with its acceptance comes the requirement by the users for validation, i.e., a measure of the accuracy of the results produced by the computer code and its range of validity. Because of this understandable and justifiable requirement, CFD is beginning to play a dominant role in stimulating validation experiments and in the development of advanced instrumentation for extracting validation data.

The aerospace research community is undergoing a cultural change. In the past, computationalists and experimentalists worked somewhat autonomously. The experimenters performed their experiments to understand the fluid physics or obtain design information and compared their data with available theory, while the computationalists performed their calculations and compared their results with available experimental data, theory, or other numerical results. This process involved little or no communication between the two camps. Anonymous was heard to say, "No one believes the analysis except the engineer who performed the calculations. Everyone believes the data except the engineer who performed the tests."

What is happening today is a result of the the need for validated computer codes by the aerospace community. The two camps are now beginning to work more closely together in an attempt to get not better experimental data, but the right

experimental data to validate the code. It is important that both concerns are treated as equal partners in this endeavor. Code validation is an evolutionary process. This cultural change, as any change, takes time, but it is happening, and the results should be enhanced CFD design tools.

Experiments are generally classified as building block, benchmark, or design. Design experiments or configurational experiments involve drag, lift, moment, heat-load, and shear-load measurements. Those measurements are obtained as close to the flight conditions as possible. Benchmark or parametrical experiments obtain surface quantities, flow-field quantities at selected locations, and the tunnel boundary conditions. These data are obtained by varying the Mach number, Reynolds number, and angle of attack over the flight range. Building block or phenomenological experiments measure surface quantities; flow-field quantities; turbulence (individual stresses, correlation lengths, structure); and boundary conditions. These data are taken at representative flight Mach and Reynolds numbers. Both benchmark and building block experiments are required for CFD validation purposes.

It is important that computational tools be validated to build the confidence of their users. This is best accomplished not only by performing experiments, but also by performing numerical tests. In general, a computer code's limitations are known to the author. These limitations are based in part on the equation set solved (small disturbance, Euler, parabolized Navier-Stokes, Reynolds-averaged Navier-Stokes, full Navier-Stokes) and the accuracy of the algorithm employed (steady or unsteady, explicit or implicit, first, second, or third order). From a computational point of view, grid refinement studies can be performed to determine error-prediction estimates. Code authors should specify the range of validity of their code and export them with those restrictions. These restrictions can, of course, be removed in time as the code's range of validity increases. For example, codes should be structured to readily accept new turbulence models and this flexibility increases their potential range of validity. In general, however, codes can never be fully validated.

There are various degrees of code validation that can inform the user as to a computer code's range of applicability. Dash[34] suggests four levels of validation. They include 1) basic operationality, 2) accuracy on unit problems, 3) accuracy on component problems, and 4) accuracy in predicting overall configuration performance. In the following description of the levels of validity, "a code" can refer to a single computer code or a sequence of computer codes necessary to analyze a given configuration (e.g., a blunt-body code plus a PNS code plus an unsteady continuation code for analyzing a hypersonic vehicle).

At the level 1 validation, obvious "bugs" have been eliminated from the code, the user can run the code for various generic problems (e.g., the user is familiar with the code parameters and grid-generation routines), and various ranges of operation of the code have been established. In attaining the level 1 validation stage, comparisons with similar code solutions for generic configurations are established, comparisons with alternate code solutions to establish limiting form validity and to validate approximations (e.g., PNS sublayer approximation) are made, and checks on conservation of mass, momentum and energy are performed.

At the level 2 validation, the parameters in the code required to analyze fundamental unit problems or standard test cases have been established and the user is knowledgeable on the use of the code for the analysis of realistic configurations. In attaining this level, different unit problems have been run for different component codes (e.g., blunt body or unsteady continuation) and the turbulence models and their thermochemical parameters have been modified to agree with the data.

At the level 3 validation, the code is capable of accurately analyzing the flow fields about realistic component configurations and predicting observed trends. This level of validation establishes the code as a design tool for use in parametric or trade-off studies to answer questions related to individual component performance. In attaining this level, realistic data are employed to assess the code's performance. These data must clearly define the initial conditions, geometry, and flow parameters, and must exhibit well-defined parametric trends that can imply correct performance of codes, but not validate details. Data such as those obtained from the design experiments mentioned above are appropriate.

At the level 4 validation, the code is capable of accurately analyzing complete configurations. This level establishes a coupled system of CFD codes called "a code" in the foregoing discussion that can be used as a design tool for evaluating overall configuration performance. In attaining this level of validity, realistic overall design data (i.e., performance data) are employed that exhibit the effects of the coupled system components.

Computer Technology

The demand for supercomputers to solve CFD problems at Ames and for a variety of other applications is exponentially increasing with time. The definition of a supercomputer is somewhat nebulous. On the lighter side, some say it is a machine that beats the fastest IBM currently available or one that performs an infinite loop in just 2 minutes. Scientists say it is a machine

that is just a bit too slow to solve their most interesting problem.

A plot of the speed of computers as a function of year since 1950 can be seen in figure 10 for various scientific machines (private communication, Landshut, West Germany, July 1986). In this figure the speed component is separated into that attributable to either the components or the architecture. As can be seen in the early years, component technology was the reason for enhanced speed. Since 1970, however, newer architectures have been responsible for increased computer speed. Future computers will be designed for specific problems in which circuit boards will be replaced, depending on the application to be run.

A computer's electronic components are mostly made of silicon. It is the most intensively studied of all materials and is the heart of the computer. Researchers say that silicon chips can be improved for another decade. Beyond that, however, they look to gallium arsenide chips, which transmit electrons faster, but are harder to work with.

It is clear that the world needs much more computer power than is available today. The computer industry produces the equivalent of one human brain per year. To perform human intelligence on the computer, the most difficult of all simulations, a computer with a speed of 1 trillion operations per second is required. It is believed that capability should be available in 40 years.

Laser technology will continue to have an impact on computer technology. Researchers are working on an optical computer that uses light to process information at a much faster rate than present systems that use electrical current. Lasers will continue to be used to advance data-storage technology devices.

If one were to envision future computer systems for computational fluid dynamics based on the discipline's current and future capability and its insatiable thirst for CPU cycles, one could imagine a "farm" of supercomputers. They would be collocated for economies of scale. As a problem arose requiring a supercomputer, e.g., the NASP, it would be assigned a computer from the bank of supercomputers. For efficiency of operation, the computer would be "tuned" to the problem it is solving and the user's requests. Unused cycles, of course, would run background jobs. Once the specific project using that supercomputer had been completed or the problem had been solved, the supercomputer would be assigned to another problem.

The computer is not discipline-dependent. Unlike experimental facilities that have a range of applicability, computers are not limited to a specific Mach or Reynolds number. If a discipline such as transonics, supersonics, or hypersonics matures, the supercomputer farm facility is virtually unaffected and can be used for other

simulations. This is in contrast to experimental simulation whose facilities could become idle and eventually "mothballed." The goal of CFD should not be to eliminate the need for experimental testing as was suggested in the past. The long-term goal of CFD should be simply to perform realistic flow simulations about aerospace vehicles and their components in order to predict performance. In the near term, CFD could eliminate the need for experimental testing of simple shapes and building block experiments and wind tunnel testing for aircraft at cruise conditions.

With improvements in both the software and hardware that exist today, it might be possible in the near future to actually fly an aircraft on the computer. Viscous flow codes exist today for simulating the flow about real aircraft, but they take a lot of time. The supercomputers are available, but they cannot compute the flow field fast enough to reflect changes in the aircraft's attitude and flow conditions for realistic visualization. Finally, the graphics display devices can depict the flow physics dramatically, but they must be made interactive with the supercomputer so that the user can control the aircraft's speed and behavior. With today's software and hardware technology, such a feat would be possible only for a two-dimensional airfoil and still portray a sense of realism.

Artificial Intelligence

The discipline of artificial intelligence (AI) has begun to play a role in some aspects of CFD, and promises to contribute to many additional aspects of CFD in the future.[35] AI is a branch of computer science concerned (from an engineering standpoint) with the study of how to program computers to do tasks at which humans are presently superior,[36] such as reasoning symbolically, understanding natural language, interpreting and understanding perceptual input, and applying common sense and/or expertise to problem-solving and decision-making. The automation of some CFD tasks, including geometry definition and discretization, code generation, code use to obtain a solution, and data reduction and interpretation, requires such capabilities.

Two areas within AI, computer symbolic mathematics and expert systems, are being applied to CFD problems with some success. MACSYMA, a symbolic mathematics program, has been used to analyze the stability and accuracy of numerical algorithms and to generate FORTRAN code from partial differential equations.[37,38] Expert systems, or knowledge-based systems, are AI programs which contain enough domain-specific knowledge (gleaned from experience as well as from textbooks) to enable them to perform at the level of a human expert in that domain. There are several first-generation CFD expert systems that have demonstrated the potential of this approach.[39] Among these pioneering efforts is a system that uses an

expert's heuristics to guide aerodynamic design of simple turbomachinery components,[40,41] a program which prepares the input parameters and aids in output analysis for users of the PANAIR linear aerodynamic design code,[42,43] a system embedded within an adaptive grid generator which performs the error recovery required by difficult cases,[44] and a system which partitions a two-dimensional flow field into well-shaped zones which are then individually discretized (in progress) (Andrew, A. E., unpublished work). These exploratory systems will provide the foundation for future generations of CFD expert systems. Use of the straightforward techniques will spread to many other areas within CFD, and the further development of the riskier techniques will enable more advanced applications.

One area to which application of present and future AI techniques may spread is intelligent data reduction, interpretation, and display. AI learning programs[45] may be of some use in detecting meaningful patterns in the vast amount of fluid dynamic data being generated both numerically and experimentally. Present software display packages are passive in that they display only what they are told to display, resulting in the possibility that interesting or undiscovered fluid physics might remain buried within the data. A system with knowledge of fluid dynamics and numerics might be useful in ferreting out flow phenomena (such as tertiary separation hidden in the confines of the high-resolution grid).[46]

The first step toward an experimental fluid dynamics counterpart to the intelligent data search described above has been taken in a project entitled "Smart Probe."[47] In this project, a conventional, computerized, probe-traversing mechanism has been augmented by a simple rule-based expert system to enhance its performance. The system locates regions of interesting fluid physics and homes in on those regions, probing each with increased resolution. With the same number of flow field samples, the enhanced system yields much better resolution of the flow phenomena of interest than the conventional system.

VI. CONCLUDING REMARKS

The future of fluid dynamics, both computational and experimental, is bright; it offers many challenges and should provide some exciting times. It is believed that most problems amenable for solution using validated CFD tools can be solved if the desire and resources are devoted to it. NASA's role in fluid dynamics will be to

1. Provide technology for industry when industry does not have the means.

2. Perform high-risk research that industry cannot afford to perform.

3. Perform basic computational fluid physics research to explain and discover flow phenomena.

4. Integrate the technologies of aerodynamic simulation, i.e., experimental, computational, and flight, to generate synergy that results in construction of a "better plane."

5. Work collaboratively with industry and universities to promulgate the technology.

6. As an added benefit, explore the application of CFD to other disciplines, e.g., fluids in space, medicine, hydrodynamics, automotive aerodynamics, etc.

It is important that NASA in its attempt to maintain its lead and remain a pioneer in the field of CFD phase out developed technologies and design new ones. Challenge breeds productivity in research scientists; communication speeds the process. It is management's duty to support the CFD scientist with the latest facilities, a good working environment, and the freedom to perform creative and innovative research.

The lead and preeminance that the United States enjoys in the commercial aircraft business is being challenged today by other countries. This is partially explained by the following: The intellect in fluid- and aero-dynamics in this country is not unique. This country's academic institutions and research laboratories have contributed immensely to the educational process of foreign scientists with the latest technology this country has to offer. The gap between the computing facilities of this country and the rest of the world is narrowing. The United States is no longer the sole manufacturer and owner of supercomputers. The Japanese are formidable competitors. Experimental facilities among competitive countries are on par with each other. Other countries realize the benefits of a strong aeronautical policy on their country's economics. According to Bulkeley,[48] pushing research is the only way the U.S. and other developed nations can maintain their economies because less developed nations will learn to produce less technically demanding materials and products.

It's not news that we live in an "information society." Computers are partly responsible for this glut of information. The management of this information is crucial to technological advancement in the aerospace business. With bigger and faster scientific computers on the drawing boards, validated CFD codes will generate enormous quantities of data on flows about aerospace vehicles and their components and hence play a much larger role in the design cycle of future aircraft. This country, with its CFD capability as a trump card, is in a good position to wage "technological warfare" with the rest of the world in the commercial aircraft business. It possesses all the necessary ingredients for success--intellect, facilities, freedom, and competitive spirit.

To maintain our competitive edge and preeminence, we must not continue to make evolutionary advancements; instead, we must make revolutionary jumps. Steps such as those outlined in the National Aeronautical R & D Goals[49] are appropriate. They include

1. Subsonics Goal: To build transcentury renewal that envisions technology for an entirely new generation of fuel-efficient, affordable U.S. aircraft.

2. Supersonics Goal: To attain long-distance efficiency by developing pacing technologies for sustained supersonic cruise capabilities.

3. Transatmospherics Goal: To secure future options by pursuing research toward the capability to routinely cruise and maneuver into and and out of the atmosphere with takeoff and landing from conventional runways.

Pioneering new technologies is this country's strength; pursuing the ambitious goals outlined above will help to enhance our preeminent position in aeronautics.

VIII. REFERENCES

[1] MacCormack, R. W.: The Effect of Viscosity in Hypervelocity Impact Cratering. AIAA Paper No. 69-354, April 1969.

[2] MacCormack, R. W.; and Warming, R. F.: Survey of Computational Methods for Three-Dimensional Supersonic Inviscid Flow with Shocks. AGARD-LS-64, 1973.

[3] Steger, J. L.; and Lomax, H.: Transonic Flow About Two-Dimensional Airfoils by Relaxation Methods. AIAA Journal, Vol. 10, No. 1, Jan. 1972, pp. 49-54.

[4] Steger, J. L.; and Lomax, H.: Generalized Relaxation Methods Applied To Problems in Transonic Flow. Proceedings of the Second International Conference on Numerical Methods in Fluid Dynamics, Vol. 8, Springer-Verlag, New York, 1971, pp. 193-198.

[5] Beam, R. M.; and Warming, R. F.: An Implicit Factored Scheme For The Compressible Navier-Stokes Equations. AIAA Journal, Vol. 16, No. 4, April 1978, pp. 393-402.

[6] Warming, R. F.; and Beam, R. M.: On the Construction and Application of Implicit Factored Schemes for Conservation Laws. Symposium on Computational Fluid Dynamics, New York, April 16-17, 1977, SIAM-AMS Proceedings, Vol. 11, 1978, pp. 85-129.

[7] Lomax, Harvard: An Operational Unification of Finite Difference Methods for the Numerical Integration of Ordinary Differential Equations. NASA TR R-262, 1967.

[8] Lomax, Harvard; and Inouye, Mamoru: Numerical Analysis of Flow Properties About Blunt Bodies Moving at Supersonic Speeds in an Equilibrium Gas. NASA TR R-204, 1964.

[9] Tannehill, J. C.; Holst, T. L.; and Rakich, J. V.: Numerical Computation of Two-Dimensional Viscous Blunt Body Flows with an Impinging Shock. AIAA Paper No. 75-154, Jan. 1975; Also AIAA J., Vol. 14, Feb. 1976, pp. 204-211.

[10] Holst, T. L.: Numerical Solution of Axisymmetric Boattail Flow Fields with Plume Simulators. AIAA Paper No. 77-224,, Presented at the 15th Aerospace Sciences Meeting, Los Angeles, Calif., January 24-26, 1977.

[11] Holst, T. L.: An Implicit Algorithm for the Conservative Transonic Full-Potential Equation Using an Arbitrary Mesh. AIAA Paper No. 78-1113, July 10-12, 1978; Also AIAA J. Vol. 20, Oct. 1979, pp. 1038-1045.

[12] Holst, T. L.; and Thomas, S.: Numerical Solution of Transonic Wing Flow Fields. AIAA Paper No. 82-0105, Jan. 11-14, 1982; Also AIAA J., Vol. 21, No. 6, June 1983, pp. 863-870.

[13] Hord, R. Michael: The Illiac IV, the First Supercomputer. 1982, Library of Congress No. IFBN 0-914894-71-4, Computer Science Press.

[14] Bailey, Frank R.; and Ballhaus, William F.: Relaxation Methods for Transonic Flow About Wing-Cylinder Combinations and Lifting Swept Wings, Vol. II. Problems of Fluid Mechanics, of Lecture Notes in Physics, No. 19, Proceedings of the Third International Conference on Numerical Methods in Fluid Mechanics; H. Cabannes and R. Teman (ed.), Springer-Verlag, 1973, pp. 2-9.

[15] Kutler, P.; and Sakell, L.: Three-Dimensional, Shock-on-Shock Interaction Problem. AIAA J., Vol. 13, No. 10, pp. 1360-1367, Oct. 1975.

[16] Kutler, P.; and Lomax, H.: Shock-Capturing, Finite-Difference Approach to Supersonic Flows. J. Spacecraft and Rockets, Vol. 8, No. 12, pp. 1175-1182, Dec. 1971.

[17] Kutler, P.; Warming, R. F.; and Lomax, H.: Computation of Space Shuttle Flow Fields Using Noncentered Finite-Difference Schemes. AIAA J., Vol. 11, No. 2, Feb. 1973, pp. 196-204.

[18] Kutler, P.; Pedelty, J. A.; and Pulliam, T. H.: Supersonic Flow Over Three-Dimensional Ablated Nosetips Using an Unsteady Implicit Numerical Procedure. AIAA Paper No. 80-63, AIAA 18th Aerospace Sciences Meeting, Pasadena, CA, Jan. 1980.

[19] Rai, M. M.: A Relaxation Approach to Patched-Grid Calculations with the Euler Equations. Journal of Computational Physics, Vol. 66, No. 1, Sept. 1986, pp. 99-131.

[20] Rai, M. M.: Navier-Stokes Simulations of Rotor-Stator Interaction Using Patched and Overlaid Grids. AIAA Paper No. 85-1519, July 15-17, 1985.

[21] Kwak, D.; Chang, J. L. C.; Shanks, S. P.; and Chakravarthy, S.: A Three-Dimensional Incompressible Navier-Stokes Flow Solver Using Primitive Variables. AIAA J, Vol. 24, No. 3, Mar. 1986, pp. 390-396.

[22] Chang, J. L. C.; Kwak, D.; Dao, S. C.; and Rosen, R.: A Three-Dimensional Incompressible Flow Simulation Method and Its Application to the Space Shuttle Main Engine, Part I - Laminar Flow. AIAA Paper 85-0175, Jan. 1985.

[23] Chang, J. L. C.; Kwak, D.; Dao, S. C.; and Rosen, R.: A Three-Dimensional Incompressible Flow Simulation Method and Its Application to the Space Shuttle Main Engine, Part II - Turbulent Flow. AIAA 85-1670, July 1985.

[24] Yang, R-J; Chang, J. L. C.; and Kwak, D.: A Navier-Stokes Simulation of the Spce Shuttle Main Engine Hot Gas Manifold. AIAA 87-0368, Jan. 1987.

[25] Chaussee, D. S.; Rizk, Y. M.; and Buning, P. G.: Viscous Computation of a Space Shuttle Flow Field. Ninth International Conference on Numerical Methods in Fluid Dynamics, Saclay, France, June 1984.

[26] Chaussee, D. S.: High Speed Viscous Flow Calculations About Complex Configurations. Paper 29, 58th Meeting of the Fluid Dynamics Panel Symposium on Applications of Computational Fluid Dynamics in Aeronautics, April 7-10, 1986, Aix-en-Provence, France.

[27] Rizk, Y.; Chaussee, D.; and Steger, J.: Numerical Simulation of the Hypersonic Flows Around Lifting Vehicles. Symposium on Aerodynamics of Hypersonic Lifting Vehicles Sponsored by the AGARD Gluid Dynamics Panel to be held in Bristol, United Kingdon, April 6-9, 1987.

[28] Guruswamy, G. P.; Goorjian, P. M.; and Tu. E. L.: Transonic Aeroelasticity of Wings with Tip Stores. AIAA Paper No. 86-1007-CP, May 1986.

[29] Guruswamy, P.; Goorjian, P. M.; Ide, H.; and Miller, G.D.: Transonic Aeroelastic Analysis of the B-1 Wing. Journal of Aircraft, Vol. 23, No. 7, July 1986, pp. 547-553.

[30] Guruswamy, G. P.; Goorjian, P. M.; and Tu. E. L.: Unsteady Transonics of a Wing with Tip Store. Journal of Aircraft, Vol. 23, No. 8, August 86, pp. 662-668.

[31] Guruswamy, P.; and Goorjian, P.M.: Efficient Algorithm for Unsteady Transonic Aerodynamic Aerodynamics of Low-Aspect-Ratio Wings. Journal of Aircraft, Vol. 22, No. 3, March 1985, pp. 193-199.

[32] Moin, P.; and Kim, J.: The Structure of the Vorticity Field in Turbulent Channel Flow. Part I. Analyses of Instantaneous Fields Statistical Correlations. J. of Fluid Mechanics, No. 155, pp. 441-464, 1985.

[33] Kim, J.; and Moin, P.: The Structure of the Vorticity Field in Turbulent Channel Flow. Part II. Study of Ensemble--Averaged Fields. J. of Fluid Mechanics, No. 162, Jan. 1986, pp. 339-363.

[34] Dash, S.: Code integration - Forebody/inlet/Com./Nozzle. Second National Aerospace Plane Symposium, Laurel, Maryland, Nov. 1986.

[35] Kutler, P.; Mehta, U. B.; and Andrews, A.: Potential Application of Artificial Intelligence Concepts to Numerical Aerodynamic Simulation. NASA TM 85967, 1984.

[36] Rich, E.: Artificial Intelligence. McGraw-Hill Book Co., Inc., 1983.

[37] Roache, P. J.; and Steinberg, S.: Symbolic Manipulation and Computational Fluid Dynamics. AIAA Paper 83-1952, July 1983.

[38] Steinberg, S.; and Roache, P. J.: A Toolkit of Symbol Manipulation Programs for Variational Grid Generation. AIAA Paper 86-0241, Jan. 1986.

[39] Andrews, A. E.: Progress and Challenges in the Application of Artificial Intelligence to Computational Fluid Dynamics. AIAA Paper 87-0593, Jan. 1987.

[40] Tong, S. S.: Design of Aerodynamic Bodies Using Artificial Intelligence/Expert System Technique. AIAA Paper 85-0112, Jan. 1985.

[41] Tong, S. S.: Coupling Artificial Intelligence and Numerical Computation for Engineering Design. AIAA Paper 86-0242, Jan. 1986.

[42] Conner, R. S.; Purdon, D. J.; and Wamsley, F. K.: Pan Air Consultation Using Expert System Techniques. AIAA Paper 85-4094, Oct. 1985.

[43] Conner, R. S.; and Purdon, D. J.: PAN AIR Knowledge System. AIAA Paper 86-0239, Jan. 1986.

[44] Dannenhoffer, J. F., III; and Baron, J. R.: Robust Grid Adaptation for Complex Transonic Flows. AIAA Paper 86-0495, Jan. 1986.

[45] Cheeseman, P.: Learning of Expert Systems From Data. Proceedings of the IEEE Workshop on Principles of Knowledge-Based Systems, Dec. 3-4, 1984, Denver, Colorado, pp. 115-122.

[46] Kutler, P.: A Perspective of Computational Fluid Dynamics. NASA TM 88246, 1986.

[47] Zilliac, G.; Cantwell, E.; and Fukunishi, Y.: Smart Probe Progress Report. Fluid Dynamics Research Branch, NASA Ames Research Center, Oct. 1986.

[48] Bulkeley, W. M.: Frontiers of Science. The Wall Street Journal, Nov. 10, 1986.

[49] Aeronautical Policy Review Committee: National Aeronautical R&D Goals. Executive Office of the President, Office of Science and Technology Policy, March 1985.
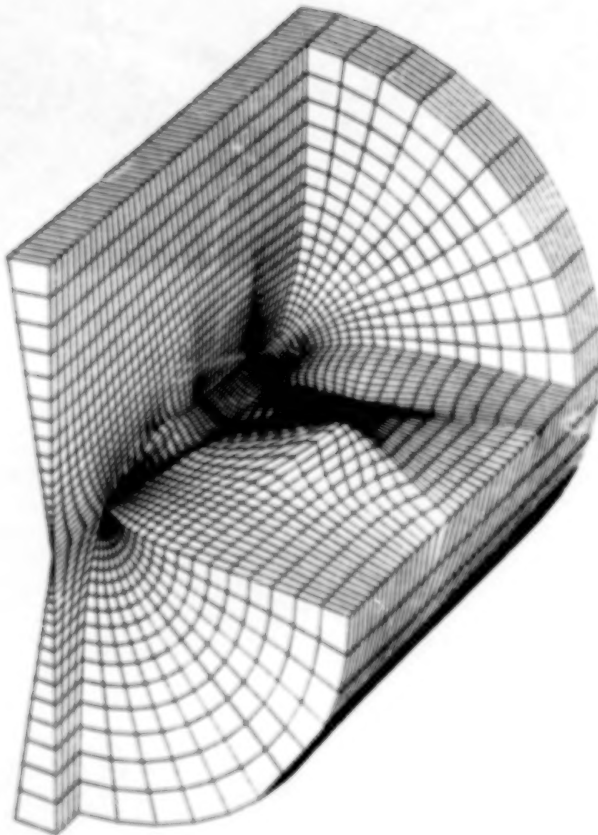
Figure 2: Particle Traces on the Modified F-16A.

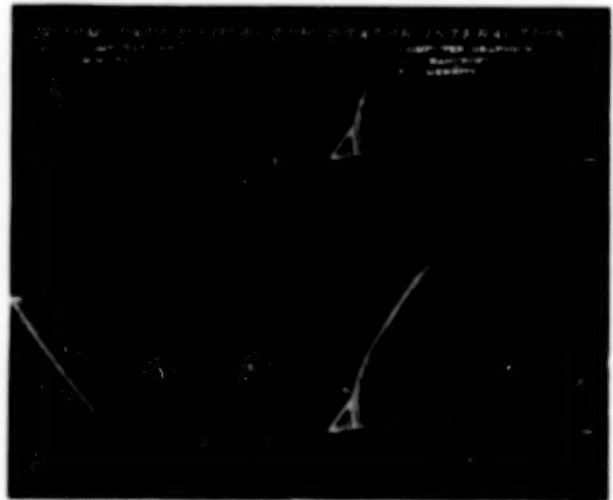Figure 1: Grid System for the Modified F-16A Simulation.

Figure 3: Supersonic Flow Through a Two-Dimensional Rotor-Stator.

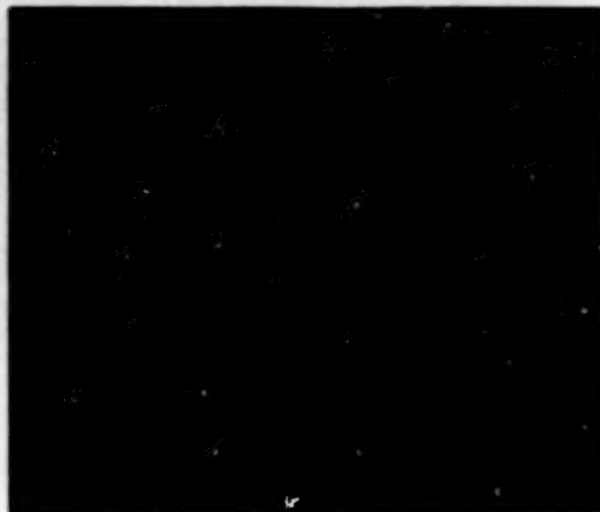Figure 4: A Navier-Stokes Simulation of Rotor-Stator Interaction.

Figure 6: Flow Field About the Space Shuttle Orbiter.

Figure 5: Flow Through Space Shuttle Main Engine Transfer Ducts.

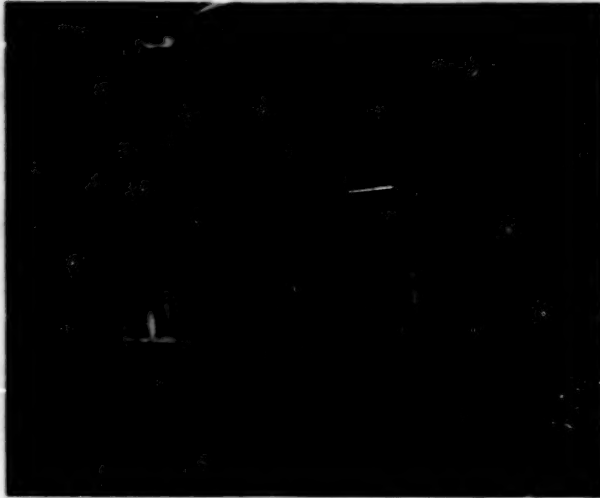Figure 7: Pressure Contour About NASP-like Configuration.

Figure 8: F-5 Wingtip Missile Simulation.

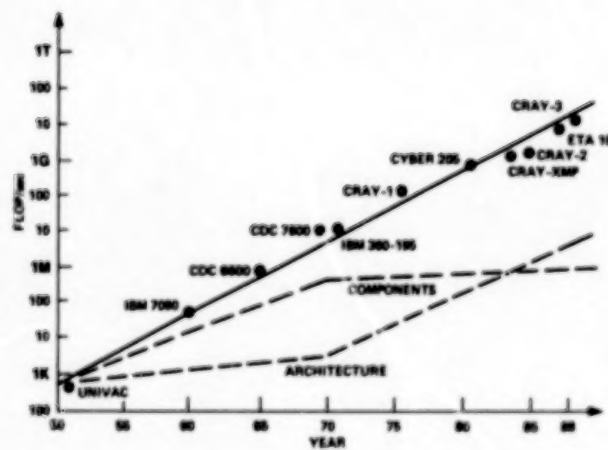Figure 9: Horshoe Vortex Simulation.

Figure 10: Computer Development Since 1950.

61

Mr. Carl Diem
Cray Research, Inc.

The Future of Supercomputing Development at Cray

Paper not available

Mr. Neil Lincoln
ETA Systems

The Future of Supercomputing Development at ETA Systems

Paper not available

Dr. Paul D. Rubbert
Boeing Military Airplane Co.

Design Applications of CFD at Boeing

Paper not available

N87
26004

COMPUTATIONAL FLUID DYNAMICS - TRANSITION TO DESIGN APPLICATIONS

R. G. Bradley, I. C. Bhateley and G. A. Howell
General Dynamics Corporation

INTRODUCTION

The development of aerospace vehicles, over the years, has been an evolutionary process in which engineering progress in the aerospace community was based, generally, on prior experience and databases obtained through wind tunnel and flight testing. Advances in the fundamental understanding of flow physics, wind tunnel and flight test capability, and new mathematical insights into the governing flow equations have been translated into improved air vehicle design. Two notable examples of this evolutionary process that resulted in significant improvements to air vehicles are the area rule and the supercritical wing technology. These examples evolved from a combination of wind tunnel experimentation and analytical advances. The analytical advances include the ability to obtain solutions to the appropriate supersonic and transonic flow equations in simplified form. The modern day field of Computational Fluid Dynamics (CFD) is a continuation of this growth in analytical capability and the digital mathematics needed to solve the more rigorous form of the flow equations.

The explosion in computer technology over the past two decades coupled with the expansive effort in the development of CFD has led to the realization of a dynamic jump in the capability to understand and to apply the governing physics for fluid flow. This capability is even now being realized in the application of CFD to critical design problems involving the solution of complicated flowfields. Industry is now aware that solving a flowfield to reveal the intricate details offers a tremendous potential to understand and improve designs.

This paper presents some of the technical and managerial challenges that result from rapidly developing CFD capabilities, some of the steps being taken by the Fort Worth Division of General Dynamics to meet these challenges, and some of the specific areas of application for high performance air vehicles. One of the primary issues for industry is the effective integration of CFD capability into the design process. What follows is written from this point of view.

CODE DEVELOPMENT AND MATURATION

Phenomenal progress in CFD has been made over the last decade, but a significant task still remains before the maturation of CFD is realized. The ultimate goal is to have fully mature codes that are (1) fully validated by comparison with detailed experimental data, (2) user

friendly, and (3) readily available for complex design applications.

A recent National Research Council study on CFD, Current Capabilities and Future Directions (Reference 1), gives a survey of the current capabilities in CFD and presents some of the areas requiring further effort. It presents a five-step developmental cycle typical for CFD codes, which is illustrated in Figure 1. NASA, the government labs, and industry have already done a great deal of work toward accomplishing many of these steps. For design cases in which the flow environment is not too severe, such as transports, the industry is applying CFD directly into the design cycle. On the other hand, the CFD capability for more complex designs, such as tactical aircraft, has not progressed as far because the flowfields are dominated by flow separations and vortex interactions.

Codes must be validated and/or calibrated before they can be used with confidence. Validation involves detailed flowfield comparisons with experimental data to verify the code's ability to accurately model the critical physics of the flow. This requires close coordination between the code developer and the experimentalist to insure that the accuracy and limitations of the experiments, as well as those of the numerical algorithms and grid densities, are understood and taken into account. Through validation, one assures that the numerical physics of the code give a true representation of the flow physics being modeled.

It is important to note that CFD codes can often be used in analyses and design applications long before the
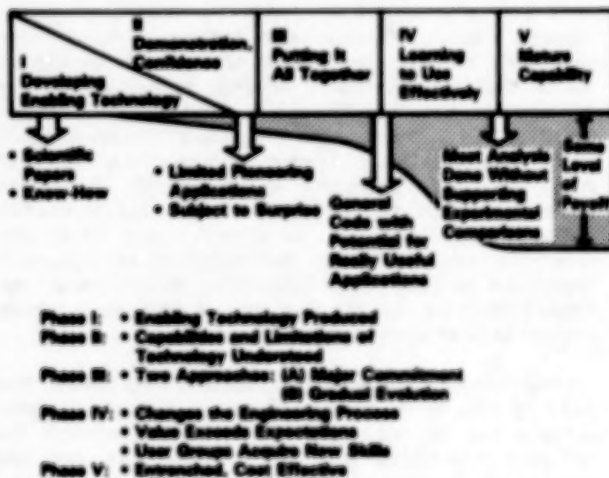

Figure 1. The CFD Development Cycle

codes are considered to be mature in the sense of Figure 1. Engineers have always been able to use less than perfect tools coupled with experience and calibration to known physical quantities to provide design guidance. Calibration and validation should not be confused. Calibration provides an error band or correction factor to enhance the ability of a particular code to predict specific parameters that are important to the design objectives for a particular design without verifying that all other features of the flow are modeled accurately. For example one might calibrate a code's ability to predict shock location and lift and moment on a wing without any assurance that the flowfield off the surface and the wake behind the wing are properly modeled. Or, one may calibrate a code's ability to compute gross pressure loss through a supersonic inlet-duct combination without concern for the distortion distribution at the compressor face. Although the use of calibrated CFD solutions is dangerous because of the subtle viscous interactions that are extremely sensitive to geometry and flowfield, skilled engineers can often obtain useful design information and guidance from relatively immature codes.

NASA has pioneered the development of CFD capability with its advanced computer centers and highly competent cadre of CFD algorithm developers. The ability to solve more complex equations efficiently, riding upon the wave of developments in computer hardware technology, has been revolutionary. More recently, emphasis has been placed on solving the governing equations for complex geometries, including full aircraft configurations. In general, at this point in time it is possible to solve complex flow equations for simple geometries or to solve simplified flow equations for complex geometries, but it is not possible to do both.

Major areas of uncertainty still remain, such as the development of grid systems for complex configurations so that they reflect the proper scales to model both the viscous and basically nonviscous flow regions. Also, in the proper modeling of physical parameters such as turbulence, heat transfer mechanisms, combustion kinetics, etc., much remains to be learned. Progress is being made in both of these areas, but there is much work to be done before the full capability of CFD is realized.

DESIGN REQUIREMENTS

If one considers CFD from the advanced design manager's point of view, one obtains a perspective completely different from that of the code developer. Recall that the aerospace designer is responsible for defining the best configuration to meet performance specifications in the shortest time and at the lowest cost. He has traditionally relied upon extensive test results to guide his design decisions and to supply the flight envelope database needed for comprehensive performance calculations. Admittedly, wind tunnel test data have many limitations, but designers have years of experience to help in understanding those limitations. Today's dilemma for the designer of high performance aircraft is illustrated in Figure 2.

The potential and promise of CFD is well known. For the first time in the history of aeronautics, the designer actually has the opportunity to generate solutions for complex flowfields and to examine the detailed microscopic features of the flow that influence a design. The challenge, now, is to provide usable, believable, cost and schedule effective codes for design application and to integrate these codes into the designer's toolset. This is

both a technical and a management challenge. A responsible designer, however, raises legitimate questions about the benefits of CFD in helping him to meet his requirements as shown in Figure 2.

Capability - The ability of the codes to model flowfields about complex geometries over a wide range of flow conditions such as Mach number, Reynolds number, angles of attack and yaw and to produce results in a form that are meaningful to the designer.

Turnaround - The time required to set up geometries, grid meshes, and obtain converged solutions.

Availability - The level of expertise required to generate the flowfield solutions (e.g., can a designer run the code or does it require a CFD specialist).

Cost - The cost effectiveness of a CFD approach relative to other options.

Confidence - The dependability of the codes to give accurate solutions over the range of design variables.

These concerns are a legitimate focus for developers of CFD codes and for engineers who are integrating the capability into the design process. While all of the concerns are vitally important, confidence is perhaps most critical at the current time. This is especially true for the tactical aircraft designer since the CFD experience level is generally low among designers, and the flowfields of tactical aircraft are most complicated. CFD code developers can raise the confidence level through careful validation of the codes being developed.

MANAGEMENT ISSUES

Becoming of age, CFD capability indeed holds the glowing promise of permitting a designer of aerospace vehicles to literally step inside a flowfield and observe the details of the flow through the use of graphics. While this exciting possibility has captured the imagination of the engineer, it has created a new set of challenges for management. As in the case of any evolving technological capability, the manager is faced with the problem of how to integrate it into his organization. To whom will the new capability be assigned for manage-
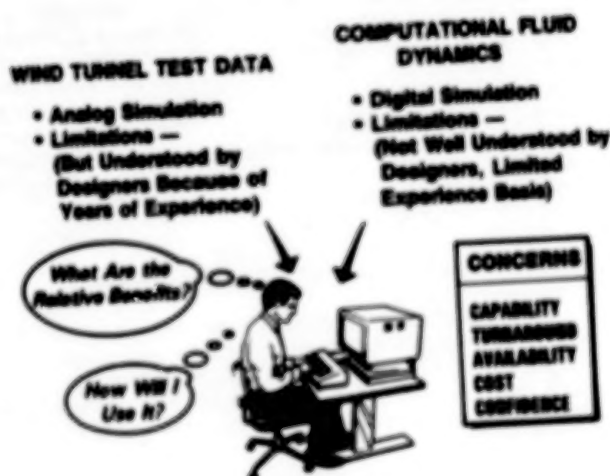

Figure 2   The Designers' Dilemma

70

ment purposes? Who will be responsible for meshing it into the design process? What procedures will be followed to ensure that only mature and/or calibrated data are used, and what measure of confidence will be placed in the CFD results for design application? These issues present the manager with a situation that is somewhat different from the customary work environment. The following paragraphs outline a management approach adopted by the Fort Worth Division of General Dynamics.

Role of CFD

The general philosophy has been to build a strong, applications-oriented CFD capability that draws heavily upon the expert development work of NASA and other government-sponsored research in labs, universities and industry. The available capability is adopted and/or modified for efficient use in design and is calibrated and/or validated for specific applications. Basic code and grid generation research is performed inhouse to fill needed voids in available methods and to develop improved techniques and interfaces.

CFD is viewed as an integral part of the fully automated factory concept and is being integrated into the shared, common database that ties all design and manufacturing functions together. Its relationship to the advanced design process is illustrated schematically in Figure 3. When fully implemented on-line, analysis of aircraft and component designs can be made and fed directly into the design database.

In the larger scheme of things, CFD capability will interface through the shared database with the model building function to provide supportive evaluation of wind tunnel test configurations and, in turn, to access wind tunnel databases for calibration/validation of the codes as illustrated in Figure 4. In the future, this loop will include a structural design interface for support of detail design activities and manufacturing. Many aspects of the concept have been implemented at this time and segments of the system are in operation. It is the responsibility of the CFD Section to develop and to support the CFD codes that are used in the design and analysis process.
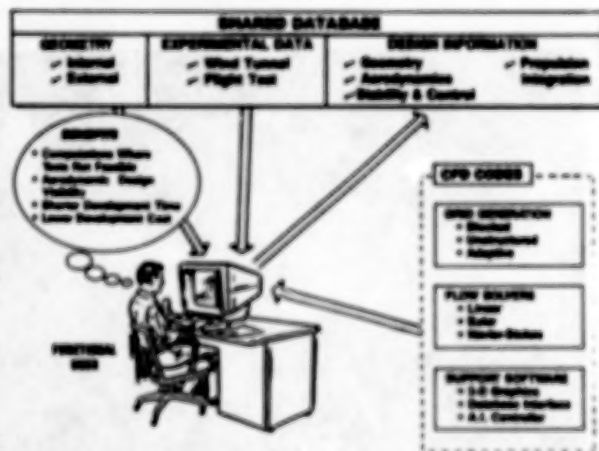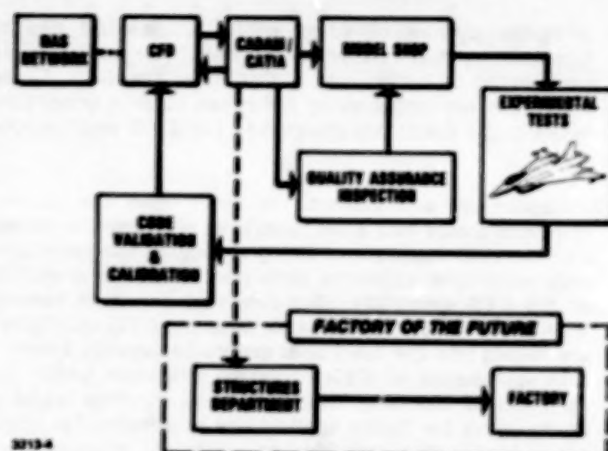

Figure 4.   CFD as an Integral Part of the Factory of the Future

Organizational Structure

The organizational structure for developing a mature CFD capability and integrating the capability into the design process, at whatever level of maturity, is outlined in Figure 5. In the matrix concept employed at General Dynamics, the functional sections are responsible for supplying direct support to the various design programs. The CFD Section is a support function charged with providing the necessary codes and expertise for use by the functional discipline areas, much as a wind tunnel test section supplies test capability and expertise.

CFD expertise is concentrated in a single section that reports to the director, who has the responsibility for the functional sections. The CFD Section is divided into two groups: (1) a group responsible for code development, and (2) a group responsible for code applications. The general division of responsibilities is shown in Figure 5.

In the dynamic environment of CFD capability maturation, a maximum degree of flexibility must be maintained. Not only must a CFD Section provide usable and dependable applications-oriented codes, but the
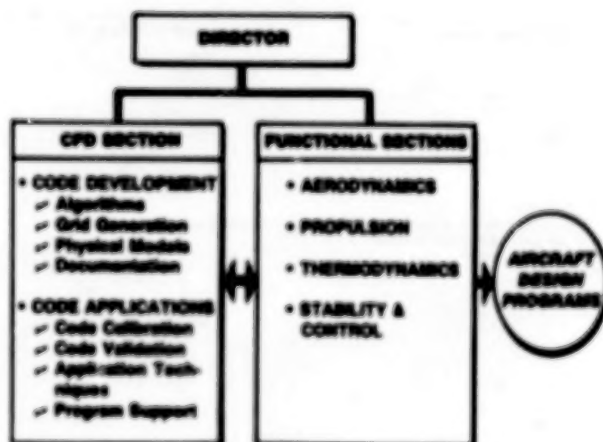

Figure 3.   CFD as an Integral Part of the Design Process

Figure 5.   Organizational Philosophy

intensive training of users skilled in making design applications must be accomplished. Organizational barriers can be detrimental to this latter function. Cross training is accomplished by a flexible loan-in procedure between the functional groups and the CFD applications group.

Under this arrangement, engineers from the various discipline groups within the functional sections are loaned into the CFD Applications Group to help in the important code calibration/validation activities, under the direction of the CFD specialists, thus receiving hands-on experience in the use of the codes. In turn, the CFD specialists are loaned into the functional groups to support specialized applications of CFD to design programs under the direction of the functional management, thus gaining appreciation for design applications requirements. This cross fertilization provides an essential element for building a strong, design-oriented CFD capability.

The CFD Section is charged with the responsibility of maintaining a documented file on all code applications that support the calibration and validation activities. This file contains the details of specific accuracy limitations of both the experimental data being used and the codes being calibrated. A documented reference source is thus available on application of all codes in order to build a base of experience for design confidence in CFD methods.

CFD APPLICATIONS

Applications of CFD to design are becoming a key element of the Fort Worth Divisions' activities. A few of the calibration activities underway in the applications areas of primary interest are discussed in the following paragraphs.

Grid generation is a complex issue that must be addressed with each configuration analysis, and often is as important as the algorithms that are used in the flowfield solution. This problem is particularly difficult when there is a high degree of integration of the aerodynamic and propulsive systems, or when there are other unique geometric features. The extreme difficulty of modeling complex regions with a single block of grid leads to the concept of multiple blocks, which is illustrated in Figure 6. With this approach, complex

problems can be subdivided into several smaller zones that can more accurately represent the geometry and the boundary conditions.

Another reason for using multiple blocks of grid is that the blocking can be controlled to divide the flowfield into zones wherein the sophistication of the analysis code can be matched to the complexity of the flowfield. Several zones of an aircraft flowfield and the types of analyses are illustrated in Figure 7. This approach also allows larger problems to be solved with a specified amount of computer core memory since only one block at a time must be in core memory, while the other blocks reside in other types of memory. The grid generation procedure is documented in References 2 and 3.

An Euler analysis of the F-16 is being accomplished as a benchmark calculation. Progress has been made and preliminary results were presented at an AGARD Symposium (Reference 4). Part of the grid system, which has over 500,000 grid points in 30 blocks, is shown in Figure 8. Detailed modeling of the inlet and nozzle with flow-through boundary conditions is essential for full aircraft simulation with power effects. Details of the inlet grid blocking are shown in Figure 9.
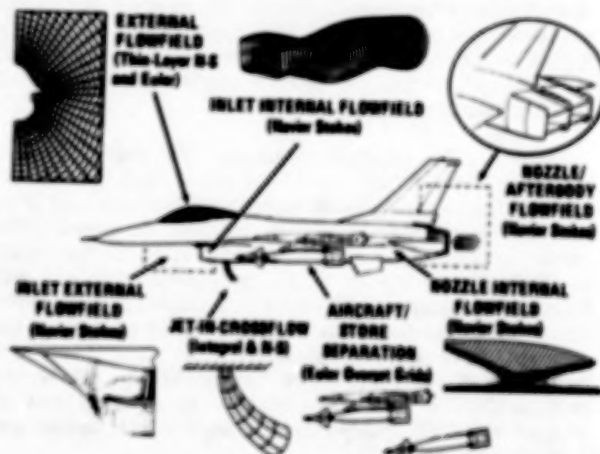

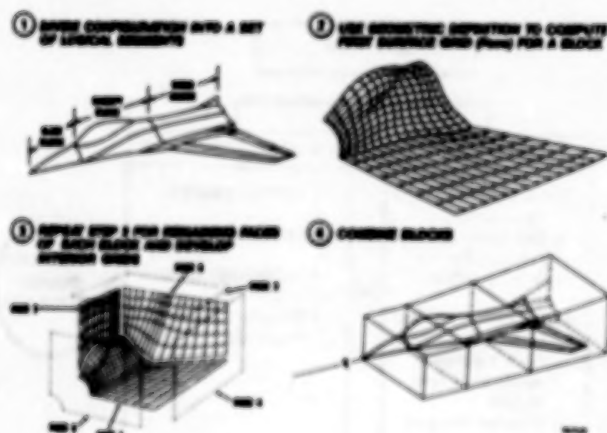Figure 7. Zonal Approach to the Computation of Aircraft Flowfields

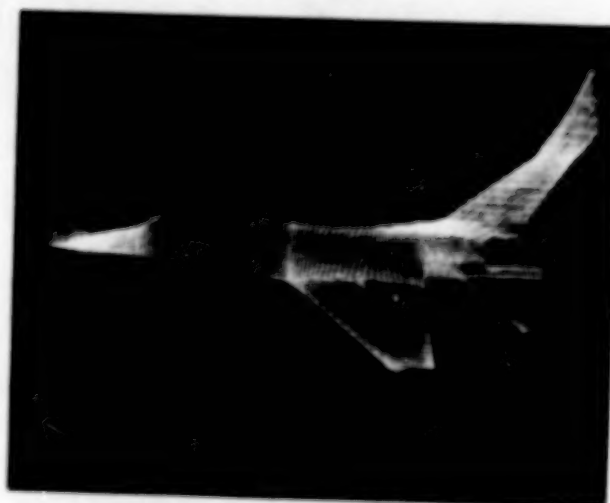Figure 6. Concept of Multi-Block Grid Systems

Figure 8. F-16 Grid System

72

Figure 9.   Blocking Scheme Applied to F-16 Inlet Region

Initial calculations, which were made on the Fort Worth Division CRAY XMP-24, utilized approximately 35 CPU hours. Computed velocity vectors on the surface of the forward fuselage are shown in Figure 10.   The accuracy of the fuselage flowfield calculations was further verified by an excellent comparison between computational results and experimental pressure coefficients from Reference 5. Sample comparisons at two fuselage stations are shown in Figure 10.

Since this was the first time that an analysis of this magnitude had been attempted, it was no surprise that problems were encountered. The code simply did not develop shock waves at the downstream edge of the
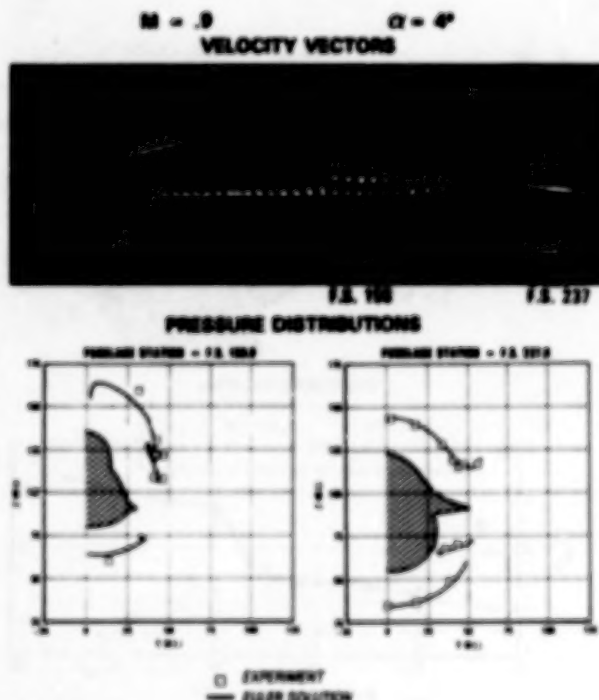
supersonic bubble on the wing upper surface; consequently, the pressures in this region were not good, as shown in Figure 11. The solution data indicate that the problem can be resolved by the use of (1) a denser grid on the wing upper surface, and (2) a revised solution algorithm that has a strong shock-capturing feature. Both the grid system and the code are being modified to incorporate these indicated improvements, and further computations are planned on the NASA/Ames Numerical Aerodynamics Simulator.

CFD can be used to solve flowfields for configurations in both pitch and yaw to determine lateral stability characteristics. This capability has not been widely explored, primarily because of the computational resources required for this type of analysis. An Euler analysis of a NASA wing/body/tail research model, illustrated in Figure 12, was performed. The analytical model contained 200,000 grid points, and about 25 CRAY CPU hours were used in obtaining the solution. As shown, the longitudinal characteristics and the lateral stability derivatives computed for a Mach number of 2.3 compared favorably with experimental force and moment data from Reference 6.   The highly-swept delta wing of this configuration offered a challenge in capturing the wing leading-edge vortex that is known to dominate this type of flowfield. The force and moment data simply indicate that the vortical flow over the wing was properly simulated. The Mach contours, shown in Figure 13, offer positive evidence that the strong wing vortex was present in the solution.

Other challenging applications for CFD are in the areas of inlets and nozzles. An example of a Navier-Stokes analysis of an axisymmetric inlet at angle of attack is illustrated in Figure 14. The results of this study were presented at an AIAA Conference (Reference 7). Computed pressures on the spike and cowl compared favorably with experimental data. A sample comparison along the upper spike centerline is shown in Figure 14 for
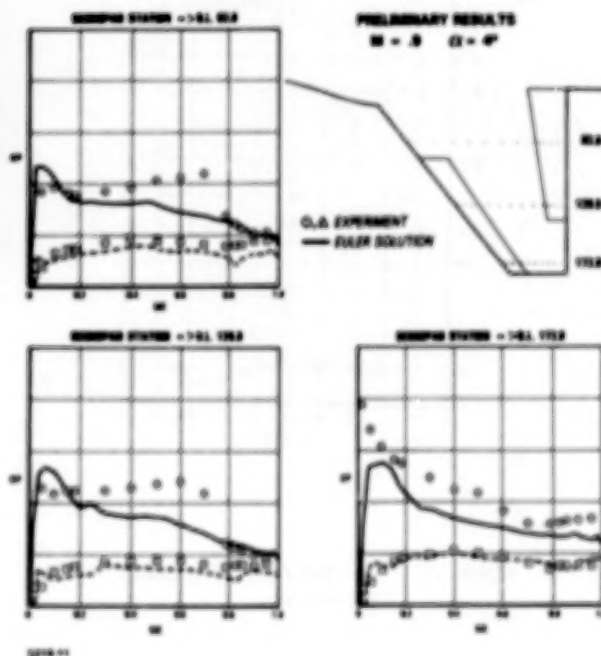

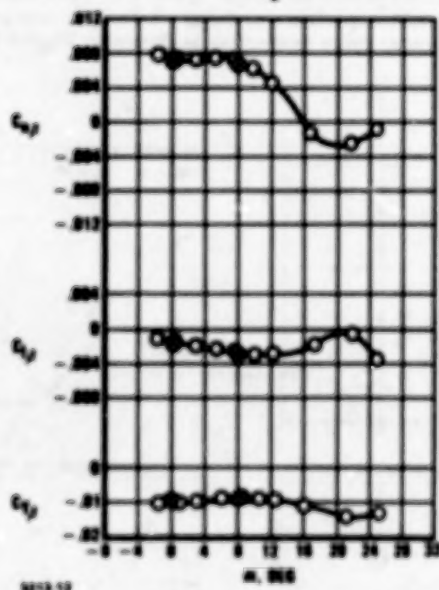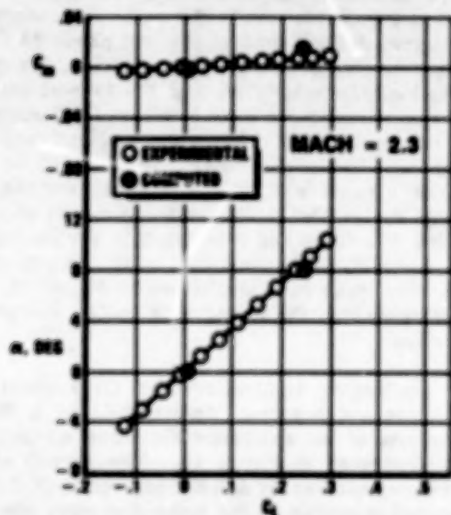**Figure 10.   Euler Solution of F-16 Fuselage Flowfield**

Figure 11.   Euler Solution of F-16 Wing Flowfield

Figure 13. Wing Vortex Defined by Mach Contours

an angle of attack of 8 degrees. Computed Mach number contours in the flowfield of this inlet, Figure 15, show the non-symmetric location of the shock and the expansion waves.

CFD also offers the potential to solve some of the special problems that are associated with high-performance military aircraft. One such problem that has defied a good experimental solution is that of an unsteady flowfield of a weapons bay. Unsteady aerodynamic flow, or weapons bay buffet as it is commonly called, has been known to damage both the weapons bay doors and the weapons inside. Although a generalized solution to this problem has not been developed, a two-dimensional, time-dependent Navier-Stokes solution was obtained for supersonic flow over a cavity in order to establish the viability of CFD as a tool to handle this problem.

Figure 12. Euler Solution for Stability Derivatives

Figure 14. Navier-Stokes Solution of a Spiked Inlet Flowfield

74

MACH
2.00
1.80
1.60
1.40
1.20
1.00
0.80
0.60
0.40
0.20
0.00

Figure 15. Mach Number Contours in the Flowfield of a Spiked Inlet
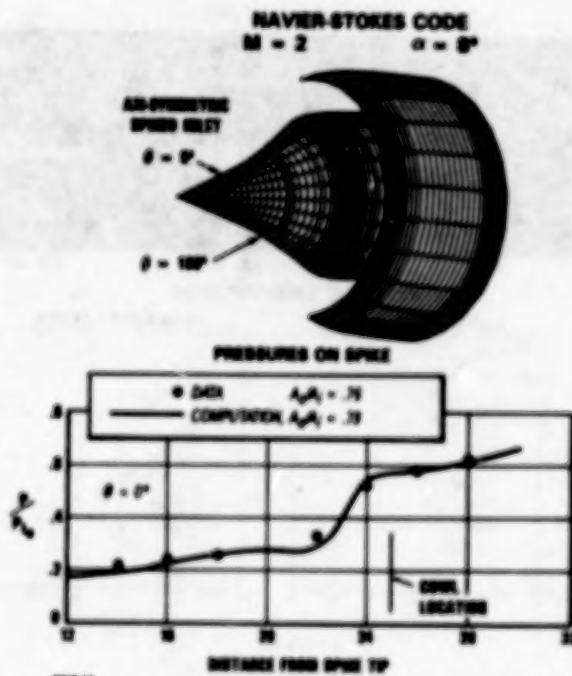
MACH = 1.5   PRESSURE CONTOURS

TIME = 4.00E-03 SECS   TIME = 5.00E-03 SECS

TIME = 6.00E-03 SECS   TIME = 6.20E-03 SECS

TIME = 8.00E-03 SECS   TIME = 8.00E-03 SECS

Figure 16 Time-Dependent Navier-Stokes Solution of a Cavity Flowfield

The two-dimensional solution of unsteady flow in a cavity was obtained with a Navier-Stokes solver. The model was comprised of approximately 36,000 grid points and was given an initial starting solution of 1.5 Mach number in the freestream and zero velocity in the cavity. The code was run for 78,000 iterations, which represented about 17 milliseconds of real time. Although this seems like a short duration, it was enough to allow cyclic fluctuations to become apparent in the solution. Some of the pressure contours in the flowfield are shown in Figure 16 at several different times during the solution to give a cursory depiction of the results. A video movie was also made that presents the data in an informative manner showing pressure waves as they move about within the cavity.

CONCLUDING REMARKS

CFD capability is maturing rapidly and is now being applied to the design process to help deal with aerodynamic phenomena encountered in the complex flowfields associated with high performance aircraft. This expanding capability is presenting new technical and managerial challenges throughout engineering. To the aircraft designer, it is the challenge to learn a new and different tool. He must responsibly question CFD and confirm that it can provide the needed capability, turnaround time, skill level, availability, cost effectiveness, and confidence level to justify its use. To the manager, it is the challenge to integrate a new capability into an existing organization. Responsibilities for CFD may sometimes overlap between functional groups and the projects on which the codes are applied. Managers must also provide safeguards to assure that only verified or calibrated codes are used in the design process. An approach to the solution of these issues has been presented.

Some sample calculations have been shown to illustrate potential design applications. While these examples, in some cases, represent early attempts at complex flow solution, it is anticipated that continued improvements in hardware and solution algorithms will make such applications routine in the future. The resurgence of interest in hypersonic technology is pressing the need for rapid advancement of CFD capability.

On this occasion of the formal opening of NASA's Numerical Aerodynamic Simulator Facility, NASA is to be congratulated for its pioneering efforts in developing both the hardware and software for this important CFD capability. The dedicated efforts of NASA's management and skilled researchers have laid the foundation for a national capability that is clearly a world leader.
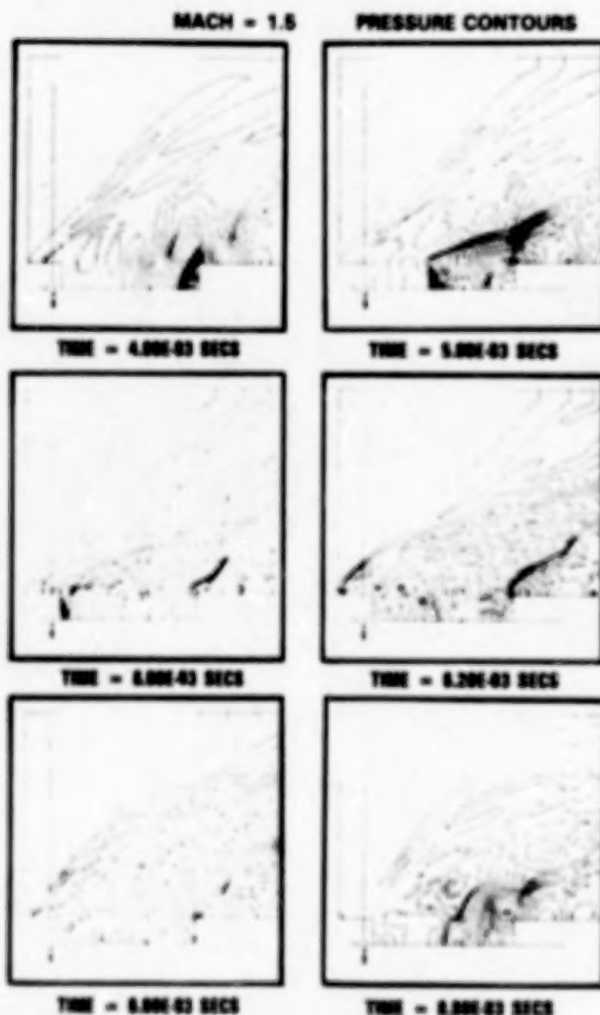
REFERENCES

1. Current Capabilities and Future Directions in Computational Fluid Dynamics. National Research Council, National Academy Press, Washington, D.C. 1986.

2. Steinbrenner, John P.: GRIDGEN2D, Interactive Elliptic Surface Grid Generation. General Dynamics Report No. CFD 063-4-8601, June 13, 1986.

3. Reed, Christopher L.; and Karman, Steve L., Jr.: Multiple-Block Grid Method Applied to Complex 3-D Geometries. Presented at 1986 National Meeting of the Society for Industrial and Applied Mathematics, Boston, Mass., July 1986.

4. Karman, Steve L., Jr.; Steinbrenner, John P.; and Kisielewski, Keith M.: Analysis of the F-16 Flow Field by a Block Grid Euler Approach. AGARD Paper No. 18, 58th Meeting of the Fluid Dynamics Panel Symposium, Aix En-Provence, France, April 1986.

5. Reue, G. H.; Doberenz, M. E.; and Wilkins, D. D.: Component Aerodynamic Loads From 1/9-Scale F-16A Loads Model. General Dynamics Report No. 16PR316, May 1976.

6. Jernell, Lloyd S.: Stability Characteristics at Mach Numbers from 1.50 to 4.63 of Several Wing-Body-Tail Models Having Wings with Arrow, Delta, and Diamond Planforms. NASA TM X-1485, December 1967.

7. Howlett, D. G.; and Hunter, L. G.: A Study of a Supersonic Axisymmetric Spiked Inlet at Angle of Attack Using the 3-D Navier-Stokes Equations. AIAA Paper No. 86-0308, 24th Aerospace Sciences Meeting, Reno, Nevada, January 1986.

CFD APPLICATIONS: THE LOCKHEED PERSPECTIVE

Luis R. Miranda
Lockheed-California Company

INTRODUCTION

The Numerical Aerodynamic Simulator (NAS) epitomizes the coming of age of supercomputing and opens exciting new horizons in the world of numerical simulation. The technological benefits likely to result from the use of the NAS may surprise even its most optimistic advocates. All this makes me both pleased and honored to be a participant of this conference which celebrates the inauguration of the NAS.

In this article I will give an overview of supercomputing at Lockheed Corporation in the area of Computational Fluid Dynamics (CFD). This overview will focus on developments and applications of CFD as an aircraft design tool and will attempt to present an assessment, within this context, of the state-of-the-art in CFD methodology. Although CFD is being actively developed and applied throughout Lockheed Corporation, the material of this paper draws heavily from activities that have taken place or are underway at Lockheed-California Company.

Of course, supercomputing in the aerospace industry is not limited to CFD. Many other disciplines either are already, or have the potential of, benefiting from supercomputing: structural analysis and optimization, vehicle signature (electromagnetic, acoustic, thermal) prediction, and signal processing, to name the obvious ones. In other areas, where the supercomputing revolution has not yet made its full impact, the payoffs are likely to be extraordinary. One such area is manufacturing. Supercomputers will make possible the effective integration of all phases and aspects of complex manufacturing processes and are bound to become essential in the development and operation of a new generation of sophisticated, versatile, and 'intelligent' robotic systems.

In spite of the wide applicability of supercomputing, I have chosen to limit my discussion to CFD and its application to aircraft design because of the following factors: 1) time and space constraints; 2) personal bias due to my familiarity with the subject; and 3) CFD was one of the first disciplines to push the limits of 'ordinary' or 'general purpose' computers, thus giving rise to the need for supercomputer capability. Moreover, the practical feasibility of CFD application demands supercomputing power, and most future developments in this area hinge on the availability of even greater computer speed and memory capability.

SUPERCOMPUTERS AT LOCKHEED CORPORATION

The term supercomputer is a relative one; what we consider supercomputer performance today may become 'ordinary' or 'general purpose' computer capability in a few years. For the purpose of the present discussion, the term 'supercomputer' will denote a machine with a performance capability of at least class VI in accordance with the following classification defined by the U.S. Department of Energy:

Class III Sustained operating speeds between 0.6 and 2 million floating point operations per second (megaflops)

Class IV 2 to 6 megaflops

Class V 6 to 20 megaflops

Class VI 20 to 60 megaflops

Class VII Greater than 60 megaflops

Presently two supercomputers are in operation at Lockheed Corporation. The first one, a Cray 1S, was installed at the Sunnyvale, California, plant of Lockheed Missiles and Space Company (LMSC) in 1982. This supercomputer is basically dedicated to serving the needs of the various LMSC divisions. The second one, a Cray X-MP/24, became operational at the Kelly Johnson Research Center, Rye Canyon, California, in April 1986.

The Cray X-MP/24 is a dual processor machine with an in-core memory capacity of 4 million 64-bit words. It is front-ended by two Digital Equipment Corporation (DEC) computers in the Lockheed installation: a DEC 8600 for unclassified processing, and a DEC 8300 for classified mode operation. This supercomputer, although it can be accessed remotely from all major Lockheed divisions, is primarily intended to cater to the Lockheed Aeronautical Systems Group companies.

The principal motivation for the acquisition of supercomputer hardware was the perceived need for processing speed. The above supercomputers have been able to fulfill that need fairly well for most present applications. At the same time, they have offered the possibility of more advanced computations. As we gain

more experience with these computations, and as we attempt to tackle more demanding problems, the need for more computer memory becomes acutely evident. This is particularly true in the engineering applications of CFD. As will be indicated later on, the use of advanced CFD methods in aircraft design applications requires fast-access memory capacity ranging from 16 megawords upwards.

THE CHALLENGE OF DESIGN APPLICATIONS

The paper is mainly concerned with CFD developments and applications within the context of aircraft design. Therefore, although it may appear obvious to many, it is important to emphasize the principal requirements that a CFD code ought to meet if it is to be used as an aircraft design tool, namely:

1) It must be a predictive tool, i.e., the accuracy and reliability of the computation should not depend on too much fine tuning or tailoring of input parameters. In many advanced applications, applicable experimental data are not available to "calibrate" the results of numerical computations.

2) It must be able to handle complex geometric configurations, including three-dimensionality, intricate aircraft components, and complete aircraft arrangements.

3) It must yield useful results in a reasonably short period of time, consistent with usually pressing program schedules.

4) Its application, although it may require a reasonable degree of expertise and experience, must not demand specialization to a degree that only its developers can effectively use it.

The above requirements are extremely important if CFD is to realize its full potential as an effective design tool. As has already been pointed out in Reference 1, these requirements directly relate to the equation:

EFFECTIVENESS = QUALITY X ACCEPTANCE

This expression has no actual quantitative meaning, it is merely a symbolism to emphasize the axiom that the effect a given process has on the activity for which it is intended depends not only on the goodness of the process itself, but also on how widely it is used or accepted. In the present context, the first couple of items listed above impact the quality factor; the last two the acceptance factor.

The ability to meet the above requirements truly differentiate between a research CFD method and one that is an engineering and design tool: for design applications, a CFD method must meet all above requirements with a reasonable degree of completeness. It is not uncommon to confuse research feasibility with design application readiness. It is the professional responsibility of the CFD code developer to fully acknowledge this difference and make it clear to the non-expert.

Unfortunately, there is a tendency amongst CFD researchers to greatly underestimate, or completely disregard, the important effort of turning a research, or pilot, code into a practical engineering tool.

Thus, the principal challenge posed by design applications to CFD practitioners is to convert what is feasible in principle (i.e., feasible in a research laboratory environment) into practical engineering tools that meet all four requirements listed at the beginning of this section.

Some of the principal CFD codes for aircraft design application in use at Lockheed are described in the following sections. These codes have been singled out for discussion herein on the grounds that they have been or are being developed specifically to be practical engineering tools. As in most engineering disciplines, there is a hierarchy in CFD methodology, namely, the various computational codes can be classified according to levels of increasing complexity and accuracy. This also implies different requirements in terms of computational resources. The codes to be discussed, all of them in practical use at Lockheed, span the CFD methodological hierarchy.

LINEAR CFD METHODOLOGY: PANEL METHODS

Methods based on linear inviscid flow assumptions are more fully developed than nonlinear methods, and they are less demanding of computer resources. The most common linear methods are the so called panel methods. The majority of these methods are limited in the flow physics they can model: they cannot deal with shock waves, transonic flows, and separated flows. On the other hand, they are capable of modeling all geometric features of the vehicle, including the most intricate details. At Lockheed, the advanced low-order panel method QUADPAN for subsonic and supersonic flows is the principal tool for linearized analysis, Figure 1. It has been under development and in use for a number of years, Reference 2.
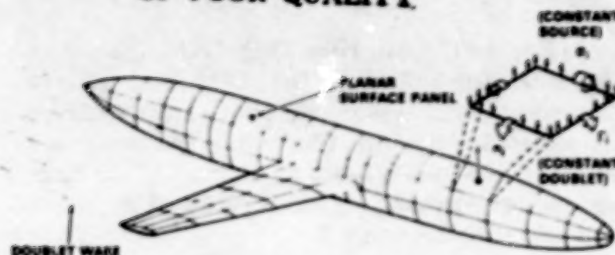
- WORK WITH PERTURBATION POTENTIAL, ϕ_p : $\vec{V} = \vec{V}_\infty + \nabla\phi_p$
- SOURCE DISTRIBUTION SET BY GREEN'S THEOREM AND CONSERVATION OF LINEARIZED MAS FLUX
- SOLVE FOR DOUBLET DISTRIBUTION
- BOUNDARY CONDITION APPLIED TO FICTITIOUS INTERNAL FLOW
- VELOCITY → 2ND ORDER BERNOULLI'S → PRESSURE

Figure 1. Advanced low-order quadrilateral element panel method QUADPAN.

In a panel method, the airplane to be modeled is represented by a large number of small contiguous surface panels. Usually these panels are flat and of a quadrilateral shape. Elementary solutions of the linearized flow equation, known as sources and doublets, are assigned to each panel, Figure 2. The individual strengths of these elementary solutions are determined by the application of the appropriate boundary conditions, e.g., no flow across solid surfaces. The shape of the distribution across a panel of these elementary solutions determine whether the method is low order (e.g., constant or linear variation) or high order (e.g., quadratic variation).
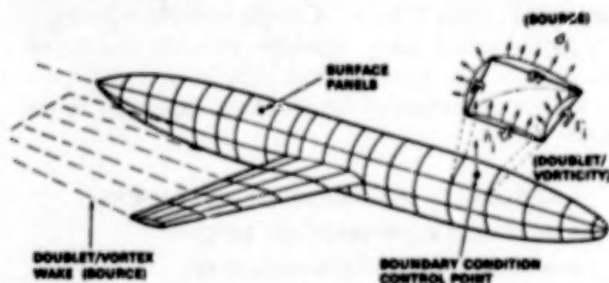

Figure 2. Concept of panel methods

Until recently it was a common belief that a high order distribution was required for better accuracy. The use of high order distribution imposes a sizeable computational cost penalty. Special numerical techniques, discussed in reference 2, can greatly improve the accuracy and robustness of low order singularity distributions. QUADPAN's advanced low order approach embodies these techniques which give it an accuracy similar to that of the high-order methods but at a fraction of the computational cost. This has been verified in evaluations conducted by NASA and U.S. Air Force researchers, References 3 and 4.

Figure 3 illustrates the result of a typical QUADPAN computation which makes evident the code's ability to model complex geometry. It shows a generic advanced fighter configuration with the corresponding elemental quadrilateral panels used to model the flow about it. The computed pressure distribution, at an angle of attack of 10 degrees at a mach number of 0.90, is shown in a color-coded display. Correlation of predicted force and moment coefficients with wind tunnel data are presented in Figure 4.
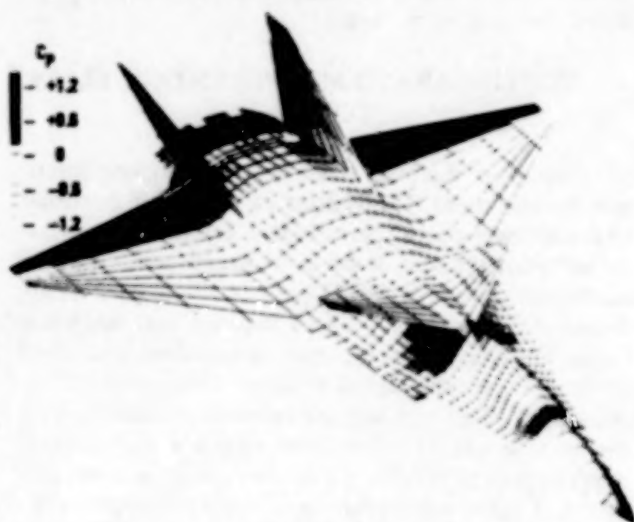

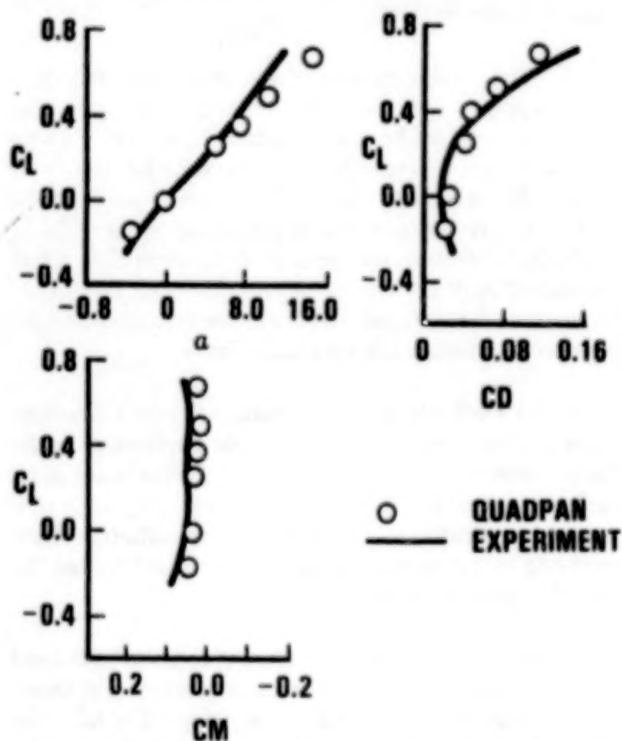Figure 3. Surface pressure distribution computed by QUADPAN on generic fighter configuration.

Figure 4. Comparison of QUADPAN predictions with wind tunnel data for generic fighter model.

79

In spite of the inherent limitations of linearized theory, QUADPAN has proven to be a valuable design tool, Reference 5. This is due to its great geometric capability and to its ease of use and computational efficiency. These factors continue to make linearized methodology the workhorse for conceptual design application. Although the routine use of a linear method such as QUADPAN does not require supercomputer capability, the effectiveness of the method is greatly enhanced by it due to resulting reductions in computational cost and cycle time.

NONLINEAR CFD METHODOLOGY: EULER CODES

Nonlinear methods have been undergoing intensive development. They either solve the full potential or the transonic small perturbation equations for inviscid irrotational flows, or the Euler equations for inviscid rotational flows, or the Reynolds-averaged Navier-Stokes equations for viscous laminar and turbulent flows. Their increased accuracy and realism is attained at the cost of substantially larger computational requirements. Furthermore, the entire space surrounding the vehicle has to be covered with a computational mesh or grid in order to solve the equations of conservation of mass, momentum, and energy throughout the flow field as is required by the nonlinearity of the equations. The generation of this computational grid for arbitrarily complex configurations is a difficult task, and it is of crucial importance for the practical application of these methods.

For flow solution algorithms, the development of time-stepping, finite volume techniques is being emphasized at Lockheed-California Company. These techniques are essentially the same whether the Euler or the Navier-Stokes equations are being solved. The principal difference is the appearance, when solving the Navier-Stokes equations, of shear stress flux terms generated by the viscosity of the fluid and the turbulence of the flow. These flux terms are zero for the Euler equations, which model inviscid flows.

Euler methods are now under advanced development and are beginning to see wide application in the design environment. Navier-Stokes methods are in an earlier stage of development and have only seen pioneering applications. The effective application of these methods in a practical design environment makes the use of supercomputers mandatory.

Although a number of different codes at Lockheed solve the Euler equations, the most advanced in terms of geometric capabilities is the TEAM (for Three-dimensional Euler Aerodynamic Method) code, Figure 5, the development of which is being partially

funded by the U.S. Air Force Flight Dynamics Laboratory, References 6, 7, and 8. The TEAM code is a modular computational system consisting of preprocessors, grid generation routines, flow solver, and postprocessors. Its flow solver is based on a variant of the finite-volume time-stepping algorithm proposed by Antony Jameson, et al, Reference 9.

$$\frac{\partial}{\partial t} \int\int\int Q \, dV + \int\int F \cdot n \, dS = 0$$

FINITE VOLUME:

• MESH CELL DEFINED BY VERTICES

TIME STEPPING:

$$Q(t + \Delta t) = Q(t) - \frac{\Delta t}{\Delta Vol} \sum_{i=1}^{6} F_i \, \Delta S_i$$

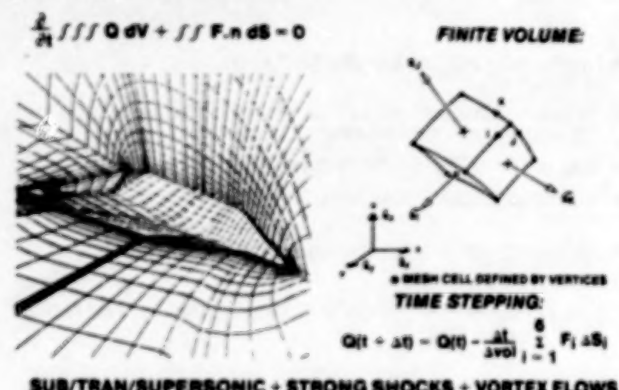**SUB/TRAN/SUPERSONIC + STRONG SHOCKS + VORTEX FLOWS**

Figure 5. Three-dimensional Euler Aerodynamic Method (TEAM) code.

The ability of the TEAM code to handle arbitrarily complex geometries is due to its zonal structure. This means that the computational domain can be divided into several zones with interfacing boundary surfaces as shown in Figure 6. The various zones can have different grid densities and the interfacing boundary surfaces can accommodate different types of boundary conditions (fluid-to-fluid interface, solid surface, transpiration, free stream). All types of grid topologies (C-H, C-O, O-H, O-O, H-H, and combinations thereof) can be dealt with, Figure 7. Complete airplane configurations including wing, fuselage, canards, horizontal and vertical tails, flow-through nacelles and inlets, etc. are within the realm of the modeling capability of the TEAM code.

• FACILITATES ANALYSIS OF REALISTIC AIRCRAFT
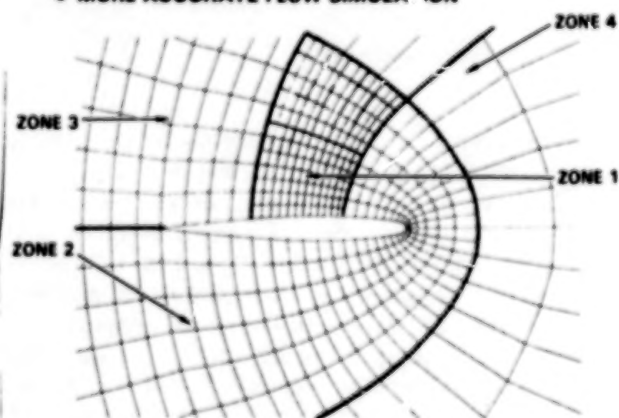• INCREASES COMPUTATIONAL EFFICIENCY
• MORE ACCURATE FLOW SIMULATION

Figure 6. Interfacing zonal grid structure.
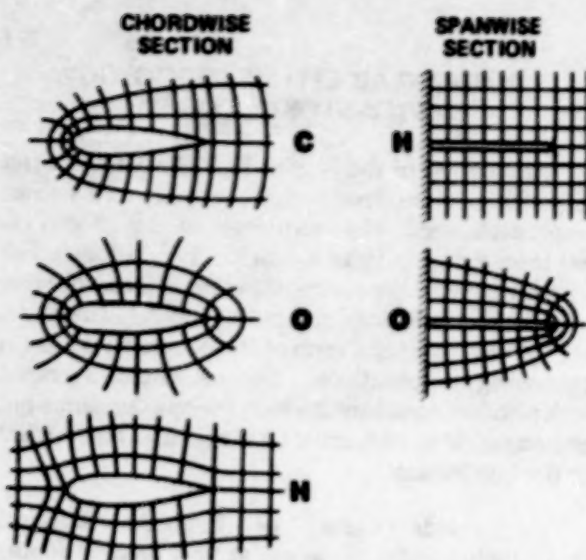
CHORDWISE SECTION **SPANWISE SECTION**

Figure 7. Typical computational mesh topologies.

The code is able to handle subsonic, transonic, and supersonic flows. It can be applied to both steady and unsteady flows, and it automatically captures shock waves and vortex flows induced by sharp edges. The ability to capture vortex flows is of great practical significance, particularly in the design of combat aircraft. Leading edge vortices, like those appearing above a delta wing at high angle of attack, induce strong nonlinear effects which cannot be predicted by classical potential flow theory. Euler methods now offer the capability of predicting these nonlinear effects for complex configurations.

Figure 8 shows the results of a TEAM code computation of the flow about a delta wing at high angles of attack. These results are compared with wind tunnel data and predictions made by classical linear theory. The improvement in accuracy provided by the Euler computations over linear theory is quite evident. Furthermore, the computed velocity field clearly displays the vortex-like structure which characterizes the flow about swept leading edges at high angles of attack.
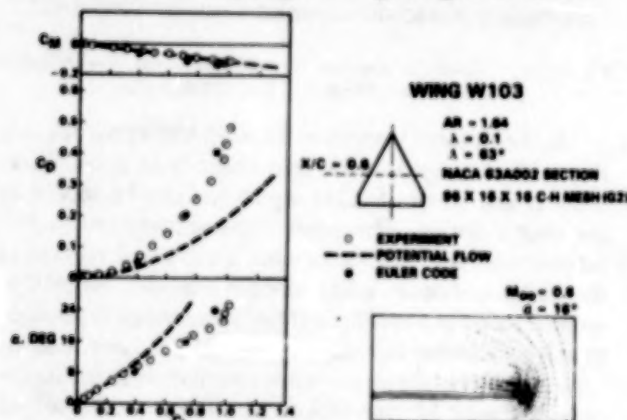

Figure 8. Comparison of computations about delta wing with experimental data.

The solution of the Euler equations appear to do an adequate job of predicting the development of vortex flows induced by sharp or highly swept edges, at least up to the point of vortex burst or breakdown. The geometrical flexibility provided by the TEAM code allows the analysis of complex vortex flow interactions about complete aircraft configurations. Our experience with the TEAM code indicates that in order to obtain reasonably accurate results, fairly dense computational grids are needed. Typically, as many as 400,000 cells may be required for a configuration consisting of a wing, fuselage, and horizontal and vertical tails in a symmetric flight condition.

Some Euler computations show the appearance of unsteadiness in vortical flows at conditions which coincide with the experimental observation of the onset of vortex breakdown. Other qualitative characteristics indicative of the effects of vortex burst have also been observed in these computations. An example of this is illustrated in Figure 9, which shows that the predicted effect of a leading edge strake upon vortex flow development correlates reasonably well with the wind tunnel data. But more study and correlations are needed before ascertaining the usefulness of Euler solutions for the prediction of vortex burst.
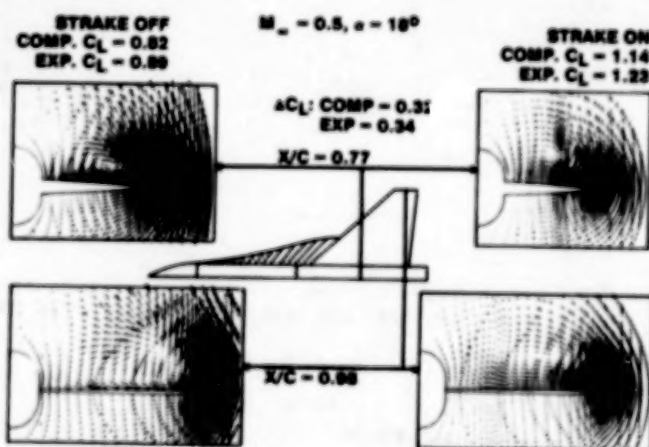
Figure 9. Effect of strake on leading edge vortex flow.

The TEAM code is also being successfully used in high supersonic mach number applications. Figure 10 presents the surface pressure distribution on one of the waverider configurations of Reference 10 at a mach number of 6 and at 4 degree angle of attack. Correlations of the computed pressure distributions with the available wind tunnel data are shown in Figure 11.

The value of Euler computations in design applications have been amply demonstrated in many cases. To what extent they will be able to satisfy the most press-

Figure 10. Surface pressure distribution computed by TEAM code on waverider configuration at Mach number = 6 and 4-degree angle of attack.

2 Y/B

LEGEND

——— AL = -4, TEAM	▲ AL = -4, EXP
·····-···-· AL = -4, TEAM	⊕ AL = -4, EXP
——— AL = 4, TEAM	⊡ AL = 4, EXP

Figure 11. Comparison of predicted lower surface pressure distribution with wind tunnel data.
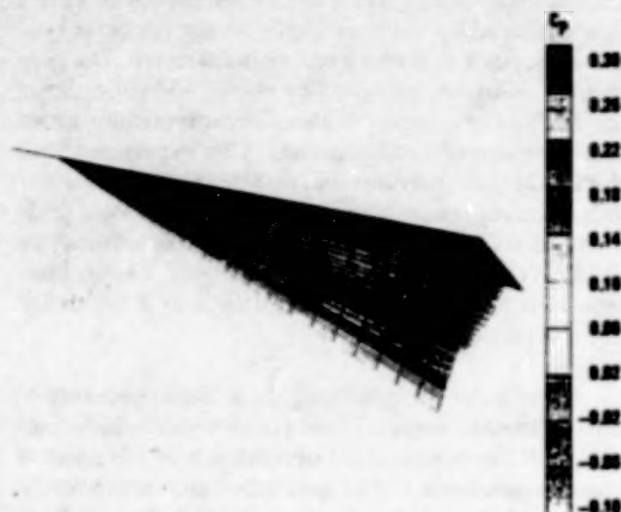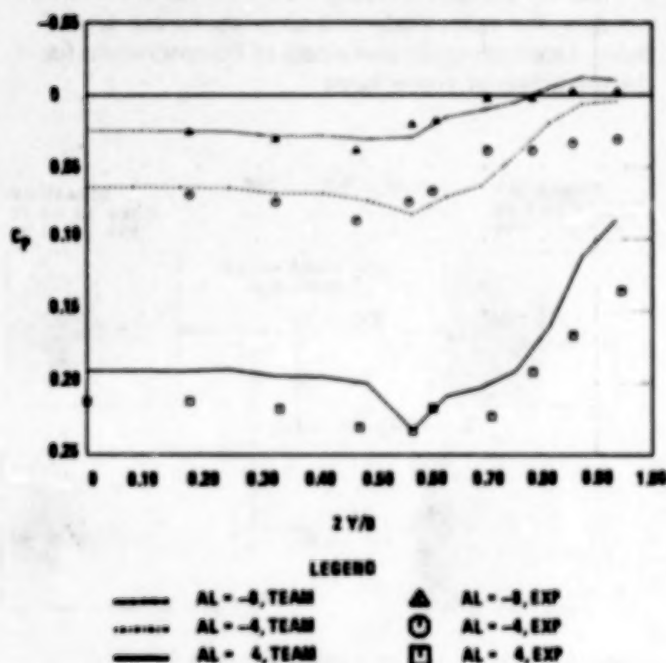
ing prediction requirements posed by the design of advanced aircraft is far from being fully established. Much work, particularly in terms of advanced computations and correlations with appropriate high quality experimental data, has to be done before the realm of practical applicability and validity of Euler solutions can be determined.

NONLINEAR CFD METHODOLOGY: NAVIER-STOKES CODES

The solution of the Navier-Stokes equations offer the potential of modeling all the physics of a viscous compressible fluid. The calculation of the viscous effects from first principles for all levels of turbulence is presently beyond the realm of practical feasibility due to the lack of adequate computing power. Therefore, the Reynolds-averaged form of the equations is used in engineering applications. The Reynolds-averaged Navier-Stokes equations include the viscous terms but semi-empirical models must be introduced to represent the flow turbulence.

A wide variety of Reynolds - averaged Navier-Stokes codes are in use at Lockheed, including codes with real gas effects and chemistry. But the most advanced from the point of view of geometric capability is the TRANSAM (for Three-dimensional Reynolds-Averaged Navier-Stokes Aerodynamic Method) code, Figure 12. Basically, it constitutes an extension of the modularized TEAM computational system to which momentum fluxes due to both viscous and Reynolds stresses have been added. Therefore, it possesses geometric flexibility and generality similar to those of the TEAM code, and it is equally able to analyze subsonic, transonic, and supersonic flows.

FINITE VOLUME:

TIME STEPPING:

SUB/TRAN/SUPERSONIC + STRONG SHOCKS + VISCOSITY
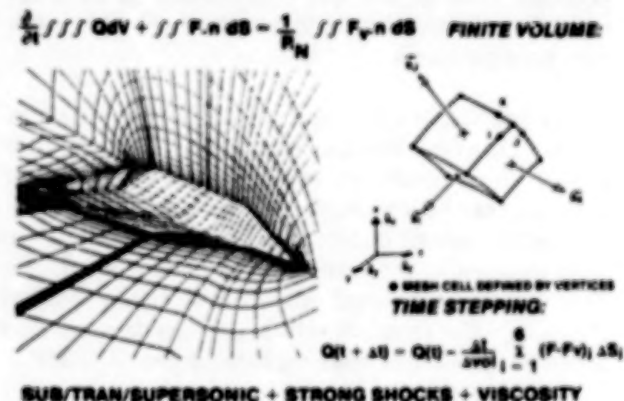
Figure 12. Three-dimensional Reynolds-averaged Navier-Stokes Aerodynamic Method (TRANSAM) code.

In the present version of TRANSAM, either the full Reynolds-averaged or the thin shear layer approximations to the Navier-Stokes equations can be solved at the user's option. The presently implemented turbulence model is an algebraic one, a modified version of the Baldwin-Lomax eddy viscosity model. Since it is architectured in a multiple zonal structure, it is possible to solve different equation types in each zone. For instance, the thin shear-layer approximation to the Reynolds-averaged Navier-Stokes equations can be solved in zones close to solid boundaries where boundary-layer behavior is to be expected; all the shear stress

terms can be accounted for in zones where fully separated flow is likely to occur; and, finally, the Euler equations can be used to model the flow for the remaining zones. This approach yields obvious economies in both computer execution time and memory requirements.

An example of the potential improvement in accuracy that can be obtained with a Navier-Stokes computation is given by the analysis of the supercritical RAE 2822 airfoil shown in Figure 13. Both viscous and inviscid calculations done with TRANSAM are compared with experimental data. The improvement that the viscous computation yields in the prediction of shock location and overall character of the pressure distribution is quite evident. The computed velocity profiles in the boundary layer, shown before and after the shock in Figure 14, show the correct behavior.
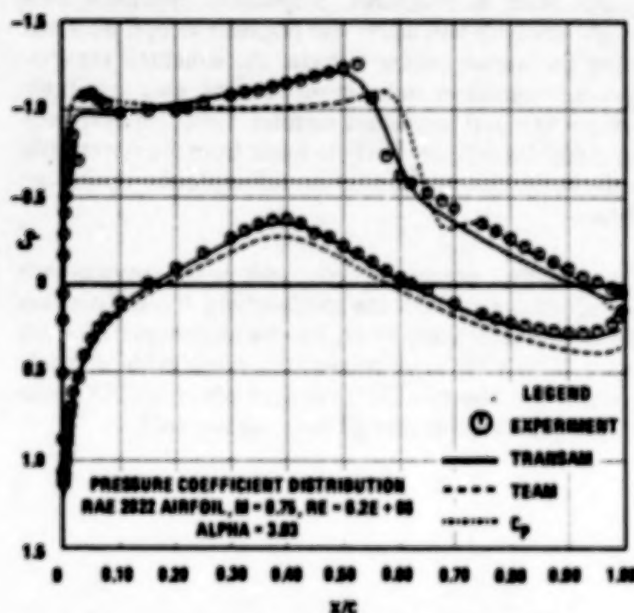

Figure 13. Comparison of computed surface pressure distributions with wind tunnel data for RAE 2822 supercritical airfoil.

We have not yet attempted the computation of separated flows about aircraft at high angles of attack because of lack of adequate memory capacity. Even using the zonal approach provided by TRANSAM, a minimum of 120 megawords of memory would be needed for such a computation. Experience with separated flows about simpler configurations indicates that the presently available algebraic turbulence models are inadequate to predict strongly separated flows with reasonable accuracy and consistency. Whether more sophisticated models (such as the two-equation or Reynolds stress models) will significantly improve the accuracy of separated flow computations remains to be determined.
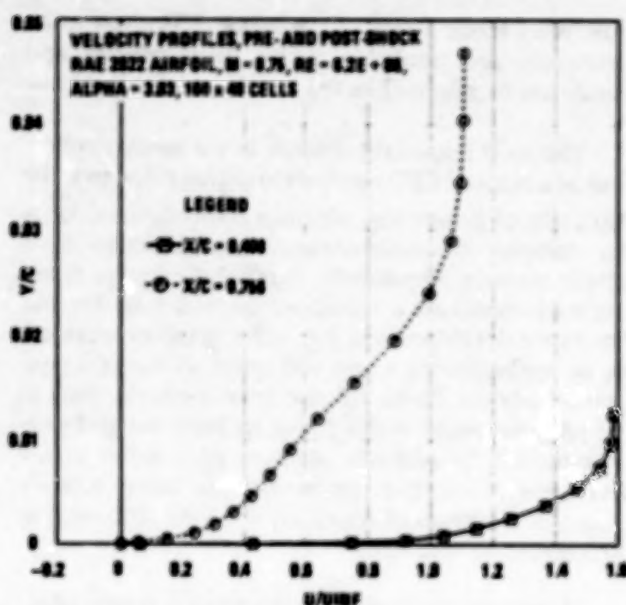

Figure 14. Before and after shock boundary layer profiles computed by TRANSAM code.

In general, the various Navier-Stokes computations of three-dimensional configurations that have been performed to date suffer from lack of adequate computational mesh resolution, and from the limitations of the turbulence models being used. Although some calculations that have recently been presented elsewhere look impressive and appear qualitatively correct, their practical value as predictive and quantitative tools is, at the present time, largely open to question.

In summary, the difficulties hampering the practical application of Navier-Stokes methods, including TRANSAM, are threefold:

1) The lack of general accuracy and reliability of present turbulence models.

2) The difficulty of generating the computational mesh or grid which engulfs the aircraft.

3) The lack of adequate computer resources.

FUTURE DEVELOPMENTS AND CONCLUDING REMARKS

In its present state of capability, CFD provides large benefits in the design process, particularly when used judiciously and synergistically with the wind tunnel. But the full realization of the great potential offered by the application of CFD to aircraft design poses formidable, but not insurmountable, technical challenges. Undoubtedly, the NAS will be highly instrumental in advancing CFD technology the level needed to success-

fully meet them. Some of the major difficulties to be overcome, and probable future developments and trends are highlighted in the remainder of this paper.

The most important obstacle to the ready application of advanced CFD methods to airplane design is the difficulty of generating adequate computational grids for complex three-dimensional configurations in a timely manner. Fortunately, significant progress is being made in this area. Advanced graphics software and hardware developments, e.g., color graphics workstations, are beginning to aid and speed up the grid generation process. Finite-volume zonal methods, such as the ones discussed in this paper, facilitate the grid generation task. In addition, alternate approaches to the treatment of complex geometries are being actively pursued, examples of which are the work discussed in References 11 and 12.

Assuming continuing development, it is very likely that soon it will be possible to generate adequate computational grids about complete and arbitrarily complex aircraft configurations in a matter of hours or days rather than weeks ,or even months, which is the time scale of present grid generation capability.

Turbulence modeling will continue to be the Achilles' heel of Reynolds-averaged Navier-Stokes codes. Reference 13 provides a concise but comprehensive survey of the state-of-the-art in turbulence modeling. This survey makes obvious that many difficulties remain. But in spite of the present short-comings of turbulence models, Navier-Stokes codes will play an increasingly useful role in many applications.

Furthermore, turbulence modeling is one area where the NAS offers great potential for advancing the state-of-the-art.

The availability of a wide variety of more capable scientific computers and supercomputers, coupled with advances in numerical solution algorithms, will greatly accelerate the application of Euler and Navier-Stokes methods to the solution of airplane design problems. Computers ranging in speed from 100 to 10,000 million instructions per second and in memory capacity from 8 to 256 million words will become commercially available at competitive prices in the near future.

The analysis and optimization of multidisciplinary interactions will become commonplace thanks to the capabilities of CFD and the foreseen increases in computer power and cost-effectiveness. Coupling CFD with the computational methodologies of other disciplines such as structures, propulsion, dynamics, and flight controls will allow the engineer to optimize not only the aerodynamics but also the structural components, propulsion and control systems, etc., in a fully interactive and integrated manner. Great performance and cost benefits are likely to result from the synergistic effects of this interactive multidisciplinary optimization.

Finally, supercomputers and wind tunnels are complementary and not exclusionary tools. This has been repeated many times, but the more experience we gain with CFD applications, the more evident it becomes. It is also true that to further advance CFD, more high-quality experimental data are required.

REFERENCES

1. Miranda, L. R. "Application of Computational Aerodynamics to Airplane Design," AIAA Journal of Aircraft, Vol. 21, No. 6, pp 355-370, June 1984.

2. Youngren, H. H.; Bouchard, E. E.; Coopersmith, R. M. and Miranda, L. R. "Comparison of Panel Method Formulations and its Influence on the Development of QUADPAN, an Advanced Low Order Method," AIAA Paper 83-1827, AIAA Applied Aerodynamics Conference, Danvers, Massachusetts, July 13-15, 1983.

3. Margason, Richard J.; Kjelgaard, Scott O.; Sellers III, William L.; Morris, Jr., Charles E. K., "Subsonic Panel Methods - A Comparison of Several Production Codes," AIAA Paper 85-0280, AIAA 23rd Aerospace Sciences Meeting, Reno, Nevada, January 14-17, 1985.

4. Strang, W. Z.; Berdahl, C. H.; Nutley, E. L. and Murn, A. J., "Evaluation of Four Panel Aerodynamic Prediction Methods (MCAERO, Pan Air, QUADPAN, and VSAERO," AIAA Paper 85-4092, AIAA 3rd Applied Aerodynamics Conference, Colorado Springs, Colorado, October 14-16, 1985.

5. Johnston, C. E.; Youngren, H. H., and Sikora, J. S., "Engineering Applications of an Advanced Low-Order Panel Method," SAE Paper 851793, SAE Technical Paper Series, Aerospace Technology Conference & Exposition, Long Beach, California, October 14-17, 1985.

6. Raj, P. R. and Long, L. N., "An Euler Aerodynamic Method for Leading-Edge Vortex Flow Simulation," NASA Conference Publication 2416, pp. 263-282, Hampton, Virginia, October 8-10, 1985.

7. Raj, P. R.; Sikora, J. S. and Keen, J. M., "Free-Vortex Flow Simulation Using a Three-Dimensional Euler Aerodynamic Method," ICAS Paper 86-1.5.2, 15th Congress of the International Council of the Aeronautical Sciences, London, United Kingdom, September 7-12, 1986.

8. Raj, P. R. and Brennan, J. E., "Improvements to an Euler Aerodynamic Method for Transonic Flow Analysis," AIAA Paper 87-0040, AIAA 25th Aerospace Sciences Meeting, Reno, Nevada, January 12-15, 1987.

9. Jameson, A.; Schmidt, W. and Turkel, E., "Numerical Solutions of the Euler Equations by Finite Volume Methods Using Runge-Kutta Time-Stepping Schemes," AIAA Paper 81-1259, 14th Fluic and Plasma Dynamics Conference, Palo Alto, California, June 23-25, 1981.

10. Jones, Kenneth M., "Application of a Supersonic Full Potential Method for Analysis of Waverider Configurations," NASA Technical Paper 2608, Langley Research Center, Hampton, Virginia, 1986.

11. Erickson, L. L. and Strande, S. M., "PAN AIR: Evolution and New Directions . . . Transonics for Arbitrary Configurations," AIAA Paper 83-1831, AIAA Applied Aerodynamics Conference, Danvers, Massachusetts, July 13-15, 1983.

12. Jameson, A., Baker, T. J., and Weatherill, N. P., "Calculation of Inviscid Transonic Flow over a Complete Aircraft," AIAA Paper 86-0103, AIAA 24th Sciences Meeting, Reno, Nevada, January 6-9, 1986.

13. Lakshminarayana, B., "Turbulence Modeling for Complex Shear Flows," AIAA Journal, Vol. 24, No. 12, December 1986, pp. 1900-1917.

DEVELOPMENT AND APPLICATION OF UNIFIED ALGORITHMS FOR PROBLEMS IN COMPUTATIONAL SCIENCE

Vijaya Shankar and Sukumar Chakravarthy

Rockwell International Science Center

ABSTRACT

This paper presents a framework for developing computationally unified numerical algorithms for solving nonlinear equations that arise in modeling various problems in mathematical physics. The concept of computational unification is an attempt to encompass efficient solution procedures for computing various nonlinear phenomena that may occur in a given problem. For example, in Computational Fluid Dynamics (CFD), a unified algorithm will be one that allows for solutions to subsonic (elliptic), transonic (mixed elliptic-hyperbolic), and supersonic (hyperbolic) flows for both steady and unsteady problems. The objective of the work reported in this paper is manyfold: 1) development of superior unified algorithms emphasizing accuracy and efficiency aspects; 2) development of codes based on selected algorithms leading to validation; 3) application of mature codes to realistic problems; and 4) extension/application of CFD-based algorithms to problems in other areas of mathematical physics. The ultimate objective is to achieve integration of multidisciplinary technologies (stealth, propulsion, aeroelasticity, ···) to enhance synergism in the design process through computational simulation.

The paper presents specific unified algorithms for a hierarchy of gasdynamic equations (full potential, Euler, and Navier-Stokes) and their applications to a wide variety of problems. Also included are extensions of the CFD methods to two other areas: 1) electromagnetic scattering, and 2) laser-material interaction accounting for melting.

INTRODUCTION

Along with rapid strides in algorithm and code development, the increasing power of super-minicomputers, supercomputers, and graphics workstations is rapidly advancing the state of the art of computational simulation of problems in mathematical physics. One area that is setting the pace is Computational Fluid Dynamics. Other disciplines such as electromagnetic scattering, semiconductor device/process modeling, material characterization, etc., are starting to benefit from the CFD experience.

Modern vehicle concepts such as the Advanced Tactical Fighter (ATF) attempt an effective compromise between the transonic maneuver and supersonic cruise conditions. Multiple design considerations of this type impose stringent constraints on the aerodynamic shape of the vehicle to achieve high buffet-free lift performance with reduced trim drag. The recent resurgence of the hypersonics program through the National Aerospace Plane (NASP) project also demands analysis and design of vehicles with requirements to fly through the entire Mach number range (subsonic to hypersonic) requiring increasingly sophisticated nonlinear methods to better understand various gasdynamic flow processes.

The Navier-Stokes equations best represent the physics of nonlinear flow. However, limitations in memory and execution speed of present-day supercomputers restrict the routine use of Navier-Stokes methods. For wider application of CFD in the aerospace industry, cost-effective methods based on less exact forms of gasdynamic equations, such as the Euler and full potential equations, are still attractive. The objective of the work reported in this paper is to develop, for all speed regimes, efficient, accurate, and robust nonlinear methods for equations ranging from the simple full potential to the complex Navier-Stokes. Development of such a spectrum of hierarchical capability is critical for efficient and cost-effective design of aerospace configurations. The general philosophy of numerical design through progression of increasingly sophisticated nonlinear tools is illustrated in figure 1, and represents a summary of the numerical design experience at Rockwell covering the HiMAT, forward swept wing, SAAB, and Air Force/Navy Research Technology contract studies[1-4].

Referring to figure 1, in designing a configuration, linear theory[5,6] is first used to establish candidate optimum thickness, twist, camber, and variable camber deflections at supersonic speeds. Second, nonlinear methods (full potential and Euler) are employed to capture embedded shock waves at transonic[7-14] and supersonic[15-21] conditions and weaken the wave system through parametric redesign. Boundary layer analysis[22] and Navier-Stokes codes[23-26] are subsequently used to assess the flow quality of the nonlinear inviscid design. The extent of separation in particular is evaluated, and a subsequent redesign is performed to minimize its extent.
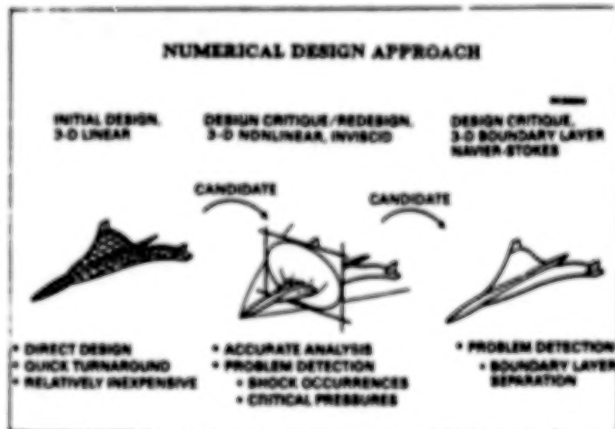

Fig. 1. Progression of improved design through nonlinear analysis.

At Rockwell, the computational activity is carried out on several fronts. 1) <u>Algorithm development</u>. Under this task, several algorithmic issues such as higher order space/time accuracy, efficiency, multizone gridding concepts, multigrid cycling, upwind total variation diminishing (TVD) schemes, vectorization concepts, implicit/explicit methods, etc., are stressed. The primary thrust of this activity is computational unification of methodologies encompassing efficient solution procedures for computing various flow phenomena occurring across the Mach number range. 2) <u>Code development</u>. Under this task, selected algorithms (based on the study from task 1)) with potential to mature into a production code capability are further developed and undergo extensive validation. Some of the issues stressed in this phase are computational efficiency through code vectorization, user orientation/documentation, code transportability, graphics interface, and user training. 3) <u>Application</u>. At this stage, codes from task 2) that have matured into a production code with established user confidence, are applied to study a wide range of realistic problems to better understand flows over existing configurations (Shuttle Orbiter, B-1B, etc.) as well as to design aerospace configurations for the next generation (ATF, NASP, Transatmospheric Vehicles (TAV), etc.). 4) <u>Extension of CFD methods to non-CFD problems</u>. Under this task, a host of problem areas in mathematical physics that are governed by appropriate partial differential equations is dealt with. The techniques developed for studying problems in Computational Fluid Dynamics are well suited for studying problems in electromagnetic scattering, laser-material interaction, and semiconductor device/process modeling, just to name a few.

Computational Fluid Dynamics is rapidly advancing. Its methods are beginning to influence how problems are and can be effectively solved in other disciplines. As this process of spreading the wealth of CFD knowledge to other areas continues, the CFD discipline is expected to play a key role in the future, together with state-of-the-art computers, in integrating multidisciplinary technologies to enhance synergism in the design process through computational simulation.

The paper presents a brief summary of some of the unified algorithms developed for various gasdynamic equations, along with their applications to many fluid dynamic problems. Also presented are some applications of CFD methods to non-fluid dynamic problems. More details on the algorithmic aspects of the unified concept can be found in the references.

This paper represents a collection of work performed by many researchers in the Computational Fluid Dynamics Department at Rockwell International Science Center.

EQUATIONS IN CONSERVATION FORM

For many problems in mathematical physics, the physical process to be modeled is governed by an appropriate set of linear or nonlinear partial differential equations. For example, many fluid dynamic processes are governed by the Navier-Stokes equations, the electromagnetic scattering from objects is modeled by Maxwell's equations[37], and problems in semiconductors are governed by Van Roos-

broeck[38] equations involving the nonlinear coupling between the electrostatic potential and the electron/hole density.

In general, many of these equations naturally lend themselves to a conservation form representation given by

$$Q_t + E_x + F_y + G_z = 0 \qquad (1)$$

where the dependent variable vector Q, and the fluxes E, F, and G take on different forms depending on the equation being modeled. The form of Q, E, F, and G for the full potential, Euler, Navier-Stokes, and the Maxwell equations are presented in the subsequent sections. Application of eq. (1) to many realistic problems requires a coordinate transformation to properly represent the physical domain of interest and to aid in the boundary condition treatment.

Under the transformation of coordinates implied by

$$\tau = t, \xi = \xi(t, x, y, z), \eta = \eta(t, x, y, z), \zeta = \zeta(t, x, y, z),$$

eq. 1 can be recast in the conservation form given by

$$\bar{Q}_\tau + \bar{E}_\xi + \bar{F}_\eta + \bar{G}_\zeta = 0 \quad , \qquad (2a)$$

where

$$\bar{Q} = \frac{Q}{J} \quad ,$$

$$\bar{E} = \frac{\xi_t}{J}Q + \frac{\xi_x}{J}E + \frac{\xi_y}{J}F + \frac{\xi_z}{J}G \quad ,$$

$$\bar{F} = \frac{\eta_t}{J}Q + \frac{\eta_x}{J}E + \frac{\eta_y}{J}F + \frac{\eta_z}{J}G \quad , \qquad (2b)$$

$$\bar{G} = \frac{\zeta_t}{J}Q + \frac{\zeta_x}{J}E + \frac{\zeta_y}{J}F + \frac{\zeta_z}{J}G \quad .$$

where, in turn, J is the Jacobian of the transformation

$$J = \partial(\xi, \eta, \zeta)/\partial(x, y, z) \qquad (2c)$$

and

$$\xi_t = -(\xi_x x_\tau + \xi_y y_\tau + \xi_z z_\tau)$$
$$\eta_t = -(\eta_x x_\tau + \eta_y y_\tau + \eta_z z_\tau) \qquad (2d)$$
$$\zeta_t = -(\zeta_x x_\tau + \zeta_y y_\tau + \zeta_z z_\tau) \quad .$$

Associating the subscripts j, k, l with the ξ, η, ζ directions, a numerical approximation to eq. (2a) may be expressed in the semi-discrete conservation law form given by

$$(\bar{Q}_{j,k,l})_\tau + (\hat{E}_{j+1/2,k,l} - \hat{E}_{j-1/2,k,l})$$
$$+ (\hat{F}_{j,k+1/2,l} - \hat{F}_{j,k-1/2,l}) \qquad (3)$$
$$+ (\hat{G}_{j,k,l+1/2} - \hat{G}_{j,k,l-1/2}) = 0$$

where $\hat{E}, \hat{F}, \hat{G}$ are numerical or representative fluxes at the bounding sides of the cell for which discrete conservation is considered, and $\bar{Q}_{j,k,l}$ is the representative conserved quantity (the numerical approximation to $\bar{Q}$) considered conveniently to be the centroidal value. The half-integer subscripts denote cell sides and the integer subscripts the cell itself or its centroid.

The semi-discrete conservation law given by eq. (3) may be regarded as representing a finite volume discretization if the following associations are made:

$$\tilde{Q}_{j,k,l} = Q V_{j,k,l} \tag{4a}$$

where V is the volume of the cell under consideration;

$$\left(\frac{\xi_{x,y,z}}{J}\right)_{j\pm1/2} =$$

$$n_{x,y,z}\{(k-1/2,l-1/2),(k+1/2,l-1/2),$$
$$(k+1/2,l+1/2),(k-1/2,l+1/2)\}_{j\pm1/2} \;,$$

$$\left(\frac{\eta_{x,y,z}}{J}\right)_{k\pm1/2} =$$

$$n_{x,y,z}\{(j-1/2,l-1/2),(j-1/2,l+1/2),$$
$$(j+1/2,l+1/2),(j+1/2,l-1/2)\}_{k\pm1/2} \;,$$

$$\left(\frac{\zeta_{x,y,z}}{J}\right)_{l\pm1/2} =$$

$$n_{x,y,z}\{(j-1/2,k-1/2),(j+1/2,k-1/2),$$
$$(j+1/2,k+1/2),(j-1/2,k+1/2)\}_{l\pm1/2} \;; \tag{4b}$$

$$\left(\frac{\xi_t}{J}\right)_{j\pm1/2} = -\left(\frac{\xi_x}{J}\right)_{j\pm1/2}(x_\tau)_{j\pm1/2}$$

$$-\left(\frac{\xi_y}{J}\right)_{j\pm1/2}(y_\tau)_{j\pm1/2} - \left(\frac{\xi_z}{J}\right)_{j\pm1/2}(z_\tau)_{j\pm1/2}$$

$$\left(\frac{\eta_t}{J}\right)_{k\pm1/2} = -\left(\frac{\eta_x}{J}\right)_{k\pm1/2}(x_\tau)_{k\pm1/2}$$

$$-\left(\frac{\eta_y}{J}\right)_{k\pm1/2}(y_\tau)_{k\pm1/2} - \left(\frac{\eta_z}{J}\right)_{k\pm1/2}(z_\tau)_{k\pm1/2} \tag{4c}$$

$$\left(\frac{\zeta_t}{J}\right)_{l\pm1/2} = -\left(\frac{\zeta_x}{J}\right)_{l\pm1/2}(x_\tau)_{l\pm1/2}$$

$$-\left(\frac{\zeta_y}{J}\right)_{l\pm1/2}(y_\tau)_{l\pm1/2} - \left(\frac{\zeta_z}{J}\right)_{l\pm1/2}(z_\tau)_{l\pm1/2}$$

In the above, $n_{x,y,z}$ are the x,y,z components of the representative normals to the surface formed by the four points a,b,c,d implied in $n_{x,y,z}(a,b,c,d)$. These four points are not necessarily coplanar. Also, $(x_\tau,y_\tau,z_\tau)_{j\pm1/2,k\pm1/2,l\pm1/2}$ are the x,y,z components of the appropriate cell-face representative velocities. These describe the motion of the cell face and will be zero for a stationary grid. In the following, we can use the notation n_t to describe the representative cell-face normal velocities:

$$(n_t)_{j\pm1/2} = \left(\frac{\xi_t}{J}\right)_{j\pm1/2}$$

$$(n_t)_{k\pm1/2} = \left(\frac{\eta_t}{J}\right)_{k\pm1/2} \tag{4d}$$

$$(n_t)_{l\pm1/2} = \left(\frac{\zeta_t}{J}\right)_{l\pm1/2}$$

The evaluation of the volume, cell-face normals and cell-face normal velocities (metrics) are presented in Ref. 14.

Within this framework of a finite volume representation, the concept of a unified algorithm/solver addresses two issues: 1) representation of the numerical fluxes $\tilde{E}$, $\tilde{F}$, and $\tilde{G}$ to account for different physical phenomena to be encountered in the problem being modeled (for example, in fluid dynamics, a unified flux representation will allow for

subsonic, transonic, and supersonic flow situations for both steady and unsteady, including proper transition through shocks and sonic rarefaction); and 2) numerical issues of solving eq. (3). Under the numerical issue, a unified algorithm will be one that performs both the space and time integration within the logic of a single solver. A unified solution treatment will allow one to consider a wide class of problem areas within the capability of a single code. For example, in fluid dynamics, a unified solver will perform space marching for supersonic flows (supersonic flow direction is treated as time like) and allow time marching for subsonic, transonic, and unsteady flows.

The objective is to solve eq. (3) for the dependent vector Q. After incorporation of proper flux representation, the discrete form of eq. (3) can be written as

$$R(Q) = 0. \tag{5}$$

If Q is known at a known neighborhood state, denoted by Q^*, then solution to eq. (5) can be written as

$$\frac{\partial R}{\partial Q}(Q - Q^*) = -R(Q^*) \tag{6}$$

where $\frac{\partial R}{\partial Q}$, in general, is a differential operator. Many numerical algorithmic issues such as implicit, explicit, relaxation, approximate factorization, algorithm unification, etc., come into play in the modeling of the differential operator $\frac{\partial R}{\partial Q}$. Issues such as higher order accuracy, proper upwinding, etc., come into $\frac{\partial R}{\partial Q}$ as well as in the modeling of the right hand side $R(Q^*)$. For a unified code that accounts for both space and time marching, one option is to split the $\frac{\partial R}{\partial Q}$ operator in the form

$$\frac{\partial R}{\partial Q} = L_\eta L_\zeta \tag{7}$$

where

$$L_\eta = L_\eta[(\tau,\zeta),\eta] \quad , \quad L_\zeta = L_\zeta[(\tau,\zeta),\zeta].$$

Equation (7) represents a double approximate factorization in the (η,ζ) plane with relaxation in the ζ-direction assumed to represent the predominant flow direction. The grouping (τ,ζ) in the L_η and L_ζ operator represents a collection of terms involving time and ζ derivative terms. For time marching, the time-step-size $\Delta\tau$ is chosen to maintain the stability and accuracy of the operator, eq. (7). For space marching, $\Delta\tau$ is usually set very large and the operator L_η becomes $L_\eta(\zeta,\eta)$ and $L_\zeta = L_\zeta(\zeta,\zeta)$ representing ζ as the marching direction. Space marching along ζ is possible only if the equation is hyperbolic with respect to that direction. A code that is based on the unified solver will include the following options:

$$\frac{\partial R}{\partial Q} = L_\zeta(\zeta,\tau)L_\eta(\eta,\tau)L_\zeta(\zeta,\tau) \quad \text{– Triple approximate factorization with time marching} \tag{8a}$$

$$\frac{\partial R}{\partial Q} = L_\eta[(\tau,\zeta),\eta]L_\zeta[(\tau,\zeta),\zeta] \quad \text{– Double approximate factorization with time marching} \tag{8b}$$

$$\frac{\partial\xi}{\partial\tau} = L_\eta(\xi,\eta)L_\zeta(\xi,\eta) \qquad \text{- Space marching along } \xi \text{ setting} \quad (8c)$$
$$\Delta\tau \to \infty.$$

If one employs an upwind differencing, $\frac{\partial\xi}{\partial\tau}$ can also be represented by a Gauss-Siedel relaxation maintaining diagonal dominance. More discussions on these ideas can be found in Refs. 12, 19, and 20.

For time marching, Q^* is usually set to be Q^n as a first guess where Q^n is the solution at the previous time plane. For space marching, Q^* is initially set to be Q_{j-1} representing the solution at the previous space marching plane in the ξ direction. Starting from the initial guess for Q^*, eq. (6) is iterated to convergence driving $\| Q - Q^* \|$ to some preset small value at every time or space marching plane. Usually, this process might involve only a few iterations.

The issue of numerical flux representation is dealt with in the subsequent sections for a variety of equations, namely 1) full potential, 2) Euler, 3) Navier-Stokes, 4) Maxwell, and 5) incompressible Navier-Stokes, representing the laser-material interaction.

Full Potential Equation

The full potential equation represents the inviscid, irrotational, and isentropic flow. In spite of these assumptions, this form of the gasdynamic equation is widely in use for analyzing complex configurations at transonic and low supersonic Mach numbers. As long as the shocks are weak (Mach number normal to a shock surface less than 1.3 to 1.5), the full potential isentropic shocks will be in agreement with the Rankine-Hugoniot jump conditions.

Referring to eq. (1), the full potential equation takes the form $Q = \rho$, $E = \rho u$, $F = \rho v$, and $G = \rho w$, where ρ is the density and u, v, and w are the Cartesian velocities. All the quantities ρ, u, v, and w are expressible in terms of a single scalar function ϕ, the velocity potential. Using Bernoulli's law, the density ρ is given by

$$\rho^{\gamma-1} = 1 - \frac{\gamma-1}{2}M_\infty^2\left[2\phi_\tau + (U+\xi_t)\phi_\xi + (V+\eta_t)\phi_\eta + (W+\zeta_t)\phi_\zeta - 1\right] \qquad (9)$$

and U, V, and W are the contravariant velocities.

Referring to eq. (3), modeling of the time term $\tilde{Q}_\tau$ will require time linearization for density to express ΔQ in terms of $\Delta\phi = \phi - \phi^*$. The density linearization is given by

$$\rho = \rho(\phi_*) + \left(\frac{\partial\rho}{\partial\phi}\right)_{\phi=\phi_*}\Delta\phi \qquad (10)$$

where

$$\left(\frac{\partial\rho}{\partial\phi}\right)_{\phi=\phi_*} = \left[-\frac{\rho}{a^2}\left\{\frac{1}{\Delta\tau_1} + U\frac{\partial}{\partial\xi} + V\frac{\partial}{\partial\eta} + W\frac{\partial}{\partial\zeta}\right\}\right]_{\phi=\phi_*} \qquad (11)$$

is a differential operator.

Equation (3) also requires evaluation of $\hat{E}$, $\hat{F}$, and $\hat{G}$ at various spatial half node points. As mentioned earlier, $\hat{E}$ represents $\overline{E}$ appearing in eq. (2a).

The concept of developing a unified full potential scheme stems from a proper definition for the numerical or representative fluxes $\hat{E}$, $\hat{F}$, $\hat{G}$ at cell interfaces derived from the theory of characteristic signal propagation. Depending on the type of flow at the cell interface (subsonic, transonic, or supersonic), the fluxes are properly defined employing an upwind bias to eliminate numerical or spurious (unphysical) oscillations by satisfying entropy conditions (no expansion shocks).

Based on the characteristic system at a cell interface in the time-space domain, the following different flux representations are made.

Subsonic at cell face $j + 1/2$ $(U < c\sqrt{a_{11}})$

$$\hat{E}_{j+1/2} = \overline{E}_{j+1/2} \qquad \text{(zero biasing)}$$

Transonic at $j + 1/2$ $(U < c\sqrt{a_{11}}, \quad q > c)$

$$\hat{E}_{j+1/2} = \tilde{\overline{E}}_{j+1/2} \qquad \text{(to be defined later)} \qquad (12)$$

Supersonic at $j + 1/2$ $(U > c\sqrt{a_{11}})$

$$\hat{E}_{j+1/2} = \overline{E}_{j-1/2} \qquad \text{(upwind biased flux)}$$

In eq. (12), c is the speed of sound and $a_{11} = (\xi_x^2 + \xi_y^2 + \xi_z^2)$. The transonic flux $\tilde{\overline{E}}$ is defined in terms of an upwind biased density based on flux biasing. Define

$$\tilde{\rho} = \frac{1}{q}\left[(\rho q) \pm \left\{\frac{U}{Q}\frac{\partial}{\partial\xi} + \frac{V}{Q}\frac{\partial}{\partial\eta} + \frac{W}{Q}\frac{\partial}{\partial\zeta}\right\}(\rho q)^-\right] \qquad (13)$$

where $Q = \sqrt{U^2 + V^2 + W^2}$.

The quantity $(\rho q)^-$ appearing in eq. (13) is defined to be

$$(\rho q)^- = \rho q - \rho^* q^* \qquad \text{if } q > q^*$$
$$= 0 \qquad \text{if } q \leq q^* \qquad (14)$$

The quantities $\rho^* q^*$, ρ^*, and q^* represent sonic values of the flux, density, and total velocity, respectively. These sonic conditions are given by (using the density and speed of sound relationships)

$$(q^*)^2 = \frac{1 + \frac{(\gamma-1)}{2}M_\infty^2\left(1 - 2\phi_\tau - 2\xi_t\phi_\xi - 2\eta_t\phi_\eta - 2\zeta_t\phi_\zeta\right)}{\frac{\gamma+1}{2}M_\infty^2}$$

$$\rho^* = (q^* M_\infty)^{2/(\gamma-1)}. \qquad (15)$$

Note that for steady flows, the sonic conditions ρ^* and q^* are only a function of the freestream Mach number, and for a given flow they are constants. For unsteady flows, ρ^* and q^* need to be computed everywhere due to the presence of ϕ_τ and other unsteady terms in eq. (15).

In the final discretized form, the full potential equation is written in the form of eq. (6) with $\Delta\phi = (\phi - \phi^*)$ as a single unknown at a grid point.

Some results are presented to illustrate the unified full potential capability in computing subsonic, transonic, and supersonic steady/unsteady flows.

Full Potential Results

Supersonic Flows — Supersonic flows are computed using the marching option within the unified solver.

Figure 2 shows the surface gridding along with cross-plane field grid points for a typical advanced generic fighter. The body-fitted grid is generated at every marching plane using standard elliptic grid solvers. Figure 3 shows pressure contours at two different axial stations at $M_\infty = 1.6$, $\alpha = 4.94°$. The crossplane geometry in figure 3 clearly shows the fuselage, vertical tail, wing, and the flow through nacelle along with the wake cut behind the trailing edge of the wing. Figure 4 shows pressure correlation between the computations and experimental data at two different span stations. Table 1 gives correlations for overall force and moment coefficients for different angles of attack and side slip angles. The impact of CFD on the development of advanced configurations is illustrated in figure 5. It shows the L/D performance for the configuration of figure 2 for across the Mach number range and compares that performance with existing fighters such as the F-14 and the F-15. A 25% to 50% increase in L/D is demonstrated.

Figure 6 shows a complex fighter configuration with canard, wing, vertical tail, swept-side-walled flow through nacelle, and a canopy. The gridding at different axial stations is shown. Figure 7 shows the pressure contours at different marching planes at $M_\infty = 2.0$, $\alpha = 4°$. A comparison of overall force and moment coefficients is given in Table 2. Figure 6 illustrates the extent of geometric complexity that can be handled by the full potential code for supersonic flows. However, for transonic and subsonic flows where the computational domain has to extend far upstream and far downstream of the configuration, the requirement for a global three-dimensional grid makes treatment of complex configurations more formidable.
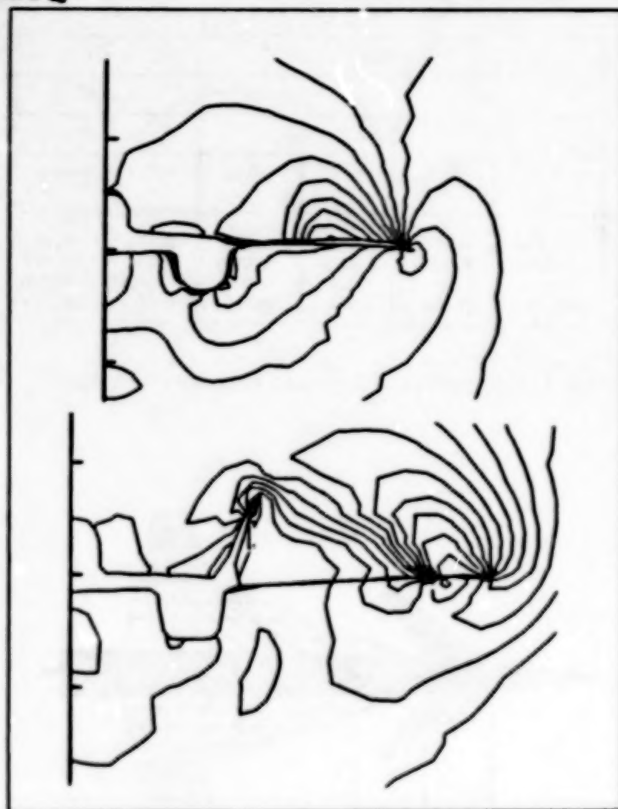

Fig. 2. Computational grid for a fighter.

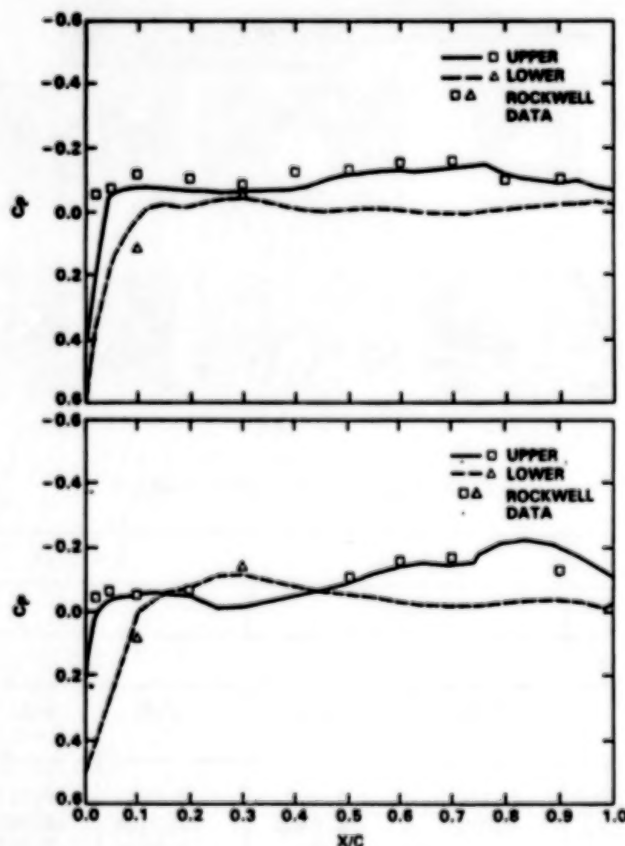Fig. 3. Pressure contours at two different axial stations.

Fig. 4. Chordwise pressure distribution at 60% and 80% span stations; $M_\infty = 1.6$, $\alpha = 1.24°$.

C-2

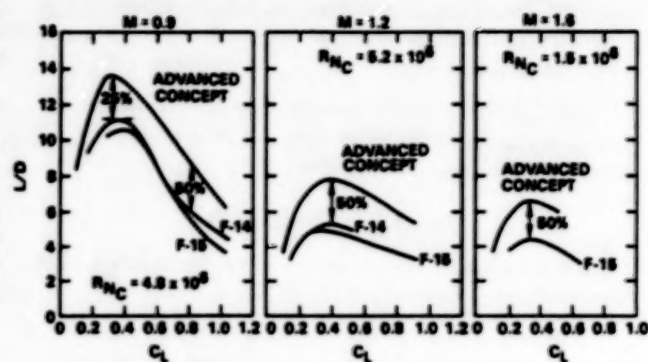|	β = 0°				β = 4.0°	
α	1.24		4.94		6.0°	
M_∞	1.6		1.6		1.6	
	F.P.	Data	F.P.	Data	F.P.	Data
C_L	0.119	0.105	0.3058	0.303	0.37	0.40
C_D	0.0293	0.0280	0.0455	0.0475	0.058	0.053
C_Y	0	0	0	0	-0.0454	0.0380
C_N	-0.0248	-0.021	-0.051	-0.045	-0.0542	-0.075

Table 1. Comparison of force and moment coefficients.

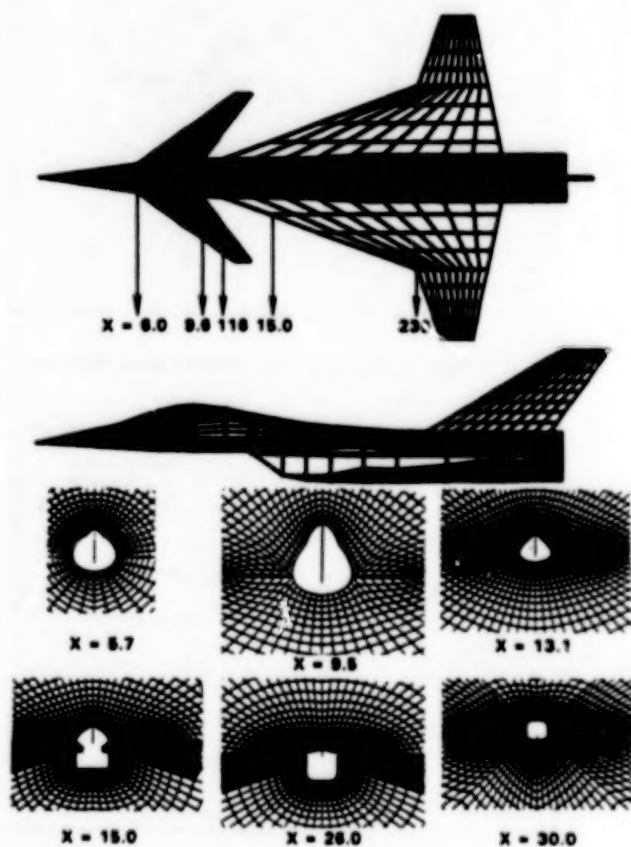Fig. 5. Impact of CFD on advanced configuration development.

Fig. 6. Modeling of a canard-wing fighter.

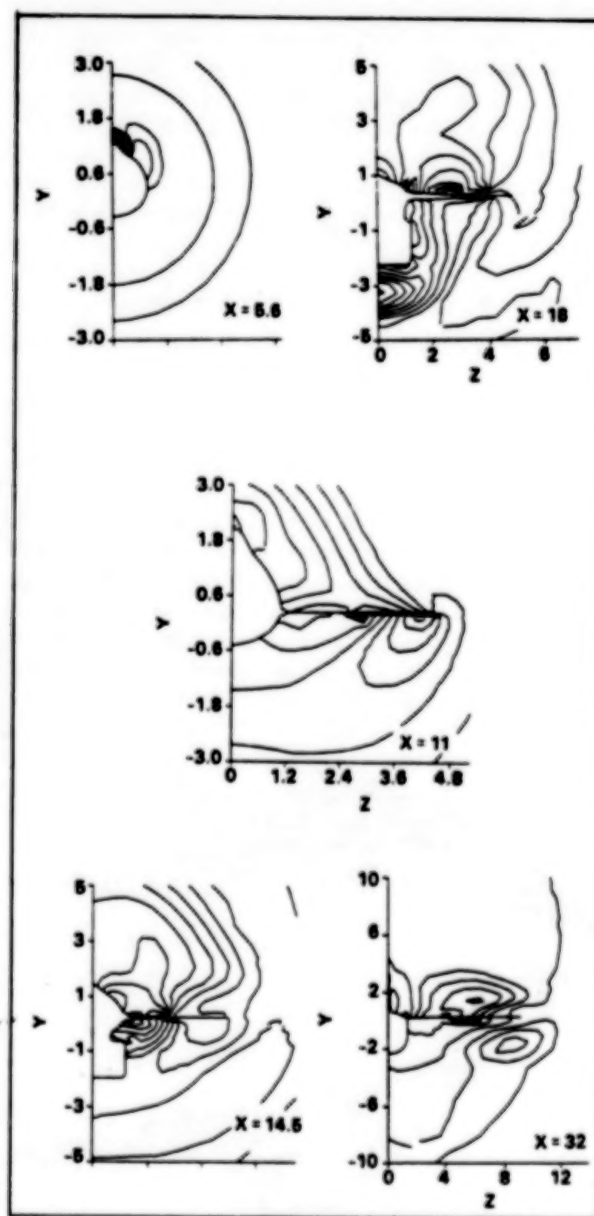|	β = 0		β = 3.18	
α	4.0		3.78	
M_∞	2.0		2.0	
	F.P.	Data	F.P.	Data
C_L	0.151	0.153	0.148	0.153
C_D	0.031	0.0302	0.0306	0.0309
C_Y	0	0	0.0350	0.037
C_N	0.0056	0.0061	0.0071	0.0066

Table 2. Comparison of force and moment coefficients.

Fig. 7. Pressure contours; $M_\infty = 2$, $\alpha = 4°$.

Transonic Flows — Figure 8 shows results for a canard-wing configuration at transonic Mach numbers. A wake cut is created between the trailing edge of the canard and the leading edge of the wing, as well as behind the trailing edge of the wing. For steady transonic computations, triple approximate factored time marching is performed until steady state is reached. A typical computation such as the one shown in figure 8 requires 100 to 200 time iterations requiring 60 seconds of CPU time on a CRAY-X/MP for 80,000 grid points.
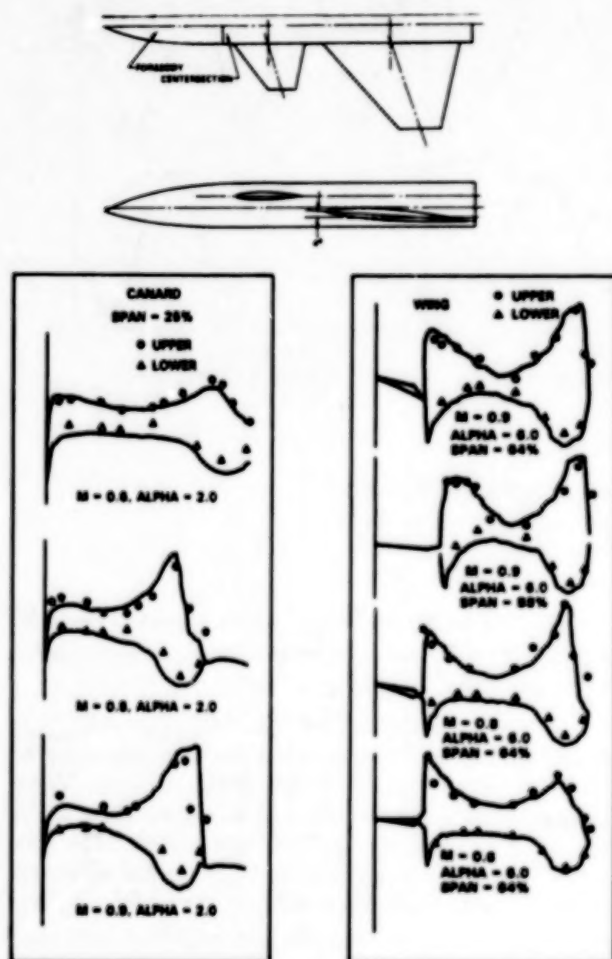

Fig. 8. Pressure correlations for a transonic canard-wing configuration.

Static Aeroelastic — Figure 9 illustrates a static aeroelastic computation for a flexible wing. The structural response is modeled using a generalized modal representation[9]. Within the aeroelastic model, a rigid wing is represented by setting the dynamic pressure to be zero. The magnitude of the structural deflection depends on the level of prescribed dynamic pressure and the generalized mode shapes. For an aeroelastically stable configuration, the tip load is reduced once the wing undergoes static deflection. This is illustrated in figure 9 which shows the deflected wing shape along with the upper and lower surface pressures. Figure 10 shows the C_L versus α variation taking into account static flexibility.
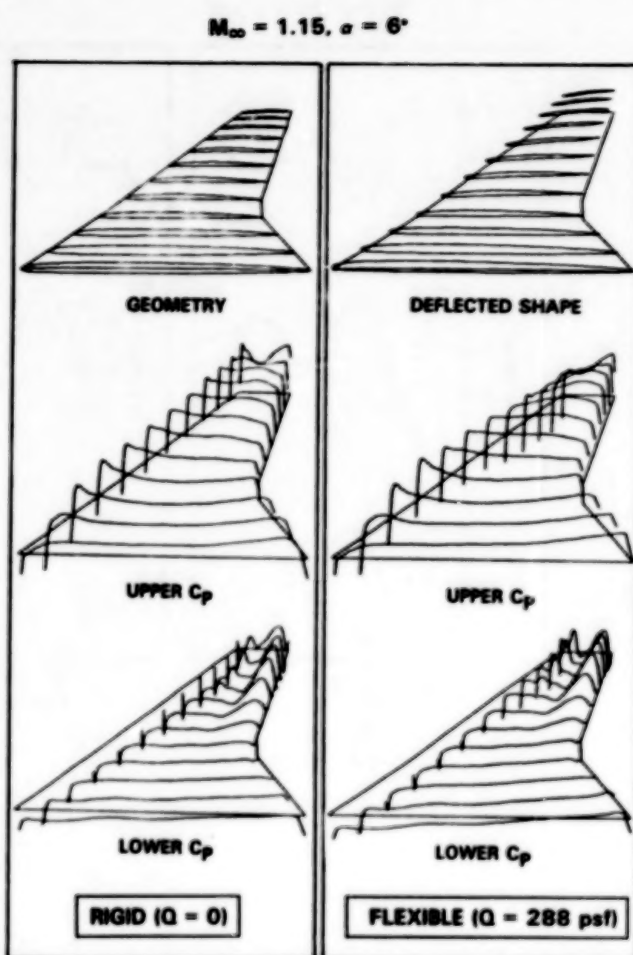
$M_\infty = 1.15$, $\alpha = 6°$
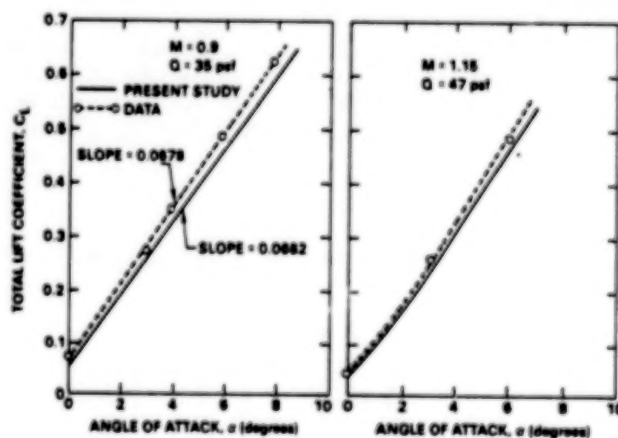

Fig. 9. Static flexible computation.

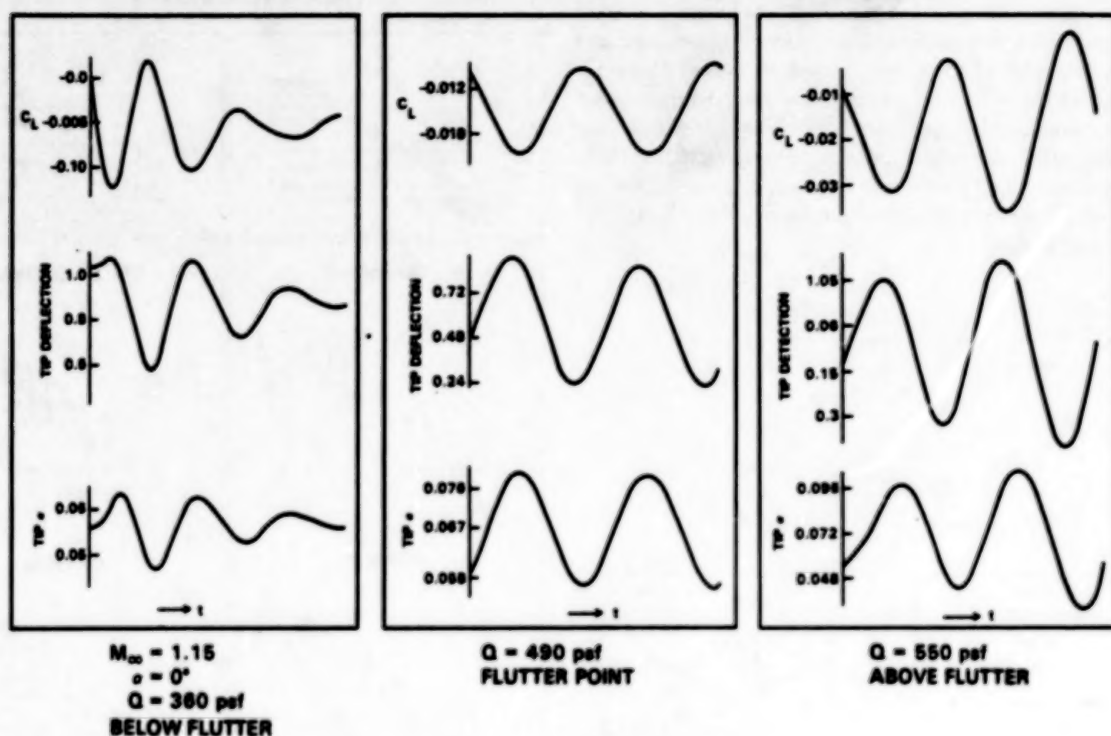Fig. 10. C_L versus α correlation for the flexible wing.

Fig. 11. Dynamic flexible computations for different dynamic pressures; a) below flutter, b) at flutter point, and c) above flutter point.

Dynamic Aeroelastic — Figure 11 shows dynamic flexible computations for three different dynamic pressure levels. Dynamic computations are performed as time–dependent calculations coupling the nonlinear aerodynamics and the structural response at a given time level invoking a time-accurate, Newton iteration procedure[9]. For a dynamic pressure level below the flutter point, the wing is aeroelastically stable as indicated by the decaying amplitude of oscillation in C_L, tip deflection, and tip α as a function of time in figure 11a. Figure 11b shows the calculation near flutter point with zero damping of the amplitude while figure 11c shows results of aeroelastic divergence above the flutter point.

Euler Equations

Referring to eq. (1), the Euler equations are given by

$$Q = \begin{pmatrix} e \\ \rho \\ \rho u \\ \rho v \\ \rho w \end{pmatrix}, E = \begin{pmatrix} (e+p)u \\ \rho u \\ \rho u^2 + p \\ \rho uv \\ \rho uw \end{pmatrix},$$

$$F = \begin{pmatrix} (e+p)v \\ \rho v \\ \rho uv \\ \rho v^2 + p \\ \rho wv \end{pmatrix}, G = \begin{pmatrix} (e+p)w \\ \rho w \\ \rho uw \\ \rho vw \\ \rho w^2 + p \end{pmatrix}. \quad (16)$$

In the above, pressure is p computed from $p = (e - \rho(u^2 + v^2 + w^2)/2))(\gamma - 1)$, density is ρ, Cartesian x, y, z velocity components are u, v, w, and the total energy per unit volume is e.

In order to define the appropriate numerical fluxes $\hat{E}$, $\hat{F}, \hat{G}$, an upwind biased scheme based on Roe's approximate Riemann solver[29] is employed.

At every cell interface $m+1/2$, let $Q^+_{m+1/2}$ and $Q^-_{m+1/2}$ denote the values of the dependent variables defined just to the right of and just to the left of the cell face. These values will be defined in the next subsection using a Total Variation Diminishing (TVD) formulation. The Riemann Solver is a mechanism to divide the flux difference between these neighboring states (between $Q^+_{m+1/2}$ and $Q^-_{m+1/2}$) into component parts associated with each wave field. These can in turn be divided into those that correspond to positive and negative wave speeds. When we compute the numerical flux at the cell face at $m+1/2$, in the finite-volume formulation, we will only use the cell-face normals defined at $m+1/2$ in the terms contributing to that representative flux. The actual fluxes $\overline{E}, \overline{F}, \overline{G}$, when evaluated with the metrics equated to cell-face normals, can all be written in the same functional form given by

$$\overline{E}, \overline{F}, \overline{G} = f(Q, n_x, n_y, n_z) = f(Q, N) \quad (17)$$

where the appropriate values of n_x, n_y, n_z are used and N denotes the set of those normals. Using such notation, it is possible to present the necessary algebra very concisely.

Let us first denote the Jacobian matrix of the flux f with respect to the dependent variables Q by $\partial f / \partial Q$. This Jacobian can also be called the coefficient matrix. Let us denote the eigenvalues of the coefficient matrix by λ^i and the corresponding left and right eigenvectors by ℓ^i and r^i,

respectively. The matrix formed by the left eigenvectors as its rows is then called the left eigenvector matrix L and the matrix of right eigenvectors comprising the right eigenvectors as its columns is R. For our purposes, we choose an orthonormal set of left and right eigenvectors which implies that $LR = RL = I$, the identity matrix. In the above, the superscript i has been used to denote the association of the i-th eigenvalue with its corresponding eigenvector. Each eigenvalue is also associated with its own wave field.

The underlying upwind scheme is based upon Roe's approximate Riemann solver. In this approach, cell interface values of density, velocities, and enthalpy ($h = \gamma p/((\gamma - 1)\rho) + (u^2 + v^2 + w^2)/2$) are computed using a special averaging procedure[14].

Knowing the cell interface values, the eigenvalues and orthonormal set of left and right eigenvectors corresponding to a cell face can be computed. These may be denoted by

$$
\begin{aligned}
\lambda^i_{m+1/2} &= \lambda^i_{m+1/2}(Q_{m+1/2}, N_{m+1/2}), \\
\ell^i_{m+1/2} &= \ell^i_{m+1/2}(Q_{m+1/2}, N_{m+1/2}), \\
r^i_{m+1/2} &= r^i_{m+1/2}(Q_{m+1/2}, N_{m+1/2}).
\end{aligned}
\tag{18a}
$$

At each cell face, the positive and negative projections of the eigenvalues may be defined by

$$
\lambda^{i\pm} = \frac{(\lambda^i_{m+1/2} \pm |\lambda^i_{m+1/2}|)}{2} \quad , i = 1, \cdots, 5 \quad . \tag{18b}
$$

Now, the numerical flux $\hat{f}_{m+1/2}$ is constructed from

$$
\begin{aligned}
\hat{f}_{m+1/2} \\
= \frac{1}{2} &\left[f(Q^+_{m+1/2}, N_{m+1/2}) + f(Q^-_{m+1/2}, N_{m+1/2}) \right] \\
- \frac{1}{2} &\left[\sum_i \left(\lambda^{i+}_{m+1/2} - \lambda^{i-}_{m+1/2} \right) \alpha^i_{m+1/2} r^i_{m+1/2} \right] \\
= f(Q^-_{m+1/2}, N_{m+1/2}) + \sum_i \lambda^{i-}_{m+1/2} \alpha^i_{m+1/2} r^i_{m+1/2} \\
= f(Q^+_{m+1/2}, N_{m+1/2}) - \sum_i \lambda^{i+}_{m+1/2} \alpha^i_{m+1/2} r^i_{m+1/2}
\end{aligned}
\tag{19}
$$

In the above equation,

$$
\alpha^i_{m+1/2} = \ell^i_{m+1/2}(Q^+_{m+1/2} - Q^-_{m+1/2}). \tag{20}
$$

We can construct upwind-biased schemes of varying accuracies by properly defining the left and right states used in the last subsection. We present here a family of schemes. For use in what follows, let us now define

$$
\begin{aligned}
\hat{\alpha}^i_{m+1/2} &= \ell^i_m(Q_{m+1} - Q_m), \\
\hat{\alpha}^i_{m-1/2} &= \ell^i_m(Q_m - Q_{m-1}),
\end{aligned}
\tag{21}
$$

where

$$
\ell^i_m = \ell^i(Q_m, (N_{m+1/2} + N_{m-1/2})/2) \tag{22}
$$

Next, we define the slope-limited values given by

$$
\begin{aligned}
\tilde{\alpha}^i_{m+1/2} &= \text{minmod}[\hat{\alpha}^i_{m+1/2}, b\,\hat{\alpha}^i_{m-1/2}], \\
\tilde{\tilde{\alpha}}^i_{m-1/2} &= \text{minmod}[\hat{\alpha}^i_{m-1/2}, b\,\hat{\alpha}^i_{m+1/2}].
\end{aligned}
\tag{23}
$$

In the above, the compression parameter b is to be taken as the following function of the accuracy parameter ϕ which is explained shortly.

$$
b = \frac{3 - \phi}{1 - \phi} \tag{24}
$$

The minmod slope-limiter operator is

$$
\text{minmod}[x, y] = \text{sign}(x) \ \max\{0, \min\{|x|, y\,\text{sign}(x)\}\} \tag{25}
$$

Then, the left state at the cell interface at $m+1/2$ and the right state at the cell interface $m - 1/2$ can be defined to be

$$
Q^-_{m+1/2} = Q_m + \sum_i \left(\frac{1+\phi}{4}\tilde{\alpha}^i_{m+1/2} + \frac{1-\phi}{4}\tilde{\tilde{\alpha}}^i_{m-1/2} \right) r^i_m
$$

$$
Q^+_{m-1/2} = Q_m - \sum_i \left(\frac{1+\phi}{4}\tilde{\tilde{\alpha}}^i_{m-1/2} + \frac{1-\phi}{4}\tilde{\alpha}^i_{m+1/2} \right) r^i_m
\tag{26}
$$

where

$$
r^i_m = r^i(Q_m, (N_{m+1/2} + N_{m-1/2})/2) \tag{27}
$$

At maxima and minima, the minmod operator returns a zero value and the left and right states reduce to

$$
\begin{aligned}
Q^-_{m+1/2} &= Q_m \\
Q^+_{m-1/2} &= Q_m
\end{aligned}
\tag{28}
$$

which result in a first-order accurate scheme locally.

More details on this Euler solver can be found in Refs. 12-14. Now some results are presented to illustrate the unified Euler solver capability.

Euler Results

Supersonic Flows — Figure 12a shows an elliptic waverider geometry typical of hypersonic configurations. Typically, waveriders are designed to have a lift–producing lower surface with a freestream aligned upper surface. Figure 12b shows Mach number contours at different Mach numbers and angles of attack. At the design point ($M_\infty = 4$, $\alpha = 0°$), the shock is at the leading edge while at off–design flow conditions the shock moves away from the leading edge. The upwind, TVD based Euler solver implemented in the code does not exhibit any numerical instability problems in capturing strong shocks. Figures 12c and 12d show comparisons of surface pressures and pitching moment coefficients with experimental data[30] and other available methods[31]. The full potential method compares well with the Euler results when the shock is weak. The shock strength starts to become more pronounced for $M_\infty > 4$, $\alpha \geq 5°$ as indicated by the deviation of the isentropic full potential results from the correct Euler solutions.
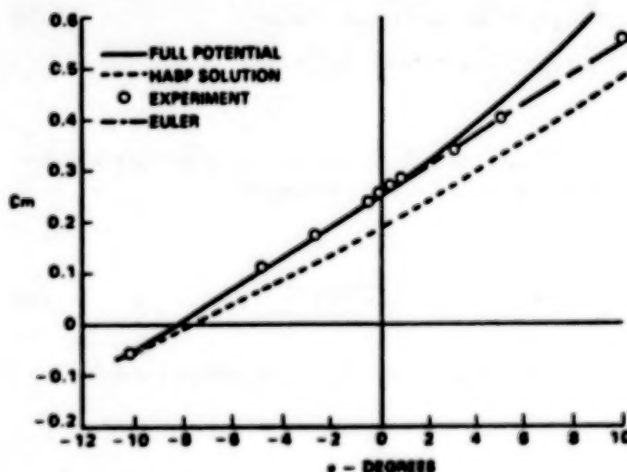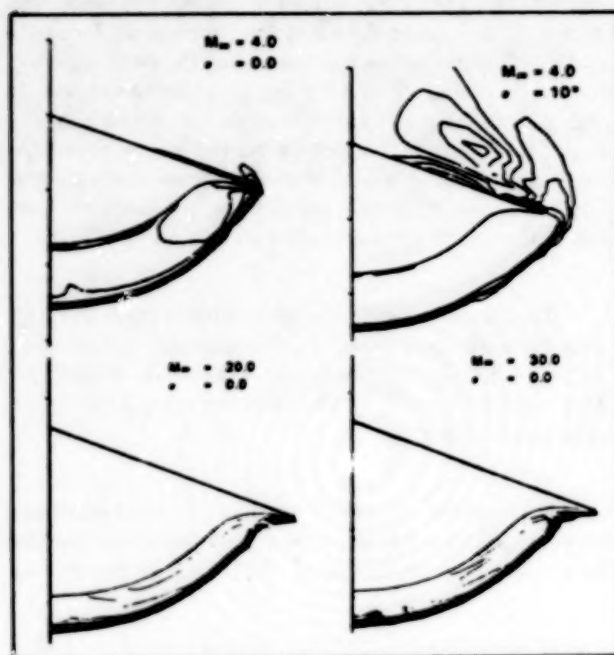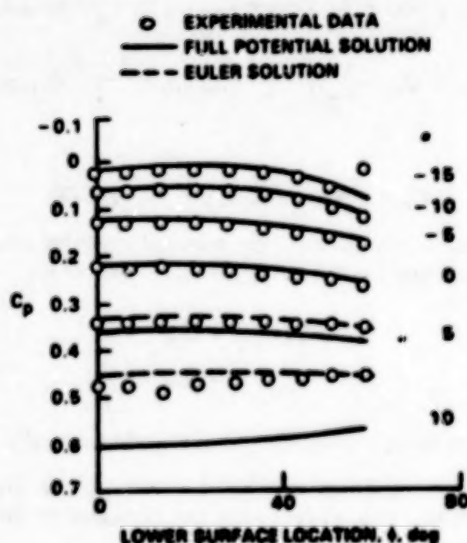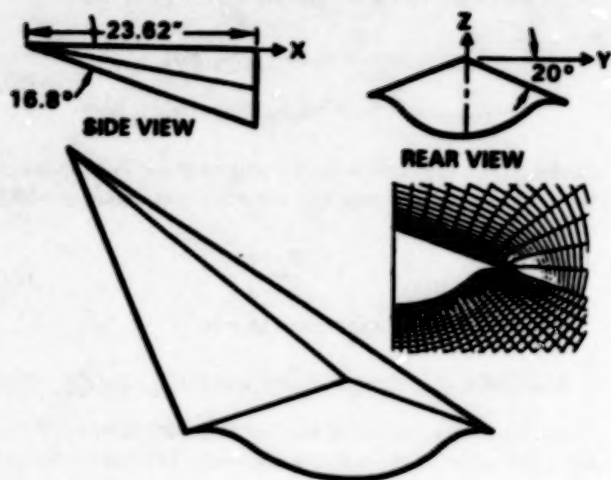
Fig. 12. Euler results for a waverider configuration; a) geometry and gridding, b) Mach contours at different Mach numbers, c) lower surface pressures, and d) pitching moment correlation.

Multizone Computation — For treatment of complex three-dimensional multibody flows, the gasdynamic solvers are provided with a multizonal capability where the physical domain of interest is subdivided into multizones requiring single gridding procedures within each zone. Across the zonal boundaries proper flux balancing is maintained to avoid spurious numerical errors originating at the interface. The zonal interface can be permeable or impermeable and can also be a boundary of flow discontinuity such as a shock or sonic surface.

Figure 13 shows the Space Shuttle mated configuration with the Orbiter mounted on top of the External Tank and the Solid Rocket Boosters. A single zone gridding that can treat every component of this multibody as a constant coordinate surface, though possible, can be cumbersome to construct. A five-zone gridding in the axial plane is generated to study this multibody problem at supersonic Mach numbers. Pressure contours and gridding are shown at different marching stations for $M_\infty = 1.8$, $\alpha = 0°$. The presence of a shock around the Shuttle OMS pod (station C) is clear.

Transonic Flow — Figure 14 shows transonic results for the ONERA-M6 wing. The double shock pattern on the upper surface at $M_\infty = 0.84$, $\alpha = 3.06°$ is well captured by the Euler code.
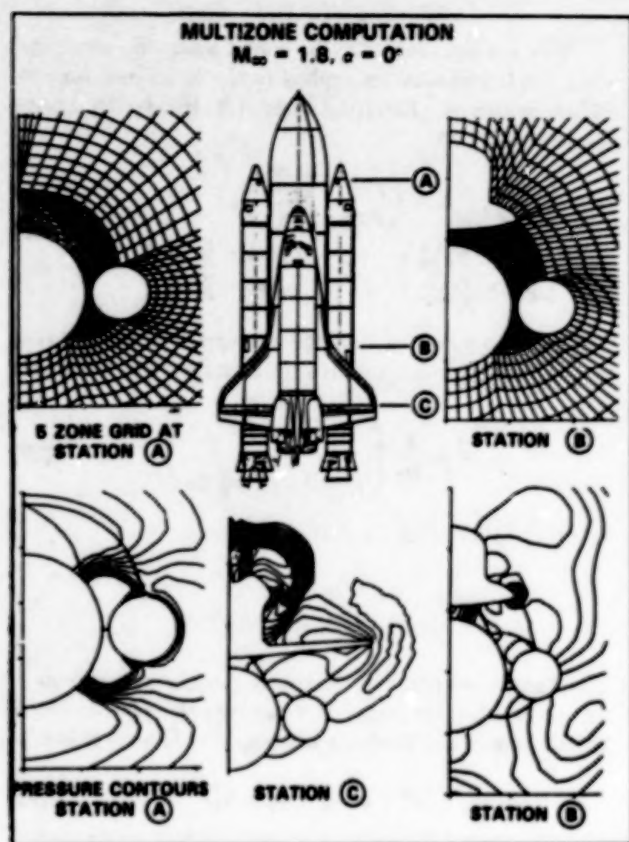
96

Fig. 13. Multizone treatment of the Shuttle mated configuration; $M_\infty = 1.8$, $\alpha = 0°$.

Fig. 14. Transonic results for the ONERA-M6 wing; $M_\infty = 0.84$, $\alpha = 3.06°$.

Navier-Stokes Equations

The purpose in developing powerful, robust and efficient Euler solvers is not just to study inviscid strongly shocked, rotational flows, but also to use them as a stepping stone in devising Navier-Stokes methods for solving viscous flow problems. Many problems of real interest in advanced aerospace and configuration development do require the use of Navier-Stokes methods. Some of the flows that can only be modeled using the Navier-Stokes equations are:

1) attached flows with a) tip vortex, b) wing/body junction vortex, and c) cross-flow leading edge vortex;

2) separated flows (leading edge separation and shock-boundary layer separation);

3) acoustics/unsteady phenomena (cavity flow and internal flow-induced vibrations);

4) high Mach number flows with significant heating; and

5) reacting flows (combustion involving chemical kinetics).

Referring to eq. (1), the Reynolds-averaged form of the Navier-Stokes equations is represented by
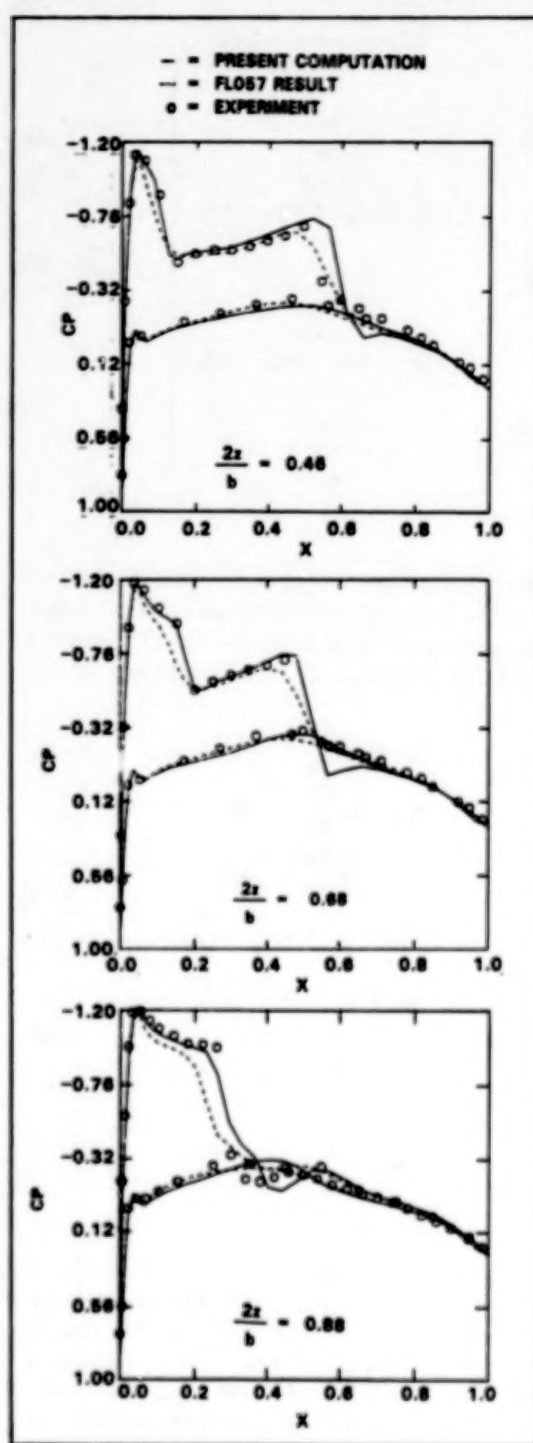
$$Q = \begin{pmatrix} e \\ \rho \\ \rho u \\ \rho v \\ \rho w \end{pmatrix}; E = E_{in} + E_v; F = F_{in} + F_v; G = G_{in} + G_v$$

(29)

where E_{in}, F_{in}, and G_{in} are the inviscid Euler fluxes given by eq. (16) and the viscous fluxes E_v, F_v, and G_v are given by

97

$$E_v = \frac{1}{Re}\begin{pmatrix} \frac{2}{Pr}\kappa\frac{\partial T}{\partial x} + u\tau_{xx} + v\tau_{xy} + w\tau_{xz} \\ 0 \\ \tau_{xx} \\ \tau_{xy} \\ \tau_{xz} \end{pmatrix},$$

$$F_v = \frac{1}{Re}\begin{pmatrix} \frac{2}{Pr}\kappa\frac{\partial T}{\partial y} + u\tau_{yx} + v\tau_{yy} + w\tau_{yz} \\ 0 \\ \tau_{yx} \\ \tau_{yy} \\ \tau_{yz} \end{pmatrix}, \qquad (30)$$

$$G_v = \frac{1}{Re}\begin{pmatrix} \frac{2}{Pr}\kappa\frac{\partial T}{\partial z} + u\tau_{zx} + v\tau_{zy} + w\tau_{zz} \\ 0 \\ \tau_{zx} \\ \tau_{zy} \\ \tau_{zz} \end{pmatrix}.$$

Here, Re is the Reynolds number, Pr is the Prandtl number, κ is the thermal conductivity, and T is the specific internal energy given by $T = p/[(\gamma - 1)\rho]$. The terms τ_{xx}, τ_{xy}, τ_{xz}, τ_{yx}, τ_{yy}, τ_{yz}, τ_{zx}, τ_{zy}, and τ_{zz} are given by

$$\begin{aligned}
\tau_{xx} &= 2\mu\frac{\partial u}{\partial x} - \frac{2}{3}\mu\Phi, \\
\tau_{yy} &= 2\mu\frac{\partial v}{\partial y} - \frac{2}{3}\mu\Phi, \\
\tau_{zz} &= 2\mu\frac{\partial w}{\partial z} - \frac{2}{3}\mu\Phi, \\
\tau_{xy} &= \tau_{yx} = \mu\left(\frac{\partial u}{\partial y} + \frac{\partial v}{\partial x}\right), \\
\tau_{xz} &= \tau_{zx} = \mu\left(\frac{\partial u}{\partial z} + \frac{\partial w}{\partial x}\right), \\
\tau_{yz} &= \tau_{zy} = \mu\left(\frac{\partial w}{\partial y} + \frac{\partial v}{\partial z}\right)
\end{aligned} \qquad (31)$$

where

$$\Phi = \left(\frac{\partial u}{\partial x} + \frac{\partial v}{\partial y} + \frac{\partial w}{\partial z}\right)$$

and μ is the coefficient of viscosity.

The viscosity coefficient for turbulent flows is modeled as the sum of the laminar and turbulent viscosities in the eddy viscosity approach. The turbulent eddy viscosity is usually computed using one of two popular techniques, 1) by using the Baldwin-Lomax or other algebraic eddy viscosity formulation, and 2) by using a two-equation model such as the $k - \epsilon$ formulation.

The k-ϵ model often used is the standard high Reynolds number form of the equations. Even though the k-ϵ model can take more time to solve than the simpler algebraic eddy viscosity models this is justifiable since the k-ϵ model is generally applicable to a much wider class of flows. The kinetic energy equation is derived from the Navier-Stokes equations with the main limiting criterion being that it assumes local isotropy. The dissipation equation is not exact but is modelled to represent physical processes similar to those of the kinetic energy equation. Even with these assumptions the k-ϵ equations have a proven capability of adequately predicting a large range of complex flows, including anisotropic ones.

The k-ϵ equations may be solved using the same upwind, TVD formulations applied to the Euler and Navier-Stokes equations. Referring to eq. (1), the k-ϵ equations can be written as

$$Q = \begin{pmatrix} \rho k \\ \rho\epsilon \end{pmatrix}, \quad E = \begin{pmatrix} \rho uk - \frac{\mu_k}{Re}\frac{\partial k}{\partial x} \\ \rho u\epsilon - \frac{\mu_\epsilon}{Re}\frac{\partial \epsilon}{\partial x} \end{pmatrix},$$

$$C = \begin{pmatrix} \rho vk - \frac{\mu_k}{Re}\frac{\partial k}{\partial y} \\ \rho v\epsilon - \frac{\mu_\epsilon}{Re}\frac{\partial \epsilon}{\partial y} \end{pmatrix}, \quad D = \begin{pmatrix} \rho wk - \frac{\mu_k}{Re}\frac{\partial k}{\partial z} \\ \rho w\epsilon - \frac{\mu_\epsilon}{Re}\frac{\partial \epsilon}{\partial z} \end{pmatrix}. \qquad (32)$$

The only exception is that the k-ϵ equations, in addition to the above, involve a source term on the right hand side given by

$$S = \frac{1}{Re}\begin{pmatrix} P - \rho\epsilon Re \\ C_1\frac{\epsilon}{k}P - C_2\rho\frac{\epsilon^2}{k}Re \end{pmatrix}. \qquad (33)$$

In eqs. (31) and (32),

$$\mu_k = (\mu + \mu_t/\sigma_k)$$
$$\mu_\epsilon = (\mu + \mu_t/\sigma_\epsilon)$$

k is kinetic energy, ϵ is turbulent dissipation, and μ_t is turbulent eddy viscosity. P represents the production of kinetic energy and the following simplified form of it is used

$$P = \mu_t(u_x^2 + u_y^2 + u_z^2). \qquad (34)$$

The k-ϵ model still employs the eddy viscosity/diffusivity concept as it relates eddy viscosity to the kinetic energy and dissipation by

$$\mu_t = C_\mu\rho\frac{k^2}{\epsilon}. \qquad (35)$$

This eddy viscosity is then used to create an effective viscosity $(\mu + \mu_t)$ which replaces μ in the Reynolds-averaged Navier-Stokes equations. To solve the above turbulence model the following constants must be specified: $\sigma_k = 1.0$, $\sigma_\epsilon = 1.3$, $C_1 = 1.44$, $C_2 = 1.92$, and $C_\mu = 0.09$.

One of the highlights of the Navier-Stokes activity is the modeling of turbulence for separated flows. The new turbulence model is based on experimental observations of separated turbulent flows. The model prescribes turbulence kinetic energy (k) and its dissipation (ϵ) analytically inside separation bubbles. A Gaussian variation of k normal to walls is assumed. The length scale of turbulence within bubbles is proportional to the local distance from the wall to the edge of the viscous sublayer, which is located outside the backflow region, as shown in figure 15. The latter feature is a basic assumption of the model.

The stress scale is the local maximum Reynolds stress, which typically occurs around the middle of the boundary layer, well outside the bubble. This scale must be supplied by the turbulence model used beyond separated regions.

The main equations of the model are given in Ref. 23. A simple formula for eddy viscosity distribution within the separation bubble results, and is used to provide eddy viscosity for the Reynolds-averaged equations when performing the calculations inside the bubble. Outside of it, another turbulence model (e.g., Baldwin-Lomax or k-ϵ) supplies the values of eddy viscosity.
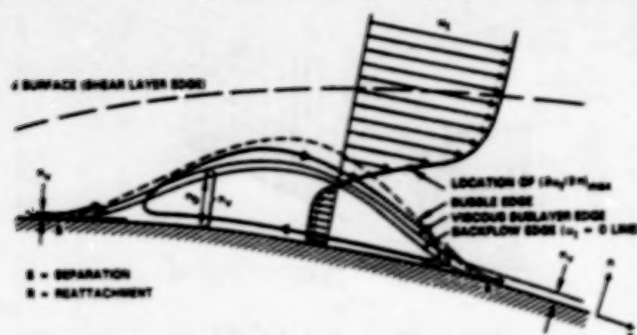
Fig. 15. Schematic view of separated flow bubble and basic nomenclature.

Navier–Stokes Results

The algebraic k-ϵ turbulence model for separated flows, in conjunction with the Baldwin–Lomax model, has been incorporated into a finite volume, time–marching, multizonal Navier-Stokes code[23-26], featuring an implicit upwind–biased scheme, approximate factorization, and Total Variation Diminishing discretization for high accuracy. When a separation bubble exists, the standard Baldwin–Lomax or the k-ϵ model is used to compute eddy viscosity outside the backflow region, while the separation model (figure 15) provided eddy viscosity within the separation bubble.

Several unit problems are computed to check the validity of the Navier–Stokes code with a turbulence model for treating separated flows.

As a first computational test of the new turbulence model, a transonic flow calculation over an axisymmetric boattail with a cylindrical extension (solid plume simulator) has been performed. Figure 16a shows the chosen geometry. This case involves a moderate–sized separation bubble at the end of the boattail. The data of Ref. 32 at $M_\infty = 0.8$ and a Reynolds number of 1.8×10^6, based on maximum model diameter, were used for comparisons with the calculations. A 65×40 grid was employed, with 23 points normal to the wall lying inside the separation bubble at the location of its maximum height. Figure 16b shows a detail of the computational mesh.

In figure 16c, pressure coefficient at the wall, calculated using the new separation turbulence model, is compared with experimental data of Ref. 32 as well as with a calculation which used the Baldwin–Lomax model by itself. The figure also indicates the location and extent of the separated region. The advantage of using the separation model is demonstrated by the significant improvement in predicting the pressure through the separated zone, compared to the corresponding calculation without the model.

Figure 16d compares skin friction distribution, as calculated using the new model, with the corresponding calculation done without it. A larger separation bubble is predicted by the former. No data are available for comparison.
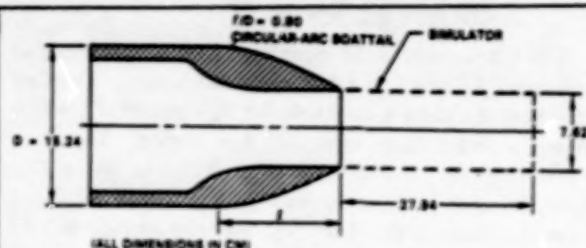

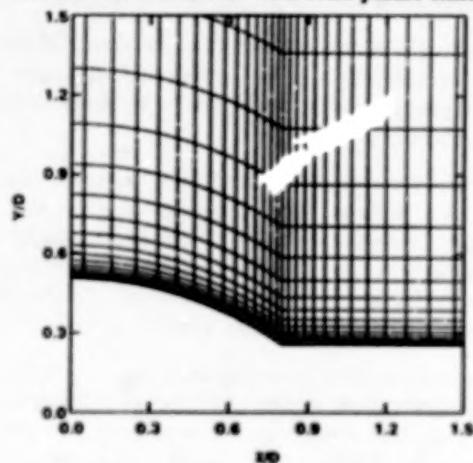Fig. 16a. Sketch of boattail with solid plume simulator.

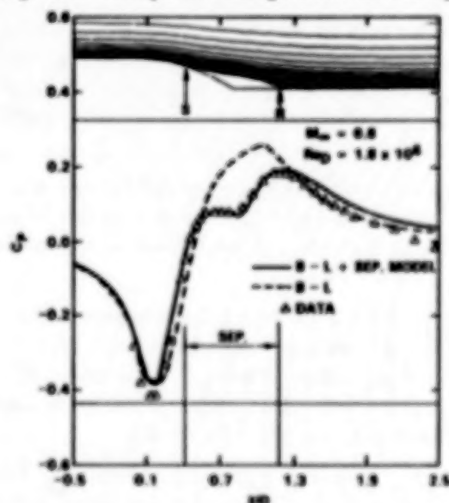Fig. 16b. Computational grid for the solid plume.

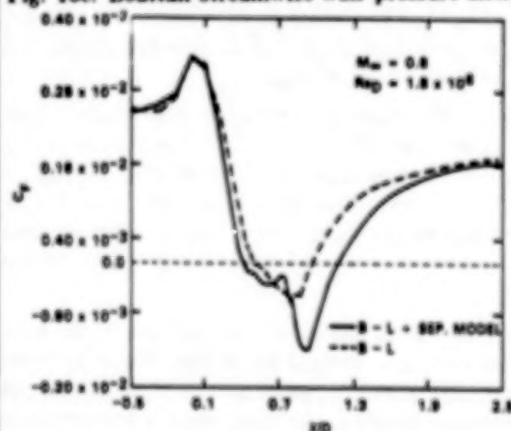Fig. 16c. Boattail streamwise wall–pressure distribution.

Fig. 16d. Boattail streamwise skin friction distribution.

The second test of the separation model was chosen to be a supersonic flow over a 24° compression ramp. Detailed experimental data are available for this case[33-35], which involves a rather large separated flow region. The 65 × 35 grid used for the calculations is shown in figure 17a. About 75% of the normal-to-wall mesh points were located within the shear layer. This case was run at $M_\infty = 2.85$ and a Reynolds number based on incoming boundary layer thickness of 1.6×10^6.

Figure 17b shows a comparison between calculations and experimental data of wall pressure distribution. The improved predictional capability due to inclusion of the separation model is evident.

Figure 17c compares calculations with experimental data of skin friction. The advantage of using the separation model over the regular Baldwin-Lomax model is evident throughout the separation bubble. Incorporation of the new model enables precise prediction of reattachment location, a difficult task for this flow.

A streamline plot, resulting from the calculation with the separation model, is shown in figure 17d. The predicted extent of the separated region agrees quite well with the experimentally observed locations of separation and reattachment, also indicated in the figure.

The third test of the new backflow model was the backward-facing step case reported in Ref. 36, with an inflow Mach number of 0.128 and a Reynolds number of 31,250 based on inflow conditions and the step height as a reference length.

Figure 18a shows the geometry and the two-zone computational grid, with a 42 × 22 mesh used in the subdomain above the step, and a 36 × 20 mesh used in the subdomain downstream of the step.

Pressure distribution along the step-side wall is shown in figure 18b, as resulting from the current approach and from Sindir's[37] calculations using the k-ϵ model. Comparison with the data indicates a slight advantage in using the new algebraic model over the k-ϵ model.

Figure 18c shows skin friction distribution on the step-side wall. The new backflow model enables improved prediction and significantly better performance in the reattachment zone. In the vicinity of the step corner, the skin friction is positive, indicating a small counter-rotating vortex, in agreement with the data.

In figure 18d, streamwise velocity profiles at two locations are shown, one upstream of the reattachment region, the other downstream of it. Agreement with the data is very good at the former location, where the flow is separated, and fair at the latter, where a somewhat sluggish boundary layer recovery is predicted for the lower part of the profile.

Figure 18e shows Reynolds stress profiles at the locations corresponding to those of figure 18d. While the shape of the calculated profile agrees with the experimental one at the upstream location, the magnitude is overpredicted roughly by a factor of two. In the downstream location, however, agreement with data is quite good, although the lower part of the calculated profile is again overpredicted.
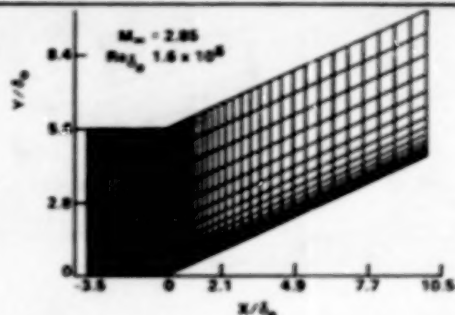

Fig. 17a. Computational grid for the 24° compression ramp.
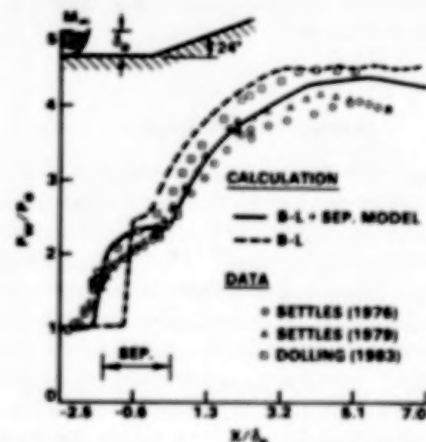
Fig. 17b. Streamwise wall-pressure distribution over ramp.
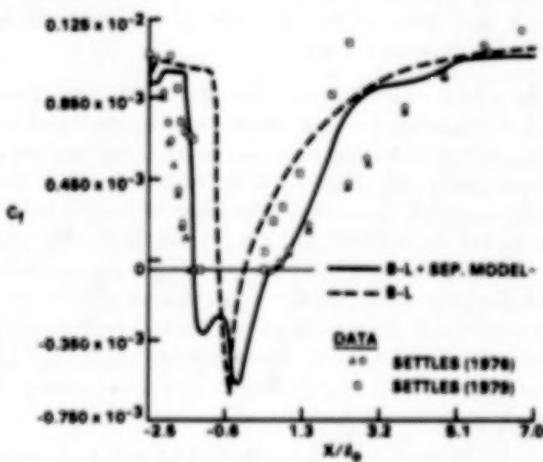
Fig. 17c. Streamwise skin friction distribution over ramp.
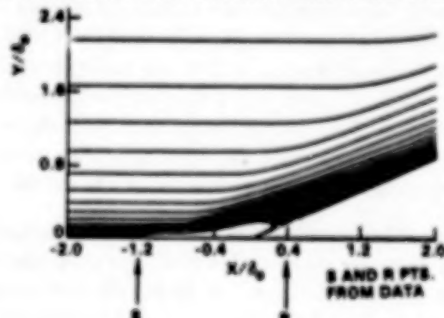
Fig. 17d. Ramp streamline plot, showing the separation bubble.
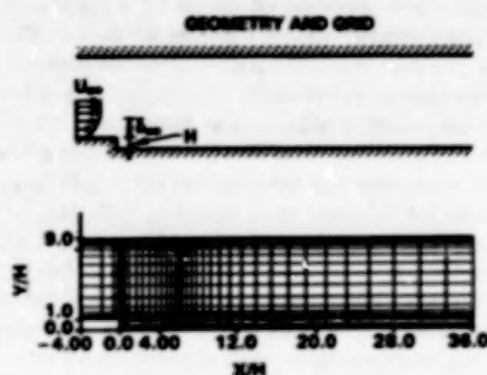
Fig. 18a. Two-zone computational grid and geometry for backward-facing step.
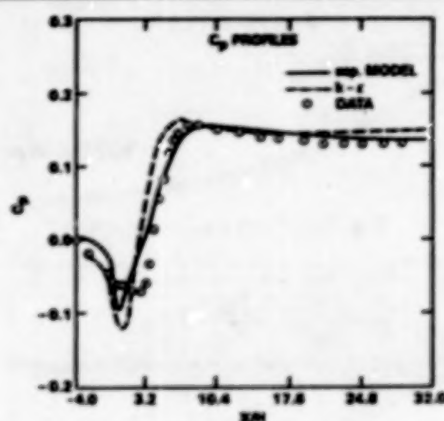
Fig. 18b. Step-side pressure distribution.
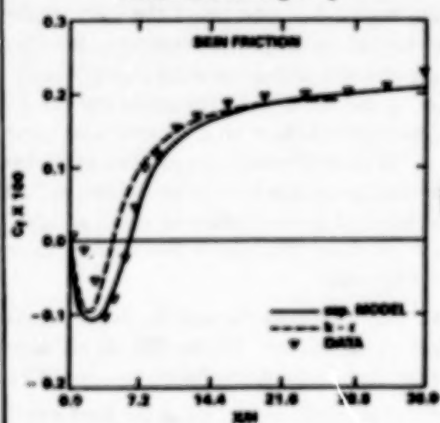
Fig. 18c. Step-side skin friction distribution.
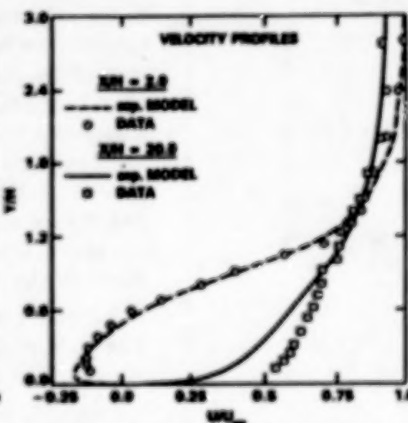
Fig. 18d. Streamwise velocity profiles upstream and downstream of reattachment.
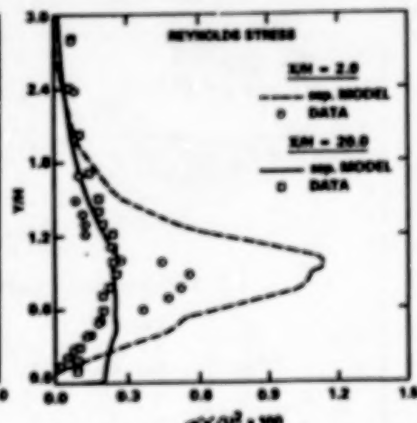
Fig. 18e. Reynolds stress profiles

Since store separation and aerodynamic drag due to open cavities are important issues in design, cavity computations are vital for validation and prediction. A laminar three-dimensional cavity computation has been done. The specific cavity is a simplified version of the F-111 weapons bay. Figure 19a shows velocity directions down the centerline of the cavity. Figure 19b shows the velocity directions of the secondary motion on a cross plane of the cavity. More cavity results can be found in Ref. 38.
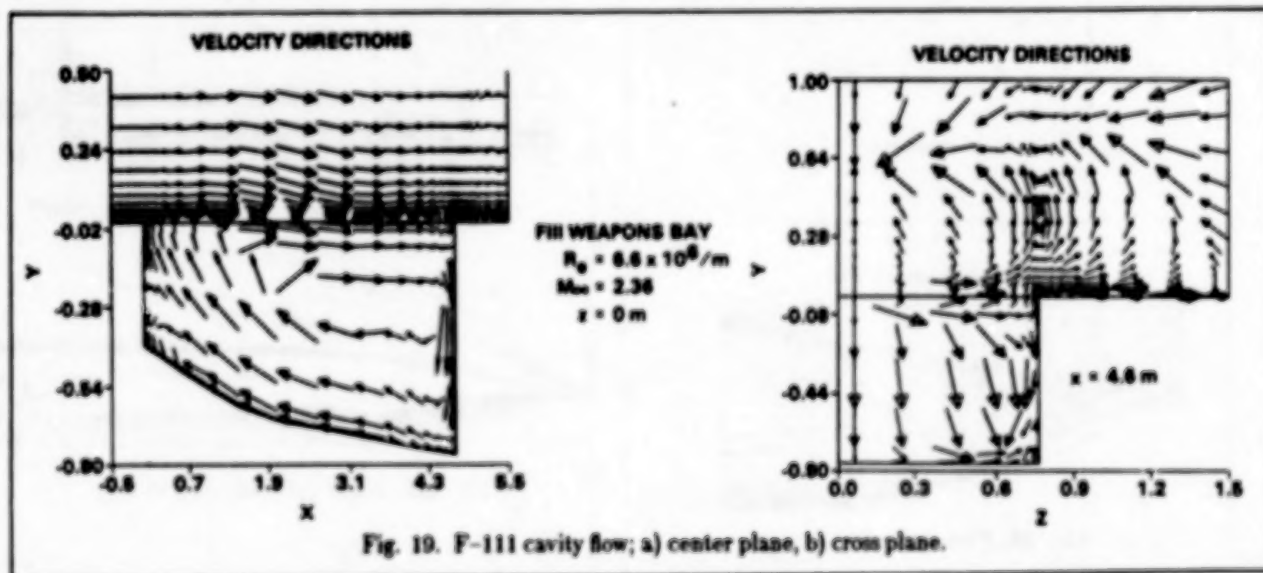
Fig. 19. F-111 cavity flow; a) center plane, b) cross plane.
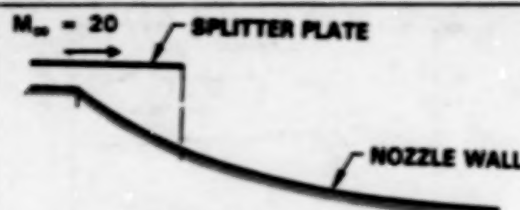
Fig. 20a. Test case geometry.
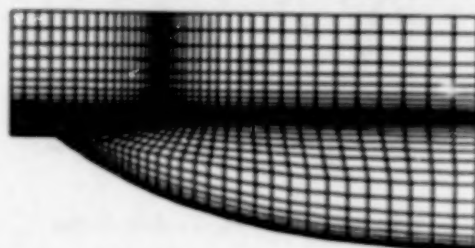
Fig. 20b. Computational grid
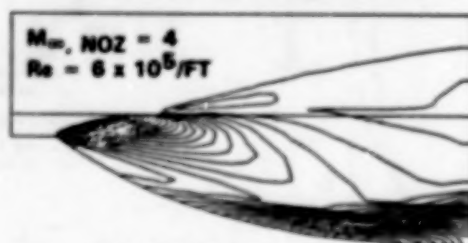
Fig. 20c. Pressure contours
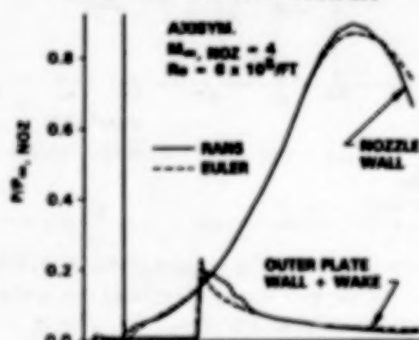
Fig. 20d. Wall pressure comparison
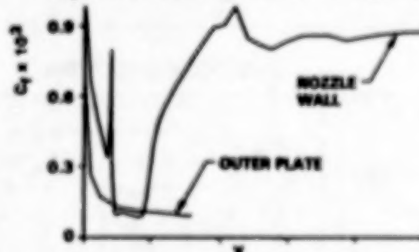
Fig. 20e. Skin friction
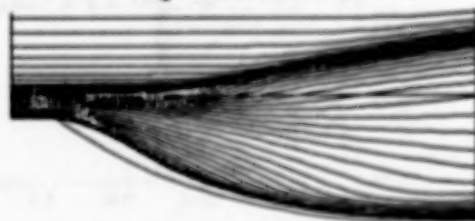
Fig. 20f. Plume development

Figure 20a shows an axisymmetric nozzle and the corresponding two-zone gridding is given in figure 20b. The external inflow was fixed at $M_\infty = 20$, while the nozzle inflow Mach number was varied from 4.0 to 1.5. The nozzle inflow pressure was 217 times that of the external inflow. For the viscous calculations, the Reynolds number based on nozzle inflow conditions was varied from 6×10^5/ft at Mach 4 to 2.25×10^5/ft at Mach 1.5. All solid surfaces were held at a constant wall temperature $T_W = 0.347 T_{\infty,\text{tot}}$. Calculations for this case were run using both the Reynolds-averaged Navier–Stokes code (RANS) and the Euler code. Figure 20c shows pressure contours for the Navier–Stokes computation. Figure 20d compares pressure distributions on the nozzle wall and on the outer plate surface plus the wake region downstream of it, as resulting from the RANS and Euler calculations. Except for the milder corner expansion due to viscous displacement effects, the two calculations predict the same nozzle wall pressure distribution. In the near wake region downstream of the splitter plate, however, the interaction between the shear layers from both sides of the plate and the plume-induced shock/boundary layer interaction in the vicinity of the plate trailing edge modify the pressure distribution as compared with the inviscid prediction. Further downstream the two predictions coincide. Figure 20e shows skin friction on the two walls, indicating no separation of the boundary layers. The streamline plot in figure 20f shows the plume development as predicted by the RANS code.

Figure 21a shows the geometry and the multizone gridding for a ramjet configuration. Figure 21b shows viscous Mach number contours for an inflow Mach number of 4.03.

The Navier–Stokes code developed at the Rockwell Science Center is still undergoing validation tests on several unit problems for possible improvements in modeling turbulence of separated flows. Future applications will involve wings, wing-body combinations at high α, and cavity-store acoustics and separation studies.
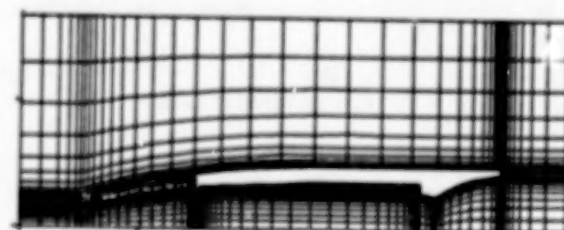
Fig. 21a. Geometry and gridding for a ramjet.

Fig. 21b. Mach contours, $M_\infty = 4.03$.

Laser-Material Interaction

The paper so far dealt with the development and application of computational algorithms for solving aerodynamic problems. Extension of these CFD methods to solving problems in other disciplines that are governed by an appropriate set of partial differential equations is very attractive. One such application is to study the problem of heat transfer in materials subjected to intense laser heating.

Laser heat treatment of materials (especially iron-base alloys and carbon-carbon composites) for various industrial applications is becoming very attractive due to ease in the controllability and in generation of laser beams. For example, use of laser as a heat source in enhancing materials resistance to surface wear and corrosion through solid state phase transformations (without melting) and rapid solidification (with shallow melting), in achieving a desired homogeneous molten weld pool, and in obtaining a unique surface composition through coating or cladding, as a viable economical process, has been well proven in laboratory settings. Transitioning this process technology from a laboratory setting to an industrial environment requires a better understanding of the role of various controlling parameters, such as the cross-section of the laser, power intensity of the laser, velocity of the moving laser or the workpiece, and the material properties themselves in determining the quality of the surface modification process. Optimization of these controlling process parameters through theoretical modeling and computational simulation can lead to achieving the desired properties of surface treatment.

Figure 22 shows the schematic of a laser melted material pool. When the workpiece is swept under the beam, a self quenched heat treated zone is obtained along the surface. Dimensions of the melted zone ($T > T_m$, where T_m is the melting temperature) and the heat affected zone ($T > T_e$) are controlled by absorbed laser beam power density, beam size, and travel speed.
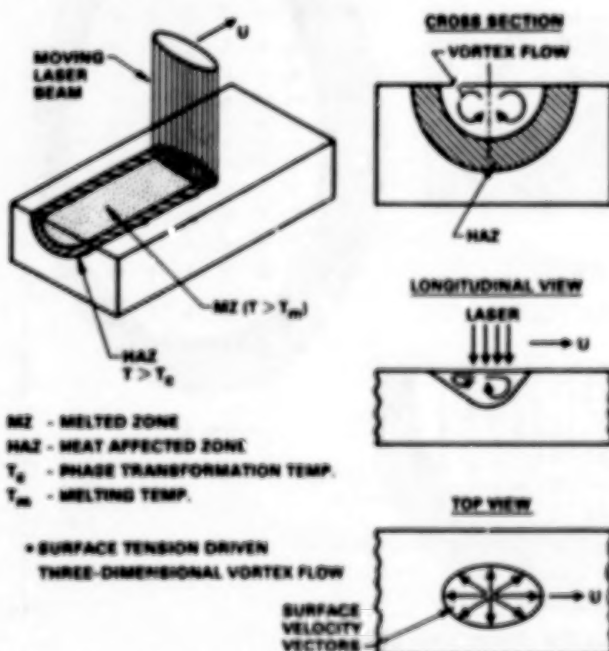
The high surface temperature gradients in the melted zone create a variation of surface tension along the surface which is balanced by shear forces. This balancing shear force is created by setting up a counter rotating vortex flow within the molten zone as described in figure 22.

The physics of modeling the heat transfer process occurring in figure 22 involves both conduction and convection in a high gradient thermal field. The equation that best describes the physical phenomena of this problem is the incompressible Navier-Stokes equations. Referring to eq. (3), the following describes the coupling between the temperature field and the velocity field.

$$
Q = \begin{Bmatrix} 0 \\ \rho u \\ \rho v \\ \rho w \\ T \end{Bmatrix} \; ; \; E = \begin{Bmatrix} u \\ p + \rho u^2 - \tau_{xx} \\ \rho uv - \tau_{xy} \\ \rho uw - \tau_{xz} \\ Tu - \alpha \frac{\partial T}{\partial x} \end{Bmatrix} \; ;
$$

$$
F = \begin{Bmatrix} v \\ \rho uv - \tau_{xy} \\ p + \rho v^2 - \tau_{yy} \\ \rho vw - \tau_{yz} \\ Tv - \alpha \frac{\partial T}{\partial y} \end{Bmatrix} \; ; G = \begin{Bmatrix} w \\ \rho uw - \tau_{xz} \\ \rho vw - \tau_{yz} \\ p + \rho w^2 - \tau_{zz} \\ Tw - \alpha \frac{\partial T}{\partial z} \end{Bmatrix} \; ; \tag{36}
$$

$$
\alpha = \frac{k}{\rho c_p}
$$

where $\tau_{ij} = \nu \left(\frac{\partial u_i}{\partial x_j} + \frac{\partial u_j}{\partial x_i} \right)$. Modeling of turbulence in τ_{ij} is neglected in the present formulation and only the laminar stress tensor is considered.

In these equations, c_p is the specific heat, ρ is the density, k is the thermal conductivity, T is the temperature, and ν is the kinematic viscosity. The induced velocity field in the molten pool is represented by u_j.

In the unmelted region of the material where the heat transfer process is purely due to conduction (temperatures below melting), only the energy equation needs to be solved for temperature (see Ref. 39).

On the outer surface of the molten pool, the force balance equations are

$$
\mu \frac{\partial u}{\partial z} = \sigma' \frac{\partial T}{\partial x}
$$
$$
\mu \frac{\partial v}{\partial z} = \sigma' \frac{\partial T}{\partial y} \tag{37}
$$

where σ' is the rate of change of surface tension ($N/m/k$) with temperature and μ is the coefficient of viscosity of the molten pool (N sec/m^2; N is Newton).

At the liquid-solid interface $u = v = w = 0$ and $T = T_m$. More details on the boundary condition can be found in Ref. 40.

The computational method employs an implicit triple approximate factorization scheme to solve the energy equation in terms of temperature and an explicit treatment for the three momentum equations and the continuity equation. The pressure field is updated at each time level using a Poisson solver to satisfy the continuity equation.

MZ - MELTED ZONE
HAZ - HEAT AFFECTED ZONE
T_e - PHASE TRANSFORMATION TEMP.
T_m - MELTING TEMP.

- SURFACE TENSION DRIVEN THREE-DIMENSIONAL VORTEX FLOW

Fig. 22. Surface tension induced convective heat transfer.

Laser Results

A sample result for a rectangular workpiece undergoing melting is presented.

Figure 23 shows results for a typical case (5000 W laser, 4 × 3 mm laser cross section, 1.26 mm/sec beam travel speed). A point in the workpiece is considered heat affected if that point experienced temperatures above 750°C and the melt zone corresponds to temperatures $\geq$ 1500°C. At a given instance of time (laser beam around the halfway length of the workpiece), the instantaneous temperature distribution, melt zone shape, and the three-dimensional vortex mixing material flow are shown in the figure. The cross-sectional view, longitudinal view (plane of symmetry), and the top view of the melted zone clearly reveal the convection process induced by the surface tension driven flow. Pure conduction treatment of this heat transfer problem (no convection model, i.e., surface tension gradients set to zero) results in temperature levels not comparable with experimental observations. The computational procedure of the present study incorporating the surface tension driven convective heat transfer process produces melt zone and heat affected zone shapes very similar to experimental data. More results are presented in Ref. 40.

Application of this work to study problems of deep welding (solute redistribution, microstructure of the heat affected zone, and residual stress state) and characterization of the surface ripples are some of the ongoing projects.

Electromagnetic Scattering

The objective is to develop time–dependent finite difference methods to solve the Maxwell equations to study the problem of electromagnetic scattering from dielectric and perfectly reflecting objects. Although techniques based on the integral form of the equations are available, they are usually restricted in their application due to various simplifications made in the formulation. Solution techniques to the differential equation usually provide a general–purpose capability with fewer restrictions than techniques based on the integral approach. Based on proven CFD methods, it is desirable to develop an efficient finite difference technique for the Maxwell equations.

Referring to eq. (1), the Maxwell equations take the form

$$
Q = \begin{Bmatrix} e_x \\ e_y \\ e_z \\ H_x \\ H_y \\ H_z \end{Bmatrix} ; \quad
E = \begin{Bmatrix} 0 \\ -\frac{1}{\mu}e_z \\ \frac{1}{\mu}e_y \\ 0 \\ \frac{1}{\epsilon}H_z \\ -\frac{1}{\epsilon}H_y \end{Bmatrix} ;
$$

$$
F = \begin{Bmatrix} \frac{1}{\mu}e_z \\ 0 \\ -\frac{1}{\mu}e_x \\ -\frac{1}{\epsilon}H_z \\ 0 \\ \frac{1}{\epsilon}H_x \end{Bmatrix} ; \quad
G = \begin{Bmatrix} -\frac{1}{\mu}e_y \\ \frac{1}{\mu}e_x \\ 0 \\ \frac{1}{\epsilon}H_y \\ -\frac{1}{\epsilon}H_x \\ 0 \end{Bmatrix}
$$

(38)
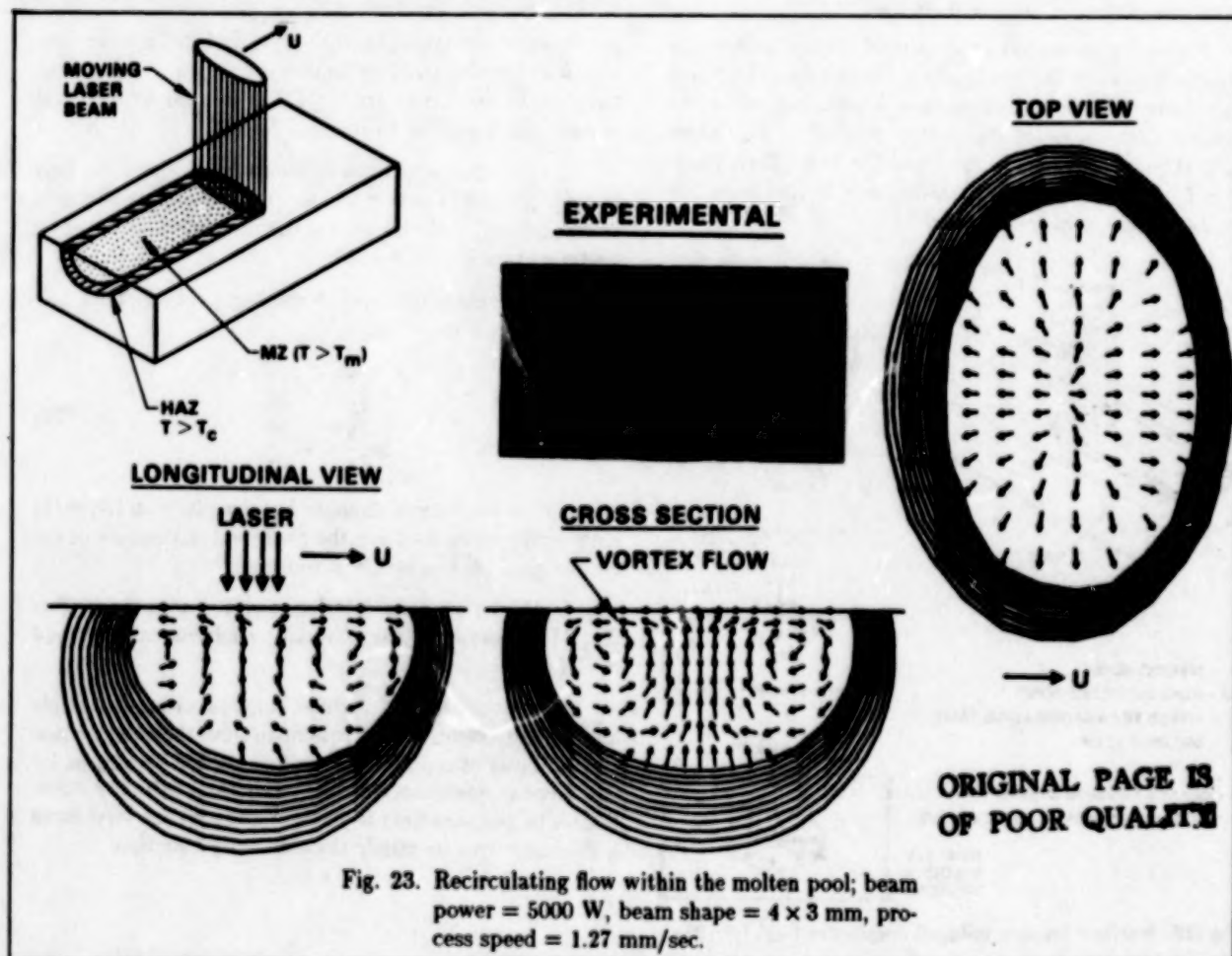

Fig. 23. Recirculating flow within the molten pool; beam power = 5000 W, beam shape = 4 × 3 mm, process speed = 1.27 mm/sec.

where e_x, e_y, and e_z are the electric field components along x, y, and z, and similarly H_x, H_y, and H_z are the magnetic field components. The parameters ϵ, μ, and σ represent permittivity, permeability, and conductivity of the medium through which the electromagnetic wave is propagating. Equation (38) is hyperbolic and has real eigenvalues and a linearly independent set of eigenvectors. Upwind schemes developed for the Euler equations are ideal for solving the Maxwell equations. The objective is to solve eq. (3) subject to an incident wave to compute the equivalent surface current on the object given by $n \times H$ where n is the surface normal and H is the magnetic field vector. Once the equivalent surface current is known on the dielectric object and around any contour encompassing the object, the radar cross section (RCS) information can be obtained using a near field–to–far field transformation (Refs. 41,42). The RCS information depends on the intensity of the scattered wave.

RCS Results

The Maxwell equations in two dimensions can be specialized for a transverse magnetic (TM) wave ($e_x = e_y = 0, H_z = 0$), or for a transverse electric (TE) wave ($H_x = H_y = 0, e_z = 0$). Development of computational algorithms for studying electromagnetic scattering from perfectly conducting or dielectric objects can benefit from solving the TM or the TE wave problem. Preliminary results are reported here for the electromagnetic scattering from a perfectly conducting square cylinder for an incident plane wave of the form $e_i = e_0 \sin k(r \cos(\phi - \phi') - ct)$ where e_0 is the amplitude, $k = 2\pi/\lambda$, λ is the wavelength, c is the wave speed, ϕ' is the angle of incident wave with respect to the x-axis. Figures 24a and 24b show the surface current $J_z = n \times H$ on the cylinder for two different incident wave angles. The correlation of $n \times H$ obtained using a simple, first-order accurate, upwind, explicit scheme with an existing method known as method of moments (MOM) is good. Knowing this J_z information, the RCS value for different viewing angles can be computed. Development of higher order accurate, upwind schemes based on Euler solvers is currently in progress. Some of the numerical issues to be addressed in this development are 1) higher order accurate nonreflecting farfield conditions based on characteristic theory, 2) grid resolution requirements for high frequency (small λ or large k) incident waves, 3) boundary condition treatment for radar absorbing materials taking into account frequency dependence on ϵ, μ and σ, 4) multizone gridding techniques for interior and external regions, and 5) near-field to far-field transformations to derive RCS values from the near-field $n \times H$ and $n \times E$ information.
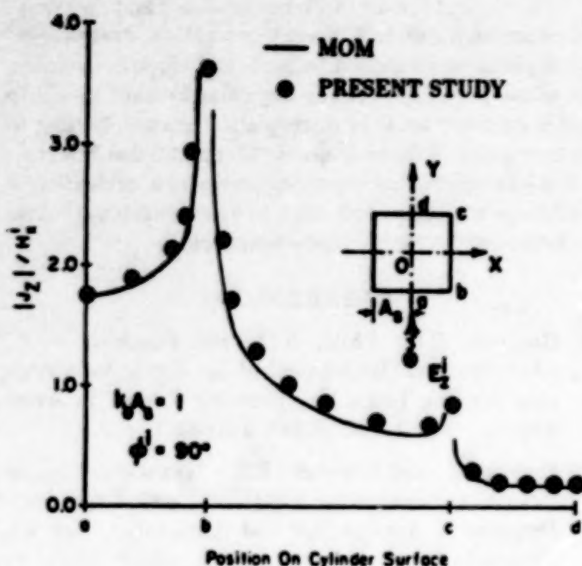

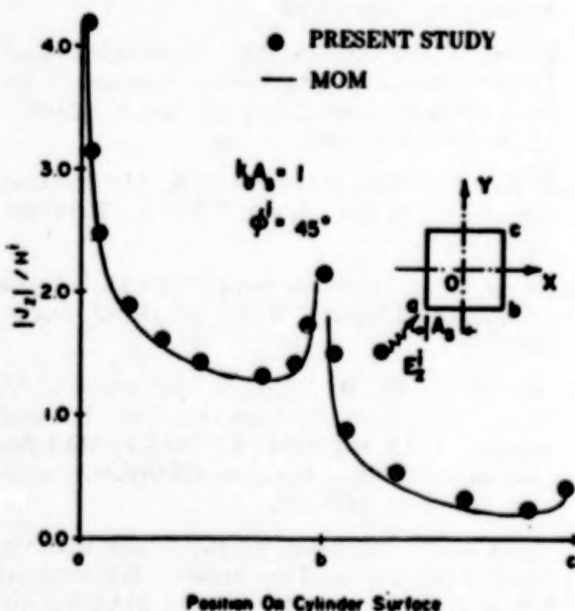Fig. 24a Surface current on a square cylinder for a right moving incident wave.

Fig. 24b Surface current on a square cylinder for an incident wave at 45°.

CONCLUSIONS

The state of the art of Computational Fluid Dynamics has taken rapid strides in recent years with the development and application of unified, robust, and efficient methods. The advances in CFD are also beginning to make a positive impact on other areas of mathematical science, leading to the emergence of the concept of "Computational Science". In this new spirit, this paper has presented a unification of algorithms and their application to fluid dynamics, electromagnetics, and material characterization.

REFERENCES

1. Gingrich, P.B., Child, R.D., and Panageas, G.N., "Aerodynamic Development of the Highly Maneuverable Aircraft Technology Remotely Piloted Research Vehicle," NASA CR-143841, June 1977.

2. Bonner, E. and Gingrich, P.B., "Transonic Computational Experience for Advanced Tactical Aircraft," *Progress in Astronautics and Aeronautics*, Vol. 81, Transonic Aerodynamics, D. Nixon, editor, American Institute of Aeronautics and Astronautics, 1982.

3. Gingrich, P.B. and Bonner, E., "Wing Design for Supersonic Cruise/Transonic Maneuver Aircraft," 13th Council of the International Council of Aeronautical Sciences, Vol. 2, American Institute of Aeronautics and Astronautics, August 1982.

4. Bonner, E. and Gingrich, P.B., "Supersonic Cruise/Transonic Maneuver Wing Section Development," Air Force Flight Dynamics Laboratory Report AFAWL-TR-80-3047, June 1980.

5. Bonner, E., Clever, W., and Dunn, K., "Aerodynamic Preliminary Analysis System," NASA CR-145284, April 1978.

6. Clever, W.C., "Supersonic Second Order Analysis and Optimization Program," NASA CR-172342, August 1984.

7. Shankar, V., Ide, H., Gorski, J., and Osher, S., "A Fast, Time-Accurate Unsteady Full Potential Scheme," AIAA Paper No. 85-1512-CP, AIAA 6th Computational Fluid Dynamics Conference, Cincinnati, July 15-17, 1985.

8. Shankar, V., "Treatment of Steady and Unsteady Flows Using a Fast, Time-Accurate Full Potential Scheme," AIAA Paper No. 85-4060, AIAA 3rd Applied Aerodynamics Conference, Colorado Springs, October 14-16, 1985.

9. Shankar, V. and Ide, H., "Unsteady Full Potential Computations for Complex Configurations," AIAA Paper No. 87-0110, AIAA 25th Aerospace Sciences Meeting, Reno, January 1987.

10. Caughey, D.A. and Jameson, A., "Recent Progress in Finite Volume Calculations for Wing-Fuselage Combinations," AIAA Paper No. 79-1513, July 1979.

11. Jameson, A., Baker, T.J., and Weatherhill, N.P., "Calculation of Inviscid Transonic Flow over a Complete Aircraft," AIAA Paper No. 86-0103.

12. Chakravarthy, S.R. and Szema, K.-Y., "Unified Euler Algorithms for the Euler Equations," in preparation.

13. Chakravarthy, S.R., "The Versatility and Reliability of Euler Solvers Based on High-Accuracy TVD Formulations," AIAA Paper No. 86-0243, presented at the AIAA 24th Aerospace Sciences Meeting, Reno, January 6-9, 1986.

14. Chakravarthy, S.R. and Ota, D.K., "Numerical Issues in Computing Inviscid Supersonic Flow over Conical Delta Wings," AIAA Paper No. 86-0440, presented at the AIAA 24th Aerospace Sciences Meeting, Reno, January 6-9, 1986.

15. Szema, K.-Y. and Shankar, V., "Full Potential Solutions of Three-Dimensional Complex Geometries and Multibody Configurations," AIAA Paper No. 85-0272, Reno, January 1985.

16. Shankar, V. and Osher, S., "An Efficient Full Potential Implicit Method Based on Characteristics for Analysis of Supersonic Flows," AIAA Paper No. 82-0974, June 1982; AIAA J. 21 (9), 1262 (1983).

17. Shankar, V., Szema, K.-Y., and Osher, S., "A Conservative Type-Dependent Full Potential Method for the Treatment of Supersonic Flows with Embedded Subsonic Regions," AIAA Paper No. 83-1887; AIAA J. 23 (1), 41-48 (1985).

18. Szema, K.-Y. and Shankar, V., "Nonlinear Computation of Wing-Body-Vertical Tail-Wake Flows at Low Supersonic Speeds," AIAA Paper No. 84-0427.

19. Shankar, V., "A Unified Full Potential Scheme for Subsonic, Transonic, and Supersonic Flows," AIAA Paper No. 85-1643, AIAA 18th Fluid Dynamics, Plasmadynamics, and Lasers Conference, Cincinnati, July 16-18, 1985.

20. Chakravarthy, S.R. and Szema, K.-Y., "An Euler Solver for Three-Dimensional Supersonic Flows with Subsonic Pockets," AIAA Paper No. 85-1703, presented at the AIAA 18th Fluid Dynamics, Plasmadynamics, and Lasers Conference, Cincinnati, July 16-18, 1985.

21. Szema, K.-Y., Chakravarthy, S.R., and Dresser, H., "Multizone Euler Marching Technique for Flows over Multibody Configurations," AIAA Paper No. 87-0592, January 1987.

22. Nash, J. and Scruggs, R., "An Implicit Method for the Calculation of Three-Dimensional Boundary Layers on Finite, Thick Wings," AFFDL TR-77-122, February 1977.

23. Goldberg, U.C., "Separated Flow Treatment with a New Turbulence Model," AIAA J. 24, 1711-1713 (1986).

24. Goldberg, U.C. and Chakravarthy, S.R., "Prediction of Separated Flows with a New Turbulence Model," submitted for publication in AIAA J., Rockwell Science Center Preprint No. SC-PP-86-183.

25. Goldberg, U.C. and Chakravarthy, S.R., "Comparison Between Navier-Stokes and Euler Calculations for a Class of Supersonic Nozzle Flows," in preparation.

26. Ota, D.K., Chakravarthy, S.R., and Gorski, J.J., "Inviscid and Viscous Simulations of High Angle of Attack Flows," SAE Technical Paper Series No. 851820, presented at the Aerospace Technology Conference and Exposition, Long Beach, California, October 14-17, 1985.

27. Stratton, J.A., Electromagnetic Theory, McGraw-Hill Book Company, Inc., New York, 1941.

28. Van Roosbroeck, W., "Theory of the Flow of Electrons and Holes in Germanium and Other Semiconductors," Bell System Tech. Journal, Vol. 29, 1950, p. 560.

29. Roe, P.L., "Approximate Riemann Solvers, Parameter Vectors, and Difference Schemes," J. of Computational Physics, Vol. 43, 1981, pp. 357-372.

30. Jischke, M.C., Rasmussen, M.L., and Daniel, D.C., "Experimental Results for Surface Pressures on Cone-Derived Waveriders in the Mach Number Range 3 to 5," AIAA Paper 82-0249, presented at the AIAA 20th Aerospace Sciences Meeting, Orlando, January 1982.

31. Gentry, A.E. and Smythe, D.E., "Hypersonic Arbitrary-Body Aerodynamic Computer Program (Mark III Version)," Vol. I - User's Manual, Report DAC 61552 (available from DTIC as 851811), McDonnell Douglas Corp., April 1968.

32. Abeyounis, W.K. and Putnam, L.E., "Investigation of the Flow Field Surrounding Circular-Arc Boattail Nozzles at Subsonic Speeds," NASA TP 1633, May 1980.

33. Settles, G.S., Vas, I.E., and Bogdonoff, S.M., "Details of a Shock-Separated Turbulent Boundary Layer at a Compression Corner," AIAA J., Vol. 14, No. 12, December 1976, pp. 1709-1715.

34. Settles, G.S., Fitzpatrick, T.J., and Bogdonoff, S.M., "Detailed Study of Attached and Separated Compression Corner Flowfields in High Reynolds Number Supersonic Flow," AIAA J., Vol. 17, No. 6, June 1979, pp. 579-585.

35. Dolling, D.S. and Murphy, M.T., "Unsteadiness of the Separation Shock Wave Structure in a Supersonic Compression Ramp Flowfield," AIAA J., Vol. 21, No. 12, December 1983, pp. 1628-1634.

36. Driver, D.M. and Seegmiller, H.L., "Features of a Reattaching Turbulent Shear Layer in Divergent Channel Flow," AIAA J., Vol. 23, No. 2, February 1985, pp. 163-171.

37. Sindir, M., "Numerical Study of Separating and Reattaching Flows in a Backward-Facing Step Geometry," doctoral dissertation, Mechanical Engineering, University of California at Davis, California, 1982.

38. Gorski, J.J., Ota, D.K., Chakravarthy, S.R., and Shankar, V., "Calculation of Three-Dimensional Cavity Flowfields," AIAA Paper No. 87-0117.

39. Shankar, V. and Gnanamuthu, D., "Computational Simulation of Laser Heat Processing of Materials," AIAA Paper No. 85-0390.

40. Shankar, V. and Gnanamuthu, D., "Computational Simulation of Heat Transfer in Laser Melted Material Flow," AIAA Paper No. 86-0461.

41. Shankar, V. and Chakravarthy, S.R., "An Approach to Computational Simulation of Problems in Electromagnetic Scattering," in preparation.

42. Umashankar, K. and Taflove, A., "A Novel Method to Analyze Electromagnetic Scattering of Complex Objects," IEEE Trans. on Electromagnetic Compatibility, Vol. EMC-24, No. 4, November 1982, p. 397.

COMPUTATIONAL FLUID DYNAMICS APPLICATIONS AT MCDONNELL DOUGLAS

R. J. Hakkinen[*]

McDonnell Douglas Research Laboratories

SUMMARY

Representative examples are presented of applications and development of advanced Computational Fluid Dynamics (CFD) codes for aerodynamic design at the McDonnell Douglas Corporation (MDC). Transonic potential and Euler codes, interactively coupled with boundary layer computation, and solutions of slender-layer Navier-Stokes approximation are applied to aircraft wing/body calculations. An optimization procedure using evolution theory is described in the context of transonic wing design. Euler methods are presented for analysis of hypersonic configurations, and helicopter rotors in hover and forward flight. Several of these projects have been accepted for access to the Numerical Aerodynamic Simulation (NAS) facility at the NASA-Ames Research Center.

1. INTRODUCTION

Computational fluid dynamics (CFD) is used as a routine design technique in the divisional engineering technology and project organizations of the McDonnell Douglas Corporation (MDC). Several groups are also active in research and development of CFD methods, both at the divisional companies in the context of their primary applications, and in a more generic sense at the McDonnell Douglas Research Laboratories (MDRL). Figure 1 shows a simplified corporate organization chart.

In addition to the computing facilities at divisional locations, a Cray X-MP/14 is available as a central resource under the management of the McDonnell Douglas Aerospace Information Services Company. When authorized, U. S. Government large-scale computing facilities are used for specific tasks; cooperative projects with NASA centers have been especially fruitful.

The following examples describe CFD applications to aerodynamic design and optimization, and new methods under development for computation of aircraft, helicopter, and missile flowfields. These projects are supported by the McDonnell Douglas Corporation Independent Research and Development Program; for several projects, the cooperation of the NASA NAS Program and/or of Cray Research, Inc., is appreciated.
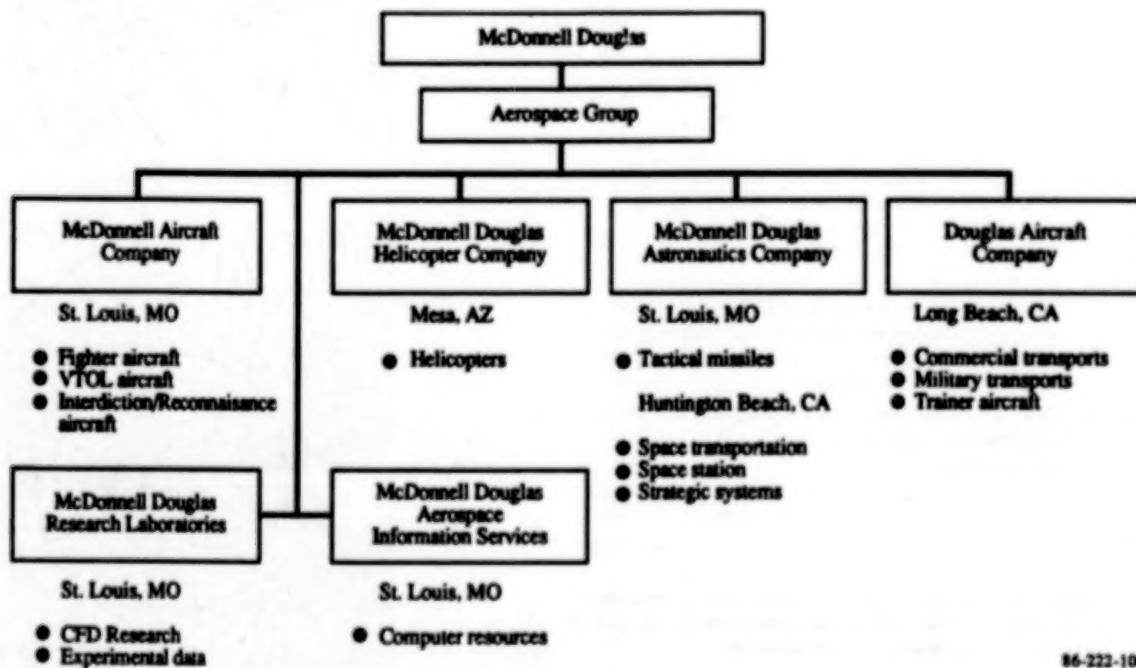

Fig. 1 McDonnell Douglas Aerospace Group components active in CFD.

86-222-100

---

[*]Director-Research, Flight Sciences Department.

2. Simulation of Power Effects on Complex Configurations with an Inviscid/Viscous Interaction Scheme Based on the Solution of Euler and Inverse Boundary Layer Equations (T. Cebeci and L. T. Chen, Douglas Aircraft Company (DAC), Long Beach, CA)

The objective of this project (fig. 2) is to combine transonic flowfield codes based on the Euler equations with a three-dimensional inverse boundary-layer method. Complex wing/body and aft fuselage/nacelle/pylon configurations, including power effects, will be computed with different grid topologies. The results will be compared with available experimental data. The computer resources used in this project include the NAS Cray-2.

Successful computation of flows with both shock-induced and trailing-edge separation requires the combination of viscous/inviscid interactive schemes with the Euler equations which provide a realistic simulation of the vorticity distribution downstream of strong shocks. In the inverse boundary-layer method of Cebeci, et al. (1986), the edge velocity is treated as an unknown and the interactive solutions are obtained with the Hilbert integral approach. The coupling of the inverse method with two-dimensional Euler equations is presented by Chen, Li and Chen (1987); Chen and Chen[*] extend this approach to three dimensional transonic flows over wings and wing/body configurations.

The computational procedure of Chen and Chen[*] also extends the hybrid mapping/numerical grid-generation method of Chen, Vassberg and Peavey (1985) to a new scheme where the mesh lines are wrapped around the wing tip into a C-mesh which allows proper modeling of wing-tip vorticity permitted by the Euler equations, as shown in figure 3.

Task 1:	Develop and validate Euler methods for wing/body and aft-fuselage/nacelle/pylon configurations, respectively, on NAS computer.
Task 2:	Develop and validate an interactive inverse boundary-layer method for coupling with the Euler method wing/body and aft-fuselage/nacelle/pylon configurations, respectively.
Task 3:	Validate solutions for both configurations on the NAS computer for a wide range of flow conditions and power settings, and study the mesh effect on the solutions by comparing them with DAC full-potential and Euler-correction solutions.
Task 4:	Develop a zonal method for coupling solutions about wing/body and aft-fuselage/nacelle/pylon configurations.
Task 5:	Compare computed solutions with available test data.

CP83-1659-5-R

Fig. 2 Simulation of power effects on complex configurations with an inviscid/viscid interaction scheme based on the solution of Euler and inverse boundary-layer equations.

---

[*]Chen, L. T. and Chen, H., "An Interactive Scheme for Transonic Wing/Body Flows Based on Euler and Inverse Boundary-Layer Equations," Douglas Aircraft Company, Long Beach, CA, 1987.
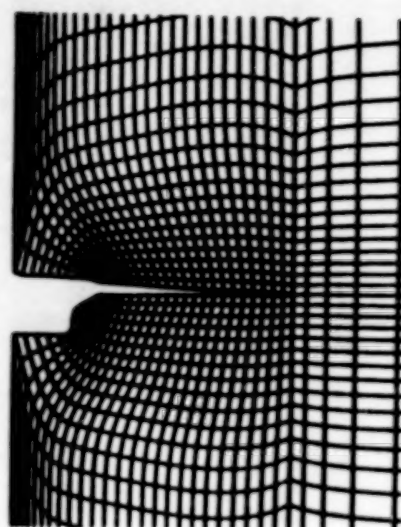
(a) KGRID (C-H-H mesh)
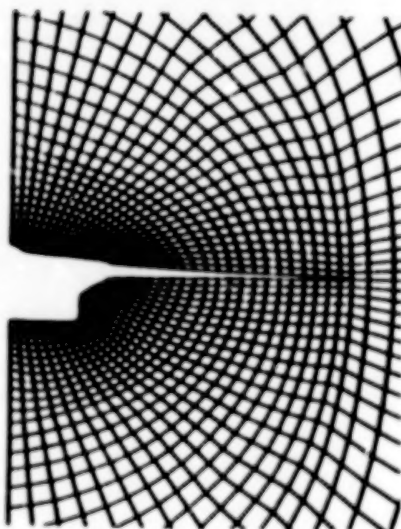
(b) PGRID (C-C-H mesh)

(c) QGRID (C-C-C mesh)

CP83-1659-5-R
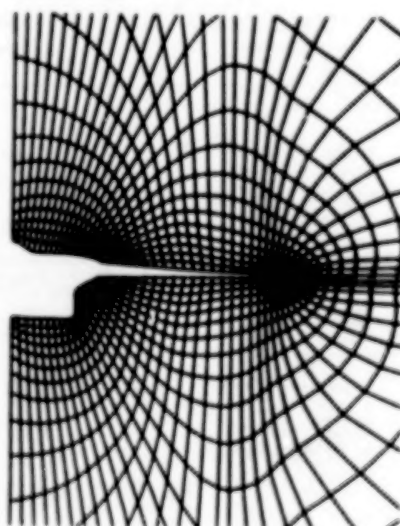
Fig. 3 Comparison of cross-sectional grid distribution for three grid-generation methods.

The three-dimensional inviscid flowfield is
calculated with Jameson's multi-grid, four-stage
Runge-Kutta time-stepping scheme, and the inverse
boundary-layer method of Cebeci et al. (1986) is
applied with a strip theory approximation. Both
displacement surface and blowing velocity
approaches are used in the interactive matching
procedure described in detail by Chen and Chen.[a]

Figure 4 shows an inviscid Euler calculation of
supersonic flow about a fighter-type wing/fuselage
configuration. The calculation was obtained with
the new grid-generation method described by Chen,
Vassberg, and Peavey (1985) and Chen and Chen.[a] A
comparison of viscous/inviscid interactive calcula-
tions with test data is shown in figure 5 for a
high-aspect-ratio transport wing/body configura-
tion. Both potential and Euler codes were used for
the inviscid flowfield, and the interactive cou-
pling was accomplished by the displacement surface
approach. The agreement between the calculations
and experiment is generally good, with some deteri-
oration toward the wing tip.

Further improvements of the grid-generation
method will include implementation of the zonal
technique for complex configurations.

3. Transonic Wing Optimization By Evolution Theory
(R. D. Gregg, Douglas Aircraft Company, Long Beach,
CA)

The present comments are based on Gregg and
Misegades (1987), which contains a more extensive
discussion of the impact of increasing computer
capability on three-dimensional optimization proce-
dures and presents detailed practical results.

The importance of computing speed is illustrat-
ed in figure 6, where the assumption of an optimi-
zation process requiring 1000 transonic wing flow-
field solutions indicates the dramatic effect of
computational speed: the approximately 250 hours
required by an IBM 3081 can be reduced to ten hours
on a single-processor Cray X-MP, and to 2.5 hours
when taking full advantage of the multitasking cap-
ability of a Cray X-MP/48.

A description of the evolution-theory approach
is shown in figure 7. Basically, a set of merit
functions related to performance requirements is
calculated repeatedly for different sets of design
variables that are allowed to vary within a chosen
range. At each step, the range and its center are
adjusted until a reasonable convergence of the
merit functions is achieved.

Figure 8 illustrates how the convergence of
merit functions was achieved in the case of an
aspect ratio of ten, taper ratio of four, 25-degree
swept NACA 0012 wing which was allowed to change
camber in the last 15 per cent of chord. The flight
condition was M=0.76 at C_L=0.55, and the base wing
exhibited excessive shock drag, buffet, and tip
stall. While induced drag increased slightly be-
cause of increased departure from an elliptic span-
wise load distribution, significant gains in other
merit functions were achieved in approximately

[a]Chen, L. T. and Chen, H., "An Interactive Scheme
for Transonic Wing/Body Flows Based on Euler and
Inverse Boundary-Layer Equations," Douglas
Aircraft Company, Long Beach, CA, 1987.

Heavy line indicates isovalue = 1.0000
Dashed line indicates isovalue = 1.3000
Increments in isovalue = 0.0500

Fig. 4 Mach number contours on a typical fighter wing/fuselage;
$M_\infty = 1.3$ and $\alpha = 4.84°$.

forty iterations, including a 50-per cent decrease
in total drag.

The procedure involved 640 FLO-22 solutions
with a total CPU-time of 7.2 hours. This example
is the first one of three in this paper where the
microtasking procedure of Booth and Misegades
(1986) was used in cooperation with Cray Research
on their Cray X-MP/48, resulting in this case in
clock-time reduction by a factor of 3.95 to 1.8
hours.

4. Accurate, Efficient Prediction Method for
Supersonic/Hypersonic Inviscid Flow (A. Verhoff and
P. J. O'Neil, McDonnell Aircraft Company, St.
Louis, MO)

The new method employs a spatial marching pro-
cedure to solve the formulation of Euler equations
described by Verhoff and O'Neil (1984). This for-
mulation is written in terms of Riemann-type vari-
ables by use of a local streamline coordinate sys-
tem shown in figure 9, and therefore models wave
propagation in a physical sense with no inherent
Mach-number restrictions. The procedure can be
extended to three-dimensional flows in a straight-
forward manner, and it is especially suitable for
efficient vector coding.

Steady-state solutions are obtained by an ex-
plicit time-integration scheme, where the local
maximum time step is used to increase rate of con-
vergence. Spatial derivatives are approximated by
one-sided finite differences to properly model the
wave propagation. At solid surfaces, the algebraic
relationship between the flow angles θ and ϕ, com-
bined with the local pressure gradient, yields an
accurate boundary condition. Neither non-physical
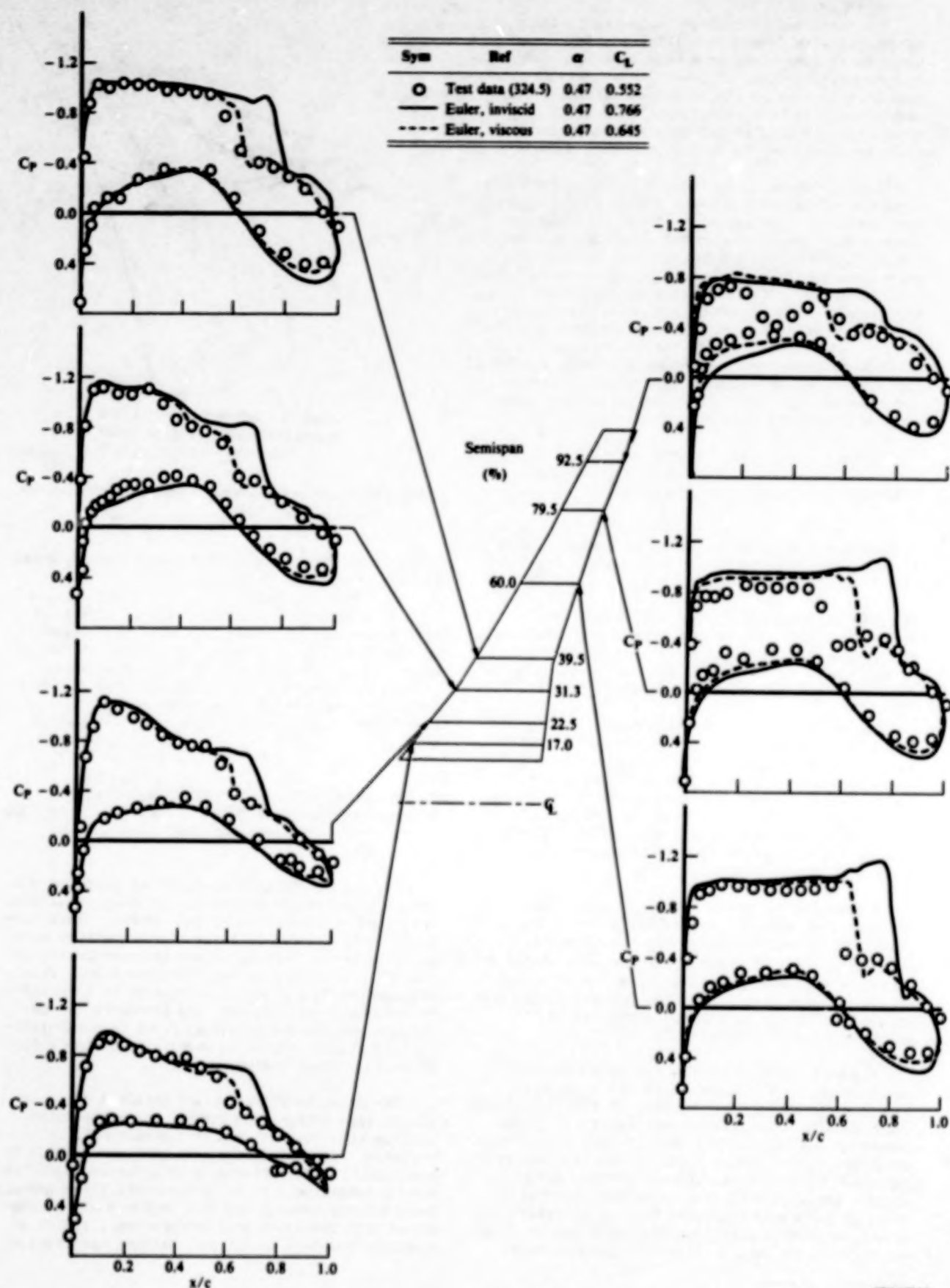
Fig. 5 Comparison of viscous/inviscid Euler solutions and test data for the LB-488 wing/body;
M = 0.82, α = 0.47; and Re_c = 5.4 × 10^6.

input parameters, artificial dissipation, nor smoothing are required in the solution algorithm.
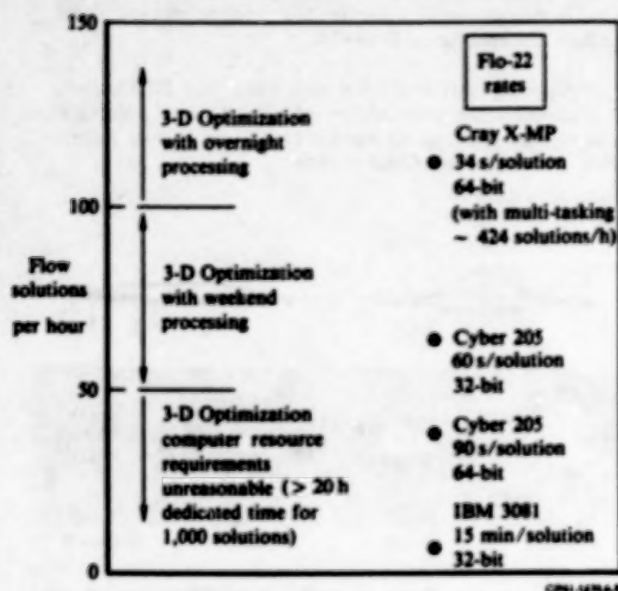
Fig. 6 Aerodynamic wing optimization: the importance of computational speed.

- User selects range of each design variable to initiate scheme

- A random sample within this range is selected and evaluated

- Best value of design variable(s) is selected as new center, and the radius is modified

Best - 1, worst - 8

- Procedure is repeated until 'convergence' of all design variables is obtained
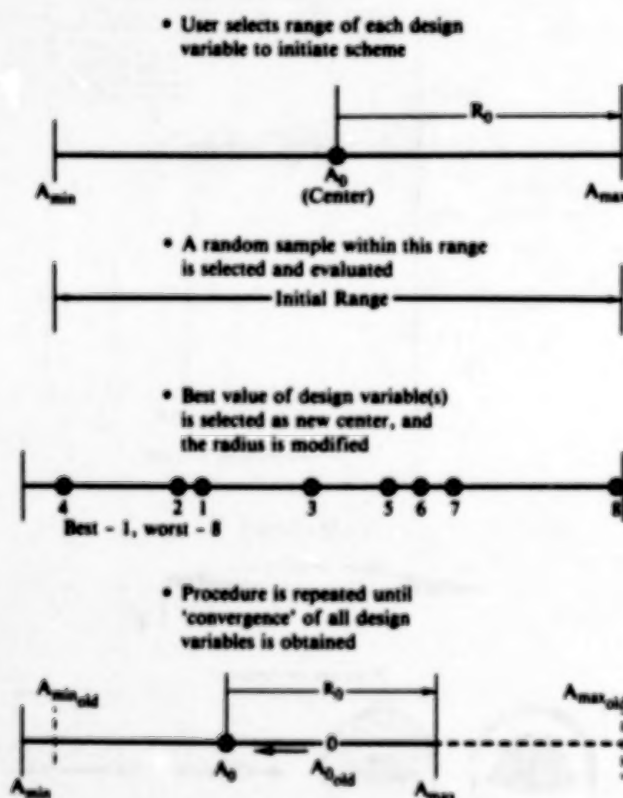
Fig. 7 Evolution theory.

For fully inviscid supersonic flow, three-dimensional flowfield analysis can be reduced to a sequence of two-dimensional problems by use of a spatial marching procedure based on this formulation. Flowfields about vehicles with wings, tails, and fins can therefore be predicted with relatively coarse computational grids. Shocks are automatically captured; the only constraint requires the outer grid boundary to include the perturbed flowfield.

A computer program called SCRAM (Streamline Coordinate Riemann Axial Marching) has been developed at McDonnell Aircraft using this formulation. The program evolved from a research code and within one year became a useful design method for routine analysis of hypersonic configurations. A detailed description of the method is presented by Verhoff and O'Neil,[*] including the following representative examples.

Figure 10 illustrates the suitability of the SCRAM-code for vector processing in the case of a simple 20-degree cone at zero angle of attack in
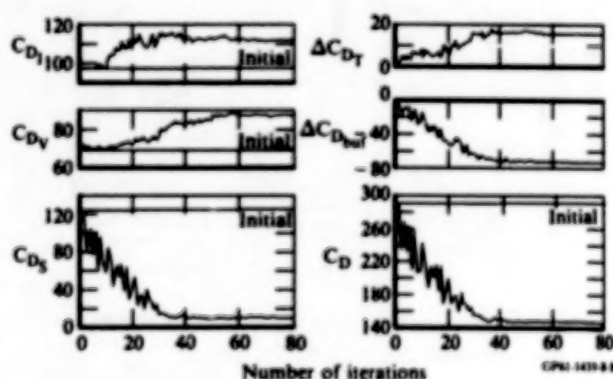
Fig. 8 Aerodynamic wing optimization for a simple, swept-wing test case (in terms of induced, viscous, shock, trim, buffet, and total drag).
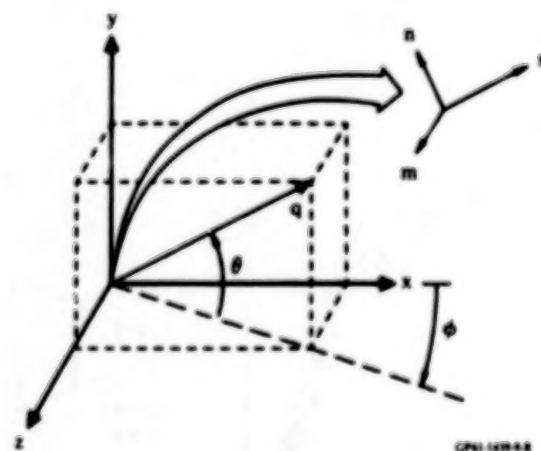
Fig. 9 Definition of flow angles and streamline coordinates.

[*]Verhoff, A. and O'Neil, P. J., "Accurate, Efficient Prediction Method for Supersonic/Hypersonic Inviscid Flow," McDonnell Aircraft Company, St. Louis, MO, 1987.

M=2.5 supersonic flow; CPU time reductions by an order of magnitude can be achieved for higher grid densities relative to scalar operation. Figure 11 shows the accuracy of the solution for various grid densities, as compared with the exact analytical solution.

Figure 12 shows the computational grid for a blended wing/body configuration. The grid has half-plane distribution of 51 by 25 nodes, with 25 axial stations, and is based on a nonlinear grid generation procedure developed at McDonnell Aircraft. For M=6, computed pressure contours in four cross-planes are shown in figure 13, and a comparison of predicted force and moment characteristics with test data is shown in figure 14; estimated skin-friction drag has been subtracted from the test data, yielding excellent agreement with the inviscid computation. Each case, including input-output processing, required only about five minutes on the Cray X-MP/14.

Figures 15 and 16 show the grid and the computed Mach number contours, respectively, for a complex conical body at M=10. The excellent grid resolution and computational efficiency contributed to the achievement of a converged solution at the first attempt, again requiring approximately five minutes on the Cray X-MP/14.

McDonnell Aircraft is applying the SCRAM code to high-quality prediction of increasingly complex flowfields, including realistic fighter and hypersonic aircraft configurations.

Fig. 12 Computational grid for AMI-X blended body; vertical tails off.

Fig. 10 Vector efficiency of SCRAM code on CYBER 205 computer; $M_\infty = 2.5$, $\delta = 20°$, and $\alpha = 0°$.
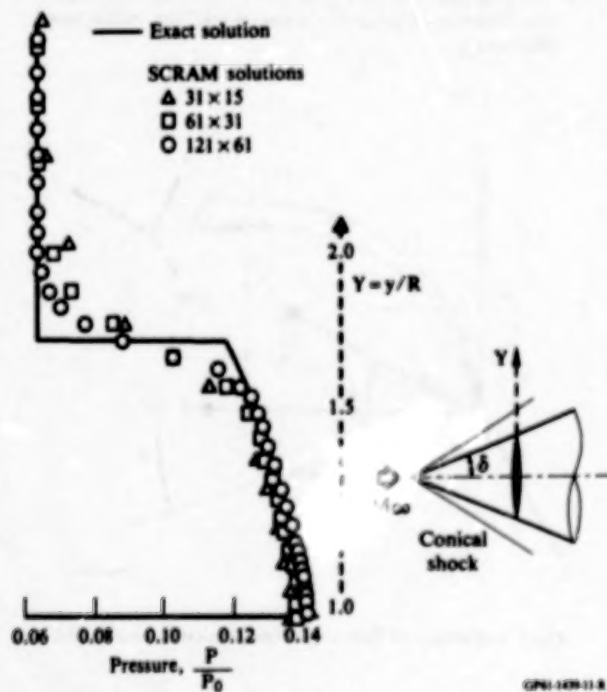
Fig. 11 SCRAM solution for circular cone; $M_\infty = 2.44$, $\alpha = 0°$, and $\delta = 20°$.

Surface pressure distributions

$51 \times 25 \times 24$ grid

Pressure contours
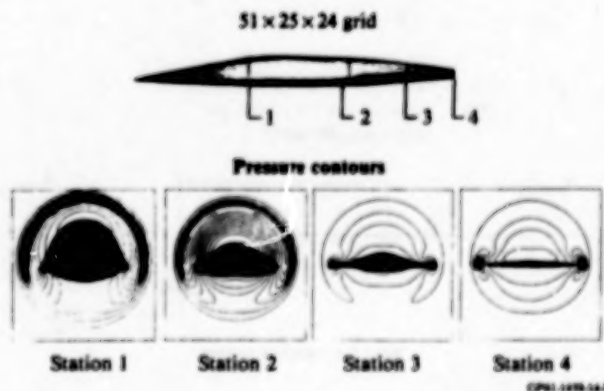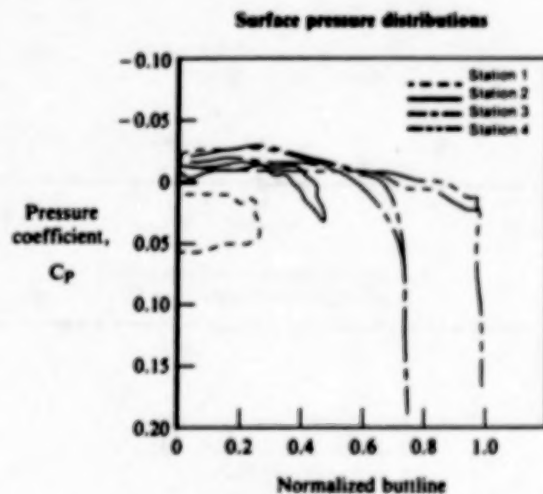
Fig. 13 SCRAM pressure predictions for AMI-X blended body; $M_\infty = 6$ and $\delta = 0°$.

114
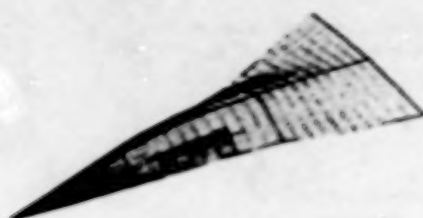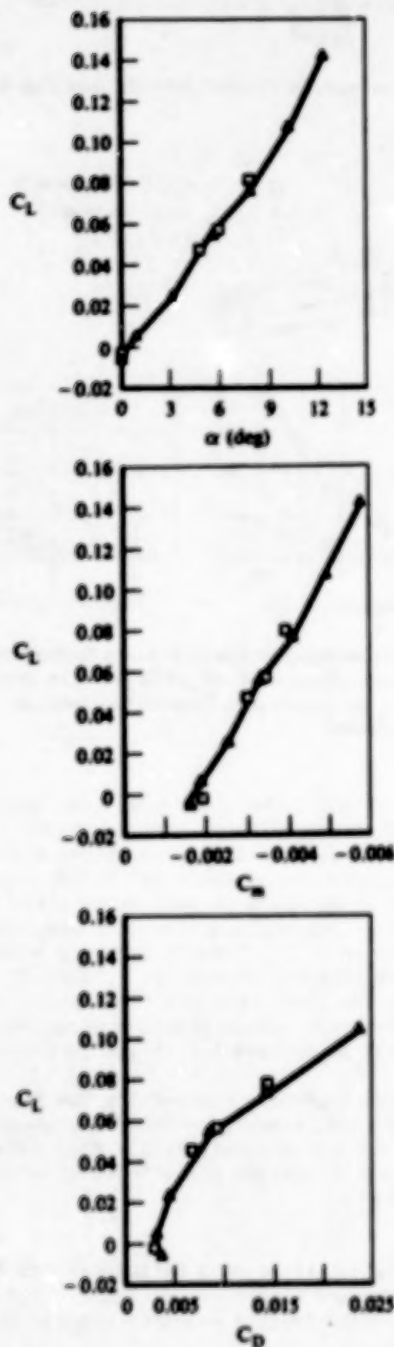
Fig. 14 SCRAM force and moment predictions for AMI-X blended body; $M_\infty = 6.6$.
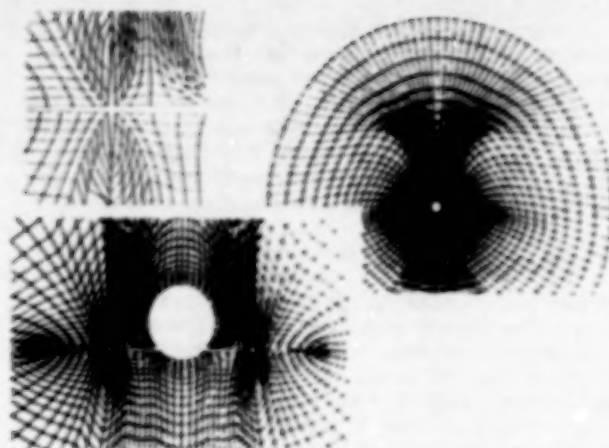
Fig. 15 MARCHG grid generation for SCRAM code.

Fig. 16 SCRAM code application to complex hypersonic vehicle; $M_\infty = 10$ and $\alpha = 0°$.

5. **Integrated Flowfield Analysis Methodology for Fighter Inlets** (R. R. Cosner, McDonnell Aircraft Company, St. Louis, MO)

A methodology to predict viscous flow over integrated fighter forebody-inlet combinations has been developed at McDonnell Aircraft Company; effects of Mach number, Reynolds number, angle of attack and engine mass flow are included in the prediction. A detailed description of the method is given by Cosner (1986), including the following examples.

The procedure is based on the velocity-splitting method which provides a relaxation solution to the steady-state Navier-Stokes equations [Cosner (1982)]. A multiple-zone mesh achieves the geometric flexibility required for representation of realistic inlet/forebody configurations. The mesh is generated by a three-dimensional implementation of Thompson's method, with wall orthogonality enhanced by a three-dimensional extension of Sorenson's technique, as described by Cosner (1982).

All terms, except time derivatives, were retained in the Navier-Stokes equations; turbulence effects were represented by the Cebeci-Smith algebraic model. Non-conservative and quasi-linearized discretization was used, and type-dependent differencing, according to the local flow velocity, ensured numerical stability without addition of artificial viscosity terms.

Separate mesh and flow solutions were executed
in each of the three zones; the flow solutions are
coupled by matching boundary conditions between
adjacent zones during the iterative solution proce-
dure. The mesh solutions were executed to a maxi-
mum of 30 iterations using an alternating-direction
implicit scheme; formal convergence was not found
to be necessary for achievement of a valid mesh.

The definition of the three computational zones
is shown in figure 17. The external flowfield up-
stream and downstream of the inlet highlight com-
prises the forebody and centerbody zones, respec-
tively; the internal zone extends from the inlet
entrance to the throat or the engine face. Mesh
parameters, such as node distribution or stretching
coefficients in each coordinate direction can be
prescribed entirely independently in each zone.
The flow solution is coupled across the interface
by interpolating Dirichlet and Neumann boundary
condition data; mesh coordinates and dependent var-
iables are modeled using piecewise bilinear func-
tions. The flow solution algorithm selects the
appropriate boundary condition according to the
type of local flow in the adjoining zones at or
near the interface.

The iterative solution procedure uses an
alternating-direction implicit scheme. The cycle
updates each zone in turn, starting with the fore-
body. In the internal zone, an algebraic correc-
tion to provide mass continuity in the potential
field significantly enhances the rate of conver-
gence. Typically, 10 to 30 solution cycles are
required; a larger number is necessary when the
free-stream Mach number approaches one from either
direction or the viscous interactions are strong.
Also, a modified procedure is used at near-choking
conditions in the inlet.

Application of the zonal forebody-inlet code to
the F/A-18 configuration used 8000 computational
nodes (16x25x20) in the forebody zone, 4000 nodes
(8x25x20) in the centerbody zone, and 6000
(12x25x20) in the inlet; the quasi-cylindrical mesh
topology is shown in figure 18. Pressure distribu-
tions on the forebody in front of the inlet are
shown in figure 19 at M=0.8 for three engine mass-
flow rates from near-maximum to zero flow. The
mass-flow rate variation was introduced into the
computation only in the inlet zone, from which the
perturbation propagated through the zone boundary
into the forebody zone. As shown in Cosner (1986),
especially good agreement with wind tunnel tests
was obtained in the critical region inside the
lower intake lip. The computations were performed
on a CDC CYBER 176, typical times being 10 to 15
minutes.

Fig. 18 Zonal mesh for F/A-18A forebody/inlet analysis.

$A_e/A_t = 0.71$ (100% power)
$A_e/A_t = 0.53$ (flight idle)
$A_e/A_t = 0$ (no flow)
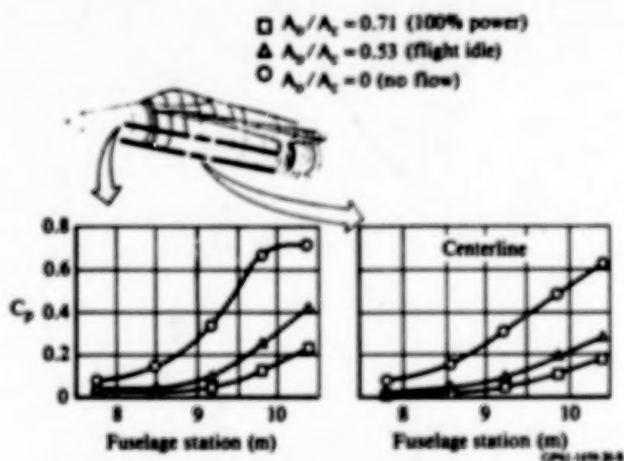
Fig. 19 Effect of engine airflow on F/A-18A forebody pressure;
Mach = 0.8 and $\alpha = 0°$ (A_e = inlet mass flow area,
A_t = inlet capture area, corrected to free-stream
conditions).

Figure 20 shows the three-zone mesh interfaces
for an AV-8B forebody/inlet configuration; a total
of 53760 nodes were used. Computations made on a
Digital Equipment Corporation VAX 11/780 computer
required 20 to 25 hours of wall-clock time. Com-
puted surface-pressure distributions and comparison
of the lower inlet lip inboard pressure with a test
at M=0.9 are shown in figure 21. Figure 22 shows,
for M=0.67, the inlet entrance flowfield from which
detailed total and static pressure distributions in
the inlet can be derived for design purposes.

The zonal procedure for solving the Navier-
Stokes equations is being extended to integrated
external compression inlets at all Mach numbers of
interest, and to include the effects of wing and
canard surfaces.

6. **Euler Calculations of a Helicopter Rotor in
Hover and Forward Flight** (R. K. Agarwal and J. E.
Deese, McDonnell Douglas Research Laboratories, St.
Louis, MO).

The progressive increase of computing power
over the last decade has advanced the computation
of helicopter rotor flowfields from solution of
transonic small-disturbance equations first to that
of the full potential equations, and recently, to

Fig. 17 Zone layout for forebody/inlet analysis.

Analysis model

Exploded view

Detail of Inlet Duct
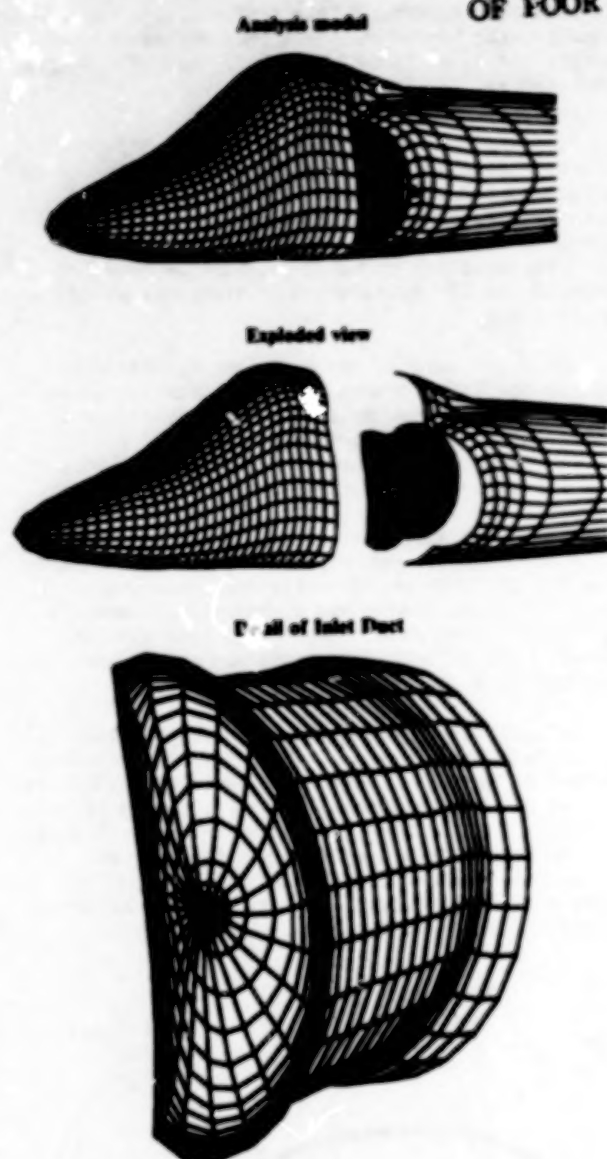
Fig. 20 Three-zone surface mesh for AV-8B forebody inlet.

Velocity vectors

Mach number

Static pressure, C_P

Total pressure, P_t/P_{t_∞}

Lip pressure comparison
(inboard lower lip)

Computed surface pressure

$\alpha = 10°$

O Test (Mach = 0.7, $\alpha = 9.9°$)

— Analysis

Distance from leading edge (cm)

Fig. 21 AV-8B forebody inlet viscous analysis; Mach = 0.67,
$\alpha = 10°$, and 186 kg/s (corrected).
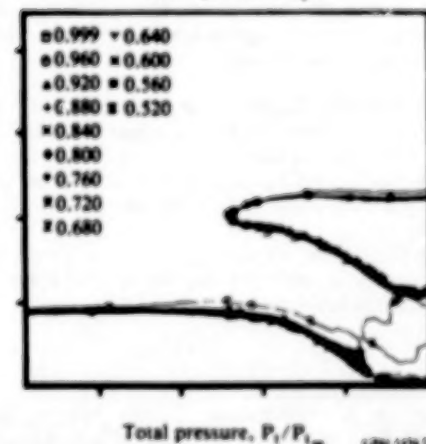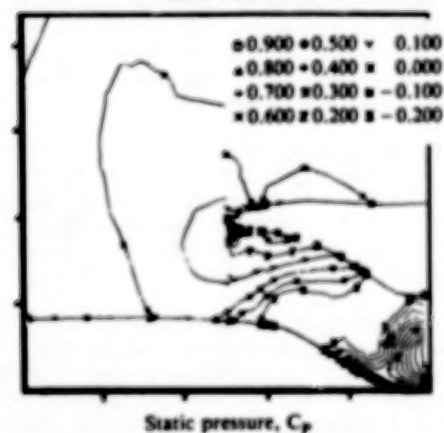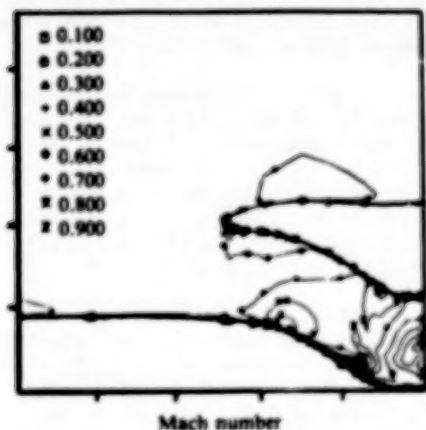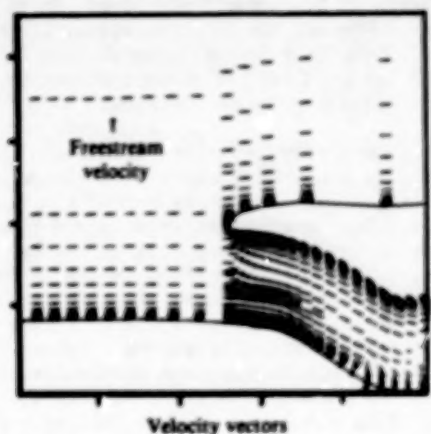
Fig. 22 AV-8B computed inlet entrance flowfield; Mach = 0.67,
$\alpha = 0°$, and 186 kg/s.

codes based on the Euler equations. An Euler code, designated MDROTH, has been developed at the McDonnell Douglas Research Laboratories for calculating the flowfield of a multibladed helicopter rotor in hover and forward flight.

The code solves the three-dimensional Euler equations in a rotating coordinate system on body-conforming curvilinear grids around the blades. Euler equations are recast in absolute flow variables so that the absolute flow in the far field is uniform, but the relative flow is non-uniform. Equations are solved for the absolute flow variables by employing Jameson's finite-volume explicit Runge-Kutta time-stepping scheme. Rotor wake effects are modeled in the form of a correction applied to the geometric angle-of-attack along the blades. This correction is obtained by computing the local induced downwash with a free-wake analysis program. The details of the methodology are described by Agarwal and Deese (1986).

A set of test calculations was performed by Agarwal and Deese[a] to verify the code for a model rotor in hover and forward flight at various collective pitch angles. The model rotor has two untwisted, untapered blades of aspect ratio equal to six and the NACA 0012 airfoil section. Computations were performed on a 97 (chordwise) x 33 (blade-normal) x 21 (spanwise) mesh.

The code has been fully vectorized for optimum performance on Cray X-MP, and has also been microtasked for peak performance on the four-processor Cray X-MP/48 [Booth and Misegades (1986)] with a speed-up factor of 3.71. A typical case requires 2 million 64-bit words of main memory and 7×10^{-6} seconds of CPU time per mesh point for each iteration. A solution for hover flowfield converged in 500 to 800 iterations. This project has been accepted for access to the NAS Cray-2.

Figure 23 shows the main features of the flowfield of a two-bladed rotor in hover, with the imbedded finite-difference grid and the coordinate system. The flowfield is characterized by transonic shocks, complex vortical wakes, and blade-vortex interactions.
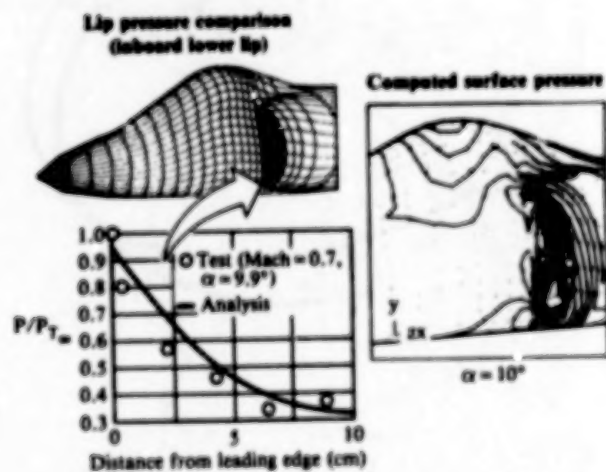
Comparisons of computed pressure distributions with experimental data are shown in figure 24 for a hovering rotor at a tip Mach number of $M_t = 0.52$ and zero collective pitch, and for $M_t = 0.877$ and collective pitch angle $\theta_c = 8°$ in figure 25. Both cases indicate good agreement; in the lifting case of figure 25, further improvement can be achieved by refining the wake model.

For forward flight, computed pressure distributions are compared with experimental data at a location near the blade tip in figure 26 for $M_t = 0.8$, advance ratio $\mu = 0.2$, and zero collective pitch. Again, good agreement is demonstrated.

The long-term objective of this project is to include viscous effects in the calculation of transonic multibladed rotor flowfields.

---

[a]Agarwal, R. K. and Deese, J. E., "An Euler Solver for Calculating the Flowfield of a Helicopter Rotor in Hover and Forward Flight," McDonnell Douglas Research Laboratories, St. Louis, MO, 1987.

7. Transonic Wing/Body Calculations Using the Slender-Layer Navier-Stokes Approximation (R. K. Agarwal and J. E. Deese, McDonnell Douglas Research Laboratories, St. Louis, MO)

With the increasing availability of supercomputers, the ability to compute transonic flowfields has progressed to solution of Reynolds-averaged Navier-Stokes equations for aircraft configurations. A viscous flow code, designated MDSSL30, has been developed at McDonnell Douglas Research Laboratories for calculation of transonic wing/body flowfields.

The code computes the turbulent flowfield by solving the three-dimensional, Reynolds-averaged, slender-layer approximation to the Navier-Stokes equations on body-conforming, curvilinear grids. In the slender-layer approximation to the Navier-Stokes equations, only streamwise diffusion terms are neglected; diffusion terms in the other directions are retained. Therefore, slender-layer equations are suitable for calculating spanwise separation and the flow along a wing-body junction. These equations are solved by employing Jameson's finite-volume explicit Runge-Kutta time-stepping scheme. The calculations performed so far have used the Baldwin-Lomax turbulence model.

The details of the methodology and the test calculations performed to verify the code are described by Agarwal, Deese, and Underwood (1985) and Agarwal and Deese (1984). Recently, fine-grid calculations for turbulent flow over an ONERA-M6 wing were performed on a Cray X-MP/48; the code was fully optimized and microtasked for peak performance on the four-processor Cray X-MP/48, as documented by Booth and Misegades (1986).
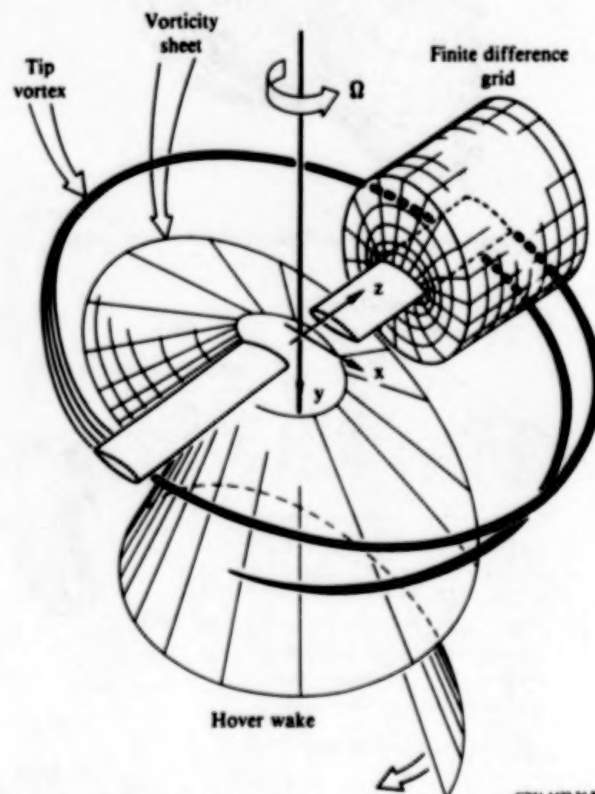
Fig. 23 Schematic of helicopter rotor flowfield in hover.
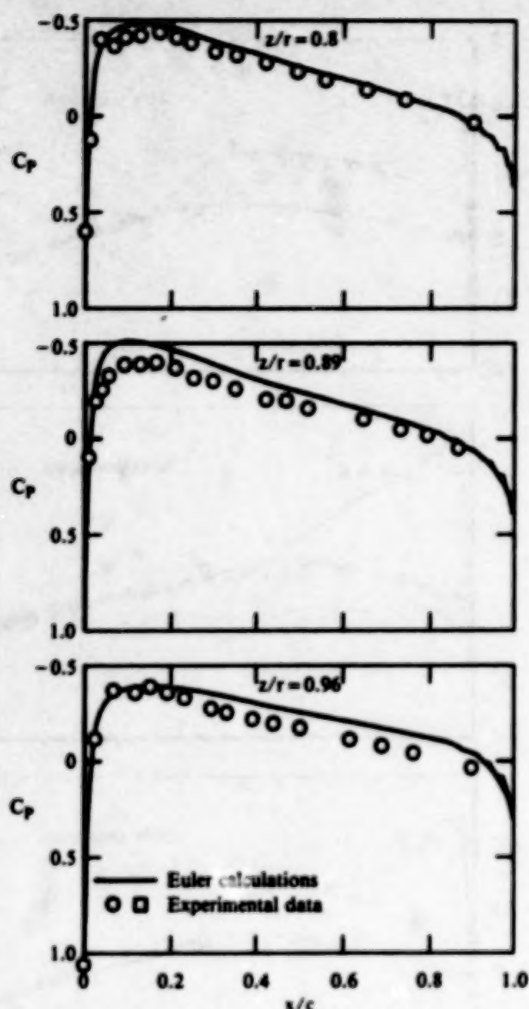
Fig. 24 Surface pressure distributions on a nonlifting rotor in hover; $M_t = 0.52$, $\theta_c = 0°$, AR = 6, NACA 0012 blade, and $97 \times 33 \times 21$ mesh.

Fig. 25 Surface pressure distributions on a lifting rotor in hover; $M_t = 0.877$, $\theta_c = 8°$, AR = 6.0, NACA 0012 blade, and $97 \times 33 \times 21$ mesh.

Computed results at various spanwise stations of the ONERA-M6 wing are compared with experimental data in figure 27, with good agreement. The code has also been exercised by Deese and Agarwal[*] for calculation of fighter- and transport-type wing/body flowfields; excellent global grids were generated with the three-dimensional procedure of Chen, Vassberg, and Peavey (1985). Surface grid-lines of a transport wing/body configuration are shown in figure 28. Comparisons of calculated pressure distributions at various spanwise stations with experimental data are shown in figure 29; the agreement is again good.

The long-term objective of this project is to calculate turbulent flowfields for increasingly complete transport and fighter aircraft configurations. The project has also been accepted for access to the NAS Cray-2.

8. Concluding Remarks

An extensive program to develop advanced CFD codes is being conducted within the components of the McDonnell Douglas Corporation for applications to helicopters, transport and fighter aircraft, and missiles and hypersonic vehicles. Efficient use of large computers, including multiple-processor facilities, is receiving special attention, and access to the NAS facility in several of these areas is greatly appreciated.

---

[*]Deese, J. E. and Agarwal, R. K., "Navier-Stokes Calculations of Transonic Viscous Flow About Wing-Body Configurations," McDonnell Douglas Research Laboratories, St. Louis, MO, 1987.
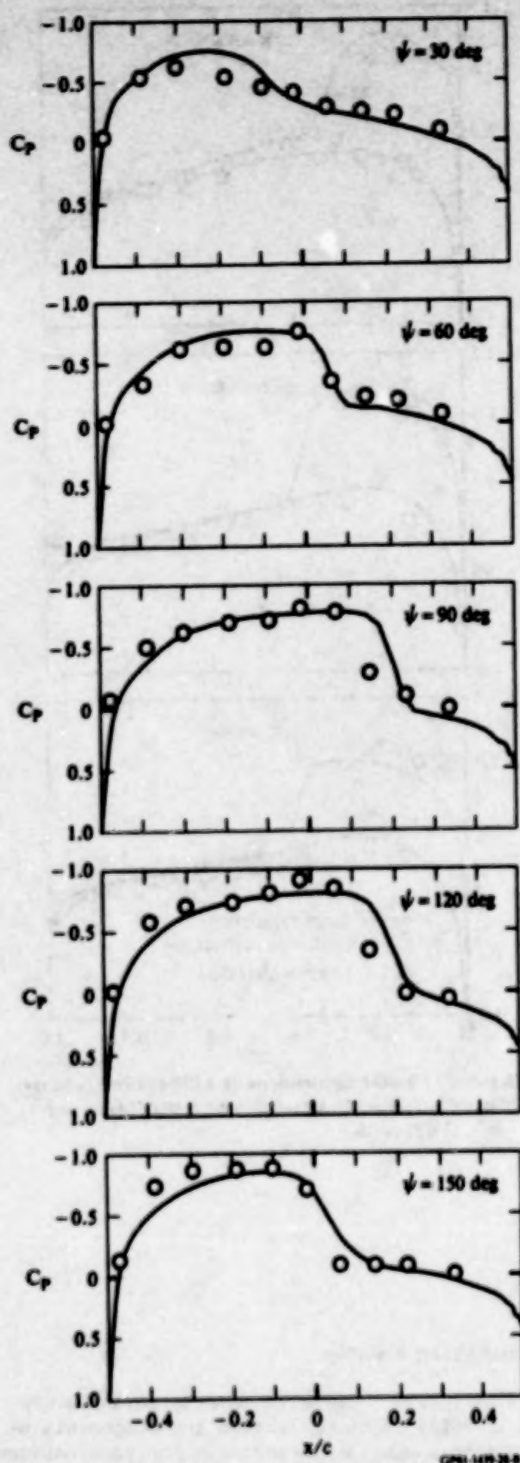
Fig. 26 Euler calculations for flowfield of a helicopter rotor in forward flight; $M_t = 0.8$, $\mu = 0.2$, and $96 \times 32 \times 32$ mesh.
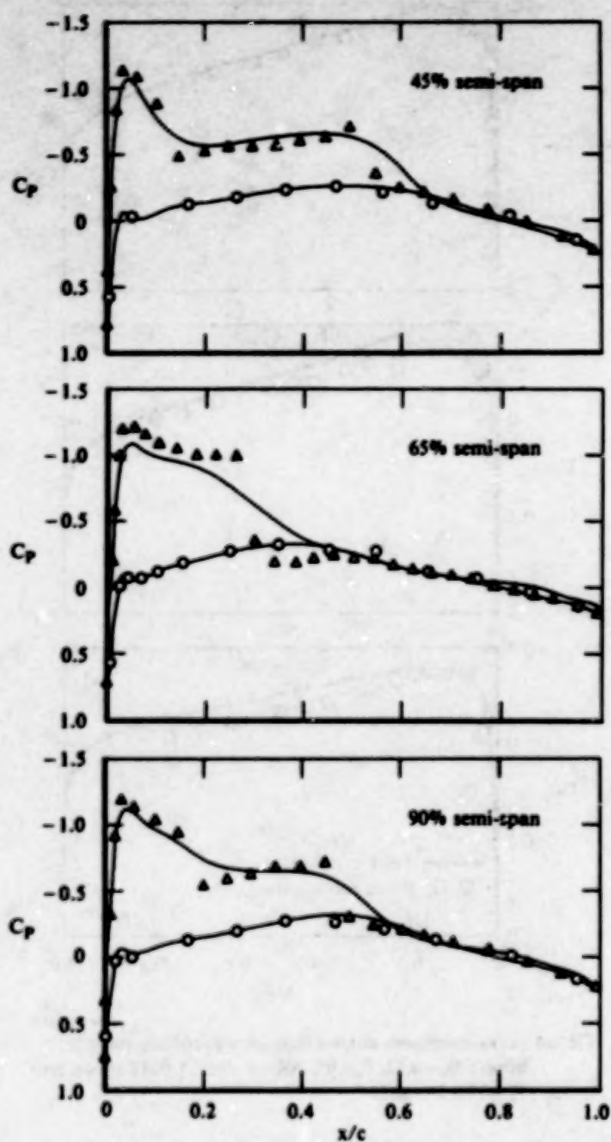
Fig. 27 Transonic viscous wing calculations on CRAY X-MP/48 for the ONERA-M6 wing; $M_\infty = 0.84$, $\alpha = 3.06°$, $Re_c = 11.72 \times 10^6$, and $140 \times 48 \times 32$ mesh.

Fig. 28 Grid lines on the surface of a transport wing-body configuration.
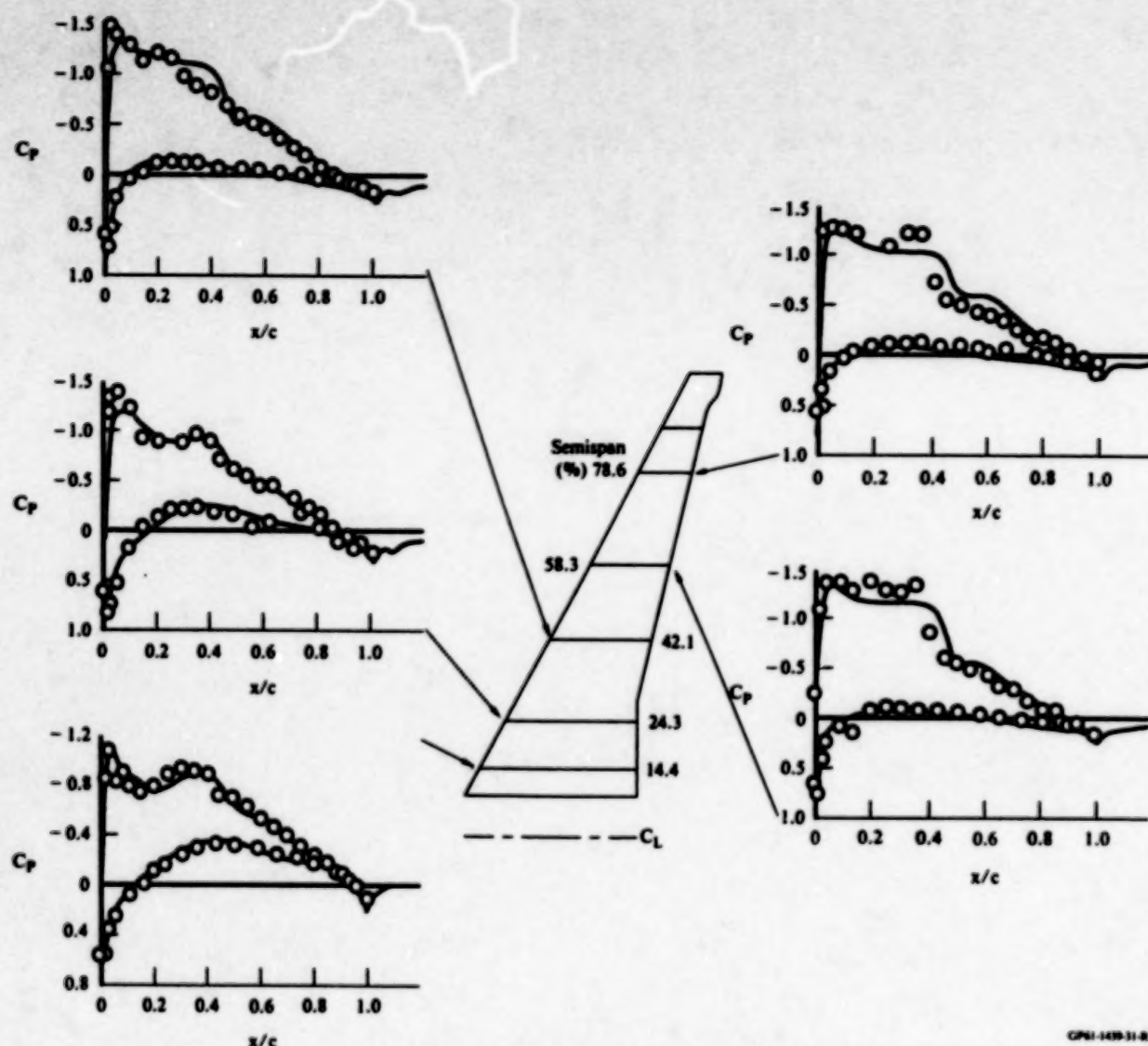
Fig. 29 Navier-Stokes solutions for flow past a transport-
type wing-body; $M_\infty = 0.76$, $Re = 6.39$ million,
$\alpha = 2°$.

REFERENCES:

Agarwal, R. K.; and Deese, J. E.: Computation of
Viscous Airfoil, Inlet, and Wing Flowfield. AIAA
84-1551, 1984.

Agarwal, R. K.; and Deese, J. E.: Euler Calcula-
tions for Flowfield of a Helicopter Rotor in
Hover. AIAA 86-1782CP, 1986.

Agarwal, R. K.; Deese, J. E.; and Underwood, R. R.:
Computation of Transonic Viscous Wing-Body Flow-
fields Using Unsteady Parabolized Navier-Stokes
Equations. AIAA 85-1595, 1985.

Booth, M.; and Misegades, K.: Microtasking: A New
Way to Harness Multiprocessors. Cray Channels,
Vol. 8, No. 2, Summer 1986, pp. 24-27.

Cebeci, T.; Clark, R. W.; Chang, K. C.; Halsey, N.
D.; and Lee, K.: Airfoils with Separation and
the Resulting Wakes. J. of Fluid Mechanics, Vol.
163, 1986, pp. 323-347.

Chen, L. T.; Li, S.; and Chen, H.: Calculation of
Transonic Airfoil Flows by Interaction of Euler
and Boundary-Layer Equations. AIAA 87-521, 1987.

Chen, L. T.; Vassberg, J. C.; and Peavey, C. C.: A
Transonic Wing/Body Flowfield Calculation with
Improved Grid Topology. AIAA J., Vol. 23, Dec.
1985, p. 1877-1884.

Cosner, R. R.: Relaxation Solution for Viscous
Transonic Flow about Fighter-Type Forebodies and
Afterbodies. AIAA 82-0252, 1982.

Cosner, R. R.: Integrated Flowfield Analysis Meth-
odology for Fighter Inlets. AIAA 86-1463, 1986.

Gregg, R. D.; and Misegades, K.: Transonic Wing
Optimization Using Evolution Theory. AIAA 87-
0520, 1987.

Verhoff, A.; and O'Neil, P. J.: A Natural Formula-
tion for Numerical Solution of the Euler Equa-
tions. AIAA 84-0163, 1984.

Dr. Robert E. Melnik
Grumman Aerospace Corp.

Title not available

Paper not available

PRECEDING PAGE BLANK NOT FILMED

APPLICATION OF COMPUTATIONAL PHYSICS WITHIN NORTHROP

M. W. George, R. T. Ling, J. F. Mangus
Northrop Corporation, Aircraft Division
Hawthorne, California

W. T. Thompkins
Northrop Research and Technology Center
Palos Verdes, California

An overview of Northrop programs in computational physics is presented. These programs depend on access to today's super-computers, such as the Numerical Aerodynamic Simulator (NAS), and future growth will depend on the continuing evolution of computational engines. Descriptions here are concentrated on the following areas: 1) computational fluid dynamics (CFD), 2) computational electromagnetics (CEM), 3) computer architectures, and 4) expert systems. Current efforts and future directions in these areas are presented. The impact of advances in the CFD area is described, and parallels are drawn to analagous developments in CEM. The relationship between further advances in these areas and the development of advanced (parallel) architectures and expert systems is also presented.

BACKGROUND

The design of modern fighter aircraft requires the analysis of many factors. Some of these, including complex flow phenomena and electromagnetic characteristics, pose serious problems for the designer. The analysis of these conditions is complicated by the fact that it is extremely expensive and time consuming to reproduce them in an experimental test environment. Fortunately, computational methods have advanced sufficiently to allow mathematical simulation of these phenomena, supplementing physical testing during the design process.

The trend towards integrating computational methods into the design process has been driven by the rapid advances made in computer hardware over the last decade. This trend has resulted in the development and application of methods capable of analyzing complete aircraft configurations.

Over the past ten years at Northrop, computational physics had its largest impact in the area of computational fluid dynamics. This began with a requirement to analyze transonic flow phenomena for fighter aircraft. In 1975 Northrop applied the 3-D Bailey-Ballhaus transonic small disturbance code developed at NASA Ames (Ballhaus, Bailey, and Frick [1976]) to the solution of this problem. This was followed by the application of the full potential codes, leading to our present use of Euler and Navier-Stokes codes. Throughout this period of development, Northrop efforts were enhanced by cooperative programs with NASA. These programs gave Northrop access to state-of-the-art computer facilities that allowed for the advanced development of methodology and application techniques that would be assimilated into Northrop's evolving project areas.

Our initial runs with the transonic small disturbance codes were done on an IBM 360 series computer. These facilities could barely handle a wing-alone configuration. On today's computers, those early codes can be run numerous times a day. Today, the Euler and Navier-Stokes codes are straining the capabilities of our equipment, which is limiting the degree to which these methods can be beneficially applied. As in the past, Northrop is working with NASA through cooperative programs to develop applications of these methods on leading-edge computing facilities.

Throughout the last decade several factors have stimulated Northrop's development and application of computational methods. These have included:

- The insight into the physics of the flow that was obtainable from computational methods

    Prior to extensive use of computational methods, the design of aircraft was based primarily on experimental testing, in particular, wind tunnel testing. Wind tunnel testing typically generates global values (lift, drag, moments) with limited surface pressure measurements, flow visualization and flowfield measurements. It is very expensive in both time and money to acquire more extensive flowfield information, such as off-body information, through experimental testing. Computational methods provided a way to see the whole picture, yielding an excellent complement to experimental testing. With this ability to see the flow phenomena in total came a better understanding of the physics of problems, providing a more complete and valuable understanding to the design process.

- The emerging emphasis on low observables

    The shifting emphasis to low observable characteristics forced new aircraft configurations towards shapes and concepts outside of the established data base. To do a parametric study on the new families of geometries, using the traditional approach of experimental testing, was prohibitive in both time and money. Computational fluid dynamics filled this void in the aerodynamic analysis of new radar cross section (RCS) driven configurations. As a result, they earned acceptance in the design process.

- Testing limitations

    Wind tunnel testing cannot accurately simulate flight conditions, especially in the transonic flow regime, where wall effects, mount effects, and scaling have a significant impact on flow characteris-

125

tics. The ability of the codes to model both free-flight conditions and test conditions results in a powerful tool for better understanding test results, and for extrapolating results to free-flight conditions.

In brief, Northrop's acceptance of these codes was the result of their ability to: 1) increase our understanding of flow phenomena associated with conceptual designs, 2) expand the number of design parameters while controlling costs and 3) improve the effectiveness of test programs.

Northrop Applications

The emphasis within Northrop, in the area of computational fluid dynamics, has shifted almost entirely to the application of the Euler and Navier-Stokes equations. The flight environment of fighter aircraft, which is dominated by a multi-sonic vortex/viscous environment, requires a level of physical detail that can only be supplied by the Euler and Navier-Stokes methods.

As a result of the advances made in the area of computational fluid dynamics in the last decade, an emerging area for the application of computational physics at Northrop has been in the solution of the Maxwell/Helmholtz equations. The similarity of the Maxwell equations to the Navier-Stokes equations allows the advances made in computational fluid dynamics to be applied to the solution of electromagnetics problems. Advances in algorithms, grid generation techniques, and specialized computer architectures, developed for computational fluid dynamics, are all readily applicable to the solution of the Maxwell equations.

Future Directions

The application of both computational Navier-Stokes and Maxwell methods to full configurations in the actual design environment is now a realistic goal. Achieving that goal will require, in addition to further algorithm development: (1) the further development of computer hardware and architectures, and (2) the development and application of expert systems to make productive and efficient use of this potential.

Useful solutions of the Reynolds-averaged Navier-Stokes equations for flow about a realistic aircraft configuration would require hours of run time on one of the current generation of supercomputers. Because the aircraft designer must study a large number of configurations, even an hour's wait for a solution is unacceptable. In addition, the high cost of such computers prohibits running them in this manner. As a possible solution to this resource problem, Northrop is studying the application of parallel architectures. By solving a large, computationally-intensive problem on a system with multiple processors working concurrently, the solution time can be reduced by a factor approaching the number of processors. In addition, parallel processing provides an advantage of flexibility in the allocation of computer resources. As small projects develop, computational resources can be increased by adding dedicated processors. While parallel processing architecture promises a viable approach to the computer resource problem, it requires a rethinking of solution algorithms.

The potential value of current and evolving computational physics codes, coupled with the development of new computers, is immense. The resulting systems will be able to analyze multiple families of parameters, exploring new and innovative concepts in relatively short time periods. The data generated in this process will be overwhelming. In order to effectively utilize these systems,

the integration of expert systems will be required. Northrop is currently addressing the need for expert design systems as part of its program in computational physics.

While Northrop is developing and applying computational physics methods to other areas (e.g. structures, avionics, controls, simulation, etc.), fluid dynamics and electromagnetics place the largest demands on computational resources. This paper will therefore address Northrop's current programs in these two areas, along with corresponding efforts in the area of computer architectures, and expert systems.

COMPUTATIONAL FLUID DYNAMICS (CFD)

Over the past decade, the aerodynamic and propulsion design processes have undergone a significant change. Where the process was once dominated by the use of wind tunnel facilities as analysis and design tools, the trend today is to rely more on CFD methods as the principal design tools. There are several reasons for this change. Wind tunnel testing has always been expensive, in terms of manpower, time, and facilities. Over the last ten years these costs have increased. At the same time, the development of sophisticated CFD methods and computing engines have made these methods more efficient and effective. In comparing the results gained by the two approaches, computational techniques are also gaining an advantage. The inherent limitations of wind tunnel testing, including the restrictions imposed by modelling, wall effects, etc., do not constrain today's CFD methods. Instead their application has been limited by the available computer hardware. With advances in "supercomputers", those limitations are rapidly being overcome.

Northrop's experience with CFD methods has been strongly influenced by the specific complexities of fighter aircraft design. Fighter aircraft incorporate geometrical features such as closely-coupled lifting surfaces, sharp or small leading edge radius, and vortex generating devices as part of a multi-point, multi-sonic design emphasizing high angle-of-attack maneuverability. These features generate a flow environment strongly dominated by viscous and vortex phenomena. Also, the strongly coupled flow environment limits the utility of the application of CFD methods to individual components. In this environment, earlier methods such as transonic small disturbance and full potential could be applied to fighter design primarily in regimes where the flow "behaved nicely", such as under cruise conditions. Application of computational methods to full fighter configurations over the complete design envelope required both more sophisticated methods, and more capable computing resources.

As a result of Northrop's emphasis on fighter design, CFD efforts have been directed towards Euler and Navier-Stokes methodology. Today, computational Euler methods are utilised on a daily basis in design projects for application to configurations as well as to isolated components. The computer resources within Northrop which provide the capability to run the Euler methods are two FPS-164 (Floating Point Systems) computers. These machines have in-core memory of four and seven million 64-bit words, which allows for the modeling of meaningful configurations. These machines have enabled the development of Euler methods at Northrop and their integration into the design environment. They have also allowed for initial exploration of Navier-Stokes methods.

The current capabilities and limitations of Euler methods are illustrated in figures 1 to 7. As stated previously, the primary

reason for the selection of Euler methodology is its ability to model the vortex-dominated environment associated with fighter aircraft, as indicated in figures 1 to 4. The Euler methods that generated the following results are based on the finite volume formulation developed by Jameson, et al (1981).

Figure 1 illustrates configuration and flow capabilities provided by current Euler methodology. The configuration in Figure 1a was generated by combining a chined forebody (Erickson and Brandon [1985]) together with the wing from the AFVFM (Air Force Vortex Flap Model, Erickson [1985]) and a tail representative of the F-18. A configuration similar to this will be tested in 1987 as part of a cooperative program between Northrop and NASA Ames. Figures 1b and 1c show the complexity of flow associated with this type of configuration, specifically the vortex-dominated environment, composed of interacting vortices generated by the chine, wing and tail. The total pressure contours in Figures 1b and 1c show the vortex structure at a wing-body fuselage station and tail-body fuselage station, respectively.

Figures 2 and 4 show the capabilities of the Euler methods to calculate total forces on fighter-type configurations. Lift versus angle-of-attack results for both Euler and experiment are compared in figure 2 for the AFVFM shown in figure 3. The agreement in both value and location of C_{LMAX} is quite good. As is typical of this type of fighter configuration, the stall characteristics are due to the burst point of the vortex generated by the wing leading edge moving forward over the wing. The nonlinear lift effects which are also associated with the wing leading edge vortex passing over the wing, and which contribute to the increasing lift curve slope prior to stall, are also modeled by the Euler code. The experimental results showed wing tip separation occuring near 15 degress angle-of-attack, which accounts for the early decrease in lift curve slope as compared to the Euler results.

Figure 4 shows comparison of experimental and Euler drag polars for the F-20 Tigershark at a Mach number of 0.80. As seen in figure 4, the comparison between experiment and computation is quite good over the entire range. Figure 4 was taken from the paper by Bush, Jager, and Bergman (1986), which gives more comprehensive coverage of Euler code application within Northrop.

Another area in which Euler codes are used extensively is in the design and analysis of inlets. The ability of the Euler methods to correctly model shock structure and corresponding total pressure losses makes them applicable to the transonic and supersonic inlet problems. Figure 5 shows the results of an Euler method applied to a 3-D supersonic compression-ramp inlet. The ability of the Euler method to model the shock structure is shown in this figure. The pressure contours show the shock emanating from the ramp combining with the standoff shock from the inlet cowl.

While the current capability of the Euler codes is proving to be extremely useful in the design environment, their limitations due to lack of viscous modeling and computer resources is placing an increased demand on the development/acquisition of larger computing engines and on the development/application of Navier-Stokes methods. While the creation of the vortex structure and its resultant gross effects on the aerodynamic characteristics are not that sensitive to mesh size, the local effects (shock-vortex interaction, surface pressures, vortex empennage interactions, etc.) are not accurately modeled in the Euler methods without adequate grid definition. The addition of viscous terms is needed to improve the calculation of drag, total pressure losses (inlets), entrainment (nozzles), and separation phenomena. Figures 6 and 7 show some of the deficiencies due to current computer resources and lack of viscous modeling.

Figure 6 shows the comparison of experimental and Euler pressure results at a forebody station of the chined forebody configuration in figure 1a. As seen in this figure the Euler results do not resolve the peak pressure due to the vortex (formed from the chine) which sits over the body. The discrepency is due to the lack of grid resolution in defining the vortex, as shown by Rizzi (1985).

The comparison of experimentally obtained pressures and pressures calculated by the Euler code are shown in figure 7 for a spanwise cut on the AFVFM, with the leading edge flap deflected 30 degrees. Experimental results are shown for both 0.4 and 0.7 Mach numbers. The primary vortex generated by the wing leading edge and the secondary vortex structure generated at the flap hinge line are not modeled well by the Euler code due to a lack of grid resolution and lack of viscous modeling.

Northrop's current computer resources do not yet allow the application of Euler and Navier-Stokes codes to complete fighter aircraft configurations. Another limitation is the current inability to grid the complete configurations. The capability of Euler and Navier-Stokes methods to adequately model a full configuration depends on a grid scheme that provides an arrangement of points to discretize the equations and model the physics. For simple configurations this process is easily accomplished, but for problems such as complete fighter configurations this becomes the most difficult part of the solution procedure. The AFVFM (figure 3) and the chined wing-body configuration (figure 1) were gridded as illustrated in figure 8. The grid is generated by defining a series of "C" type surface grids which extends forward and rearward of the wing. The portions of the surface grid forward and rearward of the wing can accomodate chines, leading edge extensions (LEXs), tails and flow-through conditions. The boundary grids and internal grids are generated by a combination of 2-D and 3-D Poisson and transfinite interpolation solvers. This grid approach, due to its contiguous nature, is limited in its applications. The current trend is to develop grid generation techniques which utilize a block structure and grid lines that are not necessarily continuous within or across blocks.

Northrop's current and future activities in the area of Navier-Stokes and Euler development involve cooperative efforts with NASA. As stated in the introduction, these cooperative programs allow access to the evolving "supercomputers" along with access to NASA personnel and methods. A current NAS program being done in conjunction with the Ames Research Center involves the application of the TNS code (Kaynak, Holst, and Cantwell [1986]) to the AFVFM. The AFVFM provides a good test basis for determining the applicability of Navier-Stokes and Euler methods to fighter configurations. The AFVFM (figure 3) provides a simple, easily gridded geometry which generates some of the primary vortex flow phenomena associated with fighter configurations. The AFVFM incorporates a swept wing with a series of leading edge vortex flaps (including sharp and round leading edges) and conventional trailing edge flaps. In addition to this NAS program, cooperative efforts exist in the areas of the development/application of Navier-Stokes methods to nozzles and the application of Euler methods to chined forebody configurations.

The growing importance of and demand for CFD in the design and project areas within Northrop is placing more emphasis on the development of Euler and Navier-Stokes methods and acquisition of more capable computing systems, along with the development of pre- and post-processing techniques. We expect that, with the current growth in computer technology and the evolving methodology, Navier-Stokes methods (Reynolds averaged) and the systems to utilize them will be commonplace within Northrop in the next five years.

COMPUTATIONAL ELECTROMAGNETICS (CEM)

Requirements for aerodynamic performance and electromagnetic characteristics, such as radar cross section (RCS), have become critical drivers in the design of modern military aircraft. Northrop has been actively involved in RCS analysis for more than twenty years. It has been a pioneer in the development of Physical Theory of Diffraction (PTD), and integral equation methods. The MISCAT/GENSCAT codes, developed by Northrop under a series of contracts to government agencies, have found widespread usage by many aircraft and missile manufacturers. These codes, like the panel method codes in CFD, are forerunners of the emerging field of computational electromagnetics (CEM). The latter is as important in the design process as computational fluid dynamics (CFD), figure 9. Just as CFD codes can be considered as numerical wind tunnels, CEM codes can be considered as numerical radar ranges and anechoic chambers. As CFD plays an increasingly important role in supplementing costly wind tunnel testing in the design process, so CEM is expected to supplement expensive testing in radar ranges and anechoic chambers.

Actually, the similarity between CFD and CEM runs much deeper than this. Since both the aerodynamic performance and the electromagnetic characteristics are configuration dependent, a unified approach can be devised for both aerodynamics and electromagnetics problems, figure 10. Starting with the same aircraft configuration, common geometry definition and grid generation procedures can be used in preparation for the solution of respective governing equations to obtain the aerodynamic and RCS characteristics. The most interesting and important aspect of the unified aero/RCS approach lies in the mathematical similarity between aerodynamics and electromagnetics problems, figure 11.

The scattering of electromagnetic waves by an aircraft can be formulated as a boundary value problem analogous to the fluid dynamic problem of flow past the aircraft. The governing Maxwell/Helmholtz equations can be solved numerically in a manner similar to the solution of governing fluid flow equations such as the Navier-Stokes/Euler equations. The far field radiation condition and media interface boundary condition can also be enforced in a manner similar to the enforcement of the freestream condition and flow tangency condition. Various numerical methods in CFD can be carried over for the computation of electromagnetic characteristics.

For the electromagnetics problem, the Maxwell/Helmholtz equations can be solved by differential equation and integral equation methods. One type of differential equation method (King, et al [1959] and Bowman, et al [1969]) involves separation of variables in specific coordinate systems. In the past few years, there have been attempts (Bayliss, et al [1982], [1982] and [1983]) to directly solve the Helmholtz equation for scalar scattering problems by finite difference methods. Besides these finite-difference, frequency-domain (FD-FD) methods, a finite-difference, time-domain (FD-TD) method has also been proposed (Umashankar, et al [1982]).

In the integral equation approach to scattering problems, an equivalent integral equation such as the Chu-Stratton equation containing Green's function can be derived for either the magnetic field or electric field and can be formulated either in the time domain or frequency domain (Mittra [1974]). Many techniques are available for reducing the integral equation to a matrix equation for numerical solution. Some of these are grouped under the title of "moment method" (Harrington [1968]). Moment method codes in general are not numerically efficient. At Northrop, they are mainly used to validate results obtained from new methods under development, for obstacles of simple geometry.

Numerical techniques developed for CFD have various degrees of applicability to nearly every CEM method mentioned above. However, the CEM method that is most closely related to common CFD methods – and therefore best suited for exploiting the advances made in CFD – is the finite difference, frequency domain (FD-FD) method based on the concept of generalized scattering amplitude (Ling [1986] and [1987]). In this CFD approach to solving electromagnetics problems, the original Helmholtz equations in terms of electric and magnetic field vectors are transformed into scalar equations in terms of generalized scattering amplitudes or related Debye amplitude functions.

The current CEM research at Northrop consists of development of methods in both the integral equation and differential equation approaches. In the former, efforts are focused on the k-space method (Bojarski [1971]). The aim here is to find efficient iterative procedures to make it practical in the design process. A CFD approach developed at Northrop has recently been applied to simple obstacle shapes including the circular cylinder and sphere (Ling [1986] and [1987]), figures 12 and 13. Numerical results agree with the exact eigenfunction expansion solutions (King [1959] and Bowman, et al [1969]).

To apply CFD methods to practical RCS problems involving complex aircraft geometry and incidence of high frequency electromagnetic waves, fast processing capability and large memory storage of a supercomputer such as the NAS are required. This is due to the large number of grid points necessary for resolution of the scattering characteristics generated by complex geometry aircraft. Though the introduction of the radially non-oscillatory generalized scattering amplitude has largely eliminated the need to resolve the field quantity oscillations along the radial distance to infinity, one still has to contend with the generalized scattering amplitude variation inside the finite volume of the aircraft. To achieve sufficiently accurate resolution of field quantities and generalized scattering amplitudes, the grid spacing should be one-tenth of a wavelength or less. Representative RCS problems encountered in the design process may involve obstacles with dimensions on the order of one hundred wavelengths or more in each of the three directions. This would require dealing with millions of grid points. Solution of matrix equations for such a large system certainly requires a supercomputer.

The CFD approach to electromagnetic wave scattering shows promise for accurate, systematic, and efficient calculations for obstacles of arbitrary material properties, size and shape. The power and capability of a supercomputer can transform CFD methods into practical tools for solving the RCS problems encountered in the military aircraft design process.

COMPUTER ARCHITECTURES

Northrop's activity in the area of computer architectures is focused on the hardware used in parallel processing. Parallel computing uses multiple processors to simultaneously execute individual parts of a larger overall task. Although this adds to the complexity of the application program, it can greatly decrease its execution time. Within the scope of Northrop's program, parallel processing is viewed as a possible alternative to supercomputers for the small project environment, and also as a concept applicable to supercomputing and other emerging computer technology.

One reason for investigating parallel architectures stems from the unique computing requirements of the Northrop engineering environment. The majority of Northrop's projects operate their own isolated computing facilities. Individual projects cannot provide the computer resources for running codes that require the power of a supercomputer. Purchase of individual supercomputers for many such projects is clearly not cost effective, and security requirements prevent the use of supercomputing resources available at NASA and other government research centers. In this environment, parallel computers offering significant power at reduced cost will enable projects with limited resources to utilize advanced computational methods.

A second reason for exploring concurrent architectures is the machine speedup they offer. As explained by Denning (1985), the maximum speed of a single processor is limited to approximately 1 GFLOPS by the speed of light. Running complex computational physics applications quickly enough to be useful in the design process will require computational speeds in excess of this figure. The only way to attain such speeds will be through the use of some form of parallelism. This trend is already apparent in supercomputers such as the CRAY-2 which uses 4 processors, and is expected to grow in the future. As concurrent processing becomes more prevalent, the knowledge now being developed in this area should enable Northrop to continue making effective use of evolving computer technology.

The Northrop effort examines parallel processing architectures with the ultimate goal of implementing computational physics codes on such machines. Our objectives in this area are as follows: 1) learn how best to parallelize computational physics algorithms, determine those algorithms most suited to concurrent execution, and examine how parallelization affects algorithm behavior; 2) examine what special demands are placed on pre- and post-processing facilities (e.g. grid generation and analysis of results) by parallelized codes; and 3) explore the effects of different computer architectures on the parallelism of specific algorithms and, conversely, what specific architectural details enable optimal performance of concurrent computational physics applications.

Of these goals, the last has proven to be the most complicated and extensive in scope. Architectural issues such as memory organization, interprocessor communication speed and configuration, and processor power will have a large impact on an algorithm's parallel execution. The most important architectural concern has been the degree of coupling between multiple processors and memories. At one end of the range of architectural options, a parallel computer can have a number of processors addressing a single global memory in a tightly coupled system. As the number of processors in the system increases however, the time overhead incurred by many processors accessing one memory over a limited bandwith data channel will degrade any potential parallel speedup. Consequently, existing shared memory machines seem to be limited to 2-8 processors.

Computers using more than this number of processors employ memories divided into small parts, each accessible by a single processor. This creates a loosely coupled system with limited memory access, and leads to a question of which processors should communicate with which others. The "crossbar" interconnect, in which each processor node communicates with every other processor in the system, becomes prohibitively complex and expensive as the number of nodes grows, eventually giving way to less extensive communication schemes. These range in complexity from simple nearest-neighbor schemes to the binary hypercube structure in which each of 2^n processors is connected to n other processors, forming one corner of an n-dimensional cube. The degree to which processors are coupled can be further decreased

until one reaches the other extreme of an uncoupled system in which individual nodes no longer communicate. These simplified interconnection schemes make loosely coupled architectures more desirable for massively parallel systems incorporating hundreds and possibly thousands of processors.

The choice of an efficient interconnection scheme depends largely on the desired application. For example, it is questionable whether a fully implicit finite difference algorithm which parallelizes efficiently on a shared memory machine will do so on loosely coupled architectures. In addition, the resolution of other architectural issues such as the bandwidth of the interconnecting communications channels, the power of individual nodes and the size of individual processor memory is also highly application dependent. In essence, one would like to balance all of these factors to create an optimal configuration for the efficient execution of a given algorithm. Ideally, a variety of applications might then be found to share some roughly similar optimal architecture which would then define our needs for a parallel processor. Whether this is a realistic goal remains to be seen.

The investigation of these issues has proceeded along two avenues, the first being the implementation of a target code on several commercially available parallel computers. This effort was undertaken to gain experience in working with a variety of parallel architectures, with emphasis on examining the relationship between architecture and parallel implementation as well as relative advantages and disadvantages between alternative architectures. It was also deemed useful to gain experience with the different ways of coding parallelism while also measuring the performance improvements gained by these various methods.

To accomplish this, two- or three-dimensional versions of an explicit Euler code which uses the finite volume algorithm due to Jameson, et al (1981) have been ported onto several parallel machines. This code is a particularly good test case because, while primarily explicit in nature, it also incorporates an implicit residual smoothing scheme, enabling us to also examine the parallelism constraints associated with implicitness.

The code was first implemented on the CRAY X-MP/48 supercomputer which uses the shared-memory, tightly coupled architecture described previously (the CRAY architecture is discussed in more detail by Hwang [1985]). This activity was part of an ongoing cooperative program in computational methods between Northrop and Cray Research, Incorporated. The code was converted for parallel execution with minimal modifications using the Microtasking facility available on Cray FORTRAN. After modification, the code executed with a speedup approaching the maximum predicted by Amdahl's law. This demonstrated that fluid dynamics algorithms of this kind may be efficiently implemented on global memory, tightly coupled machines with relative ease. In addition, running on the CRAY machine afforded an opportunity to perform CFD calculations involving very large numbers of grid points, which in turn pointed out some of the specialized post-processing capabilities needed to cope with the resulting large volume of flowfield data. It was found that high resolution color graphics such as the example reproduced (in black and white) as figure 14 (generated with the assistance of personnel from the Applications Department of Cray Research Incorporated) were most valuable in interpreting the resultant data. The variations in shading in this figure (different colors in the original) correspond to the magnitude of the crossflow velocity component near the wing-body-chine model's surface and clearly show wing and chine vortex formation. Advanced graphics capabilities of this kind are a requirement for efficient use of the sorts of computational devices under discussion here.

Additional efforts at code implementation are currently being directed toward two parallel devices, the Butterfly machine produced by Bolt, Beranek and Newman, and the T-20 computer built by Floating Point Systems. The Butterfly (described in detail by Schneck, et al [1985]) is a 16 processor, local memory machine which represents something of a hybrid architecture by virtue of its unique interconnect scheme. Because each processor is connected to a butterfly switching network (shown in figure 15) which enables it to communicate with any one other processor at a time, any processor has potential access to any other local memory, thus making the memory appear global. A 2-dimensional Euler algorithm has been implemented on this machine and has shown a speedup in execution which scales linearly with the number of processors used. In addition, the 3-dimensional version of the algorithm is being implemented and will be used to investigate optimal coding and memory allocation strategies for this architecture. The T-20 computer (detailed by Frenkel [1986]) consists of 16 processors linked in a hypercube structure as shown in figure 16. One of the unique aspects of this machine is its use of the OCCAM programming language, which is specialized for parallel processing. Current work concentrates on implementing the 2-dimensional Euler algorithm on this machine in OCCAM, and has validated the loosely coupled hypercube architecture as appropriate for this type of application.

The second approach to the architecture study has been through participation in the design of a parallel processor system. Under a contract with DARPA, Northrop is working with Paragon Pacific, Incorporated to build a parallel computer specialized for the solution of computational physics problems. Called the Custom Architectured Parallel Processing System (CAPPS), the machine will incorporate several innovative features, the most important of which is a user-configurable interconnect structure. This flexibility will increase the utility of this machine for solution of a variety of problems in computational physics.

To aid in the design of this device, the 3-dimensional Euler code described previously has been partitioned to execute in a concurrent blocked-grid mode and is being used to define interprocessor data transfer requirements. Since the algorithm operates in parallel on several subdomains of the main grid, data must be transferred at the subgrid interfaces at selected times. To reduce the time penalty associated with this communication, the frequency with which this transfer takes place has been progressively reduced, and the results on convergence rate observed. As shown in figure 17, overall convergence remains largely unaffected even when communications are reduced by a factor of 10 over the sequential case. This information can now be used to help formulate the requirements for interconnect bandwidths and individual processor speed for the CAPPS and the optimal level of parallelism to incorporate in this algorithm.

In summary, the Northrop program in parallel architectures has had the overall effect of increasing our understanding of the hardware of parallel processing as well as the basic method for introducing concurrency into computational physics algorithms. Specifically, the results show that a loosely coupled architecture such as the hypercube is an acceptable choice for explicit fluid dynamics algorithms. In the future, as additional parallel machines are examined and new parallel algorithms are implemented, the conclusions drawn should provide an accurate picture of how best to incorporate parallel processing into the aircraft design environment.

EXPERT SYSTEMS FOR DESIGN APPLICATIONS

In the past, aircraft design has generally suffered from a lack of analytical or computational predicative capability. That is to say our capacity to conceptually design aircraft has exceeded our capacity to predict performance without extensive wind tunnel testing or full-scale prototypes. Modern computational methods, when coupled with continued advances in computer power, have the potential to rectify this situation. That is to say our capacity to compute performance and perform mission simulation may exceed our intuitive design ability.

While this viewpoint may strike some as optimistic, it is already true in some important areas.

- fluid dynamics

    intuitive understanding of vortex augmented lift vs. detailed description of wing pressure distribution

- structural analysis

    intuitive understanding of the structural response of uniform, metallic parts vs. detailed description of stress levels in complex three dimensional shapes

- low observable vehicles

    intuitive understanding of low observable trade-offs vs. integration of aerodynamic, electromagnetic, structural, and materials design techniques

- mission analysis

    intuitive understanding of factors affecting fighter maneuverability vs. integration of aerodynamic performance, observable, avionics, cost, and maintainability into mission effective vehicles

Since the required performance of future vehicles demands that the benefits identified by increased computational capabilities actually be achieved, we are moving rapidly into system complexity which can only be achieved through close interaction of design engineers with extensive computational facilities.

While our capability to numerically analyse complex or innovative configurations has grown rapidly, a commensurate increase in our capability to integrate this in the design process has not occurred. Increases in aircraft performance have simply not kept up with increases in available computer power.

The difficulty is not a lack of knowledge in the disciplines but rather a lack of capability to encapsulate knowledge and share it among personnel with diverse backgrounds. While the techniques of expert systems and their promise has received far more attention than their current merit would justify, accomplishing effective knowledge sharing, to which the best of these systems are directed, is exactly the task which must be accomplished in order to efficiently cope with the diverse requirements of modern aircraft design.

Thus, the challenge is to develop software systems or environments which can aid designers in their complex technology integration and design tasks.

Design Process Review

A simplistic view of a top-down aircraft design cycle takes the following form: The process begins with system specifications, and first derives: 1) a functional decomposition among subsystems, 2) subsystem performance goals, and 3) a preliminary system design. Next, a sequence of increasingly detailed iterations between aerodynamic, observables, and structural requirements is conducted to define a detailed geometric shape. Iteration between performance goals and detailed design analysis may also occur. Once a detailed vehicle design is complete, integration of subsystems with the vehicle is performed and system performance simulated. If the system performance meets specified performance levels, the design is accepted. If not, revisions throughout the design cycle may be introduced to develop a design which meets the required system performance.

This structure has a number of important strengths since it:

1. Provides a clear logical structure for the design and development process that moves from the abstract to the concrete;

2. Allows technical details to be added a level at a time in such a fashion that provides the encapsulation of detail needed to deal with complex systems;

3. Is a pipeline like process in which many different groups are productively active.

The difficulties of incorporating rapidly evolving computational approaches into this cycle are immediately apparent when one considers that:

1. The preliminary design process for an aircraft extends over 1 to 2 years;

2. Computational algorithms are usually developed for particular analysis problems not for integration into a multidisciplinary design process;

3. Design engineers are, properly, not specialists in numerical analysis or computer systems.

Under these conditions, design engineers are unable to effectively utilise the latest analysis techniques known to be effective in the research community. Therefore, the challenge is to create environments which facilitate knowledge transfer and provide a framework for creating and testing designs.

Design Assistant Shell

In order to address this situation, a number of Knowledge Based System (KBS) shell implementations to aid design engineers are being considered. A KBS shell is a computing environment designed around similar applications and is a compromise between specific applications and general knowledge engineering tools.

One Design Assistant Shell architecture is illustrated in Figure 18. This architecture is a layered implementation which provides multiple user interfaces which serve the requirements of several different design team members. Figure 18 illustrates interfaces to: 1) CAD/CAM processors and their associated databases and specialised equipment, 2) network connections to local or remote computing resources such as CRAY class supercomputers or special purpose processors, 3) algorithm developers and their special knowledge, and 4) interactive control of design processing through the specification of design plans and stored procedural knowledge. The KBS shell provides assistance in generating and

controlling execution of the design plans, a common framework for expressing expert knowledge, automated execution of remote computational processing and display of computed results. The variety of user interfaces allows design team members with diverse backgrounds to communicate freely and isolates them from the complete design process complexity so that each may perform their tasks efficiently.

Information or knowledge about the design process is often procedural in nature and this fact is reflected in the choice of a design plan as a primary technique for knowledge representation and user interaction. A design plan is composed of:

* Objectives - what is to be achieved

* Constraints - checks and requirements to be satisfied

* Procedures - process to achieve objectives

Figure 19 illustrates a plan fragment that a design engineer might create to minimise wing drag. The most interesting section of this plan is the procedural knowledge expressed. This particular procedure creates an initial wing geometry through use of a library of known "good" pressure distributions and then passes control to a numerical optimiser to achieve an improved geometric design.

It is expected that the design engineer will be able to interactively create the procedures, call up and/or modify old procedures, or have procedures suggested to him.

In reference to Figure 19, it seems likely that a design engineer would have expert knowledge about "good" pressure distributions, but is unlikely to have expert knowledge about the Navier-Stokes algorithms used to evaluate drag or the numerical optimisation procedure. In fact, the numerical optimisation procedure of Figure 19 expands into the plan fragment illustrated in Figure 20. This optimisation plan is a simple one based on linear combinations of approximating shape functions. A plan treatment of this type would be developed and maintained by algorithm specialists on the design team. Procedures in Figure 20 may also expand into plan fragments, but a successful plan expansion by the KBS plan generator will terminate in well-defined subproblems for which computational or analytical solutions exist. It may, of course, be impossible to successfully expand a design plan, or a procedure execution inside a plan may fail.

This section has reviewed techniques which can be used to simplify and manage the design process in a more efficient manner. These techniques provide a framework for creating and testing designs as well as mechanisms for the ultimate users to create and maintain their own knowledge bases. The multiple user interfaces mirror usual organizational structures but can relieve humans of tedious chores as they build and modify the knowledge base. In this way, knowledge transfer between design team members can be facilitated and more complete designs accomplished inside the available time and resources.

SUMMARY

Computational physics has grown in influence in aircraft design over the last decade. Initial growth in this area was in the development and application of computational fluid dynamics, and today CFD remains the leading area for development and growth in computational physics. At the same time, the success of CFD has led to applications in other areas. Specifically, the similarities between the governing equations in CFD and CEM, as well as the importance of emerging design problems involving low observables, has led to major development efforts in the CEM area.

The utility and growth of computational methods in the design process depend on access to computational facilities with sufficient size and speed. Access to today's supercomputers, such as NAS, is essential in the exploration and development of future computational methods. The use of the resulting methods in a project design environment, such as at Northrop, requires exploration of alternative architectures, including parallel processing.

Finally, the depth of analysis and the volumes of data that will become available through the combination of more sophisticated methods and supercomputers will place unrealistic demands on the designer. The effective use of computational physics will therefore require the integration of expert systems. As computational engines continue to evolve, the value of fully-developed computational methods in aircraft design will increase proportionately. Within the next decade, we expect, computational methods will become the primary tools of the design engineer.

REFERENCES

Ballhaus, W. F.; Bailey, F. R.; and Frick, J.: Improved Computational Treatment of Transonic Flow About Swept Wings, Advances in Engineering Sciences, NASA CP-2001,1976.

Bayliss, A.; Goldstein, C. E.; and Turkel, E.: An Iterative Method for the Helmholtz Equation, Journal of Computational Physics, vol. 49, 1983, pp. 443-457.

Bayliss, A.; Gunzburger, M.; and Turkel, E.: Boundary Conditions for the Numerical Solution of Elliptic Equations in Exterior Regions, SIAM J. Appl. Math., vol. 42, no. 2, 1982, pp. 430-451.

Bayliss, A.; and Turkel, E.: Far Field Boundary Conditions for Compressible Flows, Jounal of Computational Physics, vol. 48, 1982, pp. 182-199.

Bojarski, N. N.: K-Space Formulation of Electromagnetic Scattering Problem, Air Force Avionics Laboratory Technical Report AFAL-TR-71-75, March 1971.

Bowman, J. J.; Senior, T. B. A.; and Uslenghi, P. L. E.: Electromagnetic and Acoustic Scattering by Simple Shapes, North-Holland Publishing Co., Amsterdam, 1969.

Busch, Richard J.; Jager, Merle; and Bergman, Brad: The Application of Computational Fluid Dynamics to Aircraft Design, AIAA Paper 86-2651, October 1986.

Denning, Peter J.: The Science of Computing – 1985, Research Institute for Advanced Computer Science, RIACS TR 85.12, September 1985.

Erickson, G. E.: Vortex/Linear Lift Augmentation, AFWAL-TR- 85-3017, Volumes I-VI, June 1985.

Erickson, Gary E.; Brandon, Jay M.: Low-Speed Experimental Study of the Vortex Flow Effects of a Fighter Forebody Having Unconventional Cross-Section, AIAA Paper 85-1798-CP, August 1985.

Frenkel, Karen A.: Evaluating Two Massively Parallel Machines, Comm. ACM, vol. 29, no. 8, August 1986, pp. 752-758.

Harrington, R. F.: Field Computation by Moment Methods, MacMillan, New York, 1968.

Hwang, Kai: Multiprocessor Supercomputers for Scientific/Engineering Applications, IEEE Computer, vol. 18, no. 6, June 1985, pp. 57-73.

Jameson, A.; Schmidt, W.; and Turkel, E.: Numerical Solutions of the Euler Equations by Finite Volume Methods Using Runge-Kutta Time-Stepping Schemes, AIAA Paper 81-1259, June 1981.

Kaynak, Unver; Holst, Terry L.; Cantwell, Brian J.: Computation of Transonic Separated Wing Flows Using an Euler/Navier-Stokes Zonal Approach, NASA TM 88311, July 1986.

King, R. W. P.; and Wu, T. T.: The Scattering and Diffraction of Waves, Harvard University Press, 1959.

Ling, F. T.: Numerical Solution for the Scattering of Sound Waves by a Circular Cylinder, AIAA Paper 86-1880, July, 1986.

Ling, H. T.: Application of Computational Fluid Dynamics (CFD) Methods to Numerical Study of Electromagnetic Wave Scattering Phenomena, AIAA Paper 87-0487, January, 1987.

Mittra, R.: Computer Techniques for Electromagnetics, Pergamon Press, New York, 1974.

Pulliam, Thomas H.: Recent Improvements in Efficiency, Accuracy, and Convergence For Implicit Approximate Factorization Algorithms, AIAA Paper 85-0360, January 1985.

Rizzi, Arthur: Euler Solutions of Transonic Vortex Flows Around The Dillner Wing, Journal of Aircraft, vol. 22, no. 4, pp. 325-328, April 1985.

Schneck, Paul B.; Austin, Donald; Squires, Stephen L.; Lehmann, John; Mizell, David; and Wallgren, Kenneth: Parallel Processor Programs in the Federal Government, IEEE Computer, vol. 18, no. 6, June 1985, pp. 43-56.

Umashankar, K.; and Taflove, A.: A Novel Method to Analyze Electromagnetic Scattering of Complex Objects, IEEE Transactions on Electromagnetic Compatibility, EMC-24, 1982, pp. 397-405.
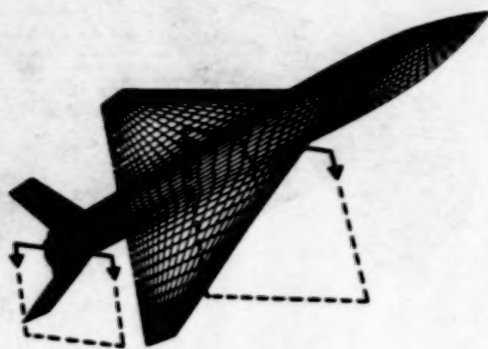
Figure 1a. Surface grid for wing-body-tail configuration
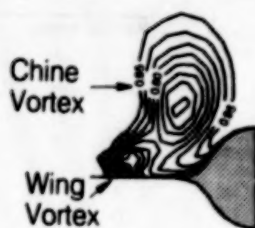
Figure 1b. Total pressure contours at wing-body station
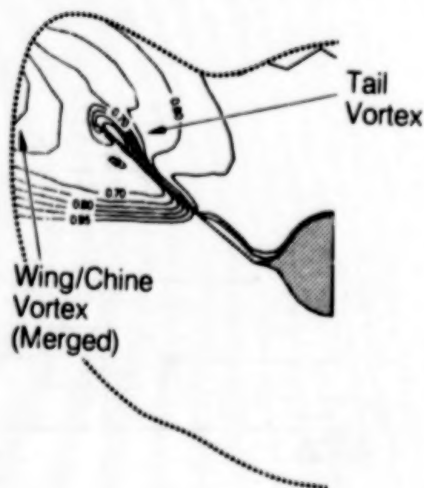
Figure 1c. Total pressure contours at tail-body station
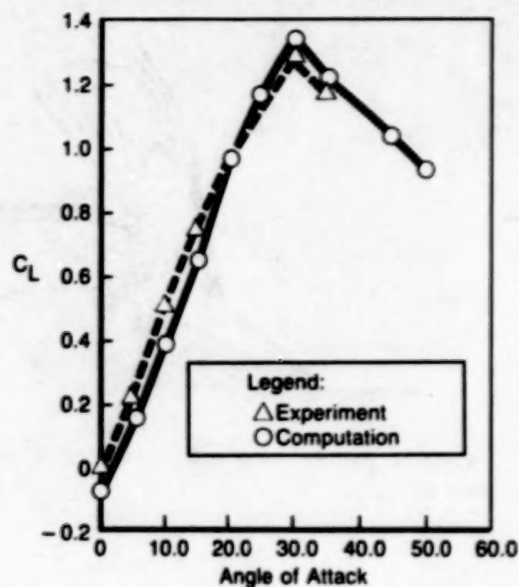
Figure 2. Comparison of test results and Euler calculations for the AFVFM
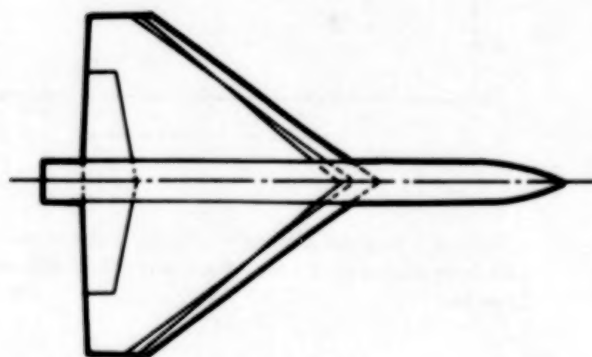
Figure 3. Planform view of AFVFM
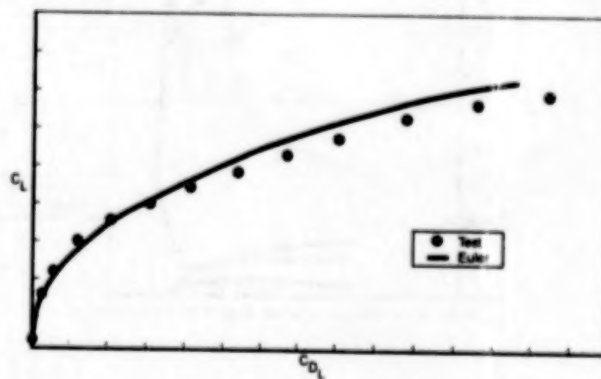
Figure 4. Comparison of F-20 Euler results with test force and moment data at Mach 0.80

133
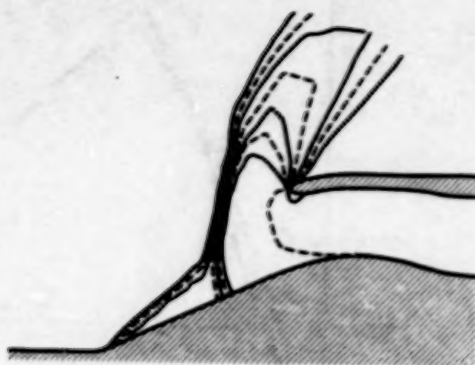
Figure 5. Pressure contours for a compression ramp inlet at Mach 2.0
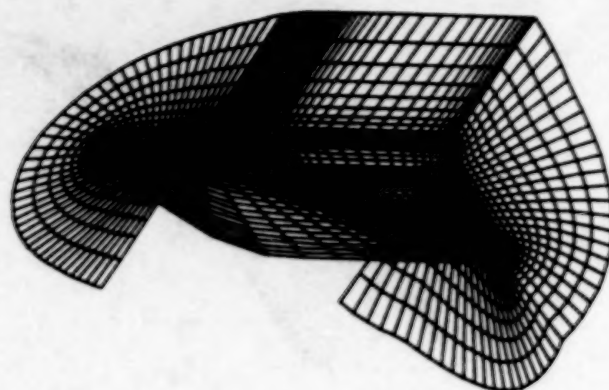
Figure 8. Grid for AFVFM (figure 3)
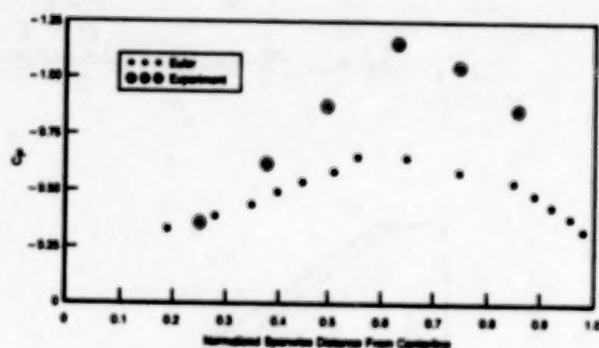
Figure 6. Comparison of test results and Euler calculations at a forebody station for the wing-body-tail configuration shown in figure 1a
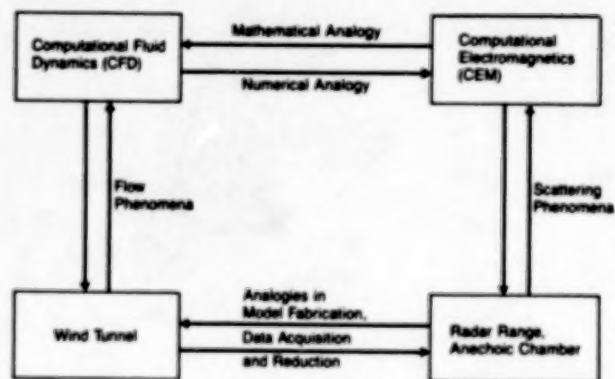
Figure 9. Aerodynamics and Electromagnetics in the design process
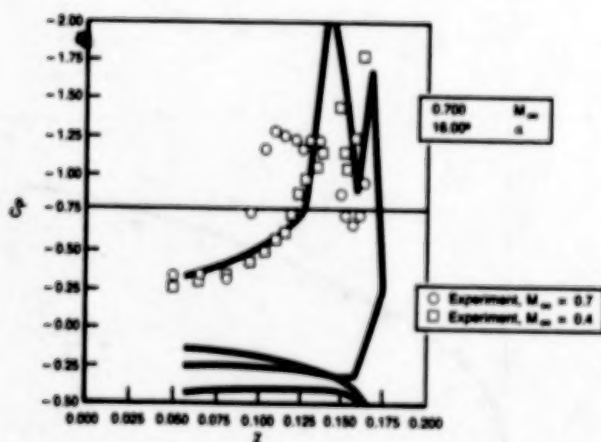
Figure 7. Comparison of test results and Euler calculations at a wing body station for the AFVFM (figure 3)
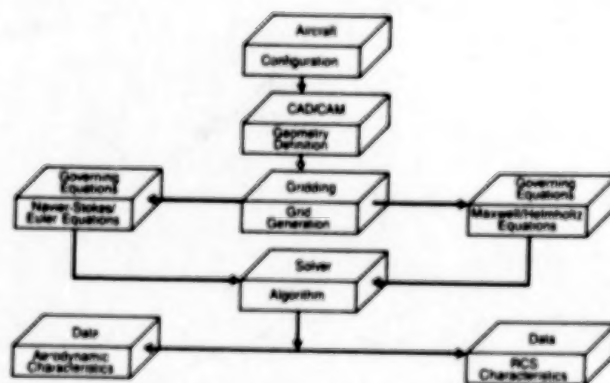
Figure 10. Unified solution of aerodynamic and RCS problems

Boundary Value Problems	Computational Fluid Dynamics (CFD)	Computational Electromagnetics (CEM)
Governing Equations	Navier-Stokes/Euler Equations	Maxwell/Helmholtz Equations
Outer Boundary Condition	Freestream Condition	Radiation Condition
Inner Boundary Condition	Flow Tangency Condition	Media Interface Condition

Figure 11. Analogy between Computational Fluid Dynamics (CFD) and Computational Electromagnetics (CEM)

Figure 14. Cross-flow velocity magnitudes on a 3-D fighter configuration
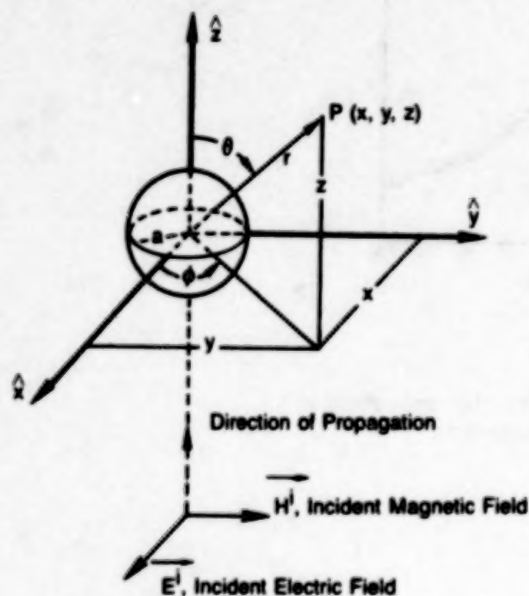
Figure 12. Plane wave incidence on a sphere and the coordinate systems
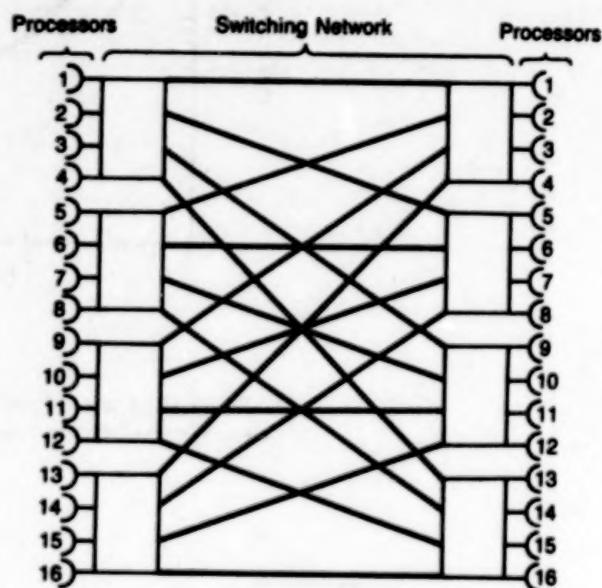
Figure 15. 16 processor system with butterfly switching network interconnect

Figure 13. Distribution of bistatic scattering cross sections for a perfectly conducting sphere in a plane wave field at ka = 2.9; $\sigma_1(\theta)$ is in the E-plane; $\sigma_2(\theta)$ is in the H-plane
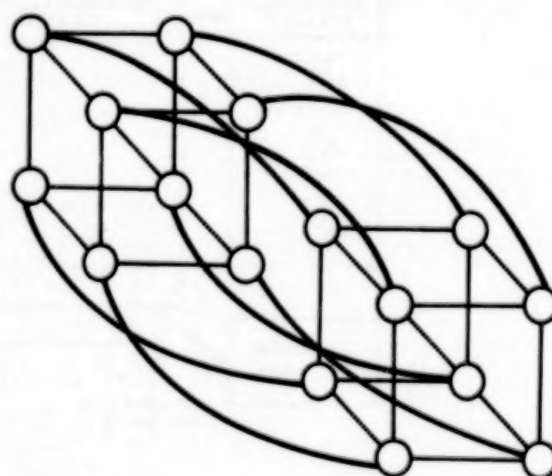
Figure 16. 16 processor system with 4-dimensional hypercube interconnect

135
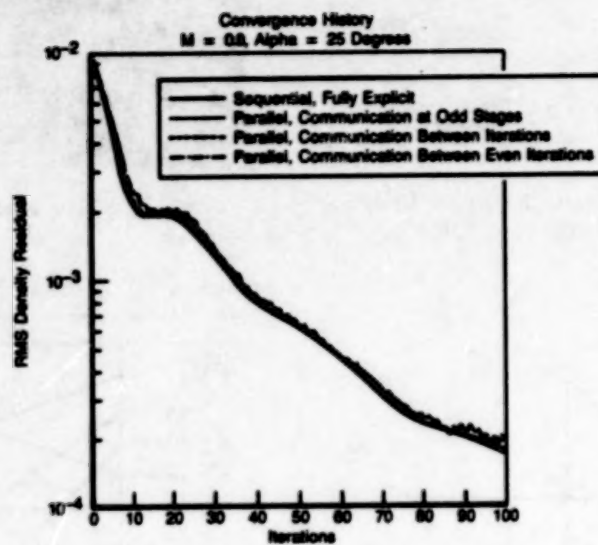
Figure 17. Finite-volume Euler algorithm convergence with varying levels of interprocessor communications
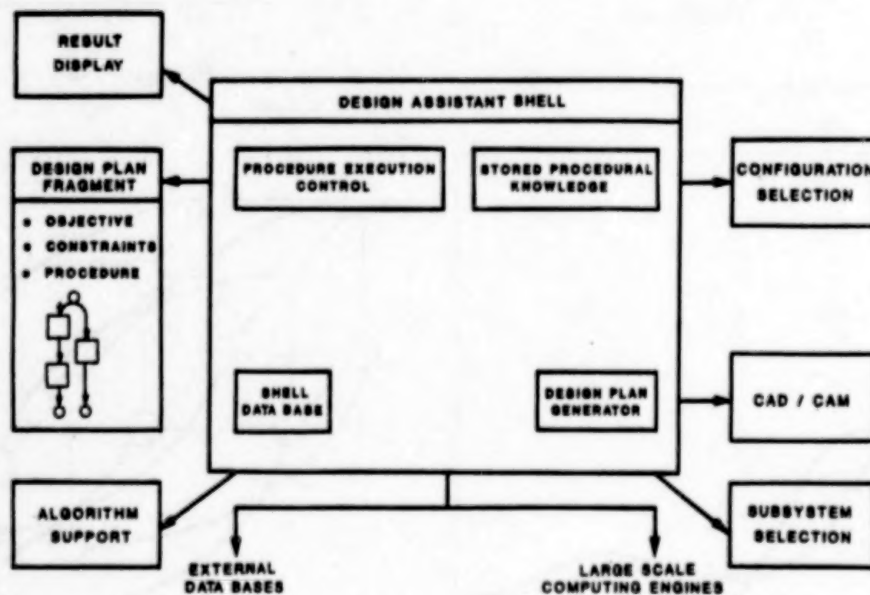
Figure 18. Design assistant shell logical architecture. Multiple interfaces facilitate design plan interaction.

OBJECTIVE: MINIMIZE DRAG AT M = 0.9

CONSTRAINTS: $C_L = 1.0$

PROCECURES:
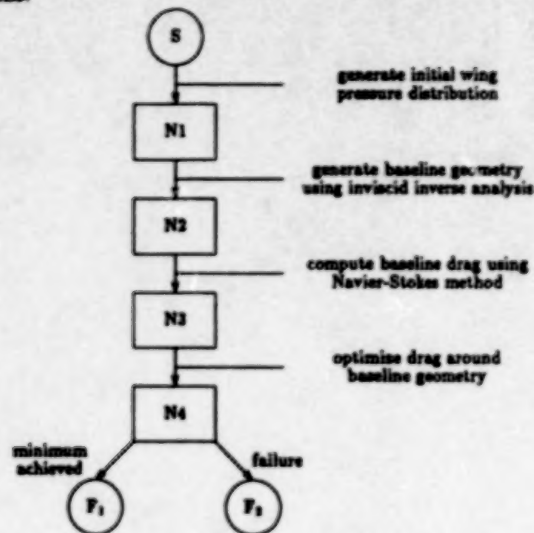
Figure 19. Design plan fragment for drag minimization step

OBJECTIVE: MINIMIZE PERFORMANCE MEASURE

CONSTRAINTS: SCALAR PERFORMANCE MEASURE, BASELINE GEOMETRIC
SPECIFICATION, TARGET PARAMETERS < C_L... >

PROCEDURES:
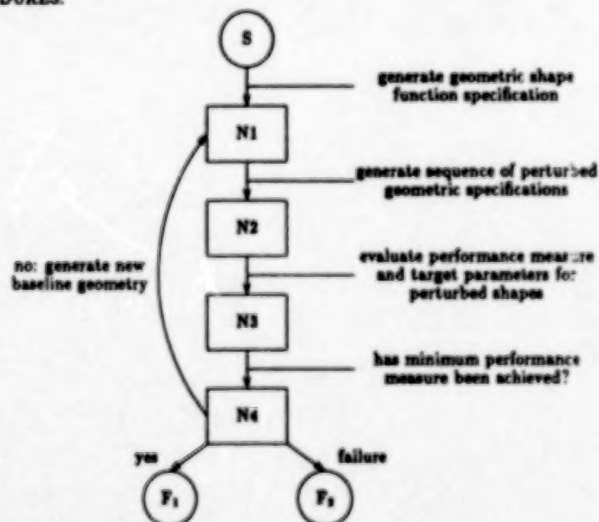
Figure 20. Design plan fragment for generalized optimization
procedure

137

APPLICATION OF CFD CODES TO THE DESIGN AND DEVELOPMENT OF PROPULSION SYSTEMS

W. K. Lord, Project Engineer
G. F. Pickett, Senior Project Engineer
G. J. Sturgess, Senior Research Engineer
H. D. Weingold, Senior Research Engineer

UNITED TECHNOLOGIES CORPORATION
Pratt & Whitney
Engineering Division
400 Main Street, East Hartford, CT 06108

SUMMARY

The internal flows of aerospace propulsion engines have certain common features that are amenable to analysis through computational fluid dynamics (CFD) computer codes. Although the application of CFD to engineering problems in engines has been delayed by the complexities associated with internal flows, many codes with different capabilities are now being used as routine design tools. This is illustrated by examples taken from the aircraft gas turbine engine of flows calculated with potential flow, Euler flow, parabolized Navier-Stokes, and Navier-Stokes codes. Likely future directions of CFD applied to engine flows are described, and current barriers to continued progress are highlighted. The potential importance of the Numerical Aerodynamic Simulator (NAS) to resolution of these difficulties is suggested.

INTRODUCTION

If an aerospace propulsion system is taken as any continuous-flow engine powering a vehicle for flight through the atmosphere, then included by this definition are gas turbines, ramjets, scramjets and liquid-fueled rocket motors. Although these engines look and operate very differently, they have certain common features that are amenable to analysis, e.g., flow turning, fuel injection, mixing, combustion, radiation, etc. In addition, certain of them have common flow systems (such as labyrinth seals, rotating cavities, cascade flow, stator-rotor blade interactions, diffusers, nozzles, etc.) that also can be addressed. Propulsion systems, with the exception of rocket motors, are usually enclosed in some kind of aerodynamic fairing. Flows over, and into and out of, these fairings form a critical part of the whole, and provide a link between the external aerodynamics of the vehicle and the internal fluid dynamics of its powerplant. It is flows such as these with which internal computational fluid dynamics (CFD) is concerned.

Computational fluid dynamics is emerging as a vitally important tool in the design and development of aerospace propulsion systems. It is a tool that is being used extensively at present, and its continued growth for these applications is assured since it makes available to the designer and development engineer information that can be provided in no other way. This use and potential of CFD is demonstrated in the next section through examples taken for convenience, from the gas turbine engine. It will be shown that efforts to obtain realistic and quantitatively accurate simulations are confronted primarily by two technical barriers. They are: (a) the availability and affordability of the computer capacity, and (b) the accuracy of the physical models that need to be incorporated into the CFD codes. It is anticipated that the existence and operation of the Numerical Aerodynamic Simulator (NAS) will help to push back the first of these barriers and to permit the extensive code validation against benchmark experimental data that eventually will generate improved physical models and so, will push back the second barrier.

The application of CFD techniques in the aerospace industry has been very successful in external aerodynamics. However, although the status of CFD code development is equivalent, successful application to complex internal flows as an engineering tool has not yet advanced to the same degree, and the engine manufacturers appear to lag the airframe manufacturers in exploiting CFD by a period of at least ten years. It is only in the last five years or so when any significant use of CFD in powerplant design and development has taken place. However, recent progress in the area has been rapid.

Much of the reason for the delay in the use of CFD codes as an engineering tool in the design and development of propulsion systems can be attributed to the considerably more difficult task associated with calculating internal fluid flows. Many of the physical simplifications and computational shortcuts applicable to problems in external aerodynamics are just not suitable for analyzing internal aerodynamic problems. Two-dimensional potential, and two and three-dimensional Euler equation CFD codes, which form the cornerstone approach for analyzing external aerodynamic flows, are used extensively to analyze turbomachinery flows; but in this internal application, they need to be calibrated to account for viscosity-generated blockage and airfoil trailing edge conditions. Boundary layer codes and inviscid/viscous interaction codes are used in conjunction with the potential and Euler equation solvers to determine estimates of airfoil heat transfer and to define regions of possible separation. However, at off-design conditions where the potential/viscous interactions cause separated regions, this approach is not adequate. Parabolized Navier-Stokes codes can be used for a class of problems provided that regions of separated flow are very small, and there exists no significant recirculation of flow. There are many situations, however, where the internal aerodynamics is dominated by secondary flow development, and such large regions of separated flow can only be addressed through solution of the full Navier-Stokes equations with the attendant costs and computer demands. In almost all cases, the enclosing geometries are extremely complex.

This is very much the case for flows in combustors and dump diffusers, regions of flow on the

endwalls near leading edges of compressor and turbine airfoils, and engine secondary flow systems such as rotating cavities and labyrinth seals. These problems can only be addressed through the solution of the full Navier-Stokes equations. Because the bounding geometries in internal aerodynamic flows are invariably complex and the flow fields are also, large numbers of grid points are needed for adequate resolution of gradients; this gives rise to high computing demands and the attendant costs. The perceived difficulties of calculating internal flows in a realistic and affordable manner did inhibit serious acceptance of CFD until such time as computer developments made the difficult task feasible. In practice, pragmatic engineers in the propulsion field utilize whatever solution-approach is physically adequate for their purposes and computationally efficient.

The application of CFD codes in the propulsion industry will be demonstrated for a variety of design problems associated with the aircraft gas turbine engine. It will be shown that some cases can be adequately analyzed with the relatively simple CFD codes, while other cases require the application of a full Navier-Stokes code. Similar examples could also be presented for liquid rocket motors and ramjet engines.

The authors wish to thank the Pratt & Whitney Engineering Division of United Technologies Corporation for permission to present this paper. The views expressed are those of the authors.

CURRENT APPLICATION OF CFD CODES

In order to illustrate the current state of the art, various applications are presented under the headings of specific CFD code types.

Potential Flow Codes

Since the mid-1970s, subsonic and transonic potential-flow codes have been widely used at Pratt & Whitney to analyze two-dimensional compressor or turbine airfoil cascades, and axisymmetric inlet flow fields. In the last five years, there has been an increasing shift toward three-dimensional flow analyses.

One area in which three-dimensional potential methods are extensively used is nacelle aerodynamics. Nacelle-related problems, such as the design of inlets and nozzles, involve a combination of external and internal aerodynamics. Since the external flow about the nacelle is essentially irrotational, the potential-flow approximation is valid for many of these problems. It is particularly applicable to the aerodynamic analysis of inlets and fan cowls on turbofan engine installations for subsonic transport aircraft. (It is not a very good approximation of the physics of nozzle flow fields, however, because of the rotational engine exhaust flow, strong shocks, and turbulent shear layers typical of nozzles at high pressure ratio.)

Panel methods have seen extensive use in the airframe industry for a number of years. They have been used at Pratt & Whitney to obtain potential solutions for the flow about complex geometries such as the installed turbofan nacelle (Lord and Zysman, 1986). Most recently, they have been applied to the aerodynamic design and analysis of

Prop-Fan nacelles. The Pratt & Whitney/Allison Gas Turbine/Hamilton Standard Prop-Fan propulsion system is a geared counter-rotating pusher. The nacelle (figure 1) has an auxiliary air intake for the gearbox air/oil heat exchanger. The engine exhaust gas exits the nacelle through discrete lobed nozzles located upstream of the propellers. Panel codes have proved to be quite useful in analyzing the flow into the auxiliary air intake and around the lobed nozzles (figure 2). Pratt & Whitney is currently using primarily the VSAERO code (Clark, et al, 1984). VSAERO is a second-generation panel code that exhibits very little leakage, and is thus well suited to problems involving combined external/internal aerodynamics.
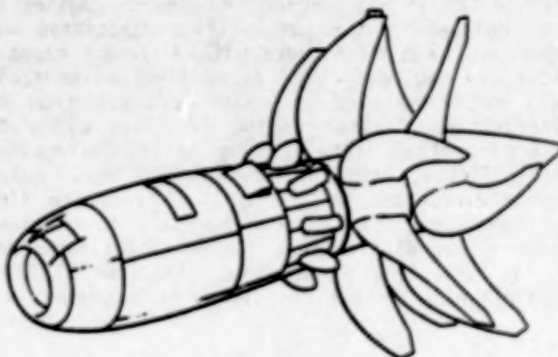
Figure 1 Arrangement of P&W/AGT/HS Pusher Prop-Fan

LOBED NOZZLE WITH FAIRING
MACH 0.76
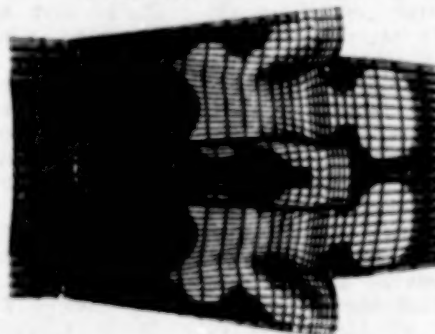
Figure 2 Distributions of Mach Numbers Over Lobed Nozzle of Pusher Prop-Fan - Panel Method (Original in Color)

The significant advantage of panel codes, of course, is that they do not require an off-body computational grid. They can handle completely arbitrary geometries, as opposed to finite-difference or finite-volume solvers for which the grids and boundary conditions are typically set up for a specific component. The computer storage and processor time requirements for panel codes are relatively modest, well within the capacity of current machines. One major drawback is that current panel-method solutions are strictly valid only in the subsonic, and not in the transonic, flow regime.

Euler Equation Flow Codes

Three-dimensional potential methods are not generally applicable to propulsion system internal flows because of rotational effects (e.g., spanwise total temperature and total pressure profiles). This fact helps to explain the intensive development effort at Pratt & Whitney of three-dimensional (3-D) Euler methods for fan/compressor and turbine aerodynamics.

Euler equation codes are being applied to the design and analysis of all the major components of the gas turbine engine with the exception of the combustor. The particular version used at Pratt & Whitney is that developed by Ni (1982). With good input/output subroutines, and the incorporation of multi-grid methods to speed-up the calculation, the Ni Euler-equation solver is extensively used by the engineer as just another design tool. The Euler code is principally used to determine the surface loading distributions on airfoils, endwalls and nacelles. It is also used, however, in conjunction with 2-D and 3-D boundary layer analyses to identify potential separated flow regions and high heat load regions in turbine airfoil passages.

The code was initially developed in two-dimensional form to calculate the blade-to-blade pressure distributions in turbine and compressor airfoils. Its main advantage over potential flow codes is that it can be applied well into the transonic flow regime. The code was extended to three-dimensional steady flow for application to turbine airfoil passage flows. In addition, because of the relatively small viscous/inviscid interactions that occur in a well-designed turbine airfoil passage away from endwalls, the code has proved to be an excellent tool for predicting airfoil loadings as a function of span for a variety of three-dimensional turbine designs.

The Ni code demonstrated early that problems in existing highly loaded airfoil designs could be avoided by changing the airfoil section stacking and also the sections to obtain improved pressure distributions. In this way, local diffusing regions could be avoided, and as a consequence, improved performance invariably was achieved. Some examples of this are presented in an American Institute of Aeronautics and Astronautics paper by Huber, et al (1985).

One of the biggest problems in applying a three-dimensional Euler solver to the design of turbomachinery airfoils is the definition of the upstream and downstream boundary conditions for each airfoil row. An approach adopted to overcome this problem was to develop a multi-stage calculation procedure, where the upstream boundary condition is defined ahead of the first vane and the downstream boundary condition is defined behind the last blade row. Interface planes between adjacent blade rows are defined, and flow conditions at these planes are calculated as part of the solution. Implementation of this approach, however, requires that certain simplifying assumptions be made. Since the flow in actual turbines is highly unsteady, and because invariably, for dynamic structural reasons, the number of airfoils in neighboring rows is different, the flow field at the interface planes has to be circumferentially

averaged before transmitting the information to the calculation of the neighboring airfoil row which, of course, is in a different frame of reference. In principle, the calculation procedure could be set up to include an integral number of neighboring blades and vanes; and the Euler code, being a time-marching scheme, could handle the unsteady boundary conditions at the interface plane due to the need to change from stationary to moving frames of reference between vanes and blades and vice versa. However, the current state of the art of computers does not allow mesh densities that would be sufficiently large to accurately capture the flow. It should be emphasized, however, that the relatively high levels of turbine performance have been obtained with time-averaged data and based on the demonstrated accuracy of predicting "mean" pressure distributions and flow angles. As such, the multi-stage analysis with circumferentially averaged interface plane conditions has provided a significant step in simulating the mean flow effects for three-dimensional, rotational flow fields in turbines.

Figure 3 shows a view of a typical two-stage high pressure turbine computational mesh. There are a total of four airfoil rows contained within the computational domain (i.e., two vanes and two blades). The lines formed by adjacent airfoil row mesh planes are the "interface" boundaries that subdivide the computational domain into four sectors. The three-dimensional flow solution for the resultant multisector problem is determined by applying the code to all the sectors and imposing an interior flow boundary condition to the interface mesh points at each time iteration step. The far-field boundary conditions for this multistage computational procedure then become the first vane upstream conditions and the second blade downstream conditions.

SAMPLE COMPUTATIONAL MESH
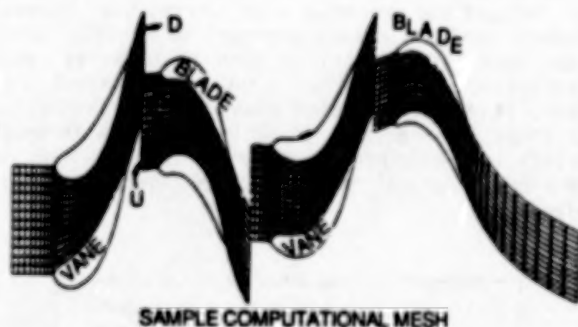
Figure 3 Computational Mesh for Turbine Vane/ Blade Rows

Several calculations of two-stage turbines have demonstrated the accuracy of predicting airfoil and endwall pressure distributions and exit flow angles from each airfoil row. In order to achieve this accuracy, the secondary flow within the passages needs to be reasonably well represented. Figure 4 illustrates the predicted vortex structure that can exist in the first blade depending on the flow field exiting the first vane. Such secondary flow can have a large effect on the flow angles exiting the blade row.

PRESSURE SIDE   SUCTION SIDE   TIP
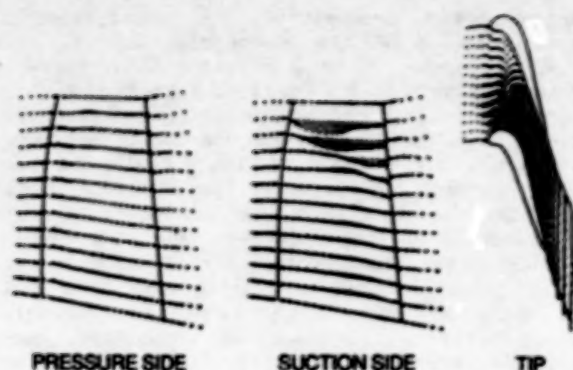
Figure 4   Predicted Secondary Flows in First Blade Passage - Euler Code

As the capacity of computers increases, multi-stage Euler codes will be extended to simulate inviscid unsteady vane/blade interaction flows, and viscous terms will be added to the governing equations so that first order viscous effects will be simulated in the calculations.

The Ni Euler code has also been used to compute the inviscid flow about inlets at angle of attack. In this case, a uniform static pressure boundary condition is applied at an internal station at or just downstream of the actual fan-face station. At low inlet air flows, the flow is isentropic and the relationship between the captured mass flow and the fan-face static pressure may be calculated directly from the one-dimensional isentropic relations. At flow approaching the maximum inlet air flow capacity, however, strong internal shocks can occur, particularly at high angle of attack (figure 5). In the case of nonisentropic flow, a static pressure boundary condition is specified; but the corresponding actual inlet mass flow must be obtained from the computed solution by integration of mass flux across an internal control surface. A mass-averaged inlet total pressure loss (shock loss) is also obtained by integration of entropy flux across the control surface. It should be noted that accurate prediction of shock loss requires an Euler algorithm in which artificial dissipation effects, which lead to spurious numerical total pressure loss, are minimized.
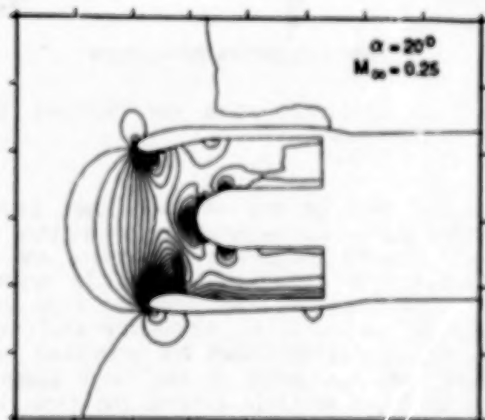
Figure 5   Mach Number Contours for Engine Inlet Showing Shock Formation - Euler Code

Parameters of interest from a design standpoint at high inlet air flow are inlet total pressure recovery and maximum inlet flow capacity. Inlet recoveries can be crudely estimated by simply adding the shock loss from the Euler calculation to the boundary-layer loss obtained from a separate strip boundary-layer calculation. A comparison with model test data (figure 6) indicates that recovery levels are fairly well predicted and that the maximum air flow capacity, due to choking at the inlet throat, is predicted quite accurately.
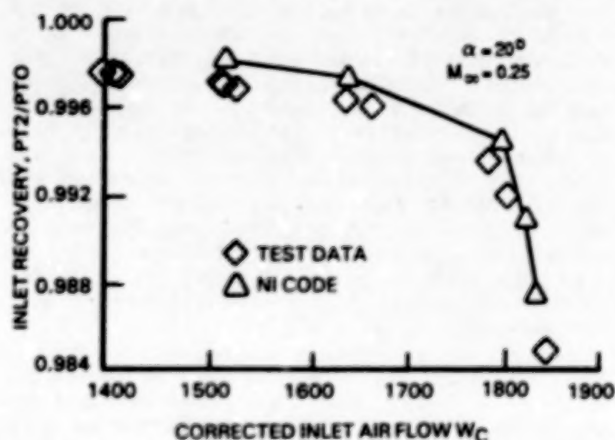
Figure 6   Comparison of Predicted and Measured Inlet Pressure Recoveries - Euler Code

Parabolized Navier-Stokes (PNS) Codes

The Parabolized Navier-Stokes (PNS) approach has been applied to both subsonic and supersonic/hypersonic flow fields. At Pratt & Whitney, the emphasis has been on development of a PNS code for subsonic internal flows in three-dimensional ducts of arbitrary cross section and curved centerline. A development version of this code is currently undergoing extensive calibration. The expected applications include fan ducts in turbofan nacelles, the radially-offset exhaust duct for the lobed nozzle in the Prop-Fan nacelle, the circular-to-rectangular transition duct in military two-dimensional nozzle exhaust systems, and several components in the Space Shuttle Main Engine.

In the PNS formulation, upwind differencing is used for transport variables, streamwise diffusion terms are neglected, and the streamwise pressure gradient is prespecified. In the case of the Pratt & Whitney PNS code, global elliptic effects are incorporated through use of a coarse-grid Euler solution; i.e., it is this solution that provides the background pressure gradients. The reduced set of PNS equations allows streamwise marching of planes of data in space, as opposed to time marching of three-dimensional data blocks for a full Navier-Stokes solver. This results in an order-of-magnitude reduction in both computer core memory and central processing unit (CPU) time requirements.

The PNS code has been applied to a well-known example case, the Boeing 727 center-engine S-duct inlet (Kunz and Rhie 1986). The computational grid and a comparison of the Euler and PNS pressure distribution with experimental results from model

test (Ting, et al, 1975) are shown on figure 7. The pressure distributions are here expressed in terms of an equivalent Mach number based on upstream total pressure. The inviscid Euler solution agrees well with the data over the forward portion of the duct but underpredicts the Mach number levels in the aft portion of the duct. This is as expected; the boundary layer builds up with distance down the duct and the displacement effect of the boundary layer raises the local Mach number levels. The PNS code viscous solution reflects the boundary-layer displacement effect and gives better agreement with the data in the aft portion of the duct.
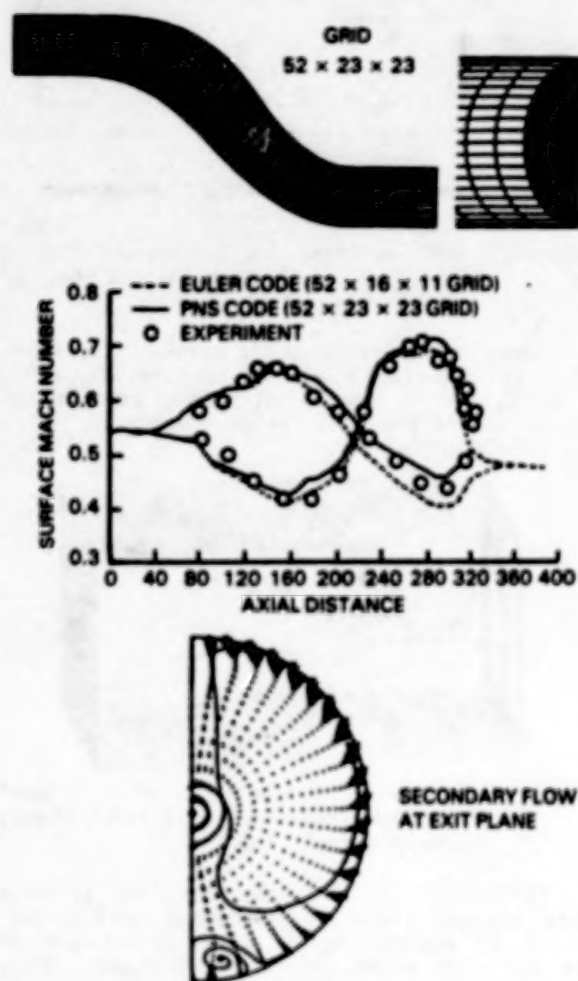
Figure 7   Calculation of B727 Center-Engine S-Duct Inlet Showing Secondary Flow Development - PNS Code

The predicted secondary flow pattern at the exit plane is also illustrated in figure 7. The cross-channel pressure gradient induced by the second bend drives a circumferential flow in the boundary layer toward the top of the duct. A much smaller region of secondary circulation is evident at the bottom of the exit plane cross section; this is the remnant of the secondary flow induced by the first bend in the duct. It shows up on a total pressure contour as a region of high loss.

Navier-Stokes Codes

Flows with dominating recirculation demand solution of the full Navier-Stokes equations. Examples of such flows are rotating cavities, labyrinth seals and combustion chambers. Two examples of such flows are presented.

Most practical internal fluid flows of interest are turbulent. This is usually dealt with through a simple turbulence management strategy in which the Navier-Stokes equations are written in Reynolds-averaged or Favre-averaged (density-weighted) form and are solved as a stationary flow. The turbulent fluxes introduced into the equations by the averaging are represented through the eddy viscosity hypothesis and gradient diffusion. Turbulence modeling is used to find relationships for the eddy viscosity. This modeling may be appropriate for both high and low turbulence Reynolds numbers, or a high Reynolds number model may be used together with turbulent wall functions for the near-wall region. For variable density and chemically reacting flows, the energy equation and species transport equations are included. The partial differential equations are arranged into a general form that consists of convection and diffusion terms, and source terms describing the generation and dissipation of the dependent variable. A heat release rate expression is provided for reacting flows. Finite differencing is used to discretize the equations. Since pressure does not appear directly in the momentum equations or the continuity equations but is a dependent variable nonetheless, an algorithm is used to obtain a pressure field and correct the velocity field in such a manner that the continuity and momentum equations are simultaneously satisfied. An implicit solution algorithm is used, with the initial guesses for the field variables being iteratively updated until convergence is reached (Sturgess, 1983). The liquid fuel is accounted for through a Lagrangian spray model that is coupled with the Eulerian gas flow field through a particle-source-in-cell technique (Sturgess, et al, 1985b).

Part of the difficulty of presenting internal flows is that they are totally enclosed. In addition, the enclosing geometry can be extremely complex. The combustion chamber of the gas turbine engine is one such component; this is illustrated on figure 8 which is a view of an annular combustor presented from an interior perspective. Although the flow can be considered as periodic about fuel injectors, it may be appreciated that definition of the many streams (film cooling air, combustion air jets, dilution air jets, dome cooling air, swirler air, and liquid fuel), entering the computational domain, as well as the basic bounding geometrical contours, demand a large computer resource. Even when reduced to a repeating segment, the combustor geometry presently has to be greatly simplified, an example of which is given in figure 9.

Calculation of the simplified combustor of figure 9 yields a tremendous amount of useful information concerning the details of the reacting flow contained therein. Figure 10 gives an isotherm contour plot at a cross-section in the dome and shows details of the film cooling, the dome cooling associated with the heatshield, and the results of local air admission around the fuel injector. Note that the temperature field is not symmetric about the axisymmetric fuel injector and heatshield geometries; this is due to the swirling

air introduced by the airblast fuel injector. An additional cross-section is contained in figure 11. This section is taken at a plane through the second row of air-addition ports. Streaklines are provided as motion-cues and are colored with the appropriate color for the local temperature field. The complex character of the flow field can be appreciated.
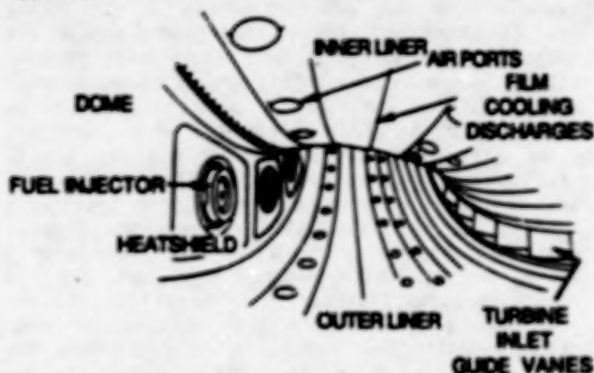
Figure 8   Interior View of an Annular Combustor for a Gas Turbine Engine

ISOMETRIC VIEW
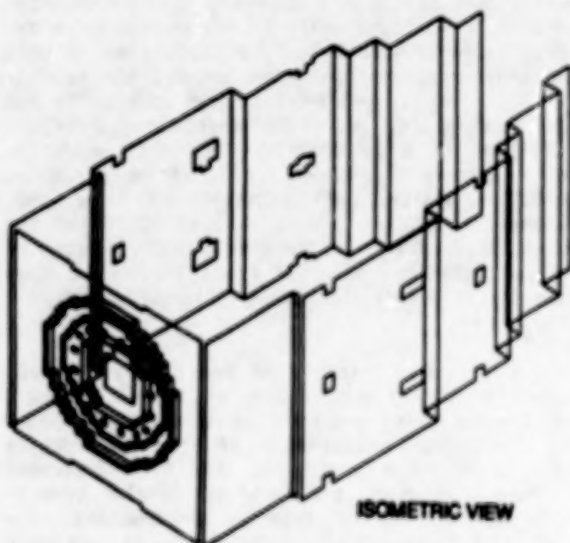
Figure 9   Simplified Repeating Sector of an Annular Combustor
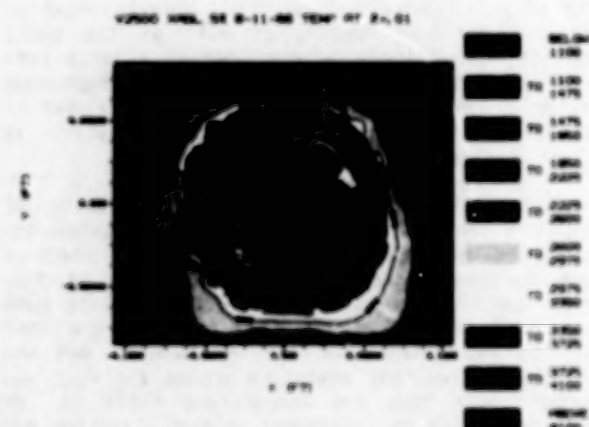
Figure 10   Isotherm Contour Plot Close to Dome in Simplified Dome - NS Code (Original in Color)
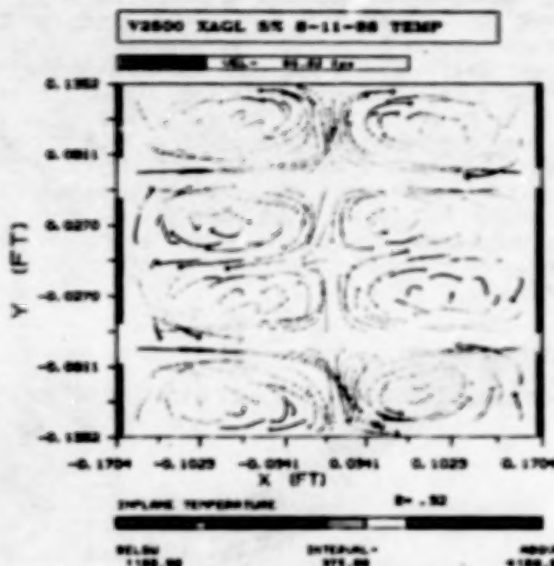
Figure 11   Combined Streakline/Temperature Plot at Cross-Section Through Second Row of Air-Ports (Original in Color)

Figure 11 demonstrates the dominant characteristic of combustor flows, i.e., they are wholly elliptic. This is best illustrated by means of animated streaklines, of which figure 12 is a "still" rendering.
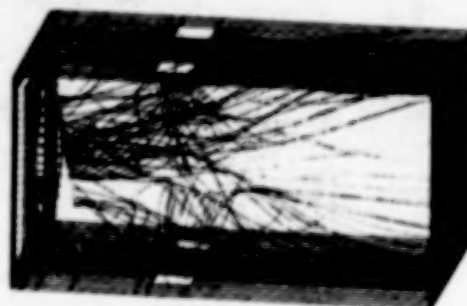
Figure 12   Isometric Projection of "Frozen" Animated Streaklines in a Model Primary Zone (Original in Color)

Calculations in the combustor such as those shown are most useful to understand the flow processes, for determining the origin of hot-spots on the confining liners and dome (Sturgess, 1980), and in investigating geometric changes to develop the outlet temperature distributions. This is all done by directly viewing the reacting, hot-gas flow field, rather than by measuring its effects on the confining boundaries and then postulating a field which is to be modified in some way.

The calculations shown were performed with a Cartesian coordinate system on a 50 x 40 x 41 grid, requiring a storage of 30 megabytes and about 11 CPU hours on an IBM 3090 (fast scalar) computer to reach a somewhat arbitrary convergence level of 5 percent (residual source sum). At this level, the definition of the combustor is inadequate, and calculations at the 200 megabyte level are being explored, although it is estimated that 300 megabytes might be necessary for adequate representation of the geometry and resolution of the flow gradients. The solutions currently obtained cannot be considered to be grid-independent. Thus, when calculations like this are used

for parametric diagnostic studies, all variations contemplated must be calculated on the same grid; this necessitates very careful thought and advanced planning in establishing the initial grid.

The accuracy of combustor simulations is being determined at present not by the numerics or the physical modeling but by computer capacity and the cost of solution.

Prepared originally for the combustion chamber, the availability of a general Navier-Stokes code written in modular form containing a suite of switchable physical models and an arbitrary geometry capability, enables application to be made to internal flows with recirculation that arise in many areas of the gas turbine engine, including secondary systems as well as the main gas path. An example of such an important secondary system is the internal cooling of turbine aerofoils where there is a need to understand and predict the effects of rotation on local heat transfer and pressure loss, especially for blades that have multi-pass coolant passages. Accurate calculation of these quantities is very important as it can lead to an improvement in the reliability of predicting turbine airfoil temperatures and, ultimately, blade life. Accurate estimates of temperature and life permit available cooling air to be used most effectively and reduces its negative impact on turbine performance.

In order to demonstrate the potential for this, a simplified geometry of a blade passage was calculated, as shown on figure 13 (Sturgess and Datta, 1987). It consisted of a single outflow leg and an inflow leg. The grid was a coarse 33 x 11 x 5, and these demonstration calculations were not considered to be grid independent, and the resolution is low. For the baseline calculation of 600 RPM, the Reynolds number was 30,000 and the Rossby number was 0.174; the passage aspect ratio was unity and its length-to-width ratio was 12.
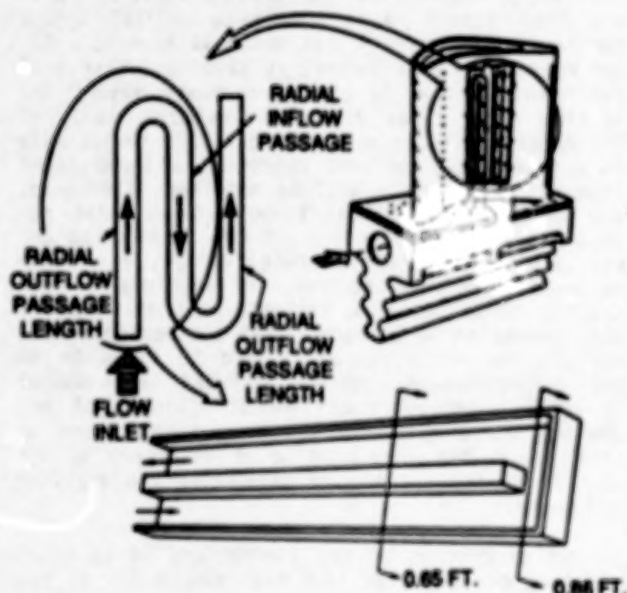
Figure 13 Schematic of Simulated Turbine Blade Coolant Passage

Figure 14 gives the flow field development along the passages at 600 RPM and at the two

cross-sections shown in figure 13 for several rotational speeds. The flow visualization technique is by streaklines, and results for four rotational speeds of 0, 60, 600 and 1900 RPM are presented. The development of secondary flows due to the influence of Coriolis forces can be seen. In the outflow (away from the axis of rotation) leg of the passage, a pair of counter-rotating vortices develop. The vortex centers are shifted slightly from the centerlines of the leg towards the pressure side, but the size and strengths of the vortices are about equal. As the vortex pair enters the turn, their rotational velocity is overcome, and the flow changes direction as mass is forced to the pressure side of the turn. The flow entering the passage inflow leg from the turn is therefore forced into a right-angled corner. As it escapes from the corner to begin flowing down the inflow leg (towards the axis of rotation), the air has no choice other than to establish a single vortex. The action of the turn is thus to coalesce the vortex pair formed by Coriolis forces into a single vortex completely filling the passage inflow leg. Other sections of the passage show that the the double vortex structure of the original system begins to reestablish itself as the flow proceeds down the inflow leg towards the axis of rotation, although initially this vortex pair is not symmetrical, of course. The flow behavior observed is intuitively correct.
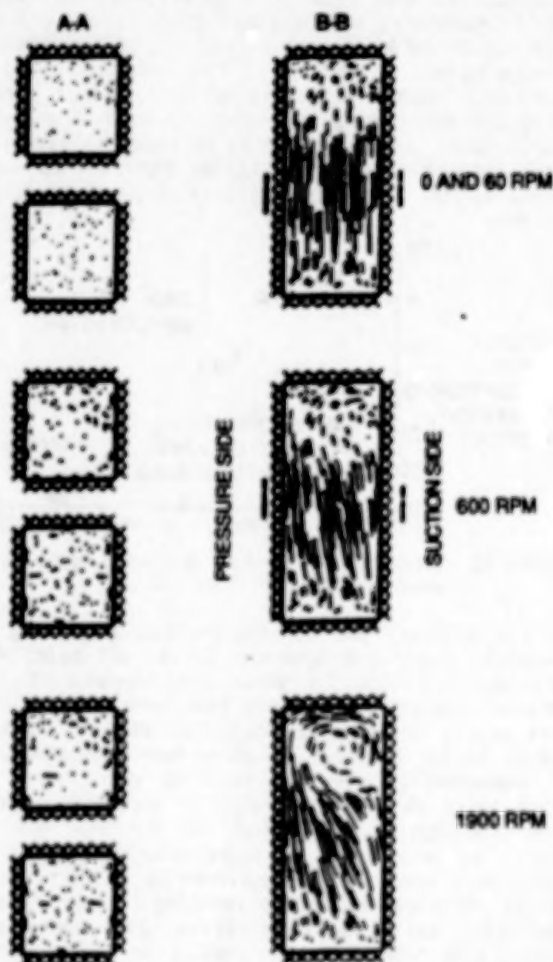
Figure 14 Flow Visualization in Simulated Coolant Passage for a Range of Rotational Speeds - NS Code

Although the code can give adequate quantitative accuracy in three-dimensional rotating passages of very simple geometry, as was established by subsequent calculations (Sturgess and Datta, 1987), the geometries of practical interest require more computer capacity than is currently available. For example, the use of trip-strips in the passages to enhance heat transfer requires that the induced disruption of the laminar sublayer in between strips be both calculated and resolved in detail. Such a calculation demands the use of appropriate low Reynolds number turbulence models and many grid lines adjacent to the walls. Again, progress is limited by the available computer facility.

FUTURE DIRECTION

It has been shown by way of example, how current CFD codes are being used in the design and development of aerospace propulsion systems. In conjunction with highly refined design criteria, advanced materials and advanced manufacturing technology, gas turbine component performances have progressively increased so that the thrust specific fuel consumption (TSFC) of commercial and transport gas turbines has been reduced at a rate better than 1% per year over the past two decades (figure 15). Also shown in figure 15 is that, with the introduction of advanced propulsion concepts like the Prop-Fan or the ducted fan, the potential for continued significant TSFC reductions will continue. Improved modeling of the gas path flows using the developing CFD codes in the new propulsion systems and in advanced versions of existing gas turbine engines will play an important role in achieving the full potential of these propulsion systems.
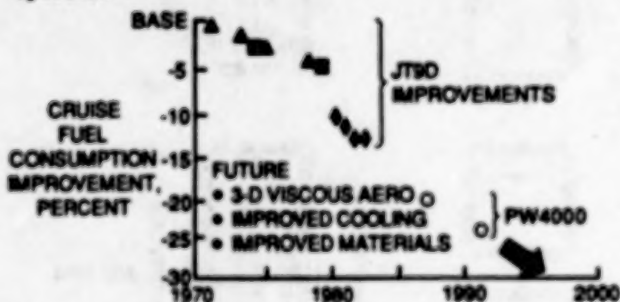
Figure 15   Improvement in Gas Turbine Engine Fuel Consumption with Time

For military gas turbine engines, high thrust-to-weight ratio and specific thrust are major requirements. Figure 16 shows the improvements in thrust-to-weight ratio that have been made in recent years, and also a projection of what is required in the future. It can be seen that the rate of improvement over the next 15 years must be about twice the current rate. It has been identified that approximately half of the improvements can be achieved with advanced materials, and the other half needs to be achieved by improved component efficiencies and by reducing the air "leakage" from the propulsion stream. Once again advanced CFD codes will be needed to achieve the necessary component performance goals and to ensure that as much as is possible of the air entering the engine goes to generate useful thrust.

The successful applications of CFD codes ob-

tained to date should not give rise to complacency. To the contrary, if the aggressive military and commercial goals needed to keep this nation competitive with outside threats are to be met, then significant advances in the development and application of CFD codes will need to be made. Two major limitations exist that currently are impeding further progress in the development and use of CFD codes. They are: the inadequacy of physical models that need to be incorporated in order to simulate realistic engine flow fields, and the limitations in computer capability associated with speed, memory capacity and cost of calculation.
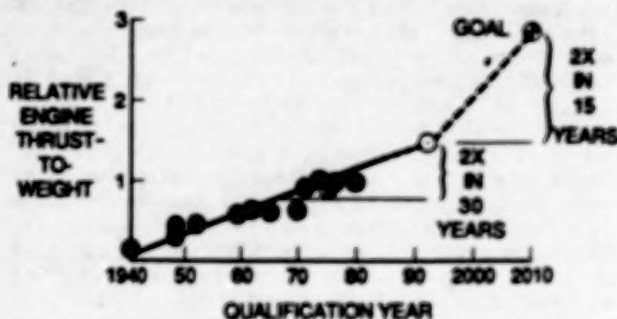
Figure 16   Increase in Engine Thrust to Weight Ratio with Time

The first and perhaps the most obvious deficiency in current CFD codes is the lack of realistic physical models. Empirical data from many different types of test are used to calibrate the codes for application to gas turbine design. For example, in turbomachinery flows, surface shear forces and trailing edge conditions are established in order to obtain the required accuracy in predicting airfoil loadings, air angles and weight flow. Turbulence models that are necessary to provide closure to the Reynolds-averaged Navier-Stokes equations have evolved to the point where relatively simple flows can be simulated, but they are insufficient to be used as a reliable means for predicting airfoil loss and heat transfer. For the reasonably near future, it seems unlikely that the complex flows in airfoil boundary layers and in free shear flows will be calculable. Thus, if CFD codes are to be used in the future to optimize on minimum loss or heat transfer, a large input from key experiments will be required. Similarly, the interactions between turbulence and heat release in the combustor are not well understood and can only be modeled in crude fashion, for which empirical input is required. The problems in generating these data are twofold: what are the key experiments to be performed that are needed to develop codes which can be applied to flows in an engine environment, and how will the large number of these experiments be funded? Attempts at answering these questions are beyond the scope of this paper, but they need to be addressed by all who are in the business of developing and applying CFD codes.

No discussion of the limitations of physical modeling can omit the fact that almost all of the CFD codes used in gas turbine design are steady, and that the so-called Navier-Stokes codes usually do not solve the Navier-Stokes equations, but employ a statistical turbulence management strategy and solve the time-averaged Reynolds or Favre equations. Yet, of course, the flow in most gas turbine components is highly unsteady. In fact, it

is quite remarkable that so much progress in calculating component flows has been made without considering unsteadiness as a first order factor. Again, using an example from turbomachinery flows, the flow in a specific turbine or compressor airfoil passage is very much dependent on the flow field exiting the upstream airfoil row. As discussed in the section on Euler codes, because the upstream row is moving relative to the specific airfoil passage in question, the flow field from the upstream row currently is pitchwise averaged and the flow is assumed steady and circumferentially constant as it enters the airfoil passage that is being analyzed. From the work of Sharma, et al (1985) it can be shown that this simplification results in the suppression of vorticity entering the airfoil passage. Since the function of the airfoil passage is to turn the flow (and the turning angle can be over 100 degrees for turbines), the redistribution of the entering vorticity is instrumental in determining the exit flow angles. Thus, if much of the inflow-vorticity is suppressed, it is not possible to obtain reliable exit flow predictions from an essentially steady CFD code. Similarly, in the combustor, the current calculation of the distribution of fuel across the reaction zone depends on the trajectories of the fuel droplets (which should include the effects of turbulent dispersion of the droplets and modulation of the gas-phase turbulence by the presence of the droplets) and the assumption of gradient diffusion. However, observations of the flow patterns in combustor primary zones show that nonstationary effects can be dominant. Thus, the actual mixing of fuel and air is largely by processes that are not accounted for in the calculation procedure which solves time-averaged equations. One solution to these problems is to develop unsteady three-dimensional CFD codes, and starts have been made in this direction. Such codes introduce such a level of complexity and calculation cost, however, that it is unlikely that unsteady codes will be used significantly in the design of gas turbine components for several years (Sturgess, 1984).

The other significant limitation in developing and applying CFD codes is the current state of the art of computer hardware. In gas turbines, the geometries and the flow fields are highly complex; thus, large numbers of grid points are desired by the code developers in order to predict the flow field with the accuracy required by the designer. The designer also wants to obtain answers fast, make some changes and re-run the code until appropriate design criteria are met. Since designs are generated within a given budget, the designer also wants the cost of each run to be reasonable in order to stay within that budget. The code developer of course also wants inexpensive and fast computing capability so that the parametric studies necessary for calibrating the code for a wide range of geometries and flow conditions can be conducted. Many papers in the literature have realistically assessed the computer hardware needs for the future, e.g., Sturgess (1985a) for the combustor, and the Numerical Aerodynamic Simulator (NAS) has a well-established program in place to meet many of these needs. Within this context, emphasis must be placed on re-configuring CFD codes to be optimally efficient on vector and parallel-processing computer architectures. Emphasis must also be placed on exploiting such techniques as adaptive grid procedures to reduce as much as possible, the computer resources needed for solution of a specific problem.

CONCLUDING REMARKS

It has been shown that internal flows for aerospace propulsion are now being extensively calculated in the industry as part of the design and development procedure of engine components. Although the illustrative examples presented have been taken exclusively from the gas turbine engine, this is so for ramjets, scramjets and liquid-fueled rocket motors also. A variety of codes is used, and the physics embodied in these codes range from potential flow to the Navier-Stokes equations. Selection of the appropriate code depends on the component flow required to be calculated and on the objectives required of the calculation. The codes are currently making a useful and important contribution to achieving the required performances of the various engines.

While the utility of the current generation of codes cannot be denied, there are some limitations to the accuracy of the calculations produced, and these were briefly touched upon. These limitations can be succinctly described as: (1) lack of physical realism in the modeling, and (2) restraints imposed by available computer resources.

The Numerical Aerodynamic Simulator (NAS) represents a great resource with immense potential for assisting with the calculation of internal flows in aerospace propulsion engines of all types. It is an opportunity for the present barriers to accuracy in such calculations to be overcome. The NAS, because of its high speed and large storage capacity, can be used as an experimental wind tunnel, or in the present circumstances, as an experimental engine component. In this role, it can be used to make calculations that are free from computer-resource limitations; therefore, it can be used to improve the understanding and modeling of relevant physical phenomena and to provide calibration information that is necessary for simpler, design-oriented codes intended for regular engineering use.

For example, the tip clearance flow field is a major contributor to loss in compressors; but because of the prohibitive number of grid points which would be necessary to incorporate it accurately in a numerical treatment of a full blade row, it is currently represented by very crude empirical modeling. The NAS would permit calculation of the actual tip clearance flow field with sufficient resolution when embedded in a full three-dimensional representation of blade row geometry to lead to more fundamental models.

In the case of non-stationary flows, the capabilities of the NAS can permit the use of unsteady codes for relevant cyclical periods. For turbomachinery applications, blade and vane row interactions can be examined and methods developed to model average flows at computational interfaces. This information can be incorporated in steady flow design codes, which will then more accurately model the interaction effects. Similarly, non-stationary mixing and chemical reaction processes in the combustor could be accurately modeled on the NAS facility, permitting full evaluation of the relative magnitude of the effect of time-dependent processes on the time-average solution.

The examples given above suggest how the NAS might contribute to engineering design capability. How useful the facility actually is will depend on the aerospace propulsion industry learning how to exploit its capabilities to the best advantage. Certainly, it seems apparent that the computational capacity offered by the NAS will be as necessary to achieving the goals of the new engine for the Advanced Tactical Fighter (Petty, et al, 1986) and the lightweight stoichiometric engine, as it is to the Space Shuttle Main Engine and the aerospace plane.

REFERENCES

Clark, D. R.; Maskew, B.; and Dvorak, F. A.: The Application of a Second Generation Low-Order Panel Method - Program VSAERO - to Powerplant Installation Studies. AIAA-84-0122, 1984.

Huber, F. W.; Rowey, R. J.; and Ni, R-H.: Application of 3D Flow Computation to Gas Turbine Aerodynamic Design. AIAA-85-1216, 1985.

Kunz, R. F.; and Rhie, C. M.: private communication, 1986.

Lord, W. K.; and Zysman, S. H.: VSAERO Analysis of a Wing/Pylon/Nacelle Configuration. AIAA-86-1523, 1986.

Ni, R-H.: A Multiple-Grid Scheme for Solving the Euler Equations, AIAA Journal, vol. 20, no. 11, Nov. 1982, pp. 1565-1571.

Petty, J. S.; Hill, R. J.; Piccirillo, A. C.; and Fanning, A. E.: The Next Hot Fighter Engine, Aerospace America, vol. 24, no. 6, June 1986, pp. 40-43.

Sharma, O. P.; Butler, T. L.; Joslyn, H. D.; and Dring, R. P.: Three-Dimensional Unsteady Flow in an Axial Flow Turbine, Journal of Propulsion and Power, vol. 1, no. 1, Jan.-Feb. 1985, pp. 29-38.

Sturgess, G. J.: Gas Turbine Combustor Liner Durability - The Hot Streak Problem. Gas Turbine Combustor Design Problems, Ed. A. H. Lefebvre, Hemisphere Publishing Company, 1980, pp. 133-150.

Sturgess, G. J.: Aerothermal Modeling - Phase I, Final Report. NASA CR-168202, May 1983.

Sturgess, G. J.: Stationary State Computational Fluid Dynamics for Aeropropulsion Devices, Computational Methods, Ed. K. L. Strange, CPIA Publication 401, Feb. 1984, pp. 25-51.

Sturgess, G. J.; James, R. H. and Syed, S. A.: Computing Gas Turbine Combustors, Proc. Symp. Computers in Engineering 1985, vol. 3, ASME Computer Engineering Division, August 1985a, pp. 261-275.

Sturgess, G. J.; Syed, S. A.; and McManus, K. R.: Calculation of a Hollow-Cone Liquid Spray in a Uniform Airstream, Journal of Propulsion and Power, vol. 1, no. 5, Sep.-Oct. 1985b, pp. 360-369.

Sturgess, G. J.; and Datta, P.: Calculation of Flow Development in Rotating Passages (to be published, 1987).

Ting, C. T.; Kaldschmidt, G.; and Syltebo, B. E.: Design and Testing of New Center Inlet and S-Duct for B-727 Airplane with Refanned JT8D Engines. AIAA-75-59, 1975.

DESIGN APPLICATIONS FOR SUPERCOMPUTERS

C. J. STUDERUS
GENERAL ELECTRIC COMPANY
CINCINNATI, OHIO

ABSTRACT

The complexity of codes for solutions of real aerodynamic problems has progressed from simple two-dimensional models to three-dimensional inviscid and viscous models. As the algorithms used in the codes increased in accuracy, speed and robustness, the codes were steadily incorporated into standard design processes. The highly sophisticated codes, which provide solutions to the truly complex flows, require computers with large memory and high computational speed. The advent of high-speed supercomputers, such that the solutions of these complex flows become more practical, permits the introduction of the codes into the design system at an earlier stage. The purpose of this paper is to present the results of several codes which either have already been introduced into the design process at GE-AEBG or are rapidly in the process of becoming so. The codes fall into the area of turbomachinery aerodynamics and hypersonic propulsion. In the former category, results are presented for three-dimensional inviscid and viscous flows through nozzle and unducted fan bladerows. In the latter category, results are presented for two-dimensional inviscid and viscous flows for hypersonic vehicle forebodies and engine inlets.

INTRODUCTION

At the General Electric Aircraft Engine Business Group (GE-AEBG), aerodynamic computer codes have been developed over the past thirty years to provide solutions for flows through a large variety of turbomachinery and propulsion systems. The capability of these codes has progressed from providing the solutions of simple two-dimensional inviscid meridional and blade-to-blade flows, and viscous boundary-layer flows, to the solutions of full three-dimensional inviscid and viscous flows. As the algorithms used in the codes increased in accuracy, speed, and robustness, the codes were steadily incorporated into standard design processes. However, the highly sophisticated codes which provide solutions to the full complexity of three-dimensional flows require computers with very large memory and extremely high computational speed. Therefore, it was not until the availability of such high-speed supercomputers that the solutions of these complex flows became more practical and permitted the introduction of these advanced codes into the design process at earlier and earlier stages. The advantage of being able to utilize these codes as design tools was one of the factors which prompted GE to purchase its own supercomputer, a CRAY-XMP.

The purpose of this paper is to present the results of several such codes which either have already become a part of the design process at GE-AEBG or are rapidly in the process of becoming so. The codes fall into two specific fluid dynamic areas: turbomachinery aerodynamics and hypersonic propulsion.

TURBOMACHINERY AERODYNAMICS

The actual flow through a turbomachinery bladerow is exceedingly complex. It is unsteady, compressible and viscous, producing strong three-dimensional effects, as indicated schematically in Figure 1. When the incoming endwall boundary layer encounters the leading edge, it rolls up to produce a so-called horseshoe vortex, which wraps around the leading edge. One leg of this vortex is convected along the suction surface. The other leg is convected across the passage to the suction surface of the opposite bladerow. The boundary layers farther along the endwalls are forced from the pressure surfaces of the blades to the suction surfaces by the cross-passage pressure gradients. They are deflected in the spanwise direction and roll up into a passage vortex. Similarly, when the endwall boundary layer flows into the corner and interacts with the boundary layer on the suction surface, corner vortices are produced. Trailing vortices result from vortex sheets created by a varying circulation along the blade span and from interaction of the different velocities over the pressure and suction surfaces. Tip clearance flows are created when the undeflected throughflow across the clearance gap combines with the flow caused by the pressure difference between pressure and suction surfaces. The relative motion between a blade and the casing boundary layer result in scraping and skewing effects. Finally, blade wakes produce viscous mixing after the trailing edges.

Efficient design of turbomachinery bladerows, especially in the transonic regime, requires accurate evaluation of these phenomena. The aerodynamic design starts with a two-dimensional circumferentially averaged solution in which the flow path is defined and the bladerows are modelled in terms of blade loadings, losses, and thickness distributions. This is followed by two-dimensional blade-to-blade analyses at several spanwise locations in order to design custom-tailored airfoil shapes that will produce the desired circumferentially averaged flow field. Additional analyses account for secondary flow effects. The blade shapes obtained are then

evaluated by means of a three-dimensional code, which provides a single unified solution for the design. Modifications to the blade shapes and flow path can then be made on the basis of additional three-dimensional solutions to achieve the final design of the bladerow.
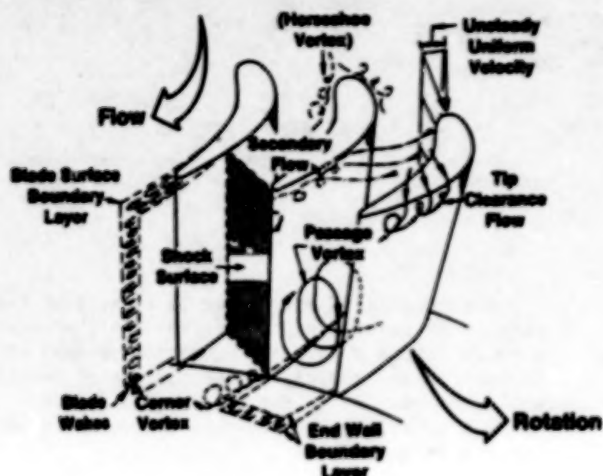
Figure 1. Complex Flow Phenomena in Turbo-
machinery.

Inviscid 3-D Nozzle Flow

A great deal of useful design information about the structure and general characteristics of turbomachinery flows can be obtained from three-dimensional inviscid analyses. The inviscid flow determines the pressure distributions on the blade surfaces, except for regions of local flow separation, and can be used to evaluate many of the features of the secondary flows produced in the bladerow passage. Therefore, the final design of conventional bladerows are now carried out with the use of a three-dimensional inviscid Euler Code, EULER3D, developed by Dr. D. G. Holmes[1] at the GE Research and Development Center (GE-R&DC). The algorithm used in that code is based on a scheme developed by Jameson, et al.[2] The Euler equations are discretized in space using a straightforward finite-volume scheme that is equivalent to central spatial differencing on a regular, rectangular grid. The discretized equations are marched forward in time to a steady state using an explicit, four-step, Runge-Kutta scheme. Some smoothing is needed to suppress wiggles and to capture shocks. Both smoothing tasks are fulfilled by a blend of second and forth-order smoothing.

The following results, taken from Reference 3, present the flow through the first-stage nozzle of a low-pressure turbine with non-cylindrical endwalls, for which experimental data was available in the form of traverses of total pressure just downstream of the trailing edge. Due to the long passage between the upstream high-pressure turbine and the low-pressure turbine, relatively thick boundary layers were present at the nozzle entrance, as indicated by total-pressure traverses taken there. To investigate the secondary flows produced in the nozzle by these thick boundary layers, an inlet profile of total pressure, based on the measured data, was specified for the computation. The three-dimensional grid used had 66825 nodes, 25 in the t   ntial, 33 in the radial, and 81 in the

axial directions, Figure 2. A three-dimensional representation of the nozzle passage is shown in Figure 3. A completely converged solution requiring approximately 900 iterations could be obtained in 9 hours on an IBM Model 3080, or in approximately 15 minutes on a CRAY-XMP. A solution sufficiently converged for design purposes could be obtained in half that time.
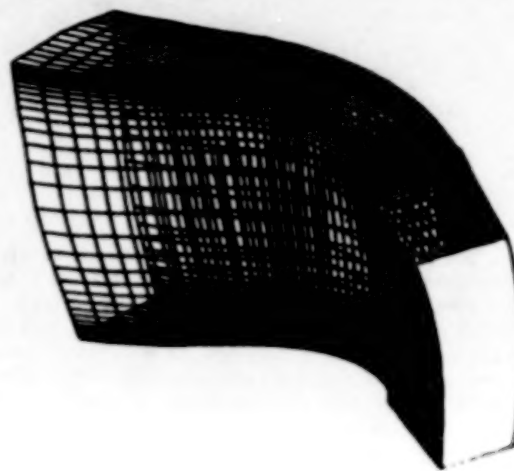
Figure 2. Grid for Inviscid Nozzle Flow Com-
putation.

Figure 3. Grid Representation of Nozzle Bladerow.

The formation of the secondary flow is shown by the streamline traces on the casing endwall and blade surfaces, Figures 4 through 6. On the casing endwall, the flow is swept toward the suction surface by the action of the cross-passage pressure gradient on the low momentum fluid near the endwall. The non-cylindrical endwalls produce generally radially outward flow in the entire passage. However, superposed on this are the radial flows due to the passage secondary flow. On the pressure surface, the secondary radial flows are from pitchline toward each endwall; on the suction surface, the secondary radial flow is toward the pitchline.

The generation of the corner vortex is shown by tracing the location of particles in several blade-to-blade streamsheets near the tip, Figure 7. As the flow progresses from leading

150

edge to trailing edge and downstream, the particles near the suction surface are generally swept radially inward, while those originating on the pressure side are swept across the passage along the tip.

Figure 4. Inviscid Streamlines on Nozzle Endwall.
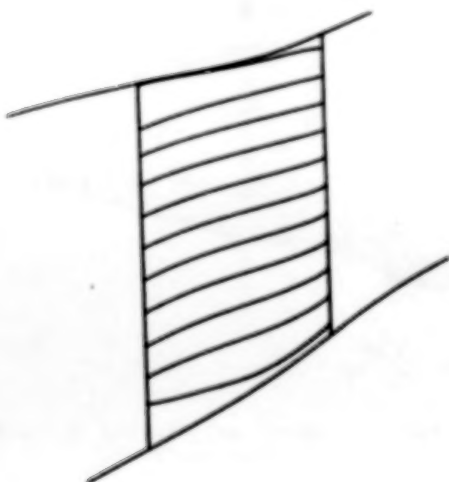
Figure 5. Inviscid Streamlines in Nozzle Pressure Surface.
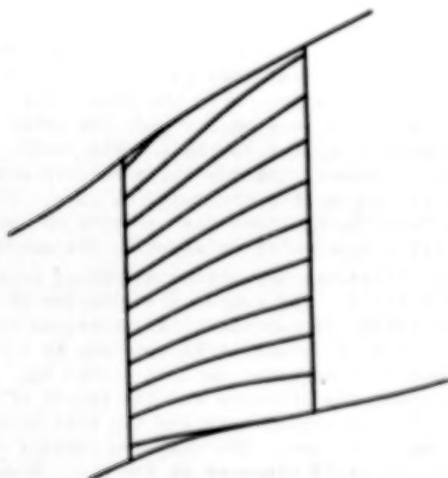
Figure 6. Inviscid Streamlines in Nozzle Suction.

Figure 7. Streamline Traces Through Nozzle Passage.

For this bladerow, contours of exit total pressure had been produced from experimental data. The calculated values are compared in Figure 8. The presence of the secondary flow vortex is clearly demonstrated. Since the inviscid computation has no provision for blade boundary layers or mixing downstream of the trailing edge, no wake effects are produced.

Test Data (Traverse Plane)

Euler 3D Result (Repeating Point)

Figure 8. Comparison of Computed and Measured Contours of Total Pressure.

151

Viscous 3-D Nozzle Flow

Although inviscid solutions can indicate many of the features of real turbomachinery flows, viscous analyses are required to evaluate local regions of separated flows, frictional forces, heat transfer, wake effects, etc. For most turbomachinery applications, these phenomena must be evaluated in environments of high Reynolds number with thin turbulent boundary layers. This places a large burden on the analysis in the form of very dense grid requirements in regions of high shear along the blade and endwall surfaces.

A three-dimensional viscous turbomachinery code has been developed at GE. Although the code is not yet a part of the design system, the availability of a supercomputer, with its number-crunching power and memory capacity, is accelerating the transition of the code into the design process. The NAH code,[4] developed by Dr. C. Hah at the GE-R&DC is a fully elliptic, compressible, turbulent, viscous flow program capable of calculating the three-dimensional flow inside a cascade of airfoils at design and off-design conditions. The Reynolds-averaged Navier-Stokes equations are solved together with either an algebraic Reynolds-stress turbulence model or a two-equation (k-ε) turbulence model. The finite-difference formulation is based on the control-volume methodology of Patankar and Spalding in which a pressure-correction equation is solved along with the governing equations. The fluid dynamic conservation equations and the transport equations for the turbulent quantities are solved sequentially on a staggered grid. The highly non-linear and coupled set of equations are solved on the grid nodes with an iterative method of solution, using an upwind discretization scheme for the convective terms.

Viscous solutions have been obtained for the same nozzle bladerow previously described for the EULER3D application. The results presented here were obtained by Dr. Hah, and documented by J. Laylek.[5] A fine grid was used, comprised of 64260 nodes, 36 in the tangential, 35 in the radial, and 51 in the axial directions. Figures 9, 10, and 11 show the grid patterns in the blade-to-blade, crossflow, and meridional planes, respectively. The solution was obtained on an IBM model 3080 mainframe computer, using double precision. Starting from a uniform flow condition, 2000 iterations were required to obtain a converged solution. The computation took approximately 70 hours of CPU time.

Figure 10. Crossplane Grid for 3D Viscous Calculations.
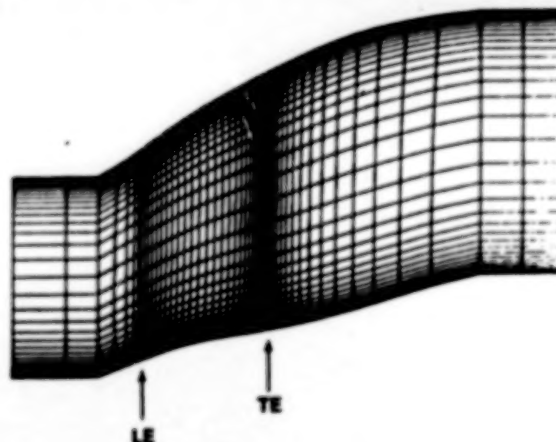
Figure 11. Meridional Grid for 3D Viscous Calculations.

The total-pressure contour levels at 0.5 percent increments are compared to the experimental data at the downstream measurement plane, Figure 12, and show good qualitiative and quantitative agreement with the data. The existence of the loss region near the outer wall is properly simulated in the computational results. However, the overall predicted wake region is larger than the measured wake. This is due to "artificial viscosity" created by the numerical scheme which is added to the molecular and eddy viscosity mechanisms naturally present in the flow field. The radial distribution of the mass-weighted, circumferentially averaged and normalized total pressure is compared to the experimentally measured data in Figure 13. This figure shows the presence and the extent of the predicted loss region near the tip with respect to the measured losses. The computed results do not exhibit the rapid recovery at the tip. However, there is excellent agreement over 85 percent of the span, which confirms the excellent comparison between computations and experiments seen in Figure 12.

Figure 9. Blade-to-Blade Grid for 3D Viscous Calculations.

Test Data

Contours represent increments of .005 in PT/PT

Creative
Surface 42
Stagnation Pressure
CONTOURS
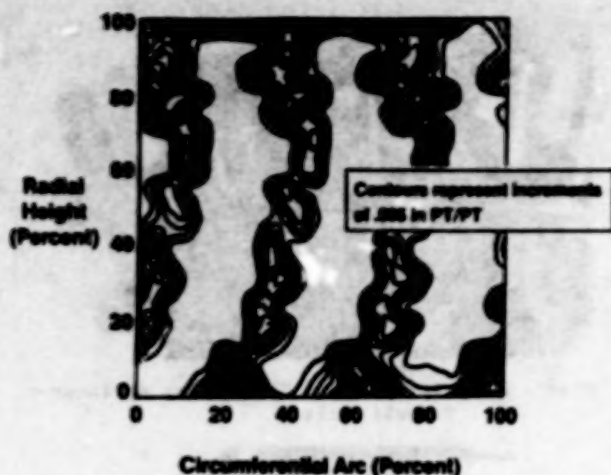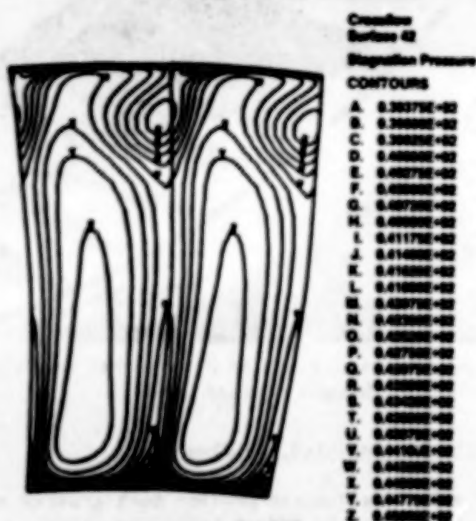
Viscous Solution

Figure 12. Comparison of Computed and Measured Contours of Total Pressure.

The following set of plots were included in Reference 5 to describe and to help verify the computed flow field. Figures 14 and 15 show the velocity vectors and the streamline pattern near the suction surface. Figure 16 is a photograph of the streamline pattern obtained on the suction surface near the stator exit area. This pattern was obtained in a flow visualization experiment using lampblack and oil traces. A careful examination of the vector plot in Figure 14 shows that the downward direction of the vectors near the outer wall agree well with the observed flow pattern in Figure 16. The region where the flow appears to move toward the pitchline corresponds to the high loss section in the total-pressure plot of Figure 13. The endwall streamlines, near the inner and outer endwall surfaces, are shown in Figures 17 and 18, respectively. Photographs of the streamline patterns on the endwall surfaces from the flow visualization experiments, Figures 19 and 20, substantiate the predicted patterns shown in Figures 17 and 18.
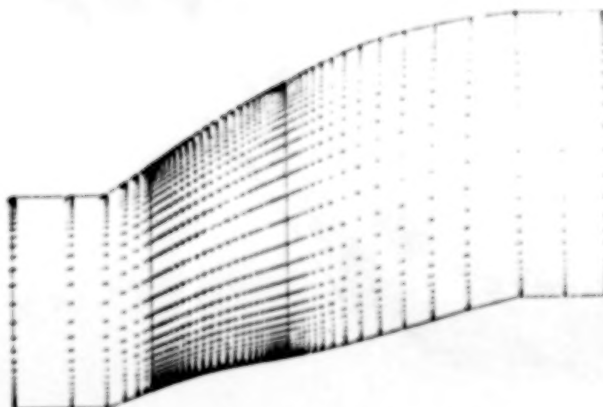
Figure 14. Velocity Vectors in Meridional Plane Near Suction Surface.

Figure 13. Radial Distributions of Circumferentially Mass-Averaged Total Pressure.
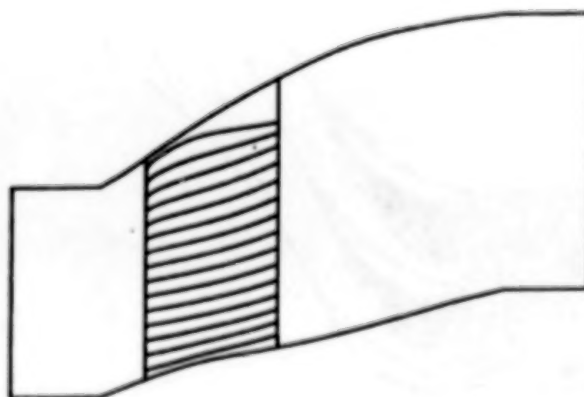
Figure 15. Streamline Pattern Near Suction Surface.

153

Figure 16. Photograph of Flow Traces on Aft Suction Surface.
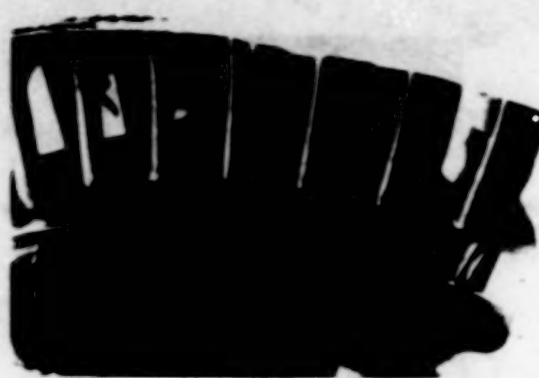
Figure 19. Photograph of Flow Traces on Inner Endwall Surface.

Figure 17. Streamline Pattern Near Hub Surface.

Figure 20. Photograph of Flow Traces on Outer Endwall Surface.

Inviscid 3-D Unducted Fan Flow

Propfan engines can provide much greater mass flows than those of modern turbofans, thus providing the potential for greater propulsive efficiency. NASA's Advanced Turboprop Program is aimed at establishing the technology for single-rotation and double-rotation propfan engines. Large fuel savings have been estimated for single-rotation propfan configurations; even greater savings are estimated for advanced counter-rotation designs. The GE Unducted Fan Engine (UDF[TM]), Figure 21, has such a counter-rotation design, in which the blades rotate at the same speed, but in opposite directions.
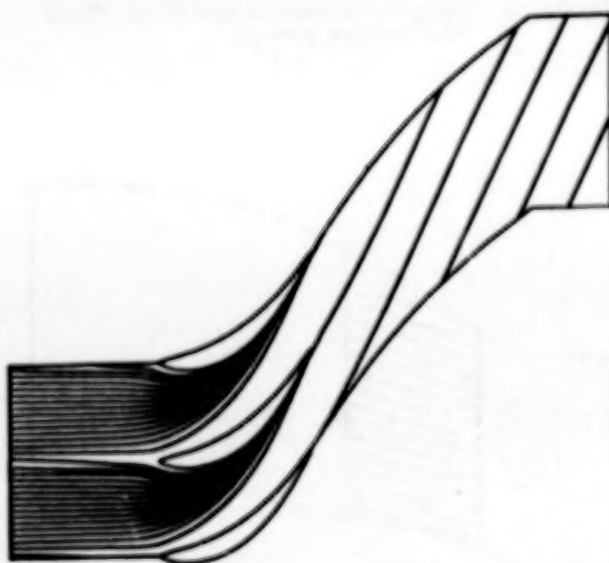
Figure 18. Streamline Pattern Near Tip.

Figure 21. General Electric Unducted Fan Engine.

154

Current aerodynamic design of the GE-UDF™ follows the same general procedure as for conventional bladerows, described previously. That is, a circumferentially averaged flow field solution is obtained, with suitably prescribed chordwise and spanwise loadings, losses, and blockage. This is followed by two-dimensional blade-to-blade and secondary flow analyses to determine the basic blade shapes. The resulting propfan bladerows are then analyzed with the EULER3D code to produce the final design. The EULER3D code has been modified to handle the far-field boundary conditions beyond the bladerow tips.

For the case of counter-rotating unducted fans, the design should include the interaction between the two bladerows. The approach presently utilized is to analyze one bladerow in detail, with the effects of the other bladerow simulated by axisymmetric source terms in the three-dimensional equations. Mass sources in the continuity equation simulate the effects of blade blockage; force terms in the momentum equations simulate the turning in the adjacent bladerow; work terms in the energy equation represent the conservation of enthalpy simultaneously. The source terms are computed by performing an axisymmetric analysis of the flow through the primary and secondary bladerows. This axisymmetric solution is passed to the Euler solver as a starting solution and the Euler source terms are calculated as the residuals of the initial solution. Thus, each bladerow can be designed separately, assuming only that the other bladerow meets its design intent. Either upstream or downstream bladerows can be simulated in this manner.

Results are shown in Figures 22 and 23 for the EULER3D solutions of each of the bladerows of a counter-rotating UDF™ at a flight Mach number of 0.72. Figure 22 presents the contours of local Mach number on the forward rotating bladerow, which include the fluid dynamic effects of the aft rotating bladerow. The location of the aft bladerow is indicated in the figure by the darkest band on the hub surface. For this solution, the aft bladerow is, of course, represented by axisymmetric source terms. Similarly, Figure 23

Figure 23. Contours of Local Mach Number on Aft UDF™ Bladerow.

presents the contours of local Mach number on the aft rotating bladerow, which include the effects of the forward bladerow. The location of the forward bladerow is indicated in that figure by the lightest band on the hub surface. High supersonic Mach numbers are present in the tip regions of both bladerows and extend almost to the hub on the aft bladerow. Although the bladerows being simulated in these solutions are represented in the analysis by axisymmetric terms, the bladerows being analyzed produces periodic flow effects in the region occupied by the simulated bladerows, as can be faintly seen by the varying width of the lightest band in Figure 23. An indication of the computational grid used for the calculations is shown on the inside surfaces of the hub. The grid consisted of 41905 nodes, 17 in the tangential, 29 in the radial, and 85 in the axial directions. The computation time for each bladerow solution was 5 minutes on a CRAY-XMP.

HYPERSONIC PROPULSION

There has been a resurgence of interest in SCRAMJET technology as the feasibility of hypersonic propulsion is re-examined. One of the factors that has been put forth as a key improved technology which can lead to successful design of hypersonic vehicles and engines is the availability of new sophisticated computational codes. These codes will provide detailed solutions to the complex flow problems which must be solved. The full Navier-Stokes equations can be solved in one form or another to analyze the internal and external flows involved. The supercomputers required to run these codes in an efficient manner are now available. An effort is underway at GE-AEBG to implement such codes in a suitable design system. The following sections illustrate the type of design problems involved in the design of engine inlets and some of the codes currently being actively pursued by GE-AEBG.

Vehicle Forebody Flows

The performance of a hypersonic propulsion engine is greatly dependent upon the vehicle forebody, since it determines the amount of air captured and the efficiency of that process. The forebody provides a system of ramps which produce external shocks to compress the air prior to

Figure 22. Contours of Local Mach Number on Forward UDF™ Bladerow.

ingestion into the engine inlet. The compression
efficiency is degraded by shock losses, wall
shear, and heat loss. Therefore, the shock layer
properties of the forebody must be accurately
determined, including the effects of local
phenomena. Since the leading edge must have
finite bluntness, a region of subsonic/transonic
flow is produced with the attendent features of
vorticity and entropy swallowing. Along the
compression surface, there are real-gas effects,
transition of the boundary layer to turbulent
flow, with high-Mach-number effects which should
be included in the turbulence model. At the
compression corners, there is always the
possibility of boundary-layer separation. The
surface effects, of course, influence the vehicle
design. The surface heating determines the
cooling requirements, and the surface friction and
pressure contribute to the force balance.

Many codes have been, and continue to be,
developed to analyze these flows, ranging from
coupled inviscid/boundary-layer codes, to
Parabolized Navier-Stokes (PNS) codes, to full
Navier-Stokes codes. Several of these are being
evaluated by GE-AEBG. One is the so-called SCRAMP
code, developed by SAIC.[6] This is a PNS code
which requires significantly less computer
capacity and computational time than an elliptic
code, and is therefore more advantageous as a
design tool. The code uses the linearized
implicit algorithm of Beam and Warming, the
near-wall subsonic layer treatment of Schiff and
Steger, either the Baldwin-Lomax or two equation
$k-\epsilon$ turbulence model, and a fitted bow shock.
The upstream influence of the flow can be
accounted for by global pressure iteration. For
blunt-nosed bodies, the space-marching procedure
is initiated from a viscous shock layer solution
produced by the VSL code.[7]

Some typical results from the SCRAMP code are
shown in Figures 24 and 25. Calculations were
made for a two-dimensional laminar flow over a
blunted double-ramp forebody at a flight Mach
number of 18. The computations were made with 75
grid points across the shock layer and took
approximately 3 minutes on the CRAY XMP. For this
case, no separation occurred at the second ramp.
Profiles of properties across the shock layer are
shown at axial locations just ahead of the second
ramp and at the entrance to the inlet. In the
figure, the profiles at point A are shown as solid
lines, with the thickness of the shock layer
indicated by the height yA. With the exception of
the viscous effects near the ramp surface, the
profiles are uniform. The profiles at point B are
shown as dashed lines. The shock layer at that
point is considerably thinner due to the
additional compression of the second ramp. Point
B is also downstream of the intersection of the
bow shock and the secondary shock produced by the
second ramp. The intersection of the two shocks
produces an expansion fan within the shock layer,
in addition to the resultant downstream shock.
This causes variations in the inviscid portions of
the shock layer near the shock. The results of
such a solution are then used to determine the
mass flow and state of the air entering the
inlet. Of particular interest for inlet design
are the variations of η_{KE}, the kinetic energy
efficiency, shown in Figure 25.
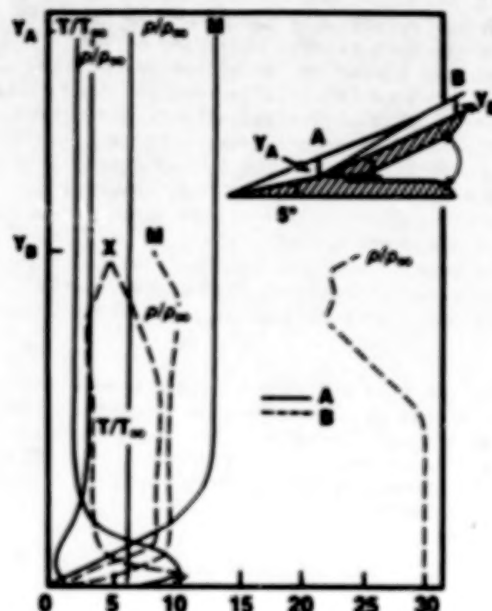
Figure 24.   Profiles of Shock-Layer Properties on
a Double-Ramp Forebody.
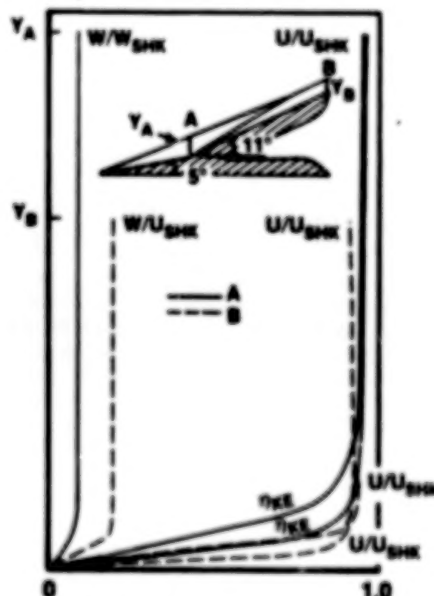
Figure 25.   Profiles of Shock-Layer Velocities and
Kinetic-Energy Efficiency.

Engine Inlet Flows

The engine inlet provides additional compres-
sion of the air to some minimum cross-section or
throat and presents its own set of flow problems.
The cowl leading edge produces an additional bow
shock, which ultimately impinges on the ramp
surface, producing a strong shock/boundary-layer
interaction, possibly causing local separated
flow. In addition, there is the existence of the
corner flows due to the inlet sideplates and the
possibility of local effects due to boundary-layer
bleed. The inlet solution provides knowledge of
the flow conditions at the throat and the losses
produced by the shocks and viscous effects. This
information is required for the engine cycle and
performance calculations. And, just as for the

forebody, the surface heating determines the engine cooling requirements, while the surface friction and pressure contribute to the force balance.

Although the internal flow is really three-dimensional, analysis of even a two-dimensional simplification of an inlet flow requires sophisticated flow field codes. Among those being evaluated are the SAIC SCRINT code,[6] the NASA/Lewis PEPSIS[8] code, the NASA/Langley NASCRIN code,[9] and an Euler code called TRIAD2D.[10] The SCRINT code is the internal-flow equivalent of the SCRAMP code, i.e., a space-marching PNS code, which relies on profiles of initial data at the inlet entrance, obtained, for example, from a SCRAMP solution. PEPSIS is a three-dimensional supersonic viscous marching analysis for the flow over the forebody and through the inlet.

The NASCRIN code utilizes the time-dependent finite-difference method to solve the full Navier-Stokes equations in conservation form, using the explicit, predictor-corrector method of MacCormack for the solution algorithm and the algebraic, two-layer eddy viscosity model of Baldwin and Lomax for calculations of turbulent flow. An illustration of the results from the NASCRIN code are presented in Figure 26 for a two-dimensional inlet. This perfect-gas solution was computed for a uniform flow along the ramp surface at a Mach number of 5; no initial ramp boundary layer was assumed. The computation, which used a 53 x 61 grid, required 2574 cpu-seconds for 60,000 iterations on the CRAY-XMP. The plot of the flow vectors indicates the grid locations. The contours of Mach number define the bow shock produced by the leading edge of the slightly blunted cowl, and the reflected shocks which occur downstream. The contours of static pressure provide a sharper picture of this shock structure. Although the contours of total pressure show the extent of the loss regions due to the surface boundary layers, they tend to smear out the shocks near the throat.
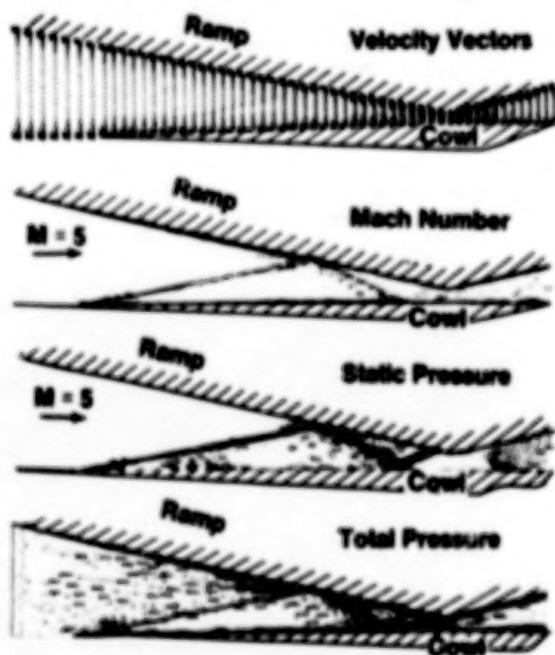
Figure 26. Contours of Inlet Flow Field Properties.

TRIAD2D code, which is currently under development by Dr. D.G. Holmes at GE-SRDC, utilizes a method recently devised by A. Jameson.[11] This calculation procedure uses a triangular adaptive grid to build an unstructured network, one without a set of coordinates, by first connecting a set of points, working outward from each boundary surface. Where the patterns from adjoining surfaces meet, the code symmetrically removes excess points and reconnects them into a fairly regular triangular array. This method of building a grid has the advantage that grid points can easily be added to any region of the flow without disturbing the grid in other regions. In the TRIAD2D code, grid points are added in those regions where local gradients are highest, such as along shock waves.

The two-dimensional code currently solves only the Euler equations for a perfect gas. Results are shown for the flow in an inlet for which the entrance Mach number is 7.7. The calculation included the region of flow along the external surface of the cowl. The resulting grid, which was adaptively changed during the calculations, is shown in Figure 27. The solid black regions indicate the large number of grid points added in the regions where shock waves occur in the
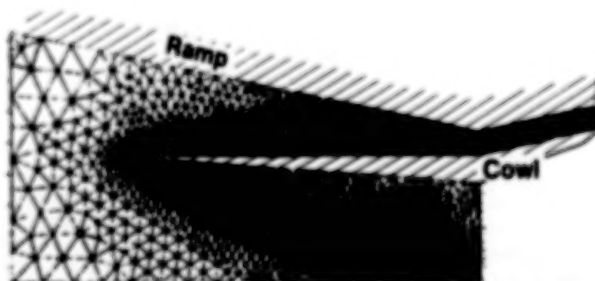
Figure 27. Triangular Grid for the TRIAD2D Code.
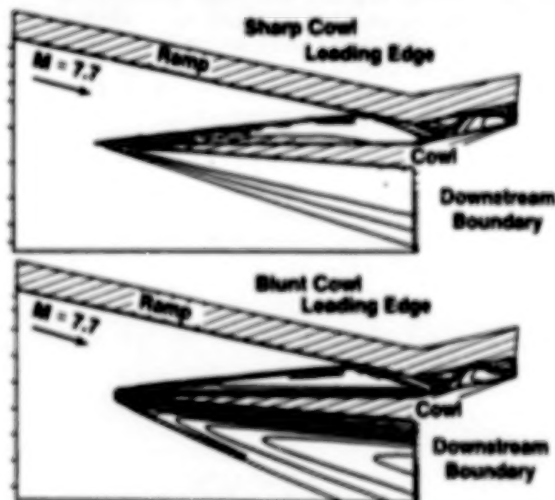
Figure 28. Inlet Contours of Mach Number.

internal flow and where expansion waves occur on the external cowl surface. The total number of grid points is 11991. Contours of Mach number are presented in Figure 28 for solutions with sharp and blunted cowl leading edges. The cowl shock and its reflection from the ramp are clearly shown in both cases. The solution for the blunted leading-edge, however, also shows a significant

variation in Mach number due to the entropy layer along the cowl inner surface . These solutions required approximately 1220 cpu-sec for 5070 iterations on the CRAY X-MP computer.

Although currently providing only an inviscid solution, the TRIAD2D code is another illustration, similar to the EULER3D code, of how a robust inviscid code can be a vital part of the design process by providing a complex flow solution in a rapid efficient manner. The shock locations and distributions of surface pressure are the paramount initial concerns in an inlet design, since they can indicate possible regions of flow separation. Rapid evaluation of candidate inlet geometries to achieve improved shock structure and strengths is enhanced by a code which requires minimum grid manipulation by the user. A unique feature of the TRIAD2D code is its adaptive grid which relieves the user of a priori specification of grid points in regions of interest whose location is not known beforehand.

SUMMARY

Supercomputers provide for more rapid development of complex aerodynamic codes and for faster introduction of the codes into the design process. The large storage capacity of these computers permits the user to specify grid sizes appropriate to the problem being analyzed. Their rapid computational time permits results to be obtained on a time scale that is useful in design studies. Important attributes of a code from a design standpoint are that they be relatively easy to use and sufficiently robust to be applied over the desired design conditions. In the turbomachinery area, the three-dimensional inviscid EULER3D code is already part of the design system, providing a single unified solution for the design of conventional and unconventional bladerows. The three-dimensional viscous NAN code is almost at that stage for conventional bladerows. Results from both of these codes were presented. In the hypersonic propulsion area, several codes are currently being exercised to determine their appropriateness for utilization in the inlet design process. Among these are the SCRAMP, SCRINT, and PEPSIS PNS codes, the MASCHEN Navier-Stokes code, and the Euler TRIAD2D code. Results from several of these codes were presented. The availability of a CRAY-XMP at GE-AEDC will accelerate the selection process.

REFERENCES

1. Holmes, D.G. and Tong, S.S., "A Three-Dimensional Euler Solver for Turbomachinery Blade Rows," ASME Paper 84-GT-79, October 1, 1984.

2. Jameson, A., Schmidt, W., et al, "Numerical Solutions of the Euler Equations by Finite-Volume Methods Using Runge-Kutta Time-Stepping Schemes," AIAA Paper 81-1259, 1981.

3. Gregory, B.A., "A Comparison of Results Obtained from the Euler Inviscid 3D Code Program (EULER3D) with Those Obtained in A Cascade Test Configuration for the E-Cubed Vane," General Electric Turbine Design and Evaluation Memo TDE 0031, December 1984.

4. Hah, C., "Navier-Stokes Calculations of Three-Dimensional Compressible Flow Across A Cascade of Airfoils With An Implicit Relaxation Method," AIAA Paper 85-0555, 1985.

5. Leylek, J., "NAN Code", GE-AEDC Memo dated August 19, 1985.

6. Krawczyk, W.J., Jr., Rajendran, N., et al, "Computational Models for The Analysis and Design of Hypersonic Scramjet Components," Paper AIAA-86-1596, presented at the AIAA/ASME/SAE/ASEE 22nd Joint Conference, Huntsville, Alabama, June 1986.

7. Curtis, J.T., "Hemisphere Viscous Shock Layer Code for Equilibrium Air," AEDC-TR-82-22, January 1984.

8. Buggeln, R.C., McDonald, H., et al, "Development of a Three-Dimensional Supersonic Inlet Flow Analysis," NASA CR 3218, January 1980.

9. Kumar, A., "Numerical Simulation of Flow Through Scramjet Inlets Using A Three-Dimensional Navier-Stokes Code," AIAA Paper 85-14, July 1985.

10. Holmes, D.G. and Lamson, S.H., "Adaptive Triangular Meshes for Compressible Flow Solutions," GE-CRAD Report CRD079, April 1986.

11. Jameson, A., and Mavriplis, D., "Finite Volume Solution of the Two-Dimensional Euler Equations on a Regular Triangular Mesh," AIAA Journal, Volume 24, No. 4, April 1986.

N87
26011
UNCLAS

COMPUTATIONAL FLUID DYNAMICS RESEARCH AT THE
UNITED TECHNOLOGIES RESEARCH CENTER REQUIRING SUPERCOMPUTERS

Anton J. Landgrebe
Manager, Aeromechanics Research

United Technologies Research Center
East Hartford, CT

ABSTRACT

An overview of research activities at the United
Technologies Research Center (UTRC) in the area of
Computational Fluid Dynamics (CFD) is presented.
The requirement and use of various levels of
computers, including supercomputers, for the CFD
activities is described. Examples of CFD directed
toward applications to helicopters, turbomachinery,
heat exchangers, and the National Aerospace Plane
are included.

Helicopter rotor codes for the prediction of rotor
and fuselage flow fields and airloads have been
developed with emphasis on rotor wake modeling.
Airflow and airload predictions and comparisons with
experimental data are presented. Work is currently
underway at UTRC for the development and application
of CFD codes related to the analysis of the inlet,
scramjet combustor, and nozzle flow fields of the
National Aerospace Plane. Examples are presented of
recent parabolized Navier-Stokes and full Navier-
Stokes solutions for hypersonic shock-wave/boundary
layer interaction, and hydrogen/air supersonic
combustion. In addition, other examples of CFD
efforts at UTRC in turbomachinery Navier-Stokes
methodology and separated flow modeling are
presented.

A brief discussion of the 3-tier scientific
computing environment at UTRC is also presented, in
which the researcher has access to workstations,
mid-size computers, and supercomputers. The recent
UTRC link to the Numerical Aerodynamic Simulation
(NAS) supercomputer system at the NASA Ames Research
Center and a helicopter code demonstration on this
supercomputer are described. A new activity to
evaluate massive parallel processing supercomputers
for CFD applications, using CFD codes for fluid flow
model problems, is also described.

INTRODUCTION

The state-of-the-art of CFD and computer technology
have simultaneously reached advanced levels such
that new capabilities are providing unique
opportunities for the CFD researcher. CFD problems
that were impossible to consider just two years ago
are now feasible, and as a result, progress is now
accelerating rapidly in the CFD field. NASA has
played a key role in leading the way for both CFD
technology and the adaptation and provision of
supercomputers for CFD research. UTRC is
interacting with NASA, universities, computer
organizations, and the Divisions of the United
Technologies Corporation (UTC) (such as Pratt &
Whitney, Sikorsky Aircraft, Hamilton Standard, and

Carrier) to adapt, develop, refine and evaluate CFD
codes for application to gas turbines, helicopters,
propellers, and heat exchangers. A wide range of
CFD problems are being investigated which include
the various levels of aerodynamics methodology
(lifting line/surface, full-potential, Euler, and
Navier-Stokes methods). Examples of UTRC CFD
activities related to the forementioned variety of
applications and methodology levels are presented
herein.

Computer access and capability level have rapidly
advanced at UTRC in the last year. UTRC's computing
system is based on the 3-tier computer environment
shown in figure 1. This consists of workstations
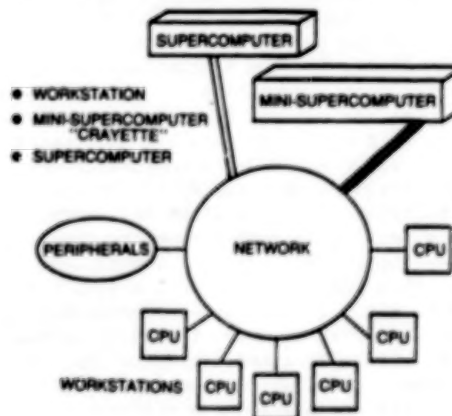
Figure 1. UTRC 3-Tier Computer Network

with built-in or accessible processors of limited
power, mini-supercomputers ("Crayettes") which
typically have one-tenth to one-third the computing
power of the supercomputers, and supercomputers of
varying types and capabilities. The computers have
been specifically selected for performing CFD
research. They cover the complete range of computer
categories (scalar/vector and serial/parallel/
massive parallel). Access is provided to the
research engineers through an internal Ethernet
network system. Many of the computers are off-site
and are accessed through a variety of network
systems which include high speed, long-haul
communications networks. On-site computers include
VAX and Apollo workstations, Perkin-Elmer computers,
and an Alliant mini-supercomputer. Off-site
computers are listed below. Of these, the UTC
supercomputer is the CRAY X-MP, operational in 1987,
and located at Pratt & Whitney Government Products
Division in West Palm Beach, Florida. It is
remotely linked to the local network systems at UTRC
and the UTC Divisions. Several off-site computers

are being used to evaluate the use of massive
paralell processors for CFD. In particular, a
unique application of cellular automata techniques
will be discussed in the last section of this paper.

Off-site computers

- UTC - West Palm Beach   Cray X-MP
- NASA-Ames   Cray - 2 (NAS)
- NASA-Lewis   Cray X-MP
- NASA-Langley   Cyber 205
- Cray Research   Cray X-MP
- Kirtland Air Force   Cray X-MP
- Air Force Weapons Lab   Cray - 1
- Los Alamos Nat'l. Lab   Cray X-MP
- IBM Kingston   LCAP
- Thinking Machine Corp   Connection Machine

UTRC was selected in 1986 as a remote site
user/demonstrator of the new NASA Numerical
Aerodynamic Simulation (NAS) supercomputer system.
NAS is the computational facility at the NASA Ames
Research Center that currently includes the CRAY-2
high-speed processor with an approximately 250
megaflops speed/256 megaword central memory
capability. A high-speed network system linking the
NAS supercomputer located in California, to UTRC in
East Hartford, Connecticut, was made operational in
1986. Initial demonstration cases were successfully
run over the 56 kb/sec link from a VAX workstation,
as shown in figure 2. The initial demonstration
cases consisted of computations of the influence of
blade sweep on the airload distribution and sonic
delocalization for a representative helicopter blade
using a state-of-the-art 3-D aerodynamics analysis
developed jointly by NASA and UTRC. This activity,
endorsed by NASA and The American Helicopter
Society, is serving to demonstrate the remote use of
NAS for helicopter CFD codes. A description and
results of this NAS/helicopter CFD activity will be
presented herein. It is planned to continue this
NAS activity at UTRC with the following general
objectives: (1) to continue the use of NAS to
develop, demonstrate, and evaluate advanced
rotary-wing CFD codes for the prediction of
helicopter/propeller airloads and performance, (2)
to interact with NASA researchers on the use of NAS
to adapt and integrate flow solver, wake, and
rotary-wing CFD methodology, and (3) continue to
perform NAS remote-site demonstrations of helicopter
CFD codes for the helicopter industry.

Remote site (UTRC)/NAS communications network
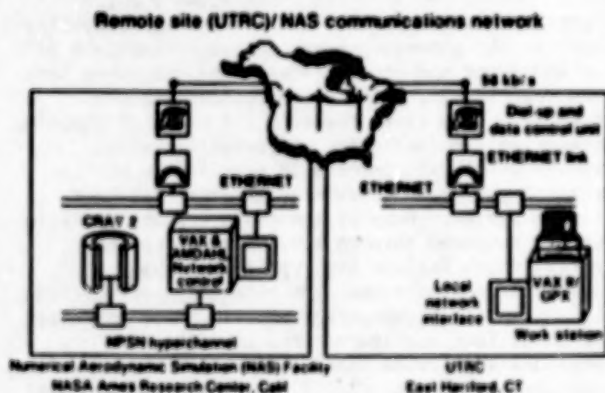
Figure 2. UTRC Remote-Site Link to NAS
Supercomputer at NASA Ames Research
Center

In addition to helicopter/propeller applications,
the use of NAS for the development and evaluation
of CFD codes related to the National Aerospace Plane
(NASP) has been separately proposed. Examples of
these codes and initial results are also presented
herein.

The following are the major subject technology areas
of this paper and the UTRC technical contributors to
each technology area are indicated accordingly:
Helicopter CFD (T. A. Egolf, P. F. Lorber, S. P.
Sparks, and A. J. Landgrebe), CFD for NASP,
Turbomachinery and Separated Flow Modeling (T. J.
Barber, J. E. Carter, R. L. Davis, and D. E.
Edwards), and Parallel Processing for CFD (A. F.
Haught, and E. B. Smith). In addition to UTC
Corporate sponsorship, NASA, Army, Navy, and Air
Force contract support has contributed to several of
the activities reported herein.

HELICOPTER CFD

The task of predicting the flow field and airloads
of a helicopter rotor continues to be of primary
importance for providing and evaluating improved
rotor designs. Also, the capability to predict
rotor induced flow velocities away from the main
rotor is important for the calculation of
aerodynamic interference effects at the fuselage,
tail rotor, and tail surfaces. Technological
advancement of rotor induced velocity and airloads
methodology has focused on the analytical modeling
of the rotor wake and the application of higher
level computational aerodynamics techniques to
represent the blades and their influence on the
airflow. This has become possible with the advent
of high-speed, large memory computers.

As part of a long-term effort to advance the
aerodynamic technology of helicopter rotors, studies
have been conducted at UTRC to develop methodology
for predicting the rotor wake, flow field and blade
airloads. Publications that document these studies,
which span a period of twenty years, are listed in
the author's overview of helicopter wake and
airloads technology (Landgrebe (1985, 1986)). The
scope of this effort has included analytical and
experimental research programs, distorted and
undistorted wake analyses, single and dual rotor
configurations, hover and forward flight conditions,
and blade airloads methods ranging from lifting line
to full potential. Aerodynamic methods pertaining
to these areas, developed or adapted at UTRC are
presented herein. Examples of related methodology,
developed by other researchers, are indicated within
the references cited in the above overview paper and
the references of McCroskey and Baeder (1985) and
Davis and Chang (1986).

Rotorcraft Wake Analysis

Several methods have been consolidated and expanded
at UTRC to form the Rotorcraft Wake Analysis, a
comprehensive helicopter aerodynamic analysis to
predict induced flow velocities both at and off the
rotor (Landgrebe and Egolf (1976)). This family of
component computerized analyses is normally used in
conjunction with rotor performance and airloads
analyses. A schematic of the Rotorcraft Wake
Analysis showing the input, output, and capabilities
of the computer program is presented in figure 3.
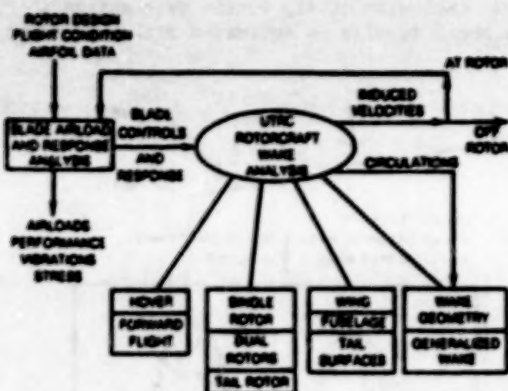
Figure 3. Schematic of Rotorcraft Wake Analysis Showing Input/Output and Capabilities of Component Codes

Briefly, the fundamental technical approach for the Rotorcraft Wake Analysis consists of the representation of each blade by a segmented lifting line, and the wake of the rotor by discrete segmented vortex filaments consisting of trailing vorticity, which result from the spanwise variation of blade bound circulation. The distribution of blade and wake circulation changes with azimuth position and is assumed periodic for each rotor revolution. The blades are divided into a finite number of radial segments, and the induced velocity at the center of each selected blade segment is computed by summing the contributions of all bound and trailing wake segments. The contribution of each vortex segment is obtained through use of the Biot-Savart law, which expresses the induced velocity in terms of the circulation strength of the vortex segment and its geometric position relative to the blade segment at which the induced velocity is desired. The blade bound circulation distribution is determined at each blade azimuth by expressing the wake circulations and induced velocities in terms of the unknown bound vortex strengths by means of the Biot-Savart law, and developing a set of simultaneous equations relating the bound circulation and local blade angle of attack at each blade segment. These equations thus involve the known flight condition, wake geometry, two-dimensional airfoil data, blade motion and control parameters, and the unknown blade bound circulation values. Solution of these equations yields the desired blade bound circulation values, which, when combined with the appropriate geometric relations in the Biot-Savart law, produce the required induced velocities at or away from the rotor blades. The influence of realistic airfoil data and blade motions and controls (e.g., for rotor trim) can be included through an iterative coupling with a blade airloads and performance program. The influence of the shed vorticity behind a blade, due to the time variation of blade bound circulation, can be included by the use of unsteady two-dimensional airfoil data in the airloads program.

Generality regarding the specification of the rotor wake geometry was retained in the computer programs by requiring only that the coordinates of the wake segment end points be stored with various options for obtaining the coordinates. Thus rotor wake geometry models ranging from the classical undeformed wake (figure 4) to the fully distorted

wake (figure 5) can be used. A computerized method for predicting the rotor distorted wake geometry is the UTRC Wake Geometry Analysis (Landgrebe (1969)). A generalized wake model has been made available which is based on generalized wake equations for hover (Landgrebe (1972)) and forward flight (Egolf and Landgrebe (1984)). A sample isometric view of the generalized wake model for forward flight is shown in figure 6.
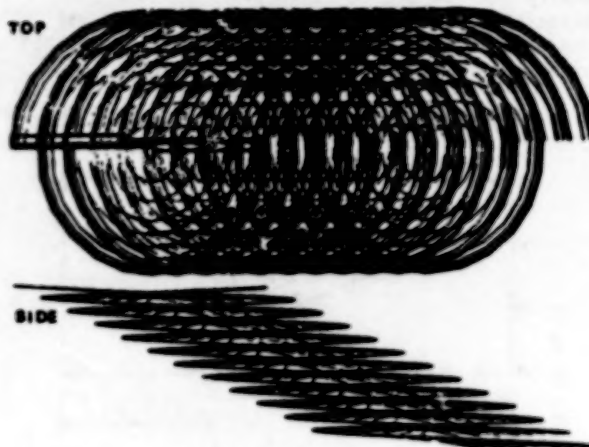
Figure 4. Classical Undeformed Wake Representation for a 30 Kt Forward Flight Condition
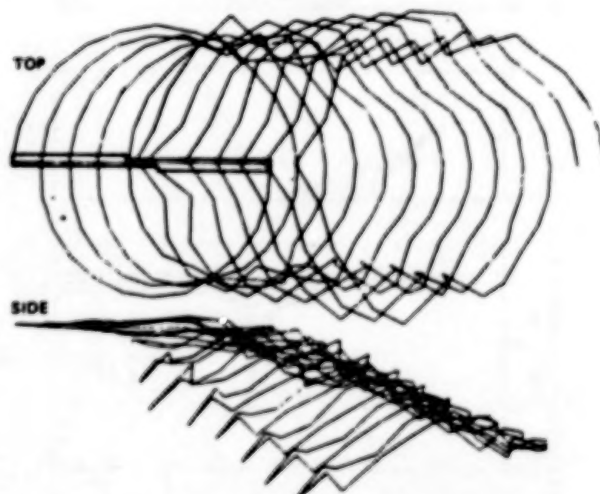
Figure 5. Distorted Tip Vortex Representation for a 30 Kt Forward Flight Condition
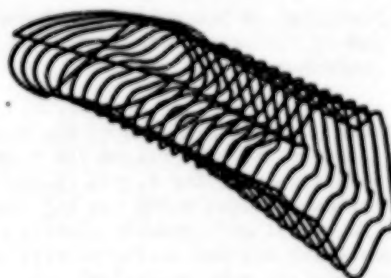
Figure 6. Isometric View of Generalized Distorted Tip Vortices

The ability of the component codes of the Rotorcraft Wake Analysis to predict rotor flow field velocities is shown for hover and forward flight conditions in figures 7 and 8 from Landgrebe and Egolf (1976). The experimental based generalized wake model was used for the hover condition and the predicted distorted wake geometry was used for the forward flight condition. It is noted that, although they are encouraging, these calculations are very sensitive to the wake model and wake geometry and the degree of correlation is not necessarily typical of all flight conditions and rotor blade designs, particularly some advanced tip designs.

indicated, inclusion of tip vortex deformation in the wake model results in increased higher harmonic
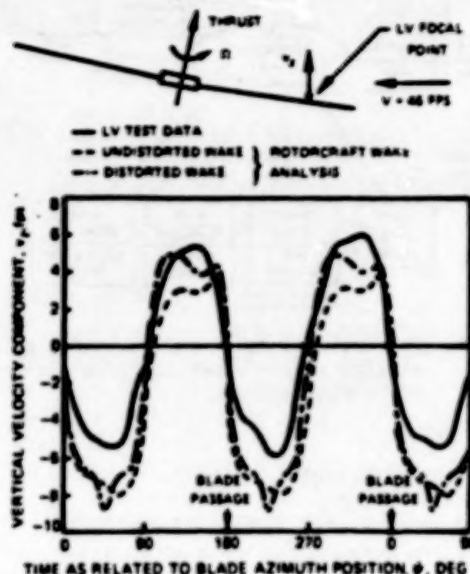
Figure 8. Predicted vs Measured Time Variations of the Flow Velocity at a Point Near a UTRC Model Rotor (Advance Ratio = 0.15)

Figure 7. Predicted vs Measured Instantaneous Induced Velocity Components of a Full-Scale Hovering Rotor

In forward flight, the deformation of the forward and lateral sides of the wake toward the rotor disk, shown earlier in figures 5 and 6, can result in close blade-vortex passages which can introduce severe local azimuthal and spanwise gradients in blade airloads which are not predicted with uniform inflow and undistorted wake analytical models. This is shown in figure 9 where the predicted airloads (blade lift distributions) based on the different inflow/wake models are presented for a representative rotor in the form of surface contour plots. As

Figure 9. Blade Lift Distributions Predicted With Various Wake/Inflow Models

162

content in the airload prediction. The outboard
advancing side of the rotor typically exhibits the
most severe vibratory airload gradients with
significant variations also on the outboard
retreating side. These impulsive airload
characteristics are of importance for helicopter
vibration and noise as well as performance.

The requirement for supercomputers for helicopter
airloads/wake predictions is well recognized when
the computational interaction of thousands of wake
elements with each other and with many blade
elements at each rotor azimuth are considered.
Also, rotor trim normally requires several airload/
wake iterations. The computer requirements are
further compounded when the aerodynamic interactions
of the rotor with other helicopter components are
computed (fuselage, tail rotor, tail surfaces etc.).
Wake modeling for airload prediction of the various
helicopter components is being pursued at UTRC.
Earlier UTRC investigations of rotor-fuselage/wing/
tail interaction are cited in the previously
mentioned overview (Landgrebe (1985, 6)).

The influence of the rotor airflow on fuselage
vibratory airloading is currently being considered
by P. F. Lorber and T. A. Egolf under a NASA/Army
contract. Experimental results have indicated that
the rotor blades and wake can produce significant
oscillating fuselage pressures at principally the
fundamental blade passage frequency. These pressure
pulses have been recognized as a fuselage vibration
mechanism, but this mechanism and its effect have
not been fully investigated analytically.
Methodology is currently being developed at UTRC to
approximate the rotor wake deformation due to the
fuselage and to calculate the unsteady fuselage
pressures. Thus far, provisions have been made for
prescribed time variant local deformation of the
rotor tip vortices around the fuselage surfaces and
the calculation of the airflow and airloads on the
panels representing the fuselage surfaces. Wake
patterns and flow vectors for sample fuselage shapes
and a 0.15 advance ratio condition are shown in
figure 10.
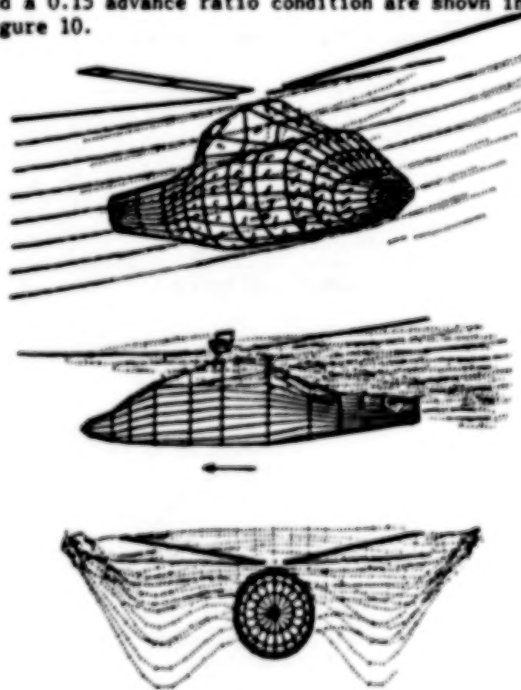
Full Potential Flow/Wake Analysis

The Rotorcraft Wake Analysis results presented
earlier are based on a lifting-line representation
for the blades. In order to provide a more accurate
aerodynamic representation of the blades and more
properly include chordwise airloading, blade
thickness and compressibility effects, a full
potential flow analysis has been extended at UTRC for
the inviscid solution of the rotor and wake flow
field. A NASA three-dimensional full potential
analysis (ROT22), by Arieli and Tauber (1979), has
been recently revised, under a NASA contract, at UTRC
by Egolf and Sparks (1985, 1986) to include the rotor
wake influence. The NASA analysis, based on an
infinite computational domain, was revised to
incorporate an inner and outer domain around each
blade and match the domain boundary solutions in
three dimensions. Blade surface flow pressure
distributions can be computed for subsonic and
transonic flow conditions.

Briefly, the ROT22/WAKE method consists of the use of
a finite difference scheme to solve the nonlinear
near blade flow (inner domain), while the remainder
of the flow field (outer domain) is computed using a
discrete vortex representation of the wake. A type
of solution matching is employed for the resulting
inner and outer domain problem. Although the
solution is based on the full potential equation,
details of the wake distortion are modeled using
prescribed wake methods. This allows for the
description of the wake to be as complex (or as
simple) as desired while maintaining the relatively
low cost full potential method for the detailed blade
airloads. The finite inner domain and its
computational boundary is shown in figure 11 with the
hovering blade wake model represented by vortex
filaments. The cut-surface that represents the blade
wake in the inner domain for the full potential
solution is adapted to the prescribed wake surface
such as that determined from the generalized wake
geometry described earlier. An embedded vortex
technique has recently been developed to accommodate
in the full potential solution the blade-vortex
interaction for finite length vortex elements near
the blade in the inner domain.

The analysis has been applied by Egolf and Sparks
(1985) to compare with hover data from model rotors.
A comparison of predicted and measured spanwise lift

Figure 10. Wake Modeling for Rotor-Fuselage
Aerodynamic Interaction
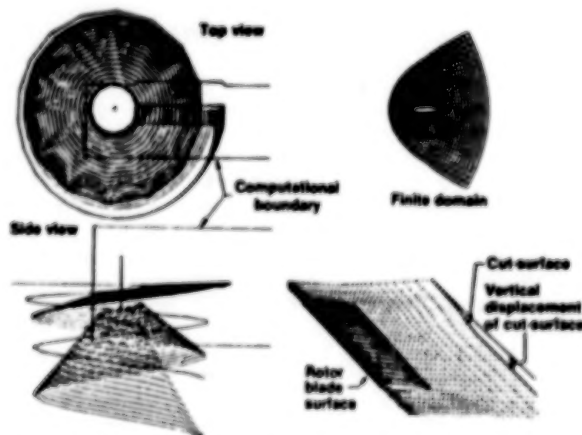
Figure 11. Schematics of Computational Domain
Boundary and Wake Representation

163

distributions are presented for an Army rotor (Caradonna and Tung (1981)) in figure 12. The influence on the chordwise pressure correlation near the blade tip of increasing the tip Mach number to transonic conditions is shown in figure 13. The formation of a shock is evident at this location as the blade progresses from low to high tip Mach number.

— Hover
— $M_{TIP} = 0.439$
— $C_T = 0.0046$

● Model test data, Army rotor
— Full potential/wake analysis
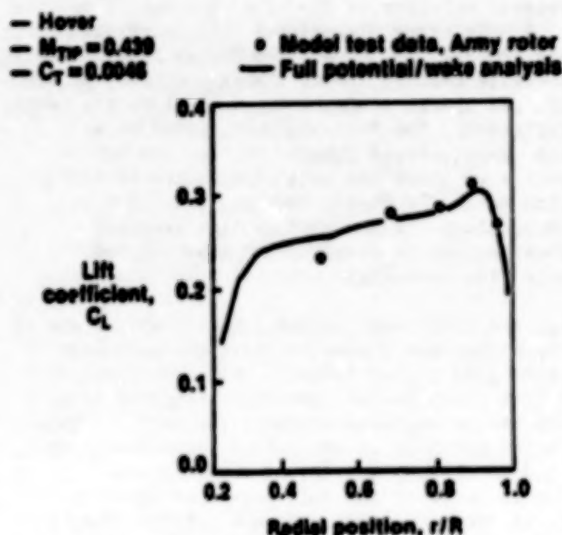
Figure 12. Comparison of Predicted and Measured Spanwise Lift Distribution
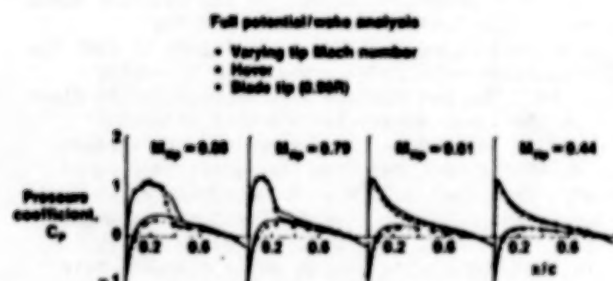
Figure 13. Comparison of Predicted and Measured Chordwise Pressure Distributions Near the Blade Tip for Varying Tip Mach Numbers

This analysis was recently extended and applied to forward flight conditions, and comparisons with test data are presented in Egolf and Sparks (1986). More recently the NAS supercomputer has been accessed remotely from UTRC, as described above, and used by T. A. Egolf to investigate the potential acoustic benefits of varying blade tip design. This is an extension of the work of Tauber (1984) of NASA, for the purpose of including the rotor wake influence. The smaller predicted supersonic zone for a swept tip with tapered thickness relative to that of a rectangular tip is shown in figure 14 in which Mach isobars are presented for a 4-bladed rotor (B=4) at a specified pitch angle. The results for the swept blade with only 1/4 rev of flat wake are included in figure 14 to show that an enlarged supersonic zone is predicted when the influence of the other blades and the more complete generalized wake is included in the computation. Typically, the NAS CRAY-2 computer time requirement is between 1/2 and 2 hours for predicting blade airloads and Mach isobars at one blade azimuth position. The requirement for a supercomputer for

rotor problems such as this is evident when it is considered that, even after the code is fully vectorized, many hours of NAS CRAY-2 time will be required for solutions over the rotor azimuth range.

The concepts involving the inclusion of the influence of the wake using an inner/outer solution domain are not limited to the quasi-steady full potential formulation. The method can be adapted to time-dependent rotor problems and more sophisticated numerical models such as Euler and Navier-Stokes analyses. This method of solution has the advantage of reduced volume for the nonlinear inner domain solution (finite difference methods) while treating the global influence of the complex rotor wake with a method based on prescribed wake models. The computational cost to obtain the complete solution is thus reduced as compared with an infinite domain solution approach. It is currently planned to apply the technique to other Ames Research Center full-potential codes by Chang (1984) and Strawn and Caradonna (1986) and include viscous airfoil characteristics using Navier-Stokes methodology (McCroskey, Baeder, and Bridgeman (1985)). It is planned to use our remote link to the NAS supercomputer for this activity. In addition to helicopter CFD, propeller CFD is of interest at UTRC to support the Prop-Fan activities of the Pratt & Whitney and Hamilton Standard Divisions of UTC. Various approaches to code development and evaluation are in progress based on 3-D lifting surface (vortex lattice), full-potential, and Euler methodology.
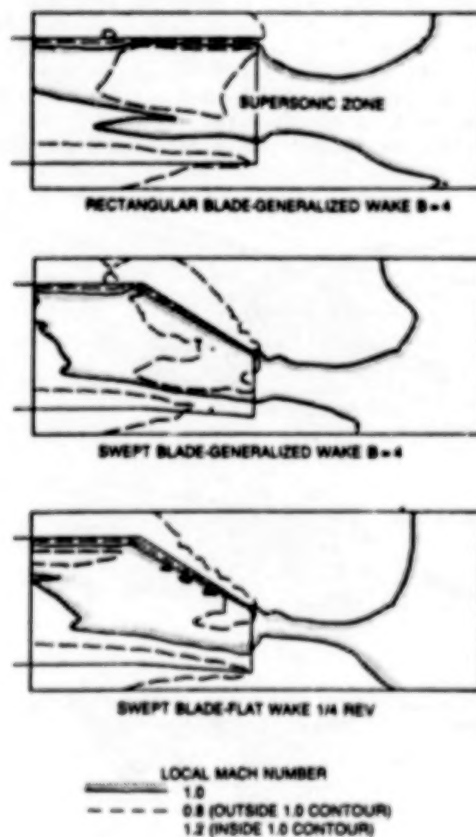
Figure 14. Predictions of Influence of Blade Design and Wake Model on Supersonic Zone

CFD FOR THE NATIONAL AEROSPACE PLANE

The design of the advanced high speed propulsion systems, such as scramjets and ramjets for a National Aerospace Plane (NASP) type vehicle operating at high Mach numbers and at extreme altitudes, cannot be based on conventional approaches utilizing extensive data bases and expensive experimental test simulations. The development of CFD techniques however has reached a state-of-the-art that will permit a designer to use Parabolized Navier-Stokes (PNS) and Navier-Stokes (NS) methods in the evolution of component designs. The current requirements for CFD codes in several high speed propulsion programs are being limited by the ability of the codes to model the relevant geometric features and physical processes.

A prime example of this problem is found in the analysis of new/novel combustor concepts. In this component, the flow is controlled by the complex three-dimensional interaction of the main stream fluid dynamics with reacting chemistry of the fuel. The flow simulation is significantly influenced by the introduction of multiple length and time scales that affect the stability of the flow as well as the numerical algorithms used in the simulation codes. Further complicating the design process is the lack of any meaningful data base to help reduce the simulation process to more tractable unit problems.

The use of CFD codes in the current NASP program is however predicated on using state-of-the-art codes with only a minimal degree of improvement. All codes related to the hypersonic propulsion problem can be categorized by their level of physical modeling, the completeness of data bases needed in these models, and by the type of numerical algorithm. In any application of these codes to the entire flight regime, the codes will have varying degrees of applicability and accuracy. A modular approach to classifying all codes helps a user to categorize a particular code, identify its capabilities and prioritize future code work.

Calibration of CFD codes for high speed applications is however, hampered by the limited availability of benchmark quality data for practical configurations. It is apparent that the need for modeling viscous and air/fuel chemistry effects over a three-dimensional hypersonic vehicle will require a blend of Parabolized Navier-Stokes (PNS) and full Navier-Stokes (NS) codes. Computer CPU and memory resources can represent a limiting factor forcing an engineer to trade geometric and physical modeling requirements with computer resource availability. Instead, our approach has been to identify unit problems that describe critical physical processes for which benchmark data are known to exist, i.e. include shock boundary layer interaction (Holden plate/ramp cases), flow three dimensionality (PB inlet), viscous mixing induced combustion, etc. and then validate the codes against these data bases (as performed by T. J. Barber for the following examples).

Shock Wave/Boundary Layer Interaction

One such example is demonstrated in the analysis of a shock wave/boundary layer interaction problem. A good data base is found in the CALSPAN data of Holden (1970). In the CFD validation study shown on figure 15, a laminar M = 14.1 flow over a flat plate/15 degree compression ramp combination is examined. Holden obtained surface static pressure, skin friction (Cf) and heat transfer rate (St) data. The static pressure contour plot shows the complexity of the flow physics in this benchmark case. A leading edge viscous interaction shock interacts with the compression corner shock. This shock/shock interaction controls the entire problem. Computed results from the SCRAMP (Kravczyyk (1986)) (SAIC) PNS code and the MASCRIN (Kumar (1986))(NASA LaRC) NS code are coplotted with the data. The MASCRIN two-dimensional code uses a MacCormack explicit time marching central difference scheme. In the calculations shown on figure 15, at least 15-20,000 time steps were required to reach a steady state. Good agreement is noted in the surface pressure and Stanton number comparisons. The wall skin friction data shows the expected drop into the compression corner. The single pass PNS results, as expected, do not reproduce this flow feature. Furthermore, with the relatively good agreement in the predicted Stanton number values on the ramp surface from the SCRAMP and MASCRIN and the poor ramp skin friction levels, one should question the applicability of Reynolds' analogy at these high Mach numbers.
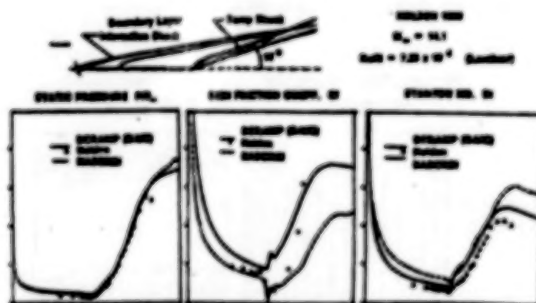
Figure 15. Unit CFD Problem: Shock Wave/Boundary Layer Interaction.   (Validation of Viscous Inlet/Forebody Codes)

Flow Three-Dimensionality

Another relevant unit problem to investigate is flow three-dimensionality. The PB inlet configuration of Seebaugh (1973), tested experimentally in the early 1970's, is a good three-dimensional configuration that does not require real gas modeling to simulate the flow physics. The incident flow Mach number was 7.4. Most of the available test data was measured along a narrow band inlet centerline. Because of flow symmetries, this problem can be initially examined in a 2D calculation. Predictions using the NASTAR (P&W) NS program of Rhie (1986) for pitot total pressure profiles are compared in figure 16(a) to the published results of Ng, Benson, and Kunik (1986) using the PEPSI-S (PNS) program and to experimental data. The PEPSI-S uses a substantially refined mesh (3000*300) to obtain the moderately better agreement at X = 42", however, its resolution of the reflected shock at X = 47" is not as good as NASTAR's prediction.

- NASTAR (180 × 72)
- PEPSI-S (3000 × 300)
- EXPERIMENT

X=42 in.   X=47 in.
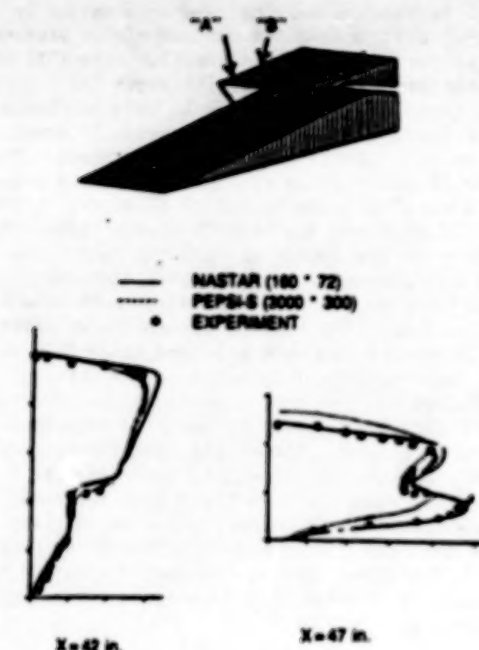
(a) Two Dimensional P8 Inlet Calculation vs. Experimental Data

PROJECTED VELOCITY VECTORS   PITOT PRESSURE CONTOURS

PLANE "A" (35.3 inches)

PLANE "B" (44.8 inches)
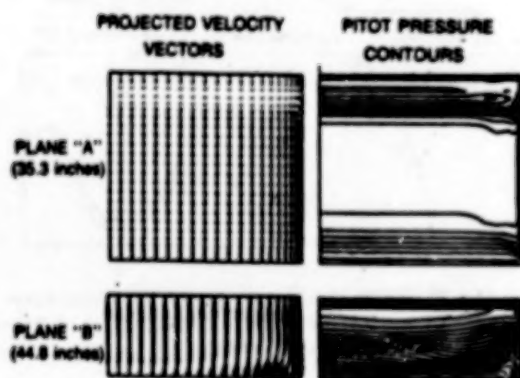
(b) Three-Dimensional P8 Inlet Calculation

Figure 16. Unit CFD Problem: Flow Three-Dimensionality. (Validation of Navier-Stokes Inlet Codes)

In the calculations shown in Figure 16(b), a full three-dimensional NASTAR (NS) solution is displayed. The computational mesh had 72 points in the axial direction, 36 points across the inlet duct height, and 28 points in the spanwise direction. A spanwise symmetry was assumed to conserve the number of grid points used in the calculation. The problem was run as a one zone domain, using a nonreflective boundary condition along the capture streamline. This grid setup assumes no internal interaction with the external flow. The implicit NASTAR procedure converged in 200 iterations, when started with an initial flow field generated from a two-dimensional calculation. The CPU required was 3.7 hours on an IBM 3090.

The results displayed on Figure 16(b) are shown at two cross-planes; one near the inlet entrance and the other substantially further in the inlet. Very little three-dimensional flow is seen to exist, and the symmetry line/2D comparisons presented previously are seen to be reasonable. The corner region of the downstream plane, however, shows some significant flow turning. This is more easily seen in the displayed velocity vector plots. The initial plane is basically 2D with upward pointing vectors corresponding to the ramp effect of the forebody. The downstream plane shows the kind of corner crossflow pattern observed by SRA/NASA LeRC in their PEPSI-S calculations.

Mixing Driven Supersonic Combustion

Finally, a mixing driven supersonic combustion validation study uses the Burrows & Kurkov (1973) experimental data to benchmark the UTRC version of the NASA LaRC SPARK NS code of Drummond (1985). In the experiment, shown schematically on figure 17, a sonic jet of hydrogen is injected tangentially into a supersonic air stream. Although the combustion efficiency is only 20 per cent, the experiment is unique in that species concentration data were obtained at an exit plane located approximately 90 slot heights downstream of the injection plane. SPARK NS calculations for the nonreacting and reacting cases are shown on figure 17. The
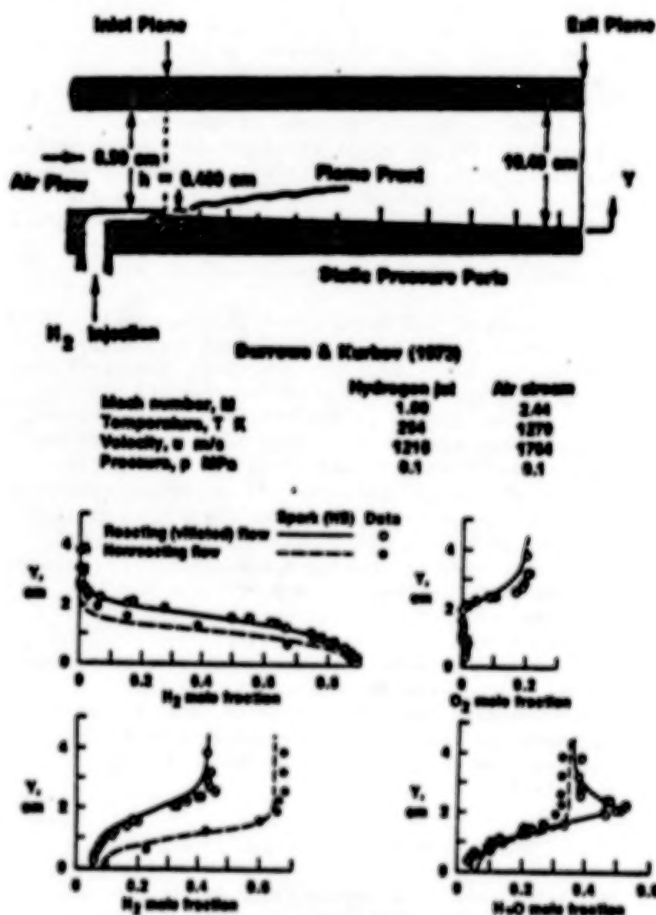
Figure 17. Unit CFD Problem: Mixing Driven Supersonic Combustion. (Validation of Navier-Stokes Combustor Codes)

166

nonreacting case represents the situation where the mainstream flow is heated through combustion in an upstream section, but the flow in the test section has no oxygen available for combustion. The reacting or vitiated case has the inlet air stream replenished with oxygen. The SPARK runs were made using a stretched 31 x 35 mesh. An algebraic model was used to simulate turbulence effects. No effort was made to model the upstream boundary layer in these calculations. Species comparisons with data for the reacting and nonreacting cases show excellent agreement in level as well as in the location of the flame front.

The ultimate goal of these types of CFD validation efforts is to apply state-of-the-art computational methods to complex hypersonic flow problems in support of the NASP design program. Frequently, critical design problems cannot be answered using classical design methodology. Since experimental verification is either difficult or too costly, a CFD based design procedure is necessary. Validated codes can then be applied with more confidence to the design of complex flow components such as a three-dimensional scramjet combustor. During portions of the flight envelope, fuel is injected at sonic velocities into a supersonic air stream, schematically shown on figure 18. The critical design issues of mixing efficiency (combustor length) and wall integrity (surface cooling) require a full three-dimensional reacting flow NS analysis. Computer main memory resources may be inadequate on most machines when sufficient mesh resolution (additional nodes) and full chemistry (additional words per node) are necessary. As part of UTRC's support of the NASP program, a new three-dimensional reacting flow Navier-Stokes Analysis will be developed from the NASCRIN/SPARK methodology. The NAS facility capabilities will be essential for expediting this effort and permitting use of the analysis in a realistic time frame.

LOW SPEED COMBUSTOR

HYDROGEN

AIR
FLOW
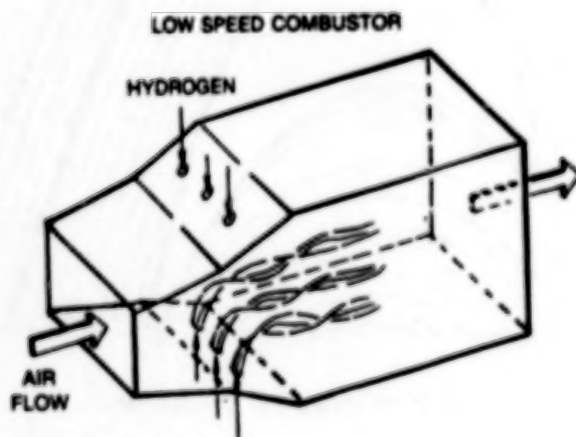
Figure 18. Three-Dimensional Scramjet Combustor Simulation: Normal Injection

Two-Dimensional Cascade Viscous Flow Analysis

The drive towards higher jet engine efficiency has resulted in increased aerodynamic and heat transfer demands on the compressor and turbine sections of gas turbine engines. As loading requirements in the blade rows and turbine inlet stagnation temperatures increase beyond the range of previous applications, the designer's job becomes increasingly difficult without the use of sophisticated three-dimensional flow analyses. Separated flow regions and hot spots in turbomachinery blade passages occur more frequently as the operation envelope is pushed to the limit. In order to determine the existence and effects of these phenomena an accurate and reliable three-dimensional viscous flow procedure becomes necessary.

The analysis and prediction of three-dimensional viscous flows in blade rows has only recently been treated. Severe demands are placed on computer storage and computational time in order to accurately resolve the wall layers adjacent to the airfoil surface and endwalls. A logical starting point for the eventual development of a three-dimensional viscous analysis for turbomachinery is the development of a two-dimensional solution technique for the Navier-Stokes equations in which the wall layers are resolved with fine grid distributions.

A technique recently developed for the solution of two-dimensional Navier-Stokes equations is a control volume algorithm presented by Davis, Ni, and Carter (1986). This algorithm uses an explicit, control volume approach combined with an efficient multiple-grid scheme, as described by Ni (1982) and Davis (1986), to update the flow variables in time until a steady state solution is obtained. The solution procedure is formally second order accurate in space for all terms in the Navier-Stokes equations. This time marching scheme is second order accurate in time for inviscid flow and first order accurate in time for viscous flow which is similar to other efforts. Several key features in this Navier-Stokes solution technique allow for the calculation of turbulent, high Reynolds number flow in cascades. A new compact operator for the calculation of the viscous terms in the Navier-Stokes equations provides high accuracy and stability in this numerical approach. A modified "C" grid generation procedure based upon the "GRAPE" Poisson solver of Sorenson (1980) and Steger (1979) is used to reduce the computational grid skewing in the mid-passage region compared to standard cascade "C" grid applications and thereby reduce numerical losses introduced by smoothing operators applied on skewed grids. The Baldwin-Lomax (1978) two layer algebraic turbulence model is implemented using a body normal grid which alleviates any apriori approximations as to the thickness of the boundary layer region adjacent to the solid surface. Finally, a combination of second and fourth difference numerical smoothing is used in this numerical procedure to dampen oscillations brought about by truncation errors on relatively coarse grids. Both second and fourth difference smoothing operators for the flow velocity variables are reduced to zero as the solid boundary is approached in order to accurately resolve the viscous layer region.

167

A case which demonstrates the ability of the current Navier-Stokes procedure to predict flows with significant separation is the subsonic turbine cascade tested experimentally by Stoeffler et. al. (1977). The 161 x 33 point grid shown in figure 19(a) was used in the viscous calculation whereas a 161 x 17 point mesh was used for the inviscid calculation. Both calculations were run with three levels of multiple-grid in addition to the fine grid solution. The viscous solution converged in 1500 time steps whereas the inviscid calculation reached convergence in 260 time steps. The flow on the suction side of the airfoil was assumed to be fully turbulent and for the pressure side of the airfoil, where a large separated region existed, transition was held fixed at x - 0.24 which was determined from the empirical correlation of Roberts (1979) for closed transitional separation bubbles. The inlet and exit aerodynamic conditions for this cascade are given in figure 19(b) along with the comparison between the predicted pressure distributions and the experimental data. Comparison of the predicted pressure distributions from both the Navier-Stokes and Euler analyses with the experimental data in figure 19(b) shows that the Navier-Stokes analysis has correctly predicted the change in the pressure due to the viscous effects. In this case it is quite clear that a significant inviscid-viscous interaction occurs due to the pressure side separation which effects the pressure distribution on both sides of the airfoil. The predicted streamline pattern shown in figure 19(c) clearly shows the extent of the separated flow region on the pressure side of the airfoil.

Accurate viscous solutions for two-dimensional cascades at near design incidence flow conditions are now obtainable with this Navier-Stokes technique of Davis, Ni, and Carter (1986). This numerical approach can now be the basis from which more challenging viscous turbomachinery flows can be attacked. For two-dimensional flows, high incidence cascade flow and total pressure loss performance prediction are two fluid dynamic problems which stretch existing numerical schemes as well as the present day computer technology to their limits. These problems are currently being pursued using the previously described Navier-Stokes approach using sophisticated supercomputer architectures. Research into the numerical approach and computational grid requirements to accurately predict cascade flows and corresponding total pressure loss over the entire incidence range is currently underway. Two types of supercomputer systems are being used in this research: a Cray XMP vector processor and the IBM LCAP parallel processing computer. The Cray XMP supercomputer has both vector and concurrent (multi-tasking) capabilities although current research will limit itself to using the vector processor of the computer. The IBM LCAP system is a research computer which consists of 10 floating Point System array processors tied in a ring to a scalar IBM host machine. A central storage area is used to communicate information between array processors. Parallel computing using this system is much different than multi-tasking on a Cray or IBM 3090/400 since data storage is local to the array processors and not in a common global storage location. The Cray and IBM LCAP computers have relatively the same peak performance. Super-computers such as these are essential in computing the complex flow structures which arise in high incidence cascade flows.
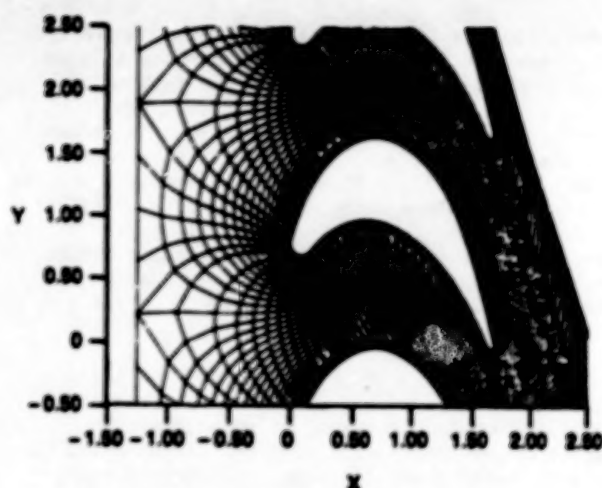
(a) Computational Grid for Turbine Cascade
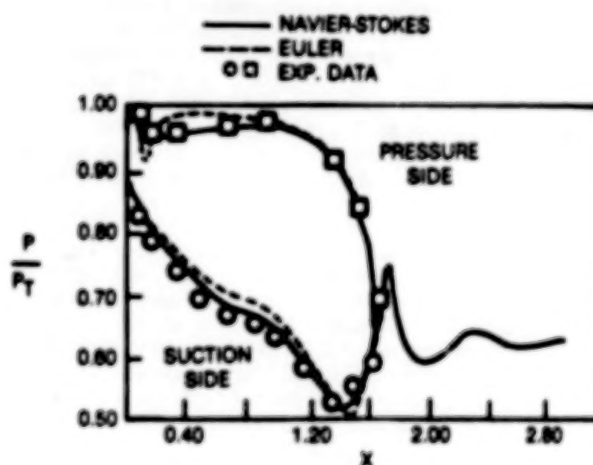
(b) Comparison Between Predicted Pressure Distributions and Experimental Data
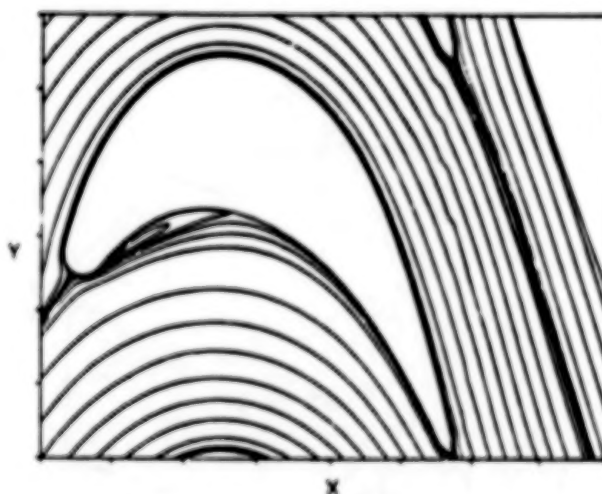
(c) Predicted Streamline Pattern

Figure 19. Navier-Stokes Calculation for Turbine Cascade with Separated Flow

THREE-DIMENSIONAL SEPARATED FLOW CFD

Viscous effects can have a substantial impact on the aerodynamic performance of external and internal flow configurations. For a significant number of high Reynolds number flows of practical interest, the viscous effects, even in the presence of boundary-layer separation, are confined to a relatively small layer near the surface. As indicated in the McDonald and Briley (1984) survey, many two-dimensional aerodynamic problems have been represented by Interacting Boundary-Layer Theory (IBLT) whereby the flow is divided into regions of viscous and inviscid flows with the two regions coupled through the displacement thickness. However, since the majority of the fluid flows in nature are three dimensional, and with the rapid advances in the development of supercomputers, it is timely to turn our attention to the analysis of strongly interacting three-dimensional flows. An objective of this present investigation is to determine if the IBLT methodology, which has been applied successfully in analyzing two-dimensional flows, can be extended to analyze three-dimensional strongly interacting flows. A second objective has been to incorporate IBLT concepts in the development of a thin-layer Navier-Stokes (TLNS) procedure in order to take advantage of the efficiency which IBLT techniques offer but retain the generality and flexiblity of Navier-Stokes procedures.

Interaction Boundary-Layer Theory

One procedure used at UTRC, in this study of three-dimensional separated flow, is Interaction Boundary-Layer Theory (IBLT) developed by Edwards (1986). In this procedure, the entire flow field is represented as regions of viscous and inviscid flow with the two regions coupled through the viscous displacement thickness. The inviscid solution is obtained from a three-dimensional small disturbance surface integral representation of an incompressible, irrotational flow field where the effect of the viscous flow is imposed by analyzing the inviscid flow over a displacement body instead of the actual geometrical surface. The flow in the viscous region is assumed to be governed by Prandtl's boundary-layer equations. The viscous equations are solved with an implicit finite difference approach, in which derivatives in the x-direction are discretized using first-order upwind approximations, and derivatives in the normal and z-directions are discretized using second order central differencing. Newton iteration is used to solve the viscous equations at each x and z location, as the solution is marched from a plane of initial data and a plane of symmetry. In this study, a three-dimensional extension of the quasi-simultaneous methodology of Veldman (1983) is used to couple the inviscid and viscous flow fields.

Thin-Layer Navier-Stokes Theory

A second procedure used in the study of three-dimensional separated flow is a thin-layer Navier-Stokes (TLNS) procedure developed by Davis, et al (1987). The objective in the development of this TLNS procedure has been to incorporate IBLT concepts in order to take advantage of the efficiency which IBLT techniques offer but retain the generality and flexiblity of Navier-Stokes

procedures. This approach has been pursued by casting the 3-D TLNS equations into a streamlike function and vorticity transport form. In this formulation, two sets of streamlike function Poisson and vorticity transport equations are solved using an implicit line Gauss-Seidel relaxation procedure. The equations describing the axial component of flow are numerically uncoupled from the spanwise component flow equations allowing an efficient implicit block 2 x 2 tri-diagonal solution procedure to be used along lines of x - constant, z - constant which are essentially perpendicular to the solid surface in a similar fashion as utilized by boundary layer techniques. Standard second order accurate central difference formula are used in the discretization of the Poisson and vorticity transport equations with the exception of the axial convection terms of the vorticity transport equations. For these convection terms, a first order windward difference operator, similar to that utilized for interacting boundary layer calculations, is used to model the parabolic nature of the vorticity transport equations. Thus, in the inviscid region where the Poisson streamlike function equations dominate the flow, central difference formula are used to model the elliptic nature of the equations, whereas in the viscous region which is dominated by the vorticity transport equations, appropriate one-sided windward differences are used to model the parabolic nature of these equations.

Application of IBLT and TLNS Methods

Results are presented for the analysis of three-dimensional incompressible separated flow using the the IBLT and TLNS methods. The model problem used in this study is laminar flow over a flat plate with either a dent or bump located downstream of the leading edge. The flat plate with the protuberance (or dent) is shown schematically in figure 20. A sign in the geometric equations determines if the flat plate has either a dent or bump. The oncoming flow for this model problem is aligned with the x coordinate. Along the vertical plane of symmetry, the surface geometry is identical to the planar trough shape studied by Carter and Vornon (1975) for two-dimensional separated flow.
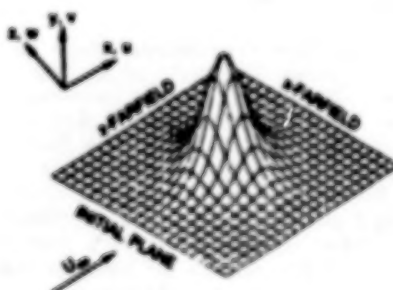
Figure 20. Schematic of Flow Over a Flat Plate With a Protuberance (Dent)

Several comparisons have been made between the present IBLT and TLNS methods (for example, Edwards (1986), Davis et al (1987), and Carter et al (1986)). One flow case is laminar flow over a flat plate with a dent (t=-.03) at Re = 8x10⁴. Both analyses used the same uniform grid consisting of 121 points in the x-direction and 31 points in the z-direction where the x-z computational domain is 1 < x < 4 and 0 < z < 1.5. The IBLT method used 21 points in the normal direction across the boundary layer while the TLNS method used 81 points in the normal direction with at least 32 points in the viscous region. Both procedures have been tested with finer normal grids with little change in the computed results. Symmetry conditions are assumed along z=0 and the Blasius flat plate solution is assumed at x=1.

A comparison of the results of the two analyses is shown in figure 21 where contours from both analyses are shown for the axial component of skin friction. From this figure, it can be seen that the results of the two analyses show nearly similar trends for the flow quantities. Figure 22 shows the limiting streamlines near the vicinity of the dent (both analyses produced essentially the same result). These limiting streamlines are the paths taken by particles located an infinitesimal distance above the surface and are determined using a technique developed by Duck and Burggraf (1986). It is noted in figure 22 that the flow is moving from left to right. Figure 22 shows the formation along the symmetry plane of two singular points on the surface (saddle point of separation and nodal point of reattachment). Lighthill (1963) has shown that the number of nodal points must exceed the number of saddle points exactly by two for a closed body. Since the model problem in this study can be regarded as a local region on such a body, then any additional nodes and saddle points must cancel in number. It is seen from figure 22 that this condition is satisfied. Also in this figure, note that there is a dividing limiting streamline (sometimes referred to as a separation line) emanating from the saddle point of separation which results in forming a region that is not accessible from the upstream. Similar types of flow structure have been observed in the work of Duck and Burggraf (1986), where laminar flow over a flat plate with a protuberance at infinite Reynolds number was examined using triple-deck theory. This favorable comparison between the present IBLT and TLNS methods shows that the IBLT methodology can be applied to the analysis of strongly interacting three-dimensional flows. Further, it demonstrates that IBLT concepts should be incoporated in TLNS and Navier-Stokes procedures.

The 3-D separated flow calculations shown in this paper were made using the Cray X-MP at Cray Research, Inc. The TLNS procedure required approximatley 3 hours of CPU time to obtain a converged solution which is based on a four orders of magnification reduction in the equation residuals. The IBLT procedure required approximately 7 minutes of CPU time to obtain a converged solution which is based on a four orders of magnification reduction in the maximum change per iteration of the displacement thickness.

(a) Thin-Layer Navier-Stokes   (b) Interacting Boundary Layer
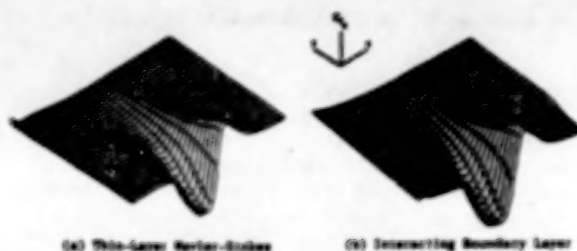
Figure 21. Flow Over a Flat Plate With a Dent. Global Comparison of Axial Skin Friction of IBLT and TLNS
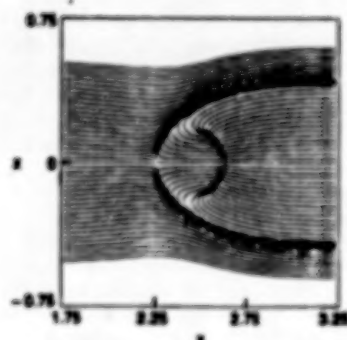
Figure 22. Limiting Streamlines for Flow Over A Flat Plate With a Dent (Re = 80,000)

PARALLEL PROCESSING FOR CFD

Computer codes for computational fluid dynamics can benefit from parallel processing. UTRC has recently established several studies to demonstrate and quantify the advantages of parallel processing for selected CFD problems with particular emphasis on evaluating new massive parallel processors. As examples of these activities, two current studies are described below.

Parallel Processing for a Combustor Flow Code

UTRC is participating in a joint program with Yale University's Computer Science Department, AFOSR and Apollo Computer, Inc. to investigate the applicability of parallel architecture computers to CFD problems. A model problem representing the energy equation for perfect gas flow through a cylinder has been solved using MacCormack's explicit difference scheme. (This problem was chosen because it contains the essential calculations for the Hankey-Shang combustor flow code.) The problem was first coded for an Apollo serial processor workstation computer at UTRC, then transfered to Yale where the code was modified for the Intel Hypercube and Encore parallel processor computers. Both the Intel Hypercube and the Encore are MIMD (Multiple Instruction stream/Multiple Data stream) machines however the hypercube has dispersed memory while the Encore has shared memory. The Intel Hypercube is basically 128 IBM PC computers linked together with a hypercube architecture (figure 23).
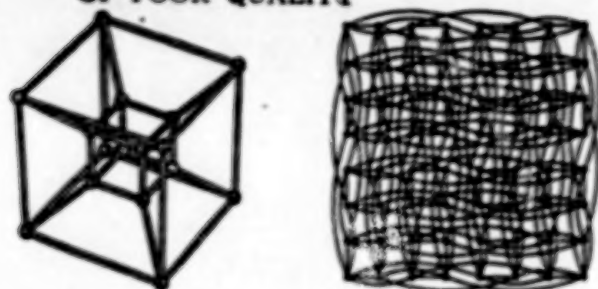
Figure 23. Hypercube Architecture

Numerous timing studies have been completed comparing the speedups for solving the model problem with different numbers of processors, different grid sizes and different domain decompositions. Basic theory such as Amdahl's Law (figure 24) is being extended to understand the difference in speedups and to permit evaluation of new and different parallel architectures. The theory shows the importance of communication time between processors in achieving desired speedups with additional processors. Future work will involve developing parallel code which is portable to different parallel architectures, evaluation of implicit solution algorithms and running the code on different parallel computers.
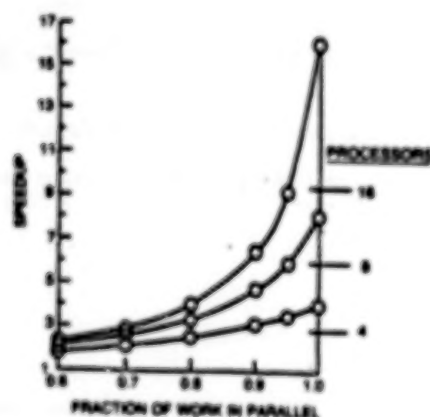
Figure 24. Computer Speedup as Determined by Fraction of Work in Parallel and Number of processors (Amdahls Law)

Parallel Processing Using Cellular Automata Techniques for Flow/Heat Transfer Modeling

Massively parallel computer architectures containing tens of thousands of processors make practicable entirely new approaches to difficult but important problems. The Connection Machine , announced this year by Thinking Machines Corporation (TMC), Cambridge, Mass., contains 65,536 processors all operating in parallel. In a cooperative program with TMC, cellular automata techniques are being examined for fluid flow/heat transfer modeling required for heat exchanger applications and as an alternative to differential equations for representing physical systems.

The massively parallel architecture represented by the Connection Machine is intrinsic to implementation of these techniques. As shown in figure 25, the Connection Machine contains 4096 chips, each incorporating 16 one-bit processors, local memory for each processor, and a router which coordinates communication. Communication between any two of the 16 processors on a chip occurs in one machine cycle, which because of the simplicity of the processors is very short. The 4096 chips are connected as a 12 dimensional hypercube, i.e., the address of each chip may be represented as a 12 bit binary number and direct communication exists between any two chips whose addresses differ by one bit. Communication between any two chips is therefore accomplished in a maximum of 12 cycles. In the Connection Machine such communication is accomplished in parallel for all chips, via the routers, and in 12 machine cycles all 65,536 processors communicate with their target. With this organization, each processor can be assigned to an element of the problem input data set, and analysis applied simultaneously to all of the data. For very large data sets, the local memory is partitioned and the data is processed in "pages" of 65,536. Such data level analysis opens up radically new approaches to problems: for example, optical lens corrections can be effected by transferring each pixel of an image from a processor representing the input pixel location to another processor representing the pixel position had the lens been perfect. In a similar manner, the cellular automata modeling of fluid flow takes advantage of the extremely efficient communication between nearest neighbor processors of the massively parallel architecture.
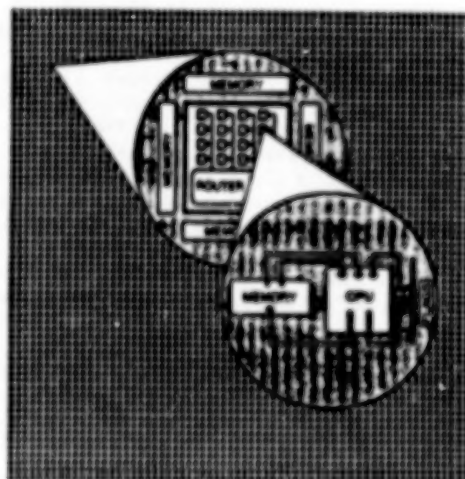
Courtesy TMC

Figure 25. Connection Machine -- Processor

The cellular automata approach models with simple interacting elements the complex behavior of natural systems. For 2D fluid flow, the elements are unit mass, unit velocity particles constrained to move along the six directions of a hexagonal lattice.

The particles interact in accord with simple
collision rules involving only particles on nearest
neighbor lattice points (figure 26). Each lattice

- Unit mass, unit velocity particles
- Simple interactions with nearest neighbors

- Flow parameters determined by average over many cells
- Formal equivalence to Navier-Stokes equations

Figure 26. Cellular Automata Fluid Flow Modeling

point (cell) is represented by one processor which
tracks the particles currently located at that
position. The macroscopic flow parameters, density,
velocity, etc., are determined by averages over many
cells providing continuum results from the discrete
particles. The behavior of this simple system is
formally equivalent to the Navier-Stokes equations
as described by Wolfram (to be published), and
although the model is deterministic, the very large
number of degrees of freedom gives rise to the rich
array of phenomena observed in fluid flow. Figure
27 is a calculation performed at TMC of the 2D flow
over a cylinder (in a coordinate system fixed on the
cylinder) and clearly displays the vortex street
observed in such flow. The UTRC contribution in the
cooperative program involves validation of the
cellular automata approach by calculation for known
behavior test flow conditions and extension of the
analysis to incorporate heat transport by analogy
with the momentum transfer of the particle
collisions. For example, as illustrated in figure
28, numerical experiments on the Connection Machine,
of the 2D flow between parallel plates, have been
used by A. Baught of UTRC to determine the effective
fluid viscosity for comparison with the viscosity
derived analytically from the cellular automata
model. The effective fluid viscosity is evaluated
from the fluid momentum decay and for the asymptotic
exponential decay agrees closely with that derived
by D. Levermore (B. Nemnich, TMC, private
communications). This simple plate problem, when
extended, will have relevance to the heat exchanger
application.

The fact that simple interaction rules can reproduce
complex behavior offers the exciting promise that
cellular automata can be used as an alternative to
differential equations for modeling a wide variety
of physical systems (Vichniac (1984)). With
cellular automata, limited, discrete information is
evaluated for each element, and each "bit"
calculated weighs equally in the results. With
differential equations, very high accuracy is
generally required during the analysis - e.g.
evaluation of a derivative as the difference of two
quantities - to obtain an answer of much lower
accuracy. The "bit democracy" of the cellular
automata approach results in efficient use of
computer resources and represents a potential
breakthrough for otherwise intractable problems.
The prospect is intriguing, and the fluid flow/heat
transfer modeling is an avenue to explore this
potential.
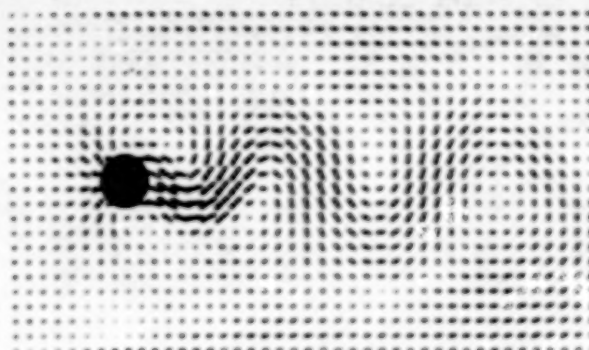
Figure 27. Two-Dimensional Flow Over a Cylinder
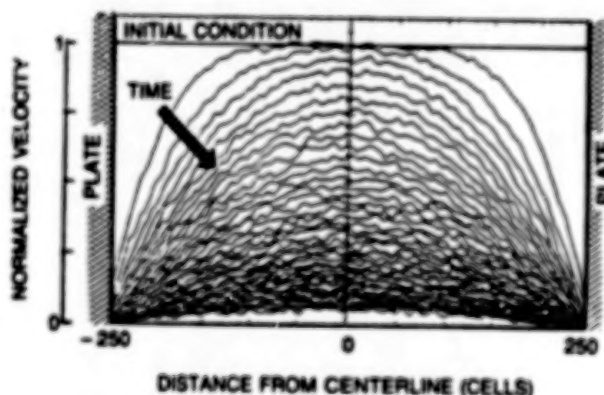
**Figure 28. Two-Dimensional Flow Between Parallel
Plates -- Velocity Profile Time History**

CONCLUDING REMARKS

With the availability of advanced supercomputers and
the rapid progress being made in computational fluid
dynamics, considerable advances in the development
of CFD codes applicable to complex aerodynamic
problems of interest to the aircraft industry are
foreseeable in the near future. Supercomputer
systems such as those of the new NAS Facility and
the new massive parallel processing systems are
anticipated to provide computational tools for
software which will significantly advance the
state-of-the-art of CFD technology for a wide
variety of design applications. Specific
methodology related to helicopters, turbomachinery,
heat exchangers, and the National Aerospace Plane
have been presented herein, but these are just
examples within a wide spectrum of potential
applications. It has been recognized and
demonstrated in the recent work that the code
developers can now conceive of incorporating and
combining the CFD features which they have had to
separate or compromise on in the past, such as
three-dimensional, viscous, compressible, unsteady,
and heat transfer effects. This will result in more
practical and accurate codes for both design and
diagnostic investigations.

REFERENCES

Arieli, R.; and Tauber, M. E.: Analysis of Quasi-Steady Flow About an Isolated Lifting Helicopter Rotor Blade, Joint Institute for Aeronautics and Astronautics TR-24, Aug. 1979.

Burrows, M.C.; and Kurkov, A. P.: Analytical and Experimental Study of Supersonic Combustion of Hydrogen in a Vitiated Airstream, NASA TMX-2828, Sept. 1973.

Baldwin, B. S.; and Lomax, H.: Thin-Layer Approximation and Algebraic Model for Separated Turbulent Flows, AIAA Paper 78-257, Jan. 1978.

Caradonna, F. X.; and Tung, C: Experimental and Analytical Studies of a Model Helicopter Rotor in Hover, NASA TM 81232 (or USAAVRADCOM TR-81-A-23), Sept. 1981.

Carter, J. E.; Davis, R. L; Edwards, D. E.; and Hafez, M. M.: Three-Dimensional Separated Viscous Flow Analyses, Presented at the Tenth International Conference on Numerical Methods in Fluid Dynamics, Beijing, China, June, 1986.

Carter, J. E.; and Wornom, S. F: Solutions for Incompressible Separated Boundary Layers Including Viscous-Inviscid Interaction, NASA SP-347, 1975.

Chang, I. C.: Transonic Flow Analysis for Rotors - Part 2 - Three-Dimensional, Unsteady, Full-Potential Calculation, NASA TP-2374, 1984.

Davis, R. L.; Ni, R. H.; and Carter, J. E.: Cascade Viscous Flow Analysis Using the Navier-Stokes Equations, AIAA Paper 86-0033, Jan. 1986.

Davis, R. L.; Carter, J. E.; and Hafez, M. M.: Three-Dimensional Viscous Flow Solutions with a Vorticity Stream Function Formulation, AIAA Paper 87-0601, 1987.

Davis, S. S.; and Chang, I. C.: The Critical Role of Computational Fluid Dynamics in Rotary-Wing Aerodynamics, AIAA 24th Aerospace Sciences Meeting, Reno, NV AIAA-86-0336, Jan. 1986.

Drummond, J. P.: Numerical Study of a Ramjet Dump Combustor Flow Field, AIAA Journal Vol. 23, No. 4, 1985, p. 604.

Duck, P. W.; and Burggraf, O. R.: Spectral Solutions for Three-Dimensional Triple Deck Flow over Surface Topography, J. Fluid Mech., Vol. 162, 1986.

Edwards, D. E.: Analysis of Three-Dimensional Separated Flow Using Interacting Boundary-Layer Theory, Presented at the International Union of Theoretical and Applied Mechanics (IUTAM) Symposium on Boundary-Layer Separation, London, U. K., August, 1986.

Egolf, T. A.; and Landgrebe, A. J.: Generalized Wake Geometry for a Helicopter Rotor in Forward Flight and Effect of Wake Deformation on Airloads, Proceedings of the 40th Annual Forum of the American Helicopter Society, May, 1984.

Egolf, T. A.; and Sparks, S. P.: Hovering Rotor Airload Prediction Using a Full Potential Flow Analysis with Realistic Wake Geometry, Proceedings of the 41st Annual Forum of the American Helicopter Society, May 1985.

Egolf, T. A.; and Sparks, S. P.: A Full Potential Rotor Analysis with Wake Influence Using an Inner-Outer Domain Technique, Proceedings of the 42nd Annual Forum of the American Helicopter Society, June 1986.

Holden, M. S.; and Moselle, J. R.: Theoretical and Experimental Studies of the Shock Wave/ Boundary Layer Interaction on Compression Surfaces in Hypersonic Flow, Calspan Report AF-2410-A-1, Oct. 1969, also ARL 70-0002, Jan. 1970.

Kravczyk, W. J.; Rahendran, N.; Harris, T. B.; York, B. J.; and Dash, S. M.: Computational Models for the Analysis Design of Hypersonic Scramjet Components - Part II, AIAA 86-1596 AIAA/ASME/SAE/ASEE 2nd Joint Propulsion Conference, Huntsville, AL, 1986.

Kumar, A.: Numerical Simulation of Scramjet Inlet Flow Fields, NASA TP-2517, May, 1986.

Landgrebe, A. J.: An Analytical Method for Predicting Rotor Wake Geometry, Journal of the American Helicopter Society, Vol. 14, No. 4, Oct. 1969.

Landgrebe, A. J.: The Wake Geometry of a Hovering Helicopter Rotor and Its Influence on Rotor Performance, Journal of the American Helicopter Society, Vol. 17, No. 4, Oct. 1972, (also, Proceedings of the 28th Annual National Forum of the American Helicopter Society, May 1972.

Landgrebe, A. J.; and Egolf, T. A.: Rotorcraft Wake Analysis for the Prediction of Induced Velocities, USAAMRDL TR-75-45, Jan. 1976. (Available from DTIC as AD A021, 202).

Landgrebe, A. J.; and Egolf, T. A.: Prediction of Helicopter Induced Flow Velocities Using the Rotorcraft Wake Analysis, Proceedings of the 32nd Annual Forum of the American Helicopter Society, May 1976.

Landgrebe, A. J.: Overview of Helicopter Wake and Airloads Technology, Proceedings of the American Helicopter Society/Nanjing Aeronautical Institute International Seminar - The Theoretical Basis of Helicopter Technology, Nanjing China, Nov. 1985, also Proceedings of the 12th European Rotorcraft Forum, Paper No. 18, Garmisch-Partenkirchen, FRG, Sept. 1986.

Lighthill, M. J.: Attachment and Separation in Three-Dimensional Flow, Laminar Boundary Layers, Oxford University Press, 1963.

McCroskey, V. J.; Baeder, J. D.; and Bridgeman, J. O.: Calculation of Helicopter Airfoil Characteristics for High Tip-Speed Application, Proceedings of the 41st Annual Forum of the American Helicopter Society, May 15-17, 1985.

McCroskey, V. J.; and Baeder, J. D.: Some Recent
Advances in Computational Aerodynamics for
Helicopter Applications, NASA TM-86777, Oct. 1985.

McDonald, H; and Briley, V. R.: A Survey of
Recent Work on Interacted Boundary-Layer
Theory for Flow with Separation, Numerical
and Physical Aspects of Aerodynamic Flows II,
Springer-Verlag, 1984.

Ng, W. F.; Benson, T. J.; and Kunik, V. G.:
Real Gas Effects on the Numerical Simulation of
Hypersonic Inlet, J. Propulsion and Power, Vol. 2,
No. 4, 1986, p. 381.

Ni, R. H.: A Multiple Grid Scheme for Solving the
Euler Equations, AIAA Journal, Vol. 20, Nov.
1982, pp. 1565-1571.

Rhie, C. M.: A Pressure Based Navier-Stokes Solver
Using the Multigrid Method, AIAA 86-0207, AIAA
24th Aerospace Sciences Meeting, Reno, NV, 1986.

Roberts, V. B.: Calculations of Laminar Separation
Bubbles and Their Effect on Airfoil Performance,
AIAA Paper 79-0285, Jan. 1979.

Seebaugh, V. R.: Hypersonic Flows in Large Scale
Inlet Models, J. Aircraft, Vol. 10, No. 1, January
1973, p. 38.

Sorenson, R. L.: A Computer Program to Generate
Two-Dimensional Grids About Airfoils and Other
Shapes by the Use of Poisson's Equation, NASA
TM-81198, 1980.

Steger, J. L. and Sorenson, R. L.: Automatic
Mesh-Point Clustering Near a Boundary in Grid
Generation with Elliptic Partial Differential
Equations, Journal of Computational Physics,
Vol. 33, No. 3, Dec. 1979.

Stoeffler, R., Dring, R. P., and Kopper, F.: United
Technologies Internal Report, 1977.

Strawn, R. C.; and Caradonna, F. X.: Numerical
Modeling of Rotor Flows with a Conservative Form
of the Full-Potential Equations, AIAA 86-0079,
Jan. 1986.

Tauber, M. E.: Computerized Aerodynamic Design of a
Transonic Low-Noise Blade, NASA Technical
Memorandum 85928, March, 1984.

Veldman, A. E. P.: A Numerical View on Strong
Viscous-Inviscid Interaction, NLR MP 83048 U,
1983.

Vichnia, G. Y.: Simulating Physics with Cellular
Automata, Physics 10D, 1984, p. 96-116.

Wolfram, S.: Cellular Automation Fluids 1: Basic
Theory, The Institute for Advanced Study,
Princeton, NJ, to be published.

N87
26012
UNCLAS

APPLICATIONS OF COMPUTATIONAL MODELING IN BALLISTICS

Walter B. Sturek
US Army Ballistic Research Laboratory, LABCOM
Aberdeen Proving Ground, Maryland 21005-5066

ABSTRACT

The development of the technology of ballistics as applied to gun launched Army weapon systems is the main objective of research at the US Army Ballistic Research Laboratory. The primary research programs at the BRL consist of three major ballistics disciplines: exterior, interior and terminal. The work done at the BRL in these areas has traditionally been highly dependent on experimental testing. A considerable emphasis has been placed on the development of computational modeling to augment the experimental testing in the development cycle; however, the impact of the computational modeling to this date has been modest. With the availability of supercomputer computational resources recently installed at the BRL, a new emphasis on the application of computational modeling to ballistics technology is taking place. The intent of this paper is to outline the major application areas which are receiving considerable attention at the BRL at present and to indicate the modeling approaches involved. An attempt has been made to give some information as to the degree of success achieved and indicate the areas of greatest need.

INTRODUCTION

The development of ballistics technology as applied to gun launched Army weapons systems is the main objective of research at the US Army Ballistic Research Laboratory. The primary research programs at the BRL consist of three major ballistics disciplines: exterior, interior and terminal. The work done at the BRL in the areas has traditionally been highly dependent on experimental testing. A considerable emphasis has been placed on the development of computational modeling to augment the experimental testing in the development cycle; however, the impact of the computational modeling to this date has been modest. This has been primarily caused by the lack of adequate computational resources at the BRL which has relied on a CDC 7600 computer since 1975. The CDC 7600 computer was replaced by a Cray XMP/48 computer in December 1986.

With the considerable increase in computational capability provided by this computer, a new emphasis on the application of computational modeling to ballistics technology is taking place. The intent of this paper is to outline the major application areas which are receiving considerable attention at the BRL at present and to indicate the modeling approaches involved. An attempt has been made to give some information as to the degree of success achieved and indicate the areas of greatest need.

Since the three ballistic disciplines represent well defined work areas, each discipline is discussed separately in the paper in the order: exterior, interior and terminal.

Exterior Ballistics

The computational modeling of exterior ballistic flows at BRL has been very active since 1973. More recently, the application of the thin layer, Navier-Stokes computational codes developed by Pulliam and Steger[1] and Schiff and Steger[2] have been applied to a variety of projectile flow fields at transonic and supersonic velocities. Our early efforts focused on the validation of the computational codes by making detailed comparisons with experimental data which were obtained for that express purpose. This code validation phase was carried out over the time period from 1975 to 1983. During this time period, the ability to predict the Magnus characteristics of spinning shell at supersonic velocities was confirmed. The Magnus coefficient is the critical parameter since it is a viscous effect and is 1/10th to 1/100th of the normal force. Figure 1 shows an illustration of the forces acting on an artillery shell. Thus, if the Magnus force can be predicted correctly, all the other static aerodynamic coefficients can also be predicted accurately.

The Aerodynamics of Spinning Shell

The critical aerodynamic behavior for a spinning artillery shell occurs in the transonic velocity regime. This critical behavior occurs between Mach = 0.9 and 1.0 and results in the gyroscopic stability of the shell being at a minimum where the Magnus moment and pitching moment are at a maximum. Figure 2 shows the expected behavior of the pitching moment coefficient as a function Mach number. Since the Magnus pitching moments have maximum values at some subsonic Mach number between 0.9 and 1.0, the determination of these coefficients is of greatest interest in this speed range. Unfortunately, this is the speed range which requires the greatest computational resources.

The geometry of a typical artillery shell, shown in Figure 3, consists of an ogive forebody with a flattened nose, cylindrical midbody and a boattailed afterbody. The flowfield for this type of shell at a transonic Mach number of 0.94 is shown as a spark shadowgraph from the BRL Transonic Range in Figure 4. The flowfield is shown to consist of significant regions of subsonic and supersonic flow, shock-boundary layer interactions, and separated flow at the base of the projectile. The modeling of this flowfield is further complicated by the loss of pitch plane symmetry that occurs due to the effect of surface spin. In order to model this flowfield, three-dimensional, time-marching, Navier-Stokes computational techniques are required.

The flowfield for a projectile in flight at supersonic velocity is shown in Figure 5. The characteristic of this flowfield of particular interest here is that the effect of flowfield disturbances are only felt downstream. Thus the Parabolized Navier-Stokes (PNS) computational

technique can be applied. The computational technique has been very successful at predicting the aerodynamic behavior of spinning shell including the Magnus effect. These results have been extensively reported[3] and will not be discussed further here.

Several papers have been written over the past five years describing our attempts to predict the aerodynamic coefficients at transonic velocities.[4-5] Figure 6 shows the results achieved on a Cray 1 using two million words of memory. The peak value of the pitching moment is about right; however, the trend of the coefficient with Mach number is unsatisfactory. Our latest attempt, which has not yet been published, was recently completed on the X-MP/48 at the NASA Ames Research Center. This computation took a year to complete due to problems of remote access, file storage and CPU availability. In order to carry out the full computation in which the entire projectile with the base region and the effect of surface spin are included, we expect to require at least eight million words of memory. The CPU time on an X-MP/48 using a fully vectorized code is expected to be of the order of 45 hours. This is the time using a single processor. It is obvious that to achieve improved turnaround time, the ability to perform computations on multiple processors is important.

Base Flow Modeling

Base region flowfield computations at zero angle of attack have been performed at BRL for several years. The results of these computational studies have been reported in References 6 and 8. The technique uses the thin-layer, time-marching Navier-Stokes computational code as reported by Nietubicz, Pulliam and Steger.[7] An important feature of the technique is the ability to preserve the sharp corner at the base of the projectile. This is achieved using a zonal gridding approach.

An example of the application of this predictive capability to current projectile development concerns is shown in Figure 7 where two examples of irregular base region configurations are shown. These base configurations are currently being considered as modifications for fielded Army shell. The configurations are known to have measurable effects on the flight performance of the shell. Computational studies are underway to predict the total drag of the shell using the axisymmetric Navier-Stokes computational code. Using the X-MP class of machine, a substantial matrix of results can be developed over the speed range of interest, .8 < M < 2.5. An example of recent results achieved is shown in Figure 8 where the total drag for the standard and modified base geometries are plotted versus Mach number. Full 3D simulations are desired in order to provide the complete aerodynamic performance; however, the scope of results needed and the timeframe involved make this achievement unattainable.

The base flow modeling has been also been extended to include mass injection into the base region.[8] This capability is desired to predict the performance of rocket assist and base bleed shell. The current configuration of the XM864 base bleed shell is shown in Figure 10 as an example. Recent results achieved in the modeling of

this type of flow is shown in Figure 9 where the mass injected is modeled as a perfect gas. This figure compares the computation to an experiment conducted for the US Army Missile Command at AEDC. The results show comparisons of surface pressures at the base of the model. These results are encouraging; however, the real problem includes effects of multi-phase flow with combustion. The modeling of these effects is of considerable interest and research in this area is in progress.

Finned Projectiles

Kinetic energy penetrator projectiles are of considerable development interest within the Army. These are long L/D, finned projectiles which are launched at high supersonic velocities (M > 4.5) and have a very short time-of-flight (3-4 seconds maximum). A simplified drawing of a typical fielded round (M735) is shown in Figure 10. A spark shadowgraph taken in the BRL Transonic Range of this projectile in flight at Mach = 4.5 is shown in Figure 12.

A series of computational studies for this type of projectile have been carried out using the PNS computational technique and are reported in Reference 9 and 10. Figure 13 shows the development of particle traces at the surface of the projectile in the vicinity of the fins. A comparison between the computations and free flight measurements of pitching moment is shown in Figure 14. In an attempt to achieve better comparisons with the experimental measurements, computations have been made with highly dense grids in the vicinity of the fins by coupling solutions from PNS and time-marching techniques. The results achieved indicate some improvement; however, further improvement in the ability to predict the aerodynamics of these shapes await the impact of greater computational resources than has been used to this date. This is especially true since current interest is in projectiles with L/D's greater than 20.

Interior Ballistic Modeling

The interior ballistic cycle involves the combustion of solid propellant in a gun tube which creates the high pressure required to propel the projectile out of the gun tube into free flight. The time of the cycle is of the order of 10-15 milliseconds. The maximum pressures reached are of the order of 50,000 psi and the flame temperature of the burning gases is of the order of 2500 R. The configuration of the propellant consists of rods or sticks which are packaged together to form a loosely packed bundle or multiple bags of material.

The ignition of the propellant is a very important aspect of the burning since the pressure-time behavior of the combustion process can, if too violent, result in the destruction of the breech of the gun. Thus, the interior ballistic problem has the following characteristics: (1) time dependent; (2) multi-phase flow (solid and gaseous); (3) combustion; (4) high temperature; (5) high pressure; (6) real gas effects; (7) chemically reacting gas.

Due to the highly complex nature of the interior ballistics problem, current computational modeling techniques are far from being able to adequately model the full physical processes of interest. Thus, current computational modeling[11-12] makes use of a combination of lumped parameter, two dimensional-two phase flow, quasi-one dimensional flow modeling and modified constitutive laws for chemical energy release, frictional losses, heat loss to the gun tube and erosive burning. A schematic illustration of a bagged charge inside of a gun chamber is shown in Figure 15. This drawing shows the basic configuration of the interior ballistic problem prior to ignition. A schematic illustration of the configuration for a multi-increment charge is shown in Figure 16. The presence of considerable ullage (or empty space) is illustrated and is an important factor in the performance of the propellant. The combination of modeling techniques used to model this multi-increment configuration is shown in Figure 17.

Terminal Ballistic Modeling

The terminal ballistics problem consists of several processes including: response of structures such as vehicles and shelters to blast waves, penetration of armor by long rod projectiles and penetration of armor by high velocity plasma jets.

Armor Penetration

There are a number of penetration and impact codes which have been developed. Eight such codes are surveyed in Reference 13. EPIC-3[14] is actively used at BRL. EPIC-3 is a finite element code in a Lagrangian formulation. Models for material properties and equations of state to account for high energy impact are an important part of the computational technique. An example of an EPIC-3 computation for impact of a steel ball onto an aluminum plate is shown in Figure 18. Excellent agreement with experiment has been obtained for this case.

Another code used extensively at BRL for armor penetration modeling is the EPIC-2 code.[15] An example of the application of this code to predict the penetration of single plate armor by a long rod is shown in Figure 19. In this figure, examples are shown of the time-dependent armor penetration process for two angles of impact, normal and oblique to the surface. The modeling of the armor penetration process is accomplished by a combination of Lagrangian and Eulerian techniques. Modeling of the dynamic response of the target material to the high energy release is an important aspect of this computational technique. The full problem of interest requires the capability to model penetration of multiple armor plates at high angles of obliquity. Fully three-dimensional computations require considerable computer resources in terms of CPU time and storage capacity.

Incident Blast Wave Effects

Blast effects are of concern in the ability of military vehicles and command post structures to withstand the effects of incident blast/thermal waves caused by nuclear bursts. The computational modeling of these effects utilize time-dependent Euler and Navier-Stokes techniques. A typical example of the problem of interest[17] is depicted schematically in Figure 20 where a vehicle is shown being struck by an incident blast wave. Reference 17 reported the application of an inviscid, finite-difference code to predict the time-dependent flow over several objects of generic interest. An example of the resulting sequence of density contours for the flow over the truck are shown in Figure 21. Fully three-dimensional viscous computations coupled with the effect of the thermal pulse are required to properly model the complex shapes and flowfield conditions of interest.

CLOSING REMARKS

A brief overview has been presented of the computational modeling applications and activities at the US Army Ballistic Research Laboratory. The topics covered are by no means complete. Several additional areas of active research are in progress. The scope of this paper was not intended to provide a complete coverage, only a partial coverage within the allowed constraints. Given the supercomputer resources now available at the BRL, the impact of computational modeling on weapon system design and development is certain to become significant.

REFERENCES

1. Pulliam, T.H. and Steger, J.L., "On Implicit Finite-Difference Simulations of Three-Dimensional Flow," AIAA Journal, Vol. 18, No. 2, February 1980, pp. 159-167.

2. Schiff, L.B. and Steger, J.L., "Numerical Simulation of Steady Supersonic Viscous Flow," AIAA Journal, Vol. 18, No. 12, December 1980, pp. 1421-1430.

3. Sturek, W.B. and Schiff, L.B., "Numerical Simulation of Steady Supersonic Flow over Spinning Bodies of Revolution," AIAA Journal, Vol. 20, No. 12, December 1982, pp. 1724-1731.

4. Nietubicz, C.J., Sturek, W.B. and Heavey, K.R., "Computations of Projectile Magnus Effect at Transonic Velocities," AIAA Journal, Vol. 23, No. 7, July 1985, pp. 998-1004.

5. Nietubicz, C.J., Inger, G.R. and Danberg, J.E., "A Theoretical and Experimental Investigation of a Transonic Projectile Flow Field," AIAA Paper No. 82-0101, January 1982.

6. Sahu, J., Nietubicz, C.J. and Steger, J.L., "Numerical Computation of Base Flow for a Projectile at Transonic Speeds," AIAA Paper No. 82-1358, August 1982.

7. Nietubicz, C.J., Pulliam, T.H. and Steger, J.L., "Numerical Solution of the Azimuthal-Invariant Thin-Layer Navier-Stokes Equations," AIAA Journal, Vol. 18, No. 12, December 1982, pp. 14   412.

8. Sahu, J., Nietubicz, C.J. and Steger, J.L., "Navier-Stokes Computations of Projectile Base Flow with and without Base Injection," AIAA Paper No. 83-0224, January 1983.

9. Weinacht, P., Guidos, B.J., Kayser, L.D. and Sturek, W.B., "PNS Computations for Spinning and Finned-Stabilized Projectiles at Supersonic Velocities," AIAA Paper No. 84-2118, August 1984.

10. Weinacht, P., Guidos, B.J., Sturek, W.B. and Hodes, B.A., "PNS Computations for Spinning Shell at Moderate Angles of Attack and for Long L/D Finned Projectiles," AIAA Paper No. 85-0273, January 1985

11. Gough, P.S., "Modeling of Rigidized Gun Propelling Charges," Contract Report ARBRL-CR-00518, US Army Ballistic Research Laboratory, Aberdeen Proving Ground, MD, November 1983.

12. Horst, A.W., Robbins, F.W. and Gough, P.S., "A Two-Dimensional, Two-Phase Flow Simulation of Ignition, Flamespread and Pressure-Wave Phenomena in the 155-mm Howitzer," ARBRL-TR-02414, US Army Ballistic Research Laboratory, Aberdeen Proving Ground, MD, July 1982.

13. Zukas, J.A., Jonas, G.H., Kimsey, K.D., Misey, J.J. and Sherrick, T.M., "Three-Dimensional Impact Simulations: Resources and Results," Computer Analysis of Large-Scale Structures, AMD Vol. 49, edited by K.C. Park and R.F. Jones, Jr., published by ASME.

14. Johnson, G.R., BRL-CR-343, US Army Ballistic Research Laboratory, Aberdeen Proving Ground, MD, 1977.

15. Snow, P., "KEPIC-2," Kaman Sciences Corporation Report K82-46U (R), August 1982.

16. Kimsey, K.D. and Zukas, Jonas A., "Contact Surface Erosion for Hypervelocity Problems," ARBRL-MR-3495, US Army Ballistic Research Laboratory, Aberdeen Proving Ground, MD, February 1986.

17. Mark, A. and Kutler, P., "Computation of Shock Wave/Target Interaction," AIAA Paper No. 83-0039, January 1983.

Figure 3. Simplified Geometry of the M483 Artillery Shell
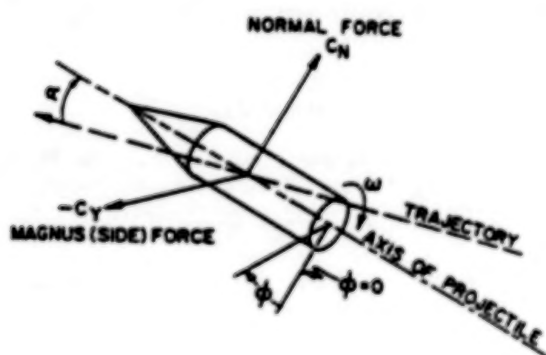
Figure 1. Aerodynamic Forces on a Spinning Shell
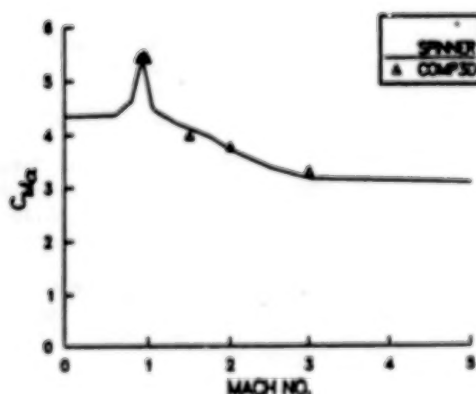
Figure 2. Critical Aerodynamic Behavior of a Boattailed Artillery Shell
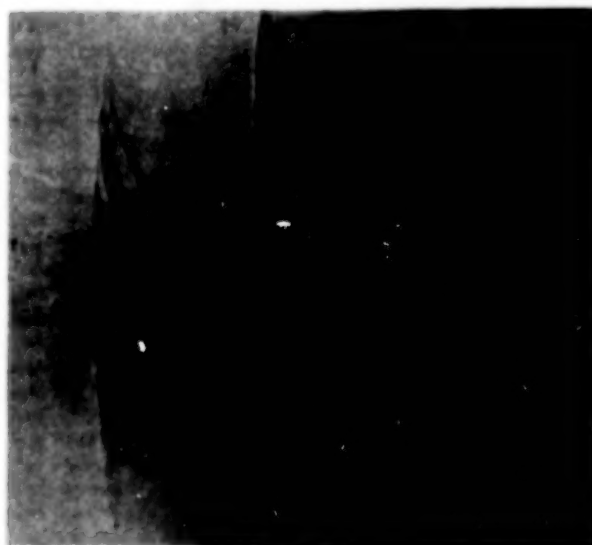
Figure 4. Spark Shadowgraph of a Shell in Flight at M = .96
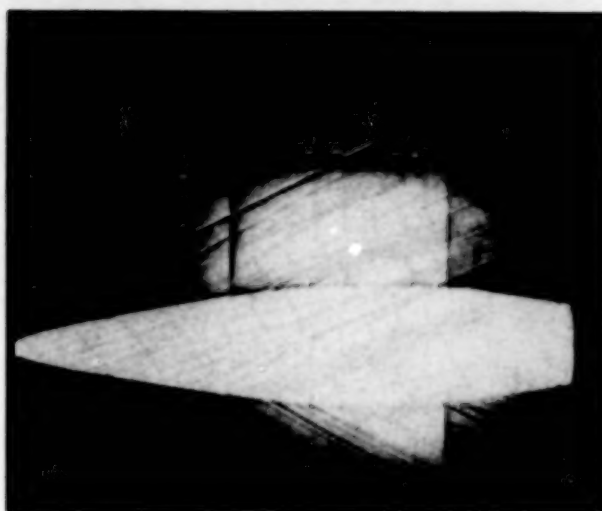
Figure 5. Spark Shadowgraph of a Shell in Flight at M = 2.3

Figure 8. Total Drag Versus Mach Number for the Standard and Domed Bases, M483
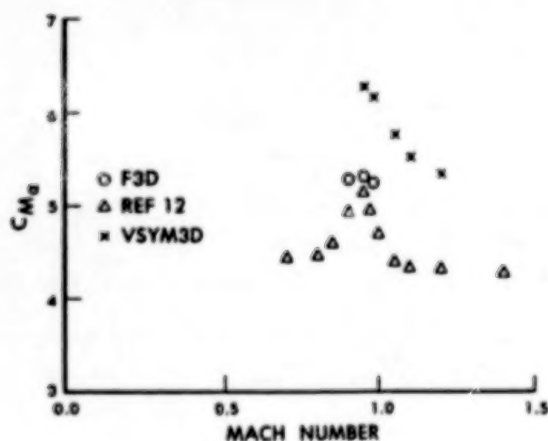
Figure 6. Pitching Moment Versus Mach Number for M549 Shell
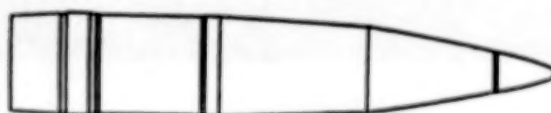
Figure 9. XM864 Base Bleed Shell

Figure 7. Standard and Domed Base Configurations for the M483
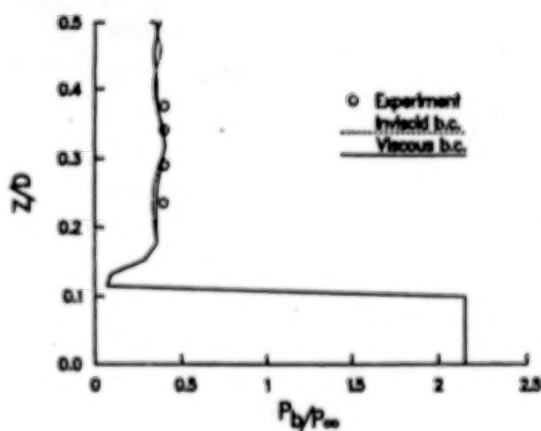
Figure 10. Base Pressure Predictions for the MICOM Test Case

179

Figure 11. Simplified Geometry of the M735 KE
Penetrator Projectile

Figure 14. Surface Flow Patterns in Vicinity of
Fins for M735 Geometry

Figure 12. Spark Shadowgraph of Flight of M735
at Mach = 4.5

Figure 15. Schematic Illustration of a Bagged
Charge/Gun Chamber Geometry

Figure 13. Slope of Normal Force Coefficient
Versus Mach Number for M735

Figure 16. Schematic Illustration of a Multi-
Increment Charge

180

2D2P - TWO-DIMENSIONAL, TWO-PHASE
Q1DA - QUASI-ONE-DIMENSIONAL, AXIAL (SINGLE- or TWO-PHASE)
Q1DR - QUASI-ONE-DIMENSIONAL, RADIAL
LP - LUMPED PARAMETER

Figure 17. Modeling Techniques for Multi-
Increment Charge
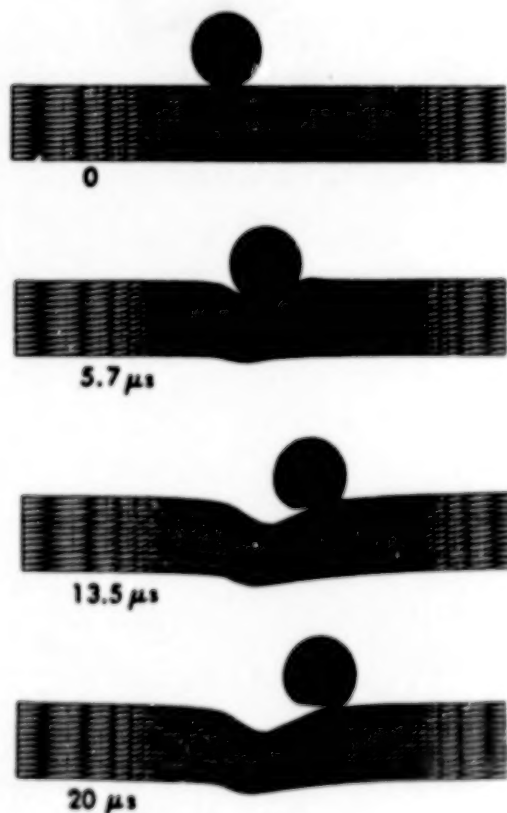
Figure 18. Impact of Steel Ball with Aluminum
Plate

Figure 19a. Penetration of a Single Plate by a
Long Rod
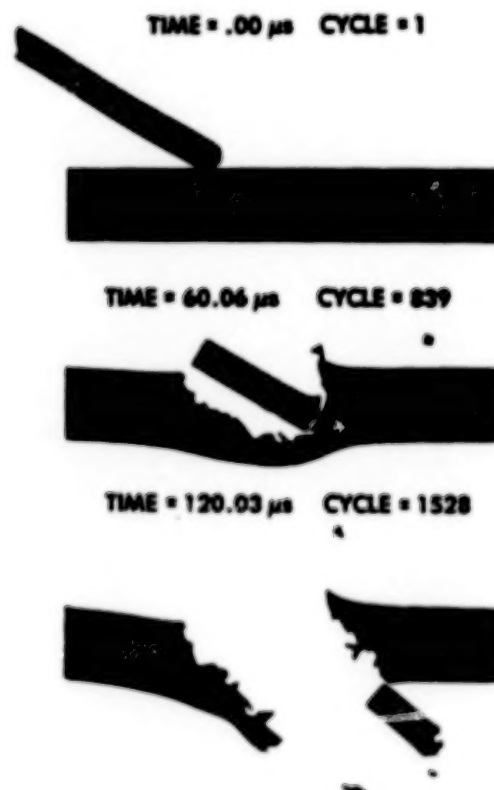
Figure 19b. Penetration of a Single Plate by a
Long Rod

181
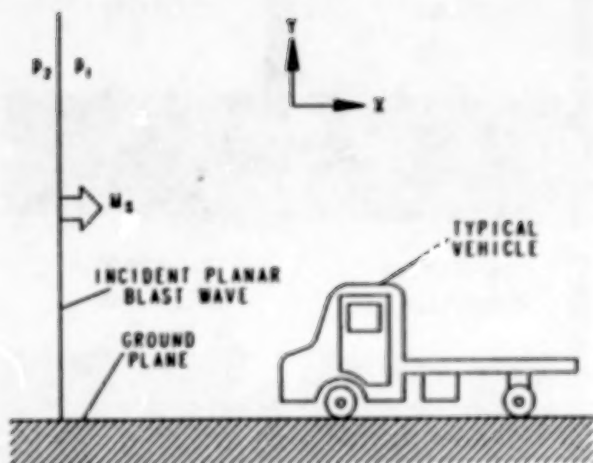
Figure 20. Schematic Illustration of a Vehicle-
Blast Wave Interaction

(a) $\Delta t_{ff} = .08$

(e) $\Delta t_{ff} = .40$

(p) $\Delta t_{ff} = .56$
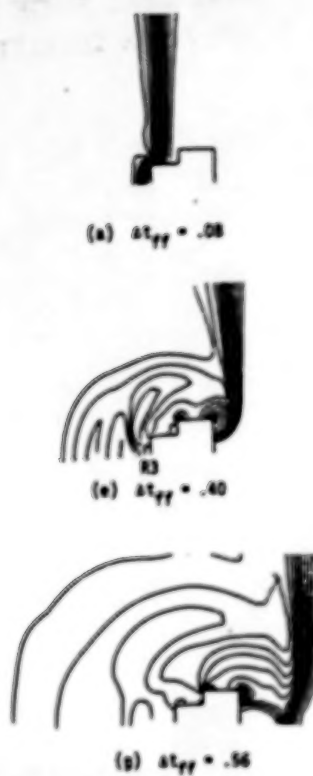
Figure 21. Density Contours for Blast Wave-
Vehicle Interaction

COMPUTATIONAL FLUID DYNAMICS IN A MARINE ENVIRONMENT

Arthur D. Carlson
Naval Underwater Systems Center

INTRODUCTION

The introduction of the supercomputer and recent advances in both Reynolds averaged, and large eddy simulation fluid flow approximation techniques to the Navier/Stokes equations, have created a robust environment for the exploration of problems of interest to the Navy in general, and the Naval Underwater Systems Center in particular. The following discussion will address the nature of problems that are of interest, and the type of resources needed for their solution. The goal is to achieve a good engineering solution to the fluid-structure interaction problem. It is appropriate to indicate that a paper by D. Chapman[1] played a major role in developing our interest in the approach discussed. Further there are several researchers who have pivotal roles in the development of and use of these computational fluid dynamic (CFD) tools. Two of these researchers are Dr. A. J. Kalinowski, who has a leadership role in the large eddy simulation code we are developing, and C. A. Wagner, who has played a similar role in the further development of the Reynolds averaged code INS3D.

NATURE OF PROBLEMS

It is convenient to divide our interests into two classes: the first is where the scale permits a more macroscopic approximation of the flow, i.e., it is not dominated by the boundary layer alone but includes a significant part of the flow outside the boundary layer, the second is dominated by the boundary layer and requires as detailed (as practical today) a description of the flow as possible. Figure 1 illustrates this first class, where we show two bodies in close proximity to one another, perhaps with a relative velocity. The flow is three-dimensional,

$$V_1 \longleftarrow$$
$$\longrightarrow V_2$$
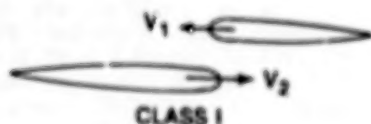
CLASS I

Figure 1.

unsteady, laminar/or turbulent and incompressible.

A second class of problem is shown in Figure 2.

VELOCITY
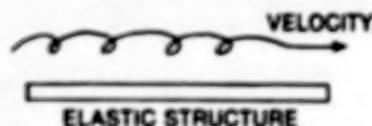
ELASTIC STRUCTURE

CLASS II

Figure 2.

Here we have an elastic structure that can respond to the boundary layer generated forces, and in turn cause the flow to be influenced by the structural motion. Further the structure may absorb energy and/or be a source of energy. We are interested in as many details of this interaction as are possible to compute.

It appears that a computer code developed at Ames Research Center called INS3D for Incompressible Navier/Stokes in 3 Dimensions will be quite appropriate for class I problems. Reference 2 provides a thorough despription of the theoretical and numerical solution techniques employed in INS3D. We are working with this code on a series of laminar problems with viscosity, and for turbulent flow situations. The turbulent solution is being tested for one example against a right circular cylinder for which good experimental data is available. The problems being addressed are quite large and require a machine the size of a CRAY 2 if we are to do practical work. Of course there is no difficulty in thinking of problems that would require N number of CRAY 2's, but for this point in time good insights can be achieved with a CRAY 2. Because the pressure field is important to the Navy, INS3D is very useful since it calculates pressure explicitly. The equation for this approximation is;

$$\frac{\partial P}{\partial t} + \beta \nabla \cdot \vec{V} = 0$$

where P is pressure, t is time, β is constant and V is velocity.

One effect not considered is any coupling of INS3D with the elasticity of a structure.

To examine class II problems NUSC is developing its own code called TURBO (Turbulent Unsteady-flow over Resilient BOundaries). TURBO is being written for a CRAY 2 environment, at first for single CPU, later as a mulitple CPU code. An important feature in TURBO is the

coupling of the three-dimensional Navier/Stokes equations to a viscoelastic structure. Following is the order of development of the code and some of its details.

. Version I - The complete Navier/Stokes equations with no modelling are coupled to an orthotropic viscoelastic plate. An analytical solution is used for the plate.

. Version II - The complete Navier/Stokes equations with no modelling are coupled to a three-dimensional viscoelastic structure. The structure is represented by finite elements.

. Version III - A turbulence model in conjunction with the large eddy simulation approximation is used to model the fluid. The structure is viscoelastic and represented by finite elements.

SOLUTION METHODOLOGY

. The fluid equations are transformed by a double Fourier transformation in the streamwise and spanwise direction into a wave number space. This is so we can sample the computational space with fewer computational points, and secondly automatically satisfy periodic boundary conditions. In the vertical direction a closed form solution to the differential equation is used. In principle this should allow us to resolve the flow character near the wall to a small scale.

. Provisions have been made for compressibility effects in the fluid. This is achieved by a formula of the form:

Change in Pressure = Constant (Change in Density)

. Periodic boundary conditions are assumed in the streamwise and spanwise direction. Currently in the vertical direction there is a rigid boundary at the top surface. Research is underway to lift this restriction and provide for a free field.

. At the bottom surface, the very complicated, but very critical, coupling of the flow equations to the flexible structure surface employs an arbitrary Eulerian/Lagrangian coordinate system. This system in effect requires that we observe, i.e., compute the solution along a predetermined, prescribed path. We perform a coordinate transformation that in effect transforms the deformed fluid mesh into a regular mesh in which the fluid equations are solved. Then the new updated forces and fluid displacement are transformed back and applied to the structural surface. The finite element method is then applied to the structural domain and a finite element solution methodology is carried out there.

. Work is currently also underway to use more than a single CPU for the solution of TURBO. The initial version though will use a single CPU.

PRE AND POST PROCESSING OF MATH MODEL

It is imperative that sophisticated graphics be employed if a comprehensive analysis is to be carried out in a production type mode, utilizing rapid turnaround and user friendliness. To this end we have acquired a Silicon Graphics 3030 color workstation along with the GAS (Graphics Animation System) and PLOT3D software developed at NASA Ames. This software enables rapid analysis of large CFD data sets along with automated movie making for visualization and presentation of interesting results. The movies are recorded in 16mm format and then translated to videotape.

OPTIMIZATION

The mathematics of optimizaton of an N dimensional space, and the computer programming for it, has reached the state where it is reasonable to explore the use of such techniques in conjunction with codes like INS3D and TURBO. Vanderplaats[3] gives an excellent outline of the optimization method. To be successful from an engineering point of view will require judicious use of optimization codes and very good estimations of a set of initial designs. Using the structures shown in Figure 3 as an example one can pose the following problem: What shape body will provide a minimum pressure distribution when
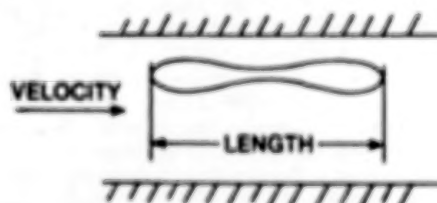
Figure 3.

subject to a set of constraints such as a fixed length and some minimum volume? The problem here is that there is no explicit way to write a relationship between drag and the body dimensions. Hence we start with an initial set of shapes that work "well" and iterate using an approximate search for the minimum objective function. An example of an optimization code that could be combined with INS3D is ADS (Automatic Design Synthesis) and is described in reference 4. This code has software for a number of solution strategies such as sequential linear programming, optimizer options such as the modified method of feasible directions method for constrained minimization, and a number of search options such as a technique to find the minimum of a constrained function using the golden sections method.

There is no guarantee that a good solution can be reached in a realistic time given the computer resources at this particular point in time, but if not today, almost certainly in the near future.

OCEAN DYNAMICS

It appears that INS3D has the necessary ingredients and flexibility for its application to questions involving ocean dynamics. To use it several key issues will have to be resolved: First one must include coriolis forces to account for the earth's rotation effects on the fluid, second the boundary condition at the ocean-air interface must be accounted for, and third the ability to account for variations in density within the fluid, and ultimately with time, will have to be made. The other boundary conditions will depend on the depth of water and the lateral extent over which the model is to be applied on a case by case basis. Our solution strategy is to start with as simple a model of the ocean as possible, and progressively build those characteristics into INS3D, verify these with an experiment(s), and proceed with further complexities. Because we have a good idea of the parameters we are looking for, our efforts will be directed to adding, within an engineering model, just enough to get working insights.

TESTING

The ultimate measure of a computed design is proof by test and then by field use. Several water tunnel test facilities exist today which can be used but these will most likely have to be expanded not only in size, but in the number and accuracy of velocity and pressure sensors that are used. Smaller pressure sensors and three-dimensional velocity measurements at many points simultaneously will be required. Laser velocimetry techniques are useful here.

CONCLUSIONS

Order of magnitude improvements in the ability to separate out cause from effect in complex flow situations is about to occur in important problems. The pacing item is the computer, although such esoteric areas as tubulence modelling will provide significant challenges. As one moves into production use of these new tools, pre and posts processing of the fluid and structure models will also require further improvement.

The immediate future will be devoted to proving out the new CFD tools by both numerical checks against analytical solutions, as well as careful experimental checks. One can think of the product of numerical solutions on supercomputers as providing a numerical microscope with which to view various flow phenomena. What ultimately remains then is the creative use of such tools to solve real problems.

REFERENCES

1. Chapman, Dean R.: Computational Aerodynamics Development and Outlook, AIAA Journal, vol. 17, no. 12, Dec. 1979, pp. 1293-1313.

2. Kwak, Dochan; and Chakravarthy, Sukumar R.: A Three-Dimensional Incompressible Navier-Stokes Flow Solver Using Primitive Variables, AIAA Journal, vol. 24, no. 3, Mar. 1986, pp. 390-396.

3. Vanderplaats, Garret N.: Numerical Optimization Techniques for Engineering Design: With Applications, McGraw-Hill Book Co., Inc., 1984.

4. Vanderplaats, Garret N.: COPES/ADS - A Fortran Control Program for Engineering Synthesis Using the ADS Optimization Program, Engineering Design Optimization, Inc., 1984.

N87
26014

COMPUTATIONAL ASTROPHYSICS

Richard H. Miller
University of Chicago

Introduction

Astronomy is an area of applied physics in which unusually beautiful objects challenge our imaginations to explain observed phenomena in terms of known laws of physics. It is a field that has stimulated the development of lots of physical laws and lots of mathematical and computational methods. Many statistical and numerical methods may be traced to 19th century efforts to determine orbits of solar system objects such as comets and asteroids. Numerical calculations were to be done by hand, with pencil and paper. Methods were needed that would guarantee a reliable orbit with minimal effort, based on imperfect observations that were not evenly spaced in time. In another area, some well-known and powerful stability techniques were developed to study the classical 3-body problem by mathematicians like Poincaré. The stability of the solar system is a problem that continues to challenge mathematicians. The story of Newton, apples, and the moon's orbit is well known to all of you.

Outstanding scientists were drawn to astronomical problems by their charm and beauty, not to deny practical usefulness, in an earlier era. The opening paragraphs of Maxwell's Adams Prize Essay (1859) on the structure and stability of Saturn's rings eloquently appeal to the charm of trying to understand a natural phenomenon for which no practical use could be imagined. He did that in an era when astronomy was the quintessence of "practical" science for navigation at sea. Techniques worked out to attack astronomical problems are useful in many other contexts, and they promise to remain useful for years to come.

Charm and beauty characterize many problems of present-day astronomy as well. As in earlier eras, astronomical problems drive us to consider phenomena in extraordinary physical conditions. Physical conditions in astronomical objects take on far more extreme values than can be mimicked in any terrestrial laboratory. Densities, for example, range from less than one atom per cubic centimeter $(\rho \sim 2 \times 10^{-24} \text{gm/cm}^3)$ in interstellar space to nuclear densities $(\rho \sim 10^{13} - 10^{16} \text{gm/cm}^3)$ in neutron stars, rising a bit higher if the star is on the verge of collapsing to a black hole. Temperatures range from around $100°K$ in molecular clouds to $10^{10} °K$ at the centers of pre-supernova stars. Magnetic fields can be found that range from a microgauss in interstellar space to 10^{12} gauss at the surface of a neutron star. Magnetic fields are important because the interstellar medium tends to be a highly ionized plasma, thus to have high conductivity.

Boundary conditions are much cleaner in astronomical problems than in laboratory experiments as well. Astrophysical plasmas (e.g., the solar wind, solar atmosphere, interstellar medium) are not contaminated by boundaries as are laboratory plasmas. Problems in which laboratory boundary conditions differ from real-world situations are familiar to people working on aircraft design as well.

Astronomers have been in supercomputing for the past century and a half as well, if we define supercomputing to mean numerical computation on an unprecedented scale for its time. Imagine the numerical work in computing ephemerides for navigational purposes in the 19th and first half of the 20th centuries. An astronomical work still stands as a landmark from the days when it was first done with punched-card calculators: the "Coordinates of the 5 Outer Planets 1653-2060," by Eckert, Brouwer, and Clemence (1951). A sign of the times: five years ago, amateur astronomers took it as a challenge to repeat that calculation on PC's like the TRS-80. Fortunately, they could refer to the original work for methods and for numerical values that could be used to check their calculations.

Three features drive present research efforts that impel astronomers to seek the computational power of supercomputers.

(1) A complex interplay of many physical processes. Interactions are almost always nonlinear. General physical situations must be taken into account to fit observations.

(2) Higher quality observational material discloses details of flow and emission patterns that require complex models. Several factors contribute. (a) Improved (multi-element, low-noise) detectors. (b) Extension to new wavelength bands (radio, infrared, ultra-violet, x-ray, gamma rays), with (c) high resolution imaging and (d) spectroscopic resolution as well. These features come from excellent new instruments such as the VLA and VLBI in radio astronomy, from KAO and IRAS and the future SOFIA and SIRTF in infrared astronomy, from IUE and the Hubble Space Telescope in visible and ultra-violet wavelengths, and a variety of satellites for x- and gamma rays. European and Japanese satellites are coming on line as well, and we saw cooperative programs with them and with the Soviets in the recent Halley missions. Scientific use of all these superb instruments requires source modeling in at least as great detail as the instruments can yield.

(3) Reduction of raw observational data to a form comprehensible by people. Instruments like the VLA (a 27-element interferometer or synthetic aperture) produce what is essentially a Fourier transform of the source brightness distribution (in two spatial dimensions for each spectral passband for possibly as many as 256 spectral bands), corrupted by sky noise, by receiver and antenna noise, by a "dirty" raw synthesized beam, and messed up by the atmosphere. Other instruments produce data encoded differently, but the data reduction problem is much the same. High data rates exacerbate the problem. These newer instruments produce a lot of data in a short time, then they switch to a new source and produce a lot more data.

We see again the pattern that techniques developed for astronomical use have uses in other areas: Modern oil field exploration uses techniques roughly equivalent to turning the VLA upside down so its antennas detect signals coming from inside the earth. Some of the astronomical imaging methods such as CLEAN, self-calibration, hybrid mapping, etc., are finding use there. Maximum entropy restoration methods are being developed actively in both camps, as they are elsewhere.

Image restoration in radio astronomy is truly impressive. Within the past couple of years, a map of the radio source Cygnus-A has been produced with 1000 or more pixels along an edge, and with a dynamic range (ratio of brightest spot to faintest detail recorded) of about 10,000 to 1. This is in the presence of sidelobes that can range to 10% for a "dirty beam." It is difficult to look at that map without a tingle of admiration and excitement.

Current Computations

Computation has had an impact on nearly every area of astrophysics. Many of the problems of astrophysical interest have their origin in trying to understand the structure and aging (evolution) of stars. Particularly interesting computational problems arise with studies of the final death-throes of a massive star—a supernova outburst. A core like a neutron star (density around 10^{15}gm/cm^3, temperature about 100 Million degrees K, size about 10 miles across, about 1 solar mass or 10^{33} gm) is thought to pass a stability limit in its equation of state that leads to a collapse. A shock is sent outward into the surrounding envelope. Time scales are milliseconds (sound speed is nearly the velocity of light). Nuclear burning in the shock front transmutes most nuclei to the doubly magic Ni^{56} (28 protons and 28 neutrons). So many neutrinos are produced, and they carry such a large fraction of the energy, that neutrino opacity limits energy transport. Things become particularly interesting when the shock encounters the innermost nuclear-burning shell of the pre-supernova star where silicon is being burnt. The

upshot is that a burst of energy (10^{54} ergs) is produced that makes a star as bright as an entire galaxy (10^{11} solar luminosity or about 10^{44} ergs/sec) that takes weeks or months to expand and cool, as the outburst gradually fades.

This is but one of the fascinating problems astrophysicists are tackling computationally today. Star formation, stellar evolution, and physics of the interstellar medium are others. Common threads run through the physics of all these situations. That physics includes (1) Radiative transfer (2) Transient fluid flows, and (3) Radiation hydrodynamics. This last term refers to situations in which radiation pressure dominates mass motions. Actual physical situations involve some cases where radiation dominates, others where fluid flows dominate, and transition cases. The fluid flows influence the radiation field and radiative transport as well. Strong shocks frequently occur in examples of astrophysical interest. The state of the art can cope with these cases, and nuclear burning is included in modern codes. Nuclear burning provides an energy source (and a sink in some cases). Nuclear reaction networks bring in several hundred nuclear species with vastly different lifetimes, so the problems are very "stiff." Magnetic fields have so far not been successfully included, so we cannot yet handle hydromagnetic cases with radiation and nuclear burning. But that is coming. It should be here in a couple of years.

Numerical relativity is another area receiving a lot of attention. Relativity here means general relativity—well known for numerical intractability because the nonlinearities affect the geometry of spacetime. Black holes were made to collide a few years ago (lots of gravitational radiation emitted). Star clusters going relativistic are just now being studied—but even that with restrictive symmetries because of numerical and conceptual difficulties. A star cluster goes relativistic when its central density and size become great enough to be near the Schwarzschild radius for a black hole.

We see once more that new methods have to be developed to handle extreme physical conditions that first come to our attention in astrophysical situations. Often these methods can help with problems in other scientific and technical areas, even if conditions are not so extreme. Algorithms must be robust and dependable.

Dynamics of Galaxies

Let me turn to another particularly beautiful area of computational astrophysics, the area of my own research, the dynamics of galaxies. Galaxies are beautiful both in photographs and in VLA maps, and they are dynamical objects. I will do this by describing an investigation that has been occupying our attention for the past couple of years. It is a good example of the method of numerical experimentation.

Experiments in terrestrial laboratories are out of the question for problems in the dynamics of galaxies as well. Distances are so great that there is no hope of going out beyond the object to get a look from the other side. There is no way to kick a galaxy to see if it bounces—to check its stability as you would check the stability (or robustness) of everyday objects in the laboratory. Even if we could, the time scales are so long we could not wait. Dynamical times are typically about 100 million years. The need for experimental checks on analytical theories is as great in galaxy dynamics as in any area of physics. Numerical experiments, based on large scale computations, are the closest thing we have to the laboratory experiments of other parts of physics. They are much closer in style and spirit to laboratory experiments than to conventional (analytic) theory. Numerical experiments are initial value problems. They are defined by the initial conditions. The same rules are used for carrying out all experiments, and those rules contain as much of the essential physics of galaxies as possible. Once an experiment is started, it runs to "completion" with no interference.

Studies in the dynamics of galaxies produce strikingly beautiful objects as well as charming dynamical insights. Galaxy dynamics is challenging because one's guesses are so often wrong. This happens, of course, because self-consistent systems have so many options open to them that they usually select one you hadn't thought about. It is exciting as you begin to see which option the system selected and as

you try to figure out why it chose that option.

The investigation reported here started out as a study of the dynamics of dark lanes in the so-called dark-lane elliptical galaxies. This investigation was started by Dr. Althea Wilkinson of the University of Manchester in England, and it was carried out by a team from which Dr. Bruce F. Smith of NASA-Ames was a driving force. Some totally unexpected and surprising phenomena turned up—phenomena that remind one of the strange things observed at the center of our own Galaxy. I want to concentrate on those phenomena.

The experiments started with a disk of particles embedded within an oblate spheroidal galaxy. Both the disk and the oblate spheroid were formed of particles, 400 000 in all. The experiments consist of following the dynamical development of this system for some time, usually several dynamical time periods, by means of a fully self-consistent fully three-dimensional n-body integration. The bulk of the mass is in the oblate spheroid, and it represents the elliptical galaxy. The disk represents the dark lane. It contains little mass (1000 particles), and notwithstanding its dominant optical appearance it has little, if any, dynamical effect on the main galaxy.

The disk was flat at the start. Its normal formed an angle of 45° with the spheroid axis. Its center coincided with the center of the galaxy. Disk particles orbit around the galaxy center so the disk is centrifugally supported against the gravitational forces of the galaxy. Disk particles have different velocities at different distances from the center, so the disk is said to "rotate differentially." It also precesses differentially, and it soon becomes warped, taking on a sequence of beautiful shapes.

We routinely make motion pictures that show the dynamical development of the systems we study. Shapes and motions are so complex that one cannot understand them otherwise. It is safe to say that every significant discovery we have made in 10 years of experimentation has started from some feature first noticed in a motion picture, whether on film or on a graphics display. Good graphics is essential for an experimenter to understand his own results. Of course, motion pictures are great for showing results to others as well, and a motion picture derived from an experiment run on the NAS Cray-2 will be shown.

The unexpected feature showed up as we were studying an earlier version of this system on the then new E&S graphics displays at Ames. We had zoomed in for a tight view of the center, watching temporal developments. The center was whipping about. We were concerned lest this be a numerical instability. A motion picture showing a close-up view of the disk center was made as one of our checks. That motion picture will be shown. The motions that troubled us are quite small. The centermost particle moves only as far from the center as the radius of a sphere that would contain but 4×10^{-5} of the galaxy's mass. Nonetheless, it is troubling to an experimenter until he can figure out what causes it. If caused by a numerical instability, it could signal a trouble with the entire sequence of experiments we've done over the past 10 years.

Checks whether we were dealing with a numerical instability led us to study $l = 1$ oscillations of galaxy models, to study the stability of the disk with the galaxy immobilized (i.e., the underlying galaxy was no longer self-consistent), to study the disk in a harmonic oscillator potential rather than the galaxy potential, and to carry out a variety of other checks. The $l = 1$ mode had too low a Q to fit the experiment. Experiments with the galaxy immobilized or with a harmonic potential showed that self-gravitation of the disk was not responsible. Next, we conducted experiments on the galaxy alone, with the disk removed. We had to invent a way to look for motions of the central parts in order to do this. The method used was to locate the extremum of the gravitational potential. We found that the center, as defined by the potential, moved about the center as defined by the mass (the centroid). The most dense part of the galaxy, indicated by the potential center, need not remain fixed, even though the equations of motion require that the mass centroid remain fixed.

Fairly early in this sequence of checks, we plotted the trajectory of the normal to a little patch at the center of the disk. That plot is shown in Figure 1. It looks like the plots of combined precession and nutation in rigid body motion in your elementary mechanics text. Indeed, that is just what it shows—combined precession and

nutation. It is not as clean as the motion shown in the mechanics text, but it is the trajectory of a genuine mechanical motion. It is not the trajectory of a numerical instability.

The second part of the check is shown in Figure 2.

Figure 1. Trajectory of normal to the center of disk as seen on the unit sphere. The trajectory starts at the right side (small amplitude) and winds downward and to the left, ending on the left side with large amplitude.

Figure 2. Plots of position vs. time. Time in the integration is plotted horizontally, the z-component of position vertically. The motion of the centermost particle is shown in the top trace, the potential center wandering in the middle trace, and the motion of a harmonically bound test particle subject to forces produced by that potential center wandering in the bottom track. All three tracks have the same vertical and horizontal scales.

So it's not a numerical instability. But then, what is it? We finally nailed this down with the experiments on the NAS Cray-2.

The potential near the center of a galaxy is harmonic-it is the potential of a (possibly anisotropic) harmonic oscillator. A particle, initially at rest at the center, feels tugged first in one direction and then in another, by the wanderings of the potential center. It acts like a harmonically bound particle in Brownian motion. That is a well-known problem. We checked whether this might be the character of the motions we were observing by integrating the response of a harmonically bound particle to forces it would feel due to the wandering center, and found those motions to match the wanderings of the centermost particle of our disk fairly well.

Now we come to the nailing. Experiments with different numbers of particles showed that the amplitude by which the potential center wanders about the mass center varied inversely with the square root of the number of particles in the galaxy. Separate checks, with a sequence of initial loads produced by different runs of random numbers produced a scatter of potential center positions about the same as the early stages of an actual integration. That confirms suspicions that $\sqrt{n}$ noise causes the potential center to differ from the mass center. Both checks were run with 25,600, with 100,000, and finally with 400,000 particles. The scatter for the integration increases at later times.

The actual motion of the centermost particle is shown in the topmost trace, and the potential center wandering in the middle trace. Finally, a separate integration of a harmonically bound test particle under the tuggings of the actual potential center wanderings is shown as the bottom trace. Notice the similarity of the top and bottom tracks-even to shapes of individual wiggles. The amplitudes are a bit different, indicating that something or other about the galaxy affects the centermost particle at late times. Further, we used oscillation frequencies from an earlier experiment for this comparison, rather than re-determining the frequencies from the actual experiment. That accounts for the phase difference in the two tracks at the end of the experiment. The increasing amplitude looks more like a linear growth rate (up to a limiting amplitude) than like the square-root of time amplitude of the classical harmonically bound particle, suggesting that something more is going on. That can be seen in the center track, where one can imagine that the potential center wanderings near the end are beginning to follow the particle. The system is actually unstable, with feedback coming from the potential center's following the driven particles. But that is a physical, not a numerical, instability.

The experiments are vindicated, but our next task is to determine whether this phenomenon is important in real galaxies. As mentioned earlier, the wanderings are very suggestive of things that happen at the center of our Galaxy, so we could be dealing with an important physical effect. But that involves a separate set of arguments, one that necessarily hinges on of astronomical details. We postpone that to a conference on the dynamics of galactic nuclei.

ALGORITHM DEVELOPMENT

Timothy J. Barth
NASA Ames Research Center

and

Harvard Lomax
NASA Ames Research Center

Introduction

Algorithm: A set of rules for solving a problem in a finite number of steps.

Development: The progression to a more effective state.

The past decade has seen considerable activity in algorithm development for the Navier-Stokes equations. This has resulted in a wide variety of useful new techniques. It would appear, however, that there is plenty of room for further improvements. That is to say, we are far from exhausting all possible sets of rules for these problems and it is highly probable that some remaining ones will be more effective than those we have now.

It is foolish and even counterproductive to anticipate or set milestones for the detailed development of basic or even applied research. The history of science tells us that we can expect something to happen in any major field if active minds capable of original thinking are allowed to pose challenging problems and seek elegant solutions.

What we can do is look backwards and find what we are doing now in a given area of science that was not anticipated ten years ago. Some examples of this type for the numerical solution of the Navier-Stokes equations form the body of this paper. These are divided into two parts, one devoted to the incompressible Navier Stokes equations, and the other to the compressible form. The discussion is far from being comprehensive, and, in fact, the examples for the incompressible case are strictly limited to experience at NASA Ames.

1. Incompressible Navier-Stokes Equations

In the middle and late 70s much attention was paid to the direct solution of homogeneous turbulent flows with periodic boundary conditions, see Rogallo (1981). The grids used at that time were 64^3 and the storage capacity of available computers was the limiting factor in the spatial resolution. The natural method to use for the numerical approximation of the space derivatives was the classical spectral method composed of finite Fourier series, and the algorithm used for implementation was the fast Fourier transform. The time advance was fully explicit so that all of the time and space scales could be resolved as accurately as possible. However, even with explicit schemes, time advance of a spectral method requires a minimum of two memory locations for every dependent variable at every point in the mesh. The standard third and fourth order Runge Kutta methods both take a minimum of three locations, so the options at that time were to use an existing second order time march method or use a coarser mesh and reduce the space accuracy. This motivated Dr. Alan Wray (Ames Research Center, unpublished) to turn to the Runge-Kutta technique and search for a subset of high order methods that require a minimum (two location) amount of storage capacity. He was successful and his third-order method, used to time march the nonlinear equation,

$$\frac{du}{dt} = F(u, t) \qquad (1.1)$$

has the predictor-corrector form

$$\hat{u} = u_n + \alpha \Delta t F(u_n , t_n)$$
$$\hat{\hat{u}} = u_n + A \Delta t F(u_n , t_n)$$
$$\dot{u} = \hat{u} + \beta \Delta t F(\hat{\hat{u}} , t_n + A \Delta t) \qquad (1.2)$$
$$\tilde{u} = \dot{u} + B \Delta t F(\hat{\hat{u}} , t_n + A \Delta t)$$
$$u_{n+1} = \dot{u} + \gamma \Delta t F(\tilde{u} , t_n + (\alpha + B)\Delta t)$$

The value of u_n is initially provided and stored. The value of $\hat{u}$ is then calculated and also stored. Then the value of $\hat{\hat{u}}$ is formed and overstores u_n which is no longer needed. The process continues through $\dot{u}$ and $\tilde{u}$, requiring at any intermediate step only two memory locations per dependent variable per mesh point. Finally, u_{n+1} overwrites $\dot{u}$, $\tilde{u}$ is discarded, and the cycle is repeated.

There are four equations for the five coefficients in eq (1.2), so we have a one-parameter family of low-storage, third-order Runge-Kutta methods. The four equations are

$$\alpha + \beta + \gamma = 1$$
$$(\alpha + B)\gamma + A\beta = 1/2$$
$$(\alpha + B)^2\gamma + A^2\beta = 1/3 \qquad (1.3)$$
$$AB\gamma = 1/6$$

One particular solution is given by

$$\alpha = 1/4 , \; A = 8/15 , \; \beta = 0 , \; B = 5/12 , \; \gamma = 3/4 \qquad (1.4)$$

This method is still being used to time march codes for homogeneous turbulent flows. It is a good example of an algorithm advance adding a new capability to an old concept.

A major advance in algorithms for wall-bounded turbulent simulations occurred in the early 1980's. At that time Leonard and Wray (1982) extended the concepts being used to compute homogeneous turbulent flows, to compute wall bounded turbulent flows in relatively simple geometries. Let U be the velocity vector, p the pressure, and ν the kinematic viscosity. One solves the vector equation expressing conservation of momentum,

$$U_t + U \cdot \nabla U = -\nabla p + \nu \nabla^2 U \qquad (1.5)$$

under the constraints of continuity in the domain and no slip at the walls:

$$\nabla \cdot U = 0 \; \text{in} \; D , \; U = 0 \; \text{on} \; \partial D \qquad (1.6)$$

In homogeneous flows harmonic basis functions are used and these automatically satisfy the periodic boundary conditions. Furthermore, it was easy to make the solutions solenoidal ($\nabla \cdot U = 0$) so the pressure term could be eliminated. The idea advanced by Leonard and Wray was to build the constraints (1.6) into the basis functions of a generalized spectral method for wall bounded flows, so that the constraints are automatically and exactly satisfied with each time advance, and do not need to be further enforced at each step in conjunction with (1.5). The solution is then expressed as a linear combination of global vector "basis functions" that each satisfy (1.6). Due to the constraints one needs to carry only two degrees of freedom per spectral mode while other methods usually carry four, the three velocity components and the pressure. Thus, less computer storage is needed to achieve the better resolution. For more details and further discussion see the paper by Leonard and Wray.

Where they can be formed (this can be difficult since they are geometry dependent), the choice of the generalized spectral basis functions greatly improves the numerical treatment of the spatial aspect of the problem. However, to get adequate resolution near the walls, the time integration tends to be stiff due to the eigenstructure of the viscous terms. Because of this Dr. Philippe Spalart (Ames Research Center, unpublished) devised the use of a hybrid time marching scheme which is implicit for the (linear) viscous terms and explicit for the (nonlinear) convection terms. Again because of low memory requirements he had been using existing 2nd order methods for the time march. However, he has recently extended Wray's Runge-Kutta technique and developed a hybrid method which is third order in time accuracy and still has the minimum (two location) storage requirements. Thus if we have the vector relation

$$u_t = N(u) + L \cdot u \qquad (1.7)$$

where L and N are matrix operators that are linear and nonlinear, respectively, the sequence can be made third order accurate with the proper

choice of the coefficients in

$$\tilde{u} = u_n + \Delta t[L \cdot (\alpha_1 u_n + \beta_1 \tilde{u}) + \gamma_1 N_n]$$

$$\tilde{\tilde{u}} = \tilde{u} + \Delta t[L \cdot (\alpha_2 \tilde{u} + \beta_2 \tilde{\tilde{u}}) + \gamma_2 \tilde{N} + \varsigma_1 N_n]$$

$$u_{n+1} = \tilde{\tilde{u}} + \Delta t[L \cdot (\alpha_3 \tilde{\tilde{u}} + \beta_3 u_{n+1}) + \gamma_3 \tilde{\tilde{N}} + \varsigma_2 \tilde{N}]$$

$$(1.8)$$

The treatment of the N terms is equivalent to that used in Wray's scheme. Only one solution for the coefficients is known. This is given by the conditions that

$$\gamma_1 = 0.7208762469, \quad \gamma_2 = 0.4001233399,$$
$$\gamma_3 = 0.5778221005, \quad \beta_1 = 0.3763996503,$$
$$\beta_2 = 0.0929740417, \quad \beta_3 = 0.1818702938,$$
$$\varsigma_1 = 0.4724519312, \quad \varsigma_2 = 0.2263697562$$

$$(1.9a)$$

and

$$\alpha_1 + \beta_1 = \gamma_1 \ , \ \alpha_2 + \beta_2 = \gamma_2 + \varsigma_1 \ , \ \alpha_3 + \beta_3 = \gamma_3 + \varsigma_2$$

$$(1.9b)$$

Equations (1.9b) assure that the length of each time substep is the same for both L and N. The numerical stability bounds for the model equation

$$u_t = i\lambda u - \nu u \qquad (1.10)$$

where $i\lambda u$ represents $N(u)$ and $-\nu u$ represents $L \cdot u$, are $\lambda \Delta t \leq \sqrt{3}$ and $\nu \Delta t < 47$, which were quite adequate for Spalart's purposes.

2. Compressible Navier-Stokes Algorithms

The development of compressible Navier-Stokes algorithms has also seen moments of inspiration in the last decade. We have taken several steps forward in the general development of algorithms. Some of these steps are via new concepts while most are the result of applying old concepts in a new setting. An example of a concept that was newly introduced to practical application in the field of fluid mechanics is the flux-vector splitting developed by Steger and Warming (1979). This opened up a wide new range of applications of "upwind" algorithms for the Euler and Navier-Stokes equations. Similar concepts have evolved since that time, most noticeably flux-difference splitting algorithms. Both of these methods have succeeded in removing much of the "fine tuning" of parameters which had plagued many algorithms previous to this time. A brief review of this work is given.

A concept that is probably as "new" as one can find is the total variation diminishing (TVD) theory extended to finite differencing schemes by Harten (1983). In this work, Harten extended ideas concerning total variation properties of scalar hyperbolic differential equations to discrete differencing schemes. This was an important step forward in determining the "ground rules" for designing good shock capturing methods, although it is not clear how religiously they need be followed. A complete review of this subject would be a formidable task by any measure. We chose not to do this, but rather to take some of the original underlying concepts involved and present a new perspective which hopefully will inspire new ideas.

Flux-Vector / Flux-Difference Splitting

In this section, we discuss two basic philosophies in the construction of upwind algorithms for systems of equations: flux-vector and flux-difference splitting. Each has proved to be a powerful technique in extending the upwind schemes for scalar equations to systems of equations. By the late 1970's, the theory for scalar hyperbolic equations was well established and several upwind schemes for these equations had appeared in the literature. The model nonlinear conservation equation

$$u_t + (f(u))_x = 0 \qquad (2.1)$$

had been analyzed extensively by Lax (1973) and others as an initial-value problem, yielding a fairly complete description of the equation and it's solution. For smooth regions of initial data, (2.1) can be represented for a small time interval by its quasi-linear form

$$u_t + a(u)u_x = 0 \qquad a(u) = \frac{df}{du}$$

While at discontinuities, an integral form of (2.1) describes the solution behavior. The quasi-linear form has characteristic solutions for small time intervals of the form: $u(x,t) = u_0(x - at)$, i.e. the solution is constant along the characteristic lines, $\frac{dx}{dt} = a$. Upwind methods (more properly referred to as characteristic oriented methods) use this information by determining the local propagation direction, $\text{sgn}(a)$, and adapting

differencing stencils accordingly. One of the simplest upwind schemes using this strategy is the Cole-Murman scheme. This scheme can be written for the discrete mesh, $u_j^n = u(j\Delta x, n\Delta t)$, as

$$u_j^{n+1} - u_j^n + \frac{\Delta t}{\Delta x}(h_{j+\frac{1}{2}}^n - h_{j-\frac{1}{2}}^n) = 0$$

$$h_{j+\frac{1}{2}}^n = \frac{1}{2}(f_{j+1}^n + f_j^n) - \frac{1}{2}|\bar{a}|_{j+\frac{1}{2}}^n(u_{j+1}^n - u_j^n) \quad (2.2)$$

$$\text{where} \quad \bar{a}_{j+\frac{1}{2}} = \begin{cases} \frac{f_{j+1}-f_j}{u_{j+1}-u_j} & \text{if } u_j \neq u_{j+1} \\ a(u_j) & \text{otherwise} \end{cases}$$

This produces the following simple (and more recognizable) schemes for cases in which a is of uniform sign:

$$u_j^{n+1} = u_j^n - \frac{\Delta t}{\Delta x}(f_j^n - f_{j-1}^n) \quad \text{if } a > 0$$

$$u_j^{n+1} = u_j^n - \frac{\Delta t}{\Delta x}(f_{j+1}^n - f_j^n) \quad \text{if } a < 0$$

Obviously, if higher order accuracy is needed, then a more elaborate scheme needs to be constructed. But even for the simplest schemes (the Cole-Murman scheme for instance) one can ask the following question: *what is the simplest and most natural way to extend the scalar upwind schemes to systems of equations?* For the Euler equations, Steger and Warming (1979) and van Leer (1982) answered this question with flux-vector splitting while Roe (1981), Osher(1981) and others answered with a flux-difference splitting technique. To illustrate these methods, we consider the 1-D Euler equations

$$Q_t + \partial_x E(Q) = 0 \quad (2.3)$$

Here Q is the vector of conserved variables for mass, momentum, and energy while E is the corresponding flux vector. Whenever needed, we assume the ideal-gas law as an equation of state.

The basic notion in flux-vector splitting is to split the flux vector into two parts

$$E = E^+ + E^-$$

The components, E^- and E^+, are to be chosen such that they can be forward and backward differenced, respectively. This choice is based on the assumption that if the individual vectors can be forward and backward differenced in a stable fashion, i.e., if

$Q_t + E_x^- = 0$ (stable for forward differencing)

$Q_t + E_x^+ = 0$ (stable for backward differencing)

$$(2.4a)$$

then the same differencing can be used for the full equation,

$$Q_t + E_x^+ + E_x^- = 0 \quad (2.4b)$$

This turns out to be the case, albeit some reduction in stability characteristics may be encountered. For the van Leer splitting described below with first order explicit upwinding, van Leer (1982) mentions that this amounts to a limit of CFL ≤ 1 for (2.4a) and CFL $\leq \frac{2\gamma}{\gamma+3}$ for the full scheme, (2.4b).

Steger and Warming constructed a general class of flux-vector splittings for the Euler equations by exploiting the fact that the flux vectors are homogeneous of degree one in the conserved variables. Euler's identity then gives

$$E = AQ \quad \text{with } A \equiv \frac{\partial E}{\partial Q} \quad (2.5)$$

To construct the splittings, they first diagonalized A,

$$X^{-1}AX = \Lambda = \begin{bmatrix} \lambda_1 & & \\ & \lambda_2 & \\ & & \lambda_3 \end{bmatrix}$$

then split the diagonal matrix into nonnegative and nonpositive parts, i.e.

$$\Lambda = \Lambda^+ + \Lambda^- \quad (2.6)$$

They define the new flux vectors by using (2.5)

$$E^\pm = X\Lambda^\pm X^{-1}Q = A^\pm Q \quad (2.7)$$

The splittings based on (2.6) are obviously not unique; Steger and Warming suggest several different splittings satisfying (2.6), of which probably the most frequently used is the "$\pm$ splitting" defined by

$$A^\pm = \frac{\Lambda \pm |\Lambda|}{2} \quad (2.8)$$

For this $\pm$ splitting they were able to determine that the resulting flux vectors had Jacobians, $\frac{\partial E^\pm}{\partial Q}$

and $\frac{\partial E^-}{\partial Q}$, with all positive and negative eigenvalues, respectively (at least for $1 \leq \gamma \leq \frac{5}{3}$). This is remarkable since nowhere in the development is any effort made to insure this. Unfortunately, this ± splitting leads to flux vectors that do not vary smoothly near sonic and stagnation points, even though the correct solution behaves smoothly there, and this produces "glitches" in the numerical solution. Several "fixes" have been proposed to remedy this, see Buning (1983).

Van Leer (1982) provided an alternate flux-vector splitting, which he devised using special Mach number polynomials to construct fluxes that remain smooth near stagnation and sonic points. His construction technique is quite different from that of Steger and Warming, in particular it is purely a vector construction (neither the Jacobian matrix nor its diagonalizing transforms is directly used). A reasonable question to ask is whether van Leer's flux vectors have an equivalent Steger-Warming representation via similarity transforms of A as in (2.7). We find that this is so by redefining new $\Lambda^\pm$ and direct calculation. In the case of van Leer's splitting they are given by

$$\Lambda^+ = \begin{bmatrix} \mu_1 & & \\ & \mu_2 & \\ & & \mu_3 \end{bmatrix} \quad , \quad \Lambda^- = \Lambda - \Lambda^+$$

with

$$\mu_1 = \frac{-((u-c)^2 - c^2(\gamma+1))(u+c)^2}{4c^3(\gamma+1)}$$

$$\mu_2 = \frac{(u-c)((\gamma-1)u + 2c)(u+c)^2}{4c^3(\gamma+1)}$$

$$\mu_3 = \frac{((\gamma-1)u^2 + (1-3\gamma)uc + 2(2\gamma+1)c^2)(u+c)^2}{4c^3(\gamma+1)}$$

In general, we find that these entries are of no particular uniform sign, (i.e. Λ^+ may have negative diagonal entries). This is not too surprising since the van Leer splitting only requires that the Jacobian matrices of the split fluxes, $\frac{\partial E^+}{\partial Q}$ and $\frac{\partial E^-}{\partial Q}$, have nonnegative and nonpositive eigenvalues, respectively. For illustration, we chose the state: $\rho = .9$, $u = .5$ and $c = 1.1$. In this case, the van Leer splitting gives: $\mu_1 = .5097, \mu_2 = -.2885, \mu_3 = 1.5098$, while the eigenvalues of $\frac{\partial E^+}{\partial Q}$ are calculated to be 0., .5795, and

1.6918. Thus it appears that defining splittings from (2.6) is certainly not a necessary condition. We have, in fact, considered other schemes which satisfy (2.6) yet fail to have eigenvalues of their Jacobians with signs consistent with (2.6). This is certainly an avenue for future investigation.

Flux-difference splitting has also provided a useful technique for extending scalar upwind algorithms to systems of equations. These methods use Riemann solvers to calculate the interaction of neighboring cells by the exact or approximate solution of Riemann's initial-value problem. The simplest explicit schemes for solving the Euler equations take the generic structure:

$$\frac{Q_j^{n+1} - Q_j^n}{\Delta t} + \frac{h_{j+\frac{1}{2}} - h_{j-\frac{1}{2}}}{\Delta x} = 0 \qquad (2.9)$$

where $h_{j+\frac{1}{2}}$ is the numerical flux at the cell interface between the grid points j and $j+1$. The role of the local Riemann solver is to determine the numerical flux at every cell interface by examining the neighboring conditions. The best known approximate Riemann solvers are those of Roe (1981) and Osher and Solomon (1982). Roe's Riemann solver is particularly popular because of its simplicity. Roe considered the exact solution to the linearized form of (2.3),

$$Q_t + A(Q^L, Q^R)Q_x = 0 \qquad (2.10)$$

with constant left and right states specified as initial data,

$$Q = \begin{cases} Q^L & x < 0, \ t = 0 \\ Q^R & x > 0, \ t = 0 \end{cases}$$

Here $x = 0$ corresponds to the local cell interface and A is the approximate Jacobian, obtained from a mean value linearization satisfying

$$E^R - E^L = A(Q^L, Q^R)(Q^R - Q^L) \qquad (2.11)$$

Equation (2.10) can be diagonalized, decoupled, solved exactly, then recoupled. This amounts to solving three linear (scalar) convection problems with step functions as initial data and constant convection velocities u, $u+c$, and $u-c$. Since the exact solution for each scalar problem is merely the translation in x of the original step function,

this results in a "shocks only" approximate Riemann solver; expansion fans, shocks, and contant discontinuities are all modelled as discontinuities. Unfortunately, this allows expansion shocks to form as solutions which must be precluded by special means (see Harten (1983) for examples).

From the local solution, the numerical flux at the cell interface can be calculated. If we construct A^+ and A^- as in (2.7) and (2.8), then the numerical flux can be written with reference to the left or right states as (details can be found in Roe (1981,1986))

$$\mathbf{h}(\mathbf{Q}^L, \mathbf{Q}^R) = \mathbf{E}^L + A^-(\mathbf{Q}^L, \mathbf{Q}^R)(\mathbf{Q}^R - \mathbf{Q}^L)$$
$$= \mathbf{E}^R - A^+(\mathbf{Q}^L, \mathbf{Q}^R)(\mathbf{Q}^R - \mathbf{Q}^L)$$
$$(2.12)$$

Taking the average and applying the local solution everywhere on the discrete grid, we obtain the final form ($|A| = A^+ - A^-$)

$$\mathbf{h}_{j+\frac{1}{2}} = \frac{1}{2}(\mathbf{E}_{j+1} + \mathbf{E}_j) - \frac{1}{2}|A(\mathbf{Q}_j, \mathbf{Q}_{j+1})|(\mathbf{Q}_{j+1} - \mathbf{Q}_j)$$
$$(2.13)$$

If we again look at cases in which the local eigenvalues are of uniform sign (supersonic flow), we obtain the following conventional schemes

$$\mathbf{Q}^{n+1} = \mathbf{Q}^n - \frac{\Delta t}{\Delta x}(\mathbf{E}_j^n - \mathbf{E}_{j-1}^n) \text{ if } [u, u-c, u+c] > 0$$

$$\mathbf{Q}^{n+1} = \mathbf{Q}^n - \frac{\Delta t}{\Delta x}(\mathbf{E}_{j+1}^n - \mathbf{E}_j^n) \text{ if } [u, u-c, u+c] < 0$$

If we contrast this with the Cole-Murman scheme (2.2), which can also be viewed as using a "shocks only" scalar Riemann solver, we see that (2.13) is a successful extension of a scalar upwind scheme to systems.

We conclude this section by remarking that we have limited our discussion to 1-D inviscid flow. This is not really as restrictive as one might guess. Remarkable success has been attained by applying these ideas "dimension by dimension" to the two and three-dimensional Navier-Stokes equations, see Chakravarthy and Osher (1985) for some excellent examples.

Basics of TVD Schemes for Scalar Equations

In this section, we briefly mention the key elements used in the development of the TVD concept. More details as well as proofs can be found

in the literature. The basic notion is to consider solutions, $u(x,t)$, of the single nonlinear conservation equation

$$u_t + (f(u))_x = 0, \qquad \frac{df}{du} = a(u) \qquad (2.14)$$

In this case, we make the usual assumption that the solutions of interest are entropy-satisfying weak solutions with convex flux functions. In the simplest case, to avoid boundary conditions, the initial value problem is considered in which the solution is specified along the x-axis, $u(x,0) = g_0(x)$, either in a periodic or compact supported fashion. This problem has been treated extensively by Lax (1973). The solution can be depicted in the $x - t$ plane by a series of converging and diverging characteristic straight lines. From the solution of (2.14), Lax provides the following observation: *the total increasing and decreasing variations of a differentiable solution between any pair of characteristics are conserved.* This means that in the absence of shocks the exact solution of (2.14) conserves the total variation of the initial data in time.

$$I(t + t_0) = I(t_0) \quad , \quad I(t) = \int_{-\infty}^{+\infty} \left| \frac{\partial u(x,t)}{\partial x} \right| dx \qquad (2.15)$$

Moreover, in the presence of shock waves it can be shown that the total variation of the exact solution actually decreases in time (i.e. $I(t + t_0) \leq I(t_0)$). A simple heuristic argument for this decrease would be to consider solution data with a shock present, $u(x,t)$, and consider reconstructing the solution data at a previous time $u(x, t - \Delta t)$. But using characteristics, it becomes quickly obvious that this cannot be done uniquely; information (solution variation) has been irretrievably lost in the shock formation. An equally important result from Lax's observation comes from considering a monotonic solution between two nonintersecting characteristics: *between pairs of characteristics, monotonic solutions remain monotonic,* (i.e. no new extrema are created).

Although the properties described previously are those of the differential equation (2.14) and its solution, Harten developed a TVD criterion for numerical schemes by considering the discrete

form of (2.15) on a mesh $u_j^n = u(j\Delta x, n\Delta t)$, $u[u_1, u_2, u_3, ...]$. The discrete total variation in this case is defined as

$$TV(u) = \sum_{-\infty}^{+\infty} |u_{j+1} - u_j| \qquad (2.16)$$

with a corresponding TVD condition

$$TV(u^{n+1}) \leq TV(u^n) \qquad (2.17)$$

It is not difficult to show that this TVD condition is sufficient for monotonic data with bounded total variation to remain monotonic, (to prove this, assume a new extremum is introduced and compute the new total variation). Although we will only use (2.17) to investigate conditions for constructing TVD schemes, equation (2.17), along with consistency of the scheme with the differential equation and satisfaction of the entropy inequality, is enough to guarantee convergence to the weak solution(s) (see Harten (1983)).

Equation (2.17) now provides us with an additional measure which will allow us to rule out many existing schemes which do not diminish the solution variation. More importantly, as we will see in the next section, it will be used to derive algebraic criteria which we can use to construct new TVD schemes.

Matrix Interpretation of TVD Criteria

Sufficient conditions for constructing TVD algorithms have been developed first by Harten (1983) and later in a more general form by Osher and Chakravarthy (1984), and Jameson and Lax (1984). In this section we demonstrate general sufficient conditions for TVD schemes. In developing the criteria for general explicit schemes, we independently followed a path similar to that of Jameson and Lax, although their claim of necessary and sufficient conditions is generally agreed to be in error (Harten (1986) notes that this is the danger of using their compact indicial notation). In the development of implicit schemes we depart from their strategy altogether and avoid the introduction of expansive operators. More importantly, we avoid the use of indicial notation in favor of a more compact matrix-vector notation whenever possible. As a result, the natural simplicity of constructing TVD schemes becomes evident, and we are able to give another

(and perhaps clearer) interpretation of sufficient conditions given by the previous authors.

An important step in the development of TVD schemes arises from the form chosen to express these schemes. We find it convenient to use a generalization of the form used by Osher and Chakravarthy. Since the objective is to obtain bounds on the variation of u, the conservative difference schemes are put in a general form which uses an "apparent" $(p + q + 2)$ explicit and $(p' + q' + 2)$ implicit stencil of the solution, u.

$$u_j^{n+1} + \sum_{i=-p'}^{q'} D(\hat{v})_{j+\frac{1}{2}} \Delta_{i+\frac{1}{2}+i} u^{n+1}$$

$$= u_j^n + \sum_{i=-p}^{q} C(\hat{v})_{j+\frac{1}{2}} \Delta_{j+\frac{1}{2}+i} u^n$$

(2.18)

where $\Delta_{j+\frac{1}{2}} u = u_{j+1} - u_j$. Because C and D are typically nonlinear functions of u at grid points which could be outside the apparent stencils, it should be clear that (2.18) is far from being unique. This nonuniqueness provides a large amount of freedom in designing schemes and is essentially the distinguishing feature of various schemes appearing in the literature. Although the algebraic details of putting a particular scheme into the form of (2.18) are important, we are only interested the general principles involved in the construction of TVD schemes and refer the reader to the literature for specific details.

We begin our analysis of TVD schemes by rewriting the discrete total variation in terms of the forward difference matrix, D, (shown here for a periodic domain)

$$D = \begin{pmatrix} -1 & 1 & 0 & 0 & \cdots & 0 \\ 0 & -1 & 1 & 0 & \cdots & 0 \\ 0 & 0 & -1 & 1 & \cdots & 0 \\ \vdots & \vdots & \vdots & \vdots & \ddots & \vdots \\ 0 & 0 & 0 & 0 & -1 & 1 \\ 1 & 0 & 0 & 0 & 0 & -1 \end{pmatrix}$$

from which $\|Du\|_1 \equiv TV(u)$ and the TVD condition can be written

$$\|Du^{n+1}\|_1 \leq \|Du^n\|_1 \qquad (2.19)$$

In these expressions we are using the notation for the conventional L_1 vector norm, $\|\mathbf{v}\|_1 = \sum_j |v_j|$. Using the forward difference matrix, eq. (2.18) can be written

$$[I + \theta \widetilde{M} D]\mathbf{u}^{n+1} = [I - (1-\theta)MD]\mathbf{u}^n \quad (2.20)$$

Here M and $\widetilde{M}$ are matrix operators which can be nonlinear functions of $\mathbf{u}$. This equation, with the free parameter θ, represents various explicit and implicit forms of the evolution of $\mathbf{u}$ in time. (We chose this particular form so that if $\widetilde{M} = M$, then the scheme would be a generalized form of Harten's "linearized" implicit TVD scheme, Harten (1984).) One can also construct a scheme representing the timewise evolution of the variation, $D\mathbf{u}$. To do so multiply (2.20) from the left by D and regroup terms.

$$[I + \theta D\widetilde{M}]D\mathbf{u}^{n+1} = [I - (1-\theta)DM]D\mathbf{u}^n \quad (2.21)$$

Symbolically this can be expressed in terms of the matrix operators R and $\mathcal{L}$ as

$$\mathcal{L}\, D\mathbf{u}^{n+1} = R\, D\mathbf{u}^n \quad \text{or} \quad D\mathbf{u}^{n+1} = \mathcal{L}^{-1}R\, D\mathbf{u}^n \quad (2.22)$$

with

$$\mathcal{L} = [I + \theta D\widetilde{M}], \quad R = [I - (1-\theta)DM]$$

Next we take the L_1 vector norm of eq. (2.22) and apply the matrix-vector norm inequalities. Thus

$$\|D\mathbf{u}^{n+1}\|_1 \le \|\mathcal{L}^{-1}R\|_1 \|D\mathbf{u}^n\|_1 \quad (2.23)$$

and we find a sufficient condition for the scheme to be TVD is that $\|\mathcal{L}^{-1}R\|_1 \le 1$.

Note that for the extremely restrictive case in which $\mathcal{L}$ and R are not functions of $\mathbf{u}$, the basic definition of a matrix norm would guarantee that $\|\mathcal{L}^{-1}R\|_1 \le 1$ is both a necessary and sufficient condition for the scheme to be TVD. (Many monotone schemes would be included in this class.) Recall that the L_1 norm of a matrix is obtained by summing the absolute value of elements of individual columns of the matrix and

choosing the column whose sum is largest. Furthermore, we have the usual matrix norm inequality $\|\mathcal{L}^{-1}R\|_1 \le \|\mathcal{L}^{-1}\|_1 \|R\|_1$, so in the more general case, it is clear from (2.23) that it is sufficient to show that $\|\mathcal{L}^{-1}\|_1 \le 1$ and $\|R\|_1 \le 1$ (L_1 contractive). As we will see, these simple estimates will be enough to obtain the TVD criteria of previous investigators.

First consider the explicit operator R and multiply it from the left by the summation vector $s \equiv [1,1,1,...,1]$. It is clear that $sD = [0,0,0,...,0]$, so that that R has columns that sum to exactly unity, regardless of the particular choice of M. Because the L_1 norm of R is simply the maximum of the sum of absolute values of elements in the columns of R, it is obvious that a sufficient and necessary condition for $\|R\|_1 \le 1$ is for R to be a *nonnegative matrix*, (i.e. $R \ge 0$). Thus for explicit schemes ($\theta = 0$) to be TVD, we have the general sufficient condition that R be a nonnegative matrix. We illustrate that this leads to Harten's criteria for explicit schemes by considering his particular explicit form of (2.18), (in his notation)

$$u_j^{n+1} = u_j^n + C_{j+\frac{1}{2}}^+ \Delta_{j+\frac{1}{2}} u^n - C_{j-\frac{1}{2}}^- \Delta_{j-\frac{1}{2}} u^n$$

The operator R in this case (again assuming a periodic domain) has the following banded structure

$$R = \begin{pmatrix} \ddots & \ddots & 0 & & 0 & & \ddots \\ \ddots & \ddots & C_{j+\frac{1}{2}}^+ & & 0 & & 0 \\ 0 & C_{j-\frac{1}{2}}^- & 1 - C_{j+\frac{1}{2}}^+ - C_{j+\frac{1}{2}}^+ & C_{j+\frac{3}{2}}^+ & 0 \\ 0 & 0 & -C_{j+\frac{1}{2}}^- & & \ddots & & \ddots \\ \ddots & 0 & 0 & & \ddots & & \ddots \end{pmatrix}$$
$$(2.24)$$

We need only require that this matrix be nonnegative to immediately arrive at Harten's criteria:

$$C_{j+\frac{1}{2}}^+ \ge 0$$

$$C_{j+\frac{1}{2}}^- \ge 0$$

$$1 - C^+_{j+\frac{1}{2}} - C^-_{j+\frac{1}{2}} \geq 0 \qquad (2.25)$$

For the general form of R, we can construct the matrix in the same fashion and arrive at the same conditions given by Harten, Jameson and Lax, and Osher and Chakravarthy by requiring that this resultant matrix be nonnegative.

Perhaps the more interesting use of a matrix interpretation comes when considering implicit schemes. Sufficient conditions would be to show that both L^{-1} and R are L_1 contractive. We have shown sufficient conditions for constructing $\|R\|_1 \leq 1$. We now consider conditions for making $\|L^{-1}\|_1 \leq 1$. From the previous development, one way to do this would be to show that L^{-1} is a nonnegative matrix with columns that sum to unity. At that point the development would be the same as previously discussed. This turns out to be a simple task and using some well known results from matrix theory, we can determine algebraic sufficient conditions on L.

Note that in the following discussion, we assume that L is invertible, but after we have found a TVD criterion we will see that this must be so. First, we show that columns of L^{-1} *must* sum to unity. We use the same trick of premultiplying L by the summation vector, $\mathbf{s} = [1,1,1,...,1]$.

$$\mathbf{s}L = \mathbf{s} \quad \rightarrow \quad \mathbf{s} = \mathbf{s}L^{-1}$$

Therefore the columns of L^{-1} sum to unity. We need only find conditions on L to make its inverse nonnegative, but from matrix theory we know that a matrix whose inverse is nonnegative ($L^{-1} \geq 0$) defines a *monotone matrix*. Therefore a sufficient condition would be that L is a monotone matrix. This is not particularly useful in itself, but a well known theorem from matrix theory allows us to develop a TVD criterion. Sufficient conditions for L monotone can be obtained from the theory for diagonally dominant M-matrices, a specific type of monotone matrix with positive diagonal entries and negative off-diagonal entries. To make this point clear we summarize a proof which appears in several books on matrix theory (see Lancaster, pp. 531-532 or Ortega, pp. 53-54). We begin by defining a real $n \times n$ matrix, a_{ij}, and assume that $a_{ii} > 0$ for each i and $a_{ij} \leq 0$ whenever $i \neq j$. If A is diagonally dominant, that is,

$$a_{ii} > \sum_{j=1, j \neq i}^{n} |a_{ij}|, \qquad i = 1, 2, ..., n,$$

then A is an M-matrix. To prove this, we first let $D = \text{diag}[a_{11}, a_{22}, a_{33}, ..., a_{nn}]$ and define $B = I - D^{-1}A$. Note that B has zero elements on the main diagonal and that $B \geq 0$. Also the fact that A is diagonally dominant implies that

$$\sum_{j=1}^{n} |b_{ij}| < 1, \qquad i = 1, 2, ..., n.$$

It follows immediately from Gersgorin's theorem that the maximum eigenvalue of B is less than one ($\mu_B < 1$). Now we have $D^{-1}A = I - B$, and $[I - B]^{-1}$ can be Neumann expanded into

$$[I - B]^{-1} = I + B + B^2 + B^3 + ...$$

Since $B \geq 0$, we conclude that $[I - B]^{-1} \geq 0$. It follows that $D^{-1}A$ is an M-matrix and consequently that A is an M-matrix.

Therefore, sufficient conditions for L to be monotone are that L be a diagonally dominant M-matrix, i.e. diagonally dominant with positive elements on the diagonal and negative off-diagonal elements. Also note that because of the diagonal dominance, we now can guarantee invertibility of L as mentioned earlier. Again, we can recover the results of other investigators from these conditions. We illustrate this using Harten's implicit form

$$u_j^{n+1} + D^+_{j+\frac{1}{2}}\Delta_{j+\frac{1}{2}}u^{n+1} - D^-_{j-\frac{1}{2}}\Delta_{j-\frac{1}{2}}u^{n+1} = u^n$$

In this case, L takes the general structure

$$L = \begin{pmatrix} \ddots & \ddots & 0 & 0 & \ddots \\ \ddots & \ddots & -D^+_{j+\frac{1}{2}} & 0 & 0 \\ 0 & -D^-_{j-\frac{1}{2}} & 1+D^+_{j+\frac{1}{2}}+D^+_{j+\frac{1}{2}} & -D^+_{j+\frac{3}{2}} & 0 \\ 0 & 0 & -D^-_{j+\frac{1}{2}} & \ddots & \ddots \\ \ddots & 0 & 0 & \ddots & \ddots \end{pmatrix}$$

$$(2.26)$$

To obtain Harten's TVD criteria for the implicit scheme, we need only require that this be an M-matrix to obtain the following conditions, as did Harten

$$D^+_{j+\frac{1}{2}} \geq 0$$

$$D^-_{j+\frac{1}{2}} \geq 0$$

We conclude this section by noting the underlying conceptual simplicity. Once the schemes are placed in the form of (2.21), then sufficient conditions become very simple and naturally give rise to the basic concepts of nonnegative and M - matrices.

3. Concluding Remark

Looking back over the last ten years, we can see that ten years ago it would have been correct to say: "There will be considerable advances in algorithm development in the next decade. " We believe it is reasonably safe to make the same statement at this time.

4. References

Buning, P.: *Computation of Inviscid Transonic Flow Using Flux Vector Splitting in Generalized Coordinates*, PhD Thesis, Stanford University, Department of Aeronautics and Astronautics, 1983.

Chakravarthy, S. and Osher, S.: *Application of a New Class of High Accuracy TVD Schemes to the Navier-Stokes Equations*, AIAA paper 85-0165, Jan. 1985.

Harten, A.: *High Resolution Schemes for Hyperbolic Conservation Laws*, J. Comput. Phys., **49** (1983),357-393.

——— : *On a Class of High Resolution Total - Variation - Stable Finite - Difference - Schemes*, SIAM J. Numer. Anal., **21** (1984),1-22.

——— :*Numerical Methods for Hyperbolic Conservation Laws*, Lecture Notes: NASA Ames short course, Oct. 1-3, 1986.

Jameson, A. and Lax, P.: *Conditions for the Construction of Multi-Point Total Variation Diminishing Difference Schemes*, ICASE Report 178076, March 1986.

Lancaster, P.L.; and Tismenetsky M.: The Theory of Matrices, Academic Press Inc, 1985, pp. 531-532.

Lax, P.: *Hyperbolic Systems of Conservation Laws and the Mathematical Theory of Shock Waves*, SIAM Regional Conf. Ser. Appl. Math., No. 11, Soc. Indust. Appl. Math, Philadelphia,Pa., 1973.

Van Leer, B.:*Flux-Vector Splitting for the Euler Equations*, ICASE Report 82-30, September, 1982.

Leonard, A. and Wray, A.: *A New Numerical Method for the Simulation of Three-Dimensional Flow in a Pipe*, NASA TM 84267, 1982.

Ortega, J.M.; and Rheinboldt, W.C.: Iterative Solution of Nonlinear Equations in Several Variables,First ed., Academic Press,Inc., 1970, pp. 53-54.

Osher S.; and Solomon, F.: *Upwind Difference Schemes Systems of Conservation Laws*, Math. of Comput.,**39**,339-374.

Osher, S.; and Chakravarthy, S.: *Very High Order Accurate TVD Schemes*, ICASE Report 84-44, September 1984.

Roe, P.L.: *Approximate Riemann Solvers, Parameter Vectors, and Difference Schemes*, J. Comput. Phys., **43**, (1981), 357-372.

——— : *Characteristic-Based Schemes for the Euler Equations*, Ann. Rev. Fluid Mech., **18**, (1986), 337-365.

Rogallo, Robert.: *Numerical Experiments in Homogeneous Turbulence*, NASA TM 81315, 1981.

Steger, J. and Warming R.:*Flux Vector Splitting of the Inviscid Gasdynamic Equations with Application to Finite-Difference Methods*, NASA TM 78605, 1979.

N87
26016

ADVANCES IN TURBULENCE PHYSICS AND MODELING
BY DIRECT NUMERICAL SIMULATIONS

W. C. Reynolds

Department of Mechanical Engineering

Stanford University, Stanford, CA 94305-3030

1. Introduction

The advent of direct numerical simulations of turbulence has opened new avenues for research on turbulence physics and turbulence modeling. Although limited to relatively low Reynolds numbers, direct simulations have already provided new insight into the structure of turbulence. Direct numerical simulation provides values for anything that the scientist or modeler would like to know about the flow, and this is beginning to have tremendous payoff. Simulations have enabled detailed evaluations to be made of turbulence models intended for use in engineering codes, as well as models of the small-scale turbulence required for Large Eddy Simulations (LES), a promising technique for practical numerical simulations of turbulence at high Reynolds numbers. This paper presents an overview of some recent advances in the physical understanding of turbulence and in turbulence modeling obtained through such simulations.

One class of turbulence that has been studied extensively by direct simulations is *homogeneous turbulence*. In homogeneous turbulence, the mean velocity gradients are prescribed and must be uniform in space, and all turbulence statistics are independent of position. One of the difficult problems in turbulence simulations is the provision of boundary conditions. It has been demonstrated that, in simulating homogeneous flows, one may use periodic boundary conditions, provided that the computational domain is larger than twice the distance between points where statistical motions are significantly correlated. Hence, the boundary motions do not have to be known to simulate homogeneous turbulence, but instead emerge as a result of the dynamics of the flow and the periodicity. It is for this reason that much of the first work on direct simulations has dealt with homogeneous turbulence.

A program developed by Dr. Robert Rogallo (1981) at Ames has become the bulwark of direct simulations of various homogeneous turbulent flows. The program uses de-aliased spectral methods to obtain high accuracy at small scales. It works in a coordinate system that deforms with the mean flow using variables that are computed exactly in the limit of very rapid distortions, and so the program has been used to cover a wide range of mean deformation conditions. The Rogallo code has been used to study the decay of isotropic turbulence, the response of isotropic turbulence to imposed mean strain and rotation, and homo-

geneous shear flow, including scalar transport. This work spans the Ames supercomputers from ILLIAC-IV to CRAY-2, and has recently been adapted for use on Masscomp supermini computers.

This paper highlights the results of three recent Stanford Ph.D. Dissertations, carried out on the Cray-XMP at NASA/Ames under the direction of the author as part of a cooperative program of turbulence research with colleagues at Ames. This program, which has spanned well over a decade, has produced many of the currently active researchers in this field, and has been instrumental in the establishment of Ames as the world center for this type of research. A key outgrowth of this prorgam is the recently-formed *NASA/Stanford Center for Turbulence Research*, which will bring together experimentalists, computational scientists, and modelers in a concerted attack on the physics and modeling of turbulence.

Two of the disserations discussed below deal with homogeneous turbulence, and were carried out using the Rogallo code. They represent the current state-of-the art in simulations of such flows, and illustrate the sort of insight into turbulence physics and models that can be obtained from direct simulations. The third dissertation was the first direct simulation of the spatially-developing turbulent mixing layer, and is characteristic of the state of affairs in the direct simulation of flows of practical interest. Current work in extending this simulation to the supersonic mixing layer, for applications in both aerodynamics and scramjet engines, will be mentioned.

2. Response of turbulence to irrotational strain

Two of the building-block flows for turbulence modelers are (1) homogeneous turbulence undergoing incompressible, irrotational mean strain and (2) relaxation to isotropy after cessation of the mean straining. These two situations apply approximately to the turbulence (1) in the contraction section of low-speed wind tunnels and (2) in the straight test section following the nozzle. Hence, this idealized case has practical importance, especially in wind tunnels designed for low free-stream turbulence.

Different types of mean deformation are of interest. Wind tunnels are either axisymmetric or two-dimensional, and the behavior of the turbulence is quite different in these cases. A simple model based on the idea that the turbulence consists of a complex tangle of vortex filaments is useful in understanding these

differences. The streamwise strain stretches the vortex filaments that form the turbulence, concentrating the vorticity and increasing the intensity of the swirling motion around each filament. The cross-stream contraction pushes these filaments closer together. In axisymmetric contraction the filaments are pushed together from both sides, whereas in plane strain (e.g. two-dimensional mean contraction), the vortex filaments are pushed together only in one direction.

In the diffuser segment of a wind tunnel, a still different type of mean deformation is imposed. In a round diffuser, vortex filaments are stretched in the two cross-stream directions, and compressed in the streamwise direction. This deforms the filaments into thin sheets, giving rise to intense local shear layers in the flow.

This line of thinking suggests that the small-scale structure of the turbulence, as determined by the tangle of vortex filaments, should be different under different mean distortions. But one of the common premises in turbulence modeling is that the small-scale structure is isotropic, which is not consistent with the model of distorted filaments. The model also suggests that the rate of return to isotropy upon cessation of mean deformation should depend on the nature of the vortex filament tangle, i.e. on the nature of the prior mean strain. These are features that one would expect to see in a numerical simulation and would like to see exhibited by analyticals model of turbulence.

Moon Lee (1986), now a Postdoctoral Researcher at NASA/Ames, performed an extensive series of direct simulations of homogeneous turbulence subjected to a variety of irrotational strains, and also studied the relaxation upon cessation of mean deformation. The objective of his dissertation was to use the simulation data to evaluate second-order closure models of turbulence. His simulations used a 128^3 mesh, a second-order Runga-Kutta time advance, carefully-configured initial conditions, and were executed at Reynolds numbers, based on the length and velocity scales of the energy-containing motions, of the order of 50. Some background necessary for understanding the impact of his work will now be outlined.

In second-order closures, one deals with the Reynolds stress tensor

$$R_{ij} = \overline{u_i' u_j'} \qquad (1)$$

or, alternatively, with the turbulent velocity scale

$$q^2 = R_{ii} \qquad (2a)$$

and the *Reynolds stress anisotropy tensor*

$$b_{ij} = (R_{ij} - \frac{1}{3}q^2\delta_{ij})/q^2. \qquad (2b)$$

In isotropic turbulence $b_{ij} = 0$. If the energy in one component, say u_1', goes to zero, then $b_{11} = -\frac{1}{3}$; and

if all of the fluctuation energy is in one component, say u_1', then $b_{11} = \frac{2}{3}$. Thus, the values of b_{ij} are limited. These limits are conveniently described in terms of the invariants of the b_{ij} tensor. The first invariant is $I_b = b_{ii} = 0$. The second and third invariants are

$$II_b = -\frac{1}{2}b_{ij}b_{ji} \qquad (3a)$$

and

$$III_b = \frac{1}{3}b_{ij}b_{jk}b_{ki}. \qquad (3b)$$

The limits outlined above translate into limits on II_b and III_b, and one finds that all possible states of turbulence must lie within a certain area on the III_b - II_b plane, which is called the *anisotropy invariant map* (AIM) for the Reynolds stress. Simple eddy viscosity models for the Reynolds stresses do not necesarily satisfy this condition, particularly in cases of very strong strain-rate, and hence sometimes these models produce *unrealisable turbulence*. The AIM is therefore a very useful tool for assessing turbulence models.

Second-order closure models for homogeneous flows require closures for the equations of evolution of R_{ij} and ϵ, the rate of dissipation of mechanical energy per unit volume by the turbulence. Alternatively, the evolution equations for b_{ij} and q^2 are used in place of those for R_{ij}. The turbulent kinetic energy equation describes the evolution of q^2, and is

$$\frac{dq^2}{dt} = 2(P - \epsilon) \qquad (4a)$$

where

$$P = -R_{ij}S_{ij} \qquad (4b)$$

is the rate of energy transfer from the mean motion to the turbulence (*production*) and

$$S_{ij} = \frac{1}{2}(U_{i,j} + U_{j,i}) \qquad (4c)$$

is the mean strain-rate (commas denote partial differentiation). No modeling is necessary in (4a) because it contains only the model variables and the prescribed mean velocity gradients.

The equation for b_{ij} is

$$\frac{db_{ij}}{dt} = A_{ij} - \frac{\epsilon}{q^2}(\phi_{ij} - 2b_{ij}). \qquad (5)$$

Here A_{ij} is a production term involving only the anisotropy tensor b and the mean velocity gradients, and hence does not require modeling. ϕ_{ij}, which involves the anisotropy of the viscous dissipation and the pressure-strain terms, must be modeled. It contains a *rapid pressure-strain* part that changes instantly when the mean velocity gradients are changed, which must be modeled as being proportional to the mean gradients, and *slow* terms that do not contain the mean

velocity gradients. For the special case of no mean gradients (the *return to isotropy* problem), ϕ_{ij} contains only the slow terms. Hence, the modeling of these terms can be examined by studying direct simulations of the return to isotropy, and this was the primary objective of Moon Lee's dissertation.

If one is going to work with b_{ij}, q^2, and ϵ as variables, then the model for ϕ_{ij} must be expressed in terms of these variables. The tensor character must be carried by tensors developed from b_{ij}. By the Cayley-Hamilton theorem, there are only two linearly independent tensors that can be involved. Thus, the most general model of the slow part of ϕ_{ij} possible in this type of second-order closure is

$$\phi_{ij} = (\alpha + 2)b_{ij} + \beta(b_{ik}b_{kj} + \frac{2}{3}II_b\delta_{ij}) \qquad (6)$$

where α and β are scalar coefficients that can depend upon the scalar invariants II_b and III_b and on other scalars, such as the turbulent Reynolds number $R_T = q^4/(\epsilon\nu)$. An immediate consequence of this model is that the return to isotropy must follow a trajectory on the Reynolds stress AIM given by

$$\frac{dIII_b}{dII_b} = \frac{3\alpha III_b + \frac{2}{3}\beta II_b^2}{2\alpha II_b - 3\beta III_b}. \qquad (7)$$

Hence, the trajectory should be a unique function of the position on the AIM (and R_T). Thus, by following the trajectory in the simulations, one should be able to deduce the parameters α and β, *provided* that the assumed model is adequate to describe the flow.

The simulations showed that the return trajectory is *not* a unique function of the AIM state; the most striking deviations were in the case of axisymmetric expansion flows, where turbulence that had been rapidly strained actually moved further away from isotropy when the strain-rates was removed, while turbulence that had been strained slowly to the same anisotropy moved *towards* isotropy upon the removal. Thus, at least for the case of strong strain-rate (but of the order of the strain rate in many practical situations), the standard second-order model simply is inadequate.

We then turned to looking for alternative ways to characterize and model the turbulence, using two other tensors characterizing the anisotropy of the small-scale motions. Analogous to R_{ij}, q^2 and b_{ij} we define the vorticity tensor by

$$V_{ij} = \overline{\omega_i'\omega_j'} \qquad (8a)$$

where ω_i' is a turbulent vorticity component. The mean-square vorticity is

$$\omega^2 = V_{ii} \qquad (8b)$$

which, for homogeneous turbulence, is related to the dissipation by

$$\epsilon = \nu\omega^2. \qquad (8c)$$

The *vorticity anisotropy tensor* is defined by

$$v_{ij} = \frac{V_{ij} - \frac{1}{3}\omega^2\delta_{ij}}{\omega^2} \qquad (8d)$$

and its invariants, II_v and III_v are defined in the same way as those for b.

The dissipation is

$$D_{ij} = 2\nu\overline{u_{i,k}'u_{j,k}'}. \qquad (9a)$$

The trace of this tensor is

$$D_{ii} = 2\epsilon \qquad (9b)$$

The associated *dissipation anisotropy tensor* is defined by

$$d_{ij} = \frac{D_{ij} - \frac{2}{3}\epsilon\delta_{ij}}{2\epsilon} \qquad (9c)$$

and its invariants, II_d and III_d are defined in the same way as those for b.

The AIMs for v and d look exactly like that for b, although the phisical meanings of the limiting boundaries are different. For example, turbulence in which the vortex filaments have been stretched infinitely in one direction has a *one*-dimensional vorticity field but a two-dimensional velocity field, and hence its state is at different points on the v and b AIMs.

The simulations revealed a very surprising result that shakes the roots of turbulence theory. The anisotropy of the small-scale turbulence was *not* found to be much smaller than the anisotropy of the large-scale turbulence, as the lore of turbulence suggests. Instead, there tended to be strong relatonships between the anisotropies at small and larges scales, as revealed by the instantaneous states of the turbulence on the vorticity/dissipation AIMS and the Reynolds stress AIM, respectively. It has been suggested that this is a result of the low Reynolds numbers used in the simulations. However, we can see no trend for the small-scale anisotropy to be less at higher Reynolds numbers. Figure 1 shows the second invariants of the vorticity and Reynolds stress anisotropies during the relaxation from simple strains. Note that for virtually every field examined the vorticity anisotropy was larger than the Reynolds stress anisotropy, as measured by their second invariants. Figure 2 shows the dissipation anisotropy vs. that for the Reynolds stress for these same velocity fields. Note that the second invariants of these anisotropies are generally of comparable value, again indicating the non-isotropic nature of the small-scale field.

Upon further reflection on this problem, it is clear from the Biot-Savart law, which relates the velocity field to the vorticity field, that anisotropy in the Reynolds stress can only arise if there is anisotropy in the two-point vorticity correlation tensor. Since

the anisotropy in Reynolds stresses persists at high Reynolds numbers, the vorticity field must also exhibit important anisotropy at high Reynolds numbers. The simulations led us to focus on this issue, and they suggest that modeling of the large-scale turbulence might be improved by explicit consideration of the anisotropies of the vorticity.

Using the simulated fields as "data", we explored a number of possible models for the return to isotropy problem, seeking a model that would describe the evolution more accurately. We found that the return-to-isotropy trajectories on the vorticity and dissipation AIM's were unique, and hence the evolution equations for u_{ij} and d_{ij} can be closed by simple models in terms of their own tensors. For example, the vorticity anisotropy was found to obey (during return to isotropy)

$$\frac{dv_{ij}}{dt} = -\gamma \frac{\epsilon}{q^2} u_{ij} \qquad (10)$$

Lee was able to obtain a tidy formula describing the coefficient γ as a function of the invariants II_b and II_v, and had similar success with the dissipation anisotropy model. Figures 3 and 4 show the comparisons of his model trajectories on the vorticity and dissipation AIMs for the return-to-isotropy cases. But unfortunately a truly satisfactory model for the evolution of b_{ij} was not discovered, and so a complete second-order turbulence model has not yet been established.

In summary, Lee's simulations of homogeneous turbulence under irrotational strain provide some very important new insight into the physics of turbulence. They raise serious questions about traditional ideas of small-scale anisotropy that have been deeply imbedded in turbulence theory and modeling, and suggest that considertation of small-scale anisotropy may be essential for development of better turbulence models for the large-scale turbulence. Lee's velocity fields have been archived at Ames and are being used to study other aspects of turbulence physics and modeling. We expect that much more can be learned from them about turbulence.

3. Scalar transport in homogeneous shear flow

Homogeneous turbulent shear flow occurs when the mean velocity gradient transverse to the flow is uniform. This situation has been studied experimentally in special wind tunnels that use variable grids to establish this unusual mean flow, and has been explored in great depth using the Rogallo code.

In homogeneous turbulence there is no net gain or loss to an elemental control volume as a result of turbulent transport (the gradients of all turbulence correlations vanish in homogeneous turbulence). But the turbulent fluxes are still present, and they can be studied by direct simulation. Experiments on heat transfer in such a flow have been limited to cases with a mean temperature gradient aligned with the mean velocity

gradient and cross-stream to it. These experiments suggest that there are strong anisotropies in the turbulent diffusion of scalars (e.g. temperature or species) in shear flow, but not enough is known about these effects to allow them to be incorporated in turbulence models.

In an effort to shed more light on this problem, Mike Rogers (1986), now a Staff Scientist at Ames, carried out detailed simulations of homogeneous shear flow with various arrangements for scalar transport, using the Rogallo code. The flow considered had the mean shear rate

$$\frac{dU_1}{ds_2} = S \qquad (11)$$

and was examined with the three linearly-independent cases, each having a mean temperature gradient in only one direction, at Prandtl numbers of 1, 0.2, and 0.7, and covered a wide range of Sq^2/ϵ, the dimensionless shear rate parameter, and Reynolds numbers. Most were carried out with a 128^3 mesh, in some cases non-square. The computed velocity and scalar fields have been preserved at selected time intervals, and represent a great resource for subsequent study of new physical ideas or modeling concepts.

The case of primary interest is case 2, having a mean temperature gradient in the x_2 direction, for this is the usual alignment of the velocity gradient and temperature gradient in shear flows. The simulations confirm the rather surprising results of experiments that the heat flux in the direction *perpendicular* to the mean temperature gradient is significantly larger than the heat flux down the imposed mean temperature gradient! Hence, *simple* gradient-transport models that assume that the heat flux vector is aligned directly opposite to the mean temperature gradient will fail to predict the strong cross-gradient transport. There are many important practical situations where this cross-gradient transport is likely to be a very important phenomena, and so it is important that the mechanisms be understood and that the models be improved so that the fluxes can be predicted.

Rogers and Moin studied the structure of the turbulence field in shear flow in great detail, using the simulations to explore such questions as the configurations of vortex lines in the flow. They found that hairpin vorticies, of the type found in inhomogeneous shear flows over solid walls, also occur in homogeneous shear flow. These vortices arise as a result of the straining of vortex filaments, and the legs of the hairpin vortices are predominantly aligned with the axis of positive principal strain rate, i.e. at 45° upward from the x_1 axis. In homogeneous shear flows there are equal numbers of "heads-up" and "heads-down" hairpins. The vorticity in the heads has the same sense as the vorticity in the mean flow; indeed, much of the transverse vorticity is concentrated in these hairpin heads. Rogers also found that persistent shearing at

the higher Reynolds numbers gives rise to structures with strong spanwise coherence over substantial distances, very much like the two-dimensional rollers in a two-stream mixing layer. Thus, the dominant large-scale structures in homogeneous shear flow are now thought to be some combinations of spanwise vortices and up and down hairpins.

This model of the structure of the turbulence allows one to understand the anisotropic nature of the turbulent heat transport. Figure 5 shows Rogers' explanation of the way in which these three types of coherent structures act to convect the scalar field in each of the three cases.

Simple extensions of the gradient transport model can be used to predict the heat fluxes for arbitrary mean temperature gradients. In suggesting these models we are not proposing that the transport process is one of gradient diffusion at the molecular level, but only that the mean temperature gradient provides the *scaling* of the heat flux. The direction of the heat flux vector is determined in a complicated way by the fluid dynamics, but it turns out that it is possible to model this in either of two rather simple ways.

The first model uses an anisotropic tensor turbulent diffusivity D_{ij}, defined by

$$F_i = \overline{\theta' u_i'} = -D_{ij}\frac{\partial T}{\partial x_j} \qquad (12)$$

where θ' is the scalar(temperature) fluctuation, T is the mean scalar quantity (temperature), and F_i is the scalar flux in the ith direction. D_{ij} is easily calculated from the simulation data, and is found to be non-symmetric. However, in a rotated coordinate system it can be made antisymmetric, and the important thing discovered by Rogers is that this coordinate system is essentially the same as the principal coordinate system of R_{ij} and b_{ij}. This means that the diagonal members of D_{ij} should be modeled in terms of the Reynolds stress tensor. In the rotated coordinate system, the off-diagonal elements must be antisymmetric, and the only antisymmetric tensor available is the mean rotation tensor,

$$\Omega_{ij} = \frac{1}{2}(U_{i,j} - U_{j,i}). \qquad (13)$$

This leads one to the model

$$D_{ij} = \frac{q^4}{\epsilon}(C_1 b_{ij} + C_2 \delta_{ij} + C_3 \tau \Omega_{ij}) \qquad (14)$$

where τ is an appropriate turbulence time scale (q^2/ϵ) and the coefficients $C_1 - C_3$ are dimensionless functions of scalars in the model. Rogers fit the coefficients as functions of the Reynolds and Prandtl numbers, and found that the resulting model could predict all of the heat fluxes for all of his fields to within 20%. This

model can be used for inhomogeneous flows to estimate the anisotropic diffusivity tensor.

A second, more sophisticated model, containing only one free coefficient, was also evaluated by Rogers. This model assumes that certain vector terms needing to be modeled in the exact equation for the turbulent scalar flux are aligned with the flux vector. This assumption had been made intuitively by earlier modelers, but Rogers was able to check it in detail using the simulations, and found that it was indeed approximately true. This assumption allows the equation for the scalar flux to be reduced to

$$-R_{ij}\frac{\partial T}{\partial x_j} - F_j\frac{\partial U_i}{\partial x_j} + C\frac{F_i}{\tau} = 0. \qquad (15)$$

This is a set of linear algebraic equations for the F_i that can be inverted immediately for special gradients and solved locally in the general cases. Rogers fit the simulation results to determine C, and found that the resulting fluxes were predicted for all cases to within about 20%.

In summary, Rogers' simulations of scalar transport in homogeneous turbulent shear flow provide physical insight on the structure of homogeneous turbulent shear flow, an explanation for the mechanisms of cross-gradient turbulent heat transfer, and simple models that can be incorporated into codes for more complicated engineering problems. The fields have been archived at Ames and continue to be explored in the study of the physics and modeling of turbulence.

4. The spatially-developing mixing layer

The mixing layer between two parallel streams of different velocity has been widely studied in the laboratory and, for the case of *time-development*, by direct numerical simulation. The time-developing case has lent itself to simulation because it permits the use of periodic boundary conditions in the flow direction, thereby eliminating the need to devise turbulent inflow and outflow conditions.

In a dissertation just completed, Pat Lowery (1986), who did his research as a NASA CFD Fellow and now works in CFD at the Battelle Northwest Research Laboratories, developed a code for the spatially-developing mixing layer, including scalar transport, with prescribed time-dependent inlet conditions. He studied the *forced* mixing layer in a series of two- and three-dimensional simulations, which included mixing studies and a fast chemical reaction calculation.

Typical two-dimensional calculations used a mesh 256 (cross-stream) by 1024 (streamwise). Three-dimensional calculations used a mesh 512 (streamwise) by 128 (cross-stream) by 64 (spanwise). Finite-difference representations were used streamwise, spectral representations were used cross-stream and spanwise, and a third-order Runga-Kutta scheme was used for time advance. TVD corrections were necessary to maintain

proper scalar fields. On the Cray XMP 4-8, approximately 60 CPU seconds were required per time step in three-dimensions. The Reynolds number at the inlet to the computational domain, based on the velocity difference across the mixing layer and the inlet vorticity thickness, was 100; the Prandtl number was 1.

The first problem to be solved was the outflow boundary condition. Other workers have set gradients to zero at the outflow boundary, but this produces a "hard" exit condition that distorts the flow near the exit. Lowery found that a "softer" condition worked extremely well. The idea is simply to convect quantities out of the computational domain at a uniform convection velocity U_c by setting

$$\frac{\partial}{\partial t} + U_c \frac{\partial}{\partial x_1} = 0 \qquad (16)$$

for all of the velocity components and the scalar field. This allows the large-scale structures to roll out of the computational domain at the convection velocity, which was taken as the average of the two free-stream speeds. Figure 6 shows a snapshot of Lowery's simulation, which strongly resembles pictures from experiments.

Most of the work was done with forcing at the inlet, which in Lowery's simulation was imagined to be just downstream of the splitter plate forming the mixing layer. Because the dynamical processes in the layer involve the interactions of modes with their subharmonics to produce vortex merging (the mechanism by which the turbulence scale grows larger downstream), it was necessary to excite the inlet flow with fundamentals and sub-harmonics of the basic instability modes for the inlet laminar shear layer ($\tanh$ profile). The response depends on the relative phases of these modes and time permitted only a modest study of the possibilities. However, it became clear (as experiments have already shown) that control over the growth of the mixing layer can be achieved by careful selection of the subharmonic phases.

One of the major experimental observations is that more high-speed fluid is entrained into the layer than low-speed fluid. This effect is not captured in time-developing mixing layer simulations, since they are symmetric with respect to the two flow streams. This effect was captured in Lowery's simulations, at a level commensurate with experiments. Probability density functions, the turbulent stress behavior, and other features of the flows were comparable in trends and magnitudes with experimental forced mixing layers, although it was impossible to make a direct comparison because of the sensitivity to the particular forcing.

There are some theoretical arguments that suggest that the mixing layer is *convectively unstable*, meaning that removal of the forcing will permit the disturbances to wash downstream and the layer to re-laminarize. Lowery studied this question by freezing the disturbance field after some computation. Indeed, the disturbances washed downstream, but only partway. It seems that the large-scale disturbances in the far-downstream region trigger instabilities in the upstream flow through the pressure field. These new disturbances then travel downstream, repeating the triggering process (an *absolute instability*). It is generally believed that the splitter plate, absent in Lowery's simulation, is an essential element in making this flow absolutely unstable. The simulation suggests that this might not be the case.

In his three-dimensional simulations, Lowery added streamwise vortices to the forcing. These produced structures very similar to those seen in the "braid" regions of the mixing layer. He ran one simulation with random excitation at the inlet, and found that these same structures were beginning to emerge naturally, although a great deal more computational time would have to be expended to allow them to develop completely. Thus, one can probably study these three-dimensional effects by judicious selection of the inlet forcing.

Experiments have shown evidence of some vorticity of opposite sign to that in the mixing layer. This could be due to the vorticity coming from the boundary layer on the low-speed side of the splitter plate, or it could be due to overturning of vortex filaments by the three-dimensional action of the turbulence. Lowery could do what an experimentalist can not, i.e. run without the low-speed boundary layer, in which case negative vorticity could result only from overturning of vortex filaments. Feeding the inlet flow with vorticity of only one sign, only vorticity of this sign was found in the two-dimensional simulations. But in the three dimensional simulations a small amount of vorticity of opposite sign was found, indicating that the vortex filament overturning process indeed takes place.

A new Ph.D. student, Neil Sandham, has used Lowery's code to study the mixing layer using inlet flows representing the splitter-plate boundary layers. These have shown very little effect of the boundary layers on the overall flow development, except very near the end of the splitter plate. In addition, we have developed a method for randomly exciting the inlet flow that looks quite promising in that it produces a mixing layer behavior much more characteristic of natural mixing layers than of the forced layers studied by Lowery.

A new effort is being devoted to simulation of the *compressible* spatially-developing mixing layer, which is of interest in both aerodynamic and scramjet engine situations. The effort involves both direct numerical simulations at low Reynolds numbers and the development of improved models for LES studies of supersonic mixing and combustion. Supersonic mixing layers are known to spread and mix much less rapidly than subsonic layers, and the reasons for this are not well understood. In the scramjet application, new ways to

enhance the mixing must be found. We are hopeful that these direct simulations will, over the next few years, shed some light on these important questions.

In summary, Lowery's simulations of the spatially-developing mixing layer provide new physical insight into the mechanisms of transport and entrainment in inhomogeneous free shear flows, and provide a basis for further studies on the modeling of such flows. Inlet conditions for turbulent flows need to be developed, but the prospects look bright. Extensions to compressible flows are within reach and should be achieved in the next two or three years.

References

Lee, M.J. and W.C. Reynolds 1985 Numerical Experiments on the Structure of Homogeneous Turbulence, Report TF-24, Department of Mechanical Engineering, Stanford University

Lowery, P.S. and W.C. Reynolds 1986 Numerical Simulation of a Spatially-Developing, Forced, Plane Mixing Layer, Report TF-26, Department of Mechanical Engineering, Stanford University

Rogallo, R.S. 1981 Numerical Experiments in Homogeneous Turbulence. NASA Technical Memo 81315

Rogers, P.M, P. Moin and W.C. Reynolds 1986 The Structure and Modeling of the Hydrodynamics and Passive Scalar Fields in Homogeneous Turbulent Shear Flow, Report TF-25, Department of Mechanical Engineering, Stanford University

FIGURE 1

$|\Pi_c|$ vs. $|\Pi_b|$ for relaxation from simple strains. ●, AxR; △, BxR; ▽, CxR; ◇, DxR; □, ExR; ■, FxR; ●, GxR; ◉, HxR where x = 2,3,4. +, relaxation from axisymmetric contraction; ×, relaxation from axisymmetric expansion. -----, locus of locking for relaxation from axisymmetric contraction ($A_0 = -1$); ——, locus of locking for relaxation from axisymmetric expansion ($A_0 = +1$).
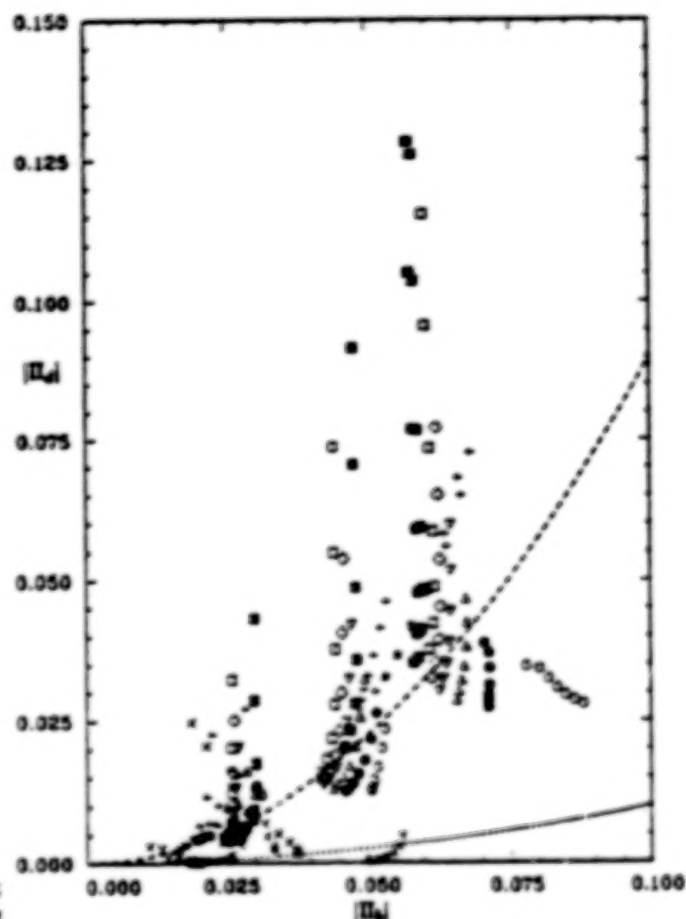
FIGURE 2

$|\Pi_d|$ vs. $|\Pi_b|$ for relaxation from simple strains. ●, AxR; △, BxR; ▽, CxR; ◇, DxR; □, ExR; ■, FxR; ●, GxR; ◉, HxR where x = 2,3,4. +, relaxation from axisymmetric contraction; ×, relaxation from axisymmetric expansion. -----, locus of locking for relaxation from axisymmetric contraction ($A_0 = -1$); ——, locus of locking for relaxation from axisymmetric expansion ($A_0 = +1$).

FIGURE 3 Comparison of relaxation trajectories on the vorticity AIM: ⊕, B2R; △, E2R; ▽, M2R; ◇, P2R; □, L2W1R; ▣, P2V1R; ●, Q2U1R; ▣, Q2W1R; ——, model prediction.
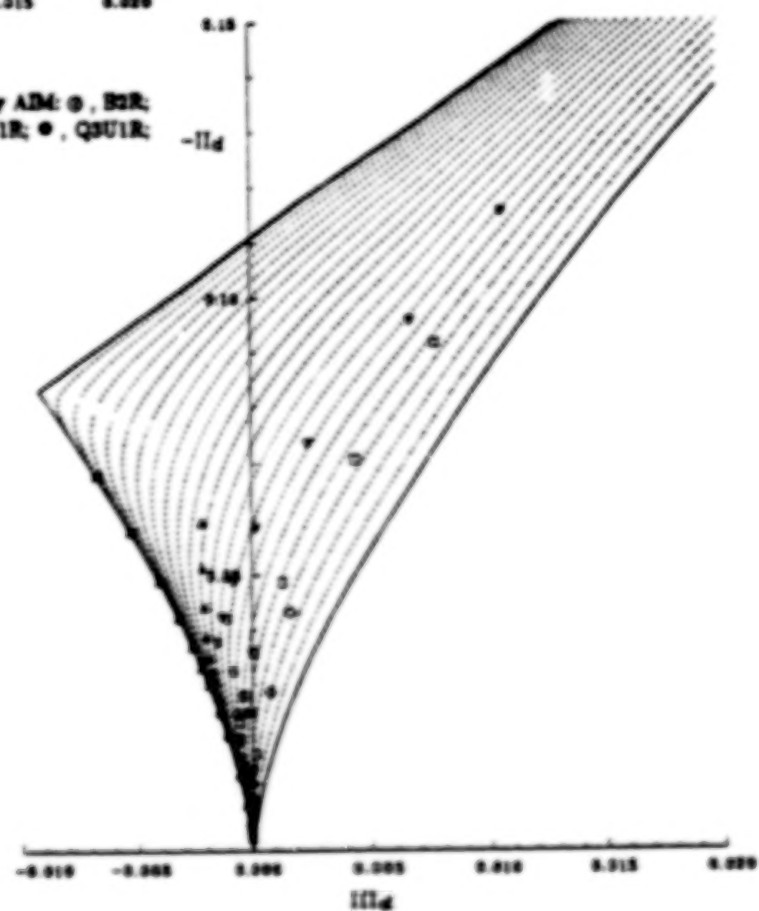
FIGURE 4 Comparison of relaxation trajectories on the dissipation rate AIM: ⊕, C2R; △, C4R; ▽, E4R; ◇, F2R; □, F2R; ▣, L4R; ●, Q6R; ▣, L2W1R; ——, model prediction.

CASE 1	CASE 2	CASE 3
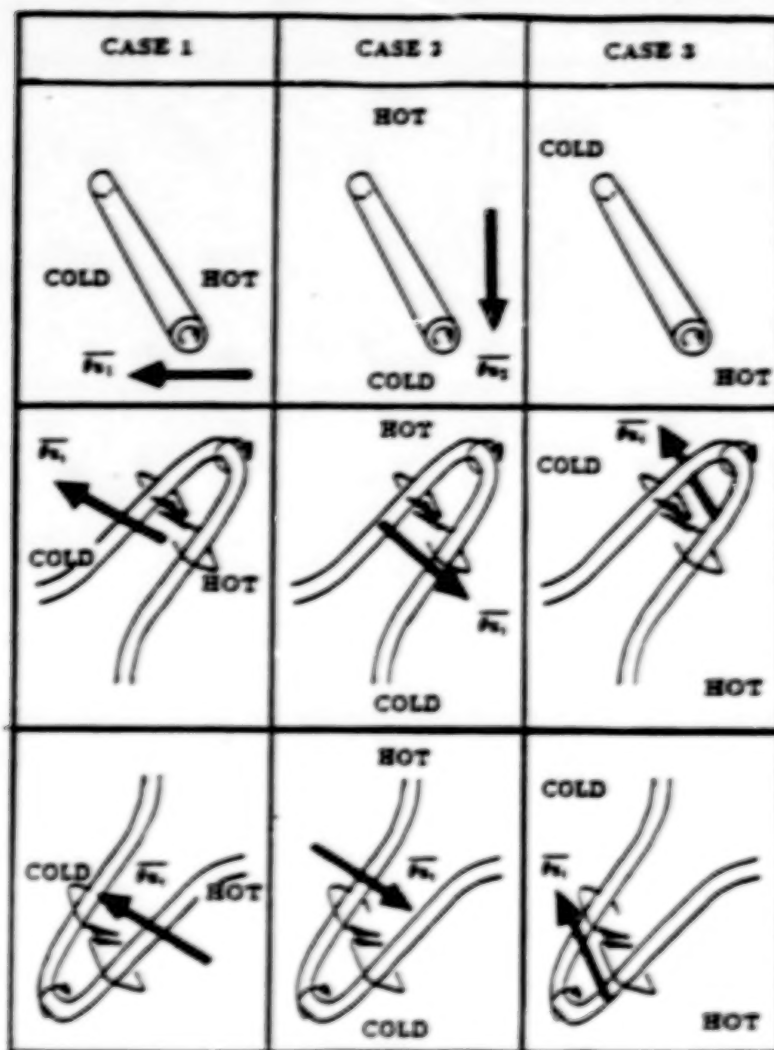
Figure 5   Schematic of the turbulent scalar flux generated by typical coherent structures for all three mean scalar gradient cases.
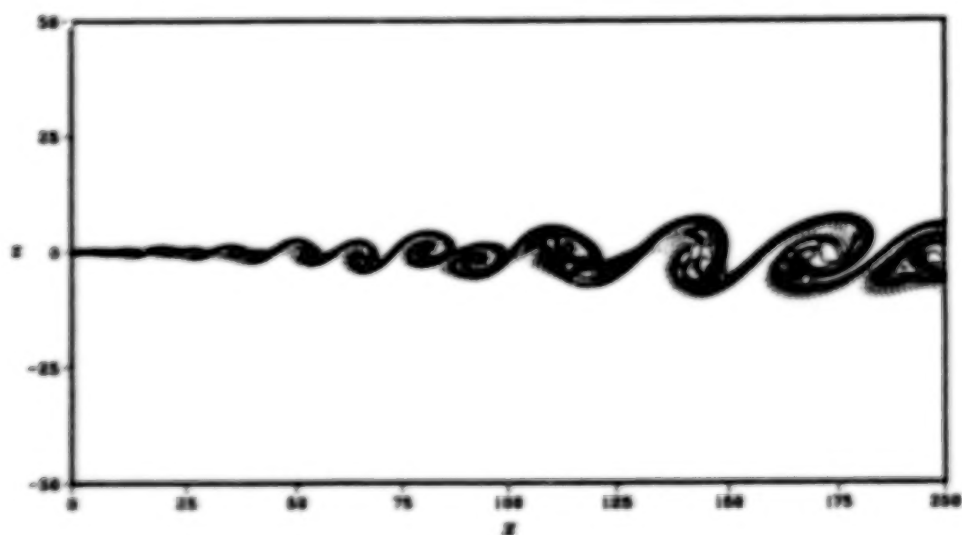
Figure 6   Snapshot" of results – passive scalar isograms

N87
26017
UNCLAS

Stability, Transition and Turbulence

M. Y. Hussaini

Institute for Computer Applications in Science and Engineering

NASA Langley Research Center

Hampton, VA 23665

1 Abstract

A glimpse is provided of the research program in stability, transition and turbulence based on numerical simulations. This program includes both the so-called abrupt and the restrained transition processes. Attention is confined to the prototype problems of channel flow and the parallel boundary layer in the former category and the Taylor-Couette flow in the latter category. It covers both incompressible flows and supersonic flows. Some representative results are presented.

Superscripts

$\bar{}$: Favre average

Subscripts

k, l : Cartesian indices
w : wall value
∞ : freestream value

2 Nomenclature

C_p : specific heat at constant pressure
C_v : specific heat at constant volume
D : average of diagonal stress components
$\mathbf{F}$: forcing function
M : Mach number
OD : average of off-diagonal stress components
p : pressure
Pr : Prandtl number
Re : Reynolds number
t : time
T : temperature
u : fluid velocity
γ : ratio of specific heats (C_p/C_v)
δ : Kronecker tensor
∇ : gradient operator
κ : thermal conductivity
μ : molecular viscosity
Φ : viscous dissipation function
ρ : density
S : average of stress components on the scalar level
σ : viscous stress tensor
θ : $(T - T_w)/(T - T_\infty)$
V : average of stress components on the vector level

3 Introduction

The phenomena of transition to turbulence are so complex as to defy a unified theory at the present time. As such, direct numerical simulations of these phenomena within the framework of Navier-Stokes equations have assumed a dimension equal in importance to experimental and even theoretical studies. An effective simulation not only mimics a physical experiment but has the added advantages of offering readily retrievable clean information wherever and whenever it is needed, and also a precise control of parameters unachievable in the physical experiment. Theoretical and mathematical approaches provide progress in understanding through the processes of abstraction and idealisation; the results of analysis then furnish, apart from specific predictions, a deeper comprehension of the underlying general principles. These features are not intrinsic to a numerical simulation. However, they can be built into the simulations to some extent. Careful considerations of such factors are the bases of the research program in this area. Here at LaRC/ICASE our research program includes both the so-called abrupt and restrained transition processes. Attention is confined to the prototype problems of the channel flow and the parallel boundary layer in the former category, and the wake and the Taylor-Couette flows in the latter category. It covers both incompressible flows and supersonic flows.

4 Poiseuille and Blasius Flows

4.1 Background

Although our knowledge of laminar-turbulent transition is by no means complete, the broad features are now clear at least in low subsonic shear flows. This is in a large measure due to the the classical experiments of Klebanoff, Tidstrom and Sargent [1], Kovasznay, Komoda and Vasudeva [2], Han and Nutant [3]. These experiments were conducted in a controlled, identifiable disturbance environment where the nondeterministic disturbances were immeasurably small. Briefly stated, the instability and transition process involves the following stages: 1) a primary instability evolving in accordance with the linear theory, 2) a secondary instability leading to the emergence of a flow of a pronounced three-dimensional nature, and the appearance of the streamwise vortex system, 3) the development of detached high-shear layers, 4) at least a tertiary instability (if not an extremely rapid succession of a sequence of instabilities) resulting in turbulent spot development and 5) convection and coalescence of turbulent spots to form a fully developed turbulent flow. Similar patterns have been observed in plane Poiseuille flow by Nishioka, Iida and Ichikawa [4]. More recently, the experiments of Kachanov and Levchenko [5], and Saric and Thomas [6] have uncovered some new details in the secondary instability stage of the transition process in boundary layers. The flow pattern outlined above is relevant to natural transition under some limited, but not all, conditions. The reviews of Stuart [7] and Tani [8] provide a detailed discussion of the classical experiments and the then available theoretical explanations of the isolated stages or events of the transition process. The more recent review of Herbert and Morkovin [9] provides an overview of applied problems in stability and transition, and a discussion of the various theoretical approaches to the secondary instability problem. Craik's monograph [10] deals with the general problem of wave interactions in various fields, and includes a discussion of the secondary instability pertinent to wall-bounded shear flows.

The primary instability has as its basis linear theory and has long been well established. The theory for the secondary instability is however more recent, but is also fairly well established (Herbert [11], Nayfeh [12]). There have been no improvements in the theoretical models for the other stages since the survey article of Stuart [7] Full scale numerical simulations provide a unified basis for investigating the

relevance and relative importance of various events right up to the formation of turbulent spots. In the present paper we shall dwell on numerical experiments which have uncovered the secondary instability associated with the center modes in plane Poiseuille flow. We shall also discuss simulations which have brought out the relative effectiveness of the various laminar flow control (LFC) techniques such as heating, favorable pressure gradient and suction. We will present some representative results in each category.

The incompressible variable property Navier-Stokes equations, in usual notation, are (Zang and Hussaini [13])

$$\nabla \cdot \mathbf{u} = 0 \tag{1}$$

$$\frac{\partial \mathbf{u}}{\partial t} + \mathbf{u} \cdot \nabla \mathbf{u} = -\nabla p + \frac{1}{Re} \nabla \cdot (\mu \nabla \mathbf{u}) + F_{\mathbf{u}} \tag{2}$$

$$\frac{\partial \theta}{\partial t} + \mathbf{u} \cdot \nabla \theta = \frac{1}{RePr} \nabla \cdot (\kappa \nabla \theta) + F_\theta \tag{3}$$

where the lengths are scaled by the half channel-width (or for the boundary layer by the displacement thickness at the streamwise station of interest), velocities by the corresponding center velocity for the channel flow (or the corresponding mainstream velocity for the boundary layer), and pressure by the dynamic head; the forcing functions $F_{\mathbf{u}}$ and F_θ are designed to ensure parallel flow. The viscosity and conductivity are given functions of temperature for the heated wall case, and constants in other cases.

The applied boundary conditions assume periodicity in the horizontal directions, and the no-slip velocity on solid walls. For the heated water boundary layer case, the no-slip condition for the velocity and a uniform temperature are enforced at the wall; perturbations are assumed to be zero in the mainstream. This permits a Fourier discretization in the streamwise and spanwise directions, and a Chebyshev discretization in the vertical direction. The initial condition consists of a triad of waves – one two-dimensional wave and two skewed waves. The general fractional step algorithm for efficiently solving the relevant equations is given by Zang and Hussaini [14]. A survey of spectral algorithms for fluid dynamic calculations is given in Hussaini and Zang [15], and Canuto, Hussaini, Quarteroni and Zang [16]. The latter is a monograph which deals with both theory and applications of spectral methods.

4.2 Instability Due To A Triad Of Center Modes

The so-called center modes of plane channel flows are in fact temporal eigenfunctions of the Orr-Sommer-

field equation which decay in time. However, a combination of a two-dimensional center mode with two skewed modes is susceptible to an instability similar to the secondary instability encountered in a similar non-resonant triad of wall modes. The essential qualitative difference between the center mode and the wall mode (as is evident from Fig. 1a and 1b) is that the maximum amplitude for the former occurs away from wall towards the channel center, while for the latter it occurs near the wall, and hence the terminology. There are of course other quantitative differences with regard to wavelengths, phase velocities and decay rates. The Reynolds number for the simulation was 8000 based on the channel half width, and both the streamwise and spanwise wavenumbers were unity; the initial two-dimensional and three-dimensional amplitudes were 10% and 3% respectively of the channel center velocity. The resolution requirements were monitored and the grid was refined to resolve the fine structures as they emerged. The finest grid was 96x128x192. Plotted in Fig. 2 is the time history of the harmonic contents of the solution. Note that the two-dimensional mode, labeled (1,0), decays almost exponentially, but the three-dimensional mode, labeled (1,1), grows after an initial decay for about three periods 2π being the characteristic period. The results are presented at $t = 87$ (a little less than 14 periods) at which time the finest grid was just about sufficient to resolve the sharp gradients of the flow field. The vortex lines are displayed in Fig. 3a, and for comparison purposes vortex lines for an analogous case of wall modes are presented in Fig. 3b. The streamwise and spanwise vorticity contours are displayed in Fig. 4 at four equidistant streamwise planes over a wavelength. Fig. 5 displays similar contours for the case of the wall modes. The qualitative similarities and differences are obvious. The center-mode vortex loop is comparatively away from the wall, and the pinching at the neck is less intense than for the wall-mode vortex loop. Also, the high-shear layer associated with the center modes is less intense than the one associated with the wall modes. The physical relevance of the center mode instability to the high-intensity bypass to transition is as yet undetermined.

4.3 Effect of Heating on the Secondary Instability of Blasius Flow

Laminar flow control (LFC) vehicles might operate in a finite-amplitude disturbance environment, so it is of interest to examine the relative performance of the various LFC techniques in the nonlinear regime.

While some experimental studies have investigated the influence of nonlinear disturbance sources such as roughness, vibrations, free-stream turbulence, etc. on the basic transition process, there have been no comparative studies on the sensitivity of the LFC techniques such as heating, pressure gradient and suction in the nonlinear regime. In the absence of any relevant nonlinear stability theories due to the complexity of the problem, numerical simulations can play a crucial role in this field. As an example of such a use of simulation, we have performed a Navier-Stokes calculation involving conditions similar to those used in the experiment of Kovasznay, Komoda and Vasudeva [2] except that in our simulation the wall was heated. The idealisation of a parallel boundary layer was used mainly in order to meet the resolution requirements while keeping the computing time within reasonable limits. The Reynolds number of the simulation was 1100 based on the displacement thickness, and the initial amplitudes of the two-dimensional and three-dimensional Tollmien-Schlichting waves (wall modes) were respectively 2.7% and 0.8% of the free stream velocity. The finest grid was 72x162x192.

Three different situations were studied: 1) the uncontrolled case, 2) the heated fixed temperature case, and 3) the heated active temperature case. In the heated fixed temperature case, the temperature was kept fixed at the initial value pertinent to the mean flow conditions, and the temperature evolution was totally neglected. In the heated active temperature case, the temperature evolution was taken into account by solving the temperature equation along with the momentum equations. In both the cases the wall temperature was 2.75% above the free stream temperature. Fig. 6 shows the harmonic history of the perturbation energy. Note that the (1,0) mode which grows in the uncontrolled case decays in the heated almost up to 4 periods. Heating damps the (1,1) mode initially, but it starts growing within the first period. It appears that when the energy in the three-dimensional wave overtakes that in the two-dimensional wave, it feeds energy partly into the two-dimensional wave. Fig. 7 shows the spanwise vorticity contours on the peak plane. In the uncontrolled case (Fig. 7 top left) a kink develops in the high-shear layer at time t equal to three Tollmien-Schlichting periods. It is generally accepted that a irrevocably quick succession of events follows thereafter leading to a turbulent spot formation. Heating the wall to 2.75% above the free stream temperature diffuses the high-shear layer as is obvious from Fig. 7 (bottom left). However, within the subsequent one and one fourth period, turbulent spot formation appears to become imminent (Fig. 7 top right). In the fixed

temperature case, it is clear from Fig. 7 (bottom right) that the high-shear layer formation is mellowed down even up to four and one fourth periods. The fixed temperature case overpredicts the weakening effect of heating on the secondary instability. In other words, the effect of temperature evolution is significant and deleterious in the nonlinear regime whereas it is quite negligible in the linear regime.

5 Taylor-Couette Flow

The instability and abrupt transition process are typical of aerodynamic flows. On the other hand, the transition to turbulence by spectral evolution are typical of geophysical fluid dynamics where there is a destabilising force field. The Taylor-Couette flow in the annulus of concentric rotating circular cylinders typifies a class of geophysical problems involving instabilities and turbulence due to the presence of a destabilising centrifugal force field. DiPrima and Swinney [17] provide an excellent review of instabilities and transitions in Taylor-Couette flows. Our interest lies in finite-length Taylor-Couette flow as it offers the situation of weak turbulence which is amenable to direct simulation. The prime objective of our research effort to examine the various qualitative mathematical theories (Benjamin [18]). Some of the routes to mathematical chaos appears to have been observed in these flows. The chaos theories are based on model equations. Our investigations will establish the relevance of these theories to Navier-Stokes equations.

This problem, unlike those considered in the preceding sections, is truly inhomogeneous in two directions. A spectral algorithm necessarily involves Chebyshev polynomial expansions in radial and axial directions, and Fourier expansion in the azimuthal direction. The fractional step algorithm used to study the channel flows and the parallel boundary layers is easily extended to treat this problem (Streett and Hussaini [19]).

The initial phase of study focussed on the steady-state bifurcations in axisymmetric Taylor-Couette flow (with the inner cylinder rotating, and the outer cylinder and end walls remaining stationary) for aspect ratios of order unity. These problems provide a stringent test for a time-accurate method designed to simulate the delicate unsteady processes leading to transition. Among the numerous simulations carried out to compare with the available experiments, we present some typical results for the geometry of Benjamin and Mullin [20] which had an aspect ratio

of 1.05 and radius ratio of 0.615. The symmetric two-cell mode is established at a relatively low Reynolds number of 62, and then the Reynolds number is impulsively raised to 150. The development of the asymmetric single-cell flow represented by the streamlines in a cross-sectional plane is shown in Fig. 8, and Fig. 9 displays the order parameter (which is a measure of the asymmetry of the flow) and energy as functions of time in units of characteristic diffusion time scale. The continuing simulations are on the verge of capturing bifurcations into time-dependent states. The final objective is to calculate the dimension of the strange attractor which is supposed to represent the weak turbulence.

6 Compressible Transition and Turbulence

Transition to turbulence in supersonic and hypersonic flows is a gray area. There are differing experimental results, and unexplained visual observations. The picture is quite piecemeal compared to low Mach number flows. The purpose of the research program is to answer questions such as: a) do secondary instability mechanisms observed in low subsonic flows persist in supersonic flows, b) is the turbulent spot formation the usual way transition occurs, and c) is the transition process abrupt or restrained. The initial focus of our research program is on question (a), i.e., whether the known prototypes of instabilities in incompressible flows persist at high Mach numbers. A spectral simulation of a three-dimensional instability process in a parallel boundary layer at Mach number 4.5 was carried out.

The full compressible Navier-Stokes equations are, in dimensionless form, (Erlebacher and Hussaini [21])

$$\frac{\partial \rho}{\partial t} + \nabla \cdot (\rho \mathbf{u}) = 0 \qquad (4)$$

$$\frac{\partial (\rho \mathbf{u})}{\partial t} + \nabla \cdot (\rho \mathbf{u}\mathbf{u}) = \frac{1}{Re} \nabla \cdot \boldsymbol{\sigma} \qquad (5)$$

$$\frac{\partial p}{\partial t} + \mathbf{u} \cdot \nabla p + \gamma p \nabla \cdot \mathbf{u} = \frac{\gamma}{RePrM_\infty^2} \nabla \cdot (\mu \nabla T) + (\gamma - 1)\Phi \qquad (6)$$

where

$$\sigma_{kl} = [\mu(\frac{\partial u_k}{\partial x_l} + \frac{\partial u_l}{\partial x_k}) - \frac{2}{3}\mu(\nabla \cdot \mathbf{u})\delta_{kl}] \qquad (7)$$

$$\Phi = \frac{1}{2}(\frac{\partial u_k}{\partial x_l} + \frac{\partial u_l}{\partial x_k})\sigma_{kl} \qquad (8)$$

and the equation of state is

$$\gamma M_\infty^2 p = \rho T \qquad (9)$$

with $\gamma = C_p/C_v$, the ratio of specific heats. At high Mach number, temperature variations across the boundary layer become important and the temperature dependence of viscosity must be taken into account. The Prandtl number was assumed equal to 0.7, and the Sutherland's law was prescribed for viscosity variation with the temperature. The free stream Mach number was 4.5, and the Reynolds number was 10000 based on the displacement thickness. The boundary conditions were identical to those used in the incompressible boundary layer simulations discussed in the earlier section. The initial condition consisted of an unstable two-dimensional wave and a pair of three-dimensional oblique waves superimposed on a prescribed parallel mean flow. These waves were the eigenfunctions of an eighth order eigenvalue problem, the compressible analogue of the incompressible Orr-Sommerfeld equation. The initial amplitudes of the two-dimensional and three-dimensional perturbations were taken to be respectively 5.4% and 1.2% of the free stream velocity. The temporal evolution of this triad of waves was followed for about eight periods of the initial two-dimensional Tollmien-Schlichting wave (TS wave). The time history of several Fourier harmonics of the perturbation kinetic energy (integrated in the vertical direction) is shown in Fig. 10. After a period of slow growth of the three-dimensional wave, labeled (1,1) mode, the nonlinear interactions between the (0,1) spanwise mode and the primary (1,0) mode trigger the secondary instability after approximately 5 TS periods. Contour plots of the streamwise velocity (Fig. 11) at the time of 5 TS periods illustrate the incipient stages of a K-type breakdown (Erlebacher and Hussaini [21]). In the supersonic simulations, the critical layer is an order of magnitude further from the wall than in the incompressible cases. One consequence is that the structures are farther removed from the walls. Initial results indicate that compressibility retards the onset of the secondary instability. However, a more extensive parameter study is required before any firm conclusion can be drawn.

Our research program has recently focused its attention on the development of subgrid-scale models for compressible turbulence. A compressible extension of Bardina's linear combination model [22] has been developed. Favre-averaging was employed to produce spatially averaged compressible Navier-Stokes equations which closely resemble the incompressible ones. For compressible as opposed to incompressible flow, the trace of the subgrid stresses

cannot be incorporated with the pressure since the pressure is a true thermodynamic variable. These isotropic stresses must now be modeled, and a new model constant, termed the isotropic constant, must be included.

This new model has been tested against direct simulations at Mach numbers ranging from 0.0 to 0.6 and on grids of 64^3 to 128^3. The turbulence model was compared against this direct simulation (DS) data suitably injected onto a coarser grid. The coarse grid would normally be used in a large eddy simulation. A least square fit between the total stress calculated from the DS and the modeled stress computed from spatially filtered velocities allows the constants to be determined. The constant determination was performed on the vector level (Erlebacher, Hussaini, Speziale, Zang [23]). Table 1 summarizes the correlation coefficients between the modeled and the exact

	$M_0 = 0.0$	$M_0 = 0.6$
D	82	81
OD	85	84
V	72	71
S	73	74

Table 1:

total stresses at Mach 0 and Mach 0.6. Results are presented on the tensor, vector and scalar levels. The vector level is the divergence of the tensor, while the scalar level is defined by the product of $\nabla \cdot \tilde{u}$ and $\tilde{u}$. The Leonard stress is omitted from the total subgrid stress because it can be calculated exactly. Correlation coefficients of over 80% are obtained on the tensor level, and above 70% on both the vector and scalar levels. A more thorough study can be found in Erlebacher et al. [23].

7 Concluding Remarks

Numerical algorithms for studying the physics of transition and turbulence in simple geometries have been developed. Detailed studies of the highly nonlinear stages of transition prior to turbulent spot formation have been made. The use of simulations to study the sensitivity of laminar flow control techniques in the nonlinear regime has been demonstrated. A new instability mechanism associated with the center modes in channel flows has been uncovered, although

its physical significance is as yet undetermined. The first numerical simulations of their kind are being carried out for supersonic boundary layer flows. The preliminary results revealed the existence of a secondary instability similar to the one in incompressible flows.

References

[1] Klebanoff, P. S.; Tidstrom, K. D.; and Sargent, L. M.: The Three-Dimensional Nature of Boundary-Layer Instability, J. Fluid Mech., Vol. 12, 1962, pp. 1-34.

[2] Kovasznay, L. S.; Komoda, H.; and Vasudeva, B. R.: Detailed Flow Field in Transition, Proc. 1962 Heat Transfer and Fluid Mechanics Institute, pp. 1-16, Stanford Univ. Press, Palo Alto, 1962.

[3] Hama, F. R.; and Nutant, J.: Detailed Flow-Field Observations in the Transition Process in a Thick Boundary Layer, Proc. of the 1963 Heat Transfer and Fluid Mechanics Institute, pp. 77-93, Stanford Univ. Press, Palo Alto, 1963.

[4] Nishioka, M.; Asai, M.; and Iida, S.: An Experimental Investigation of the Secondary Instability in Laminar-Turbulent Transition, Laminar-Turbulent Transition, R. Eppler and H. Fasel (eds.), pp. 37-46, Springer-Verlag, Berlin, 1980.

[5] Kachanov, Yu. S.; and Levchenko, V. Ya.: The resonant interaction of disturbances at laminar-turbulent transition in a boundary layer, J. Fluid Mech., Vol. 138, 1984, pp. 209-247.

[6] Saric, W. S.; and Thomas, A. S. W.: Experiments on the subharmonic route to turbulence in boundary layers, Turbulence and Chaotic Phenomena in Fluids, T. Tatsumi (ed.) North Holland, 1984.

[7] Stuart, J. T.; Hydrodynamic Stability, Appl. Mech. Rev., Vol. 18, 1965, pp. 523-531.

[8] Tani, I.: Boundary-Layer Transition, Ann. Rev. of Fluid Mech., Vol. 1, 1969, pp. 169-196.

[9] Herbert, T.; and Morkovin, M. V.: Dialogue on bridging some gaps in stability and transition research, Laminar-Turbulent Transition, R. Eppler and H. Fasel (eds.), pp. 47-70, Springer Verlag, Berlin, 1980.

[10] Craik, A. D. D.: Wave Interactions and Fluid Flows, Cambridge University Press, 1985.

[11] Herbert, T.: Floquet analysis of secondary instability in shear flows, Stability of Time Dependent and Spatially Varying Flows, D. L. Dwoyer and M. Y. Hussaini (eds.), pp. 43-57, Springer Verlag, New York, 1987.

[12] Nayfeh, A. H.: On secondary instabilities in boundary layers, Stability of Time Dependent and Spatially Varying Flows, D. L. Dwoyer and M. Y. Hussaini (eds.), pp. 43-57, Springer Verlag, New York, 1987.

[13] Zang, T. A.; and Hussaini, M. Y.: Numerical Experiments on the Stability of Controlled Shear Flows, AIAA Paper No. 85-1698, 1985.

[14] Zang, T. A.; and Hussaini, M. Y.: On Spectral Multigrid Methods for the Time-Dependent Navier-Stokes Equations, Appl. Math. Comp., Vol. 19, 1986, pp. 359-372.

[15] Hussaini, M. Y.; and Zang, T. A.: Spectral Methods in Fluid Dynamics, Ann. Rev. Fluid Mech., Vol. 19, 1987.

[16] Canuto, C.; Hussaini, M. Y.; Quarteroni, A.; and Zang, T. A.: Spectral Methods in Fluid Dynamics, Springer-Verlag, Berlin, 1987.

[17] DiPrima, R. C.; and Swinney, H. L.: Transition in Flow between Rotating Concentric Cylinders, Transition and Turbulence, R.E. Meyer (ed.), Academic Press, 1981.

[18] Benjamin, T. B.: Bifurcation Phenomena in Steady Flow of a Viscous Fluid I. Theory, Proc. Roy. Soc. London, Vol. A 359, 1978, pp. 1-26.

[19] Streett, C. L.; and Hussaini, M. Y.: Finite Length Effects in Taylor-Couette Flow, ICASE Report No. 86-59, 1986.

[20] Benjamin, T. B.; and Mullin, T.: Anamalous modes in the Taylor Experiment, Proc. Roy. Soc. London, Vol. A377, 1981, pp. 221-249.

[21] Erlebacher, G.; and Hussaini, M. Y.: Incipient Transition Phenomena in Compressible Flows over a Flat Plate, ICASE Report 86-39, 1986.

[22] Bardina, J.; Ferziger, J. H.; and Reynolds, W. C.: Improved Turbulence Models Based on Large Eddy Simulation of Homogeneous, Incompressible, Turbulent FLows, Report TF-19, Department of Mechanical Engineering, Stanford University, Palo Alto, CA, 1983.

[23] Erlebacher, G.; Hussaini, M. Y.; Speziale, C. G.; and Zang, T. A.: Subgrid-Scale Models for Compressible Turbulence, ICASE Report, 1987.

ORR-SOMMERFELD EIGENFUNCTION
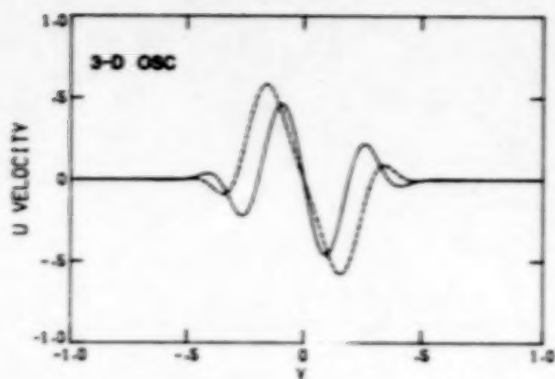
3-D OSC

U VELOCITY

Figure 1a. Center mode.

Figure 3a. Vortex lines at t = 87 for the center mode transition in channel flow at a Reynolds number of 8000.

ORR-SOMMERFELD EIGENFUNCTION

3-D TS

U VELOCITY

Figure 1b. Wall mode.

Figure 3b. Vortex lines after 3-7/8 TS periods for a (fundamental) K-type transition in a boundary layer at a Reynolds number of 1100.

10% 2-D CEN. 3.0% CEN

LOG (ENERGY)

(1,0)
(0,2)
(0,1)
(1,1)
(2,1)
(2,0)
(2,1)

TIME
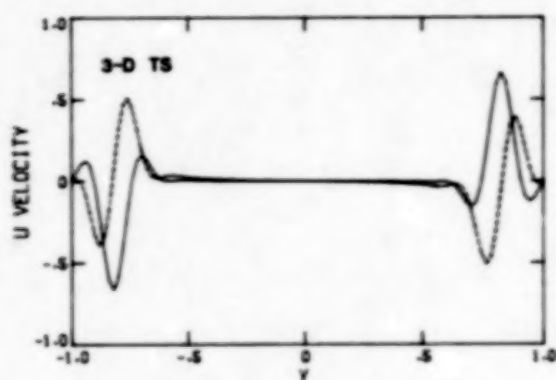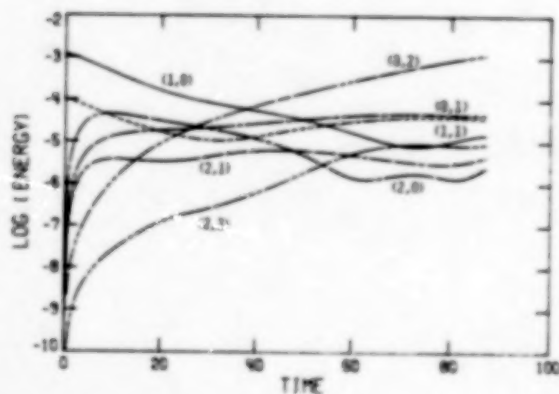
Figure 2. Harmonic history for a Re = 8000 center mode simulation.
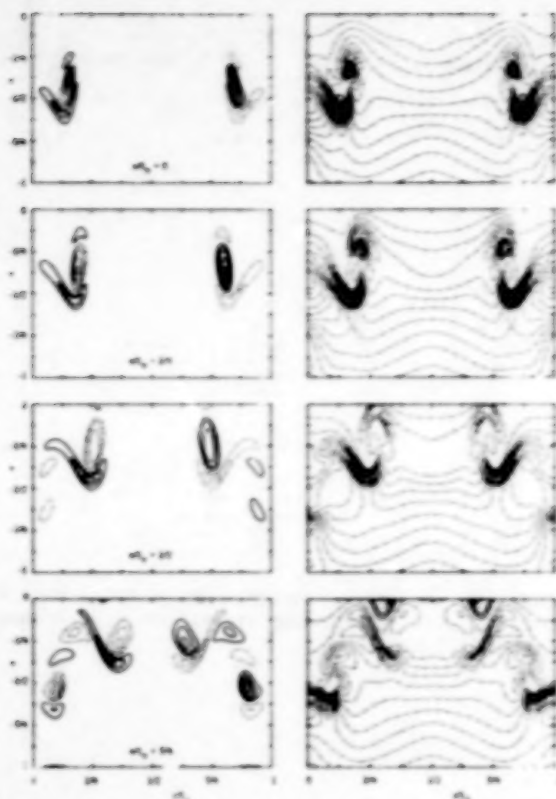
Figure 4. Streamwise (left) and spanwise (right) vorticity contours at t = 87 for a channel center mode at a Reynolds number of 8000. The contour interval is 0.20. Dashed lines indicate negative contours.
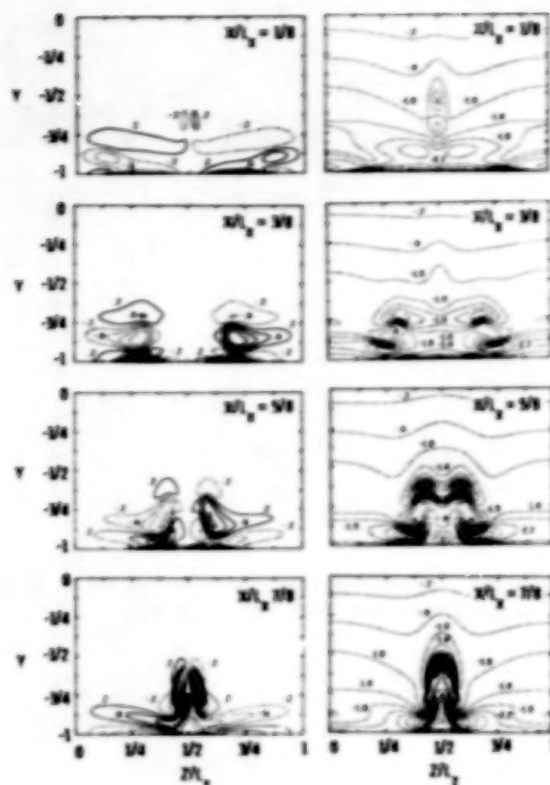
Figure 5. Streamwise (left) and spanwise (right) vorticity contours at t = 182 for a channel wall mode at a Reynolds number of 8000. The contour interval is 0.40. Dashed lines indicate negative contours.
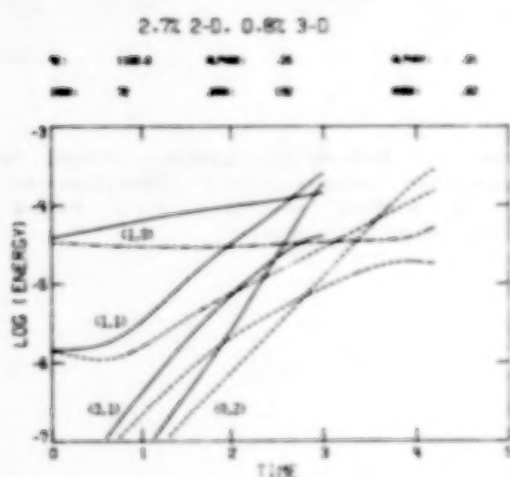
Figure 6. Harmonic energy history of an uncontrolled (solid lines) and a heated (dashed lines) boundary layer undergoing a K-type transition at a Reynolds number of 1100.
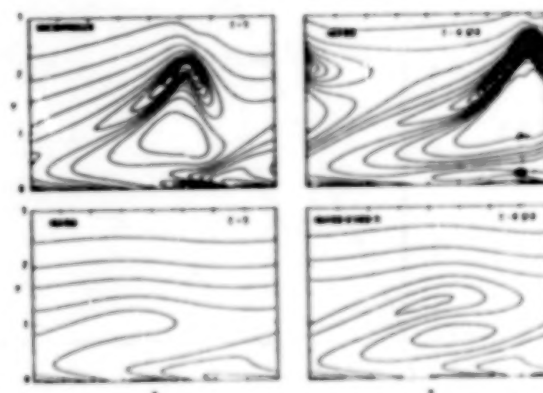
Figure 7. Vertical shear in the peak plane for Re = 1100 boundary layer simulation.
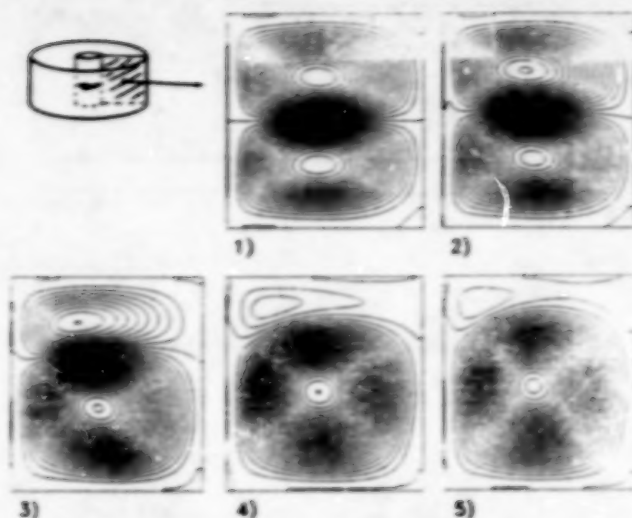
Figure 8. Cross-sectional streamline at 5 stages of two-cell/one-cell exchange process.

Harm. Cont. M=4.5 Re=10000
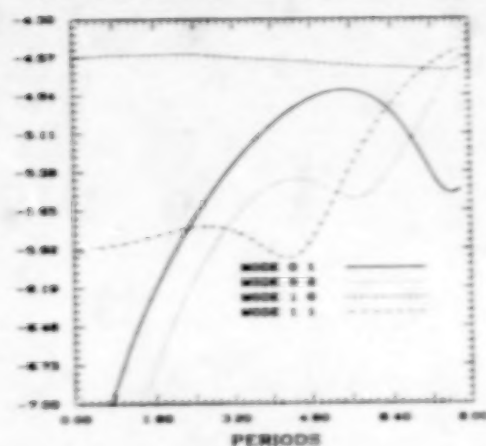
Figure 10. Harmonic energy history for a Mach 4.5 boundary layer undergoing transition at a Reynolds number of 10,000.

$\Gamma = 1.05$

$\eta = .615$

$R = 150$
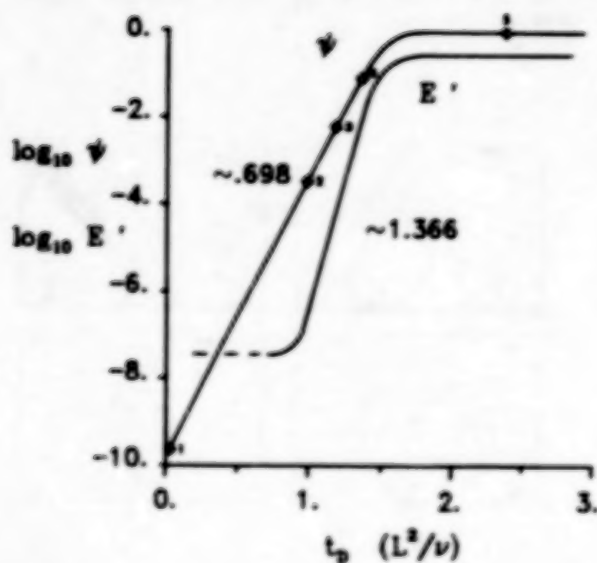
Figure 9. Time history of order parameter and perturbation energy.
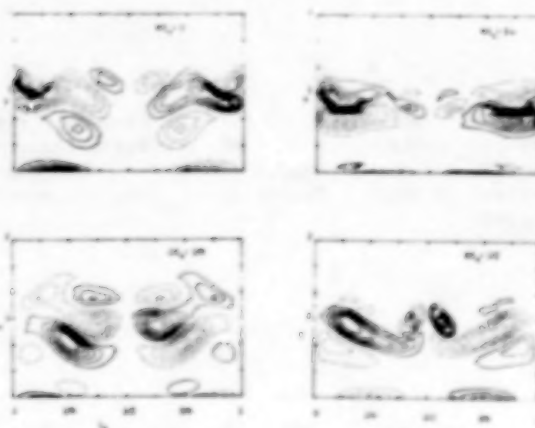
Figure 11. Streamwise vorticity contours for the compressible boundary layer transition at Mach 4.5. The contour interval is 0.20. Dashed lines indicate negative contours.

N87
26018
UNCL

TURBULENCE MODELING

Morris W. Rubesin
NASA Ames Research Center

ABSTRACT

Recent developments at several levels of statistical turbulence modeling applicable to aerodynamics are briefly surveyed. Emphasis is on examples of model improvements for transonic, two-dimensional flows. Experience with the development of these improved models is cited to suggest methods of accelerating the modeling process necessary to keep abreast of the rapid movement of computational fluid dynamics into the computation of complex three-dimensional flows.

NOMENCLATURE

$C_{\epsilon 1}$ = modeling coefficient in production of dissipation rate

$C_{\epsilon 2}$ = modeling coefficient in destruction term of dissipation rate

C_ν = modeling coefficient in eddy viscosity formulation

D_k = diffusion of kinetic energy

D_{ij} = diffusion of Reynolds stress, $\overline{u_i' u_j'}$

k = mean kinetic energy of turbulence

K = von Karman constant, 0.4

L = characteristic length scale

P_k = production of kinetic energy

P_{ij} = production of Reynolds stress, $\overline{u_i' u_j'}$

S_{ij} = strain rate, $\dfrac{1}{2}\left(\dfrac{\partial \bar{u}_i}{\partial x_j} + \dfrac{\partial \bar{u}_j}{\partial x_i}\right)$

t = time

u = velocity component in streamwise direction

U_e = velocity at boundary-layer edge

v = velocity component normal to surface

V = characteristic velocity scale

w = velocity component in transverse direction

x = coordinate in streamwise direction

$\bar{x}$ = space location vector

y = coordinate normal to surface

z = coordinate in transverse direction

β^* = modeling coefficient

δ^* = displacement thickness

δ_{ij} = Kronecker delta

ϵ = dissipation rate of kinetic energy

ϵ_{ij} = dissipation rate of Reynolds stress, $\overline{u_i' u_j'}$

ν = kinematic viscosity of fluid

ν_t = turbulent eddy viscosity

ρ = fluid density

τ_w = wall shear stress

ϕ_{ij} = pressure/rate-of-strain production of Reynolds stress, $\overline{u_i' u_j'}$

ω = specific dissipation rate, $\epsilon/\beta^* k$

Ω_{ij} = vorticity,

$$\frac{1}{2}\left(\frac{\partial \bar{u}_i}{\partial x_j} - \frac{\partial \bar{u}_j}{\partial x_i}\right), \quad \Omega = (2\Omega_{mn}\Omega_{mn})^{1/2}$$

$(\bar{\ })$ = mean or averaged quantity

$(\ )'$ = turbulent fluctuating quantity

$(\ )_i$ = vector component in ith direction, $i = 1, 2,$ or 3

$(\ )_{ij}$ = ijth tensor

INTRODUCTION

Numerical codes for the computation of fluid dynamical problems contain several distinct elements. These include the basic equation set, grid-generation and nesting techniques for complex configurations, efficient solution algorithms, and appropriate boundary condition treatments. In addition, if the fluid flow is turbulent, the effects of all the scales of the flow field that cannot be resolved by the numerical scheme either in time or space must be modeled. It is through this "turbulence modeling" that the numerically

unresolved physics of fluid motion is introduced into the flow-field computation.

The purpose of this paper, then, is to illustrate the current status of "turbulence modeling" as it is applied to aerodynamic flow fields, and to suggest some means of accelerating progress in its development. That the latter is particularly important was recognized by two National Academy of Sciences (NAS) groups that studied the rate of progress of computational fluid dynamics (CFD) in general and turbulence modeling in particular. In 1983, the committee headed by Robert Smelt concluded, "If the gap between progress in turbulence modeling and developments in numerical algorithms and computer hardware is allowed to continue, it could seriously impair the accuracy and usefulness of CFD towards the end of this century" (Smelt, 1983). This view was reflected again in a yet to be published 1986 National Research Council Report. As turbulence is a feature of almost every aerodynamically important flow field, this situation deserves the serious attention of the CFD community.

To examine why it is generally perceived that progress in turbulence modeling has been rather slow, it is important to understand what is involved in the creation or modification of a turbulence model. Basic to this understanding is the knowledge of the actual features of fluid turbulence and what the models can or cannot be expected to emulate.

What then is fluid turbulence? Turbulence is a fluid flow, not a fluid property. And it possesses many extremely complex characteristics. At a point in space, even when the gross flow is steady, the turbulent flow appears to be a chaotically, or randomly, unsteady event about some mean value. Over an extended space, however, some coherence can be observed in the large-scale turbulent motions under certain conditions. The turbulent flow is always three-dimensional, even when it exists within a mean motion that is one- or two-dimensional. This three-dimensionality is very important, for it provides the degrees of freedom to allow local vortices to stretch, and in so doing it transmits energy from larger-scale motions to those that are smaller. As a consequence, the turbulent flow possess an extremely large range of scales in time and space, and the range of scales between the largest, related to body dimension, and the smallest, where the turbulence dissipates quickly, increases with larger Reynolds numbers.

For an aircraft, the largest scales are a few percent of its length and carry most of the kinetic energy of the turbulence. The smallest scales, where the turbulence dissipates into heat, are about one thousandth of the local boundary-layer thickness, depending somewhat on the Reynolds number of the flow in question. Turbulence is also very diffusive and promotes mixing of sensible properties, such as temperature,

chemical constituents, or momentum. For example, within aircraft engines this is a favorable property which enhances the distribution of fuel prior to combustion. On a surface of an aircraft, however, this enhanced mixing contributes to increased drag. Finally, turbulence is dissipative in that the fluid viscosity can destroy the motions of the smallest scales and convert their energy into heat. It has been observed experimentally that the large scales of turbulence are unique to individual flow situations, whereas the smaller scales tend to have a universal character. The range of scales broadens with increased Reynolds number.

Up to about 15 years ago, the limitations of available computational power forced all turbulence calculations to be confined to the use of steady-state, statistical descriptions of the turbulence. Most of the features described in the previous paragraph could not be considered in detail. Turbulence models were applied only to averaged equations, and the information contained in the real dynamical features could only be restored, approximately, through the use of empirical constants that were contained in the statistical model formulations. Then, about 15 years ago, computers were developed that had sufficient power to allow the computation of the dynamic behavior of some very simple flow fields at very low Reynolds numbers where the range of scales present is relatively small. Underlying these computations is the assumption that the Navier-Stokes equations, together with the energy-transport equation, constitute the basic equations for continuum fluid flow. It is further assumed, without rigorous mathematical proof, that these three-dimensional nonlinear equations can be solved accurately in time and space and that the solutions lie within narrow bounds despite large numbers of uncertainties that exist in defining initial and time-dependent boundary conditions.

Although these computations can capture all of the features of real turbulence described earlier, they are extremely costly and have been confined to studies of the "physics" of turbulence in idealized flow situations. These studies have resulted in descriptions of the dynamic mechanisms that take place in free and wall-bounded turbulent flows in much greater detail than can be measured in physical experiments. They also provide information on quantities that can only be measured inaccurately, if at all, for example, static pressure fluctuations or local rates of turbulence dissipation. Even though these computations deal with relatively simple flow fields of limited extent, they fill the capacity of the largest computers and require many tens of hours of computer time to reach statistically meaningful results. Some of these computations have yielded results that will be of inestimable value to the turbulence modeler, but this approach cannot be considered an engineering design tool even in the reasonably near future. The reasons for this are illustrated in figure 1.

Figure 1 compares the computer speed and memory requirements for different classes of aerodynamic computational methods with the capabilities of some large existing computers and of some that are projected for the near term (Chapman, 1978). For example, application of turbulence simulation where all the significant scales of turbulence are resolved for an airfoil (A, fig. 1) would require computer capabilities about 4 orders of magnitude larger than that labeled "Large Eddy Simulation." Clearly, such calculations cannot be considered in the foreseeable future. The regions labeled Large Eddy Simulation were estimated by Chapman under the assumption that only the sublayer regions of boundary layers need to be resolved to the small scales and that the the outer parts of the boundary layers, the regions of separation, and shedding vortices could be treated inviscidly (Chapman, 1978).

Even with the major economies afforded by these assumptions, the abilities to perform time-accurate simulations of the turbulent flow fields about aerodynamic bodies lie outside the abilities of the computers projected in the immediate future. Chapman's estimates relative to the fully resolved computational needs, however, show the importance of the development of good sub-grid turbulence models to account for turbulence scales smaller than the grids employed for the bulk of the flow. In addition, if a good sub-grid model were developed for the near-wall region of the boundary layer, the computer requirements could be reduced further from those shown, and large eddy simulations of turbulent flow about an airfoil could be anticipated in the reasonably near future, not necessarily as a design technique, but at least as a research tool. The development of good sub-grid turbulence models for large-eddy simulations, then, is a research topic that should be given considerably more emphasis than it has had in the United States. The French and the Japanese have recognized this for several years, and are well ahead of us in this research topic.

Figure 1 also illustrates that projections of computer requirements for the solution of turbulent aerodynamic flow fields about aircraft shapes with the Reynolds-averaged Navier-Stokes equations are within the capabilities of near future computers. In particular, the current NAS computer is capable of handling the turbulent flow over a complete wing with the Navier-Stokes approach and use of simple algebraic models of turbulence. It is the turbulence modeling for this class of computation that is the focus of the remainder of this paper.

STATISTICAL TURBULENCE MODELING

Reynolds-Averaged Equations

Statistical turbulence modeling begins with the derivation of the equations to represent the

mean or average motions of the turbulent flow. This process can be illustrated simply by examining only the single equation representing the velocity parallel to the surface in an incompressible fluid, the instantaneous u-component equation of the Navier-Stokes system of equations:

$$
\frac{\partial u}{\partial t} + u \frac{\partial u}{\partial x} + v \frac{\partial u}{\partial y} + w \frac{\partial u}{\partial z}
$$
$$
= \frac{1}{\rho} \frac{\partial p}{\partial x} + \frac{\partial}{\partial x} \left(\nu \frac{\partial u}{\partial x} \right) + \frac{\partial}{\partial y} \left(\nu \frac{\partial u}{\partial y} \right)
$$
$$
+ \frac{\partial}{\partial z} \left(\nu \frac{\partial u}{\partial z} \right) \tag{1}
$$

For a steady-state turbulent flow, the dependent variables are then expanded as the sum of their mean parts plus their turbulent fluctuations, namely,

$$
u(\hat{x},t) = U(\hat{x}) + u'(\hat{x},t) \tag{2}
$$

where $\hat{x}$ represents a point in space and t is time. The overbar indicates an average quantity, and the prime represents the instantaneous fluctuation. The components of velocity v, normal to the surface, and w, in the transverse direction, are expanded similarly. Note that the steady-state requirement of this example eliminates time as an independent variable in the mean quantity.

When these velocities are introduced into equation (1), and the resulting equation is averaged over time, there results the following:

$$
\bar{u} \frac{\partial \bar{u}}{\partial x} + \bar{v} \frac{\partial \bar{u}}{\partial y} + \bar{w} \frac{\partial \bar{u}}{\partial z}
$$
$$
= \frac{1}{\rho} \frac{\partial \bar{p}}{\partial x} + \frac{\partial}{\partial x} \left(\nu \frac{\partial \bar{u}}{\partial x} - \overline{v'u'} \right) + \frac{\partial}{\partial y} \left(\nu \frac{\partial \bar{u}}{\partial y} - \overline{v'u'} \right)
$$
$$
+ \frac{\partial}{\partial z} \left(\nu \frac{\partial \bar{u}}{\partial z} - \overline{w'u'} \right) \tag{3}
$$

It is noted that only the nonlinear moments of the fluctuating turbulent velocity components have survived the averaging process, which has eliminated most of the real physical details of the turbulence that were described earlier. The chaotic time dependence, the phase relationships between the turbulence velocity components, and the multitude of turbulence scales are merged into just three averaged moments of the fluctuating velocity components. The resulting equation resembles the original Navier-Stokes equation, restricted to steady flow, except for the averaged moments of velocity fluctuations that reside in positions corresponding to those of the viscous stress terms and which, consequently, are called Reynolds stresses, after their original discoverer (Reynolds, 1895).

Note that these Reynolds stresses constitute three new dependent variables, whereas no new additional equations resulted from the averaging process. Thus, more unknowns are created than

equations, and the problem is not closed, at this level, unless the Reynolds stresses can be expressed in terms of the independent variables (which are the coordinates) or the dependent variables (which are the velocity components) or both. If the six equations for the Reynolds stresses are derived from moments of the Navier-Stokes equations, it is found that these new equations contain many more than six new higher-order terms, including those that contain averages of the fluctuating velocity derivatives (Chou, 1945). The proliferation of dependent variables greatly exceeds the number of new equations derived, and this process continues as more and more equations are derived. This is called the closure problem and is the central problem of statistical turbulence theory that forces the modeling of the turbulence.

Levels of Turbulence Modeling

The turbulence models required to evaluate the Reynolds stresses in equation (3) have been expressed at a variety of levels. These will be illustrated in this section, beginning with the field equations for the Reynolds stresses. By starting with the more complex models, it can be shown that some of the simpler models follow from the imposition of certain assumptions onto the more general models.

The Reynolds-stress-transport model (RSE) can be expressed as

$$\frac{D}{Dt}\left(\overline{u_i'u_j'}\right) = P_{ij} - \epsilon_{ij} + D_{ij} + \phi_{ij} \quad (4)$$

The terms on the right-hand side of the equation are divided into four quantities identified with the physical processes known to occur in a turbulent flow: P_{ij} is the production of the Reynolds stress tensor; E_{ij} is the dissipation rate of the Reynolds stress tensor; D_{ij} is the diffusion of the Reynolds stress; and ϕ_{ij} is the pressure/rate-of-strain production of the Reynolds stress tensor. Of these, only the production term P_{ij} can be expressed in terms of the Reynolds stresses, the mean velocities, and the coordinates; consequently, it does not need to be modeled. The other terms are composed of third-order moments, moments of derivatives, or pressure fluctuations, all new quantities that have to be modeled. This level of modeling is called second-order closure, that is, the closure occurs in the Reynolds stress equations instead of in the Reynolds-averaged momentum equations. The equation for ϵ, the rate of dissipation of the turbulence kinetic energy, used to define the ϵ_{ij} and the length scales, requires all of its terms to be modeled. For at least two reasons, the use of second-order closure is now limited to a few practitioners: first, the addition of seven additional field equations increases computation costs by a factor of about 5 over that of the simplest models; second, the advantages that result from the use of the stress-transport equations do not

justify these costs for most problems. Later in this paper, some examples will be presented for which the use of the Reynolds-stress-transport equations indicates some advantages that may merit application of these equations to certain problems.

A turbulence model that takes advantage of the inherent characteristics of the Reynolds-stress-transport equations, but only adds two field equations to the system, is called the Algebraic Stress Model (Rodi, 1976). Here the stress-transport equation is rewritten as

$$\frac{D}{Dt}\left(\overline{u_i'u_j'}\right) - D_{ij} = P_{ij} - \epsilon_{ij} + \phi_{ij}$$
$$= \frac{\overline{u_i'u_j'}}{k}\left(\frac{Dk}{Dt} - D_k\right) \quad (5)$$

The basic assumption of the method is represented by the term on the extreme right, where it is assumed that the convection minus the diffusion of the Reynolds stresses is proportional to the same quantities in the turbulence kinetic energy equation. The Reynolds stresses can be written algebraically as

$$\frac{\overline{u_i'u_j'}}{k} = \frac{P_{ij} - \epsilon_{ij} + \phi_{ij}}{P_k - \epsilon} \quad (6)$$

Recall that the production term also contains the Reynolds stresses, so that equation (6) has to be solved in an iterative manner. The kinetic energy and rates of dissipation are found from equations of the form

$$\frac{Dk}{Dt} = P_k - \epsilon + D_k \quad (7)$$

$$\frac{D\epsilon}{Dt} = C_{\epsilon 1}\frac{\epsilon}{k}P_k - C_{\epsilon 2}\frac{\epsilon^2}{k} + D_\epsilon \quad (8)$$

The next lower level of turbulence modeling utilizes the eddy-viscosity concept, that is, the effects of turbulence are expressed in terms of an effective kinematic viscosity acting on the fluid rate of strain. The constitutive relations between stress and strain that have been utilized are shown in the following equations from Wilcox and Rubesin (1980)

$$-\overline{u_i'u_j'} = -\frac{2}{3}\delta_{ij}k + 2v_t\left(S_{ij} - \frac{1}{3}\frac{\partial \bar{u}_\ell}{\partial x_\ell}\delta_{ij}\right)$$
$$+ \frac{8/9 k (S_{\ell m}\Omega_{mj} + S_{jm}\Omega_{m\ell})}{(\beta^* \omega^2 + 2S_{mn}S_{mn})} \quad (9)$$

and in that from Boussinesq (1877)

$$-\overline{u_i'u_j'} = -\frac{2}{3}\delta_{ij}k + 2v_t\left(S_{ij} - \frac{1}{3}\frac{\partial \bar{u}_\ell}{\partial x_\ell}\delta_{ij}\right) \quad (10)$$

Equation (9) accounts for the effects of the interaction of vorticity and the rates of strain, which allows experimentally observed anisotropies to develop in a homogeneous shear flow. Those effects are neglected in the classic form of equation (10).

The manner of evaluating the eddy viscosity distinguishes most of the currently popular turbulence models. In general, the eddy viscosity can be written as

$$\nu = C_\nu L V \qquad (11)$$

where C_ν is an empirically established coefficient or function, V is a characteristic velocity scale, and L is a characteristic length scale.

The various eddy-viscosity models are classified in Table 1; the terminology used in the table will be used in the discussion of the results to be shown later.

Table 1 Classification of eddy-viscosity models

Two-equation models:

$$V = \sqrt{k}, \quad L = L(k, \epsilon)$$

One-equation models:

$$V = \sqrt{k}, \quad L = L(y)$$

One-half-equation models:

$$\frac{\partial}{\partial x} (\tau_{max} - \tau_{max,0}) = -C_1 (\tau_{max} - \tau_{max,0})$$

Zero-equation models:

$$V = \left(\frac{\tau_w}{\rho} \right)^{1/2}, \quad L = Ky \text{ (inner zone)}$$

$$= U_e = C_2 \delta^* \text{ (outer zone)}$$

$$\text{or} \quad V = V(\Omega), \quad L = L[(y\Omega)_{max}]$$

The two-equation models utilize the kinetic energy and dissipation rates found from equation (7) and from forms of equation (8); thus, they require the solution of two additional field equations. This increases computer costs by about a factor of 3 over computations based on the zero-equation models shown at the bottom of the table. The reason for this increased cost is that the turbulence modeling equations are stiff; as a result, they require very small mesh dimensions near the surface when they are modified to allow their integration to the surface. It will be shown later that these cost penalties can be eliminated through the use of wall functions, that is, algebraic relationships that span the distance between the surface and the first mesh points

located well into the regions where the turbulence dominates the viscous forces.

Particular attention should be given to the model in Table 1 designated as a one-half-equation model. The "one-half" is used to emphasize the fact that an ordinary differential equation is added to the Reynolds-averaged Navier-Stokes system instead of another partial differential field equation. In the example shown here, the subscript 0 under the shear-stress symbol means an equilibrium value or one given by the zero-equation models indicated on the lower portion of the table. The subscript max means the maximum shear stress at some point within the boundary layer at the station, x. Thus, the one-half-equation model accounts for the lag in the development of the turbulence that occurs when the mean motion is modified by the imposition of a large streamwise pressure gradient. The dependent variable, the maximum shear stress in this case, is then used to scale the turbulence algebraically across the entire viscous region at station x.

The zero-equation models (Table 1) represent the eddy viscosity in two zones, or layers, of the viscous region. Near the surface, the velocity scale usually used is the local friction velocity, $\sqrt{\tau_w / \rho}$, and the length scale is merely proportional to the distance from the surface. In the outer zone, the velocity scale is the velocity at the edge of the viscous region and the scale depends on the displacement thickness (Cebeci and Smith, 1974). In those situations where it is difficult to define these terms, that is, where the inviscid region has a non-uniform velocity field, the velocity and length scales have been expressed in terms of the local vorticity that occurs where the moment of vorticity is a maximum (Baldwin and Lomax, 1978). Since all of these quantities are expressible algebraically in either the dependent or independent variables of the mean-flow equations, no additional partial differential equations for field variables are required and these are termed zero-equation models.

Difficulties in Applying and Developing Turbulence Models

In a particular application, the level of turbulence model that can be considered must reflect the computational power available and the solution algorithms to be used. Limited computational power permits only the simplest of turbulence models to be considered. Also, the turbulence model employed has a strong influence on the numerical behavior of the algorithms. Not all algorithms that can solve laminar flows can be applied to turbulence models, especially those that use field equations for turbulence quantities such as the Reynolds stresses, kinetic energy, or dissipation rate. Iteration processes are influenced considerably by the stiffness of the turbulence field equations. Also, algorithms that require conservative forms have difficulty with

the source and sink terms that are inherent in the
turbulence field equations to reflect the turbu-
lence production and dissipation that occur within
the real turbulent flow. Finally, the turbulence
models also impose constraints on the usable mesh
configurations by requiring very close spacings
between meshes in the vicinity of surfaces.

This strong influence of the turbulence model
on the numerical scheme has made it difficult to
assess the quality of particular turbulence
models, because often a significant part of the
disagreement between computed results and experi-
mental data is numerical, resulting from a pre-
viously verified algorithm's difficulty with the
constraints introduced by a new turbulence model.
Once these numerical difficulties are overcome and
the turbulence models can be applied with confi-
dence, the resulting disagreement with experi-
mental data for a particular flow field can be
ascribed to the limitations of a the particular
turbulence model being employed. At this point,
provided fundamental experimental turbulence data
are available to guide its improvement, it is
possible to remodel the turbulence model to
improve its performance for the complex flow in
question, and to do so in a manner that does not
alter its behavior for simpler flow fields for
which it had already proved successful. Some
examples of this process are shown in the follow-
ing section where the state of the art of statis-
tical turbulence modeling is summarized with a few
selected flow conditions.

APPLICATION OF VARIOUS LEVELS OF TURBULENCE
MODELING

In this section, in order to provide a brief
overview of the state of the art of turbulence
modeling, various levels of turbulence modeling
will be applied to a variety of flow fields of
interest to aerodynamics. Both original models
and the consequence of "remodeling" will be shown
in several examples. Care has been taken in most
of these calculations to eliminate numerical
uncertainties, so that any differences shown
between the computed results and experimental data
can be ascribed to turbulence-model deficiencies.

The first flow to be considered deals with
the effect of large streamwise pressure variations
on the skin friction of an attached turbulent
boundary layer (Kussoy et al., 1978). In
figure 2, a sketch is shown of the experimental
arrangement. The boundary layer being measured
was formed on the inside surface of a tube down-
stream from a supersonic nozzle creating an axi-
symmetric flow at $M = 2.3$. The pressure distri-
bution impressed upon the boundary layer was
created by a center body that compressed and then
expanded the flow. The resulting pressure
distribution, normalized by the upstream wall
pressure where $M = 2.3$, is shown in the upper
left corner of this figure. In this example, the

pressure rise almost doubles its original value
before relaxing. This nondimensional pressure
distribution remained essentially fixed as the
wind-tunnel pressure was altered to obtain a large
range of Reynolds numbers. The skin friction was
measured with a buried wire gauge (Rubesin et al.,
1975). The skin-friction distribution was
achieved with a fixed skin-friction gauge by
moving the centerbody upstream and downstream
about 20 cm along its axis. This provides about
the same distribution of skin friction that would
be achieved with a fixed centerbody and a moving
skin-friction gauge, because the boundary layer
ahead of the pressure rise was close to uniform
thickness.

Measured and calculated skin-friction distri-
butions are shown in figure 2 for four values of
Reynolds number. Five levels of turbulence model-
ing are shown: a zero-equation model by Cebeci
and Smith (1974) in its original form and as sub-
sequently "remodeled" to account better for
streamwise pressure gradients (Cebeci and Smith,
1974); a two-equation model by Wilcox and Rubesin
(1980); and two stress-transport models. One of
the stress-transport models utilizes a length
scale that is prescribed algebraically (Sullivan,
1976), whereas the other uses a field equation for
specific dissipation to create a length scale
(Wilcox and Rubesin, 1980).

With the exception of the original zero-
equation model at the lowest Reynolds number,
which tends to separate prematurely, all the
models show similar variations relative to the
experimental data. The computed results drift
through the data with increases in the Reynolds
number. Computed results that are low at the
lower Reynolds numbers tend to be high when the
Reynolds numbers are high. No one model is
clearly superior to the others over the entire
Reynolds-number range, though they do seem to
maintain their relative positions to each other.
One can conclude from this work that for an
attached boundary layer there is little advantage
to using the more complex models, but if it were
necessary to know the skin friction in attached
boundary layers in strong streamwise pressure
gradients to a few percent, improvements to all
the levels of models would be required.

Streamwise curvature of a surface has a pro-
nounced effect on the behavior of a boundary layer
flowing over it (Bradshaw, 1973). This is demon-
strated in figure 3, where skin friction and
shape-factor data obtained on a convex surface in
an adverse pressure are shown (So and Mellor,
1972). The data are expressed in terms of the
streamwise distribution of the skin-friction coef-
ficient and the shape factor of the turbulent
boundary layer flow. Also shown in the figure are
the computed results utilizing four turbulence
models (Wilcox and Rubesin, 1980). The dashed and
dot-dashed curves are based on a two-equation and
a Reynolds-stress transport model in which the
effects of curvature have been neglected. These

skin-friction coefficient curves depart considerably from the experimental data. The shape factor on a flat plate would remain at a value of about 1.4, again showing curvature effects that are large in affecting the boundary-layer velocity profiles. The solid and dotted curves represent the same models modified to account for the surface curvature through the introduction of a curved coordinate system. The modification to the two-equation model also required the introduction of a new centrifugal force term in the turbulent kinetic energy equation; that term vanishes on a flat surface. This was done in a rather ad hoc manner, utilizing some guidance from the the the form of the Reynolds-stress equation for $\overline{v'v'}$. On the other hand, no physical modifications were made in the Reynolds-stress model. In both of these models, the specific rate-of-dissipation equation used to define the length scale was not altered except for the coordinate modifications. Figure 3 shows that the effects of the streamwise curvature in these data are represented very well by these latter computations.

It is very significant that no modifications had to be made to the Reynolds-stress turbulence model to allow it to capture the effects of streamwise curvature; it is thereby an example in which, at least in principle, the more complex form of modeling has a fundamental advantage. Another conclusion, however, is that the simpler two-equation model can also be "remodeled" to give good results on a convex surface, without altering its behavior, for cases in which the streamwise curvature is absent. A cautionary note is in order here: concave surfaces may not be calculated well with any of these models because the models completely ignore the possibility of the existence of Gortler vortices that are present over such surfaces and that can enhance the transport within the boundary layer.

Figure 4 shows the experimental data and computed results for the distribution of surface pressure and skin friction in the vicinity of a normal shock wave in an $M = 1.48$ airstream. These measurements were obtained on the inner surface of a circular tube with a static pressure tap and a flush hot-wire skin friction gage (Mateer et al., 1976). The shock-wave position could be moved relative to the fixed gauges by increasing or decreasing the blockage of a downstream shock generator.

The experimental data are compared with computations utilizing four different turbulence models: 1) two-equation models from Wilcox and Rubesin (1980), Jones and Launder (1972), and Chien (1982); and 2) a zero-equation model from Cebeci and Smith (1974), which did not incorporate the pressure-gradient modification discussed in connection with figure 2. All of these models were used in computations that extended to the surface. It should be noted that each of the models performs quite well on a flat plate at uniform pressure. The models of Jones and Launder

and of Chien are very similar, except that the latter was more closely fitted to experimental channel data.

When these models are applied to the shock-wave and boundary-layer interaction of this experiment, it is found that all of them yield excellent surface-pressure distributions. The skin-friction results, however, are far from satisfactory for all but the Wilcox-Rubesin model. The Chien model, which behaves so well on a flat plate, yields surprisingly poor results in the vicinity of the shock wave. The Jones-Launder and Cebeci-Smith models fail to agree, in opposite ways, with the skin friction, the latter model indicating an extensive region of separation where none existed experimentally.

Qualitatively, this behavior is consistent with the behavior of the Cebeci-Smith model in figure 2, when it was not altered to account for pressure gradients. From a comparison of the different skin-friction results based on the different two-equation models, it can be concluded that models at the same level that are "calibrated" with flat-plate data can behave much differently when applied to a complex flow. This suggests that in general, the predictability of any turbulence model should be suspect until it is verified for a variety of complex flows.

In an effort to determine why the Jones and Launder and the Chien turbulence models predicted such different skin-friction results, Viegas and Rubesin (1983) eliminated the near-surface modeling in these turbulence models by applying the concept of wall functions to the computations shown in figure 4. This concept requires the first mesh point off the surface to lie well within the fully turbulent flow and therefore connect the flow at this point to the surface conditions with algebraic formulas. For example, a wall function in its simplest form is the conventional "law of the wall" applied to a zero-equation turbulence model on a flat plate with small streamwise pressure gradients. The two-equation models require more complex wall functions that account for the growth of turbulence kinetic energy in regions of strong pressure gradients, the mean values of kinetic energy and dissipation rates within the first mesh volume off the surface, and the changes to the law of the wall caused by local pressure gradients.

Figure 5 shows the results of applying such wall functions to the test conditions described in figure 4. Again, the surface pressure is well predicted when the different models use wall functions at distances from the wall shown by the corresponding upstream values of $y+$ indicated in the figure. The skin friction results show clearly that it is the individual near-wall treatments of the two-equation models by Jones and Launder and by Chien that causes their anomalous behavior shown in figure 4.

With wall functions, the results given by the two models are essentially identical and quite consistent with the other two-equation model by Wilcox and Rubesin. The Cebeci-Smith model with its wall function is quite consistent with the earlier results where it was computed to the surface, except in the immediate region of the separation zone where the pressure gradients are sufficiently high to bring into question the use of a usual law of the wall. It is gratifying that the wall functions not only collapse the results of the different two-equation models, but that results agree quite well with the experimental skin-friction data. Another significant bonus of the use of wall functions is that the costs of the computations were reduced by a factor of 8 because of the reduced number of mesh points needed to resolve the near-wall region and the elimination of much of the stiffness of the turbulence modeling equations. In this case, accuracy and economy were achieved together.

Figure 6 shows the results of improvements to two different levels of turbulence models applied to the computation of a shock-wave and boundary-layer interaction in transonic flow. The experimental data used in this comparison are from Johnson et al. (1982) and they were measured on an axisymmetric circular-arc bump indicated schematically in figure 6. The free-stream Mach number of the examples shown here is $M = 0.876$ and the unit Reynolds number is 13.1×10^6/m.

The upper part of figure 6 shows the distributions of surface pressure measured in the experiment and computed from four turbulent models. The abscissa begins at mid-chord of the bump and continues about a half-chord downstream after its trailing edge. The lower part of the figure shows the distribution of skin friction from two of the computations and the experimental points of separation and attachment, as they were indicated by an oil-film technique. This demonstrates that there was a rather extensive region of separated flow in this experiment.

The computed surface pressures based on the zero-equation turbulence model of Cebeci and Smith (1974) are represented by the dashed line. These results indicate that this model predicts a shock-wave position that is well downstream of its measured location. The computations also show much higher pressure in the region of separation than do the data. The dotted line represents the computed results obtained with the half-equation model of Johnson and King (1985). The latter model accounts for the history of the development of maximum shear stress in the streamwise direction through the use of an ordinary differential equation. This maximum shear stress is then used to scale an algebraic model, similar to that of Cebeci and Smith, at each station. Although these experimental data, for a range of Mach and Reynolds numbers, were used to evaluate the lag constants used in this model, the resulting agreement of the computed results with the shape of the

entire pressure distribution for this particular case is remarkable. Without altering the modeling coefficients, good results have been obtained by Johnson and King in comparisons with other two-dimensional data under widely different flow conditions (Simpson et al., 1981). In addition, this model is economical to use, for it requires very little more computer time than do the standard zero-equation models.

When a two-equation model is applied to this flow, the dot-dashed line (fig. 6) results for the predicted pressure distribution. Although it performs better than the zero-equation model, the pressure distribution calculated with the two-equation model also shows a shock-wave location that is downstream of the experimental position, and the pressure is overpredicted to some extent in the region of separation. When improved wall functions (Viegas et al., 1985; Rubesin and Viegas, 1985) are applied to this Jones-Launder model, the calculated pressure distribution is considerably improved, giving results equivalent to the Johnson-King model except at the upstream foot of the shock wave. It should be noted that the forms of the wall functions or the original model were not altered to fit these particular pressure data. The use of wall functions with the Jones-Launder model also improves the prediction of the location of separation and reattachment as is seen in the skin-friction coefficient figure.

In conclusion, figure 6 shows that two turbulence models are available that can give good surface-pressure distribution results in a transonic flow over an airfoil-like body. For two-dimensional flows with a closed separation region, the model of choice is the Johnson-King model for accuracy and economy of application. It is not clear at present, however, how or if this model can be extended to three-dimensional flows. The two-equation model is directly extendable to three dimensions; however, it requires some additional modeling regarding the degree of isotropy of the eddy viscosity, and the wall-function approach in its present form is constrained to no skewing of the mean-velocity vector within the first mesh volume off the surface.

Figure 7 shows the results of applying several levels of turbulence modeling (Coakley, 1986) to the prediction of the lift and drag of an RAE 2822 airfoil for three test Mach numbers and angles of attack (Cook et al., 1979). The computations are shown here in lift-drag form to allow comparison of the results relative to a constant lift-drag ratio as shown by the lines passing through the three starred data points. Coakley (1986) used six different turbulence models: two zero-equation models, that of Cebeci and Smith and of Baldwin and Lomax; the Johnson-King half-equation model; and three versions of the two-equation model, Chien's and two originated by Coakley. The symbols used for the results found from these models are indicated on the figure.

The comparison of the experimental data and the computed results can be observed from two points of view. First, a small vector distance between the experimental and computed points reflects good agreement between the experimental data and computation for both 1) surface-pressure distributions and shock-wave locations, and 2) skin-friction distributions. Second, the alignment with the constant L/D line suggests that a particular model can yield a result that happens to provide good L/D, although in reality it misses the details.

The cases represented by the three Mach numbers correspond, with increasing Mach number, to unseparated subcritical flow, unseparated supercritical flow, and separated supercritical flow, respectively. Except for two cases at $M = 0.73$, the computed results yield values of lift and drag that are higher than the measurements. At all three Mach numbers, the Johnson-King model lies closest to the data, even at the severest flow with separation. The other models generally become poorer as the flow becomes more complex. The $q-\omega2$ model of Coakley, while second-best overall in agreeing with the experimental results, yields a much poorer lift-drag slope than do the other models when separation takes place.

The earlier conclusion that the Johnson-King model is the model of choice for two-dimensional transonic flows is further supported by these data. For those interested only in the ratio of lift to drag, the simplest models of Cebeci-Smith and Baldwin-Lomax are reasonably adequate. These conclusions, however, are subject to the caveat that these data resulted from flows that were entirely attached or flows that separated and then reattached on the airfoil. Cases with massive separation may favor other turbulence models.

The next few figures will show the performance of various turbulence models for three-dimensional flows. Although the first two examples are strictly two-dimensional from a mathematical viewpoint, that is, axisymmetric flow or flow over an infinitely long, swept-back airfoil, the flows exhibit the skewing of the velocity vector parallel to the surface that is characteristic of three-dimensional boundary-layer flows.

Figure 8 describes skin-friction results obtained on the surface of a circular cylinder whose axis was mounted colinear with that of a low-speed wind tunnel (Higuchi and Rubesin, 1981; Driver and Hebbar, 1985). The particular feature of this experiment was that the cylinder was segmented so that a central portion of the cylinder could be rotated to introduce a shear-driven cross flow (see sketch in fig. 8). In the stationary region ahead of the rotating segment, the boundary layer develops the four Reynolds stresses, $\overline{u'u'}$, $\overline{v'v'}$, $\overline{w'w'}$, and $\overline{u'v'}$, which are characteristic of two-dimensional flow. Over the spinning portion, the additional Reynolds stresses,

$\overline{u'w'}$ and $\overline{v'w'}$, are activated, and it is the latter stress that causes the mean-velocity vector to skew in a three-dimensional boundary layer. In the experiment, the relaxation of the Reynolds stresses back to their two-dimensional character is studied on the downstream stationary cylinder.

Figure 8 shows the development of the axial and cross-flow skin friction with distance along the stationary downstream cylinder. The experimental data were measured with a variety of techniques: buried hot-wire gauges, surface fences (Higuchi, 1983), and momentum integral balances. Computed results based on three levels of turbulence modeling are also shown. These include the zero-equation Aquilar (1976) model which is an extension to three dimensions of the Cebeci-Smith model, and the two-equation and Reynolds-stress-transport models of Wilcox and Rubesin. Note that both the zero-equation and the two-equation models utilize the additional assumption that the eddy viscosity is a scalar quantity that acts equally on the axial and cross-flow strains. Generally, all the models capture the behavior of the relaxation of the skin friction in both directions. Of the three models, however, the Reynolds-stress-transport model yields the best agreement with the data, except for the short region at the beginning of the stationary cylinder where the relaxation process is occurring very rapidly. Since this flow remains attached, it is believed the shortcomings of the zero-equation and two-equation models, both of which are eddy-viscosity models, are caused by the the scalar eddy-viscosity assumptions and not by problems of length scale.

Figure 9 shows oil-film streaks on the surface of flow over a transonic wing, swept back at an angle of $32°$ in an airstream at $M = 0.74$ and $Rec = 4.7 \times 10^6$ (Mateer and Brosh, 1983). The airfoil shape is a NACA 0012 at zero angle of attack. The wing spans the wind tunnel, but the experiment is unique in that the side walls of the wind tunnel were contoured to follow the expected inviscid flow, thereby causing the model to behave as one of infinite length where surface pressures are essentially uniform in the spanwise direction. Also shown on the figure are the surface streamlines as computed by three levels of models. Line 1 refers to a Reynolds-stress-transport model; line 2 to a two-equation model; and lines 3 and 4 refer to a mixing-length model. These models are identical to those shown in the previous figure for the spinning cylinder experiment.

Two results for the mixing-length model are shown to demonstrate the influence of the location of transition, which can be specified in this turbulence model. In the other models the location of transition is established by stability criteria built into the models. The mixing-length model shows an increased deviation from the oil-flow data as transition is moved downstream. As with the spinning cylinder, the Reynolds-stress-transport model gives slightly better results as

represented by the oil-flow pattern near the suction peak.

Figure 10 also shows a comparison of experimental and computed surface skin-friction lines for a three-dimensional flow (Horstman et al., 1985). In this case, the test body consists of a cylinder followed by skewed flare. The airstream conditions are $M = 3$ and the length Reynolds number of the boundary layer just upstream of the flare is 18×10^6. The flare is a 60° total-angle cone tilted to an angle of attack of 23°. The computations for this flow were based on the Jones-Launder two-equation turbulence model with boundary conditions supplied by wall functions (Viegas and Rubesin, 1983). The use of wall functions was critical to reduce the cost of these computations.

The oil-flow lines on the left of this figure show that for these conditions the shock wave generated by the flare is sufficiently strong to cause the boundary layer on the cylinder to separate well upstream of the cylinder-flare junction and to reattach about halfway up the flare. Considerable amounts of turning of the near-surface flow takes place within this separation zone and in the immediate region after reattachment. The computed surface shear lines show the general character of measured oil streaks; however, the details are off to quite an extent. The computed upstream separation location is only about one-half its experimental distance from the flare junction. The poor behavior of the computations is also reflected in a generally smaller upstream movement in the computed results in the vicinity of the flare. Although the reattachment region is predicted fairly well, the flow direction on the cylinder downstream of the flare also departs from the experimental data.

How these differences are felt quantitatively is shown in a comparison of the computations with the experimentally measured surface pressures in figure 11, where the surface pressures on the windward ray are plotted along the cylinder, flare, and afterbody. The smaller predicted separation zone is again evident in this figure. These quantitative results of the computations show the position of the maximum pressure to be a bit upstream of the measured location and to yield a smaller value than measured. These results suggest that the computed side force and pressure drag are low. Recently, Brown et al. (1987) made measurements of mean flow and the Reynolds stresses under these same flow conditions. These data have not yet been analyzed with the view of improving the turbulence modeling; however, this activity is under way and should lead to a remodeling of the turbulence model that will result in computations that are considerably improved over those shown here.

CONCLUDING REMARKS

Certain observations can be drawn from this brief survey of recent developments in statistical turbulence modeling applicable to aerodynamics. For attached boundary layers upstream of pressure gradients, all levels of turbulence modeling give about the same results. This is not surprising because the attached flat-plate boundary layer has been used universally to "calibrate" these models. Under severe pressure gradients, however, many popular models still yield results that differ from experimental skin-friction data by as much as 40% when the Reynolds numbers are about 100×10^6 or larger. This is a turbulence modeling topic that requires additional attention.

The manner of modeling streamwise curvature effects is also still an open question. The simplest zero-equation models use an ad hoc correction method recommended by Bradshaw (1973). On a convex surface, the two-equation models account for curvature by either increasing the rate of production of dissipation (Ha and Lakshminarayana, 1980), by diminishing the rate of destruction of dissipation (Launder et al., 1977), or by letting the dissipation rate alone and altering the rate of production of kinetic energy by introducing the work of centrifugal forces (Wilcox and Rubesin, 1980; Pulliam et al. 1985). The full Reynolds-transport model, on the other hand, requires no changes other than the introduction of curved coordinates (Wilcox and Rubesin, 1980). This variety of approaches for the introduction of the effects of surface curvature into the zero- and two-equation turbulence models illustrates the fact that these models are merely such gross approximations to the physical turbulence that there is no unique way of modeling a particular phenomenon. Consequently, a model can only be gauged by its success or failure in its application to a particular flow field or to a range of flow fields. There is no a priori way of assessing the accuracy and breadth of application of turbulence models other than by comparison with experimental data. From such comparisons, it is generally observed that the higher levels of turbulence models tend to have broader ranges of application, but that for a given application they are likely to be less accurate than simpler models that have been fitted to the particular application. The simple, or low-level, models, though computationally economical, need a data base for every class of flow likely to be encountered, and their use places an enormous burden on the numbers of experiments required. Without such a data base, the simple models are not much sounder than intelligent guesses. It is this burden on experiment that stimulates the search for more general models that are sufficiently accurate for a variety of applications even though they may cost more to compute. The user must gauge these trade-offs in deciding which model he will employ.

With respect to the rate of progress in turbulence modeling, the development of the Johnson-King model is a good example. From the time of the first experiment on airfoils in which Johnson was measuring turbulence quantities (Johnson and Bachalo, 1980) to the recent successful tests of the model he and a colleague developed (Johnson and King, 1985), 6 years elapsed. Much of this time was spent by Johnson in analyzing his data with a variety of borrowed computer codes, some of which were in development and were extremely difficult and time-consuming to operate. During this period, he also performed an additional experiment on the axisymmetric bump model that was used to complement the original airfoil data. This short history demonstrates that turbulence modeling is composed of a variety of activities that encompass analysis of the modeling equations, experimentation, the use of and modification of complex computer codes, and, most important, a dedication to do the necessary labor to improve an existing model.

When one or two individuals attempt this, the level of effort required is bound to take considerable elapsed time. Something as relatively direct as developing wall functions for compressible flows, utilizing the experimental work of others and making small modifications to existing computer codes (Viegas and Rubesin, 1983; Viegas et al., 1985), took a little longer than 2 years. Because of its dependence on a variety of disciplines, turbulence modeling is a slow process and its development can be accelerated only by an increased level of the coordinated efforts of dedicated people possessing a variety of complementary talents in analysis, experimentation, and computational-code development. This is especially required now as the CFD community begins to emphasize complex three-dimensional flow fields and requires improved turbulence models for such flows.

REFERENCES

Aquilar, F.: A Numerical Analysis of Turbulent Flow along an Abruptly Rotated Cylinder. Ph.D. Thesis, Virginia Polytechnic Institute and State University, Blacksburg, Va., 1976.

Baldwin, B. S.; and Lomax, H.: Thin-Layer Approximation and Algebraic Model for Separated Turbulent Flows. AIAA Paper 78-257, Jan. 1978.

Bradshaw, P.: Effects of Streamline Curvature on Turbulent Flow. AGARD-AG-169, 1973.

Brown, J. D.; Brown, J. L.; Kussoy, M. I.; Horstman, C. C.; and Holt, M.: Two-Component LDV Investigation of 3-Dimensional Shock/Turbulent Boundary Layer Interactions. AIAA Paper 87-0553, Reno, Nev., 1987.

Cebeci, T.; and Smith, A. M. O.: Analysis of Turbulent Boundary Layers. Academic Press, 1974.

Chapman, D. R.: Computational Aerodynamics Development and Outlook. AIAA Journal, Vol. 17, No. 12, 1978.

Chien, K. Y.: Predictions of Channel and Boundary Layer Flows with a Low-Reynolds-Number Turbulence Model. AIAA Journal Vol. 20, Jan. 1982, pp. 33-38.

Chou, P. Y.: On Velocity Correlations and the Solutions of the Equations of Turbulent Fluctuation. Quarterly of Applied Mathematics Vol. 3, 1945, pp. 38-54.

Coakley, T. J.: Impact of Turbulence Modeling on Numerical Accuracy and Efficiency of Compressible Flow Simulations. NASA TM-88333, 1986.

Cook, P. H.; McDonald, M. A.; and Firmin, M. C. P.: Aerofoil RAE 2822 Pressure Distributions, and Boundary Layer and Wake Measurements. AGARD Advisory Report No. 138, 1979.

Driver, D. M.; and Hebbar, S. K.: Experimental Study of a Three-Dimensional, Shear-Driven, Turbulent Boundary Layer Using a Three-Dimensional Laser Doppler Velocimeter. AIAA Paper 85-1610, Cincinnati, Ohio, 1985.

Ha, C.; and Lakshminarayana, B.: Prediction of Two-and Three-Dimensional Asymmetrical Turbulent Wakes, Including Curvature and Rotation Effects. AIAA Journal, Vol. 18, Oct. 1980, pp. 1196-1204.

Higuchi, H.: A Miniature Directional Surface-Fence Gage for Three-Dimensional Turbulent Boundary Layer Measurements. AIAA Paper 83-1722, Danvers, Mass., 1983.

Higuchi, H.; and Rubesin, M. W.: An Experimental and Computational Investigation of the Transport of Reynolds Stress in an Axisymmetric Swirling Boundary Layer. AIAA Paper 81-0416, St. Louis, Mo., 1981.

Horstman, C. C.; Kussoy, M. I.; and Lockman, W. K.: Computation of Three-Dimensional Shock-Wave/Turbulent Boundary-Layer Interaction Flows. Third Symposium on Numerical and Physical Aspects of Aerodynamic Flows, California State University, Long Beach, Calif., Jan. 1985.

Johnson, D. A.; and Bachalo, W. D.: Transonic Flow past a Symmetrical Airfoil--Inviscid and Turbulent Flow Properties. AIAA Journal, Vol. 18, Jan. 1980, pp. 16-24.

Johnson, D. A.; Horstman, C. C.; and Bachalo, W. D.: Comparison between Experiment and Prediction for a Transonic Turbulent Separated Flow. AIAA Journal, Vol. 20, June 1982, pp. 737-744.

Johnson, D. A.; and King, L. S.: A Mathematically Simple Turbulence Closure Model for Attached and Separated Turbulent Boundary Layers. AIAA Journal, Vol. 23, Nov. 1985, pp. 1684-1692.

Jones, W. P.; and Launder, B. E.: The Prediction of Laminarization with a Two-Equation Model of Turbulence. International Developments in Heat Transfer, Vol. 15, 1972, pp. 303-314.

Kussoy, M. I.; Horstman, C. C.; and Acharya, M.: An Experimental Documentation of Pressure Gradient and Reynolds Number Effects on Compressible Turbulent Boundary Layers. NASA TM-78488, 1978.

Launder, B. E.; Priddin, C. H.; and Sharma, B. I.: The Calculation of Turbulent Boundary Layers on Spinning and Curved Surfaces. ASME Journal, Vol. 5, July 1967, pp. 1231-1237.

Mateer, G. G.; and Brosh, A.: Contouring Tunnel Walls to Achieve Free-Air Flow over a Transonic Swept Wing. AIAA Paper 83-1725, Danvers, Mass., 1983.

Mateer, G. G.; Brosh, A.; and Viegas, J. R.: A Normal Shock-Wave Turbulent Boundary Layer Interaction at Transonic Speeds. AIAA Paper 76-161, 1976.

Pulliam, T. H.; Jesperson, D. C.; and Barth, T. J.: Navier-Stokes Computations for Circulation Controlled Airfoils. AIAA Paper 85-1587, Cincinatti, Ohio, 1985.

Reynolds, O.: On the Dynamical Theory of Incompressible Viscous Fluids and the Determination of the Criterion. Philosophical Transactions of the Royal Society of London, Series A, Mathematical and Physical Sciences, Vol. 186, No. 123, 1895.

Rodi, W.: A New Algebraic Relation for Calculating the Reynolds Stresses. ZAMM, Vol. 56, 1976, pp. 219-221.

Rubesin, M. W.; Okuno, A. F.; Mateer, G. G.; and Brosh, A.: Flush-Mounted Hot-Wire Gage for Skin Friction and Separation Detection Measurements. Sixth International Congress on Instrumentation in Aerospace Simulation Facilities, Ottawa, Canada, Sept. 1975.

Rubesin, M. W.; and Viegas, J. R.: A Critical Examination of the Use of Wall Functions as Boundary Conditions in Aerodynamic Calculations. Third Symposium on Numerical and Physical Aspects of Aerodynamic Flows, California State University, Long Beach, Calif., Jan. 1985.

Smelt, R.: The Influence of Computational Fluid Dynamics on Experimental Aerospace Facilities, A Fifteen Year Projection. National Academy Press, Washington, D. C., 1983.

Simpson, R. L.; Chew, Y.-T.; and Shivaprasad, B. G.: The Structure of a Separating Turbulent Boundary Layer. Part. 1. Mean Flow and Reynolds Stresses. Journal of Fluid Mechanics, Vol. 113, 1981, pp. 23-51.

So, R. M. C.; and Mellor, G. L.: An Experimental Investigation of Turbulent Boundary Layers along Curved Surfaces. NASA CR-1940, 1972.

Sullivan, R. D.: GYC: A Program to Compute the Turbulent Boundary Layer on a Rotating Cone. Aeronautical Research Associates of Princeton, Working Paper No. 76-2, Aug. 1976.

Viegas, J. R.; and Rubesin, M. W.: Wall-Function Boundary Conditions in the Solution of the Navier-Stokes Equations for Complex Compressible Flows. AIAA Paper 83-1694, Danvers, Mass., 1983.

Viegas, J. R.; Rubesin, M. W.; and Horstman, C. C.: On the Use of Wall Functions as Boundary Conditions for Two-Dimensional Separated Compressible Flows. AIAA Paper 85-0180, Reno, Nev. 1985.

Wilcox, D. C.; and Rubesin, M. W.: Progress in Turbulence Modeling for Complex Flow Fields Including Effects of Compressibility. NASA TP-1517, 1980.
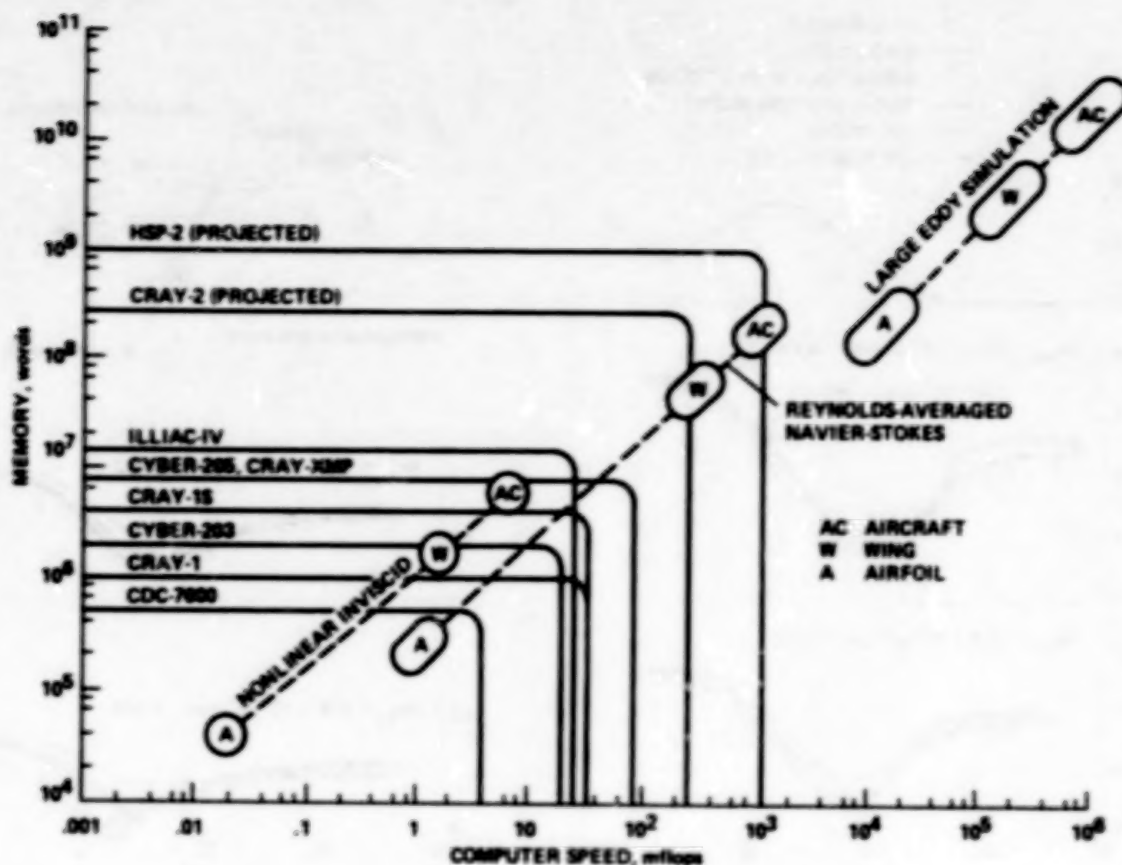
Fig. 1 Computer speeds and memory requirements
for various classes of turbulence computations-
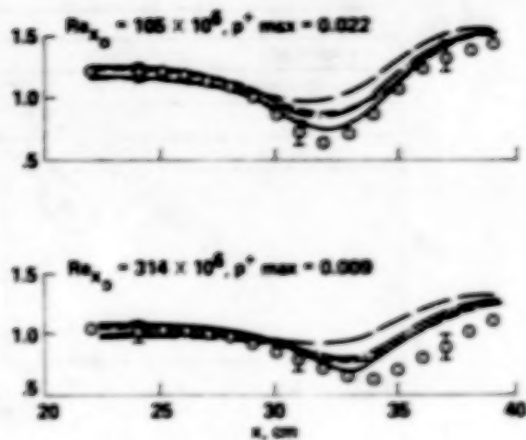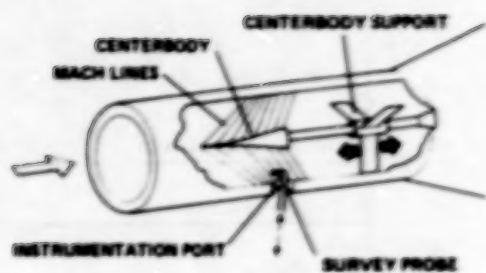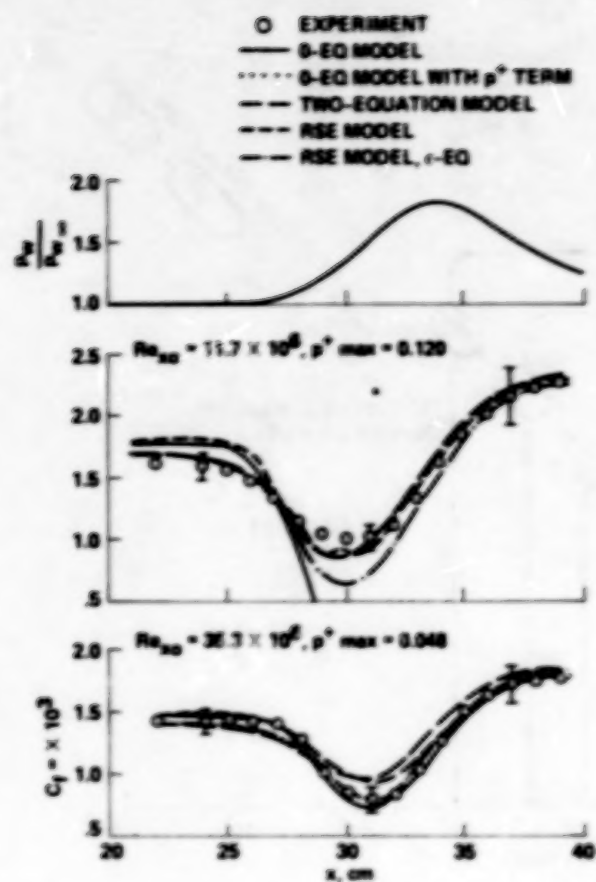based on 15 min runs with 1985 algorithms.

Fig. 2 Compressible boundary layer skin friction
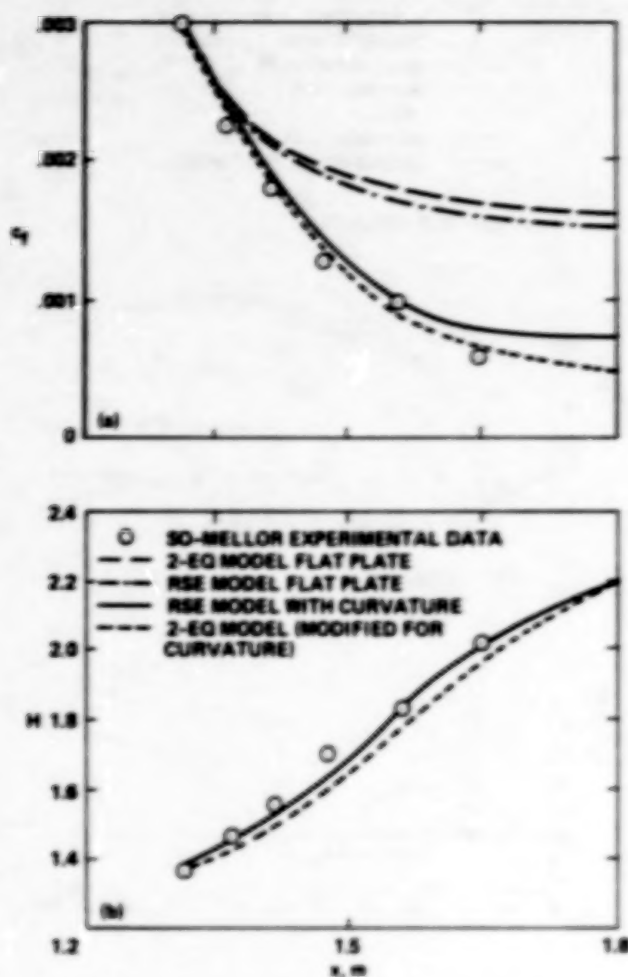in an axial pressure gradient.

Fig. 3 Boundary layer development on a convex surface in a low speed flow with an axial pressure gradient. (a) Skin friction; (b) shape factor.
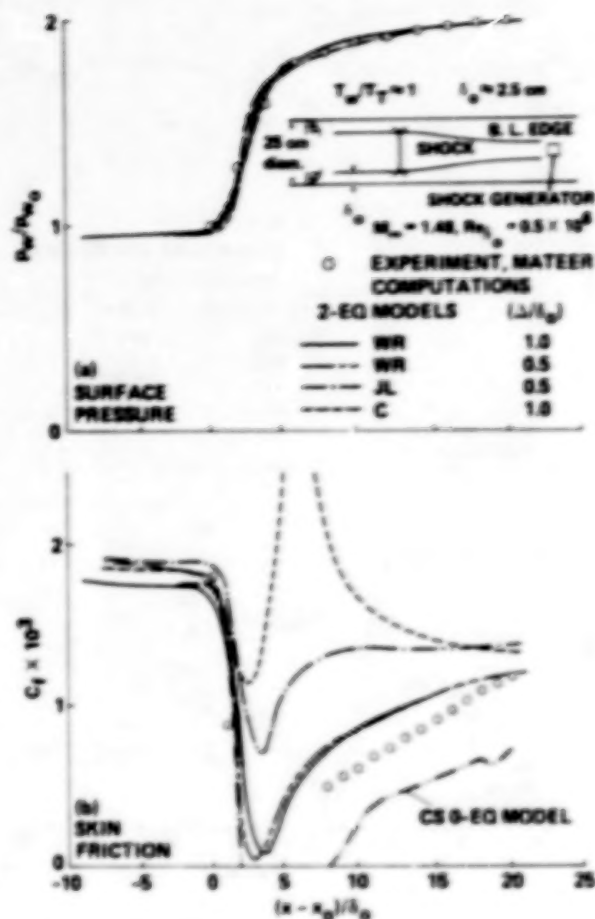

Fig. 4 Distribution of surface properties in the vicinity of normal shock wave-computations with integration to the wall.
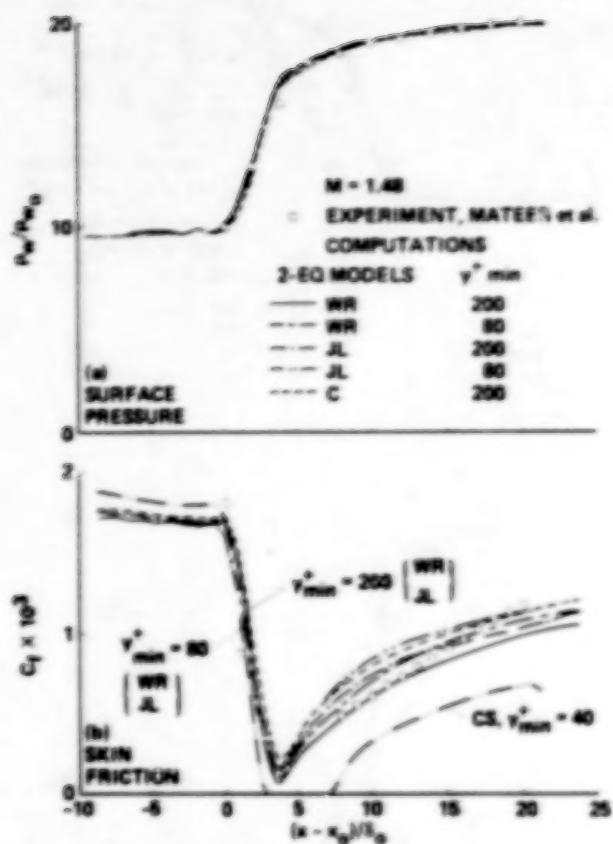
Fig. 5 Distribution of surface properties in the vicinity of normal shock wave-computations with wall functions.
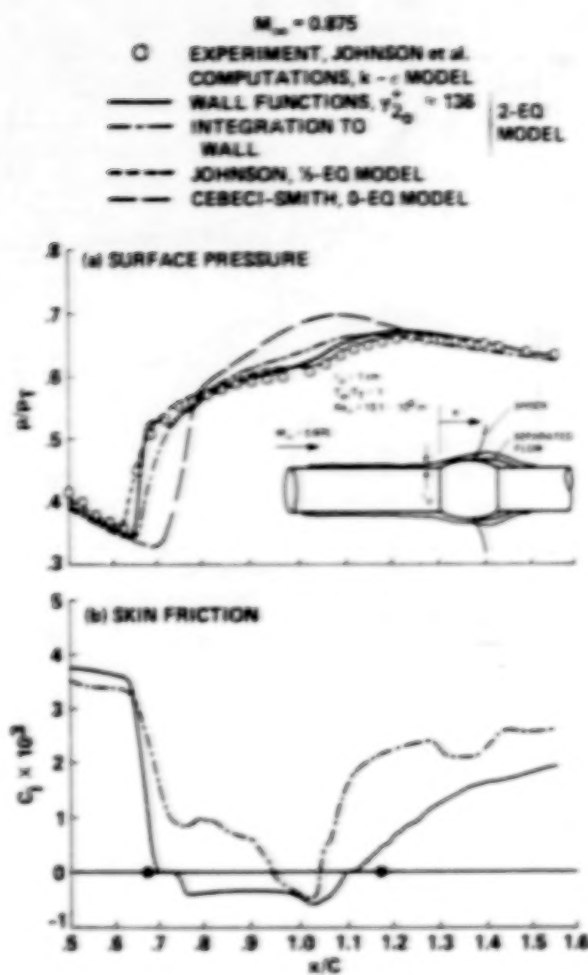
Fig. 6 Distribution of surface properties on an axisymmetric bump in transonic flow.
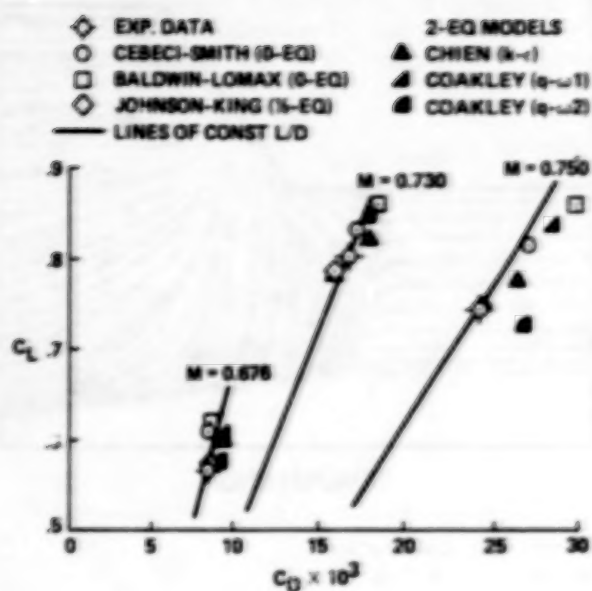
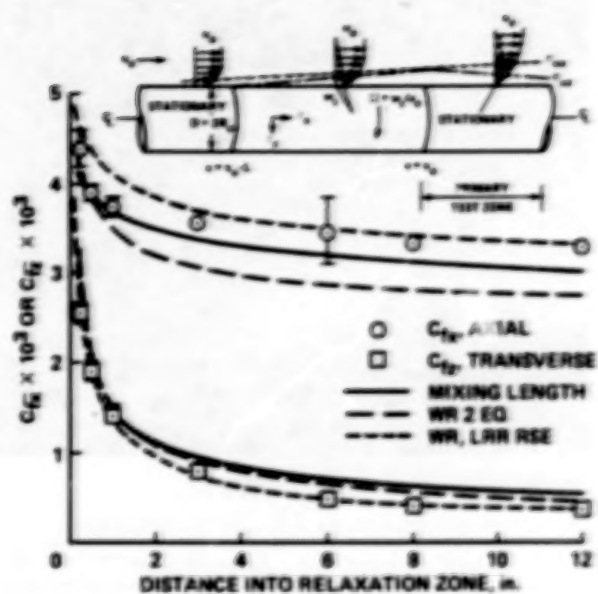Fig. 7 Lift-drag relationships for an RAE 2822 airfoil.

Fig. 8 Skin friction in the relaxation zone downstream of transversely sheared boundary layer.

Fig. 9 Comparison of experimental and computed surface flow lines on a swept, infinitely long wing-NASA 0012 at zero angle of attack.

EXPERIMENT   COMPUTATION

Fig. 10 Comparison of experiment and computation
for a three-dimensional shock wave, turbulent
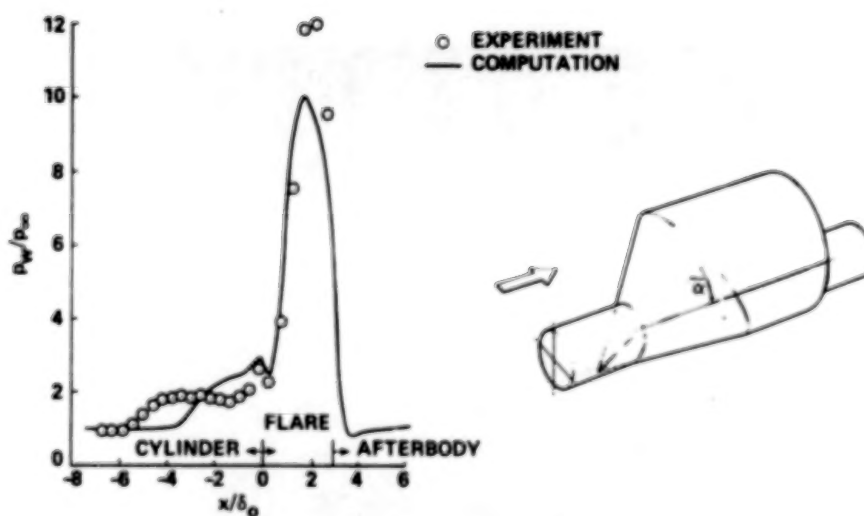boundary layer interaction.

Fig. 11 Surface pressure distribution on the
upwind ray of a skewed flare.

COMPUTATIONAL ANALYSIS OF HYPERSONIC AIRBREATHING AIRCRAFT FLOW FIELDS

Douglas L. Dwoyer* and Ajay Kumar**
NASA Langley Research Center
Hampton, Virginia

Abstract

The general problem of calculating the flow fields associated with hypersonic airbreathing aircrafts is presented. Unique aspects of hypersonic airplane aerodynamics are introduced and their demands on CFD are outlined. Example calculations associated with inlet/forebody integration and hypersonic nozzle design are presented to illustrate the nature of the problems considered.

Introduction

Over the past several years, there has been a substantial increased interest in airbreathing propulsion systems for hypersonic airplanes. A hypersonic airplane powered by airbreathing engines can gain a performance advantage over a rocket powered vehicle by using the atmosphere as the oxidizer. In order to maintain this advantage, however, these airbreathing engines with their associated large capture areas must be closely integrated with the airframe aerodynamics in order to avoid excessive drag penalties. This requirement has led the Langley Research Center to pursue the development of the airframe integrated modular scramjet engine concept as shown in Figure 1. In this concept, the forebody is designed to provide the initial inlet compression through its bow shock, and the flared afterbody acts as a part of the nozzle. Cut-back cowls, spill windows, or spill doors must be provided on the inlets to allow startup over a wide Mach number range. Struts or centerbodies in the inlets may be necessary to provide additional compression and location for fuel injection.

Through the 1970's and early 1980's, research in hypersonic airbreathing propulsion focused on the development of the individual scramjet module. Since this research occured during the time period of rapid maturation of computational fluid dynamics (CFD), it was natural to develop CFD techniques for analyzing scramjet components. An excellent paper describing the development of CFD techniques for analyzing scramjet

---

*Head, Computational Methods Branch, High-Speed Aerodynamics Division.

**Senior Research Scientist, Computational Methods Branch, High-Speed Aerodynamics Division.

component flows is presented by White, et al.[1] According to Reference 1, inlet analysis techniques have reached a relatively high level of maturity, while techniques for combustor and nozzle analysis are somewhat less mature. For all of these components, however, Navier-Stokes (NS) and Parabolized Navier-Stokes (PNS) codes exist which account for all of the relevant physics. Further, as shown in Reference 1, the ability of the PNS and NS codes to account for three-dimensional viscous effects is crucial to the accurate prediction of component flows.

The same advancements in CFD technology that led to the scramjet engine component codes have also led to great improvements in the ability to predict hypersonic external aerodynamic flows. Throughout the 1970 interest in hypersonic, external aerodynamic predictions focused on reentry bodies and the shuttle orbiter. Sophisticated codes based on the viscous shock layer (VSL) approximation, as well as PNS and NS codes were developed for predicting hypersonic reentry body flows which included real gas, radiation, ablation, and wall catalysis effects. Codes such as the COLTS code[2] have been extensively validated and are widely used today for reentry bodies.

In dealing with complex, complete configurations such as the shuttle orbiter, a different strategy evolved for flow-field prediction. In this case, inviscid analysis codes based on solving the Euler equations were coupled with approximate three-dimensional viscous techniques to provide the required solution. The STEIN code,[3] a shock fit, space marching Euler code, was specifically developed for this purpose. STEIN was later followed by HALIS,[4] a time-dependent Euler code. In recent years, a complete vehicle viscous analysis capability for hypersonic aircraft has evolved around PNS and NS codes. The PNS/UNS approach[5] involves the use of both a PNS code and an unsteady Navier-Stokes (UNS) code to provide complete vehicle solutions about the shuttle orbiter. In Reference 6, an unsteady Navier-Stokes code has been used to provide the complete flow-field solution about the X-24C lifting body.

The flow-field analysis problem described above only deals with a part of the engineering problem of hypersonic aerodynamics. The analysis codes provide the engineer with flow-field data which

can be used to derive aerodynamic performance information for given configurations. Another, and perhaps more important, problem is the development of the configurations themselves with some attempt at optimization subject to constraints. The use of analysis codes for the optimal design of hypersonic configuration components is a largely unexplored subject. A major exception is, of course, in the design of wind-tunnel and rocket nozzles where techniques based on the method of characteristics with boundary-layer correction have been in use for many years. These techniques are restricted to either two-dimensional or axisymmetric flows. Three-dimensional designs, or designs whose contraints force the relaxation of the requirement of shockless flow, will require more sophisticated CFD tools. The recent effort to design the aerolines for new nozzles for the NASA Langley Research Center 8' High Temperature Structures Tunnel[7] is an example of the kind of design project which can be undertaken using modern CFD techniques.

In summary, the status of CFD for analyzing the flow fields associated with hypersonic airbreathing airplanes is as follows. Full viscous analysis codes exist today for hypersonic gliders. Additionally, viscous analysis codes exist for the components of the most likely engine for hypersonic airplanes, the scramjet engine. Of these components, the inlet analysis capability is the most mature with somewhat less capable codes available for nozzles and combustors. Also, an attempt has been made to incorporate such codes into a design strategy for the nozzle portion of the flow field.

The time, thus, appears ripe to consider the extension of current CFD technology to one of the most crucial problems to be dealt with in the development of the hypersonic airbreathing airplane--propulsion/airframe integration. Additionally, further development of design strategies should occur over the next several years, with a heavy focus on inlets and nozzles. In this paper, we will first discuss the CFD requirements for hypersonic airplanes as compared to reentry vehicles. We will then review the status of the key CFD technologies incorporated into the current airframe and engine component codes. This will be followed by a discussion of the design problem using the constrained nozzle design problem as an example. Finally, we will discuss those areas of CFD technology requiring further development to deal with the propulsion/airframe integration problem.

CFD for Hypersonic Airplanes Vs. Reentry Vehicles

The hypersonic airplane concept places a somewhat different set of demands on CFD than does the reentry vehicle. Table I summarizes these differences in the view of the authors. The CFD demands for the hypersonic airplane stem largely from several dominating issues:

1. The requirement to fully integrate the airframe and propulsion system to achieve high Mach number performance.

2. The requirement that the vehicle be reusable with a minimum of refurbishment between flights.

3. The requirement to optimize vehicle performance over a wide Mach number range.

It is assumed herein that in both the airplane and reentry vehicle cases the flow fields have strong viscous effects. Thus, throughout the paper, emphasis will be on viscous flow-field prediction methods.

The development of a highly integrated airframe and propulsion system at high Mach numbers requires a CFD analysis capability which can treat flow fields of geometric complexity substantially greater than that of reentry vehicles including the Shuttle Orbiter. For example, an accurate prediction of the state of the three-dimensional boundary layer developed by the forebody at the inlet face is important for predicting installed inlet performance. The forebody geometry can be relatively simple, and the reusability of the vehicle implies a nonablative surface. Thus, the forebody flow-field analysis appears relatively straightforward in that the wall boundary conditions need not account for surface deformation and surface injection as would be the case with an ablative heat shield. On the other hand, an accurate prediction of this entire shock-layer profile is crucial in addition to the prediction of wall properties such as skin friction, heat transfer, and pressure. Such calculations are necessary to predict the shape of the bow shock and all embedded shocks as well as the mass and momentum flux entering the inlets. Of course, real gas effects on the forebody flow will become important for flight Mach numbers beyond about M = 10. Further, sophisticated surface boundary conditions which include wall catalysis effects and possible thermal deformation of the walls can be important in forebody flow-field prediction.

After the inlet face, the geometric complexity of the flow-field boundaries increases dramatically. At off-design

conditions, the inlets will spill a substantial amount of air thereby setting up a complex inlet/forebody flow-field interaction which can substantially effect both the inlet and forebody flow field. This flow region can be further complicated by the presence of wings. The geometric complexity of the forebody/multiple inlet/wing interacting flow field is far greater than the most geometrically complex reentry vehicles such as the Shuttle Orbiter.

The geometrical complexity of the forebody/inlet region extends to the aft end of the hypersonic airplane. The flow here is dominated by the interaction of the multiple internal/external nozzle system flow with the vehicle wing/body flow. The nozzle flow field will include real gas effects throughout the operating envelope of the vehicle, and at off-design conditions possible flow separation on the external nozzle surface must be accounted for. Requirements for accurate prediction of the complete three-dimensional flow field are again important on the external nozzle in order to estimate the nozzle thrust coefficient and the direction of the net thrust vector. Prediction of surface properties such as skin friction, heat transfer, and pressure are also vitally important. The real gas models incorporated in the nozzle flow analysis must include the chemistry of the combustor products as well as the air chemistry.

Engine combustor flow-field calculations require prediction of many complex physical phenomena not encountered on reentry vehicles. Important physical/chemical processes in the combustor include fuel/air mixing, ignition, combustion, and shock/turbulence interactions. The chemistry models in the codes must account for fuel combustion. There are a number of locations in a typical combustor where highly detailed analysis of very localized processes is required. Such regions include the immediate flow fields in the neighborhood of fuel injectors and flameholders. Accurate and detailed prediction of such highly localized phenomena is required if CFD is to be used in the analysis and design of combustors.

A major issue in CFD, common to both reentry vehicles and hypersonic airplanes, is transition and turbulence modeling. In transition modeling there is an important difference between the airplane and reentry vehicle, however. A typical reentry vehicle enters the atmosphere from above, and the flow transits from the rarefied state to the laminar continuum state to the turbulent continuum state. The hypersonic airplane, on the other hand, enters the atmosphere from below and goes from turbulent to laminar to rarefied. Transition and turbulence

models for the hypersonic airplane must, therefore, account for this laminarization process. Important turbulence modeling issues for hypersonic airplane CFD are high Mach number mixing, shock/turbulent interaction, and three-dimensional separation. Real gas effects, very high Mach number compressibility effects, and kinetics/turbulence interaction are also important in the hypersonic airplane flow field.

The purpose of this discussion is not to argue that CFD for hypersonic airplanes is more difficult or complex than for reentry vehicles. Indeed, many crucial phenomena for the reentry vehicle such as transitional flow have been glossed over here. Rather, the thrust of this discussion is to point out that development of successful CFD analysis tools for hypersonic airplanes involves addressing a somewhat different set of problems. Given that hypersonic CFD has been primarily aimed at reentry problems for the past 25 years, it is clear that the hypersonic airplane CFD presents a variety of new research problems for the CFD community. Successful solutions of these problems will require an unprecedented level of cooperation between CFD researchers, experimentalists and theoreticians for many years to come.

Algorithms for Hypersonic Airplane CFD

The algorithms available today for computing the types of 3-D, viscous, hypersonic airplane flow fields described above can generally be categorized as: (1) parabolized Navier-Stokes (PNS) algorithms based on central-difference methods, (2) Reynolds averaged Navier-Stokes (RANS) algorithms based on central-difference methods, and (3) RANS algorithms based on upwind-difference methods. Of these three categories, PNS and RANS central-difference algorithms are the most mature and have been extended to include the most complete physical/chemical models. The upwind-difference based RANS codes are relatively new, and to date only perfect gas codes are available for the 3-D case. Thus, extensive research and code development work can be expected over the next several years to include more advanced physical and chemical models in upwind codes.

PNS Algorithms

The most widely used PNS codes today for high-speed viscous flow problems evolved from an implicit formulation first proposed by and later extended by Schiff and Steger.[8] This algorithm forms the basis of the AFWAL PNS code,[9] the NASA Ames PNS code,[5] and the PNS code of Gnoffo.[10] All of these codes rest on the assumption that there is a predominant flow direction which is roughly aligned

with one of the coordinate directions in a body fitted coordinate system. The steady RANS equations are then simplified by eliminating terms involving derivatives in the primary flow direction in the viscous stress tensor. Remaining derivatives, with respect to the primary direction, are then upwind differenced and for flows whose Mach number components in the primary direction is entirely supersonic a well posed initial value problem ensues. The flow field may then be solved as a forward marching problem in the primary direction.

In order to make the discussion more concrete, it will be assumed that the PNS equations written on the x, y, z Cartesian coordinate system have been transformed to the curvilinear ξ, η, ζ coordinates. Here ξ is taken to be the primary flow, or marching, direction. In this case, the PNS equations become

$$\frac{\partial \hat{F}}{\partial \xi} + \frac{\partial(\hat{G} - \hat{G}_v)}{\partial \eta} + \frac{\partial(\hat{H} - \hat{H}_v)}{\partial \zeta} = 0 \quad (1)$$

Here $\hat{F}$, $\hat{G}$, and $\hat{H}$ represent the inviscid part of the flux vectors and $\hat{G}_v$ and $\hat{H}_v$ represent the viscous part. Forming the discrete analog of Equation (1), the term $\partial \hat{F}/\partial \xi$ will be replaced with an upwind difference while the $\partial/\partial \eta$ and $\partial/\partial \zeta$ terms will be replaced by central differences. In forming the discrete equations, one can choose either an explicit or implicit formulation in the marching direction. Gelda and McRae[11] have recently explored an explicit formulation of Equation (1) in 2-D, and this formulation holds promise of good efficiency on vector computers, particularly those which favor long vectors such as the CY-205. All of the 3-D codes are based on an implicit formulation, however. The implicit formulation takes the form

$$\frac{\frac{3}{2}\hat{F}^{i+1} - 2\hat{F}^i + \hat{F}^{i-1}}{\Delta \xi} + \bar{\delta}_\eta (\hat{G} - \hat{G}_v) +$$
$$\bar{\delta}_\zeta (\hat{H} - \hat{H}_v)^{i+1} = 0 \quad (2)$$

The superscript i denotes the grid point index in the ξ direction. Development of the solution algorithm for Equation (2) involves two steps; the first being linearization of the nonlinear terms, and the second an approximate solution of the linearized equations on the i+1 plane by approximate factorization. The linearization proceeds in a straightforward way from a Taylor expansion as

$$\hat{F}^{i+1} = \hat{F}^i + (\frac{\partial \hat{F}}{\partial U})^i \Delta U + \ldots = \hat{F}^i + \hat{A}^i \Delta U$$

where

$$\Delta U = U^{i+1} - U^i \; ;$$

U represents the conserved variables vector. With similar linearization in the η, ζ directions, the resulting equation assumes the form

$$[\frac{3}{2} \Delta\xi^{-1} \hat{A}^i + \bar{\delta}_\eta (\hat{B}^i - \hat{B}_v^i) + \bar{\delta}_\zeta (\hat{C}^i - \hat{C}^i - \hat{C}_v^i)]\Delta U$$
$$= -[\frac{-\frac{1}{2}\hat{F}^i + \hat{F}^{i-1}}{\Delta\xi} + \bar{\delta}_\eta (\hat{G} - \hat{G}_v)^i + \bar{\delta}_\zeta (\hat{H} - \hat{H}_v)^i] \quad (3)$$

The system of Equation (3) with suitable additional artificial viscosity is then solved noniteratively on each successive i plane.

As discussed extensively by Chitsomboon, et al.[12], although Equation (3) is formally second-order accurate, the linearization of the ξ-difference term is not fully conservative. As shown in Reference 12, this lack of fully conservative differencing can lead to problems in accurate shock capturing. An example comparison between a PNS and RANS prediction of an inlet flow is shown in Figures 2 and 3. This calculation is for a 2-D scoop-type inlet. The calculations were done with the PNS code of Reference 5 and the RANS code of Reference 13. In Figure 2, the inlet geometry is shown along with plots of pressure versus axial distance through the inlet for both the scoop (top) surface and innerbody (bottom) surface. Examination of the scoop surface pressure shows a substantial difference in shock location and strength between the PNS and RANS prediction. Figure 3 shows the velocity vectors and pressure contours for the flow as predicted by the RANS calculation. The first pressure rise on the scoop is from the leading-edge shock, which reflects off the innerbody and hits the scoop at the second pressure rise. The PNS calculation predicts the formation of the leading-edge shock to be further downstream than the RANS calculation. The reflected shock intersection with the scoop is also more downstream in the PNS calculation as well as being substantially weaker. The shock reflection on the innerbody surface is also much weaker in the PNS case as well as far downstream. The RANS prediction indicates a small separation to be associated with the shock reflection from the innerbody, an effect not predicted in the PNS calculation. The scoop pressure comparison with data are far better for the RANS calculation than for the PNS calculation. The discrepancy between the calculations is attributed to the poor shock capturing of the PNS code along with too much artificial dissipation that allows it to march past the shock

reflection with no indication of
separation. The PNS shock capturing error
in this case, which is typical of a
hypersonic inlet, leads to a completely
erroneous flow-field prediction.

Central-Difference RANS Algorithms

CFD algorithms most commonly in use for
high-speed RANS calculations are the
MacCormack method[14] and the Beam and
Warming method.[15] Both methods are
designed to provide steady solutions to
the RANS equations by embedding the steady
problem in the properly posed time-
dependent problem and marching the
solution to large time with steady
boundary conditions. For the hypersonic
airplane problems, this approach has as
its principle advantage over the PNS
algorithms the ability to maintain fully
conservative differencing. Additionally,
this approach can accommodate separated
flow in the streamwise direction.

The explicit methods have a substantial
computer cost penalty associated with them
when compared to the PNS approach or the
implicit RANS approach. Unfortunately,
the implicit RANS method of Beam and
Warming suffers from stability
restrictions in the 3-D case.[16] Thus, the
explicit method is more robust than the
implicit and it has been applied to a
wider variety of problems associated with
hypersonic airplanes as shown in
References 1 and 5 and in the remainder of
this paper. Additionally, inclusion of
real gas effects is somewhat more
straightforward in the explicit case than
in the implicit case. Equilibrium gas
chemistry has been incorporated into
explicit algorithm codes by several
authors including References 2, 7, and 17
and finite-rate chemistry in References 17
and 18.

A final point to be made about both
types of central-difference RANS methods
is about their shock capturing
capability. Dissipative terms must be
appended to the basic algorithms of
References 14 and 15 to allow shock
capturing. Very sophisticated artificial
viscosity terms have been devised for this
purpose which degrade the spatial accuracy
of the methods only in the immediate
vicinity of shocks. Even with the
inclusion of these terms, the ability of
central-difference codes to capture strong
shocks is limited. Codes based on the
central-differnce approach which are aimed
at hypersonic flows generally rely on
shock fitting to capture the bow shocks.

Upwind-Difference RANS Algorithms

In the last several years, an
alternative to the central-difference
approach has appeared which alleviates
several of the difficulties mentioned with
the central-differenced based PNS and RANS

methods. This alternative has its basis
in the total variation dimishing (TVD)
methods developed by solving the Euler
equations in the early 1980's. A number
of investigators have combined these TVD
methods for the convective terms in the
RANS equations with central differencing
to the viscous terms to yield this new
class of algorithms. Methods under
current development include those of
References 19, 20, 21, and 22. This new
class of algorithms is herein refered to
as the upwind RANS algorithm.

The upwind RANS methods generally
retain the superior shock capturing
capability of the Euler method on which
they are based. The method can be
implemented in both explicit and implicit
form, with the majority of implementation
to date being implicit. In the implicit
form, the coefficient matrix associated
with the change in the dependent variable
vector is in relatively well conditioned
and hence a number of innovative new
solution strategies have evolved for the
upwind methods. In addition to the
conventional three factor ADI approach for
solving the implicit upwind RANS
equation,[23] relaxation methods have also
been introduced. The use of planar Gauss-
Seidel relaxation has been used by a
number of authors. Walters and Dwoyer[24]
have also shown that this technique can
serve as the basis for an algorithm for
combining the PNS and RANS approach.

The upwind RANS methods have not been
extended to include real gas effects to
date. There is no fundamental restriction
on such an extension, and a number of
groups are currently exploring real gas
upwind RANS methods. Until these
extensions are proven, applicability of
the upwind RANS methods to the hypersonic
airplane problem will be limited.

Algorithm Summary

The comments presented above can be
summarized in the following way. The
central-difference PNS algorithms are the
least expensive of the currently available
methods for computing hypersonic airplane
flow fields. They are useful for problems
in which the shocks radiate out of the
computational domain without interacting
with vehicle components. For situations
where the shocks can impinge on vehicle
components, or for the internal flow case,
the central-difference PNS methods are
generally unsatisfactory due to their
nonconservative property.

The central-difference RANS methods are
today the most general and useful
methods. The most popular explicit and
implicit solution algorithms have
shortcomings in computational complexity
and stability respectively which has led
to the search for alternatives.
Additionally, the central-difference

methods are limited in shock capturing capability. Despite this, as will be demonstrated later in the paper, they are currently the algorithms of choice for complex hypersonic airplane flow-field prediction.

The upwind RANS methods alleviate several of the central-difference method shortcomings. The solution algorithms appear to be more robust and they possess superior shock-capturing capability. To date, however, the applicability of the method to the hypersonic airplane problem is still in the exploratory stage.

Real Gas Effects

The high temperatures encountered in hypersonic flight can lead to vibrational excitation, dissociation, and ionization of the air. These high temperatures would occur in the blunted regions of the vehicle due to strong shocks and in the boundary layers due to extreme viscous dissipation. Further complicating factors that may need to be considered are radiative heating and deformation of the surface, and surface catalysis for chemical reactions. Additionally, in the analysis of combustor and nozzle flows, the fuel/air chemistry must be considered. These high-temperature reacting flows can have significant influence on the vehicle and propulsion system performance. Generally speaking, at moderate hypersonic Mach numbers, the reaction rates associated with the air chemistry are fast enough that the air may be considered in chemical equilibrium but at higher hypersonic Mach numbers, the effects of nonequilibrium chemistry must be considered.

Inclusion of nonequilibrium chemistry in the codes results in significant complexity and increased computational time whereas equilibrium chemistry can be added rather easily. Most advanced flow-field analysis codes still do not have nonequilibrium chemistry whereas equilibrium chemistry is being added to a significant number of codes. A brief description is given below on how the equilibrium gas chemistry can be included in the code.

In the equilibrium gas chemistry approach, the gas is assumed to be in chemical and thermodynamic equilibrium at all points in the flow field. The simplest way to include these effects is through the use of variable equivalent gamma (VEG) approach.[2,18] Gamma is determined by assuming a locally linear relationship between temperature and enthalpy at every grid point. The enthalpy, in turn, is calculated from a benchmark equilibrium code such as EQUIL.[25] The code EQUIL uses free energy minimization technique to calculate

mixture composition, its enthalpy and molecular weight and other thermodynamic and transport properties given the pressure, temperature, and elemental composition of the mixture as input. This code is very general and can be used in situations with surface mass addition, ablation, etc. For simple air chemistry only, one can use other simpler equilibrium chemistry routines. The preceding VEG approach can be included in any perfect gas code with relatively little effort.

The real gas effects start to show up for freestream Mach numbers greater than ten in atmospheric flight. Figure 4 shows typical velocity, temperature, and pressure profiles in a cone shock layer at two flight Mach conditions in air, the first at $M = 10$ and the second at $M = 24.5$. The most important effect of gas property variation is on the temperature profile, and hence also on the heat transfer.

Advanced Applications

This section presents examples of some advanced applications of CFD in analysis and design studies. In the first application, integration and interaction of multiple inlet modules are studied whereas in the second application, the use of CFD codes is demonstrated in nozzle design subject to some external constraints.

Multiple Module Inlet Integration

As mentioned in the preceding sections, one of the major requirements in the development of the hypersonic vehicle is to closely integrate the vehicle airframe and the propulsion system. In an effort to investigate this problem, an experimental as well as analytical program has been devised at NASA Langley. The goal of this program is to predict performance and interactins of multiple scramjet inlets mounted on the vehicle undersurface. Figure 5 shows the schematic of the test model. It has three modules mounted on a flat plate that simulates the forebody boundary layer. The compression sufaces of each module are swept wedges. The aft body expansion is simulated by an expansion on the plate. Experimentally, the model will be tested over a Mach number range, small angles of attack, and possibly some yaw. The experimental results will be compared against the numerical result obtained from a three-dimensional Navier-Stokes code.[26] This code solves the governing equations in conservation form by MacCormack's method. It has an algebraic eddy viscosity model for turbulent flow and is highly vectorized for VPS 32 (an upgraded CDC CYBER-200 series computer) or CRAY computers. No experimental results are

yet available, but a series of numerical calculations have been made using the expected geometry of the test model and tunnel flow conditions. Sample results from one such calculations are presented here. The flow conditions used in the calculation are as follows:

$$M_\infty = 4.03$$

$$p_\infty = 8724 \text{ N/m}^2$$

$$T_\infty = 70K$$

Each inlet module has a geometric contraction ratio of 4.0, and the cowl closure begins at the throat of the inlets. The results presented here are for zero angle of attack and yaw.

Figure 6 shows the grid in a cross plane and the symmetry plane of the configuration beginning from the face of the inlet modules. The extended portion of the grid below the cowl in the symmetry plane is for accounting the interaction between the internal and external fow. This interaction arises due to the aft placement of the cowl that exposes the high-pressure internal flow to the low-pressure external flow. The grid in the cross plane shows grid lines going through the module sidewalls. This is done to avoid elaborate grid generation procedure which will be required to embedd the module sidewalls which are not present in the extended region of the grid under the cowl. If a cross plane lies above the cowl plane, the grid points lying within the sidewalls are ignored and suitable boundary conditions are applied on the surface of the sidewalls but if the cross plane lies below the cowl plane, all the grid points are used in the analysis. The calculations presented here are made with a grid of about 340,000 points (61 points in the x-direction, 91 points in the y-direction, and 61 points in the z-direction). Only half of the configuration is analyzed due to flow symmetry at zero angle of attack and yaw. Out of the 61 grid planes in the z-direction, 25 planes lie below the cowl plane to account for the end effects.

A two-dimensional Navier-Stokes code[13] is used on the front part of the flat plate to calculate the profiles of flow quantities as the flow approaches the modules. The three-dimensional code is then used for the flow from the face of the modules to the end of the configuratio.. Figure 7 shows the velocity vector field and pressure contours in a cross plane located slightly above the cowl plate. Slight blunting of the sidewall leading and trailing edges, caused by the grid lines through the sidewalls, is obvious. Pressure contours show the shock and expansion waves and

their interactions. Since it is a cold flow with no fuel injection, the flow expands bac to low pressure behind the inlet throat. The velocity vector plot shows relatively small regions of separated flow caused by the shock/boundary-layer interactions.

Figure 8 shows the pressure contours and velocity vector field in the plane of symmetry. The velocity vector plot shows a significant downturn in flow direction ahead of the cowl resulting in some flow spillage. The downturn is caused by the sidewall sweep and the interaction between the internal and external flow. Once the inlet flow passes behind the cowl leading edge, it is turned back parallel to the cowl plane, and this turning result in a cowl shock which is evident in the pressure contour plot. Other features of flow are maked on the figure.

As mentioned earlier, not all the flow approaching the inlet modules is captured by them. Some of it is spilled out due to the swept compression surfaces and effects. Figure 9 shows axial distribution of the capture. It is seen that a significant amount of flow is spilled ahead of the cowl.

Although not included here, calcuations have also been made at small angles of attack and yaw. These results will be compared with the experimental results when available.

Multiple Inlet Interactions

One of the concerns that need to be investigated both numerically as well as experimentally is the potential for interactions between closely mounted multiple inlets. In order to examine the potential for such interactions, a two-strut scramjet inlet shown in Figure 10 is used as a model problem for a three-inlet system. As is seen, the inlet has three separate passages. The two center struts have an initial compression angle of 9°, and the initial cowl closure begins at the throat for which $x/x_T = 1$. To study the interactions, an attempt is made to unstart the center passage and see the impact of this unstart on the two side passages. In the initial attempts to unstart the center passage, the cowl location is fixed at the throat but the geometric contraction ratio of the center passage, W/G, is increased substantially by increasing the strut compression angle from 9° to 10.75°. This increase in center passage contraction ratio did not cause it to choke and resulted in no interaction with the side passages as is evident from the pressure contours in Figure 11 which remain unchanged with increase contraction ratio. However, the increased contraction ratio results in much higher pressure in the center passage as well as a increased downturn of the

flow ahead of the cowl as is seen from Figures 12 and 13. A capture plot of the inlet is shown in Figure 14. It is seen that as the center passage is gradually closed, the total inlet capture goes down, but the capture plots of individual passages show that all the decrease in capture is due to the increased spillage from the center passage. The capture of the side passages remains constant. This again confirms that there is no interaction between the center and side passages.

The second attempt to choke the center passage is made by moving the cowl forward from its initial location of $x/x_T = 1$. Two cowl locations of $x/x_T = .85$ and $.67$ are tried with strut compression angle remaining at $9°$. For both cowl locations, the center passage still did not choke but the inlet capture increased significantly as is seen from Figure 15. But for $x/x_T = .67$, when the strut compression angle is increased to $10°$, choking or unstart of the center passage is observed. Figure 16 shows the pressure contours in the symmetry plane of the inlet. The results of $9°$ strut compression angle are used as the starting solution. Pressure contours at 5,500, 10,000, 13,000, and 17,500 clearly show the development and formation of a bow shock ahead of the cowl. This bow shock stands in front of the cowl producing a region of subsonic flow between the shock and the cowl and resulting in significantly increased spillage from the center passage. The pressure contours in the cross plane located slightly above the cowl plane are shown in Figure 17. It is seen that the flow in the side passages has also been modified due to the unstart of the center passage. Obviously, once the subsonic flow ahead of the cowl is established, it interacts with the flow in the side passages and modifies it.

Nozzle Design

The analysis codes are still not widely used in the design of hypersonic configuration components. A major exception is, of course, in the design of wind tunnel and rocket nozzles where techniques based on method of characteristics with boundary-layer correction have been in use for many years. These design techniques are restricted to either two-dimensional or axisymmetric flows. Three-dimensional designs or designs whose constraints force the relaxation of the requirement of shockless flow, will require more sophisticated CFD tools. The recent effort to design the nozzle contours for the NASA Langley 8' High-Temperature Tunnel (HTT) provides an example of the use of advanced CFD codes in design projects. Under this effort, two nozzles for Mach 4 and 5 are being designed such that they smoothly blend with the existing

Mach 7 nozzle about 200 inches upstream of the test section. The specified contraints are: (1) the axial position and radius of the entrance to the subsonic region; (2) the throat axial location; and (3) the axial station where current and new nozzle walls must smoothly blend together. The Mach number variaton is required to remain below $±0.1$ about its mean value across 60% of the core flow. The high temperature flow in the tunnel requires the possibility of foreign gas injection for transpiration cooling in the nozzle throats. Furthermore, the large static temperature variation in the nozzles leads to a significant variation in gas properties, and those variations must be properly modeled.

Due to the imposed constraints, it was found that the conventional shockless nozzle design procedure was not applicable. A new iterative design procedure was developed in the present effort that couples an Euler code, a method of characteristics code, and boundary-layer code. A Navier-Stokes code is used to check the overall flow quality of the final design. All codes include consistent real gas chemistry packages for H-C-O-N gas system. In addition, the Navier-Stokes and boundary-layer codes have the capability to account for foreign gas injection for transpiration cooling. A detailed discussion of this iterative design procedure is given in Reference 7.

Figures 18 and 19 show some results obtained from the design of the Mach 5 nozzle. Figure 18 shows the Mach number profiles in the exit plane of the nozzle calculated by the Navier-Stokes and Euler codes. The profile has a mean value of 4.96 with a variation of $±0.06$ over more than 70% of the test section radius, thus satisfying the Mach number variation constraint. However, a weak shock forms near the nozzle throat and intersects the exit plane, as is clearly seen from the Mach number contours in Figure 19. It appears that the weak shock cannot be avoided under the present geometric constraints. Figures 18 and 19 also illustrate the qualitative similarities in the flow solution obtained from the iterative design procedure and the Navier-Stokes code.

The preceeding design procedure is general and can easily be modified to treat perfect gas or any other real gas mixture.

Conclusions

The purpose of this paper has been to discuss CFD technology as it relates to the computation of flow fields associated with hypersonic airbreathing airplanes. It has been shown that the unique aerodynamics of these vehicles places

different demands on CFD than reentry body aerodynamics does. The major areas requiring the use of advanced CFD techniques are the prediction of airframe aerodynamics, propulsion/airframe flow-field interaction, and internal engine flows. All of these applications require use of 3-D viscous codes, most often RANS codes. PNS codes appear to have limited applicability to the hypersonic airplane problem. Advances in algorithm robustness and speed, geometric flexibility, and inclusion of real gas effects are required in the 3-D Navier-Stokes codes if they are to be widely used in the development of hypersonic airbreathing airplanes.

References

1. White, M. E.; Drummond, J. P.; and Kumar, A.: Evolution and Status of CFD Techniques for Scramjet Applications. AIAA Paper No. 86-0160, Jan. 1986.

2. Kumar, A.; Graves, R. A., Jr.; Weilmuenster, K. J.; and Tiwari, S. N.: Laminar and Turbulent Flow Solutions with Radiation and Ablation Injection for Jovian Entry. AIAA Paper No. 80--0288, Jan. 1980.

3. Marconi, F.; and Yaeger, L.: Development of a Computer Code for Calculating the Steady Super/Hypersonic Inviscid Flow Around Real Configurations. NASA CR-2676, May 1976.

4. Weilmeunster, K. J.; and Hamilton, H. H., II: Calculation of Inviscid Flow Over Shuttle-Like Vehicles at High Angles of Attack and Comparisons With Experimental Data. NASA TP-2103, May 1983.

5. Chaussee, D. S.; Rizk, Y. M.; and Bunning, P. G.: Viscous Computations of a Space Shuttle Flow Field. NASA TM-85977, June 1984.

6. Shang, J. S.; and Scherr, S. J.: Navier-Stokes Solution of the Flow Field Around a Complete Aircraft. AIAA Paper No. 85-1509 CP, July 1985.

7. Erlebacher, G.; Kumar, A.; Anderson, E. C.; Rogers, R. C.; Dwoyer, D. L.; Salas, M. D.; and Harris, J. E.: A Computational Design Procedure for Actively Cooled Hypersonic Wind-Tunnel Nozzles Subject to Wall Shape Constraints. Proceedings of Computational Fluid Dynamics in Aerospace Design Workshop, University of Tennessee Space Institute, UTSI Pub. E02-4005-029-85, June 1985.

8. Schiff, L. B.; and Steger, J. L.: Numerical Simulation of Steady Supersonic Viscous Flow. AIAA Paper No. 79-0130, Jan. 1979.

9. Kaul, U. K.; and Chaussee, D. S.: AFWAL Parabolized Navier-Stokes Code: 1983 AFWAL/NASA Merged Baseline Version. AFWAL-TR-83-3118, May 1984.

10. Gnoffo, P. A.: Hypersonic Flows Over Biconics Using a Variable-Effective Gamma, Parabolized Navier-Stokes Code. AIAA Paper No. 83-1666, July 1983.

11. Gielda, T.; and McRae, D.: An Accurate, Stable, Explicit, Parabolized Navier-Stokes Solver for High-Speed Flows. AIAA Paper No. 86-1116, May 1986.

12. Chitsomboon, T.; Kumar, A.; and Tiwari, S. N.: A Parabolized Navier-Stokes Algorithm for Separated Supersonic Internal Flows. AIAA Paper 85-1411, July 1985.

13. Kumar, A.: Numerical Analysis of the Scramjet Inlet Flow Field by Using Two-Dimensional Navier-Stokes Equations. NASA TP-1940, Dec. 1981.

14. MacCormack, R. W.: The Effect of Viscosity in Hypervelocity Impact Cratering. AIAA Paper No. 69-354, 1969.

15. Beam, R.; and Warming, R. F.: An Implicit Factored Scheme for the Compressible Navier-Stokes Equations. AIAA Journal, vol. 16, April 1978, pp. 393-402.

16. Abarbanel, S.; Dwoyer, D. L.; and Gottlieb, D.: Stable Implicit Finite-Difference Methods for Three-Dimensional Hyperbolic Systems. ICASE Report No. 82-39, 1982.

17. Gnoffo, P. A.; and McCandless, R. S.: Three-Dimensional AOTV Flow Fields in Chemical Nonequilibrium. AIAA Paper No. 86-0230, Jan. 1986.

18. Uenishi, K.; Rogers, R. C.; and Northam, G. B.: Three-Dimensional Computations of Transverse Hydrogen Jet Combustion in a Supersonic Airstream. AIAA Paper No. 87-0089, Jan. 1987.

19. Thomas, J. L.; and Walters, R. W.: Upwind Relaxation Algorithms for the Navier-Stokes Equations. AIAA Paper No. 85-1501 CP, July 1985.

20. Gnoffo, P. A.; McCandless, R. S.; and Yee, H. C.: Enhancements to Program LAURA for Computation of 3-D Hypersonic Flow. AIAA Paper No. 87-0280, Jan. 1987.

21. Chakravarthy, S. R.; Szema, K-Y.; Goldberg, U. C.; and Gorski, J. J.: Application of a New Class of High

Accuracy TVD Schemes to the Navier-Stokes Equations. AIAA Paper No. 85-0165, Jan. 1985.

22. Lombard, C. K.; Bardina, J.; Venkatapathy, E.; Yang, J. Y.; Luh, R. C-C.; Nagaraj, N.; and Raiszadeh, F.: Accurate, Efficient, and Productive Methodology for Solving Turbulent Viscous Flows in Complex Geometry. Tenth Intl. Conf. on Numerical Methods in Fluid Dynamics, June 1986.

23. Anderson, W. K.; and Thomas, J. L.: Multigrid Acceleration of the Flux Split Euler Equations. AIAA Paper No. 86-0274, Jan. 1986.

24. Walters, R. W.; and Dwoyer, D. L.: An Efficient Iteration Strategy Based on Upwind/Relaxation Schemes for the Euler Equations. AIAA Paper No. 85-1529-CP, July 1985.

25. Kumar, A.; Graves, R. A., Jr.; and Weilmeunster, K. J.: Users Guide for Vectorized Code EQUIL for Calculating Equilibrium Chemistry on Control Data Star-100 computer. NASA TM-80193, April 1980.

26. Kumar, A.: Numerical Simulation of Scramjet Inlet Flow Fields. NASA TP-2517, May 1986.

TABLE I

REENTRY BODY VS. HYPERSONIC AIRPLANE CFD

REENTRY	HYPERSONIC AIRPLANE
Axisymmetric and 3-D	3-D
Simple Wave System	Complex Wave System
	Shock/Boundary-Layer Interactions
Wall Effects - Ablation/Injection - Catalysis - Roughness/Deformation	Wall Effects - Catalysis - Thermal Deformation - Local Injection
Gas Model - Transition/Turbulence - Air Chemistry - Radiation	Gas Model - Transition/Turbulence - Laminarization - Air & Fuel Chemistry
Simple Geometry	Complex Geometry
External	External/Internal
Projectile/Glider	Powered
	Design/Optimization
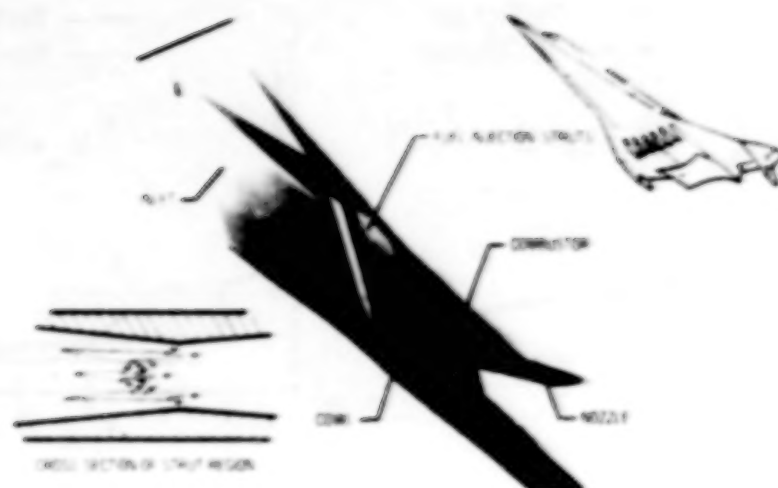
Fig. 1.- Scramjet engine module and its
cross section.
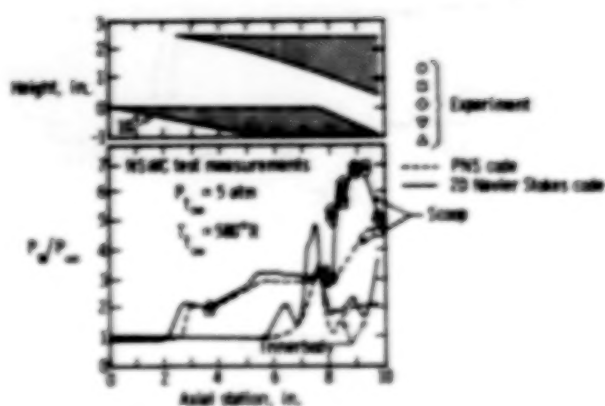
Fig. 2.- Surface pressure distribution
for the 2-D multiple inward-
turning scoop inlet model.
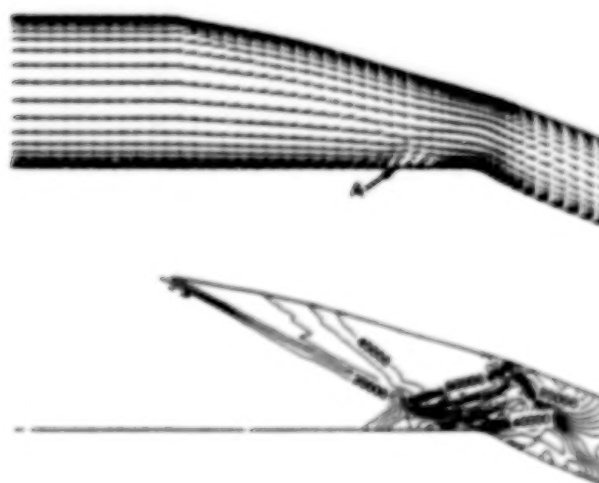
Fig. 3.- Velocity vector field and
pressure contours for the 2-D
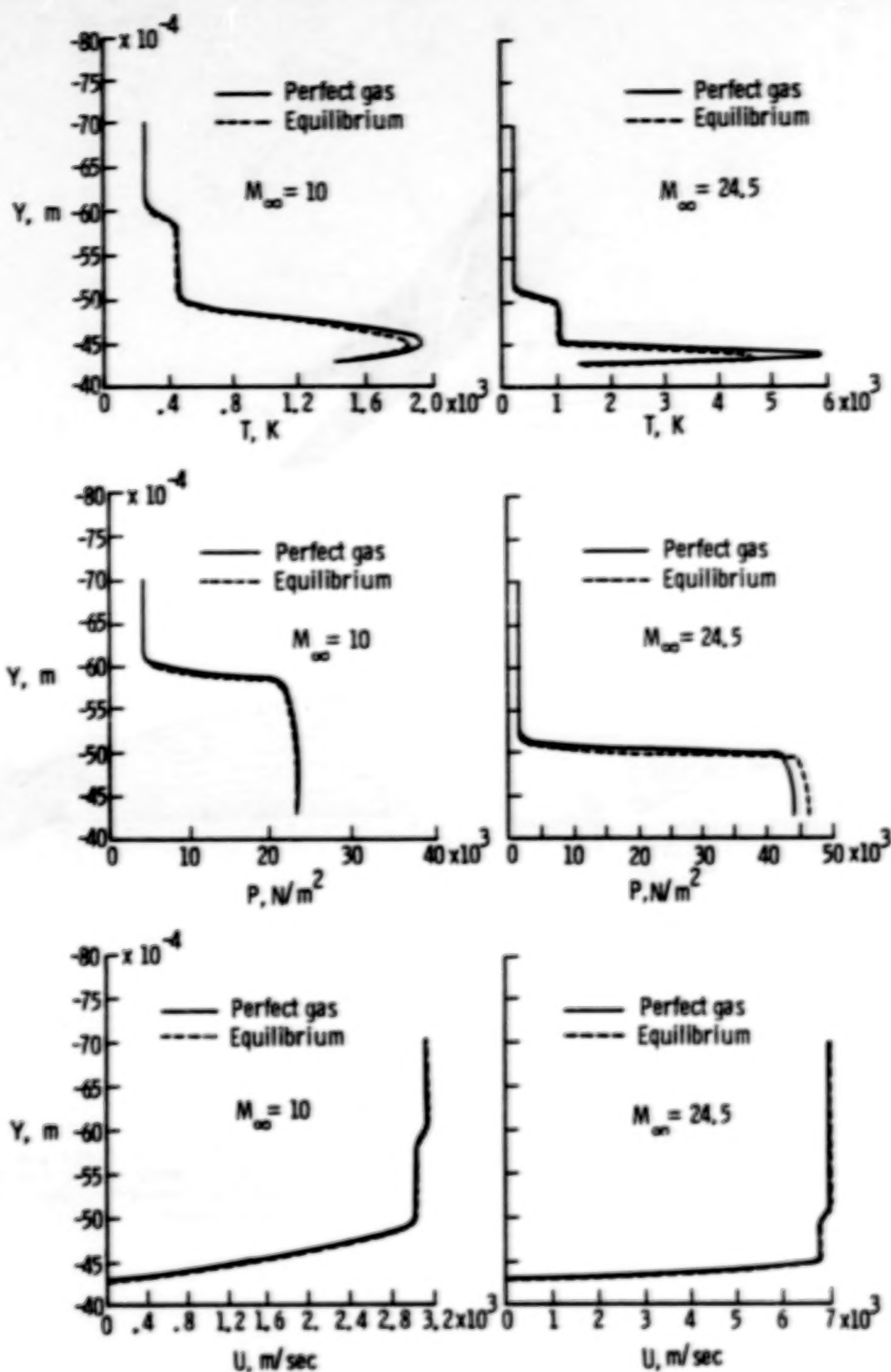multiple inward-turning scoop
inlet model.

Fig. 4.- Perfect and equilibrium gas
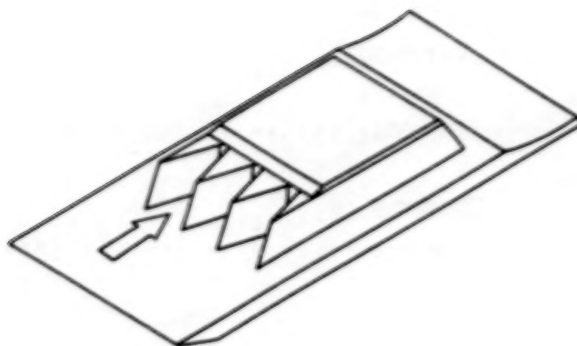shock-layer profiles over a
cone.
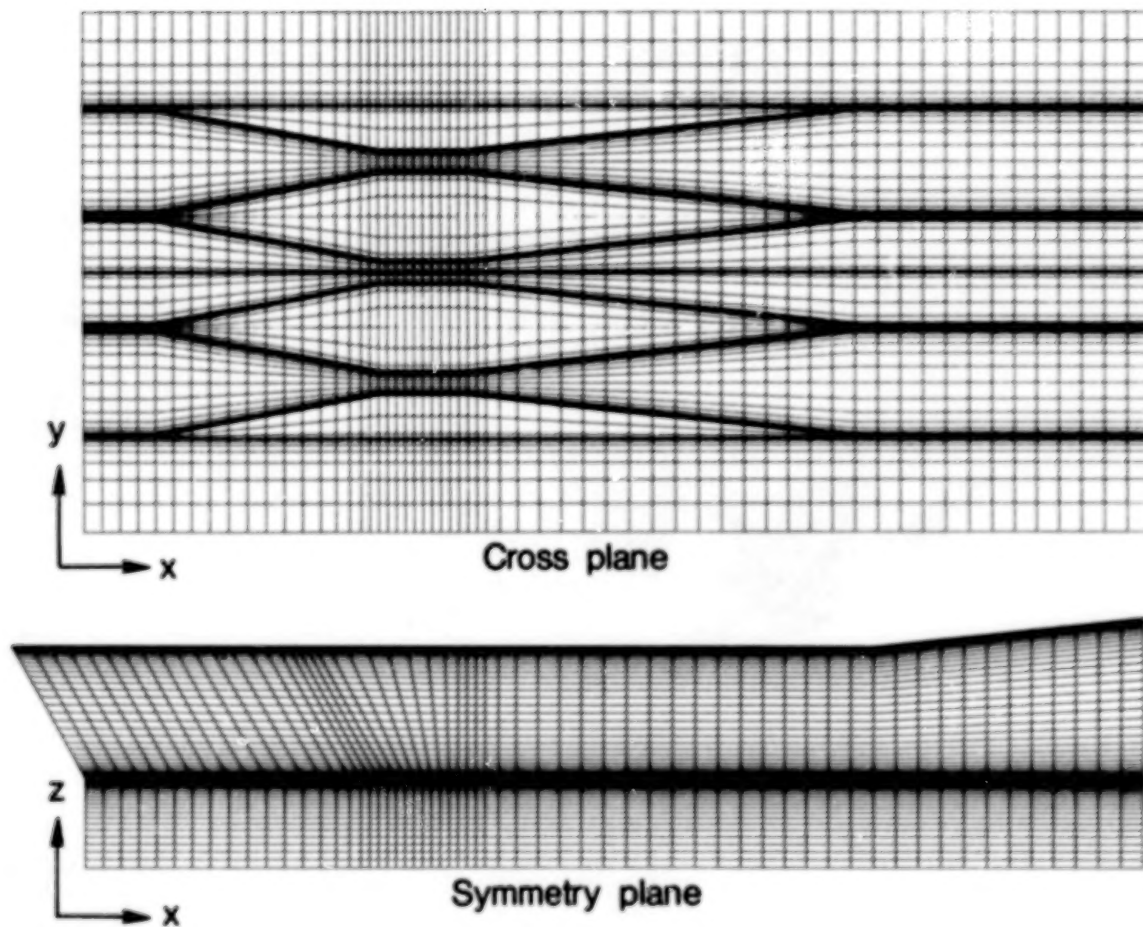
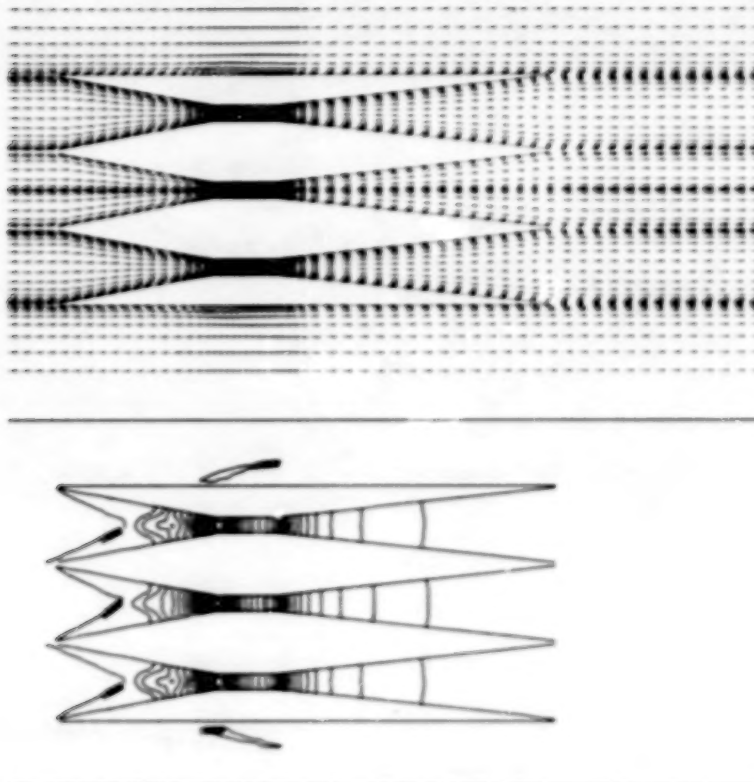Fig. 5.- Schematic of a multiple module
scramjet engine.

Cross plane

Symmetry plane

Fig. 6.- Computational grid.

Fig. 7.- Velocity vector field and pressure contours in a cross plane slightly above the cowl plane.
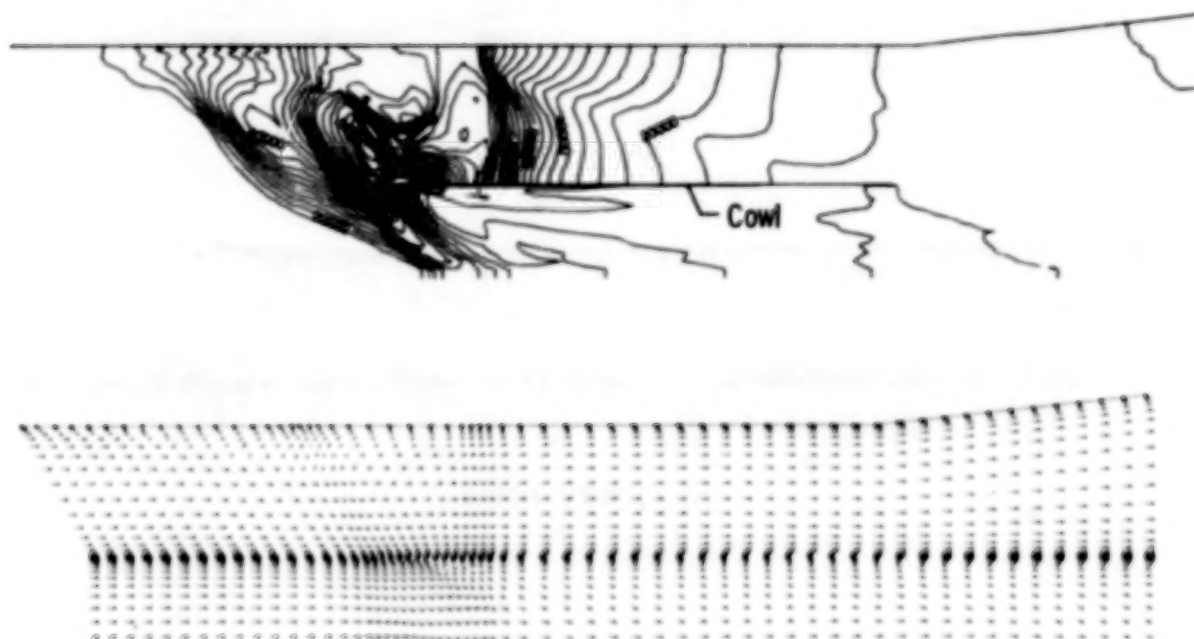
Fig. 8.- Pressure contours and velocity vector field in the symmetry plane.
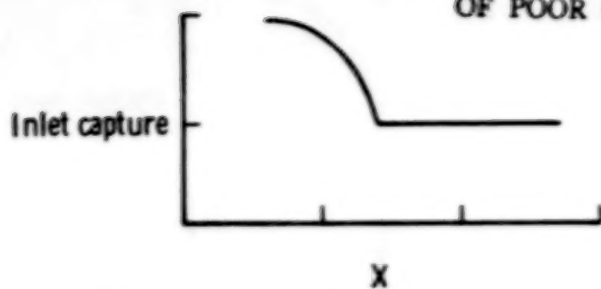
Fig. 9.- Axial capture distribution.

Fig. 10.- Two-strut scramjet inlet.
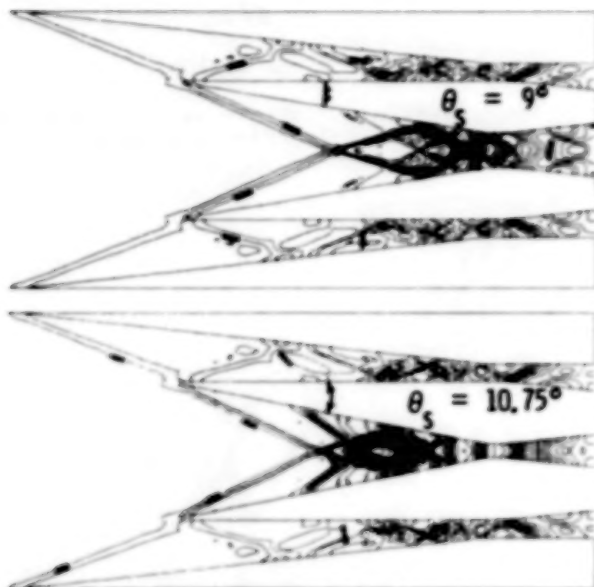
Fig. 11.- Pressure contours in a cross
plane located at 12% of the
inlet height from the cowl
plane.
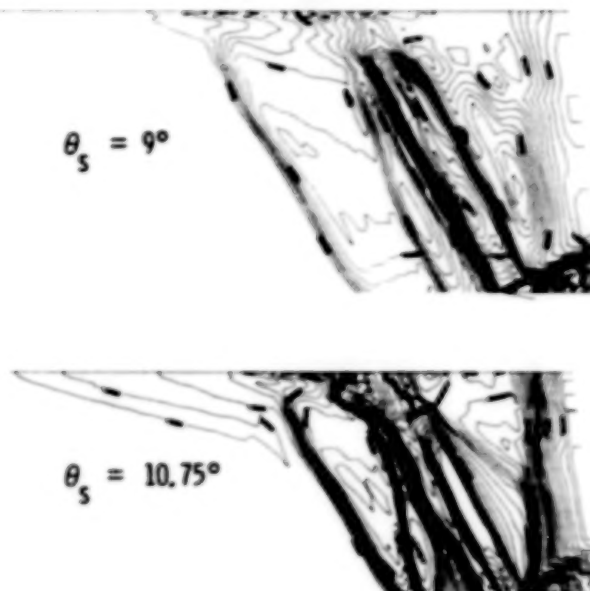
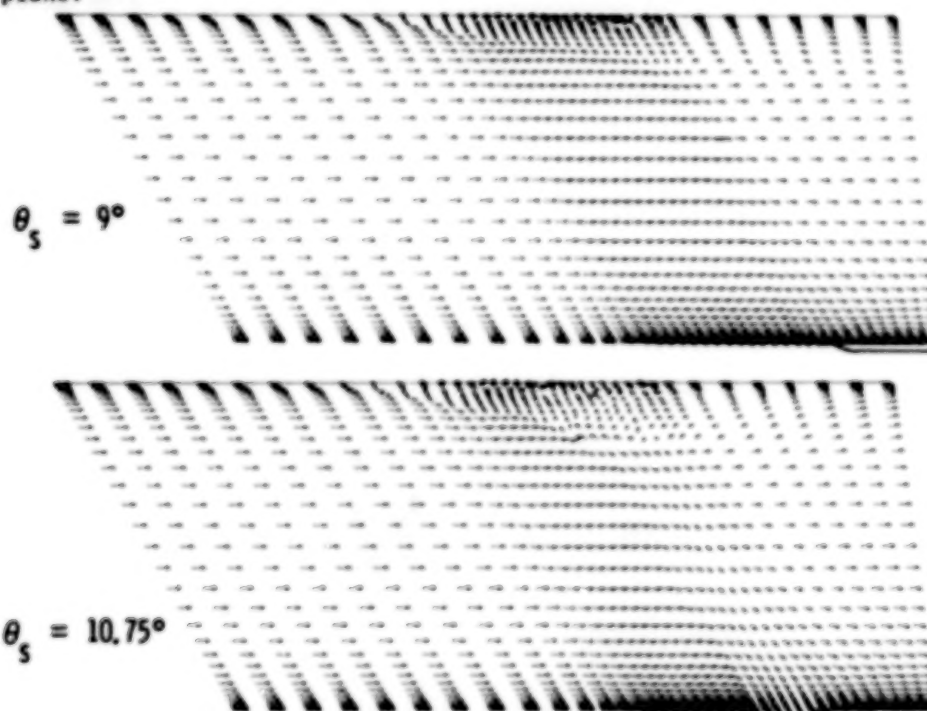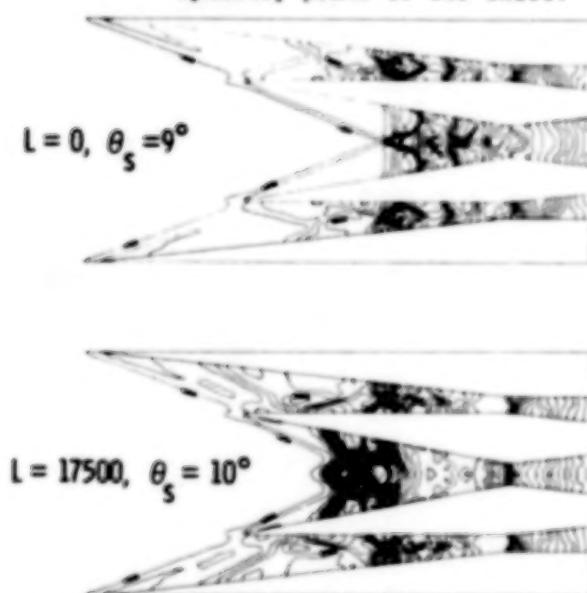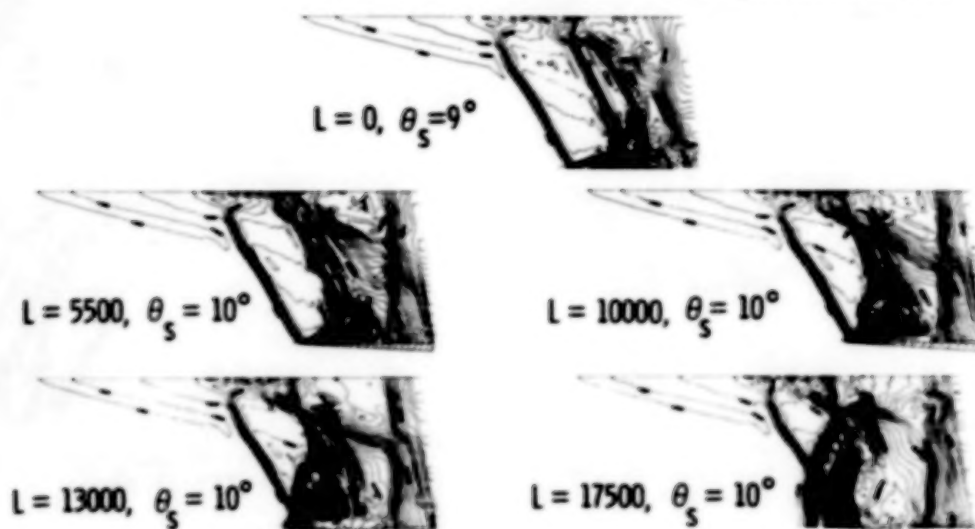Fig. 12.- Pressure contours in the
symmetry plane.

Fig. 13.- Velocity vector field in the
symmetry plane.

253

Fig. 14.- Inlet capture as a function of strut compression angle, θ_s.

Fig. 15.- Inlet capture as a function of cowl location for strut compression angle, $\theta_s = 9°$.

$L = 0, \theta_s = 9°$

$L = 5500, \theta_s = 10°$

$L = 10000, \theta_s = 10°$

$L = 13000, \theta_s = 10°$

$L = 17500, \theta_s = 10°$

Fig. 16.- Pressure contours in the symmetry plane of the inlet.

$L = 0, \theta_s = 9°$

$L = 17500, \theta_s = 10°$

Fig. 17.- Pressure contours in a cross plane located at 12% of the inlet height from the cowl plane.

Navier-Stokes

Euler

Mach number

4.970

3.976

2.982

1.988

.994

.000

-.0 9.5 19.1 28.7 38.3 48.0

Radial coordinate, in.

5.10

4.08

3.06

2.04

1.02

.00

-.0 9.2 18.4 27.6 36.8 46.0
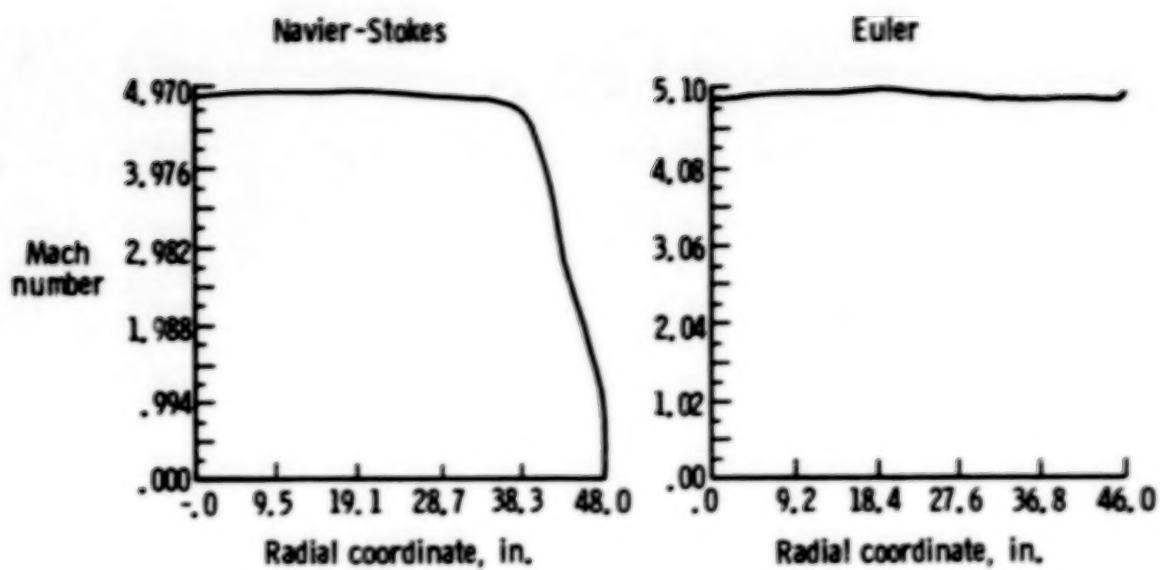
Radial coordinate, in.

Fig. 18.- Exit plane Mach number profile
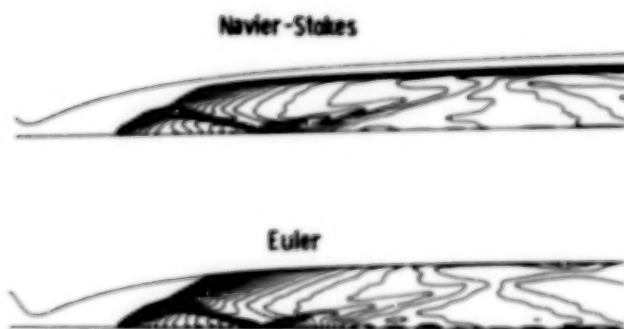in the designed Mach 5 nozzle.

Navier-Stokes

Euler

Fig. 19.- Mach number contours in the
designed Mach 5 nozzle.

NUMERICAL SIMULATION OF UNSTEADY VISCOUS FLOWS

Wilbur L. Hankey
Wright State University

Abstract

Most unsteady viscous flows may be grouped into two categories, i.e., forced and self-sustained oscillations. Examples of forced oscillations occur in turbomachinery and in internal combustion engines while self-sustained oscillations prevail in vortex shedding, inlet buzz and wing flutter. Numerical simulation of these phenomena have been achieved due to the advancement of the vector processor computer. Recent progress in the simulation of unsteady viscous flows is addressed in this paper.

1.0 Introduction

Unsteady flows have always been an important subject of fluid mechanics. Rotating turbomachinery, turbulence, flutter, buzz, buffet, aircraft spin, autorotation, noise and vortex shedding are common examples. Although these topics were subjected to intensive analysis in the past, the fluid mechanics community had to rely on experiment to produce the necessary design information. Fortunately, CFD now offers the potential for providing future design details based upon first principle computations.

Early CFD efforts concentrated on producing steady solutions, even though time-dependent methods were used, but only as an iteration technique. The introduction of the vector processor computer with higher computational speed has now made unsteady calculations possible. This paper will present a survey of some of the recent progress made in the field of unsteady viscous flows. Most unsteady flows may be divided into two categories, i.e., forced oscillations and self-sustained oscillations. In a forced oscillation an external force adds work to the fluid. Computationally this means an unsteady boundary condition must be prescribed. In a self-sustained oscillation no external forcing function is imposed, therefore, the boundary conditions are steady. According to Den Hartog (1947) the distinguishing difference between these two categories is that the force will still exist in a forced oscillation if one stops the motion, while in a self-sustained oscillation stopping the motion will also remove the force.

Before embarking on a numerical investigation, it is well to perform a linear analysis of an unsteady flow in order to gain insight into the fundamental physics (Hankey, 1980).

2.0 Linearized Analysis of Unsteady Fluid Flows

Consider a two-dimensional parallel flow of an incompressible, inviscid (but rotational) fluid. The governing equations are as follows:

$$\nabla \cdot \underline{V} = 0 \qquad (2.1)$$

$$\rho \frac{D\underline{V}}{Dt} = -\nabla p \qquad (2.2)$$

The mean flow is assumed to be parallel and rotational with small perturbations of the following form assumed:

$$
\begin{aligned}
u &= \bar{u}(y) + u'\,(x,y,t) \\
v &= \phantom{\bar{u}(y)+} v'\,(x,y,t) \\
p &= p_\infty + p'\,(x,y,t)
\end{aligned}
\qquad (2.3)
$$

Inserting these relationships into the governing equations and retaining only first order terms produces a linear system of equations.

$$u'_x + v'_y = 0 \qquad (2.4)$$

$$\zeta'_t + \bar{u}\zeta'_x = \bar{u}_{yy}\,v' \qquad (2.5)$$

where

$$\zeta' = v'_x - u'_y = \text{vorticity} \qquad (2.6)$$

Disturbances of the following form are assumed

$$v' = \phi(y)\,e^{i\alpha(x-ct)} \qquad (2.7)$$

where $\qquad c = c_r + i\,c_i \qquad (2.8)$

$\qquad c_r$ = propagation velocity
$\qquad c_i$ = amplification factor
$\qquad \alpha$ = wave number

Substitution of this relationship into the governing equation produces the Rayleigh equation (Rayleigh, 1880) which is a degenerate Orr-Sommerfeld equation appropriate for large Reynolds numbers)

$$\phi'' - (\alpha^2 + \frac{\bar{u}''}{\bar{u}-c})\,\phi = 0 \qquad (2.9)$$

with boundary conditions requiring that disturbances vanish at the wall and at the undisturbed outer edge.

$$\phi(0) = 0 \qquad \text{and} \qquad \phi(\infty) = 0$$

For prescribed values of $\bar{u}$ this is an eigenvalue problem in which $c(\alpha)$ can be obtained subject to the boundary condition constraint. The resulting solution takes on the following form:

$$v' = \phi e^{\alpha c_i t}\,e^{i\alpha(x-c_r t)} \qquad (2.10)$$

For positive values of c_i an instability occurs which is equivalent to a negative damping case. Rayleigh (1880) first investigated this type of flow and proved that velocity profiles with inflection points are unstable. In order to further explore this fact, a class of separated flows was analyzed. The stability of Stewartson's Lower Branch solutions of the Falkner-Skan equation was investigated. The Rayleigh equation was solved for several different values of the pressure gradient parameter, β, for the entire range of separated flows from incipient to a free shear layer (Verma, et al. 1979). Figure 2. represents the values of the amplification factor for the unstable frequency range. (Note f = $\omega_r c /2\pi\omega$). For reference purposes, these amplification factors are nearly two orders of magnitude greater than the more familiar Tollmien-Schlichting waves. The propagation speed $(c)_r$ for the disturbances was generally between 0.4 and 0.9 of u_e. Therefore, one can deduce from these results that flow instabilities do exist (positive c_i) but over a very limited frequency range for similar separated laminar boundary layers. By analogy, the frequency for which maximum c_i occurs can be viewed as the natural frequency of the shear layer. This corresponds to the most probable Strouhal number likely to occur for periodic disturbances and is always numerically less than unity. In Reference 5, compressibility effects of a free shear layer were investigated and the instability was found to diminish as Mach number increased (Figure 2.2). Although only one class of flows with inflection points has been examined, one is tempted to generalize these findings for all separated flows. One can speculate that (Den Hartog, 1947) separated flows become more unstable in progressing from incipient to fully separated; (Hankey, 1980) separated flows possess a relatively low natural frequency for which they are most likely to be self-excited and are stable on either side of that frequency; (Rayleigh, 1880) the instability diminishes as Mach number increases. Based upon these hypotheses, one can embark upon an analysis of unsteady flow problems.

3.0 Linear Oscillator Model

Separated flows were shown to possess a natural frequency for which small disturbances are highly amplified over a limited frequency range. However, for a self-sustained oscillation to persist a continuous string of disturbances is required to excite the shear layer. In this section the mechanism necessary to attain this result will be discussed.

It is informative at this point to compare a fluid dynamic oscillator with an electronic oscillator (Glassford, 1965). To create an electronic oscillator the circuit must contain an amplifier with a positive feedback loop (Figure 3.1). A self-excited fluid dynamic oscillator therefore must also contain these two components. In the previous section the shear layer was shown to play the role of the amplifier. The feedback loop is postulated to be a subsonic path in which pressure waves (acoustical signals) are returned to the shear layer origin and selectively reamplified.

The condition for oscillator resonance can be ascertained by examining the transfer functions for the two components.

If A in Figure 3.1 is the transfer function (a complex number) of the amplifier and B is the transfer function of the feedback loop, then the overall gain is as follows:

$$\text{Gain} = \frac{A}{1-AB} \qquad (3.1)$$

The existence of a frequency for which the return ratio, AB, equals unity is a sufficient condition for infinite gain and is hence the criterion for a sustained oscillation.

To summarize, three ingredients are necessary to produce an oscillator, i.e., (Den Hartog, 1947) amplifier with, (Hankey, 1980) positive feedback at (Rayleigh, 1880) a return ratio of unity.

Examination of the linear equations for a self-excited oscillation identifies the essential components and predicts the resonant frequency. However, it provides no capability to predict the amplitude of the disturbance or produce detailed flow field features for large disturbances. To proceed further it becomes necessary to examine the nonlinear characteristics, i.e., Navier-Stokes equations. This will be accomplished in the next section.

4.0 PROCEDURE FOR NUMERICALLY SOLVING THE NAVIER-STOKES EQUATIONS

4.1 Governing Equations

The two-dimensional or axisymmetric Navier-Stokes equations for a compressible perfect gas are listed below (7,8). This system of equations will be used to analyze several cases involving self-excited oscillations discussed later in this paper.

$$U_t + E_x + y^{-k}(y^k F)_y = k y^{-k} H \qquad (4.1)$$

where

$$U = \begin{array}{c} \rho \\ \rho u \\ \rho v \\ \rho e \end{array} \qquad ; \qquad E = \begin{array}{c} \rho u \\ \rho u^2 - \sigma_{11} \\ \rho u v - \tau \\ \rho u e - u\sigma_{11} - v\tau - kT_x \end{array}$$

$$F = \begin{array}{c} \rho v \\ \rho u v - \tau \\ \rho v^2 - \sigma_{22} \\ \rho v e - v\sigma_{22} - u\tau - kT_y \end{array} \qquad ; \qquad H = \begin{array}{c} 0 \\ 0 \\ -\sigma_{\phi\phi} \\ 0 \end{array} \qquad (4.2)$$

and

$$\tau = \mu(u_y + v_x) \qquad \sigma_{11} = -p - 2/3\mu\theta + \nabla + 2\mu u_x$$

$$e = C_v T + \frac{u^2 + v^2}{2} \qquad \sigma_{22} = -p - 2/3\mu\theta + \nabla + 2\mu v_y$$

$$p = \rho RT \qquad \sigma_{\phi\phi} = -p - 2/3\mu\theta + \nabla + 2\mu\frac{v}{y}$$

$$\nabla \cdot \vec{V} = u_x + y^{-k}(y^k v)_y$$

$k = 0$ for 2 dimensional flow
$k = 1$ for axisymmetric flow

This system of equations contains four dependent variables (u,v,T,p) where μ, k, C_v and R are prescribed for the gas. The three independent variables (x,y,t) are expressed in a Cartesian framework. A Cartesian system is unsatisfactory for most problems and therefore a general coordinate transformation must be employed. The physical space (x,y) is mapped into computational domain (ξ,η) where numerical calculations are performed.

4.2 Boundary Conditions

Four types of boundary conditions are required for the cases to be computed, i.e., (a) wall, (b) inflow, (c) outflow, and (d) symmetry surfaces. These shall now be addressed.

(a) Wall (η=0)

On an impermeable wall a no-slip condition for the velocity is required.

$$u(\eta=0)=0$$
$$v(\eta=0)=0$$

The wall temperature is also specified.

$$T(\eta=0)=Tw$$

The pressure on the wall does not require a boundary condition but must be determined from the flow field equations. The finite difference algorithm does require specification of a pressure relation at the wall and therefore a "compatibility condition" is used which is obtained from a degenerate normal momentum equation, i.e.,

$$\frac{\partial p}{\partial \eta}(\eta=0) = 0 \neq 0 \quad \text{to order Re}^{-1}$$

(b) Inflow (ξ=0)

At the inflow surface all flow variables are prescribed using characteristic variables.

$$U = \text{constant for self-sustained oscillations}$$
$$U = U(t) = \text{temporally specified for forced oscillations}$$
$$U = \quad p/\rho^\gamma$$
$$v$$
$$u+p/\rho_\infty a_\infty$$
$$u-p/\rho_\infty a_\infty$$

Note: One notable exception is that for subsonic flows the gradient of the last characteristic variable is set to zero.

(c) Outflow (ξ=L)

At a downstream boundary in which outflow occurs a simple wave equation is used to minimize reflections.

$$U_t + c_r U_s = 0$$

where s is aligned with the main streamline.

$$U = \quad p/\rho^\gamma$$
$$v$$
$$u+p/\rho_\infty a_\infty$$
$$u-p/\rho_\infty a_\infty$$

c_r = propagation velocity of disturbances.

$$c_r = \quad u_\infty$$
$$u_\infty$$
$$u_\infty + a_\infty$$
$$u_\infty - a_\infty$$

(d) Symmetry (y=0)

For axisymmetric flows the axis requires a symmetry condition as follows:

$$v(y=0) = 0$$
$$u_y(y=0) = 0$$
$$T_y(y=0) = 0$$
$$p_y(y=0) = 0$$

This concludes the description of the principle boundary conditions for the problems to be investigated. These four types are not implied to be a complete set to be used to investigate all flows but are representative of the type used in many present day calculations. Research is in progress in this area to improve the description of boundary conditions; especially for subsonic flows.

5.0 NUMERICAL RESULTS OF SELF-SUSTAINED OSCILLATIONS

In the previous section the numerical procedure was described for solving the time-dependent Navier-Stokes equations. In this section the results of several large scale computations will be explored. The configurations investigated include a cylinder, spike-tipped body, inlet, cone, and dump combustor configuration.

5.1 CYLINDER

The periodic shedding of large scale eddies from a cylinder immersed in a flowing stream is probably the most commonly recognized self-sustained oscillation in fluid mechanics. A stability analyses of a series of potential vortices representing this flow was accomplished by Von Karman (1911). This wake analysis of the "Karman Vortex Street" unfortunately contains little information about the true physics of the phenomenon and hence further investigation is required. Von Karman was limited at that time since the only tool available was linear potential theory. Today, however, the computer provides us with the ability to numerically integrate the Navier-Stokes equations and investigate problems of this type.

In Reference 10, the flow behind a cylinder at a Mach number of 0.6 and a Reynolds number of 1.7×10^5 was computed and compared with an experiment for similar conditions (Owen, 1981). By use of the techniques described in Section 4, the time dependent flow over a cylinder was determined by numerically integrating the Navier-Stokes equations. No turbulence model was used

for this case since the cylinder was in the subcritical (laminar) regime at this Reynolds number. Therefore, all large scale "turbulent" eddies in the wake were computed based upon first principles.

The flow was impulsively started. All points in the field were initially at the free stream state and suddenly the nonslip boundary condition on the cylinder walls applied. Initially, symmetric vortices developed behind the cylinder which became asymmetric after one cycle period and developed into periodic asymmetric vortex shedding after about three periods. The wall pressure history for the 90° and 270° polar angle location covering over twenty cycles of oscillation is shown in Figure 5.1.

The computed Strouhal number, fd/u, was 0.21; in general agreement with experiment. Numerically computed Reynolds stresses for the wake are presented in Figure 5.2. The comparison is favorable considering only large scale, low frequency eddies were simulated. This investigation shows that it is possible to numerically generate the production of large scale turbulent eddies and generally duplicate the experiment without accurately simulating the dissipation of the fine scale structure.

The mean velocity wake profile possesses two inflection points. A linear stability analysis of this profile (Betchov, 1967) shows two unstable modes to exist due to these two inflection points. The first mode produces an asymmetric oscillation while the second mode (with a lower amplification factor) produces a symmetric one. Since the asymmetric mode has the greater amplification, this accounts for the observed asymmetric serpentine wake pattern behind the cylinder. The Strouhal number, f d/u, for which the amplification factor is maximum is 0.2. The symmetric mode still exists, however, although lower in amplitude and higher in frequency. This tends to explain the modulation by a higher frequency of the wave form (Figure 5.1).

5.2 Buzz of Spikes

The numerical solutions of the time dependent Navier-Stokes equations for the cylinder confirmed the linear oscillation model for a self-oscillation, i.e., (a) the shear layer with an inflection point is the fluid dynamic amplifier; (b) feedback is achieved by acoustic waves returning to the origin; (c) resonance occurs at discrete integer values of the fundamental frequency when the return signal is "in phase" with the original disturbance. The existence of all three features is required to produce a self-excited oscillation. The removal of any one feature should eliminate the oscillation. (In most practical flight problems, the oscillation is undesirable and must be avoided.) The elimination characteristics of the oscillation shall now be discussed.

A configuration to demonstrate this phenomenon is a blunt body with a spike tip operating a supersonic speed. Spike tipped bodies are noted for producing violent buzz under

a restricted range of spike lengths (Harney, 1979). Figure 5.3 shows the experimental pressure intensity for different spike lengths at a Mach number of three. Buzz exists, but only for spike lengths above 20 mm for this configuration. Oscillations are not encountered at shorter lengths. Separated flow will always occur in the concave region between the spike and face of the blunt-nose body, and hence amplification is always present. However, resonance will not occur if the spike length is less than one wavelength of the unstable wave (a critical). Two numerical calculations were conducted (Shang et al., 1980) for spike lengths of 13 mm and 39 mm. The shorter spike length had an $\frac{l}{\lambda}$ of 1.5 and resulted in a stable flow. However, the longer spike length (39 mm) had an $\frac{l}{\lambda} = 9$ and produced a self excited oscillation comparable to the experiment. The spike pressure history comparison is shown in Figure 5.4. The spectral analysis for both computation and experiment is depicted in Figure 5.5. Outstanding agreement is observed between the computation and experiment for frequency, amplitude and wave form, showing the ability of the numerics to simulate self-excited oscillations.

5.3 Inlet Buzz

A supersonic inlet operating at subcritical flow conditions possesses the necessary features for buzz, i.e., a large region of intermittent separated flow and a downstream interface to reflect acoustical signals. When an inlet with a supersonic diffuser is throttled back to subcritical flow conditions, the normal shock is expelled from the diffuser causing separation on the centerbody. This separated shear layer is unstable and the principal cause of the oscillation. Standing waves occur in the duct. The upstream end of the inlet behaves as an open end (pressure node) while the downstream end behaves as a closed end (pressure antinode). Antisymmetric modes occur with all harmonics being odd. Two very significant results can be obtained from this standing wave analysis. First, the frequencies should be commensurable in which harmonics occur at exact integer values of the fundamental frequency. Secondly, antisymmetric mode shapes occur in the duct. One can also anticipate frequency modes to jump discretely to the next integer eigenvalue as flow conditions are changed by different throttle settings. This indeed is the experimental finding (Hankey, 1980).

One calculation (Newsome, 1983) using the complete Navier-Stokes equations for inlet buzz has been accomplished and compared with experimental data (Nagashima, 1972). An external compression axisymmetric inlet and diffuser configuration was modeled for flow conditions corresponding to a Mach two free stream with a Reynolds number based upon 6 cm diameter of $Re_D = 2.34 \times 10^5$. Because the turbulence model was found to artificially damp the occurrence of instabilities it was deleted from the program. The justification for the omission is that the numerical code is capable of resolving a finite number of low frequency components up to the shortest wave length ($2\Delta x$). Current turbulence models over-predict the appropriate eddy viscosity. When the turbulence model is omitted,

the turbulent transport process is resolvable
while the turbulent dissipative processes is
not. This approach was used to compute through
three buzz cycles. The instability developed
immediately as a consequence of the
non-equilibrium state of the initial conditions.
A sequence of Mach contours covering the third
buzz cycle is shown in Figure 5.6. During buzz
the bow shock was forced to the tip of the
centerbody as a result of the interaction with a
reflected compression wave. In the expulsion
phase a region of reverse flow extended between
the base of the bow shock and the cowl lip. As
the shock reached the centerbody tip, the shear
layer ruptured and flow was spilled. The bow
shock remained in this position for a time
corresponding to the propagation and reflection
of an expansion wave from the downstream choked
throat. The inlet then ingested mass and the
shock retreated to the cowl lip with the flow
reattaching to the centerbody.

5.4 Boundary Layer Transition

As alluded to in previous sections, a
portion of the turbulence spectrum can be
resolved in computing self-excited oscillations.
One then wonders if boundary layer transition can
be simulated numerically as a self-excited
oscillation on todays' computers. To explore
this area, the onset of transition was computed
for a hypersonic boundary layer (Hankey, 1982).
For highly compressible flow, the generalized
inflection point, $(\rho u')'<0$, replaces the low
speed Rayleigh condition of $u''<0$. At hypersonic
speed, linear theory shows that the second mode
instability dominates (which is fortunately two
dimensional). Examination of this case by use of
the linear stability theory results of Mack
(1965) showed the numerical computation to be
feasible. Numerical solution of the time
dependent Navier-Stokes equations was
accomplished (with steady boundary conditions)
using step sizes sufficiently small to resolve
the unstable waves predicted from linear theory.
The configuration was a 7° cone at a Mach number
of 8 and a Reynolds number of 10^6 based on a one
meter length. Temperature fluctuations with a
regular periodic behavior were obtained in the
numerical computation. The amplitude of these
self-excited waves varied across the boundary
layer with a maximum occurring near the edge.
Good agreement was obtained with experiment for
both the temperature and velocity fluctuations
(Figure 5.7).

A comparison of the computed spectral
analysis (Figure 5.8) with experiment shows
agreement in the frequency at peak amplitude,
however, the experiment has a broader band.
Further, research is required to resolve the
disparity, however, the results are encouraging
for the first phase in the prediction of
turbulence.

5.5 Dump Combustor

The flow in an efficient combustor must be
inherently unsteady in order to enhance mixing
and expell the burned products before they quench
the flame. A computation of cold flow in a dump
combustor was accomplished in order to ascertain

if the vortex shedding phenomenon could be
simulated (Guelda, 1987). Figure 5.9 is a time
sequence of vortex patterns computed for a dump
combustor configuration with choked flow at the
nozzle exit. The sequence shows periodic
shedding and downstream propagation of the
vortices. Also, shown in Figure 5.10 is a
comparison of the computed pressure histograms
with the experimental (Davis, 1981) for three
different locations. These results show
encouragement in the ability to numerically
simulate unsteady viscous flows.

6.0 Forced Oscillations

Forced oscillations in unsteady viscous
flows occur in examples, such as the piston
motion of an internal combustion engine, movement
of an aircraft control surface, rotation of a
turbine blade in a jet engine, flapping of a
bird's wing, and pumping of blood through the
heart. In all cases, an external force adds work
to the fluid to produce a desired result. To
simulate these forced oscillations, the time
dependent Navier-Stokes equations must be used.
Time dependent boundary conditions and 3-D
adaptive grid systems are required. This field
is certainly a challenge for the CFD community of
the future. In the interim more modest, yet
still challenging efforts, are in progress.

6.1 Turbomachine Rotor Stator Stage

Rai (1985) simulated the motion of a 2-D
rotor-stator stage of a turbomachine and produced
an impressive movie of the flow field. Scott
(1985) also simulated a similar case by imposing
a stator time varying wake profile onto a
multiple-blade rotor and obtained the temporal
flow features. The case computed depicted the
combination of 54 stator and 72 rotor blades of a
compressor stage. Figure 6.1 displays the flow
field for four rotor blades at one instant in
time.

6.2 Acoustically Excited Jet

Another form of forced oscillation is the
acoustic excitation of a shear layer. Since a
shear layer possesses a "natural frequency," a
resonance type phenomenon occurs when the shear
layer is excited near this frequency. Acoustic
excitation regularizes the quasi-periodic vortex
shedding of the self-sustained oscillations in a
shear layer. This modest excitation results in
higher amplitudes and enhanced mixing of the
jet. Figure 6.2 is a comparison between the
experimental (Scott, 1985) and computed vortex
patterns (Scott, 1986) of a jet for an excitation
Strouhal number of 0.45.

6.3 Dynamic Lift

Still another type of forced oscillation is
the rapid rotation of a wing (such as a helicop-
ter blade) to produce dynamic lift. The sudden
change in angle of attack creates a starting
vortex which migrates through the flow field.
During this transient phase, the dynamic lift
coefficient exceeds the static lift value but
later falls below before recovering to the static
value. This phenomenon is also of interest for

the dynamic maneuvering of an aircraft in the post-stall regime.

Figure 6.3 is an example of a numerical calculation (Tassa, 1981) of the dynamic lift coefficient for an airfoil under high rotational pitch rate.

7.0 Summary

Self-excited and forced oscillations in fluid flows have been analyzed. The concept of a fluid amplifier within a separated shear layer was presented. Signals entering the shear layer are selectively amplified over a limited frequency range and returned through a feedback loop as acoustic pressure waves. Resonance occurs when the return signal is "in phase" with the original disturbance wave. Under these circumstances no external forcing function is required and a self-excited oscillation can occur. If a forced excitation signal is imposed on a shear layer at its "natural frequency," resonance occurs. Linear theory is useful in predicting the frequency of the instability and providing a qualitative description of the phenomenon. Quantitative description of unsteady viscous flows are possible through the numerical solution of the time dependent Navier Stokes equations.

REFERENCES

ATWA, K.K.; and LEPICOVSKY, J.: Acoustic Control of Free Jet Mixing. AIAA 85-0569, Free Shear Flow Control Conference, Boulder, CO, Mar. 1985.

BETCHOV, R.; and CRIMINALE, W.: Stability of Parallel Flows. New York Academic Press, p 37-40, 1967.

DAVIS, D.L.: Coaxial Dump Ramjet Combustor Combustion Instabilities. AFWAL TR 81 2047, July, 1981.

DEN HARTOG, J.P.: Mechanical Vibrations. McGraw Hill Book Co., Inc. 1947.

CIELKA, T.; SCOTT, J.N.; and HANKEY, W.L.: Investigation of Unsteady Flow in a Dump Combustor Configuration (to be published).

GLASFORD, G.M.: Linear Analysis of Electronic Circuits. Addison Wesley, 1965.

HANKEY, W.: Analysis of Inlet Buzz. AFWAL TR-FIMM 1980.

HANKEY, W.L.; and SHANG, J.S.: Analysis of Self-Excited Oscillations in Fluid Flows. AIAA 80-1346, Snowmass, CO, 14-16 July, 1980.

HANKEY, W.L.; and SHANG, J.S.: Natural Transition - A Self-Excited Oscillation. AIAA Paper No. 82 1011, AIAA/ASME Conference, St. Louis, MO, June, 1982.

HANKEY, D.J.: Oscillating Shocks on Spiked Nose Tips at Mach 3. AFFDL TR 79 9 FX, 1979.

MACCORMACK, R.W.: Numerical Solutions of the Interactions of a Shock Wave with Laminar Boundary Layer. Lecture notes in physics, Vol. 59, Springer Verlag, 1976.

MACK, L.M.: The Stability of the Compressible Laminar Boundary Layer According to a Direct Numerical Solution. AGARDograph 97, Pt. 1, pp 329-362, May 1965.

NAGASHIMA, T.; OBRATT, T.; and ASANUMA, T.: Experiment of Supersonic Air Intake Buzz. Report No. 481. University of Tokyo, 1972.

NEWSOME, R.W.: Numerical Simulation of Near-Critical and Unsteady Subcritical Inlet Flow Fields. AIAA Paper No. 83-0175, Jan 1983.

OWEN, F.K.; and JOHNSON, D.A.: Measurements of Unsteady Vortex Flow Field. AIAA Journal, Vol. 18, pp 1173-1179.

RAI, M.M.: Navier Stokes Simulations of Rotor-Stator Interaction Using Patched and Overlaid Grids. AIAA Paper No. 85-1519, Jul. 1985.

RAYLEIGH, LORD: On the Stability or Instability of Certain Fluid Motion. Scientific Papers, Vol. 1, pp. 474-484, Cambridge University Press, 1880.

ROSCOE, D.; and HANKEY, W.L.: Stability of Compressible Shear Layers. AFWAL TR 80-3016, April 1980.

SCOTT, J.N.: Numerical Simulation of Unsteady Flow in a Compressor Rotor Cascade. AIAA 85-0133, 23rd Aerospace Sciences Meeting, Reno, NV, Jan. 1985.

SCOTT, J.N.; and HANKEY, W.L.: Numerical Simulation of Unsteady Flow in an Axisymmetric Shear Layer. AIAA 86-0202, 24th Aerospace Sciences Meeting, Reno, NV, Jan. 1986.

SHANG, J.; SMITH, R.; and HANKEY, W.: Flow Oscillations of Spike Tipped Bodies. AIAA Paper 80-0062.

SHANG, J.S.; BUNING, P.C.; HANKEY, W.L.; and WIRTH, M.C.: Performance of a Vectorized Three Dimensional Navier-Stokes Code on the CRAY 1 Computer. AIAA J., Vol. 18, No. 9, pp. 1073-1079, Sept 1980.

SHANG, J.S.: Oscillatory Compressible Flow Around a Cylinder. AIAA Paper No. 82-0098, 1982.

TASSA, Y; and SANKAR, J.L.: Dynamic Stall of an Oscillating Airfoil in Turbulent Flow Using Time Dependent Navier-Stokes Solver. IUTAM Symposium on Unsteady Turbulent Shear Flows, Toulouse, France, 1981.

VERMA, G.; HANKEY, W.L.; and SCHERR, S.: Stability Analysis of the Lower Branch Solutions of the Falkner-Skan Equations. AFFDL TR 79 3116, July 1979.

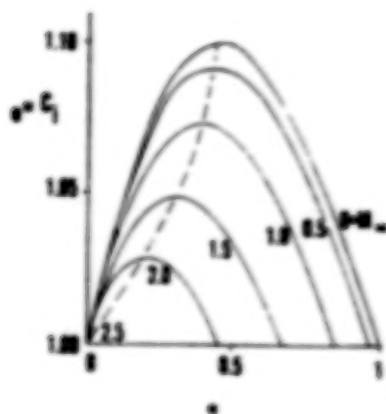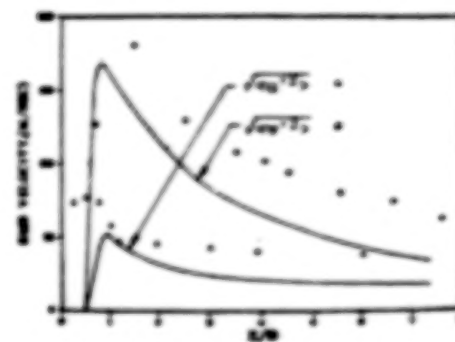VON KARMAN, T.; and Nachr. d. wiss. ges. gottinger: Mathe. Phys. Klasse, 509 (1911).
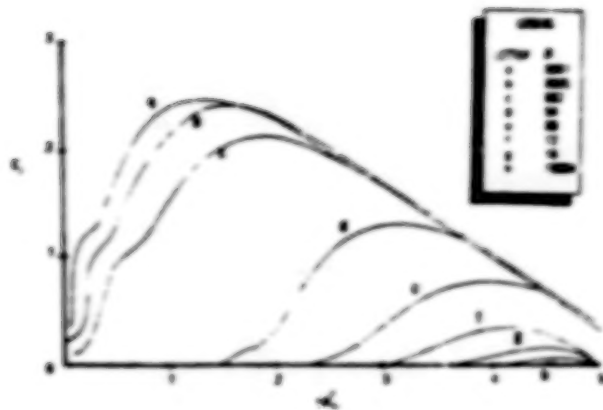
2.1 Amplification Factor vs. Wave Number for Various B (Ref 4)
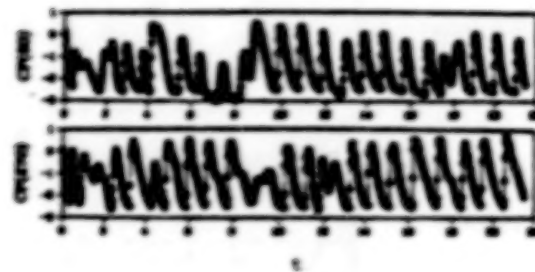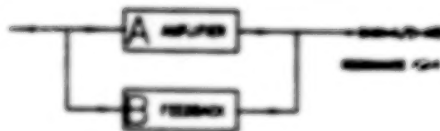

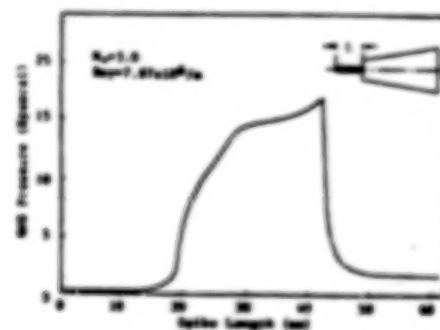5.1 Temporal Evolution of Pressure Coefficient

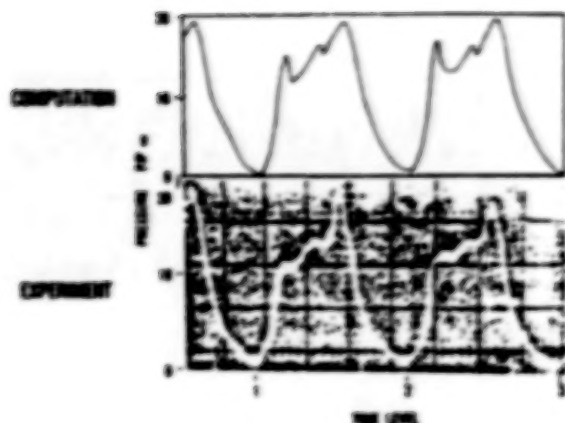2.2 Variation of C_1 with a for Various Mach Number

5.2 Comparison of Turbulent Intensity (Data Ref P.K. Owen and D.A. Johnson, 1981)
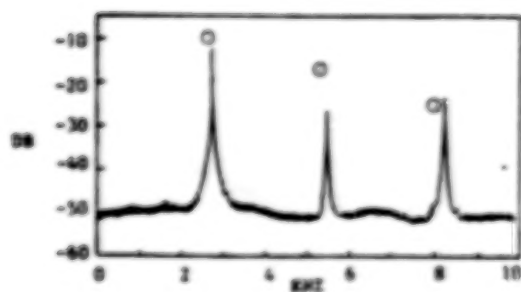

3.1 Diagram of Oscillator with Feedback
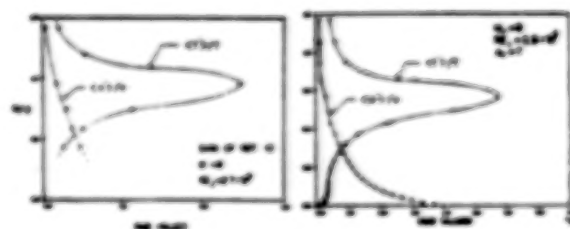

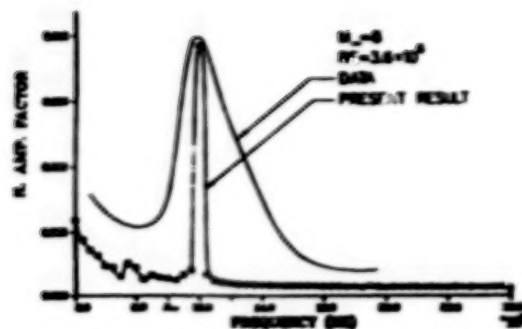5.3 RMS Pressure Level for Spike Buzz

5.4 Comparison of Predicted and Experimental Wave
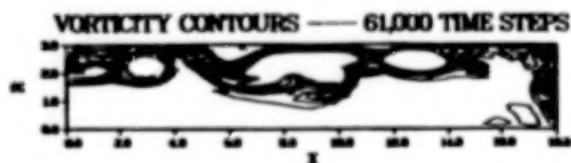Forms for Spike-Buzz

5.6 Forebody Flow Field, Third Buzz Cycle

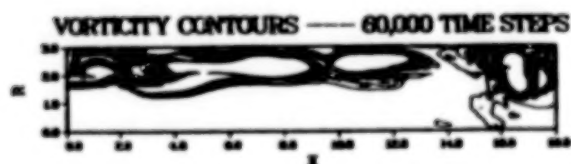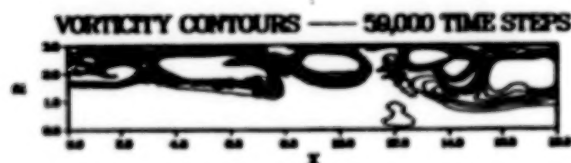5.5 Comparison of Predicted and Experimental Spectral Analysis for Spike-Buzz

5.7 Computed RMS Profiles of Temperature and
Velocity

5.8 Spectral Analysis for Instability over Cone

Theory

VORTICITY CONTOURS —— 57,000 TIME STEPS

VORTICITY CONTOURS —— 58,000 TIME STEPS

VORTICITY CONTOURS —— 59,000 TIME STEPS

VORTICITY CONTOURS —— 60,000 TIME STEPS

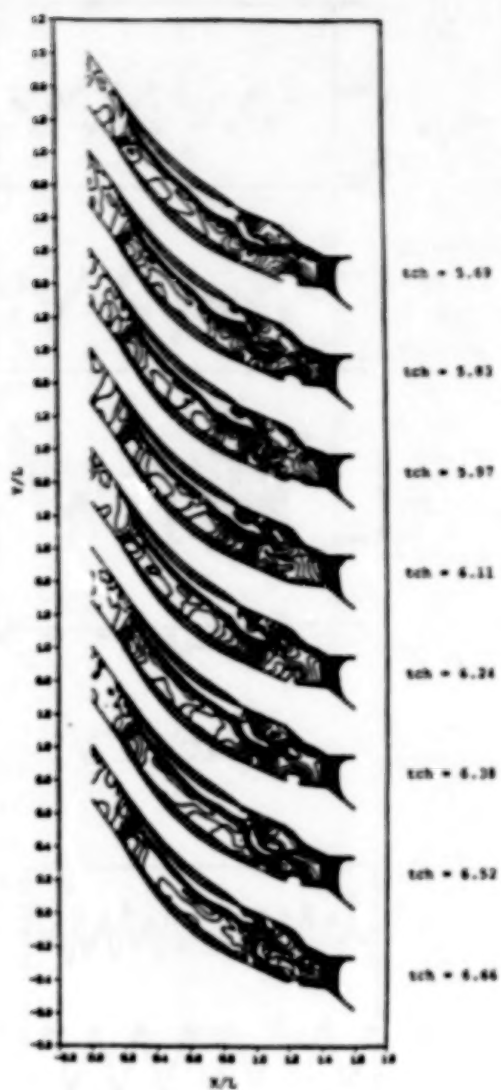VORTICITY CONTOURS —— 61,000 TIME STEPS
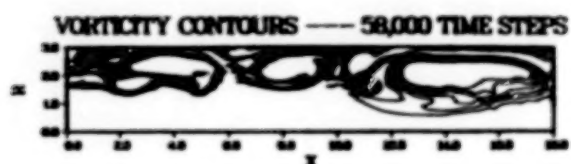
Experiment

5.9 Vortex Sequence for Dump Combustor
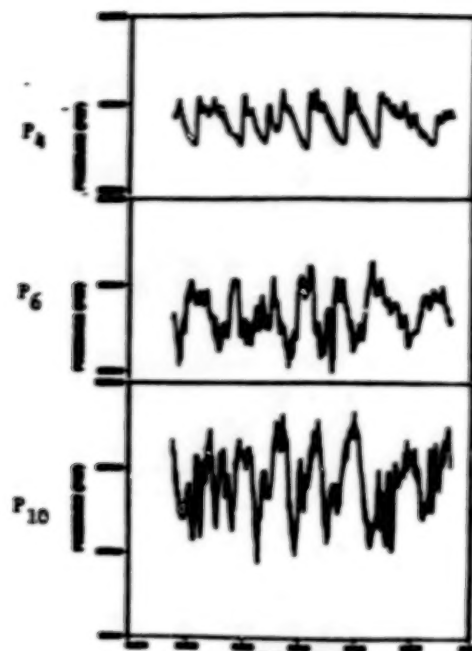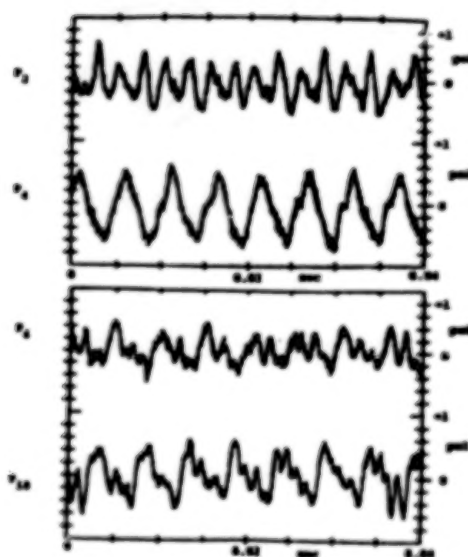
5.10 Pressure Histogram Comparison

6.1 Compressor Cascade Flow Field History

TIME = 0.24994E-01

0.25223E-01

0.25449E-01

0.25666E-01

0.25895E-01

0.26117E-01

0.26335E-01

0.26566E-01

0.26789E-01

a. $\Delta\phi = 0$ deg.

b. $\Delta\phi = 60$ deg.

c. $\Delta\phi = 120$ deg.

d. $\Delta\phi = 180$ deg.

e. $\Delta\phi = 240$ deg.

f. $\Delta\phi = 300$ deg.
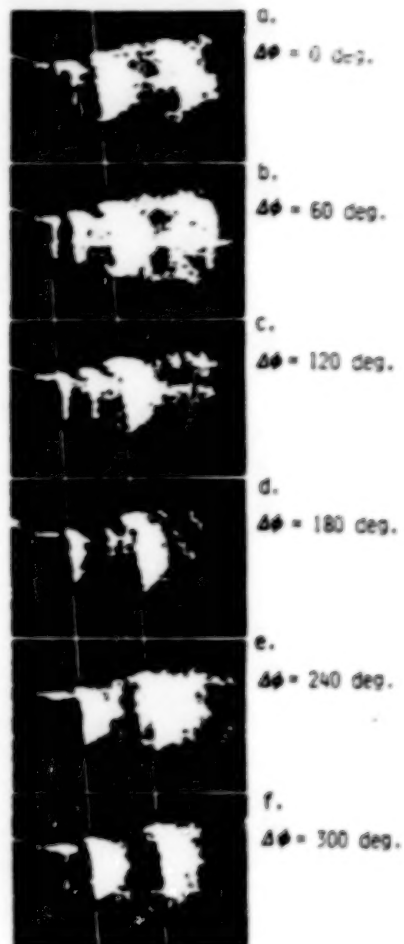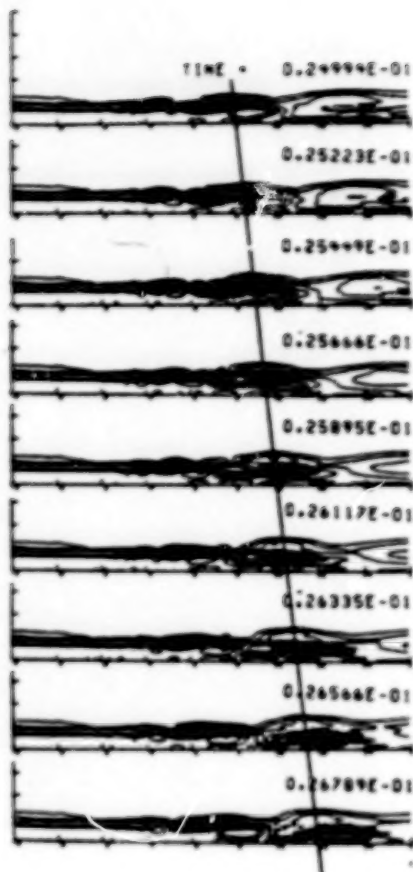
$M_j = 0.29$, $T_t = 673$ K, $St_j = 0.25$, $L_e = 144$ dB

6.2 Comparison of Vortex Structure for Excited Jet
Theory/Experiment
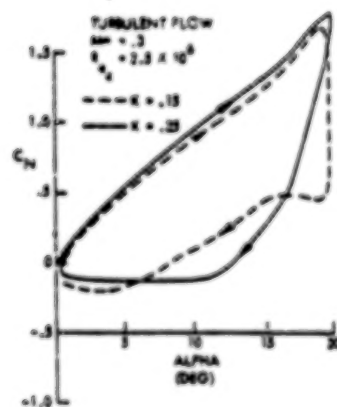
6.3 Dynamic Lift Hysterisis

267

Dr. Forester Johnson
Boeing Military Airplane Co.

3-D Configurations--Panel Methods

Paper not available

EXPERIENCE WITH 3-D COMPOSITE GRIDS*

J. A. Benek, T. L. Donegan and N. E. Suhs
Calspan Corporation/AEDC Division

ABSTRACT

Experience at the AEDC with the three-dimensional (3-D), chimera grid embedding scheme is described. Applications of the inviscid version to a multiple-body configuration, a wing/body/tail configuration and an estimate of wind tunnel wall interference are described. Applications to viscous flows include a 3-D cavity and another multi-body configuration. A variety of grid generators is used, and several embedding strategies are described.

1.0 INTRODUCTION

In the last ten years, Computational Fluid Dynamics (CFD) has evolved from an interesting spectator sport into a necessary, if not integral, part of aircraft design and development. Two circumstances have stimulated this change: the maturation of fast numerical algorithms for solution of the Euler and Navier-Stokes equations and the reduction of the price of the large supercomputers required to perform the computations. As the entry costs decrease and the value of flow simulations becomes more widely recognized, the demands for ever more complex simulations increase. The heightened level of expectation also increases pressure to produce "timely" solutions. This pressure can only be expected to increase as CFD becomes more closely coupled to the design and development processes. Frequently, the most critical phase in meeting the demand for computations is the construction of a suitable mesh. To ameliorate the difficulties experienced with grid generation, alternative computational strategies are being explored. Basically, they can be divided into two categories: global approaches and domain decomposition approaches.

The global mesh approach uses a single computational net to discretize the geometry and flow field [e.g., Thompson (1982), Rubbert and Lee (1982), and Shang and Scherr (1985)]. Complex geometry frequently requires the introduction of internal boundaries (e.g., cuts) into the domain and may result in very skewed grids and regions of unacceptably low spatial resolution. The introduction of internal boundaries increases the bookkeeping required in the flow solver and can require modifications to the solution algorithm. One novel approach utilizing a global mesh is described by Jameson, Baker, and Weatherhill (1986). The major thrust of this work is to use a finite volume algorithm based on tetrahedrons and eliminate the requirement for an ordered mesh. More data structure is required to define the relationships among the grid points comprising the volumes.

Domain decomposition includes many techniques: zonal or grid patching [e.g., Hessenius and Pulliam (1982), Rai (1984), and Holst et al. (1985)], and grid embedding/oversettings [e.g., Atta and Vadyak (1982), Benek et al. (1983), Venkatapathy and Lombard (1985), and Berger (1982)]. The basic idea of this strategy is the subdivision of the computational domain into regions (not necessarily disjoint) that can be more easily meshed. An additional advantage is that each subdomain may be treated separately and a different flow model or solution algorithm used in each. Such flexibility provides economies in computer resources as the more expensive viscous flow solvers can be confined to regions where viscosity dominates the flow. The key to successfully implementing this strategy is provision of a means of intergrid communication. This is the point at which the various techniques differ most widely. All these techniques require additional bookkeeping to facilitate communication.

Presently, no one method has been demonstrated to be clearly superior. It seems likely that some synthesis of the various strategies will become the method of choice. In the meantime, we have chosen the grid-embedding approach as it includes grid patching as a special case and thus provides a flexible method for accomplishing a broad range of flow simulations. In this paper we will describe our experience with the chimera scheme which was first developed by Benek, Steger and Dougherty (1983). The three-dimensional, color graphics code required to support this effort was developed by Buning and Steger (1985).

2.0 DESCRIPTION

The chimera grid-embedding technique is a domain decomposition strategy and as such has two principal elements: (1) decomposition of the domain into subdomains which typically overlap and (2) communication among the subdomains. The division into subdomains is arbitrary; the major considerations are the identification of regions that may be easily meshed, and perhaps the isolation of special regions of the flow (e.g., where viscous effects are important). The chimera implementation increases the flexibility of subdomain selection by removing regions of a mesh common to an embedded grid. That is, an embedded mesh introduces an artificial boundary or "hole" into the mesh in which it is embedded, figure 1. Because the regions interior to the hole do not enter into the solution process, intergrid communication is simplified since communication among the grids is restricted to the transfer of boundary data. Appropriate boundary values are interpolated from the mesh or meshes in
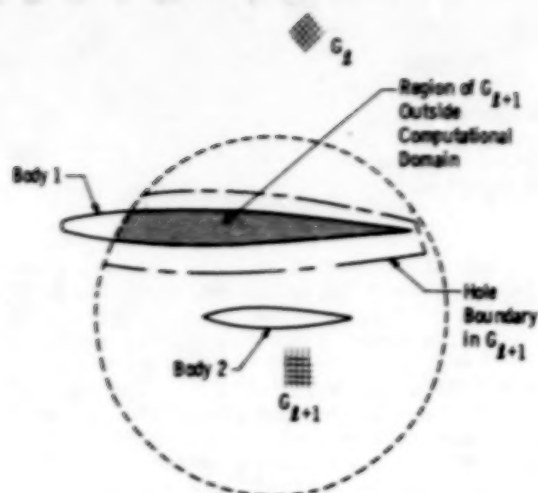
Figure 1. Hole boundary in embedded grid G_{l+1} caused by solid boundary in G_l.

which the boundary is embedded. The chimera procedure naturally separates into two parts, (1) generation of the composite mesh and associated interpolation data and (2) solution of the flow model or models on each mesh. Each part is embodied in a separate computer code, PEGSUS and XMER3D. PEGSUS takes independently generated component or subdomain grids and the embedding specifications as input and automatically constructs the composite mesh and computes the interpolation data which are output. XMER3D takes the PEGSUS output and flow specifications as input and solves the appropriate flow model on each grid.

2.1 PEGSUS

Automatic generation of a composite mesh from the input component grids requires PEGSUS to (1) establish the proper lines of communication among the grids through appropriate data structure, (2) construct holes within grids, (3) identify points within holes, (4) locate points from which boundary values can be interpolated, and (5) evaluate interpolation parameters. In addition, PEGSUS performs consistency checks on the interpolation data to assure their acceptability and constructs output files with the data structures appropriate to XMER3D. The most recent version of PEGSUS allows very general interactions among grids as indicated in figure 2. In addition, any grid may introduce a hole into any other mesh. Details of the hole construction process, and associated data structures, are provided by Benek et al. (1983, 1985, and 1986). A trilinear interpolation is used to obtain boundary data.

2.2 XMER3D

The implementation of the chimera scheme must provide for the use of multiple flow models. The current choice of models is the 3-D Euler equations for inviscid flow and the 3-D thin-layer Navier-Stokes equations for viscous flow. The algebraic model of Baldwin/Lomax (1978) is used to simulate turbulent flow. The implicit, approximate factorization scheme of Beam and Warming (1976 and 1977) is used to solve the model equations. The

implementation follows that of Pulliam and Steger (1978) and uses explicit boundary conditions. Modifications to accommodate the chimera scheme are described by Benek et al. (1986).
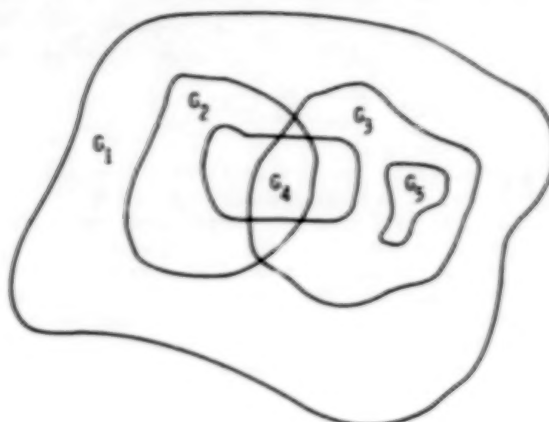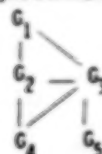

Intergrid Communication Paths

Figure 2. Structure of embedded grids.

3.0 APPLICATIONS

A major motivation for the development of the chimera scheme at the AEDC was the requirement to provide routine computational support to testing. Estimates of the effects of the wind tunnel environment on aerodynamic data are of particular interest. Typically, lead times are short and grid generation is usually the pacing item in performing CFD simulations. Also, there is the requirement to compute time-dependent flows involving aerodynamic configurations in relative motion as exemplified by the Space Shuttle booster configuration and store separation from military aircraft.

The 3-D chimera scheme has been used to compute both viscous and inviscid flows over a variety of configurations. These include wing/body/tail, bodies in close proximity, cavity flows, and base flows for Mach numbers spanning the range from subsonic to supersonic. The following sections will illustrate some of these applications of the chimera scheme.

3.1 Inviscid Flows

The flow about a three-body configuration (fig. 3) consisting of three ellipsoidal bodies in a triangular arrangement was computed for a free-stream Mach number, $M_\infty = 0.8$, and angle of attack, $a = -2.0$ deg. The composite mesh contained three grids and 57,750 points. The component grids were constructed using a hyperbolic grid generator described by Steger and Chaussee (1980) and Kinsey and Barth (1984). Mach number contours are shown in figure 4. The contours indicate that the expected symmetries exist in the flow.
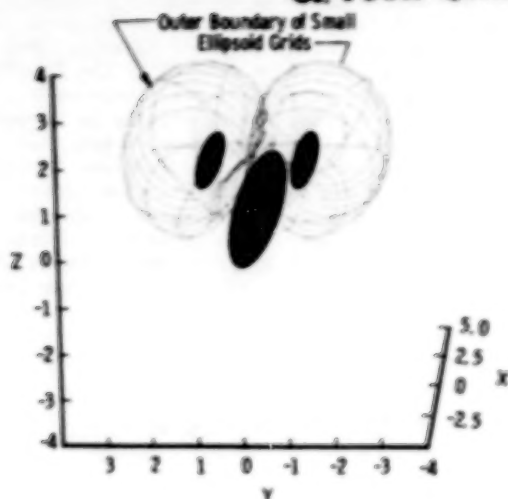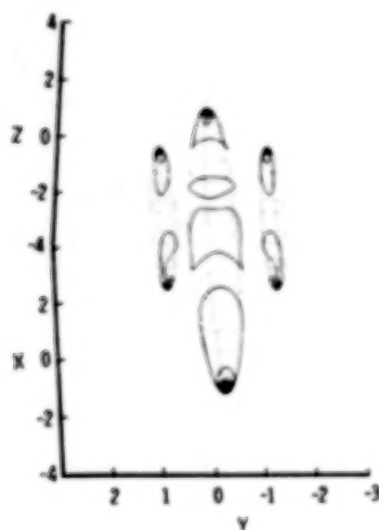
Figure 3. Three-ellipsoid-body configuration and grids.

Figure 4. Mach number contours on surfaces of ellipsoids, $M_\infty = 0.80$, $\alpha = -2$ deg.

Figure 5. Wing/body/tail configuration.

Figure 6. Composite grid for fuselage, sting, wing, and tail grids.

One of the intended uses of the chimera scheme at the AEDC is the computation of wind tunnel wall and support interference [e.g., Kraft et al. (1986) and Suhs (1985)]. A version of the scheme was converted to this purpose. The model shown in figure 5 was designed for assessment of wind tunnel wall interference and it consists of a blunted ogive-cylinder and a mid-mounted wing and tail. The wing and tail are constant chord planforms swept back at 30 deg and have no twist or taper. Cross sections parallel to the plane of symmetry are NACA-0012 airfoils. Figure 6 illustrates the meshes used to represent the wall interference model shown in figure 5. The wind tunnel walls and a portion of the sting support are also represented. Figure 6 shows the outer boundaries of the grids about the fuselage, wing, and tail; figure 7 illustrates the model embedded in the tunnel mesh. The region devoid of mesh lines on the tunnel symmetry plane in figure 7 represents the hole in the tunnel grid introduced by excluding points in the vicinity of the model from the solution in the tunnel grid.
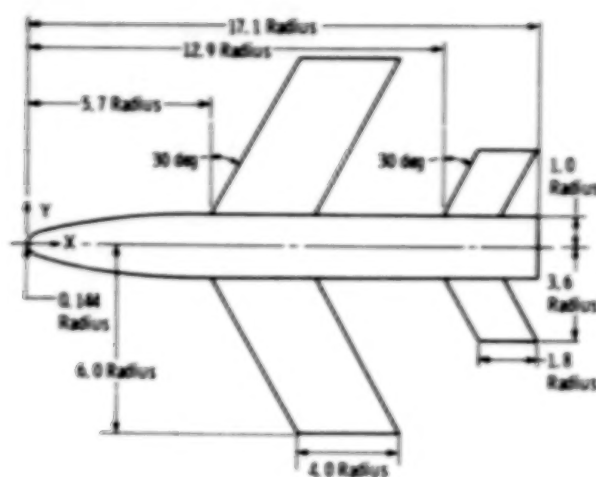

Figure 7. Model grids embedded in the tunnel grid.
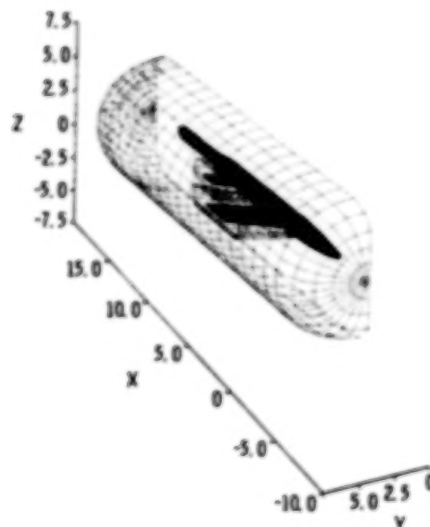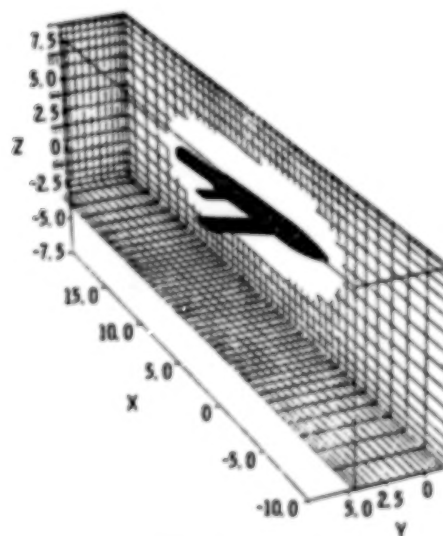
Figure 7 illustrates the flexibility inherent in the chimera scheme. The model geometry and sting grids were constructed by adding a mesh containing the sting to an existing mesh used to model the fuselage. The component-by-component construction process is particularly useful for wall interference calculations because no additional grid generation is required to change model angle of attack. All that is required is that the grids representing the wind tunnel model be rotated relative to the tunnel mesh and be re-embedded in it. PEGSUS performs such transformations on component grids by a single change of input.

Figure 8 illustrates the component grids used to represent a generic transport configuration for a wall interference assessment. In this case, three grids containing a total of 201,000 points are used.

Several grid generators were used to construct the component grids shown in figures 6 through 8. These include a two-dimensional grid generator developed by Sorenson (1980) and the three-dimensional generators developed by Soni (1985) and Thompson (to be published in 1987).

Mach number contours on the wall interference model are presented in figure 9 [Benek et al. (1985 and 1986)]. The tunnel solution obtained on the grids shown in figures 6 and 7 corresponds to $M_\infty = 0.90$ and $\alpha = 4$ deg. The contours join smoothly across mesh boundaries. The shock wave on the

wing can be seen to continue around the fuselage. The figure illustrates the effect of decreasing spatial resolution in high gradient regions. The shock wave can be seen to be smeared on the fuselage compared to the wing because of the decreased resolution in the fuselage grid. Figure 10 [Benek et al. (1985)] presents a comparison of computed and measured wing and fuselage pressure coefficients for $M_\infty = 0.9$ and $\alpha = 2$ deg. The solution corresponds to an interference-free flow on a composite mesh with 157,540 points. Details of wall interference computations will be presented at the AIAA 19th Fluid Dynamics, Plasma Dynamics and Laser Conference, June 1987.
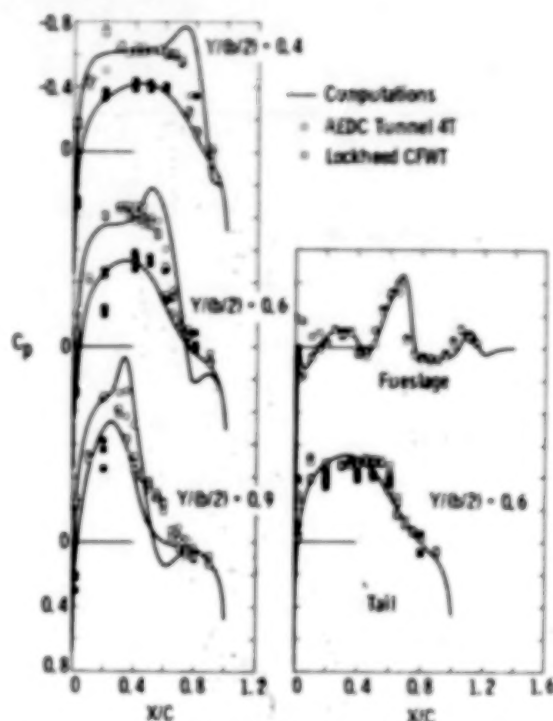
Figure 10. Wing/body/tail solution, $M_\infty = 0.90$, $\alpha = 2$ deg (open symbols, upper surface; solid symbols, lower surface).

3.2 Viscous Flows

The chimera scheme was used to compute several 3-D viscous flows: cavity flow, the flow about a three-body configuration and the flow about a blunt-based projectile. The cavity flow simulation is time-dependent because of the fluctuating free shear layer over the cavity. The cavity has a length-to-depth ratio of 5.6 and a length-to-width ratio of 3.35. Figure 11 illustrates the composite mesh used to represent the cavity/flat-plate flow field. The composite mesh has two grids, a total of 157,627 points, and no holes. The component grids are stretched cartesian nets with clustering near the solid boundaries and in the shear layer. Figure 12 presents computed Mach number contours in the streamwise plane of symmetry for $M_\infty = 0.74$. The contours correspond to the flow at a single instant of time. The three-dimensional nature of the flow is demonstrated in figure 13 which shows the flow in a plane normal to the stream direction and located half way down the cavity. Details of this computation and additional solutions will be presented at the AIAA 19th Fluid Dynamics, Plasma Dynamics and Laser Conference in June 1987.
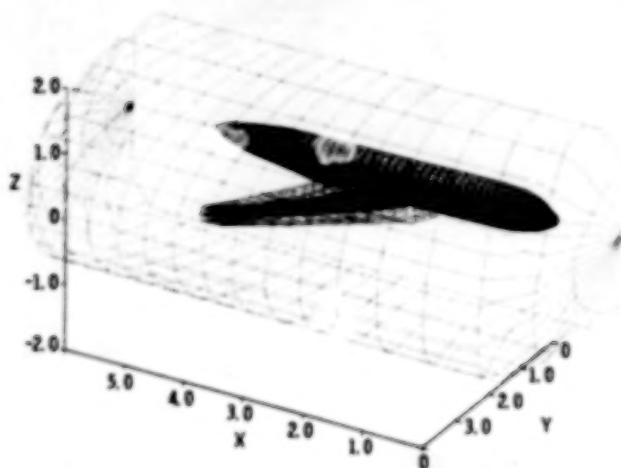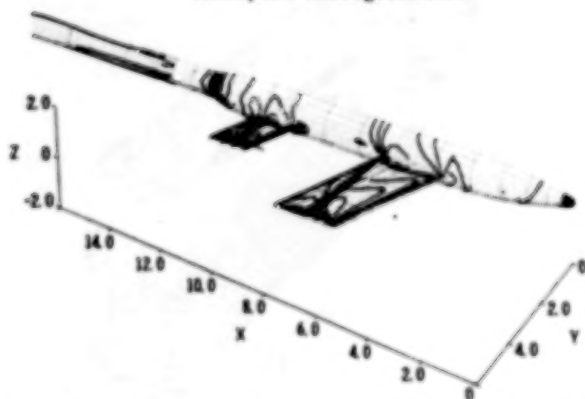
Figure 8. Fuselage and body grids for a transport configuration.

Figure 9. Mach number contours for tunnel solution of wing/body/tail configuration, $M_\infty = 0.9$, $\alpha = 4$ deg.
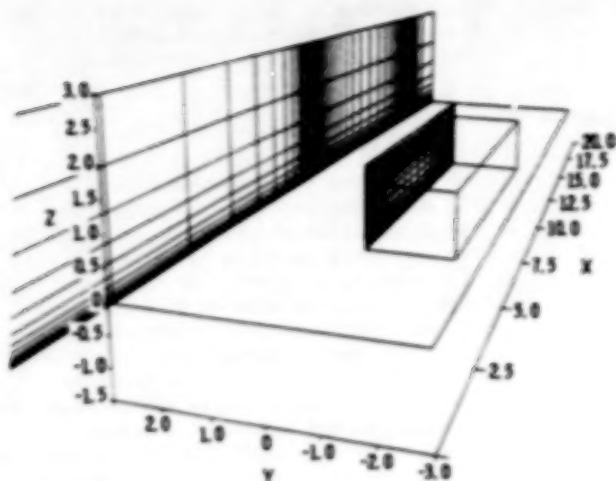
Figure 11. Composite mesh for a cavity flow.
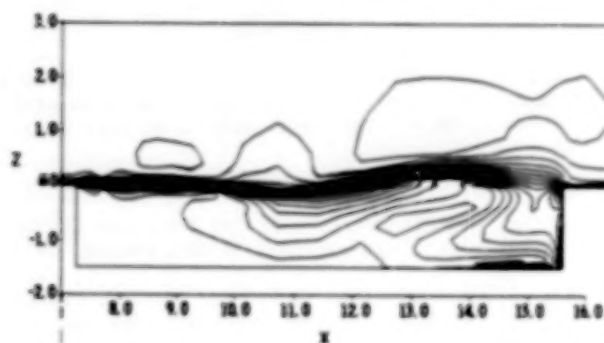
Figure 12. Symmetry plane Mach number contours, $M_\infty = 0.74$.
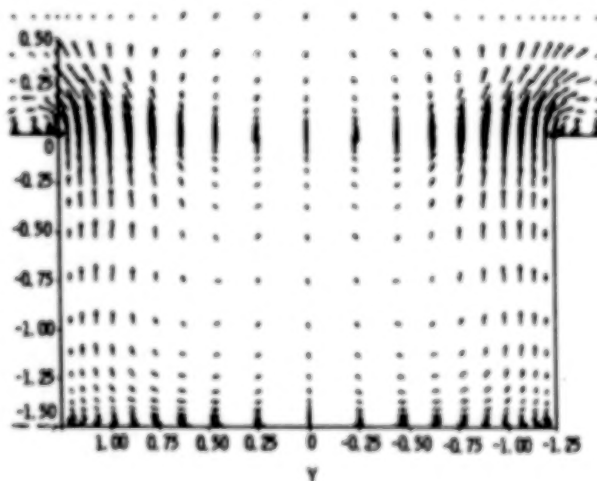
Figure 13. Cross flow vector vectors at center of cavity for $M_\infty = 0.74$.

The flow about a configuration of three bodies in close proximity was computed. Figures 14 and 15 show the structure of the composite grid. Seven component grids with 496,216 points represent the flow field. Each body has a single viscous grid and is embedded in a cylindrical mesh which has been segmented into three overlapping sections. A hemispherical mesh surrounds the entire configuration Figure 15 shows a projection of the grids onto the symmetry plane of the lower body in figure 14 and

illustrates the overlaps among the component grids. The composite mesh shows a range of grid interactions: patching among grids, e.g., G_2, G_3 and G_4, hole production by grids, e.g., G_5, G_6, G_7 in meshes G_2, G_3, and G_4, and holes crossing grid boundaries, e.g., G_5 across G_2, G_3, and G_4. Detailed comparisons of computations and experimental data at several transonic Mach numbers and angles of attack will be presented at the 8th AIAA Computational Fluid Dynamics meeting in June 1987.
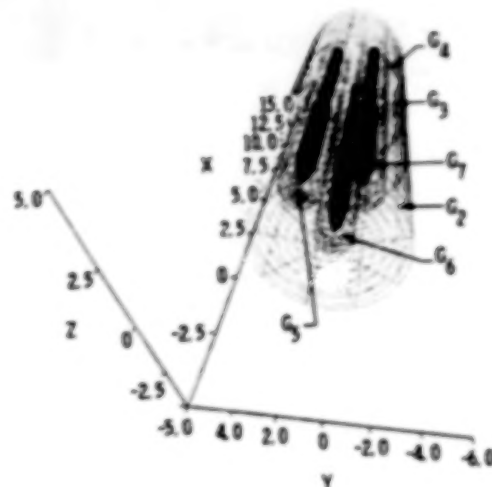
Figure 14. Multiple bodies in close proximity.
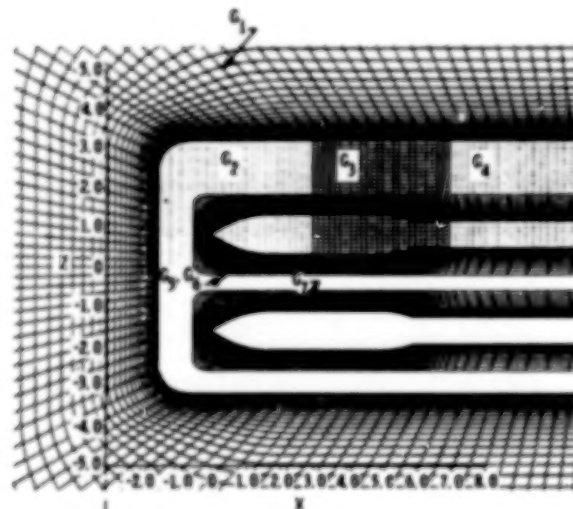
Figure 15. Projection of grids for multiple body configuration in symmetry plane of G_7.

The final example is the flow about a blunt-based projectile. The composite mesh shown in figure 16 consists of two "patched" grids containing a total of 68,000 points. This flow is being examined as part of a sting interference study. A comparison of computed and measured pressure coefficients [Kayser and Whiton (1982)] is given in figure 17 for the transonic flow conditions of $M_\infty = 0.91$ and $\alpha = 0$ deg. Comparisons of experimental and predicted values of base pressure are also in good agreement. Additional computations on similar configurations are being made.
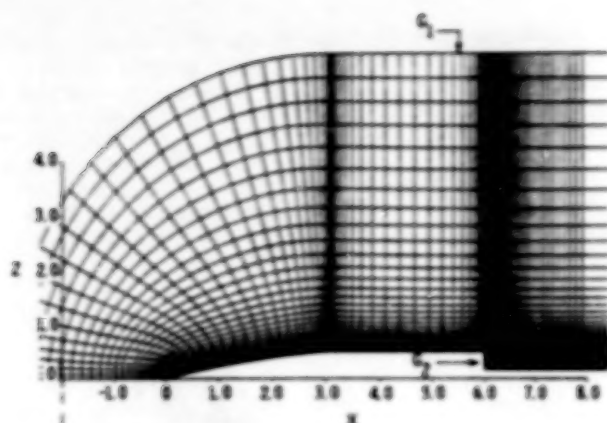
Figure 16. Composite mesh for blunt-based projectile.
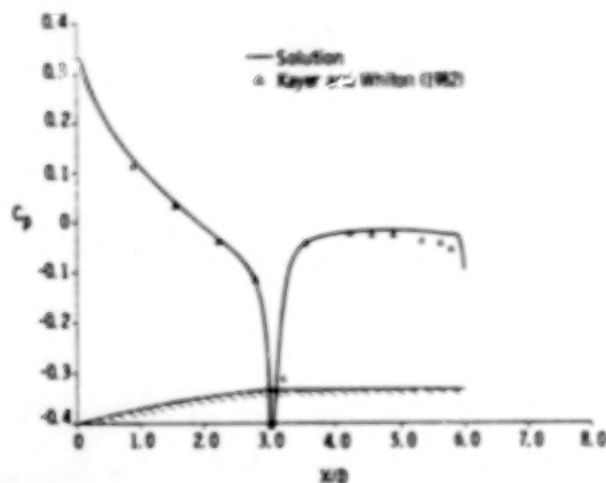
Figure 17. Comparison of computed and measured pressure coefficients for blunt-based projectile, $M_\infty = 0.91$, $\alpha = 0$ deg.

4.0 DISCUSSION

Sections 2 and 3 described our experience with the chimera scheme. However, there are several other aspects of its use that cannot be as clearly documented and several questions remain unanswered. Perhaps, the most significant change that was made from the two-dimensional (2-D) work reported by Benek et al. (1983) was a change from the mixed 2nd/4th-order accurate approximations of Pulliam and Steger (1978) to a consistently 2nd-order approximation. Large oscillations in the solution with the mixed-order scheme occurred when grid boundaries crossed high gradient regions. Switching to a 2nd-order scheme has eliminated this problem.

Another question that commonly arises involves the interpolation at grid boundaries. Is the boundary approximation conservative? Our experience indicates that the major factor affecting accuracy at the boundaries is the resolution between the grids in the neighborhood of the boundary. Whenever there is a "large" mismatch in resolution, convergence slows and large oscillations in the solution are evident near the interface. Should the mismatch occur where the interface crosses a high gradient

region, the situation is exacerbated. A more detailed and systematic study of this aspect of domain decomposition techniques is in order.

SUMMARY

We have described our experience with the chimera grid-embedding scheme. The method was applied to the computation of transonic wall interference with particular success and is being used routinely for support to testing at the AEDC. Experience with the viscous version is still being accumulated, but the potential to compute a wide range of flows has been demonstrated. Component grids have been generated by several two- and three-dimensional grid codes which employ algebraic and partial differential equations as generators. We experienced no difficulties combining grids constructed by the various methods into a composite mesh.

REFERENCES

Atta, E. H.; and Vadyak, J. A.: A Grid Interfacing Zonal Algorithm for Three-Dimensional Transonic Flows About Aircraft Configurations, AIAA Paper No. 82-1017, June 1982.

Baldwin, B. S.; and Lomax, H.: Thin Layer Approximation and Algebraic Model for Separated Turbulent Flows, AIAA Paper No. 78-257, January 1978.

Beam, R.; and Warming, R. F.: An Implicit Finite Difference Algorithm for Hyperbolic Systems in Conservation Law Form, Journal of Computational Physics, vol. 22, no. 1, September 1976, pp. 87-110.

Beam, R.; and Warming, R. F.: An Implicit Factored Scheme for Compressible Navier-Stokes Equations, AIAA Paper No. 77-645, June 1977.

Benek, J. A.; Steger, J. L.; and Dougherty, F. C.: A Flexible Grid Embedding Technique with Application to Euler Equations, AIAA Paper No. 83-1944, July 1983.

Benek, J. A.; Buning, P. G.; and Steger, J. L.: A 3-D Chimera Grid Embedding Technique, AIAA Paper No. 85-1523, July 1985.

Benek, J. A.; Steger, J. L.; Dougherty, F. C.; and Buning, P. G.: Chimera: A Grid Embedding Technique, AEDC-TR-85-64 (AD-A167466), April 1986.

Berger, M. J.: Adaptive Mesh Refinement for Hyperbolic Partial Differential Equations, Stanford University STAN-CS-82-924, August 1982.

Buning, P. G.; and Steger, J. L.: Graphics and Flow Visualization in Computational Fluid Dynamics, AIAA Paper No. 85-1507, July 1985.

Hessenius, K. A.; and Pulliam, T. H.: A Zonal Approach to Solutions of the Euler Equations, AIAA Paper 82-0969, June 1982.

Holst, T. L.; Kaynak, U.; Gundy, K. L.; Thomas, S.D.; Flores, J.; and Chaderjian, N. M.: Numerical Solution of Transonic Wing Flows Using an Euler/Navier-Stokes Zonal Approach, AIAA Paper No. 85-1640, July 1985.

Jameson, A.; Baker, T. J.; and Weatherhill, N. P.: Calculation of Inviscid Transonic Flow over a Complete Aircraft, AIAA Paper No. 86-103, January 1986.

Kayser, L. D.; and Whiton, F.: Surface Pressure Measurements on a Boattailed Projectile Shape at Transonic Speeds, U. S. Army Ballistic Research Laboratory, Aberdeen Proving Ground, Maryland, ARBRL-MR-03161, March 1982.

Kinsey, D. W.; and Barth, T. J.: Description of a Hyperbolic Grid Generating Procedure for Arbitrary Two-Dimensional Bodies, AFWAL TM 84-91, FIMM, July 1984.

Kraft, E. M.; Ritter, A.; and Laster, M. L.: Advances at AEDC in Treating Transonic Wind Tunnel Wall Interference, Presented at the 15th Congress, International Council of the Aeronautical Sciences, London, UK, September 1986.

Pulliam, T. H.; and Steger, J. L.: On Implicit Finite Difference Simulations of Three-Dimensional Flows, AIAA Paper No. 78-10, January 1978.

Rai, M. M.: A Conservative Treatment of Zonal Boundaries for Euler Equation Calculations, AIAA Paper 84-0164, January 1984.

Rubbert, P. E.; and Lee, K. D.: Patched Coordinate Systems, Numerical Grid Generation, J. F. Thompson, ed., North-Holland, New York, NY, 1982.

Shang, J. S.; and Scherr, S. J.: Navier-Stokes Solution of the Flow Field Around a Complete Aircraft, AIAA Paper 85-1509, July 1985.

Soni, B. K.: Two and Three-Dimensional Grid Generation for Internal Flow Applications of Computational Fluid Dynamics, AIAA Paper No. 85-1526, July 1985.

Sorenson, R. L.: A Computer Program to Generate Two-Dimensional Grids About Airfoils and Other Shapes by Use of Poisson's Equations, NASA TM 81198, May 1980.

Steger, J. L.; and Chaussee, D.: Generation of Body Fitted Coordinates Using Hyperbolic Partial Differential Equations, SIAM Journal on Scientific and Statistical Computing, vol. 1, December 1980, pp. 431-437.

Suhs, N. E.: Computational Estimates of Strut Support Interference at Transonic Mach Numbers, AIAA Paper No. 85-5018, October 1985.

Thompson, J. F., ed.: Numerical Grid Generation. North-Holland, New York, NY, 1982.

Thompson, J. F.: A Composite Grid Generation Code for General 3-D Regions, AIAA Paper No. 87-275 (to be published).

Venkatapathy, E.; and Lombard, C. K.: Flow Structure Capturing on Overset Patch Meshes, AIAA Paper No. 85-1690, July 1985.

Prof. Anthony Jameson
Princeton University

3-D Configurations--Inviscid

Paper not available

N87
26022
UNCLAS

NUMERICAL SOLUTION OF THE NAVIER-STOKES EQUATIONS
ABOUT THREE-DIMENSIONAL CONFIGURATIONS – A SURVEY

Terry L. Holst*

NASA Ames Research Center, Moffett Field, California

Abstract

The numerical solution of the Navier-Stokes equations about three-dimensional configurations is reviewed. Formulational and computational requirements for the various Navier-Stokes approaches are examined for typical problems including the viscous flow field solution about a complete aerospace vehicle. Recent computed results, with experimental comparisons when available, are presented to highlight the presentation. The future of Navier-Stokes applications in three-dimensions is seen to be rapidly expanding across a broad front including internal and external flows, and flows across the entire speed regime from incompressible to hypersonic applications. Prospects for the future are described and recommendations for areas of concentrated research are indicated.

Introduction

The fields of Computational Fluid Dynamics (CFD) and computer hardware design have been rapidly advancing over the last decade. It is now possible to demonstrate the importance of CFD in the field of aircraft design and performance prediction for general flow conditions including reasonably complete viscous effects. The problem of solving the Navier-Stokes equations about complex three-dimensional geometries has been undertaken and significant results have already been produced. The purpose of this paper is to review the current status of CFD applications in this area and to give prospects for the future especially for those applications involving complex geometries. Computational requirements for producing these results both now and in the future will be addressed.

The first pioneering calculations with the Navier-Stokes equations generally involved turbulent solutions with simple algebraic turbulence models (or laminar solutions with no turbulence models) in two dimensions with generally simple geometric shapes. These aspects were required to eliminate the complexity of turbulence and to reduce computational requirements to fit the computational facilities that existed in the early and mid 1970s. A good review of early work in this area is given by Peyret and Viviand.[1] Several years after the first two-dimensional Navier-Stokes solutions appeared, three-dimensional simulations were presented, again using algebraic turbulence models (or a laminar flow assumption) and simple geometries. Since then improvements in computers and algorithms have allowed tremendous advances in CFD across a broad front of different applications.

The rate of increase in the number and size of three-dimensional Navier-Stokes simulations is displayed in Fig.

* Chief, Applied Computational Fluids Branch.

1. This figure shows grid size for a representative sample of three-dimensional Navier-Stokes simulations plotted versus the year the results were published. Several observations are immediately obvious. The first three-dimensional simulations did not start appearing until the mid-1970's and since then the growth in both number and size of simulations has been almost exponential. This trend is due to improved algorithms, faster computers with larger main memories and to the availability of more computer time. The approximate cost of these computations can be inferred from Fig. 2 where the number of operations is plotted versus grid size. Note that the speed regime associated with each computation ranging from incompressible to hypersonic is also indicated. The solid line is an estimate of projected growth that appeared in Ref. 2 in 1983. This estimate was based on only the studies available in the pre-1983 time frame, and yet the curve represents a reasonably valid trend. Actually, the number of operations required to obtain a solution for the finer grids is somewhat underpredicted by this estimate. This is probably due to additional "stiffness" associated with finer grids and the fact that these solutions are newer and therefore probably less efficient.

This survey is divided into several sections listed as follows: CFD Formulations, where the major governing equations used in CFD are described with special emphasis on the Navier-Stokes formulation; Previous Survey Work, where past surveys are listed; Status of Navier-Stokes CFD, where Navier-Stokes CFD is surveyed including the areas of incompressible flow, transonic flow, supersonic/hypersonic flow and high-alpha/vortex-dominated flow; and Concluding Remarks. Because of the breadth associated with this review and the Navier-Stokes CFD
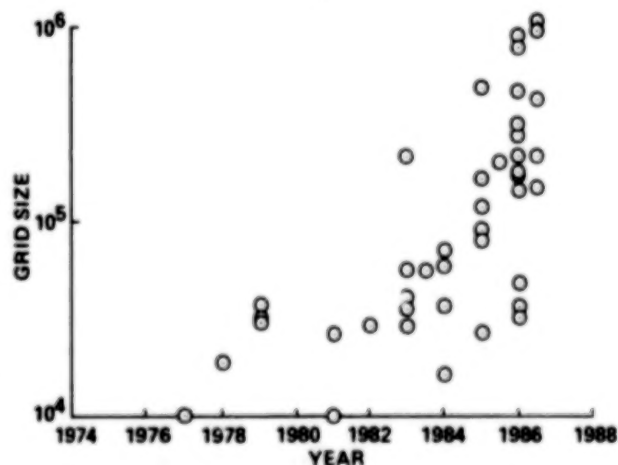

Fig. 1. Growth in the number and size of three-dimensional Navier-Stokes simulations using the time-asymptotic approach to obtain steady solutions.
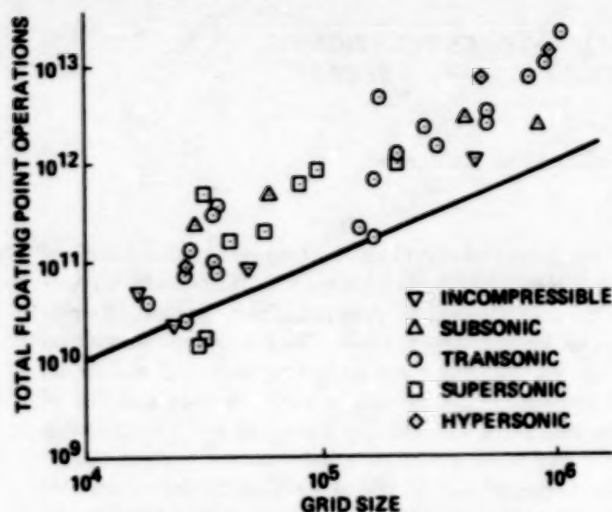
Fig. 2. Estimated floating-point operations required for a converged solution as a function of grid size for selected three-dimensional time-asymptotic RANS solutions.

Fig. 3. Computational Fluid Dynamics formulational ladder.

field in particular, no claim of completeness is made nor should one be assumed. The first item for discussion is how the Navier-Stokes formulation, and in particular, the Reynolds-Averaged Navier-Stokes (RANS) formulation, fits into all the other CFD formulations.

CFD Formulations

The aforementioned improvements in computer execution speed and main memory capacity achieved in the past several years has made it possible to dramatically expand the field of CFD. This has resulted in significant progress up the hierarchal "ladder" of CFD formulation complexity as shown in Fig. 3. Panel method solutions, which effectively solve the linear Laplace equation using the principle of superposition, have been studied thoroughly during the past three decades. As a result, panel method computer codes are well established within industry as efficient and reliable design tools for aircraft in the subsonic and supersonic speed regimes.

The next rung on the CFD formulational ladder is occupied by nonlinear potential formulations including the transonic small-disturbance and full potential equations. Both of these formulations have been extensively studied for the past 15 years and except for some grid generation limitations associated with complex geometry applications, these methods are well developed and heavily utilized within the aircraft industry design environment. Of course, these potential methods extend the range of applicability of CFD to the transonic speed regime and therefore have the capability of capturing weak shock waves and wave-drag levels. Appropriate reviews of this area can be found in Refs. 3 and 4.

The Euler equation formulation, which occupies the next rung on the CFD formulational ladder, is currently at the center of research in the Aerospace CFD community. New algorithms and applications in three dimensions
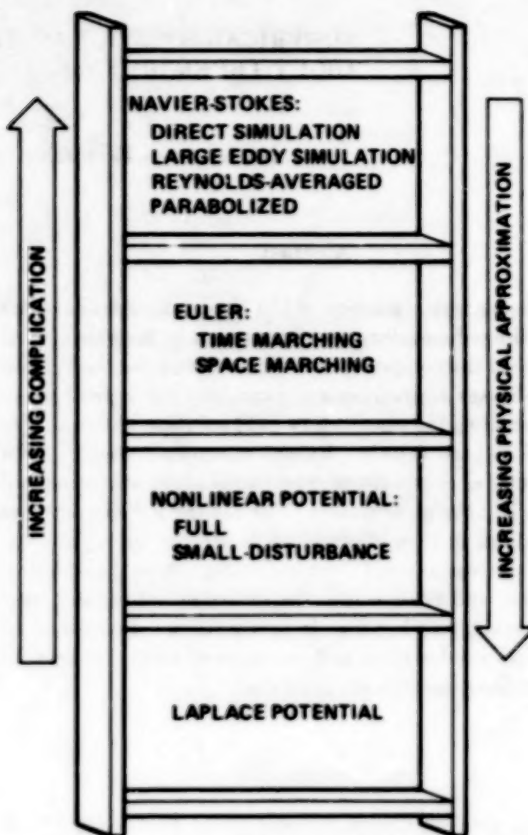
have proliferated at a very fast rate in the past five years. The various design groups within industry have already started using Euler codes for many applications but significant improvements in code and/or computer efficiency have to be realized before the Euler formulation will be used extensively. The Euler formulation provides better accuracy for strong shock calculations and has the ability to properly track vorticity gradients. These features are important for a variety of advanced flow field situations including vortical aerodynamic studies, strong shock calculations, high angle-of-attack leading-edge flow separation, high-speed blunt body problems, and blast wave studies.

The highest entry on the CFD formulational ladder is occupied by the Navier-Stokes equations. This formulation is the most complex and represents the smallest level of physical approximation. Like the Euler formulation, much work has been completed in the three-dimensional Navier-Stokes area during the past five years. However, the application of typical Navier-Stokes computer codes in the industry design environment has been slow to evolve. This is largely due to two reasons: First, the Navier-Stokes equations are several times more expensive to solve (at least) than the Euler equations. This is due to more terms in the Navier-Stokes equations; more grid points required to resolve a given problem, because in addition to the inviscid region, the boundary layer has to be resolved; and in separated flow cases, more iterations are required to achieve convergence because of the more complicated vis-

cous/inviscid interaction. The second major reason that the Navier-Stokes equations have not been used in design applications is due to the complications of turbulence. To discuss this subject a further breakdown of the Navier-Stokes formulation is required.

The Navier-Stokes equations intimately describe the motion of most fluid flow phenomena including large scale motions associated with the inviscid features of a flow field and small scale motions associated with turbulence. The numerical procedure which directly solves the Navier-Stokes equations and resolves all flow length scales including the smallest turbulent length scales is called direct simulation (DS). When the numerical grid resolution is not capable of resolving all length scales problems occur. Because for high Reynolds number flow the range of length scales is so immense, it is not currently possible to simulate this type of flow with schemes based on the DS approach. Thus, the first level of approximation to the Navier-Stokes equations, called Large Eddy Simulation (LES), is introduced. In the LES formulation the Navier-Stokes equations are solved on a grid which is capable of resolving all length scales except the smallest turbulent length scales. These length scales are associated with the smallest turbulent eddies in the flow field. Because these smallest eddies tend to be isotropic, they are easier to model than the larger eddies which tend to be random and can vary in nature for different flow conditions. A good review of the DS and LES areas is given in Ref. 5.

The LES formulation is still quite expensive and is restricted to problems with limited geometrical complexity and to moderate and low Reynolds numbers. This leads to the Reynolds-averaged Navier-Stokes (RANS) formulation where all turbulent eddies are modeled. The RANS formulation is derived by decomposing all dependent variables, e.g., density, pressure, and velocity components, into two parts, a mean part and an unsteady part. The unsteady part contains the unsteadiness due to high-frequency turbulent fluctuations and the mean part contains the average local flow value for that variable including any low-frequency time variation. After this variable decomposition process the resulting Navier-Stokes equations are time averaged over a time scale which is large in comparison with turbulent fluctuations but small in comparison with mean flow field unsteadiness. As a result of the time-averaging process, certain new terms arising from turbulent eddy correlations remain. These new terms account for the mean or average effect of turbulence and must be modeled. This allows the numerical solution of the Navier-Stokes equations for many applications involving realistic Reynolds numbers on grids that will fit on existing supercomputers.

One variation of the RANS equations first suggested by Baldwin and Lomax[6] and used in a variety of applications, is the so-called "thin-layer" formulation. This formulation requires a no-slip boundary surface to be aligned with a constant coordinate surface, which is a typical facet in most applications. The thin-layer formulation is obtained by dropping all viscous terms containing transverse spatial derivatives. The justification for this assumption is that these terms are typically small in most regions of flow and that in regions where they are potentially large, for example, near separation, grid resolution is not generally adequate to resolve them. In addition, numerical experimentation using both the full and thin-layer forms has shown little or no difference in the computed results, and the thin-layer formulation is approximately 30% cheaper. It should be stressed that although the thin-layer Navier-Stokes assumptions are similar to certain classical boundary layer assumptions, the resulting equations are quite different. All time terms are retained, that is, the thin-layer Navier-Stokes equations are still hyperbolic, while the boundary layer equations are parabolic. Thus, the thin-layer Navier-Stokes formulation has no numerical difficulty with either streamwise or cross-flow separations.

The last Navier-Stokes formulation discussed here is the Parabolized Navier-Stokes (PNS) formulation. This formulation is derived from the RANS equations and therefore requires the modeling of all turbulent length scales. The PNS approach also requires the flow to be supersonic in the streamwise direction (although under certain conditions when the pressure field is specified the freestream can be subsonic) and that there be no streamwise separations in the boundary layer. In addition, all time-dependent terms and streamwise diffusion terms are neglected. Under these assumptions the Navier-Stokes equations become parabolic in the streamwise direction and can be solved numerically using a space-marching procedure instead of the standard time-asymptotic approach. Thus, the computer requirements (both memory and cpu time) are much less demanding for the PNS approach relative to the time-dependent approach.

A comparison of the estimated memory and execution time requirements for several different formulations is given in Fig. 4. An additional horizontal scale indicates the amount of execution time required by a theoretical gigaflop computer, which should be available in the near-term future. This figure was constructed from information given in Refs. 7-11. The Euler formulation and three of the Navier-Stokes formulations just discussed (DS, LES, and RANS) are all included. Note that several variations of the RANS formulation (steady ideal gas, steady nonequilibrium real gas, and unsteady ideal gas) are presented. Including nonequilibrium real gas effects associated with hypersonic flight or the unsteadiness effects associated with (for example) high-alpha flight, may increase the computational costs of a typical steady RANS calculation by an order of magnitude. This additional expense while prohibitive today may not be prohibitive in the near-term future.

The prospects of computing three-dimensional flows at realistic flight Reynolds numbers using the LES formulation in the near future do not seem bright. As indicated in Fig. 4 the cpu time for such a calculation on a theoretical gigaflop computer would be on the order of one month. The DS picture is even more dismal with cpu times for a single three-dimensional calculation requiring on the order
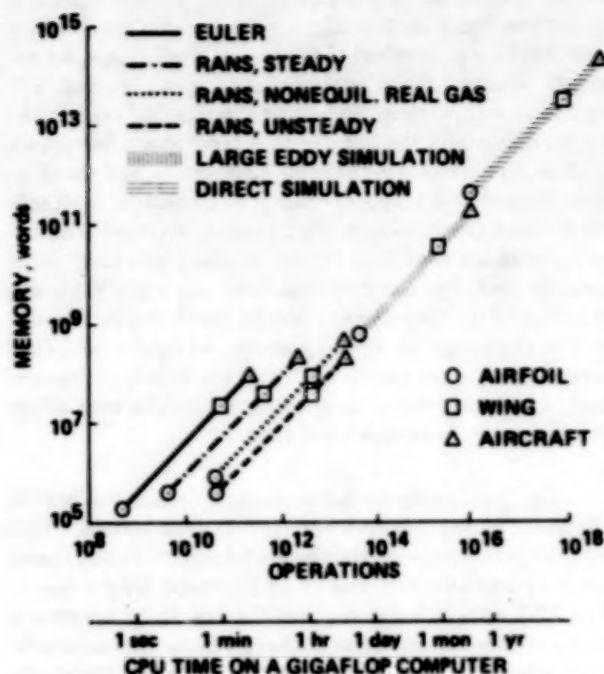
Fig. 4. Estimated memory and execution time requirements for several different CFD formulations.

of years. Hence, it seems that the most appropriate Navier-Stokes formulations for attention in the area of applications involving realistic Reynolds numbers and reasonably complex geometries, are the time-dependent RANS and PNS formulations. The remainder of this survey will be solely devoted to these areas with primary emphasis on the time-dependent RANS formulation. For an indepth technical discussion of most of the CFD formulations just discussed, the interested reader is referred to Ref. 12.

Previous Survey Work

Several interesting surveys on the subject of Computational Aerodynamics have been produced recently. Two particularly important articles are from Chapman[11,13] where the entire field of Computational Aerodynamics is reviewed; pacing items including turbulence modeling, three-dimensional grid generation, algorithm development, and computer speed limitations are discussed in detail; and computational requirements and projected computer capabilities are examined. More recent surveys along the same line are by Kutler.[10,14] The same critical pacing items are examined and updated.

Other pertinent reviews in the area of CFD are by Shang[15] where the RANS formulation is discussed for various geometric applications, Mehta and Lomax[16] where the RANS formulation for transonic flow is discussed with special emphasis on algorithmic details and aspects of turbulent physics, Chaussee[17] where the PNS approach is described with special emphasis on applications, Orszag and Israeli[18] where early work associated with the solution of the incompressible Navier-Stokes equations is reviewed, and Turkel[19] where computational physics is re-viewed with emphasis on algorithms and convergence acceleration. Additional areas related to the numerical solution of the Navier-Stokes equations are grid generation, which is reviewed in detail by Thompson,[20] and turbulence modeling, which is described with particular emphasis on three-dimensional flows involving curvature, separation, and vorticies, by Lakshminarayana.[21]

An important aspect associated with CFD research is the area of experimental fluids research. A good review in this area is given by Marvin[22] where CFD code verification experiments are described and in Ref. 2 where the projected influence of CFD on experimental facilities is discussed. Of course, the influence of the experimental world on CFD has been profound. The opposite is also true, CFD has begun to influence the experimental world as well. The CFD field has generated the need to conduct a whole new series of experiments to validate CFD code results.[22] These experiments generally take advantage of the latest developments in sophisticated measurement techniques and generally get more involved with fundamental flow phenomena. Having intimate CFD/experimental interaction is an important feature and must remain as an essential ingredient in CFD research, especially in areas involving unexplained flow phenomena such as shock-induced or angle-of-attack induced flow separation.

Before proceeding with the main emphasis of this review, an additional statement regarding experimental validation of numerical solutions is in order. A typical steady three-dimensional Navier-Stokes solution produced today consists of 100,000-200,000 grid points each with 5 dependent variables resulting in a total data base of perhaps one million words for each set of free-stream conditions. Corresponding experimental data bases, not counting qualitative flow visualization results, generally consist of perhaps only a few hundred data points for each set of free-stream conditions. These data are usually in the form of surface pressures. This general lack of extensive data, including interior flow field data, makes thorough validation of CFD results difficult. If the experimental and computational surface pressures agree, this by no means requires other aspects of the flow field to agree. If the surface pressures disagree, the physical reasons for this disagreement are usually not apparent. Thus, it is imperative that sufficient detail associated with CFD validation experiments be obtained to fully evaluate numerical results and to provide the maximum understanding of basic fluid flow phenomena.

Status of RANS/PNS CFD

This survey is divided into several different areas of application as follows: incompressible flow, transonic flow, supersonic/hypersonic flow, and high-alpha/vortex-dominated flow. The first two areas will be limited to time-dependent RANS applications and the latter two will include both time-dependent RANS and PNS applications. All the research surveyed will be restricted to three spatial dimensions and most of the applications will be associated with steady flow. First, the discussion centers on

the numerical solution of the Navier-Stokes equations for incompressible flow.

Incompressible Flow Applications

Numerical solution of the incompressible Navier-Stokes (INS) equations in three dimensions has received much attention during the past several years. In the study of incompressible flow algorithms, it is interesting to study compressible algorithms and the connections between the two fields. The overwhelming majority of all steady compressible algorithms applied to flows that are partially or totally subsonic outside the boundary layer, utilize a time-accurate or time-like iteration to asymptotically approach steady-state solutions with increasing time. The application of this approach to incompressible problems is difficult because of the basic difference in incompressible and compressible continuity equations. The incompressible continuity equation is the familiar condition that requires the divergence of the velocity vector to vanish. Thus, there is no time-dependent term as with the compressible continuity equation. Also associated with this problem is the lack of an explicit relation for the pressure. These two features cause the primary difference between incompressible and compressible algorithms. Note: Certain two-dimensional algorithms, for example, stream-function/vorticity schemes, deal with these difficulties quite nicely but are difficult to extend to three dimensions, and therefore, will not be discussed further.

Early numerical work in the incompressible flow area was presented by Harlow and Welch,[23] Chorin,[24] and Patankar and Spalding[25] where three basically different approaches were presented. In the first approach, a Poisson equation for the pressure was derived by taking the divergence of the momentum equation. This equation is then solved iteratively using the velocity field at time level n to predict the pressure such that the continuity equation is satisfied at time level n+1. This process is time accurate and can be continued until a steady-state solution is reached. Needless to say, because of the additional iteration required to solve the pressure Poisson equation, this method is computationally expensive.

In the second approach, the method of artificial compressibility was introduced. An artificial time-dependent pressure term is added to the steady continuity equation which allows the resulting equations to be solved using standard time-dependent compressible algorithms. As the solution converges, the time-dependent pressure term is driven to zero and the flow approaches the incompressible limit. In the last approach, a space marching procedure was developed by reducing the incompressible Navier-Stokes equations to a set of parabolic equations. The pressures are determined by first computing the velocities from estimated pressures, then a correction is applied to the pressure so as to satisfy the continuity equation. Of course, the latter approach does not work successfully if streamwise flow separation occurs.

More recent work in the area of INS solvers has been presented in Refs. 26-32 where three-dimensional ducts with curvature were considered for a wide variety of flow conditions, Himeno et al.[33] where the wake structure downstream of various bluff bodies was computed using the INS method described by Kawamura and Kuwahara,[34] Kwak et al.[35] where a variety of applications were reported including a rectangular duct flow with a 45 deg bend, Gorski et al.[36] where turbulent corner flows were presented using two different turbulence models, and Refs. 37-41 where various internal elements of the Space Shuttle Main Engine were analyzed. The algorithm used in Refs. 37-41 was the method of pseduo compressibility devised by Chang and Kwak.[42] This method is similar to Chorin's artificial compressibility method and is an outgrowth of the work of Steger and Kutler.[43] A recent upgrade to this algorithm was presented by Rogers et al.[44] where the original block-matrix ADI algorithm has been diagonalized to yield a scalar-matrix ADI algorithm which is about three times faster.

A typical incompressible flow result showing particle traces downstream of a circular-cylinder post mounted on a flat plate is displayed in Fig. 5 (taken from Ref. 40). This calculation is laminar with a Reynolds number of 1000. Note the formation of a saddle point of separation forward of the post and a horseshoe vortex downstream of the post. The secondary flow in front of the post wraps around the post and forms a "tornado-like" vortical flow in the wake of the post, which is strikingly different than the flow downstream of a simple post in the absence of the flat plate. An oil-flow photograph appearing in Ref. 40 provides qualitative validation for this type of vortical wake flow.
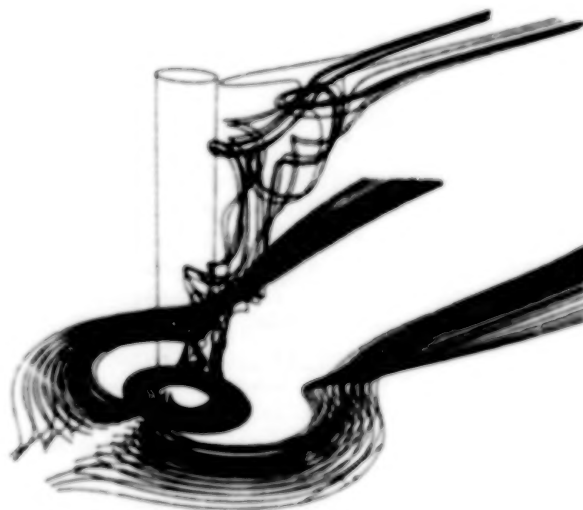

Fig. 5. Computed three-dimensional particle paths around and downstream of a circular-cylinder post mounted on a flat plate, incompressible flow, $Re = 1000$, Kwak et al.[40]

Transonic Flow Applications

The transonic flow area has perhaps received the widest attention during the past five years in the three-dimensional RANS research community. In this area there are a whole host of unsolved and interesting research topics that have practical applications for both commercial and military circles. A few of these include shock/boundary-layer interation including boundary-layer separation effects, wing/fuselage interference, performance prediction especially drag prediction, afterbody boundary-layer separation, and helicopter rotor-tip transonic performance.

Literally all transonic numerical methods for the Navier-Stokes equations utilize time-dependent formulations to obtain steady-state solutions asymptotically with increasing time. The time-integration algorithms used to implement this strategy vary from application to application. Most schemes utilize implicit methods, for example, the Beam-Warming,[45] Briley-McDonald,[46] or MacCormack[47] methods, or algorithms with suitable convergence acceleration, for example, multigrid. This theoretically allows large time steps to be taken, and therefore, provides rapid approach to the desired asymptotic solution. This philosophy works well but requires several hundred to several thousand iterations to produce acceptable levels of "convergence." The number of iterations generally increases as the mesh is refined and as the physics of the problem becomes more difficult, that is, stronger shock waves, larger separations, etc. Time-step limitations due to nonlinear numerical instabilities are common. This allows explicit time-integration methods, for example, MacCormack,[48] which generally have quite severe time-step limitations but which are cheaper per iteration and easier to code, to be appropriate alternatives for some applications.

The problem which has received the most attention in the transonic flow area is wing flow-field prediction. The first calculation of this type was presented by Mansour[49] where the RANS formulation was solved for the flow field about "Wing C" (defined in Ref. 50). The numerical scheme used in this study was a fully-implicit, ADI-like scheme developed by Beam and Warming[45] and Briley and McDonald[46] and first demonstrated in three dimensions by Pulliam and Steger.[51] The grid used in this study, while having an efficient topology, was coarse and produced only fair agreement with experiment. Another simil calcula-tion for transonic wing geometries was presented by Agar-wal and Deese.[52] In this study the explicit Runge-Kutta scheme of Jameson et al.[53] was extended to handle the RANS equations for the transonic flow about the ONERA-M6 wing (defined in Ref. 54). The grid was again coarse, but for the simple calculations reported (attached and non-lifting), the experimental/computational agreement was good.

More recent transonic RANS calculations for wing geometries have been given by Holst et al.,[55] Flores,[56] Kaynak et al.,[57,58] and Srinivasan et al.[59] These studies have utilized a computer program called TNS (Transonic Navier-Stokes) which uses the diagonalized-implicit algorithm of Pulliam and Chaussee[60] coupled with a zonal grid

arrangement to solve the thin-layer form of the RANS equations. In addition, the Baldwin-Lomax turbulence model[6] was used in each case. In the TNS approach for grid zones near the wing surface, the RANS equations are solved and for zones away from the wing surface, where viscous terms are not important, the Euler equations are solved. In Holst et al.[55] solutions are presented for a low-aspect-ratio wing derived from the NACA 0012 airfoil section. Comparisons with the experimental data of Lock-man and Seegmiller[61] for this wing at various transonic flow conditions including cases with shock/boundary-layer separation are presented and discussed. A significant aspect of this set of calculations is that the wind tunnel walls are very important and must be modeled to obtain good agreement with experiment. Generally good agreement was obtained when the walls were modeled and the flow was attached. For separated cases the agreement was not good, and this was attributed to the lack of proper grid refinement and inappropriate turbulence modeling.

Computed pressures produced by Kaynak et al.[57,58] for the previously discussed Wing C geometry are compared with experimental results from two sources, Hinson and Burdges[50] and Keener,[62,63] in Fig. 6. The free-stream Mach number for this set of results is 0.85, the angle of attack is 5 deg, and the Reynolds number is 8 million. The computed and experimental results are in good agreement; as much scatter between the two experimental results exists as between the computed and experimental results. Figure 7 shows the computed particle paths on the wing surface for the same case. Note the small shock-induced separation near the wing tip which is generally in good agreement with the corresponding experimentally produced oil flow pattern. Detailed computational/experimental comparisons for other cases are also presented in Kaynak et al.[57,58]

The computed results presented by Srinivasan et al.[59] also deal with the Wing C geometry as well as various helicopter rotor geometries. The main emphasis in this study is on tip vortex formation. With this purpose in mind special grid clustering at the wing tip was used. Computed particle paths on the surface of an ONERA wing designed to represent a typical helicopter rotor blade, are shown in Fig. 8. For this calculation the free-stream Mach number was 0.85, the angle of attack was 5 deg, and the Reynolds number was 8.5 million. A strong transonic shock wave near mid chord causes a large region of separated flow as shown in Fig. 8. An outward spiralling vortex emanates from the separated flow region near the tip. This can be seen in Figs. 9 and 10, which show standard and close-up views, respectively, of computed three-dimensional parti-cle paths about the tip. As explained by Srinivasan et al.,[59] the cross flow created by the tip sweep enables the fluid particles released in the vincinity of the tip to first braid and then roll up and lift off of the surface.

Other notable transonic wing calculations are pre-sented by Obayashi and Fujii[64] and Fujii and Obayashi.[65] In the later case high-aspect-ratio transport-type-wing flow fields are obtained using a new LU-ADI algorithm. This algorithm utilizes the flux vector splitting techniqu
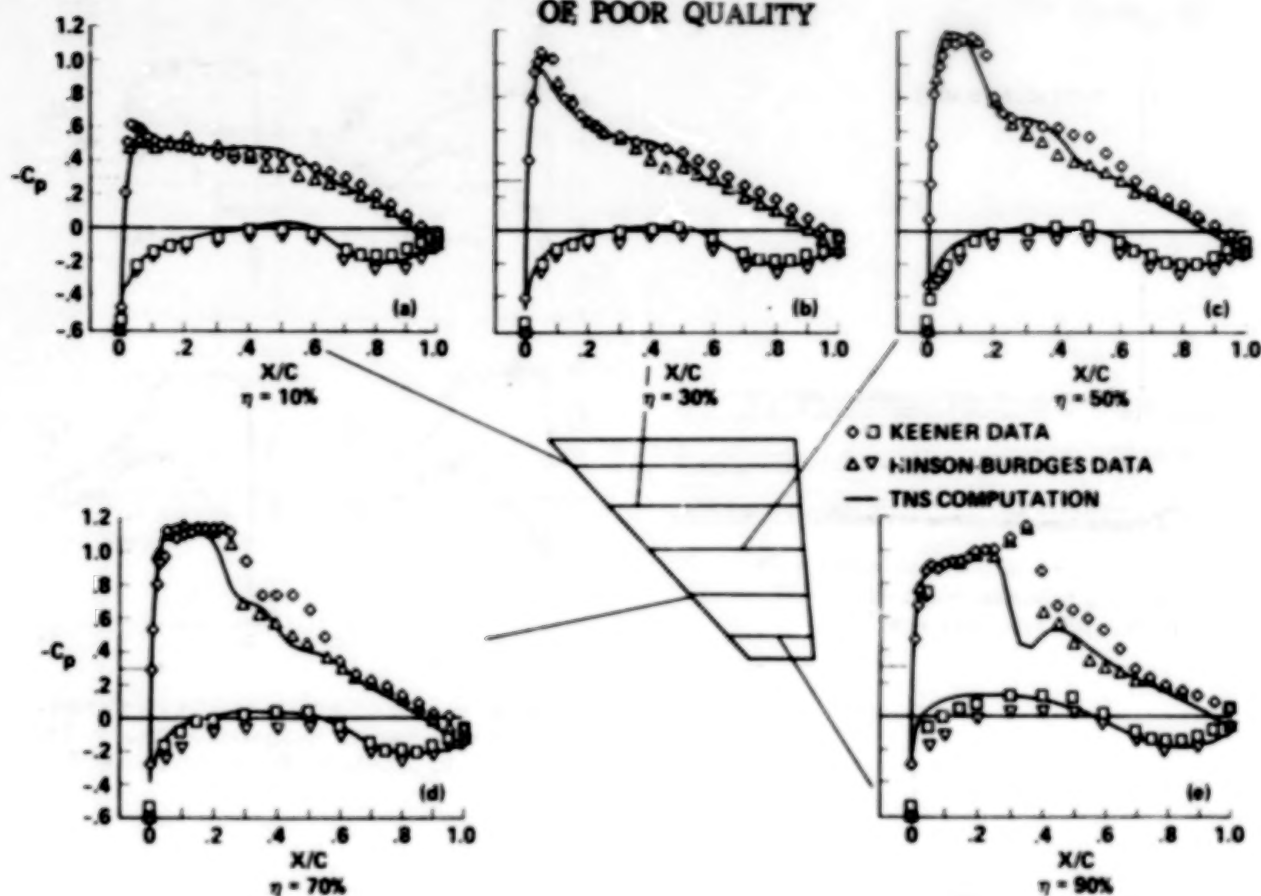
Fig. 6. Pressure coefficient comparisons for the "Wing C" geometry, $M_\infty = 0.85$, $\alpha = 5°$, $Re = 8 \times 10^6$, Kaynak et al.[58]
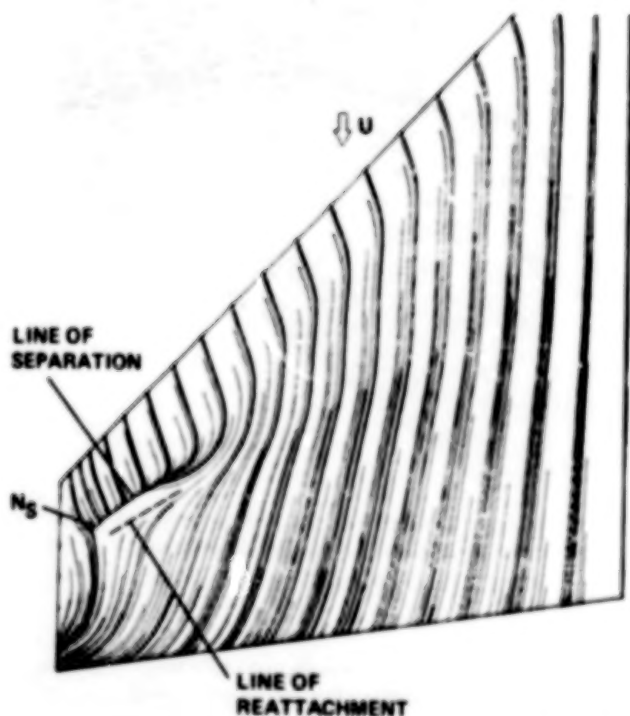

Fig. 7. Computed surface particle paths for the "Wing C" geometry, $M_\infty = 0.85$, $\alpha = 5°$, $Re = 8 \times 10^6$, Kaynak et al.[58]
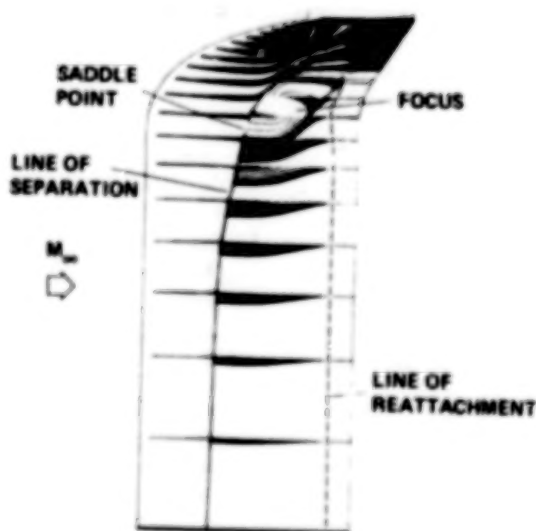

Fig. 8. Computed surface particle paths for a swept-tip helicopter blade, $M_\infty = 0.85$, $\alpha = 5°$, $Re = 8.5 \times 10^6$, Srinivasan et al.[59]

PARTICLE TRACES

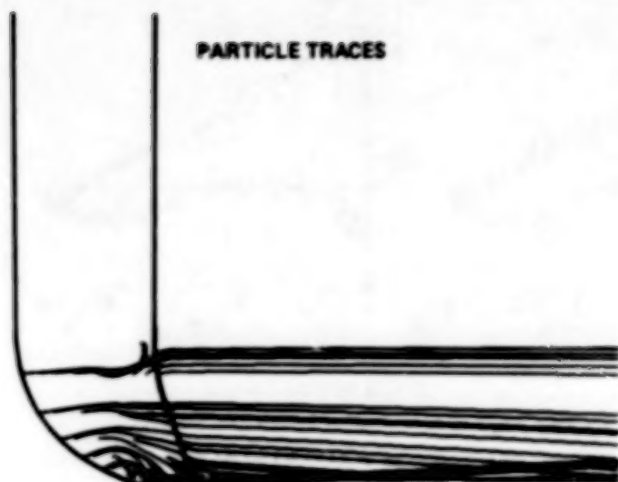Fig. 9. Computed three-dimensional particle paths around a swept-tip helicopter blade, $M_\infty = 0.85$, $\alpha = 5°$, $Re = 8.5\times10^6$, Srinivasan et al.[59]

Fig. 11. Pressure coefficient comparisons for a high-aspect-ratio wing/fuselage configuration, $M_\infty = 0.82$, $\alpha = 4°$, $Re = 1.67\times10^6$, Fujii and Obayashi.[68]

Fig. 10. Blow-up view of Fig. 9 showing tip flow-field detail, Srinivasan et al.[59]

of Steger and Warming[66] and the diagonally dominate factorization of Lombard et al.[67] to decompose the usual block tridiagonal system into the product of lower and upper scalar bidiagonal matricies. In this study flow fields with strong shock/boundary-layer interation and the resulting massive boundary layer separation are computed for a series of cases. Good correlations with experimentally measured pressures are presented.

The LU-ADI transonic wing method just discussed has also been extended to handle wing/fuselage geometries by Fujii and Obayashi.[68] A typical result from this study is shown in Figs. 11 and 12. This case invloves a high-aspect-ratio wing low-mounted on a transport-type fuselage. The Mach number, angle of attack, and Reynolds number for this solution are 0.82, 4.0 deg, and 1.67 million, respectively. Computed and experimental pressure distributions are compared in Fig. 11 and computed surface particle paths are shown in Fig. 12. Note the shock-induced sepa-

Fig. 12. Computed surface particle paths for a high-aspect-ratio wing-fuselage configuration, $M_\infty = 0.82$, $\alpha = 4°$, $Re = 1.67\times10^6$, Fujii and Obayashi.[68]

ration at about mid chord and the wing-fuselage/juncture separation which is highlighted by a large spiral node on the aft-wing-root surface. This set of calculations is also quite unique due to the level of grid refinement used. For these calculations a grid of 119 x 71 x 92 = 777,308 points was used and represents the finest RANS grid with a published solution to date.

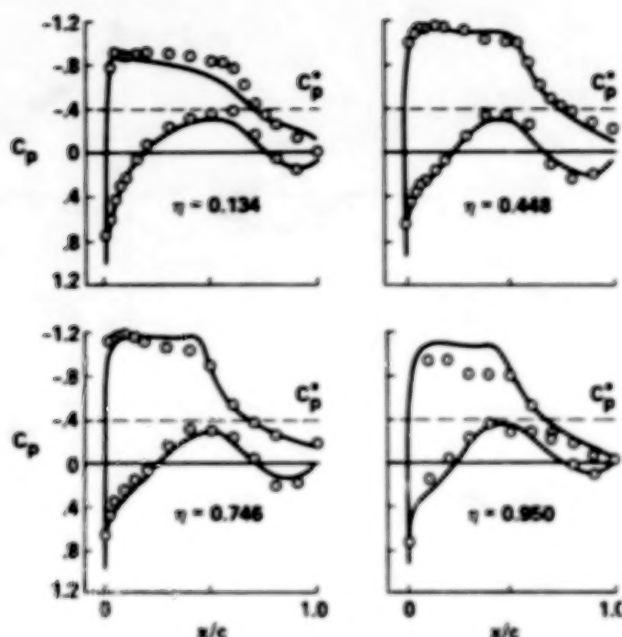Additional RANS calculations have been published for a wide variety of other types of transonic applications. These studies include the simulation of nacelle/inlet flow fields by Vadyak,[69] calculations through swept-blade cascades by Swisshelm and Johnson,[70] the simulation of forebody flow fields by Chaussee et al.[71] and Cosner,[72] the simulation of three-dimensional boattail afterbody flows by Deiwert,[73] and computations to determine the wake structure downstream of a three-dimensional turret by Purohit et al.[74,75] Another area with a lot of RANS research activity is transonic projectile aerodynamics. In this field the prediction of lift, drag, and magnus forces is very important and is intimately related to viscous effects. Interesting studies in this area include Nietubicz et al.[76] where the Magnus forces associated with a spinning projectile were first computed, Nietubicz et al.[77] where detailed computations to predict various aerodynamic coefficients were presented, and Sahu et al.[78] where the projectile base flow field was computed at transonic speeds. This group of studies, ranging from inlets to projectiles, used a variety of different integration schemes ranging from the classical explicit MacCormack[48] scheme to all types of implicit and multigrid schemes. The turbulence models used are largely dominated by the Baldwin-Lomax model[8] with all of the models being in the algebraic category. The more complicated one- and two-equation models have not generally found their way into three-dimensional transonic Navier-Stokes applications.

Supersonic/Hypersonic Flow Applications

Supersonic flow field solutions are somewhat easier to obtain relative to transonic flow fields. This is because the physics of supersonic flow typically allows smaller computational domains, the supersonic equation type is consistently hyperbolic (at least for inviscid regions) while for transonic flows the type is mixed between hyperbolic and elliptic, and the shock/boundary-layer interactions associated with supersonic flows are not as complicated as those associated with transonic flows. In addition, as already discussed, the supersonic free-stream characteristic allows the introduction of marching algorithms, that is, the PNS formulation. Hypersonic flows, while enjoying the same advantages of supersonic flow, contain other complications that even today have not been fully evaluated. These include more complicated transition and turbulence physics, real gas effects, merged shock and boundary layers, stronger shock waves, and radiation effects.

The field of supersonic CFD utilizing both the time-dependent Navier-Stokes and PNS formulations for computing three-dimensional applications has been widely researched in the past 6-8 years. Early pioneering Navier-Stokes calculations in this area include Li[79] where laminar flow separation on blunt flared cones at angle of attack was studied, Holst and Tannehill[80] where viscous blunt body flows with an impinging shock were studied, Shang and Hankey[81] and Hung and MacCormack[82] where the flow in a three-dimensional compression corner was solved, Hung[83] where the flow over an inclined body of revolution was obtained, Hung[84] where the impingement of an oblique shock wave on a cylinder was investigated, Knight[85] and Hung and MacCormack[86] where an oblique-shock/boundary-layer interaction flow field was simulated, and Hung and Kordulla[87] and Hung and Buning[88] where the flow about a blunt-fin/flat-plate interaction was computed. The Mach number for these calculations ranged from low supersonic to hypersonic with the maximum being 12.5. About half of the calculations, especially the earlier ones, were laminar, and the other half were turbulent with a variation of the Baldwin-Lomax turbulence model used in all cases.

As seen in the previous examples, turbulence modeling associated with the three-dimensional RANS formulation has not reached a very sophisticated level. For attached flow cases, existing algebraic, or "zero-equation" models as they are formally called, seem to do a good job for a wide variety of circumstances. When the flow experiences moderate or massive separation, these models do a poor job. For example, the most commonly used turbulence model is the Baldwin-Lomax model, which tends to underpredict the level and height of reversed flow in separation regions. This is probably due to an effective overprediction of dissipation in regions of separated flow. More sophisticated models of the so-called one- or two-equation variety seem to improve the correlation in some cases while making it worse in others. Two difficulties associated with their use are additional complication, that is, new differential equations have to be solved, and additional numerical stiffness which causes the need for more flow solver iterations. Because of this lack of a clear direction and because of the additional complication, movement to use these more sophisticated turbulence models in three-dimensional applications has been slow.

Additional supersonic Navier-Stokes calculations are given by Horstman et al.[89] for swept compression corners and axisymmetric bodies with either skewed or segmented conical flares; Horstman[90] for swept compression corner flows; and Knight,[91] Knight et al.,[92] and Horstman[93] for swept-shock-wave/boundary-layer interaction studies. All of these three-dimensional computations involved Mach 3 flows with significant shock-induced boundary layer separation. In addition, most of these studies utilize some form of the more sophisticated two-equation k-ϵ eddy-viscosity turbulence model. In Ref. 92 computations with both the Baldwin-Lomax algebraic model and the Jones-Launder[94] two-equation model were performed. The Jones-Launder computations also utilized Viegas-Rubesin[95] wall function boundary conditions which permit the use of coarse grids in the lower portion of the boundary layer. This reduces the amount of computer time required for a converged solution. Results from Ref. 92 indicate that, at least for the swept-shock/boundary-layer interaction flows studied, the overall structure of the three-dimensional flow was insensitive to the turbulence model, except within a small portion of the boundary layer near the surface.

The difficulties associated with obtaining good turbulence models for complex applications exists for all speed regimes. However, the problems associated with the hypersonic flow regime are the most severe. At hypersonic

speeds certain incompressible flow assumptions used in formulating turbulence models, which are still valid up to Mach numbers of about 5, start to break down. In addition, hypersonic flows, especially for Mach numbers well above 10, will have chemical reactions which may interact with the turbulence. For moderate to high altitudes, hypersonic flows will be transitional, further complicating the situation. It is clear that much work in the area of turbulence modeling in general, and for the hypersonic regime in particular, will be required in the near future.

Flow field computations about more complicated geometries have been explored in the supersonic/hypersonic flow regime. Examples of time-dependent RANS calculations in this area include Shang[96,97] where the hypersonic wing-fuselage interference problem was studied with two different grid topologies, Kumar[98] where the supersonic flow upstream and through a two-strut scramjet inlet was computed, Howlett and Hunter[99] where the supersonic flow around and inside an inlet with spiked centerbody was simulated, Rizk and Ben-Shmuel[100] where the low-supersonic flow field about the space shuttle orbiter was investigated, and Li[101] where the hypersonic flow about an aerobrake body was considered. Another significant study in this area is the work of Shang and Scherr.[102] In this paper the entire flow field over the X-24C Lifting Body at a Mach number of 5.95, an angle of attack of 6 deg, and a Reynolds number of 16.4 million/m was obtained with a time-dependent RANS approach. The computational grid was extremely fine, consisting of 475,200 points, and represented the finest-grid RANS solution published up to 1985. The explicit MacCormack numerical scheme was used and the turbulence was modeled with the Baldwin-Lomax model. A typical set of results from Ref. 102 is shown in Figs. 13-15. Figure 13 shows the surface streamline pattern over the lifting body and demonstrates the level of complication that can be captured with the RANS approach when fine grids are used. Pressure distributions are compared with experiment in Figs. 14 and 15. Figure 14 shows comparisons over the fore part of the lifting body and Fig. 15 comparisons over the aft part. For all stations the agreement is excellent.

An additional complex-geometry study performed by Deiwert and Rothmund[103] involved the computation of flow about a three-dimensional body of revolution at angle of attack. This configuration consisted of a cone-cylinder forebody with a conical afterbody and contained a centered, supersonic propulsive jet. Surface streamlines on the afterbody and density contours on the bilateral plane of symmetry are displayed in Fig. 16. For this computation the free-stream Mach number was 2.0, the jet exit Mach number was 2.5, the angle of attack was 5 deg, and the jet-to-free-stream pressure ratio was 3.0. The flow was turbulent with a Reynolds number based on cylinder diameter of 1.5 million, and turbulence was modeled with the Baldwin-Lomax model. This particular set of calculations is unique because of the complex data-base handling scheme utilized. The total data base associated with the 216,000 point grid was about 5 million words and was divided into a series of blocks each consisting of 8000 grid points. Manipulations of these blocks were performed us-
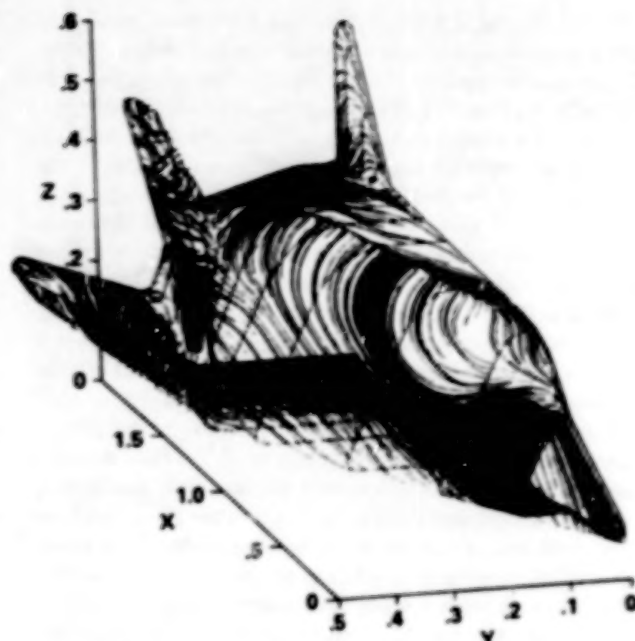
Fig. 13. Computed surface streamlines over the X-24C Lifting Body, $M_\infty = 5.95$, $\alpha = 6°$, $Re/m = 16.4$ x10^6, Shang and Scherr.[102]
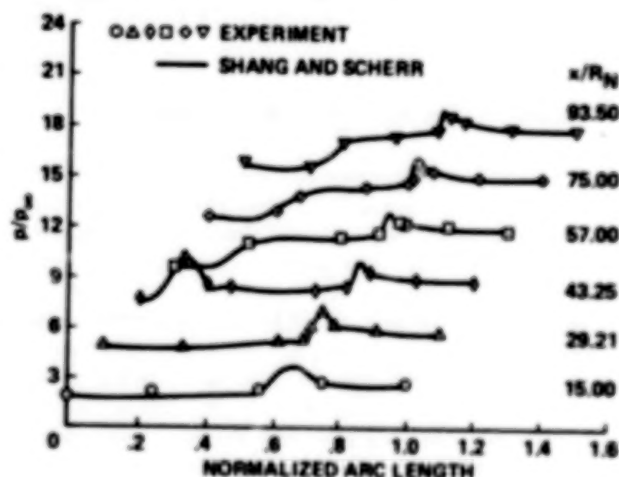
Fig. 14. Forebody pressure comparisons for the solution of Fig. 13, Shang and Scherr.[102]

ing the block data-base handling scheme described by Pulliam and Lomax.[104] With this approach very large grids were accomodated on a computer with a limited main memory for a flow field of considerable complexity.

The level of geometric complication, exhibited by the results from the preceeding paragraph and the section on transonic flow, has advanced rapidly during the past several years. However, a significant amount of work still remains. This area, along with turbulence modeling, was identified by Chapman[11,12] as one of the chief items pacing further development of computational aerodynamics. The key feature required to mature this area for three-dimensional applications is automation. Elements of this automation process must include surface grid generation,

○△◇○◇ EXPERIMENT
— SHANG AND SCHERR
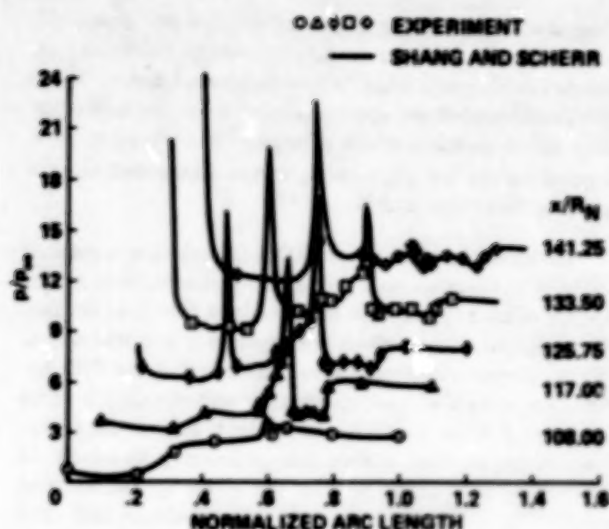
Fig. 15. Afterbody pressure comparisons for the solution of Fig. 13, Shang and Scherr.[102]
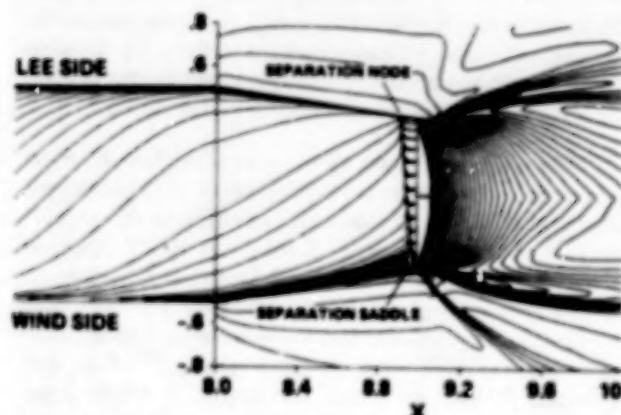
Fig. 16. Afterbody flow detail: surface streamlines and density contours on the bilateral plane of symmetry, $M_\infty = 2$, $M_J = 2.5$, $\alpha = 6°$, $P_J/P_\infty = 3$, $Re_D = 1.5 \times 10^6$, Deiwert and Rothmund.[103]

soning algorithms, and interior grid generation with solution adaptive capabilities. One possible alternative which may have a significant impact on the automation process is Artificial Intelligence as described by Andrews.[105] Progress in individual applications is anticipated to proceed at a fast rate, however, progress in automating the whole geometry and grid generation process will be slower to evolve.

A large amount of work associated with viscous supersonic flows has been completed using the PNS formulation. This includes the pioneering work on cones and blunt cones at angle of attack by Lin and Rubin,[106] Lubbard and Helliwell,[107] and Agarwal and Rakich;[108] the work on jets by McDonald and Briley;[109] and the work on ogive-cylinders by Rakich et al.[110] Applications of the PNS formulation to supersonic projectile aerodynamics have been presented by Schiff and Sturek[111] and Sturek and Schiff[112]

using the formulation described in Schiff and Steger.[113] Sensitive magnus force calculations are reported and described in the Ref. 112.

Additional results utilizing the PNS formulation for more complicated geometries have been presented by Rai and Chaussee[114] and Rai et al.[115] for finned missiles and projectiles, by Kaul and Chaussee[116] and Chaussee et al.[117] for the X-24C lifting body, by Chaussee et al.[118] for the Space Shuttle Orbiter, and by Chaussee et al.[119] and Wai et al.[120] for a generic supersonic-cruise fighter configuration. A typical result for the Space Shuttle Orbiter study of Ref. 118 is shown in Fig. 17. The free-stream Mach number for this calculation was 7.9, the angle of attack was 25 deg, and the Reynolds number was 2.4 million/m. Three-dimensional particle paths are displayed over the orbiter and show vortices forming on the leeside of the orbiter and at the wing/fuselage juncture. Another interesting PNS result is presented by Chaussee[17] for the blunt-nosed, biconic configuration displayed in Fig. 18. This configuration contained slices on both the windward and leeward sides and a control surface protruding from the windward surface. The heat transfer distribution is
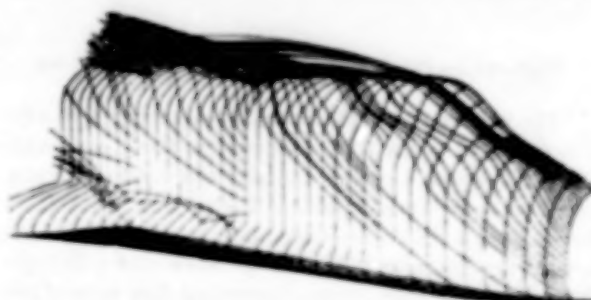

Fig. 17. Computed three-dimensional particle paths about the Space Shuttle Orbiter configuration, PNS formulation, $M_\infty = 7.9$, $\alpha = 25°$, $Re/m = 2.4 \times 10^6$, Chaussee.[17]
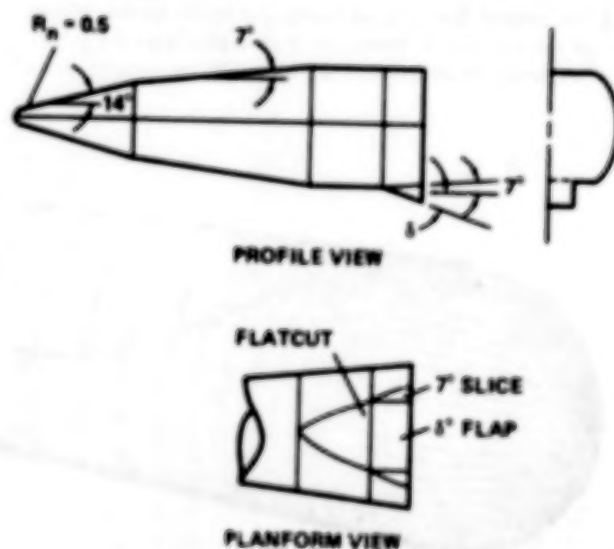

Fig. 18. Blunt biconic configuration with top and bottom slices and a flap control surface, Chaussee.[17]

compared with experiment along two meridional planes in Fig. 19. The Mach number for this calculation was 10, the angle of attack was 10 deg and the Reynolds number was 0.3 million/m. Agreement is generally good with slight discrepancies caused by problems in predicting flow transition from laminar to turbulent.
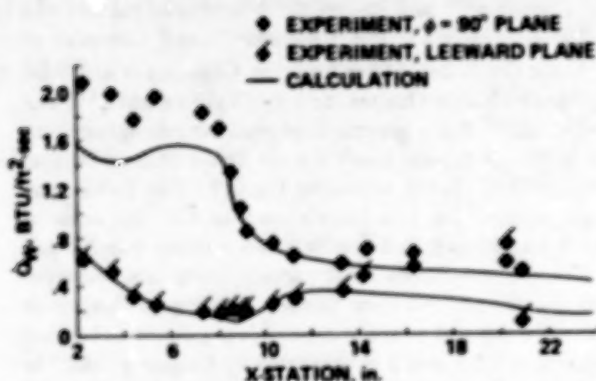

Fig. 19. Axial variation of the heat transfer over the biconic configuration in Fig. 18, PNS formulation, $M_\infty = 10$, $\alpha = 10°$, $Re_D = 8.3 \times 10^4$, Chaussee.[17]

High-Alpha/Vortex-Dominated Flow Applications

The field of high-alpha flows has recently gained a lot of momentum in the CFD community. Early work with PNS applications has been complemented with emerging activities in the time-dependent RANS area. High-alpha flows are more difficult to understand and to compute because of several factors. First of all, associated with high-alpha flows are large vortex-dominated flow separations with complicated flow physics that are not well understood. Computing these flow fields accurately means predicting vortex formation in the boundary layer, the lift-off process, the vorticity transport process, and the vortex-vortex interaction process. Because a significant amount of flow detail can exist out of the boundary layer, providing the proper level of grid resolution in the proper places is more complicated. Secondly, high-alpha flows are generally unsteady in nature and can be wildly asymmetric even

when the boundary conditions of the flow are essentially symmetric. Turbulence modeling is another difficulty associated with computing vortex-dominated flows. What turbulence models are appropriate for these flows, is a typically asked question which is largely unanswered to date. A good survey for high-alpha, vortex-dominated flows is given by Newsome and Kandil.[121]

Much of the work on the PNS formulation presented above in the section on supersonic/hypersonic flow is intimately related to the field of high-alpha flow field studies. For high-alpha flows which are supersonic and which contain no streamwise separations, utilization of the PNS approach may be the most appropriate and certainly is more economical than the time-dependent RANS approach. Two examples that utilize this philosophy to study, in particular, high-alpha physics are given by Degani and Schiff[122] and Vigneron et al.[123] The results of Ref. 122 are interesting in that the standard Baldwin-Lomax turbulence model was modified for high angle-of-attack flows involving vortex lift off. The boundary layer thickness is computed from the vorticity distribution in the standard Baldwin-Lomax model. This quantity is inappropriately determined when vorticies lift off the surface. The Degani-Schiff modification fixes this difficulty and produces good agreement with experiment even for vortex lift off.

Computational work in the area of high-alpha flows has more recently centered on the use of the time-dependent RANS approach. Interesting examples in this area include Pulliam and Steger,[51] Kordulla et al.,[124] Obayashi et al.,[125] Aki and Yamada,[126] and Ying et al.[127] where solutions over hemisphere-cylinder configurations have been studied in the transonic and low-supersonic regime; Fujii and Kutler,[128,129] Rizzetta and Shang,[130] Pan and Pulliam,[131] Mehta,[132] and Chaderjian[133] where high-alpha flows over wings, delta-wings, yawed wings, and wing-strake combinations have been studied; and Newsome and Adams[134] where the vortical flow over elliptical bodies at high angles of attack have been studied.

Results from Refs. 127 and 134 are particularly striking and are displayed in Figs. 20 and 21, respectively. Figure 20 shows computed surface velocity vectors over a
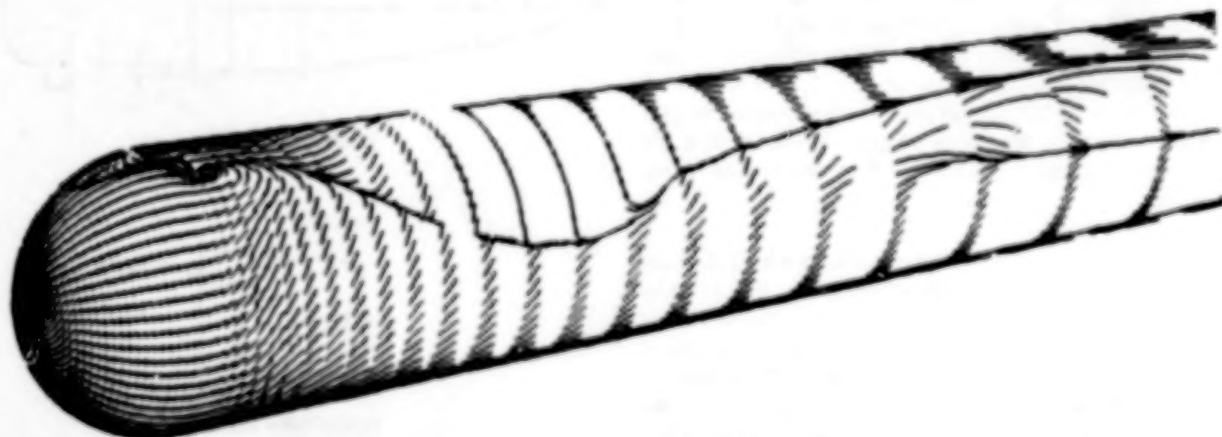

Fig. 20. Computed particle paths on the surface of a hemi-sphere-cylinder configuration, $M_\infty = 1.2$, $\alpha = 19°$, $Re_D = 4.45 \times 10^5$, Ying et al.[127]

hemisphere-cylinder combination inserted into a Mach 1.2 stream at an angle of attack of 19 deg and a Reynolds number based on the cylinder diameter of 445,000. This calculation was laminar and therefore no turbulence model was used. The surface velocity vector pattern, which is in good agreement with the experimental oil flow, was computed with a new upwind algorithm described in Ref. 127
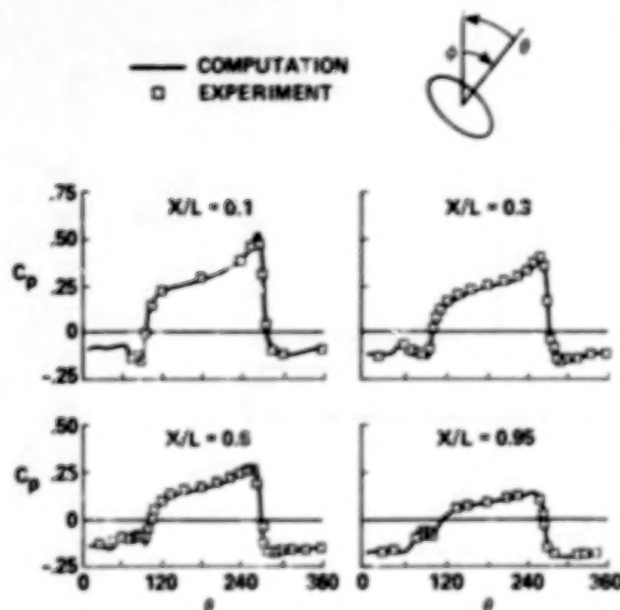

Fig. 21. Pressure coefficient comparisons for an elliptical lifting body with angles of attack (α) and roll (ϕ), $M_\infty = 2.5$, $\alpha = 20°$, $\phi = 45°$, $Re/m = 6.6 \times 10^6$, Newsome and Adams.[134]

on a fine grid consisting of $(60 \times 50 \times 60 =)$ 180,000 points. Figure 21 shows computed pressure results from Ref. 134 compared with experiment for the flow around an elliptical body. The Mach number for this calculation was 2.5; the angles of attack and roll were 20 and 45 deg, respectively; and the Reynolds number was 6.6 million/m. The numerical grid for this calculation was quite fine consisting of $(35 \times 101 \times 61 =)$ 215,635 points. The explicit MacCormack method was used to integrate the RANS equations and a modified Baldwin-Lomax turbulence model was used to simulate turbulence. The excellent correlation of this calculation to experiment is obvious from Fig. 21. The reader is referred to additional interior flow field numerical/experimental comparisons, all in good agreement, in the original paper of Ref. 134.

Another set of results dealing with the computation of vortical flows is the work of Reznick and Flores[135] and Flores et al.[136] In these studies the previously mentioned TNS computer code was upgraded to include more complicated geometries. In particular, a modified F-16A configuration with a fared inlet and the tail removed was simulated with a zonal grid topology consisting of 16 grid zones. Par-

ticular emphasis in Ref. 135 was given to the study of the strake-leading-edge vortex. A comparison of computed wing pressures with experiment at a Mach number of 0.9, an angle of attack of 6 deg, and a Reynolds number of 6 million is shown in Fig. 22. The two results are in generally good agreement. The discrepancies in shock location and leading-edge pressure levels are perhaps due to coarse grid effects or the fact that the experimental data contained a flow-through inlet that was not modeled computationally. Details of the vortex formation at the strake leading edge for a Mach number of 0.6 and an angle of attack of 10 deg are shown in Figs. 23 and 24. Figure 23 shows a view of the modified F-16A with selected three-dimensional particle paths in the vicinity of the wing-root/strake juncture. Figure 24 shows a close-up view of the wing-root/strake juncture. From these two views, the formation of a vortex from both the strake and wing-root leading edges is obvious. The wing-root vortex draws the strake vortex beneath it and creates a strong spanwise flow toward the tip. This behavior is qualitatively displayed in experimental flow visualizations described in Ref. 135.

Concluding Remarks

The numerical solution of the Navier-Stokes equations in three space dimensions has been reviewed. The areas of incompressible flow, transonic flow, supersonic/hypersonic flow, and high-alpha/vortex-dominated flow have all been considered. Applications research in all of these areas is seen to be increasing at an exponential rate. In addition, the geometrical complication of applications is advancing but at a slower rate. Areas which need concentrated attention in the near future are listed as follows:

1) Grid generation for complex geometries including surface grid generation, zoning algorithms, and solution adaptive grid concepts.

2) New developments in turbulence models for applications, especially those types of models that can be applied to obtain engineering answers for separated flow problems.

3) More complete CFD validation experiments which will allow more complete validation of CFD results and a physical assessment of why disagreements occur when they do occur.

4) More concentrated effort in the hypersonic flow regime including the development of sophisticated strong-shock capturing schemes, hypersonic turbulence models including the effects of transition, and the development of chemical equilibrium and nonequilibrium real-gas effects.

5) Convergence acceleration techniques for time-asymptotic problems, especially new algorithms which will lend themselves to vectorization and be efficient for new more sophisticated turbulence models and the more complicated physics associated with hypersonic flow.
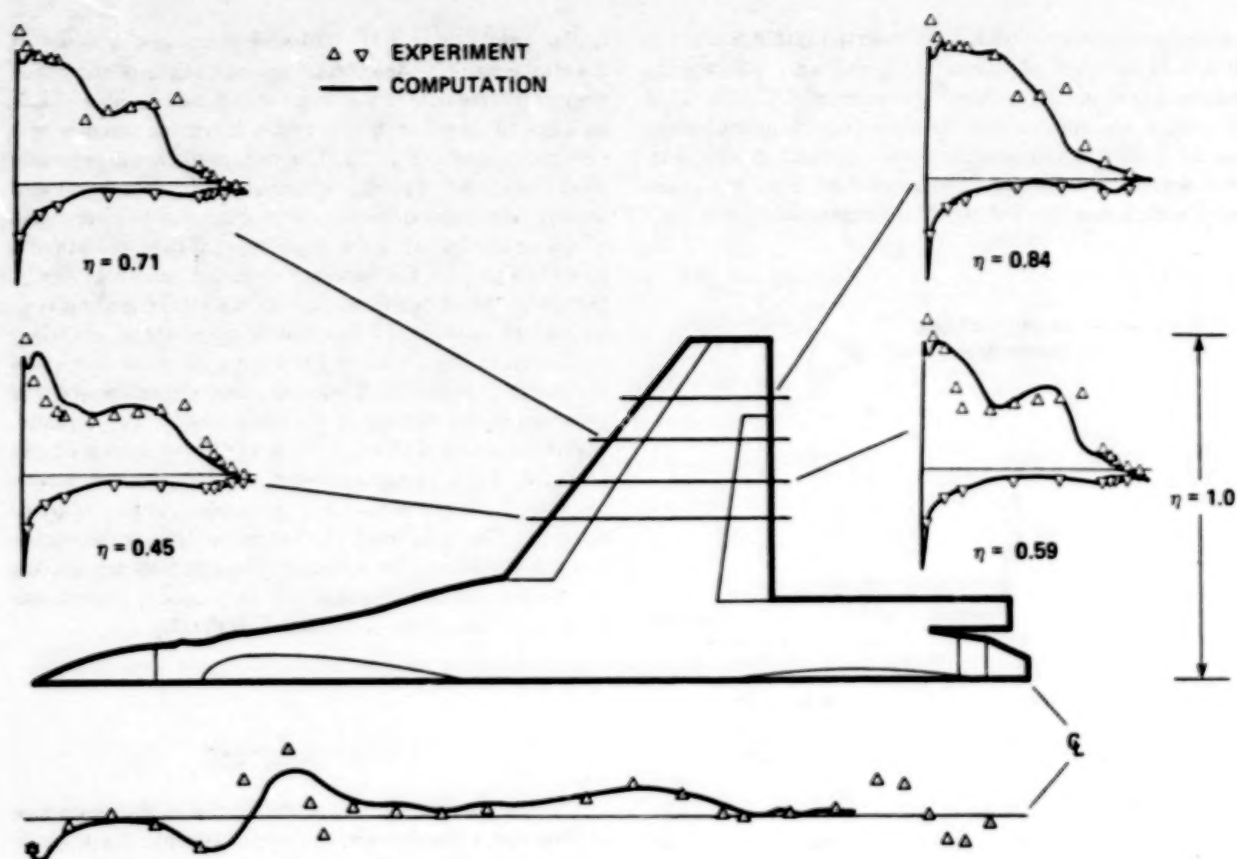
Fig. 22. Pressure coefficient comparisons on the wing and fuselage of a modified F-16A configuration, $M_\infty = 0.9$, $\alpha = 6.2°$, $Re_C = 4.5 \times 10^6$, Reznick and Flores.[135]

Fig. 23. Computed three-dimensional particle paths in the vicinity of a modified F-16A strake/wing juncture, $M_\infty = 0.6$, $\alpha = 10°$, Reznick and Flores.[135]

Fig. 24. Blow-up view of the three-dimensional particle paths shown in Fig. 23, Reznick and Flores.[135]

References

[1]Peyret, R. and Viviand, H., "Computation of Viscous Compressible Flows Based on the Navier-Stokes Equations," AGARDograph No. 212, 1975.

[2] "The Influence of Computational Fluid Dynamics on Experimental Aerospace Facilities, A Fifteen Year Projection," Prepared by the Committee on Computational Aerodynamics Simulation Technology Developments, Aeronautics and Space Engineering Board, Commission on Engineering and Technical Systems, National Research Council, National Academy Press, Washington, D.C., 1983.

[3]Holst, T. L., Slooff, J. W., Yosihara, H., and Ballhaus, Jr., W.F., "Applied Computational Transonic Aerodynamics," AGARDograph No. 266, Aug. 1982.

[4]Holst, T. L., "Numerical Computation of Transonic Flow Governed by the Full Potential Equation," Presented at the 1983 VKI Lecture Series on Computational Fluid Dynamics in Brussels, Belgium, March 7-11, 1983; Also NASA TM-84310, Jan. 1983.

[5]Rogallo, R. S. and Moin, P., "Numerical Simulation of Turbulent Flows," Ann. Rev. Fluid Mechanics, Vol. 16, 1984, pp. 99-137.

[6]Baldwin, B. S. and Lomax, H., "Thin Layer Approximation and Algebraic Model for Separated Turbulent Flows," AIAA Paper No. 78-0257, Jan. 1978.

[7]Ballhaus, Jr., W. F., "Computational Aerodynamics and Supercomputers," Proceedings of the COMPCON 1984 28th IEEE Computer Society International Conference, Feb. 27-Mar. 1, 1984, pp. 3-14, IEEE Computer Society, Silver Spring, MD.

[8]Peterson, V. L., Ballhaus, Jr., W. F., and Bailey F. R., "Numerical Aerodynamic Simulation (NAS)," Large Scale Scientific Computation, Academic Press, 1984, pp. 215-236.

[9]Peterson, V. L., "A New Opportunity for Rotorcraft Technology," Presented at the American Helicopter Society 42nd Annual Forum and Technology Display, June 1986.

[10]Kutler, P., "A Perspective of Computational Fluid Dynamics," NASA TM 88246, May 1986.

[11]Chapman, D. R., "Computational Aerodynamics-Development and Outlook," AIAA J., Vol. 17, No. 12, Dec. 1979, pp. 1293-1313.

[12]Anderson, D. A., Tannehill, J. C., and Pletcher, R. H., Computational Fluid Mechanics and Heat Transfer, Hemisphere Publishing Corp., Washington, 1984.

[13]Chapman, D. R., "Trends and Pacing Items in Computational Aerodynamics," Lecture Notes in Physics, Vol. 141, Eds. Reynolds, W. C. and MacCormack, R., Springer-Verlag, Berlin Heidelberg, Germany, 1981.

[14]Kutler, P., "A Perspective of Theoretical and Applied Computational Fluid Dynamics," AIAA J., Vol. 23, No. 3, Mar. 1985, pp. 328-341.

[15]Shang, J. S., "An Assessment of Numerical Solutions of the Compressible Navier-Stokes Equations," J. of Aircraft, Vol. 22, No. 5, May 1985, pp. 353-370.

[16]Mehta, U. and Lomax, H., "Reynolds-Averaged Navier-Stokes Computations of Transonic Flows-the State of the Art," In Transonic Aerodynamics, Ed. Nixon, D., Vol. 81, Progress in Astronautics and Aeronautics, 1982, pp. 297-375.

[17]Chaussee, D. S., "High Speed Viscous Flow Calculations About Complex Configurations, NASA TM 88237, April 1986.

[18]Orszag, S. A. and Israeli, M., "Numerical Simulation of Viscous Incompressible Flows," Annual Review of Fluid Mechanics, Vol. 6, 1974, pp. 281-318.

[19]Turkel, E., "Progress in Computational Physics," ICASE Report No. 82-23, Aug. 1982.

[20]Thompson, J. F., "Grid Generation Techniques in Computational Fluid Dynamics," AIAA J., Vol. 22, No. 11, Nov. 1984, pp. 1505-1523.

[21]Lakshminarayana, B., "Turbulence Modeling for Complex Flows," AIAA Paper No. 85-1652, July 1985.

[22]Marvin, J. G., "Future Requirements of Wind Tunnels for Computational Fluid Dynamics Code Verification," AIAA Paper No. 86-0752-CP, Jan. 1986.

[23]Harlow, F. H. and Welch, J. E., "Numerical Calculation of Time-Dependent Viscous Incompressible Flow with Free Surface," Physics of Fluids, Vol. 8, Dec. 1965, pp. 2182-2189.

[24]Chorin, A. J., "A Numerical Method for Solving Incompressible Viscous Flow Problems," J. Comp. Phys., Vol. 2, 1967, pp. 12-26.

[25]Patankar, S. V. and Spalding, D. B., "A Calculation Procedure for Heat, Mass and Momentum Transfer in Three-Dimensional Parabolic Flows," Int. J. Heat Mass Transfer, Vol. 15, 1972, pp. 1787-1806.

[26]Briley, W. R., "Numerical Method for Predicting Three Dimensional Flows in Ducts," J. Comp. Phys., Vol. 14, No. 1, 1974, pp. 8-28.

[27]Ghia, K. N. and Sokhey, J. S., "Laminar Incompressible Viscous Flow in Curved Ducts of Regular Cross-Sections," J. of Fluids Engr., Vol. 99, 1977, pp. 640-648.

[28]Ghia, U., Ghia, K. N., and Studerus, C. J., "Three-Dimensional Laminar Incompressible Flow in Straight Polar Ducts," Int. J. of Comp. and Fluids, Vol. 5, No. 4, 1977, pp. 205-218.

[29]Buggeln, R. C., Briley, W. R., and McDonald, H., "Solution of the Navier-Stokes Equations for Three-Dimensional Turbulent Flow with Viscous Sublayer Resolution," AIAA Paper No. 81-1023, June 1981.

[30]Ghia, U., Ghia, K. N., and Goyal, R. K., "Three-Dimensional Viscous Incompressible Flow in Curved Polar Ducts," AIAA Paper No. 81-1455, June 1981.

[31]Pouagare, M. and Lakshimarayana, B., "A Space-Marching Method for Viscous Incompressible Internal Flows," J. Comp. Phys., Vol. 64, No. 2, June 1986, pp. 389-415.

[32]Roberts, D. W. and Forester, C. K., "Parabolic Procedure for Flows in Ducts with Arbitrary Cross Sections," AIAA J., Vol. 17, No. 1, Jan. 1979, pp. 33-40.

[33]Himeno, R., Shirayama, S., Kamo, K., and Kuwahara, K., "Computational Study of Three-Dimensional Wake Structure," AIAA Paper No. 85-1617, July 1985.

[34]Kawamura, T. and Kuwahara, K., "Computation of High Reynolds Number Flow around a Circular Cylinder with Surface Roughness," AIAA Paper No. 84-0340, Jan. 1984.

[35]Kwak, D., Chang, J. C., Shanks, S., Chakravarthy, S. R., "A Three-Dimensional Incompressible Navier-Stokes Flow Solver Using Primitive Variables," AIAA J., Vol. 24, No. 3, March 1986, pp. 390-396.

[36]Gorski, J., Govindan, T., and Lakshiminarayana, B., "Computation of Three-Dimensional Turbulent Shear Flows in Corners," AIAA Paper No. 83-1733, July 1983.

[37]Chang, J. L. C., Kwak, D., Dao, S. C., and Rosen, R., "A Three-Dimensional Incompressible Flow Simulation Method and Its Application to the Space Shuttle Main Engine, Part I - Laminar Flow," AIAA Paper No. 85-0175, Jan. 1985.

[38]Chang, J. L. C., Kwak, D., Dao, S. C., and Rosen, R., "A Three-Dimensional Incompressible Flow Simulation Method and Its Application to the Space Shuttle Main Engine, Part II - Turbulent Flow," AIAA Paper No. 85-1670, July 1985.

[39]Ziebarth, J. P., Barson, S., and Rosen, R., "Computational Fluid Dynamics as a Design Tool for Hot Gas Manifold of the Space Shuttle Main Engine," Institute for Computational Studies, Report No. 86002, Jan. 1986.

[40]Kwak, D., Rogers, S., Kaul, U. K., and Chang, J. L. C., "A Numerical Study of Incompressible Juncture Flows," NASA TM 88319, Aug. 1986.

[41]Rogers, S. E., Kwak, D., and Kaul, U. K., "A Numerical Study of Three-Dimensional Incompressible Flow Around Multiple Posts," AIAA Paper No. 86-0353, Jan. 1986.

[42]Chang J. L. C., and Kwak, D., "On the Method of Pseudo Compressibility for Numerically Solving Incompressible Flows," AIAA Paper No. 84-0252, Jan. 1984.

[43]Steger, J. L. and Kutler, P., "Implicit Finite-Difference Procedures for the Computation of Vortex Wakes," AIAA J., Vol. 15, No. 4, April 1977, pp. 581-590.

[44]Rogers, S. E., Chang, J. L. C., and Kwak, D., "A Diagonal Algorithm for the Method of Pseudo Compressibility," AIAA Paper No. 86-1060, May 1986.

[45]Beam, R. M. and Warming, R. F., "An Implicit Finite-Difference Algorithm for Hyperbolic Systems in Conservation-Law Form," J. Comp. Phys., Vol. 22, No. 1, 1976, pp. 87-110.

[46]Briley, W. R. and McDonald, H., "Solution of the Multidimensional Compressible Navier-Stokes Equations by a Generalized Implicit Method," J. Comp. Phys., Vol. 24, No. 4, 1977, pp. 372-397.

[47]MacCormack, R. W., "A Numerical Method for Solving the Equations of Compressible Viscous Flow," AIAA J., Vol. 20, No. 9, Sept. 1982, pp. 1275-1281.

[48]MacCormack, R. W., "The Effect of Viscosity in Hypervelocity Impact Cratering," AIAA Paper No. 69-354, April 1969.

[49]Mansour, N. N., "Numerical Simulation of the Tip Vortex Off a Low-Aspect Ratio Wing at Transonic Speed," AIAA Paper No. 84-0522, Jan. 1984.

[50]Hinson, B. L. and Burdges, K. P., "Acquisition and Application of Transonic Wing and Far-Field Test Data for Three-Dimensional Computational Method Evaluation," Report No. AFOSR-TR-80-0421, Lockheed Georgia Co. Marietta, Ga., 1980.

[51]Pulliam, T. H. and Steger, J. L., "Implicit Finite-Difference Simulations of Three-Dimensional Compressible Flow," AIAA Paper 78-10, Jan. 1978. Also AIAA J., Vol.

18, No. 2, Feb. 1980, pp. 159-167.

[52]Agarwal, R. K. and Deese, J. E., "Computation of Transonic Viscous Airfoil, Inlet and Wing Flowfields," MDRL Report No. 84-29, June 1984.

[53]Jameson, A., Schmidt, W., and Turkel, E., "Numerical Solution of the Euler Equations by Finite Volume Methods Using Runge-Kutta Time-Stepping Schemes," AIAA Paper No. 81-1259, July 1981.

[54]Schmit, V. and Charpin, F., "Pressure Distributions on the ONERA-M6 Wing at Transonic Mach Numbers," AGARD Report AR-138, May 1970.

[55]Holst, T. L., Kaynak, U., Gundy, K. L., Thomas, S. D., Flores, J., and Chaderjian, N., "Numerical Solution of Transonic Wing Flows Using an Euler/Navier-Stokes Zonal Approach," AIAA Paper No. 85-1640, July 1985.

[56]Flores, J., "Convergence Acceleration for a Three-Dimensional Euler/Navier-Stokes Zonal Approach," AIAA Paper 85-1495, July 1985.

[57]Kaynak, U., Holst, T. L., Cantwell, B. J., and Sorenson, R. L., "Numerical Simulation of Transonic Separated Flows over Low Aspect Ratio Wings," AIAA Paper No. 86-0508, Jan. 1986.

[58]Kaynak, U., Holst, T. L., and Cantwell, B. J., "Computation of Transonic Separated Wing Flows Using an Euler/Navier-Stokes Zonal Approach," NASA TM 88311, July 1986.

[59]Srinivasan, G. R., McCroskey, W. J., Baeder, J. D., and Edwards, T. A., "Numerical Simulation of Tip Vortices of Wings in Subsonic and Transonic Flows," AIAA Paper No. 86-1095, May 1986.

[60]Pulliam, T. H. and Chaussee, D. S., "A Diagonal Form of an Implicit Approximate-Factorization Algorithm," J. Comp. Phys., Vol. 39, No. 2, Feb. 1981, pp. 347-363.

[61]Lockman, W. K. and Seegmiller, H. L., "An Experimental Investigation of the Subcritical and Supercritical Flow About a Swept Semispan Wing," NASA TM-84367, June 1983.

[62]Keener, E. R., "Computational-Experimental Pressure Distributions on a Transonic low-Aspect-Ratio Wing," AIAA Paper No. 84-2092, Aug. 1984.

[63]Keener, E. R., "Boundary-Layer Measurements on a Transonic Low-Aspect Ratio Wing," NASA TM-88214, May 1986.

[64]Obayashi, S. and Fujii, K., "Computation of Three-Dimensional Viscous Transonic Flows with the LU Factored Scheme," AIAA Paper No. 85-1510, July 1985.

[65]Fujii, K. and Obayashi, S., "Practical Applications of New LU-ADI Scheme for the Three-Dimensional Navier-Stokes Computation of Transonic Viscous Flows," AIAA Paper No. 86-0513, Jan. 1986.

[66]Steger, J. L. and Warming, R. F., "Flux Vector Splitting of the Inviscid Gasdynamic Equations with Application to Finite-Difference Methods," J. Comp. Phys., Vol. 40, 1981, pp. 263-293.

[67]Lombard, C. K., Bardina, J., Venkatapathy, E., and Oliger, J., "Multi-Dimensional Formulation of CSCM - An Upwind Flux Difference Eigenvector Split Method for the Compressible Navier-Stokes Equations," AIAA Paper No. 83-1895, July 1983.

[68]Fujii, K. and Obayashi, S., "Navier-Stokes Simulation of Transonic Flow over Wing-Fuselage Combina-

tions," AIAA Paper No. 86-1831, June 1986.

[69]Vadyak, J., "Simulation of Transonic Three-Dimensional Nacelle/Inlet Flowfields Using an Euler/Navier-Stokes Algorithm," AIAA Paper No. 85-0084, Jan. 1985.

[70]Swisshelm, J. M. and Johnson, G.M., "Numerical Simulation of Three-Dimensional Flowfields Using the CYBER 205," Inst. for Comp. Studies, ICS Technical Report 85002, Nov. 1984.

[71]Chaussee, D. S., Buning, P. G., and Kirk, D. B., "Convair 990 Transonic Flow-Field Simulation About the Forward Fuselage," AIAA Paper No. 83-1785, July 1983.

[72]Cosner, R., "Relaxation Solution for Viscous Transonic Flow about Fighter-Type Forebodies and Afterbodies," AIAA Paper No. 82-0252, Jan. 1982.

[73]Deiwert, G. S., "Numerical Simulation of Three-Dimensional Boattail Afterbody Flow Field," AIAA Paper No. 80-1347, July 1980.

[74]Purohit, S. C., Shang, J. S., and Hankey, Jr., W. L., "Numerical Simulation of Flow Around a Three-Dimensional Turret," AIAA Paper No. 82-1020, June 1982.

[75]Purohit, S. C., Shang, J. S., and Hankey, Jr., W. L., "Effect of Suction on the Wake Structure of a Three-Dimensional Turret," AIAA Paper No. 83-1738, July 1983.

[76]Nietubicz, C. J., Sturek, W. B., and Heavey, K. R., "Computations of Projectile Magnus Effect at Transonic Velocities," AIAA Paper No. 83-0237, Jan. 1983.

[77]Nietubicz, C. J., Mylin, D. C., and Sahu, J., "Aerodynamic Coefficient Predictions for a Projectile Configuration at Transonic Speeds," AIAA Paper No. 84-0326, Jan. 1984.

[78]Sahu, J., Nietubicz, C. J., and Steger, J., "Navier-Stokes Computations of Projectile Base Flow With and Without Base Injection," AIAA Paper No. 83-0224, Jan. 1983.

[79]Li, C. P., "A Numerical Study of Laminar Flow Separation on Blunt Flared Cones at Angle of Attack," AIAA Paper No. 74-585, June 1974.

[80]Holst, T. L. and Tannehill, J. C., "Numerical Computation of Three-Dimensional Blunt Body Flow Fields with an Impinging Shock," Iowa State University, Engineering Research Institute, Report No. ISU-ERI-Ames-75169, July 1975.

[81]Shang, J. S. and Hankey, W. L., "Numerical Solution of the Compressible Navier-Stokes Equations for a Three-Dimensional Corner," AIAA J., Vol. 15, No. 11, Nov. 1977, pp. 1575-1582.

[82]Hung, C. M. and MacCormack, R. W., "Numerical Solution of Supersonic Laminar Flow over a Three-Dimensional Compression Corner," AIAA Paper No. 77-694, June 1977.

[83]Hung, C. M., "Numerical Solution of Supersonic Laminar Flow Over an Inclined Body of Revolution," AIAA Paper No. 79-1547, July 1979.

[84]Hung, C. M., "Impingement of an Oblique Shock Wave on a Cylinder," J. of Spacecraft and Rockets, Vol. 23, No.6, May-June 1983, pp. 201-206.

[85]Knight, D. D., "A Hybrid Explicit-Implict Numerical Algorithm for the Three-Dimensional Compressible Navier-Stokes Equations," AIAA Paper No. 83-0223, Jan. 1983.

[86]Hung, C. M. and MacCormack, R. W., "Numerical Solution of Three-Dimensional Shock Wave and Turbulent Boundary-Layer Interaction," AIAA J., Vol. 16, No. 10, Oct. 1978, pp. 1090-1096.

[87]Hung, C. M. and Kordulla, W., "A Time-Split Finite-Volume Algorithm for Three-Dimensional Flow-Field Simulation," AIAA J., Vol. 22, No. 11, Nov. 1984, pp. 1564-1572.

[88]Hung, C. M. and Buning, P., "Simulation of Blunt-Fin-Induced Shock Wave and Turbulent Boundary-Layer Interaction," J. Fluid Mechanics, Vol. 154, May 1985, pp. 163-185.

[89]Horstman, C. C., Kussoy, I., and Lockman, W. K., "Computation of Three-Dimensional Shock-Wave/Turbulent Boundary-Layer Interaction Flows," Proceedings of the Third Symposium on Numerical and Physical Aspects of Aerodynamic Flows, Long Beach, CA, Jan 1985.

[90]Horstman, C. C., "A Computational Study of Complex Three-Dimensional Compressible Turbulent Flowfields," AIAA J., Vol. 23, No. 10, Oct. 1985, pp. 1461-1462.

[91]Knight, D., "Numerical Simulation of 3-D Shock Turbulent Boundary Layer Interaction Generated by a Sharp Fin," AIAA J., Vol. 23, No. 12, Dec. 1985, pp. 1885-1891.

[92]Knight, D., Horstman, C., Shapey, B., and Bodnonoff, S., "The Flowfield Structure of the 3-D Shock Wave-Boundary Layer Interaction Generated by a 20 deg Sharp Fin at Mach 3," AIAA Paper No. 86-0343, Jan. 1986.

[93]Horstman, C., "Computation of Sharp-Fin-Induced Shock Wave/Turbulent Boundary-Layer Interactions," AIAA J., Vol. 24, No. 9, Sept. 1986, pp. 1433-1440.

[94]Jones, W. P. and Launder, B. E., "The Prediction of Laminarization with Two-Equation Model of Turbulence," Inter. J. of Heat and Mass Transfer, Vol. 15, Feb. 1972, pp. 301-314.

[95]Viegas, J. R. and Rubesin, M. W., "Wall-Function Boundary Conditions in the Solution of the Navier-Stokes Equations for Complex Compressible Flows," AIAA Paper No. 83-1694, July 1983.

[96]Shang, J. S., "Numerical Simulation of Wing-Fuselage Interference," AIAA Paper No. 81-0048, Jan. 1981.

[97]Shang, J. S., "Numerical Simulation of Wing-Fuselage Aerodynamic Interaction," AIAA Paper No. 83-0225, Jan. 1983.

[98]Kumar, A. J., "Numerical Simulation of Flow Through Scramjet Inlets Using a Three-Dimensional Navier-Stokes Code," AIAA Paper No. 85-1664, July 1985.

[99]Howlett, D. G. and Hunter, L. G., "A Study of a Supersonic Axisymmetric Spiked Inlet at Angle of Attack Using the Three-Dimensional Navier-Stokes Equations," AIAA Paper No. 86-0308, Jan. 1986.

[100]Rizk, Y. M. and Ben-Shmuel, S., "Computation of the Viscous Flow Around the Shuttle Orbiter at Low Supersonic Speeds," AIAA Paper No. 85-0168, Jan. 1985.

[101]Li, C. P., "Numerical Procedure for Three-Dimensional Hypersonic Viscous Flow Over Aerobrake Configurations," Proceedings of the Inter. Sym. on Comp. Fluid Dynamics, Tokyo, Japan, Sept. 1985, pp. 833-844.

[102]Shang, J. S. and Scherr, S. J., "Navier-Stokes Solution of the Flow Field Around a Complete Aircraft," AIAA Paper No. 85-1509, July 1985.

[103]Deiwert, G. S. and Rothmund, H., "Three-Dimensional Flow Over a Conical Afterbody Containing a Centered Propulsive Jet: A Numerical Simulation," AIAA Paper No. 83-1709, July 1983.

[104]Lomax, H. and Pulliam, T. H., "A Fully Implicit Factored Code for Computing Three-Dimensional Flows on the ILLIAC IV," Parallel Computations, G. Rodrigue, Ed., Academic Press, New York, 1982, pp. 217-250.

[105]Andrews, A. E., "Progress and Challenges in the Application of Artificial Intelligence to Computational Fluid Dynamics," AIAA Paper No. 87-0593, Jan. 1987.

[106]Lin, T. C. and Rubin, S. G., "Viscous Flow Over a Cone at Moderate Incidence: I - Hypersonic Tip Region," Inter. J. of Comp. and Fluids, Vol. 1, 1973, pp. 37-57.

[107]Lubbard, S. C. and Helliwell, W. S., "Calculation of the Flow on a Cone at High Angle of Attack," AIAA J., Vol. 12, No. 7, July 1974, pp. 965-974.

[108]Agarwal, R. and Rakich, J. V., "Computation of Hypersonic Laminar Viscous Flow Past Spinning Sharp and Blunt Cone at High Angle of Attack," AIAA Paper No. 78-65, Jan. 1978.

[109]McDonald, H. and Briley, W., "Three-Dimensional Supersonic Flow of a Viscous or Inviscid Gas," J. Comp. Phys., Vol. 19, No. 2, Oct. 1975, pp. 150-178.

[110]Rakich, J. V., Vigneron, Y.C., and Agarwal, R., "Computation of Supersonic Viscous Flows Over Ogive-Cylinders at Angle of Attack," AIAA Paper No. 79-0131, Jan. 1979.

[111]Schiff, L. B. and Sturek, W. B., "Numerical Simulation of Steady Supersonic Flow Over an Ogive-Cylinder-Boattail Body," AIAA Paper No. 80-0066, Jan. 1980.

[112]Sturek, W. B. and Schiff, L. B., "Computations of the Magnus Effect for Slender Bodies in Supersonic Flow," AIAA Paper No. 80-1586, Aug. 1980.

[113]Schiff, L. B. and Steger, J. L., "Numerical Simulation of Steady Supersonic Viscous Flow," AIAA Paper No. 79-0130, Jan. 1979.

[114]Rai, M. M. and Chaussee, D. S., "New Implicit Boundary Procedures: Theory and Applications," AIAA Paper No. 83-0123, Jan. 1983.

[115]Rai, M. M., Chaussee, D. S., and Rizk, Y., "Calculation of Viscous Supersonic Flows over Finned Bodies," AIAA Paper No. 83-1667, July 1983.

[116]Kaul, U. and Chaussee, D. S., "A Comparative Study of the Parabolized Navier-Stokes (PNS) Code Using Various Grid Generation Techniques," AIAA Paper No. 84-0459, Jan. 1984.

[117]Chaussee, D. S., Patterson, J. L., Kutler, P., Pulliam, T. H., and Steger, J. L., "A Numerical Simulation of Hypersonic Flows over Arbitrary Geometries at High Angle of Attack," AIAA Paper No. 81-0050, Jan. 1981.

[118]Chaussee, D. S., Rizk, Y. M., and Buning, P. G., "Viscous Computations of a Space Shuttle Flowfield," Lecture Notes in Physics, Ninth International Conference on Numerical Methods in Fluid Dynamics, Vol. 218, 1984, pp. 148-153.

[119]Chaussee, D. S., Blom, G., and Wai, J. C., "Numerical Simulation of Viscous Supersonic Flow Over a Generic Fighter Configuration," NASA TM-86823, Dec. 1985.

[120]Wai, J. C., Blom, G., and Yoshihara, H., "Calculations for a Generic Fighter at Supersonic High-Lift Conditions," AGARD Fluid Dynamics Panel Symposium on Applications of Computational Fluid Dynamics in Aeronautics, France, April 1986.

[121]Newsome, R. W. and Kandil, O. A., "Vortex Flow Aerodynamics - Physical Aspects and Numerical Simulation," AIAA Paper No. 87-0205, Jan. 1987.

[122]Degani, D. and Schiff, L. B., "Computation of Supersonic Viscous Flows Around Pointed Bodies at Large Incidence," AIAA Paper No. 83-0034, Jan. 1983.

[123]Vigneron, Y. C., Rakich, J. V., and Tannehill, J. C., "Calculation of Supersonic Viscous Flow over Delta Wings with Sharp Subsonic Leading Edges," AIAA Paper No. 78-1137, July 1978.

[124]Kordulla, W., Vollmers, H., and Dallmann, U., "Simulation of Three-Dimensional Transonic Flow with Separation Past a Hemisphere-Cylinder Configuration," AGARD CPP-412, Appls. of Comp. Fluid Dynamics in Aero., Paper 31, April 1986.

[125]Obayashi, S. and Fujii, K., "Computation of Three-Dimensional Viscous Transonic Flows with the LU Factored Scheme," AIAA Paper No. 85-1510, July 1985.

[126]Aki, T. and Yamada, S., "A Supercomputer Simulation of Three Dimensional Viscous Flow," Proceeding of the Inter. Sym. on Comp. Fluid Dynamics, Sept. 1985, Tokyo, Japan, pp. 821-832.

[127]Ying, S. X., Steger, J. L., Schiff, L., and Baganoff, D., "Numerical Simulation of Unsteady, Viscous, High-Angle-of-Attack Flows Using a Partially Flux-Split Algorithm," AIAA Paper No. 86-2179, Aug. 1986.

[128]Fujii, K. and Kutler, P., "Numerical Simulation of the Leading-Edge Separation Vortex for a Wing and Strake-Wing Configuration," AIAA Paper No. 83-1908, July 1983.

[129]Fujii, K. and Kutler, P., "Numerical Simulation of the Viscous Flow Fields Over Three-Dimensional Complicated Geometries," AIAA Paper No. 84-1550, June 1984.

[130]Rizzetta, D. P. and Shang, J. S., "Numerical Simulation of Leading Edge Vortex Flows," AIAA Paper No. 84-1544, June 1984.

[131]Pan, D. and Pulliam, T. H., "The Computation of Steady Three-Dimensional Separated Flows over Aerodynamic Bodies at Incidence and Yaw," AIAA Paper No. 86-0109, Jan. 1986.

[132]Mehta, U., "The Computation of Flow Past an Oblique Wing Using the Thin-Layer Navier-Stokes Equations," NASA TM-88317, June 1986.

[133]Chaderjian, N. M., "Transonic Navier-Stokes Wing Solutions Using a Zonal Approach: Part 2. High Angle-of-Attack Simulation," Presented at the AGARD meeting in Aix En Provence, France, April 7-10, 1986; Also, NASA TM-88248, April 1986.

[134]Newsome, R. W. and Adams, M. S., "Numerical Simulation of Vortical-Flow Over an Elliptical-Body Missile at High Angles of Attack," AIAA Paper No. 86-0559, Jan. 1986.

[135]Reznick, S. G. and Flores, J., "Strake Generated Vortex Interactions for a Fighter-Like Configuration," AIAA Paper No. 87-0589, Jan. 1987.

[136]Flores, J., Reznick, S. G., Holst, T.L., and Gundy, K., "Transonic Navier-Stokes Solutions for a Fighter-Like Configuration," AIAA Paper No. 87-0032, Jan. 1987.

COMPUTATIONAL CHEMISTRY

J. O. Arnold
NASA Ames Research Center
Moffett Field, CA 94035

ABSTRACT

With the advent of supercomputers, modern computational chemistry algorithms and codes, a powerful new tool has been created to help fill NASA's continuing need for information on the properties of matter in hostile or unusual environments. Computational resources provided under the NAS program have been a cornerstone for recent advancements in this field. Properties of gases, materials, and their interactions can be determined from solutions of the governing equations. In the case of gases, for example, radiative transition probabilities per particle, bond-dissociation energies, and rates of simple chemical reactions can be determined computationally as reliably as from experiment. The data are proving to be quite valuable in providing inputs to real-gas flow simulation codes used to compute aerothermodynamic loads on NASA's aeroassist orbital transfer vehicles and a host of problems related to the National Aerospace Plane Program. Although more approximate, similar solutions can be obtained for ensembles of atoms simulating small particles of materials with and without the presence of gases. Computational chemistry has applications in studying catalysis, properties of polymers, etc., all of interest to various NASA missions, including those previously mentioned. In addition to discussing these applications of computational chemistry within NASA, the governing equations and the need for supercomputers for their solution is outlined.

INTRODUCTION

The availability of large-scale computers at the NASA Ames Research Center during the past decade has been a key element in developing an aggressive effort by NASA to use a computational approach to provide reliable information on the properties of gases, materials and their interactions. The impact of this effort has been growing rapidly as a result of continuing advances in computational methods and, concurrently, with increases in computer speed and memory. Specifically, the advanced computational capabilities being provided for this endeavor through the Numerical Aerodynamic Simulation (NAS) program have markedly increased the utility of computational chemistry as practiced at NASA Ames. Further, this resource is also providing benefits to the international community by enabling advanced state-of-the-art benchmark calculations which assess the reliability of approximate approaches that require less computational power.

The objectives of Ames' computational chemistry activities are specified in figure 1. The gas phase studies provide computed properties of isolated atoms and molecules, and rates of chemical reactions which occur between them. Systems composed of one to eight atomic nuclei and up to 30 electrons are treated rigorously by solving the Schrodinger equation for the quantum mechanical interaction energy of the electron in the field of all atomic nuclei. Typical molecular properties computed are potential energy surfaces for ground and excited electronic states (i.e., the set of electronic energies for all atomic geometries), equilibrium geometries, probabilities for transitions between electronic states and molecular spectra. Rate constants for chemical reactions are computed by solving Hamilton's classical equations of motion for a potential energy surface obtained from the aforementioned solutions of Schrodinger's equation.

The gas/solid calculations begin with solutions of wavefunctions and total energies for "atomic clusters" such as those illustrated for a diatomic molecule interacting with an inverted pyramid of five metal atoms. In such calculations, the metal atoms are sometimes held fixed at spacings corresponding to the bulk surfaces to simulate gas-surface interactions at the atomic scale. The quantal calculations usually account only for the outer valence electrons since all-electron calculations are too large even for machines like the Cray 2. Such calculations have progressed to the point of considering its application to systems as large as $Ni_{25}O_5$ or $Fe_{64}H$. In addition to providing information on clusters of this size, interatomic forces deduced from these calculations are used as input to atomistic simulations of large ensembles of up to 10,000 atoms. These calculations provide better simulation of the interaction of gases and bulk surfaces, as shown on the far right of figure 1. Obviously, going from left to right (fig. 1), the systems grow enormously, and the reliability of the calculations range from being competitive with the best experiments available, to being helpful in interpreting experimental findings and suggesting solutions to materials problems of crucial National concern. This work constitutes the computation of properties of matter and the results are being

used in a broad range of applications that are of current concern to NASA.

The gas phase work has great utility in providing inputs to chemically reacting, radiating, real-gas flow-field simulations like those which will occur about future space-based aerobraking orbital transfer vehicles (AOTVs). These vehicles will move men and materials between low and high Earth orbits and the Moon and Mars. These vehicles will fly very high (above 60-70 km) in the atmosphere during their aerobraking maneuver at speeds of approximately 9-13 km/sec. Under these conditions, as much as 10-15% of the gaseous species will be ionized.

Another program of National importance which requires the basic information on the properties of shock-heated air, as well as information on the hot air/hydrogen combustion process, is for the National Aerospace Plane (NASP). The NASP, in various implementations, will be capable of taking off from a conventional airport, cruising at Mach 5-12 (Los Angeles to Tokyo in 2 hr) or going into low Earth orbit, and returning to any other airport on Earth.

Discussions of the exciting missions of these vehicles and their future importance can be found in the report to the President by The National Commission on Space (1986).

Each of the missions discussed above, and others involving hypersonic flight require knowledge of the properties of materials and how they behave in the presence of hot gases or other hostile environments. For example, flight experiments on the Space Shuttle (Stewart et al., 1983) have shown that the thermal protection system (TPS) catalytic efficiency for recombination of boundary-layer atomic species effects the local heat transfer, i.e., a highly catalytic metal must absorb the diatomic heat of molecular recombination. On the other hand, a low-catalytic efficiency ceramic material such as the shuttle tile inhibits the recombination process, thereby preventing this heating and thus reducing the TPS weight requirement. Computational chemistry is helping us understand the differences in catalytic and noncatalytic materials. Such understanding clearly has the potential to aid in the development of new classes of advanced thermal protection materials for aerospace applications.

COMPUTATIONAL METHOD

Schrodinger's equation for gaseous molecules and atomic clusters is usually solved under the assumption that electronic motion is very fast compared with that of the constituent nuclei, allowing one to solve for the electronic degrees of freedom separately. Potential curves or surfaces are mapped out by obtaining several solutions corresponding to differing internuclear

separations. (The time-independent form of the equation is studied for the determination of the properties previously mentioned.)

Figure 2 illustrates the approach (generally known as "ab-initio" in the field) for a diatomic molecule where the Hamiltonian contains a ∇_i^2 operator that corresponds to the electronic motion of the ith electron, the Z/r_{iA} terms account for electron-nuclear attraction and the $1/r_{ij}$ term accounts for electrons-electron repulsion, Ψ_e is the electronic wave function and E is the electronic energy, both being sought in the solution. The expansion approach assumes that the wave function can be expanded in terms of configuration state functions (CSFs) constructed from Slater determinates composed of unknown molecular orbitals, ϕ_i. The orbitals are taken to be linear combinations of either Gaussian (GTO)- or Slater (STO)-type atomic orbitals. The GTOs or STOs used in an n-particle molecular problem are often referred to as the one-particle basis set. The solution first involves selecting a STO- or GTO-basis set, and the quality of the solution depends critically upon this choice.

The next step involves evaluating spatial integrals for the one-particle basis set and sorting for the subsequent determination of the coefficients for the molecular orbitals, c_{ip}, and the expansion coefficient, a_K. The a_K coefficients weigh the importance of a CSF to the total wave function, Ψ_e. The number of CSFs used in a calculation can range from one (self-consistent field SCF) to more than 10 million (configuration interaction CI). The CI calculation, called electron correlation, accounts for the instantaneous repulsion each electron feels, and to all other electrons constituting the molecule. The CI calculation is an eigenvector-value problem in which one gets the lowest eigenvalue by an iterative numerical procedure.

For the purpose of discussion, assume that a quality calculation may involve a basic set of size M (generally M = 50-100). The order of the subsequent steps is specified in figure 2, and the corresponding times, in seconds, of a calculation for a single internuclear separation of a typical diatomic molecule are also shown on the figure. Note that the possible number of CSFs, each corresponding to a different occupation of electrons within the possible orbital space, grows as M^6. Clearly, these calculations use large amounts of computer resources. Reasonable progress with our computational chemistry program will continue to require sizable percentages of the Ames Central Computing Facility (CCF) and NAS resources. As the available computer power grows, the utility of computational chemistry will also grow, continuing to add insight into the nature of matter, and changing the way we conduct experiments.

BENCHMARK CALCULATIONS

In the past, expansions involving all possible CSFs (or full configuration interaction (FCI) calculations) were generally not possible except for two- or three-electron single-atoms and molecules. Work on larger systems with reasonably sized, atomic basis sets were truncated because of limitations in computer memory and speed. Bauschlicher, Langhoff, Taylor, and Partridge have recently been using the NAS Cray 2 to study the impact of truncating the number of CSFs for small molecular systems, and these are serving as benchmarks for the international computational chemistry community. In one of these studies, Bauschlicher and Langhoff (work submitted, Chemical Physics and Letters, 1986) first carried out full CI calculations on the molecular ground states of CH, NH, and OH, using a modest one-particle GTO basis for each molecule. The full CI calculations accounted for each and every possible occupation of the electrons within the n-particle basis.

For NH, the FCI calculations were conducted with a one-particle [5s4p2d/4s2p] GTO basis and involved 9,240,000 Slater determinants (37,110,150 CSFs) and required 8,000 sec of Cray 2 time/iteration to optimize the expansion coefficients. These FCI calculations and similar calculations for CH and OH were compared against the standard high-quality complete active space, self-consistent field/multiple reference singles and doubles configuration interaction CASSCF/MRSDCI. The CASSCF approach is one in which an active space is defined, and all configurations possible within this space are included in a calculation to determine the molecular orbital coefficients defined above. These molecular orbitals are then used in a CI calculations in which all configurations corresponding to single and double electronic excitations from any of the CASSCF configurations are included. Finally, a very small correction to account for the missing configurations corresponding to higher-order excitation is applied. For the modest-basis set calculations, only small differences (.015 eV max) in dissociation energies between the FCI and CASSCF/MRSDCI + Q computed results were noted, as can be seen from the tabulations in figure 3. These calculations clearly indicate that the standard truncated approach widely used and previously calibrated against experimental results (of which accurate ones are available) yield quality results.

In addition to these benchmark calculations, Bauschlicher and Langhoff also used a good quality basis set in conjunction with larger MRSDCI + Q calculations (Q = Quadruples) to predict values of the bond-dissociation energy for CH, NH and OH. As can be seen from the results shown in figure 3, Bauschlicher and Langhoff achieved chemical accuracy for CH and OH, for which accurate experimental data exist. On the basis of their calculations and estimates of the remaining error caused by basis set incompleteness, they recommend a dissociation energy of $3.37 \pm .03$ eV for NH and assign a 99% confidence limit to this value. This illustrates how computational chemistry is complementing the experimental approach in determining molecular properties, such as the bond-dissociation energy.

CALCULATION OF RADIATIVE PROPERTIES FROM FIRST PRINCIPLES: DIATOMIC MOLECULES

Figure 4 illustrates the computational procedure used to determine the radiative properties of molecules. The first step is to solve the Schrodinger equation for the electronic energy, E, and the wave function, ψ_e, using the internuclear separation as a parameter as previously described. Potential-energy curves for the low-lying electronic states from a typical molecular calculation are shown on the left side of the chart. One can compute other electronic properties from the electronic wavefunction, such as the transition moments, which control the total strength of the transition between two electronic states, and the spin-orbit matrix elements, which control molecular and spectral fine structure. Once this is done, the next step is to solve the Schrodinger equation for the vibration-rotation motion. Then, by summing the product of the transition moments and the vibrational-rotational wavefunctions for all upper and lower states, one obtains the total cross section. The cross section shown on the right-hand side of figure 4 is for all the transitions between the potential-energy curves given on the left-hand side of the figure. The banded structure in the cross-section plot corresponds to bound-bound transitions and the underlying continuum corresponds primarily to transitions between bound and repulsive states (i.e., those with no minimum in the energy curve). The computated data for transition probabilities and spectral intensities are comparable to those from high quality experiments.

The cross sections yield the radiative intensity per molecule per excited state. Combining them with the appropriate distributions of species and excited states yields spectral and integrated intensity predictions in gases either in equilibrium or thermochemical nonequilibrium environments.

Thus, one can obtain a first principles absorption or emission spectrum of molecules which can be used as an input for the various flow-field codes which predict absorption, radiative heating, etc. These data are of key importance as inputs to fluid-flow simulations which predict radiative heating for the AOTV missions previously discussed. Radiative properties are also required for predictions of heat transfer in scramjet-combustor flows for the NASP and development of wind tunnel nonintrusive-flow diagnostics.

CALCULATION OF REACTION-RATE CONSTANTS

Rate constants for chemical reactions can be computed from first principles provided one is given the potential-energy surface resulting from the solution of Schrodinger's equation at all possible values of the interatomic coordinates.

A two-dimensional representation of such a potential surface for the reaction $N+O_2 \rightarrow NO+O$, recently computed by Walsh and Jaffe (1986), is shown on the left side of the figure (fig. 5). The surface corresponds to the N atom approaching the O_2 molecule at an angle of $110°$. The diatomic potential curve for O_2 is recognizable at the left-hand side of the potential surface grid. Similarly, the potential curve for molecule NO can be seen on the lower-right-hand corner of figure 5 which corresponds to this diatomic leaving the O atom after the reaction occurs. The union of these limits with short bond distances between all three constituent atoms corresponds to the tri-atomic molecule NOO. The R_{NO} and R_{OO} coordinates correspond to bond distances between atoms while the electronic energy E increases in the vertical direction. Reactive trajectories on this surface are simulated by solving Hamilton's equations of motion written on figure 5 in which P_i are momenta and Q_i are the generalized coordinates, and $V(Q)$ is a function representing the potential-energy surface. Many solutions corresponding to different initial vibrational states and approach conditions (orientation, impact parameter, etc.) are simulated giving rise to computed reaction cross section. By averaging these cross sections over the appropriate vibrational and rotational distribution (vibrational and rotational temperatures for the reactant O_2) and collision-energy distribution (translational temperature) one can determine rates of reactions as shown on the right-hand side of figure 5.

MOLECULAR-EXCITATION CROSS SECTIONS

Flow fields on AOTVs exhibit nonequilibrium, chemically reacting and radiative flows in which radiating heating is an important consideration in the design of the forebody heat shield. These flows are also weakly ionized. Preliminary analyses indicate that the collision of electrons with molecules is a very important mechanism for the production of the vibrationally and electronically excited molecules from whence flow-field radiation originates. Accurate flow simulations must account for the number density of excited-state molecular species, which depends upon the cross section for electron-molecule collisions. Computational chemists are using these techniques to provide this information, which has not been reliably provided by experimentation. Lima et al. (1986) have studied these cross sections using a Schwinger multichannel formulation, and validated against high quality experiments obtained on H_2.

Figure 6 shows the comparison of the theoretical differential cross sections for the electron impact excitations of molecular Nitrogen, $e^- + N_2(X^1\Sigma_g^+) \rightarrow N_2(B^3\Pi_g) + e^-$, at an impact energy of 10 eV versus the scattering angle in degrees. Clearly there is a dramatic difference in the angular distribution resulting from the two available experimental studies (Mazeau et al., 1973 and Cartwright et al., 1977), although there is rough agreement in the magnitude of the cross sections between 60 and 120°. The first-principal quantal calculation is also shown. The cross section agrees with the magnitude in this region, and tends to support the experiments by Cartwright et al. (1977).

Results for the total cross section as a function of impact energy for this process are shown in figure 7. In this figure, four sets of experimental data are available (Cartwright et al., 1977, Borst and Chang, 1973, McConkey and Simpson, 1969, and Shemansky and Broadfoot, 1971) and shows that these data differ roughly by a factor of five, and which also exhibit different dependences on collision energy. The computational results again support Cartwright's data, and are consistent with the results for the differential cross sections discussed above.

These theoretical results (while using some approximations) clearly demonstrate the capability of ab-initio methods to predict collision cross-sections and illustrate their value in evaluating experimental data.

STUDIES OF ATOMIC CLUSTERS

As mentioned in the introduction, the quantum/classical approach, which works well for gases, is also being used in studies of the properties of materials and their interactions with gases. The favored geometrical orientation of an ensemble of metal atoms corresponds to that structure with the lowest total energy. For a small number of atoms (less than about 75), this property is amenable to the total energy calculations by quantal means as previously outlined, if one assumes that the inner electrons of each atom can have its presence accounted for by effective core potentials. These calculations are reliably determined in separate ab-initio calculations on isolated atoms. Alternatively, the classical approach (given interatomic forces as input) uses solutions of Hamilton's equations of motion to describe the behavior of the constituent atoms (up to 10,000 atoms can be included). The interatomic forces are assumed to be given as a summation of n-body interactions but of which only the two-body and three-body terms are retained. These forces have previously been determined from bulk or surface properties for pure metals, but in general have been difficult to obtain for mixtures of elements. Recently, Pettersson et al. (1986) have completed a dual study in which they compared

predicted geometry for a series of aluminum-atom clusters using the results of both quantal and classical approaches on the same clusters of aluminum atoms.

The objective of the Pettersson et al. (1986) work was to find an alternative approach to the very large and computationally expensive ab-initio methods used to determine the properties of clusters and to extend the calculations to much larger clusters. In this study, the structure and stability of aluminum clusters containing from 2-6 and 13 atoms were calculated using both the ab-initio, quantum chemical approach and the classical atomistic simulations using a simplified parameterized interaction potential function. For each cluster, several different states and structures were considered. Two-dimensional structures were found by both methods to have the lowest energy up to Al_5. Figure 8 illustrates the different Al_6 structures considered. The two D_2h (D_2h hexagonal and D_2h triangular) and the C_2h structures are three-dimensional (3-D). The lowest energy structure according to the ab-initio calculations is the 3-D octahedron (O_h) while the parameterized modeling method predicts the planar C_2h to be the lowest-lying structure. However, the energy difference between the 3-D and planar structures is very small. Since the electron correlation energy is substantially larger for the 3-D O_h structure than for the planar one, the difference may be due to the method/level at which the correlation is treated and of which is currently under investigation.

For Al_{13}, only selected structures were calculated using the ab-initio methods. While the icosohedral structure had the lowest energy, the planar structure, D_{6h}, (predicted by the modeling method to be the lowest) was found to be low-lying and nearly equal in energy to the icosohedral structure. Otherwise, the calculated ordering of the structures was the same for both methods. Since there was only a small energy difference between the 3-D and planar Al_{13} structures, the three-body term in the modeling approach was systematically adjusted in an attempt to duplicate the ab-initio results (the value of the three-body term previously used was not necessarily the optimum value). This value was then used to predict the lowest-lying structure of Al clusters for up to 17 atoms. Figure 9 shows the results of these calculations for Al clusters containing from 7-15 atoms. Clusters with 7, 8, 10, and 12 atoms are planar. All clusters with 13 or more atoms are 3-D.

These calculations by Pettersson et al. (1986) show very promising results. First of all, they clearly demonstrate the need to account for three-body forces in the classical calculations. Secondly, with the three-body term included, the relative stabilities of all of the structures considered were correctly predicted with only two exceptions. Finally, the parameterized modeling approach should allow the study of substantially

larger clusters (than can currently be treated by ab-initio methods) and enable predictions of the effects of temperature and characterization of vibrational frequencies. In addition, the computational cost of this method is significantly less than the previous approaches.

DISSOCIATION OF H_2 ON THE NI(100) SURFACE

Figure 10 displays an example of the ability and power of computational chemistry to study and predict gas-surface interactions. The figure shows the results of calculations (Bauschlicher et al., 1984) used to predict the dissociation of H_2 on a Ni(100) surface. Experimental studies have shown that certain molecules dissociate on some metallic surfaces but not on others. This calculation was performed to predict the activation energy for dissociation and to determine the role of metal d-electrons (electrons with multiple lobes and high angular momentum) in the dissociation process. The calculations used a Ni_{14} cluster, shown on the left side of the chart, to represent the metal surface. (The 14th Ni atom, not shown, lies below those shown in a third layer. Consequently, the Ni surface is represented by the base of an inverted equilateral pyramid.) The hydrogen-molecule (represented by the two small particles in the figure) was allowed to interact with each of the possible site locations on the surface. The hydrogen-molecule is shown in figure 10 in an "on-top" site since this location is the preferred site with the lowest barrier for dissociation. The figure on the right side of this chart is a potential contour of the hydrogen molecule in a "on-top" site. The top of the figure represents a diatomic-molecule approaching the Ni surface. As the molecule gets close to the Ni surface it interacts with the surface and dissociates as illustrated.

By turning the d-electrons "on" and "off", Bauschlicher et al. (1984) showed that the d-electrons play a significant role in the dissociation process and their presence reduces the computed dissociation barrier by 44 kcal/mole. The computed barrier for dissociation of 4 kcal/mole ±3 is in good agreement with the experimental value of 0-1 kcal/mole. Further, the computed results show that once dissociated, the chemisorbed H atoms do not interact with the d-electrons, and these findings are also consistent with experiment. Finally, these calculations are capable of providing great insight into the catalytic nature of materials, and future studies will be directed toward developing a fundamental understanding of catalytic processes.

PROPERTIES OF POLYMERS

NASA is interested in advanced polymers for new aerospace applications. The Ames Computational

Chemistry group undertook studies several years ago to develop a program in which the computational approach could compliment NASA's ongoing experimental program for polymer development. Many macroscopic properties of polymers depend upon their molecular structure and upon the motions of their constituent subgroups. Calculations of polymers have been undertaken for model compounds which represent selected polymers in an attempt to relate their macroscopic- and molecular-level properties. These calculations use the single-configuration SCF method since it was previously demonstrated that this approach could give quantitative information on the torsional potentials corresponding to rotation of subgroups about chemical bonds. Several systems were studied, and it was concluded by Laskowski et al. (1986) that the energy differences between rotated groups can be generally determined to an accuracy of about 0.5 kcal/mol ($150-200$ cm^{-1}) and that torsional barriers can be determined to an accuracy of 1.0 kcal/mole (300 cm^{-1}).

Figure 11 is an example of the calculations by Laskowski et al. (1986) compared with an experiment in which the geometries and energies of the methacryloyl fluoride were studied; specifically, rotations of the COF group about the $C_2 - C_3$ bond as shown on the figure.

As can be seen from the figure the energy differences at values of $\zeta = 0°$ and $180°$ are in excellent agreement with the experimental data. The torsional potential for the COF group rotation about the $C_2 - C_3$ bond was determined by computing the energy defined by interpolating between the two geometries. Note that the computed torsional barrier is somewhat higher than the experimental results. However, it is believed that experimentally determined barrier heights are likely to be underestimated and that the theoretical values are likely to be more accurate.

In the same paper, Laskowski et al. (1986) also report studies of the 2-Methyl 2-carbomethoxy butane molecule shown in figure 12, which is a monomer model of PMMA. Experimentalists originally believed that a high-energy transition in the molecule arose from the rotation of the ester side chain corresponding to the angle Ψ_2. However the calculations by Laskowski et al. showed that the observed peak is due to the rotation of the smaller methoxy group (Ψ_3) in figure 12. Subsequent to these calculations, new temperature-dependent nuclear magnetic resonance (NMR) measurements confirmed the computations, and it was established that the original experimental assignments were incorrect.

The initial study of quantum chemical calculations were on small-model compounds and macroscopic properties and measurements. For a system in which the molecular-level motions were localized (i.e., involved a single segment of the polymer). The current effort is being applied to another prototype system in which the motions are not localized -- the large amplitude motion of the relaxation process in polycarbonate. It is believed that the ability of this polymer to undergo large amplitude motions in the glassy state at very low temperatures (i.e., $-100°$ C) is the origin of its high-impact strength (toughness).

Jaffe and Laskowski (work to be published) have undertaken SCF-level calculations of the geometries, energies and vibrational frequencies of various polycarbonate models to identify all possible stable conformers and the barriers for their interconversion. Most of these calculations used minimal basis sets (currently the use of larger basis sets is not feasible for such large compounds). However, they have found this approach to yield fairly good geometries (with known correction factors) and extremely good relative energies. The model compounds studied include diphenyl carbonate (DPC), and 2,2-diphenyl propane (DPP). The polycarbonate chain consists of alternating DPC and DPP components. This work to date has successfully predicted the most stable conformers, related the motion of the phenyl rings to coupling strength, and predicted both energy differences for selected geometries and torsional barriers.

A first step in modeling the macroscopic properties of polycarbonate has also been taken using a statistical model. The computed fragment geometries and conformer energies are used to construct the partition function for a model polymer chain of length 100,000 segments. From this model, the average chain extension can be determined and the bulk viscosity computed. The computed value of 1.18 at 25° C compares favorably with the experimentally determined value of 1.28 ± 0.19. Previously Yoon and Flory (1981) had obtained values of $0.84 - 1.1$ using a similar model that included adjustable parameters. They could adjust the model to "agree" with any experimental result (an older experimental study gave a value of 0.78), but they could not test the accuracy of the model nor could they use the model for predictive purposes. Here again, computational chemistry is complementing the experimental approach in developing a fundamental understanding of the properties of materials.

SUMMARY

The approach and illustrative example of work by the Ames Computational Chemistry Branch have been discussed. Currently, the results of this work is finding application in filling NASA's need for information on the properties of matter in hostile and unusual environments such as in the flow field about and on the surface of vehicles moving at hypervelocity speeds in the Earth's atmosphere.

Computational chemistry has changed the way NASA supplies its need for gas properties (much more reliance on results calculated with codes validated against experimental results) and has affected our level of understanding of materials properties.

The field of computational chemistry clearly has a great promise of expanding its importance and utility provided that computational speed and memory continue to increase as is being championed by the NAS program.

References

Bauschlicher, C. W., Jr.; Siegbahn, P. E. M.; and Blomberg, M. E. A.: The Dissociation of H_2 on the Ni(100) Surface. J. Chem. Phys., vol. 81, 1984, p. 2103.

Borst, W. L.; and Chang, S. L.: Excitation of Metastable $N_2(A^3 \Sigma^+)$ Vibrational Levels by Electron Impact. J. Chem. Phys., vol. 59, 1973, p. 5830.

Cartwright, D. C.; Chutjian, A.; Trajmar, S.; and Williams, W.: Electron Impact Excitation of the Electron States of N_2 I. Differential Cross Section at Incident Energies from 10 to 50 eV. Phys. Rev. A., vol. 16, 1977, p. 1013.

Laskowski, B. C.; Jaffee, R. L.; and Komornicki, A.: Theoretical Study of the Conformational Properties and Torsional Potential Functions of Polyalkylmethacrylate Polymers. Applied Quantum Chemistry, Smith, V. H. et al. (eds.), D. Reidel Publishing Co., 1986.

Lima, M.; Luo, Z. P.; Nagano, S.; Pritchard, H.; McKoy, V.; and Huo, W. M.: Study of Electron-Molecule Collisions, Proceedings of the Indian Society of Atomic and Molecular Physics, 1986.

Mazeau, J.; Gresteau, F.; Hall, R. I.; Joyez, G.; and Reinhadt, J.: Electron Impact Excitation of N_2 I. Resonant Phenomena Associated with the $A^3 \Sigma^+$ and $B^3 \Pi_g$ Valence States, J. Phys. B., vol. 6, 1973, p. 867.

McConkey, J. W.; and Simpson, F. R.: Electron Impact Excitation of the $B^3 \Pi_g$ State of N_2, J. Phys. B., vol. 2, 1969, p. 923.

Pettersson, L. G. M.; Bauschlicher, C. W., Jr.; and Halicioglu, T.: Small Aluminum Cluster II Structure Binding in Al_n ($n = 2-6$, 13), J. Chem. Phys., 1986. (To be published).

Pioneering the Space Frontier, The Report of the National Commission on Space, Bantam Books, 1986.

Shemansky, D. E.; and Broadfoot, A. L.: Excitation of N_2 and N_2^+ Systems by Electrons-- II Excitation Cross Sections and $N_2$1PG Low-Pressure Afterglow, JQSRT, vol. 11, 1971, p. 1401.

Stewart, D. A.; Rakich, J. V.; and Lenfranco, M. J.: Catalytic Surface Effects on Space Shuttle Thermal Protection System During Earth Entry of Flights STS-2 through STS-5, AIAA Conference on Shuttle Performance, "Lesson Learned," Langley Research Center, Hampton, VA, Mar. 1983.

Walsh, S. P.; and Jaffee, R. J.: Calculated Potential Surfaces for the Reactions: $O + N2 \rightarrow NO + N$ and $N + O2 \rightarrow NO + O$, J. Chem. Phys., 1986. (To be published).

Yoon, D. Y.; and Flory, P. J.: Intermediate Angle Scattering Functions and Local Chain Configurations of Semi-Crystalline and Amorphous Polymers, Polymer Bulletin, vol. 4, 1981, p. 693.
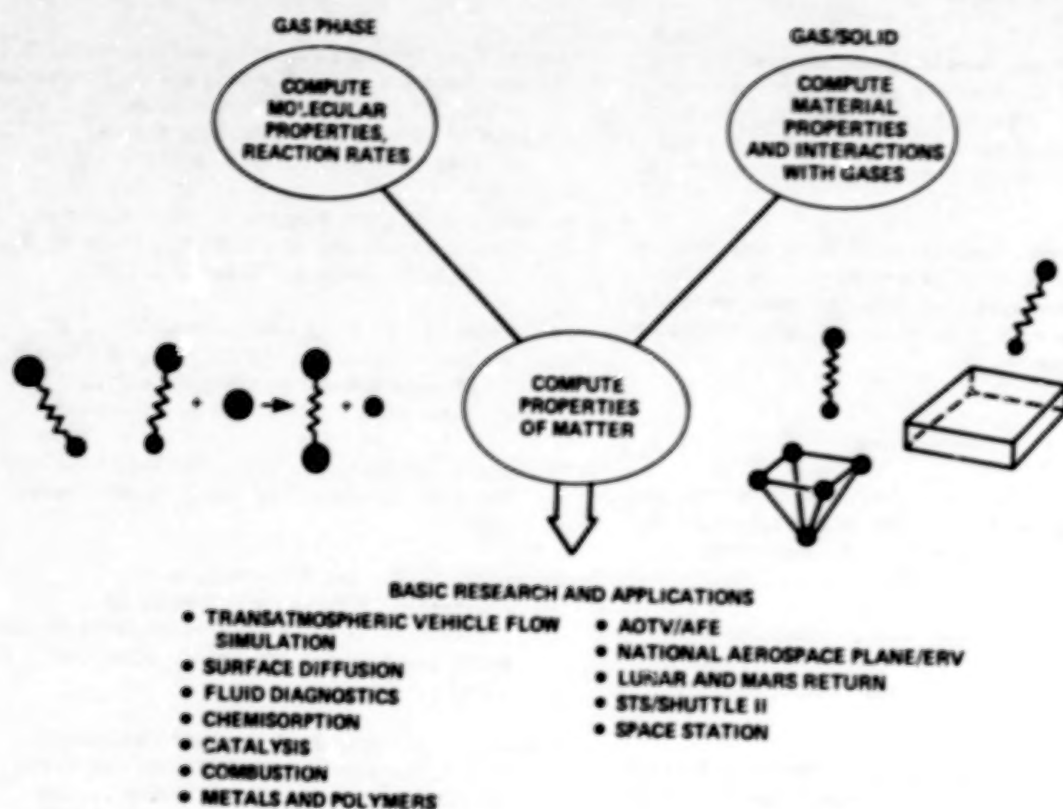
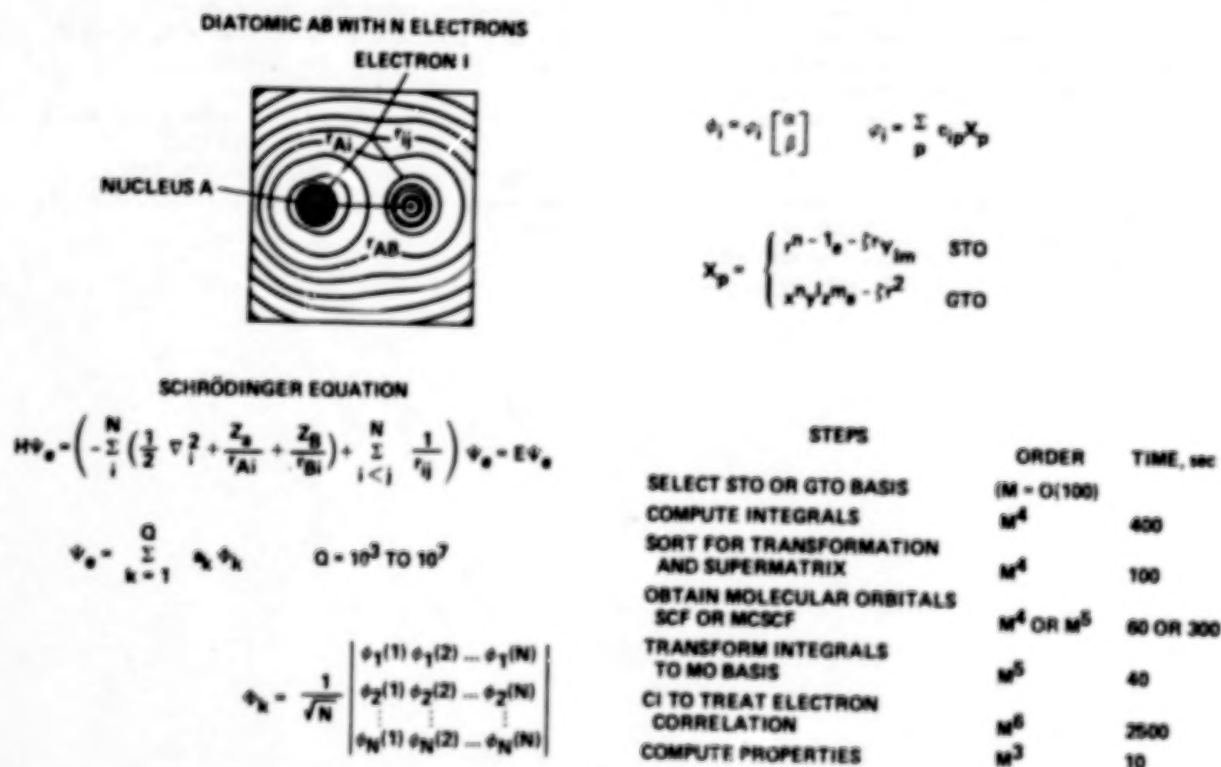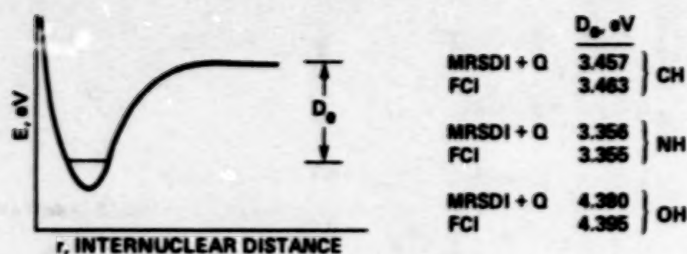Fig. 1. Objectives of NASA Ames Computational Chemistry Branch.

Fig. 2. Approach for calculating electronic wave functions for diatomic molecules and typical times on a Cray XMP to execute the calculations.

	CH	NH	OH
	MRSDI + Q	3.457	CH
	FCI	3.463	
	MRSDI + Q	3.356	NH
	FCI	3.355	
	MRSDI + Q	4.380	OH
	FCI	4.395	

D_e, eV

	CH	NH	OH
THIS WORK (COMPUTED)[†]	3.433	3.344	4.360
THIS WORK (RECOMMENDED)[†]		3.37 ± 0.03	
EXPERIMENT	3.465	>3.29 <3.47	4.392
MEYER AND ROSMUS CEPA	3.29	3.18	4.11
MEYER AND ROSMUS (ESTIMATE)		3.40	
MELIUS AND BINKLEY		3.35	

† CASSCF/MRSDCI CALCULATIONS BY BAUSCHLICHER AND LANGHOFF

Fig. 3. CASSCF/MRSDCI and full CI calculations on small molecular systems: CH, NH and OH.
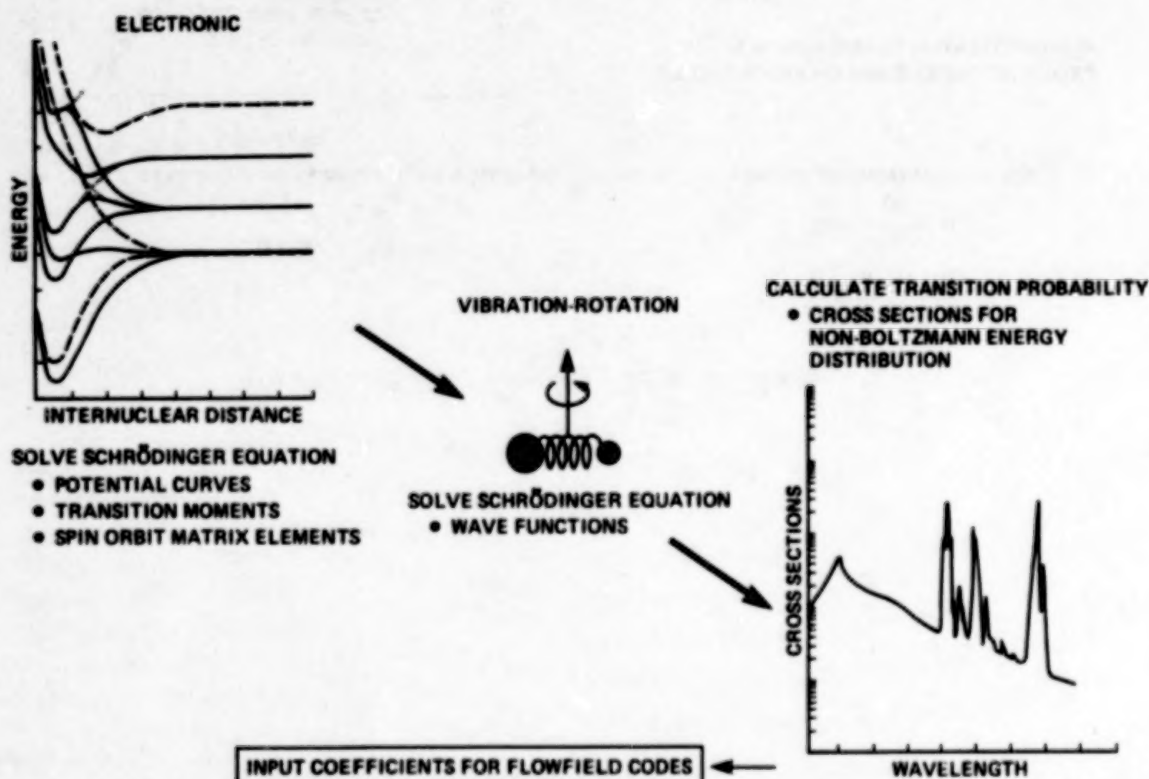
Fig. 4. Calculation of molecular spectra or optical cross sections from first principles.
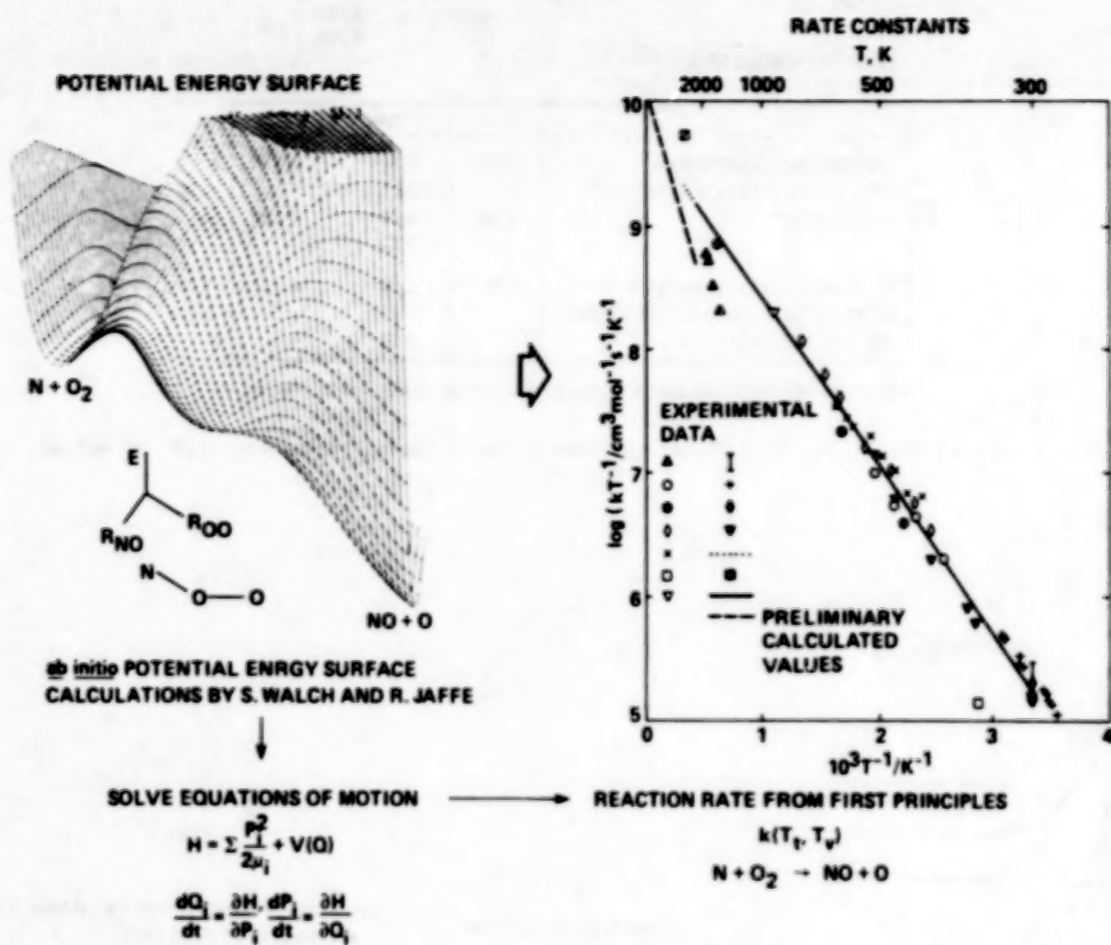
POTENTIAL ENERGY SURFACE

RATE CONSTANTS
T, K

$N + O_2$

E

R_{NO} R_{OO}

N—O—O

NO + O

ab initio POTENTIAL ENRGY SURFACE
CALCULATIONS BY S. WALCH AND R. JAFFE

EXPERIMENTAL
DATA

PRELIMINARY
CALCULATED
VALUES

SOLVE EQUATIONS OF MOTION

$$H = \sum \frac{P_i^2}{2\nu_i} + V(Q)$$

$$\frac{dQ_i}{dt} = \frac{\partial H}{\partial P_i}, \frac{dP_i}{dt} = \frac{\partial H}{\partial Q_i}$$

REACTION RATE FROM FIRST PRINCIPLES

$k(T_t, T_v)$

$N + O_2 \rightarrow NO + O$

Fig. 5. Calculations of rate constants for $N+O_2 \rightarrow NO + O$.
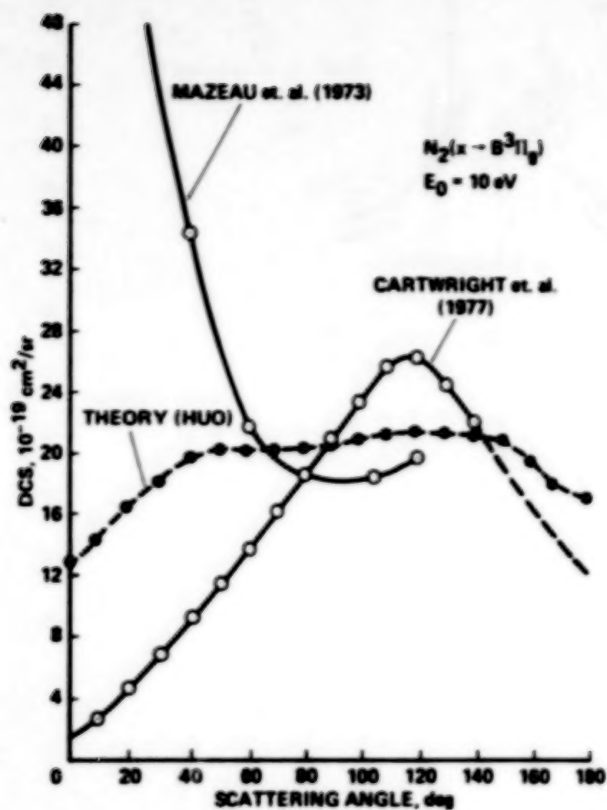
Fig. 6. Differential cross section for $N_2 \; X^1\Sigma_g^+ - B^3\Pi_g$ by electron impact at 10 eV.
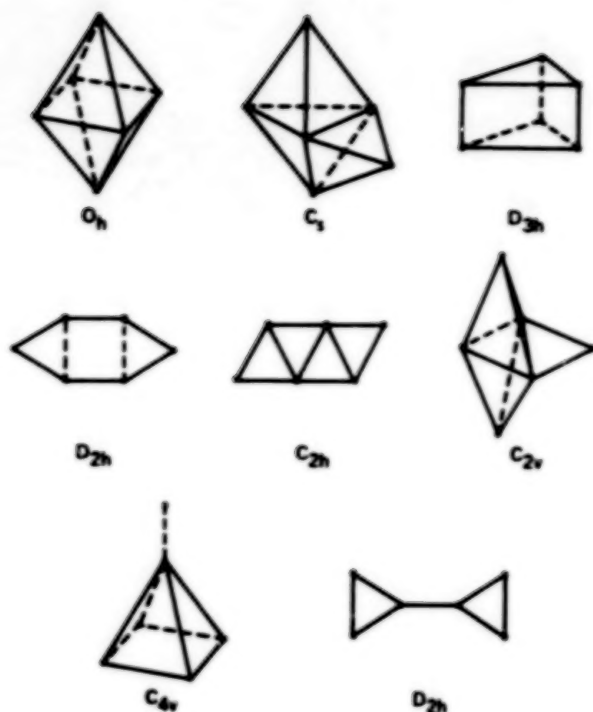
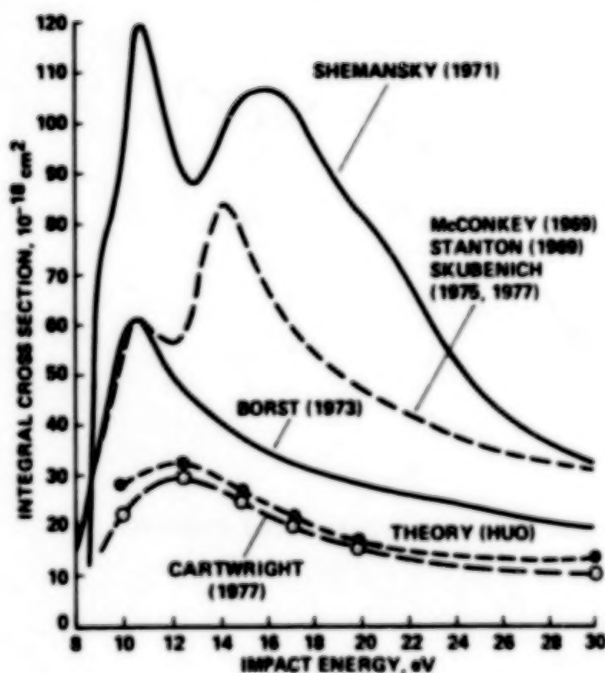Fig. 8. Possible structures constituted of 6 aluminum atoms.

Fig. 7. Total cross section of $N_2 \; X^1\Sigma_g^+ - B^2\Pi_g$ by electron impact.
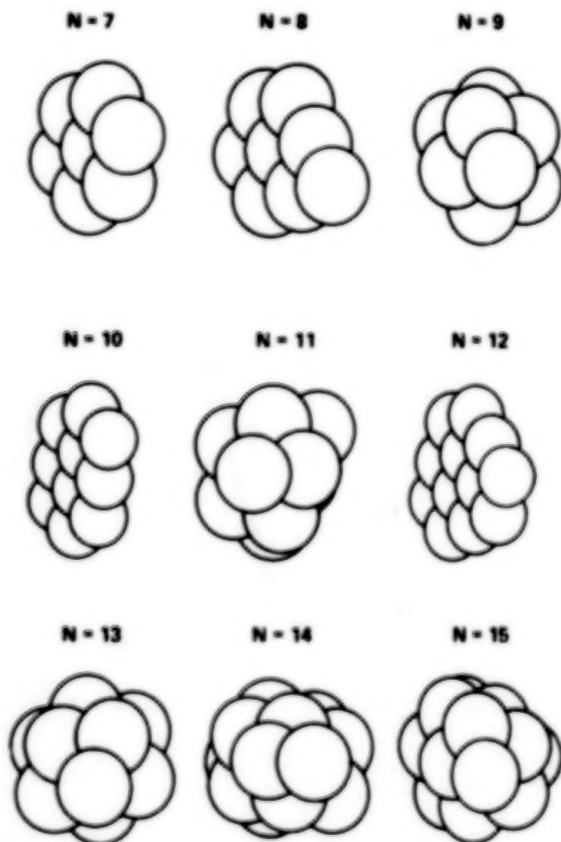

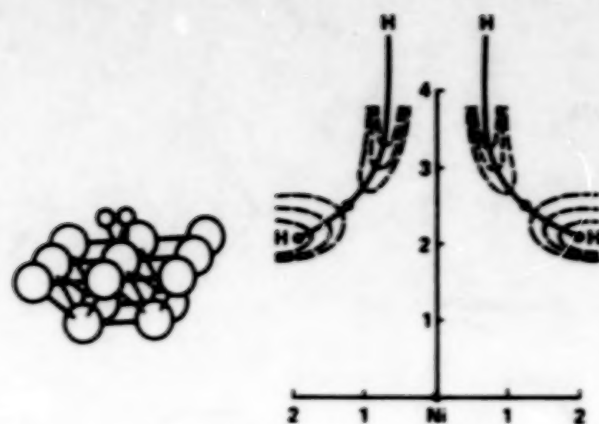Fig. 9. Lowest-lying structures of aluminum clusters constituted of up to 17 atoms.

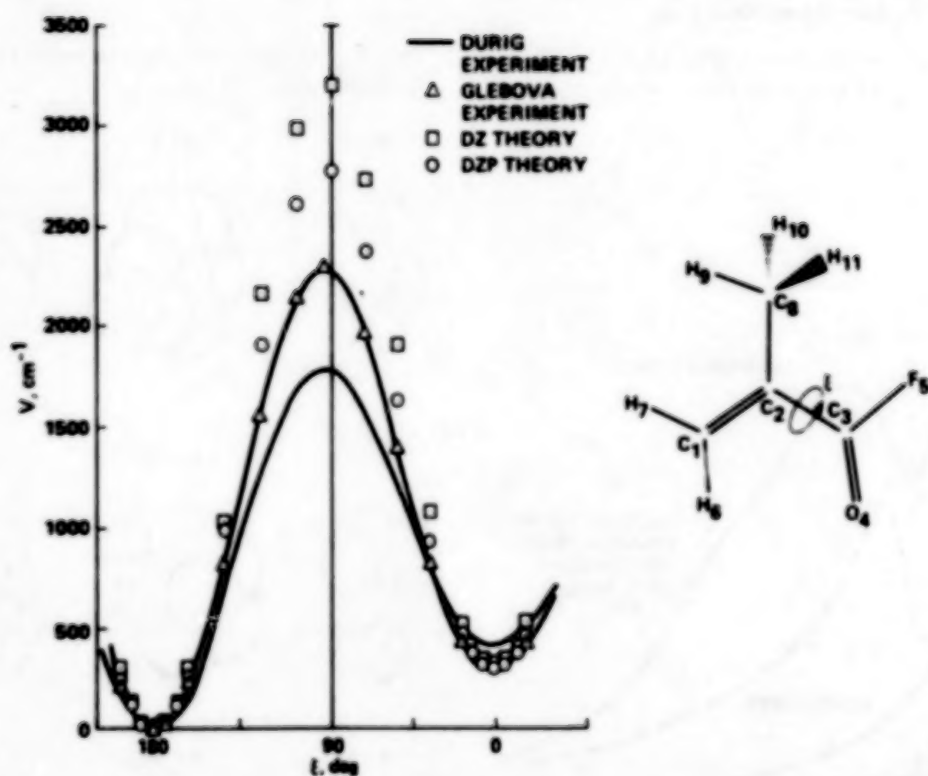Fig. 10. Computational chemistry study of H_2 dissociation on nickle surface.

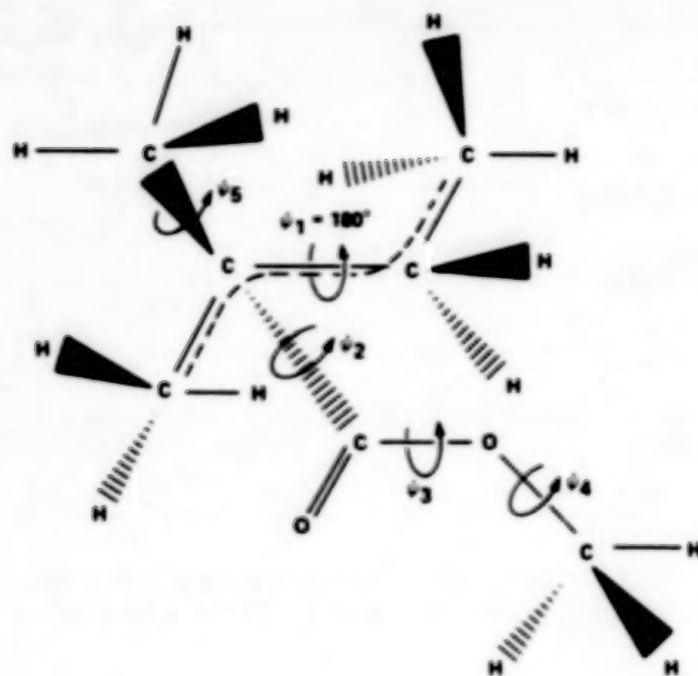Fig. 11. Energy differences and torsional potential function for Methacryloyl Flouride.

Fig. 12. Optimal conformation of 2-Methyl 2-Carbomethoxy butane, a model for a monomeric segment of PMMA.

Report Documentation Page

NASA
National Aeronautics and
Space Administration

1. Report No. NASA CP-2454	2. Government Accession No.	3. Recipient's Catalog No.
4. Title and Subtitle SUPERCOMPUTING IN AEROSPACE		5. Report Date March 1987
		6. Performing Organization Code
7. Editor(s) Paul Kutler and Helen Yee		8. Performing Organization Report No. A-87082
		10. Work Unit No. 505-01
9. Performing Organization Name and Address Ames Research Center Moffett Field, CA 94035		11. Contract or Grant No.
		13. Type of Report and Period Covered Conference Publication
12. Sponsoring Agency Name and Address National Aeronautics and Space Administration Washington, DC 20546		14. Sponsoring Agency Code

15. Supplementary Notes

Point of Contact: Paul Kutler, Ames Research Center, M/S 229-2
Moffett Field, CA 94035 (415) 694-4007 or FTS 464-4007

16. Abstract

This conference on "Supercomputing in Aerospace" is being held as part of the opening of the Numerical Aerodynamic Simulation (NAS) facility, which will be officially operational early in 1987. The theme for the meeting is "Computational Aerophysics and the NAS system--Essential Elements of the U.S. Aerospace Program." The conference will consist of invited speakers from industry, government, and academia.

17. Key Words (Suggested by Author(s)) Supercomputing Numerical aerodynamic simulation Aerospace	18. Distribution Statement Unclassified-Unlimited Subject Category - 02

19. Security Classif. (of this report) Unclassified	20. Security Classif. (of this page) Unclassified	21. No. of pages 333	22. Price A14

NASA FORM 1626 OCT 86

END

DATE

FILMED

OCT – 1987